Physics of Atomic Nuclei, Vol. 63, No. 7, 2000, pp. 1111–1118. From Yadernaya Fizika, Vol. 63, No. 7, 2000, pp. 1189–1195.

NEUTRINO PHYSICS AT ACCELERATORS

Results from the NOMAD Experiment*

B. A. Popov**
(for the NOMAD Collaboration)
Joint Institute for Nuclear Research, Dubna, Moscow oblast, 141980 Russia

Abstract—The NOMAD experiment has sought $\nu_\mu \longleftrightarrow \nu_\tau$ oscillations by looking for the emergence of τ^- in events from the CERN SPS neutrino beam. With some improvements in the techniques of analysis in relation to the results published previously and with the inclusion of data from the 1998 run, no evidence for the oscillations has been found, which results in an updated limit on the oscillation probability [$P(\nu_\mu \longrightarrow \nu_\tau) < 0.5 \times 10^{-3}$ at a 90% C.L.]. The corresponding limit on the oscillation mixing angle is given by $\sin^2 2\theta_{\mu\tau} < 1.0 \times 10^{-3}$ for large Δm^2. By using a 1% contamination of ν_e in the neutrino beam, we can also rule out $\nu_e \longleftrightarrow \nu_\tau$ oscillations and constrain the probability of the relevant transition as $P(\nu_e \longrightarrow \nu_\tau) < 3 \times 10^{-2}$ at a 90% C.L. ($\sin^2 2\theta_{e\tau} < 6 \times 10^{-2}$ at large Δm^2). © *2000 MAIK "Nauka/Interperiodica".*

1. INTRODUCTION

NOMAD (neutrino oscillation magnetic detector, WA-96) is an experiment seeking $\nu_\mu \longleftrightarrow \nu_\tau$ oscillations in the CERN SPS wideband neutrino beam. Neutrino oscillations are possible if the neutrinos have masses and if their flavor and mass eigenstates are different. In the simplified two-flavor scenario, the probability of oscillation is given by

$$P(\nu_\mu \longrightarrow \nu_\tau) = \sin^2(2\theta)\sin^2(1.27\Delta m^2 L/E), \quad (1)$$

where $\Delta m^2 = |m_1^2 - m_2^2|$ is the absolute value of the difference of the squared mass of the two mass eigenstates, θ is their mixing angle, L is the source–detector distance measured in kilometers, and E is the neutrino energy in GeV.

Given the average neutrino energy in the CERN SPS beam and the average target–detector distance (see below), the experiment is sensitive to the cosmologically relevant neutrino mass range ($\Delta m^2 > 1$ eV^2) and to small mixing angles. Potential ν_τ candidates are identified by the kinematical signatures from the decay of a τ^- lepton produced in a charged-current (CC) interaction. The detector is sensitive to 82.5% of the decay modes $\tau^- \longrightarrow e^-\bar{\nu}_e\nu_\tau$, $\tau^- \longrightarrow h^-(+n\pi^0)\nu_\tau$, and $\tau^- \longrightarrow \pi^+\pi^-\pi^- + n\pi^0(n \geq 0)\nu_\tau$. This article updates the results already reported in [1, 2], which were based on data taken between 1995 and 1997, by more sensitive analyses, including data collected during the run of 1998 (which was the last year of NOMAD data taking).

2. CERN NEUTRINO BEAM

The CERN West Area neutrino beam [3] uses 450 GeV/c protons from the SPS accelerator. These protons impinge on a beryllium target, 110 cm long, producing secondary mesons (mainly pions and kaons), which are focused by two magnetic focusing elements, a horn and a reflector. These secondary particles are allowed to decay in a 290-m vacuum decay tunnel, with 369 m of iron and earth shielding used as an absorber. The total distance between the beryllium target and

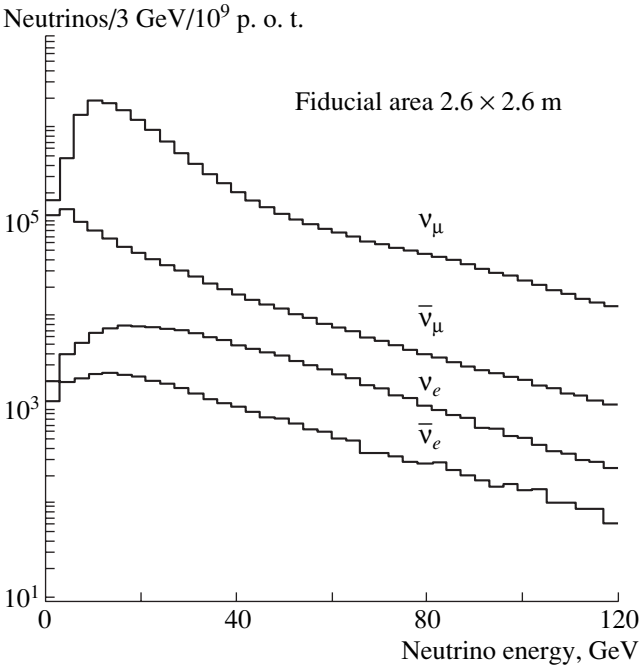

Fig. 1. Flux predictions for the various neutrino species within a fiducial area of 2.6×2.6 m^2 at the NOMAD detector.

* This article was submitted by the author in English.
** e-mail: popov@nusun.jinr.dubna.su

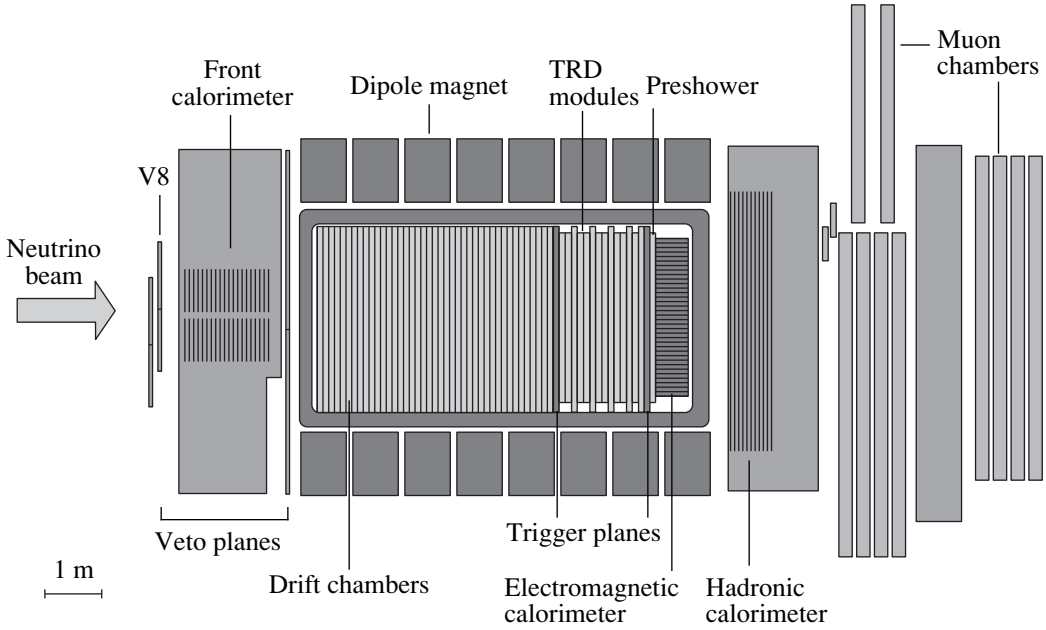

Fig. 2. Side view of the NOMAD detector.

NOMAD setup is 835 m, while the average distance between the neutrino-production point and the detector is only 620 m.

The beam consists predominantly of ν_μ, but a GEANT [4] simulation of the beamline predicts contaminations of 6.1% $\bar{\nu}_\mu$, 0.9% ν_e, and 0.2% $\bar{\nu}_e$ in the neutrino flux. The corresponding neutrino spectra are shown in Fig. 1. The intrinsic contamination of ν_τ (from D_s decays) has been calculated to provide a ratio of 5×10^{-6} ν_τCC interactions with respect to ν_μCC interactions in NOMAD [5], a negligible background given the sensitivity of the experiment.

3. NOMAD DETECTOR

A schematic view of the NOMAD apparatus is displayed in Fig. 2. The detector was described in more detail elsewhere [6]. It consists of an active target of 44 drift chambers, with a total fiducial mass of 2.7 t, within a dipole magnetic field of strength 0.4 T. The drift chambers serve a double role, appearing to simultaneously a target mass and the tracking medium. The average density of the drift-chamber volume is 0.1 g/cm^3, with each drift chamber providing only 2% of the radiation length. The momentum resolution is approximately 3.5% for momenta less than 10 GeV/c.

Electron identification is achieved with a transition-radiation detector (TRD) [7] consisting of nine modules, each module featuring a polypropylene radiator followed by a plane of straw tubes. The pion rejection achieved is 10^3 with a 90% electron efficiency (for isolated tracks). A lead-glass electromagnetic calorimeter [8] provides an energy resolution of $3.2\%/\sqrt{E(\mathrm{GeV})} \oplus 1\%$, and a preshower detector provides additional electron identification (a pion rejection of 10^2 for an electron efficiency of 90%). A hadronic calorimeter is used to identify hadrons, and a set of muon chambers provides a muon-detection efficiency of 97% for momenta greater than 5 GeV/c.

4. STRATEGY OF THE ANALYSIS

The resolution of the drift chambers is not sufficient to observe a τ candidate directly, as in the case of CHORUS experiment [9], which used nuclear emulsion. The recognition of potential ν_τCC interactions is achieved by identifying the τ-decay products by means of kinematical criteria.

4.1. Kinematical Method

There are two main criteria used in NOMAD to separate ν_τ candidates from background events:

Isolation of the τ decay products from the hadronic jet. In a ν_τCC interaction in which τ decays, for example, into a pion, the pion is isolated with respect to the hadronic jet. On the other hand, a pion from a ν_μ neutral-current (NC) background event is part of the hadronic jet. An isolation variable Q_T, the component of the momentum of visible τ-decay products orthogonal to the total visible momentum vector, can be used to isolate the decay products (see Fig. 3).

Kinematical configuration in the plane orthogonal to the incoming-neutrino direction. In the transverse plane, one can identify the following vectors (see

Fig. 4): $\mathbf{p}_T^l$, the transverse momentum of the outgoing lepton; $\mathbf{p}_T^{\text{jet}}$, the transverse momentum of the hadronic jet; and $\not\mathbf{p}_T$, the missing transverse momentum. For a ν_τCC event, the missing transverse momentum is associated with undetected neutrinos from τ decay, while, in the case of a ν_eCC background event, this quantity is, on average, less and is due largely to undetected neutrals, reconstruction failures, and the Fermi motion of nucleons. The amount of imbalance is related to the magnitude of the missing momentum and related to the transverse mass variable: $M_T = \sqrt{(|\not\mathbf{p}_T| + |\mathbf{p}_T^l|)^2 - (\mathbf{p}_T^{\text{jet}})^2}$. The direction of the imbalance is also important, as can be seen in Fig. 4, because the angle between the missing transverse momentum and the transverse momentum of the hadronic jet (Φ_{mh}) in a ν_τCC event is generally greater than in the background from ν_μ and ν_eCC interactions. The angle Φ_{lh} between the transverse momenta of the lepton and the hadronic jet will normally be less in the signal than in the background.

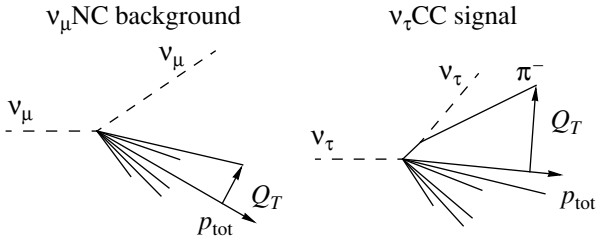

Fig. 3. Isolation of the τ-decay candidate (a pion in this example) for ν_μNC and ν_τCC.

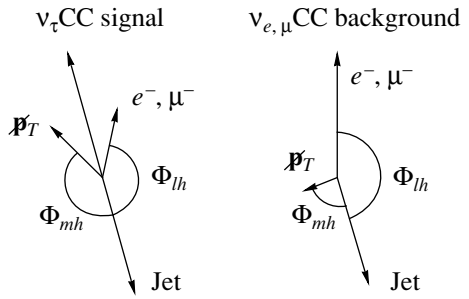

Fig. 4. Kinematical configuration in the transverse plane for a ν_τCC and a background ν_μ or ν_eCC.

4.2. Likelihood Functions

None of the variables used to perform the separation of τ candidates from background can unambiguously make the τ selection. The strength of NOMAD lies in the combination of these different kinematical variables to perform the separation. NOMAD uses the likelihood technique to make the combinations of the relevant kinematical variables (for example, Φ_{mh}, Φ_{lh}, Q_T, M_T). A likelihood function is the product of the probability-distribution functions for each of the variables or a set of variables (one can also compose multidimensional functions that take into account correlations among the variables). The logarithm of the ratio of the likelihood functions for a signal and a background describes the degree of separation between them.

4.3. Data Simulator

The level of background rejection on the order of 10^5 requires using a technique that can simulate the behavior of our data over five orders of magnitude. Due to differences in the simulation and reconstruction mainly of the hadronic system, it is not expected that our Monte Carlo (MC) simulations reproduce the data to this precision. For example, the missing-p_T distribution is not well reproduced by the data [1, 2]; therefore, NOMAD has adopted the data-simulator technique to overcome this problem.

A data simulator (DS) is based on the assumption that one can calculate the expected background and the efficiency to the signal by using the data. This is achieved by commencing from an identified ν_μCC event, removing the muon and substituting another lepton for it. If the lepton is a neutrino, this corresponds to a fake NC event; if it is an electron, it is a fake ν_eCC event; and, if it is a τ lepton followed by its subsequent decay, then a fake ν_τCC event is simulated. One has to make a further correction to eliminate any charge and energy bias and threshold effects that might ensue. Furthermore, one can apply the identical procedure to Monte Carlo data and produce samples of Monte Carlo Simulator (MCS) events.

A comparison of the difference between the DS and MCS samples is a direct measure of the differences between the behavior of the hadronic system in the data and in the Monte Carlo simulation. The signal and background efficiencies are then calculated as

$$\epsilon = \epsilon_{\text{MC}} \frac{\epsilon_{\text{DS}}}{\epsilon_{\text{MCS}}}, \tag{2}$$

where ϵ_{MC} is the efficiency of the MC, ϵ_{DS} is the efficiency of the DS, and ϵ_{MCS} is the efficiency of the MCS.

4.4. Blind Analysis

Another feature of the NOMAD analysis is the application of a "blind-box" approach. A blind box is defined around the region where we expect the signal to appear, and all cuts and corrections are performed outside the signal region to show that the analysis is robust and can reproduce the data where we do not expect the signal to be strong. A further cross-check can be applied in which the data and MC are compared for an equivalent analysis selecting positive candidates since a τ^+ signal from oscillations is not expected.

The position of the box is selected at the level corresponding to a minimal (or stable) sensitivity. The sensi-

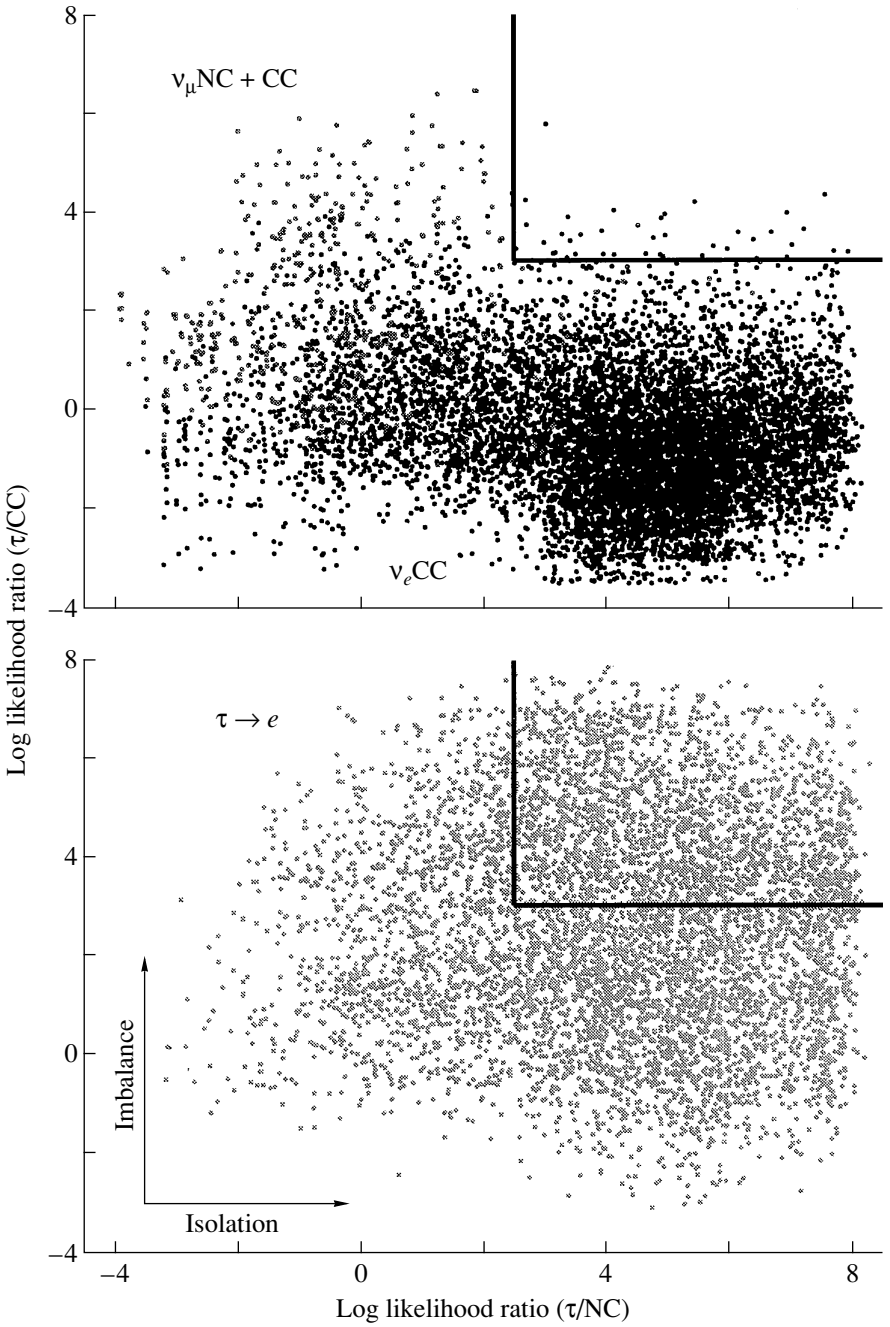

Fig. 5. Likelihood ratios for CC rejection and NC rejection for a Monte Carlo background and a $\tau \longrightarrow e$ signal. The signal box is defined in the top right corner.

tivity is defined as the average upper limit that would be obtained from an ensemble of experiments with the expected background and no true signal [10]. Additionally, one can create several bins inside the box region that can enhance the global sensitivity of the experiment owing to a variation in the signal-to-background ratio as a function of the bin size. An unbiased choice of the closed box region and its internal bins ensures the robustness of the result. Once the analysis is well understood, one is allowed to "open the box" and see whether there is an excess of signal above the expected background in the signal region.

5. SEARCH FOR $\nu_\mu \longleftrightarrow \nu_\tau$ OSCILLATIONS

5.1. $\tau^- \longrightarrow e^- \bar{\nu}_e \nu_\tau$ *Channel*

The most sensitive channel available to NOMAD is the electronic decay of τ due to the reduced background from a ν_e background of about 1% and excellent elec-

tron-identification capabilities of the NOMAD detector. The data set used for this analysis corresponds to all available data (from 1995 to 1998 runs) consisting of approximately 1.3×10^6 ν_μCC events.

The selection of the electron candidate is carried out by requiting that there only be one prompt electron in an event emerging from the primary vertex ($\Delta z < 15$ cm) and that it be identified as an electron by the TRD, the preshower detector, and the electromagnetic calorimeter. The energy of the electron has to be above 1.5 GeV, and it should not be consistent with photon conversion (the invariant mass between the electron candidate and any positive track should be greater than 50 MeV).

The rejection of NC interactions is achieved by a multidimensional likelihood function that is a measure of the "isolation" of the electron candidate and includes the following variables: $\theta_{\nu T}$, the angle between the incident-neutrino momentum and the total momentum of the event; $\theta_{\nu h}$, the angle between the incident-neutrino momentum and the total hadron momentum; $\theta_{\min}$, the minimum angle between the electron momentum and any momentum of the hadrons; Q_T, the electron energy; and the transverse mass M_T.

The rejection of ν_μ and ν_eCC interactions is achieved with a second likelihood function that measures the momentum imbalance in the transverse plane and which involves the following variables: the transverse momentum of the electron, the transverse momentum of the hadronic jet, Φ_{lh}, the total visible energy of the event, $\theta_{\nu T}$, Q_l, and the electron momentum component orthogonal to the hadronic-jet momentum. The distributions of Monte Carlo background and signal events for a scatter plot of the two likelihood functions are shown in Fig. 5. The box in the upper right hand corner defines the signal region, and this has been divided into six bins at the later stage of the analysis.

Table 1. Results of the analysis in the $\tau^- \longrightarrow e^-$ channel

Bin	N_τ	Exp. background	Data
1	178	$1.15^{+0.26}_{-0.17}$	2
2	208	$0.53^{+0.23}_{-0.12}$	1
3	903	$0.28^{+0.31}_{-0.09}$	0
4	654	2.13 ± 0.23	2
5	473	0.98 ± 0.16	0
6	1694	0.25 ± 0.09	0
Total	4110	5.3 ± 0.8	5

Table 2. Results of the analysis in the $\tau^- \longrightarrow h^-$ channel

Likelihood	N_τ	Exp. background	Data
7.2–9.0	918	4.4 ± 1.9	3
>9.0	1133	2.4 ± 0.8	3
Total	2232	6.8 ± 2.1	6

After applying the data-simulator corrections to the Monte Carlo predictions, one obtains excellent agreement with the data for all e^+ in the entire likelihood range and for e^- in the region outside of the signal box. After opening the box, the number of events found is consistent with the expected background (see Fig. 6).

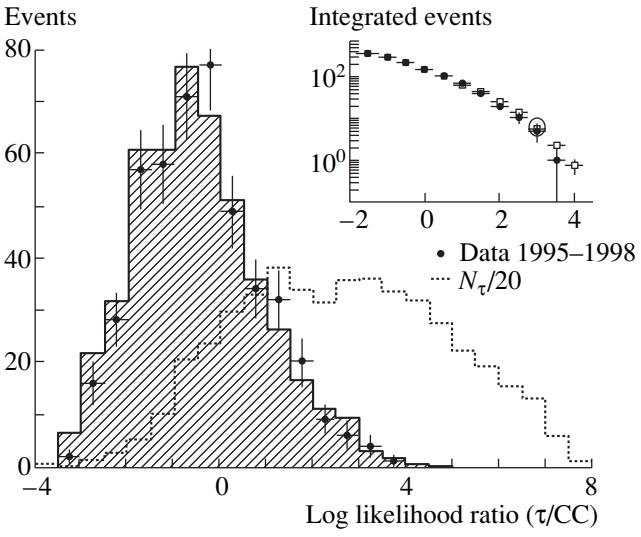

Fig. 6. Data-simulator-corrected logarithm of the likelihood function to reject CC events for (dotted histogram) the signal, (hatched histogram) the background, and (points) the data. The integrated distribution is also shown in the top right corner.

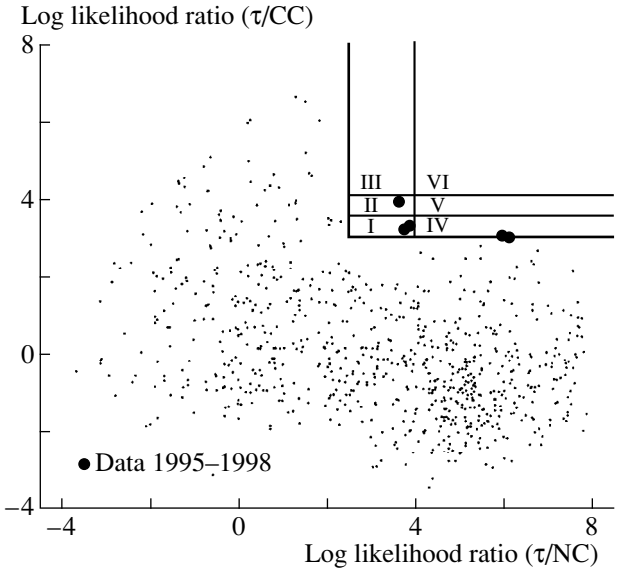

Fig. 7. Distribution of data events in the plane spanned by the two likelihood functions. The upper right corner is the signal region divided into six bins with the surviving candidates.

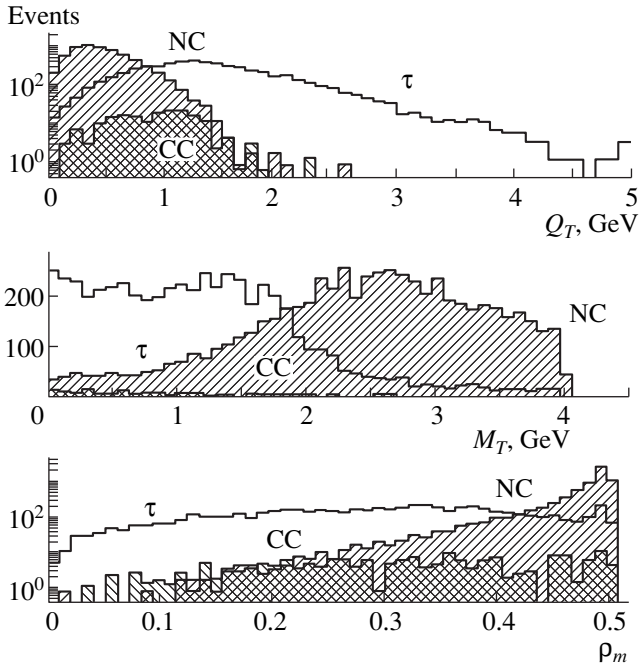

Fig. 8. Variables used for the $\tau^- \longrightarrow h^- + X$ likelihood functions.

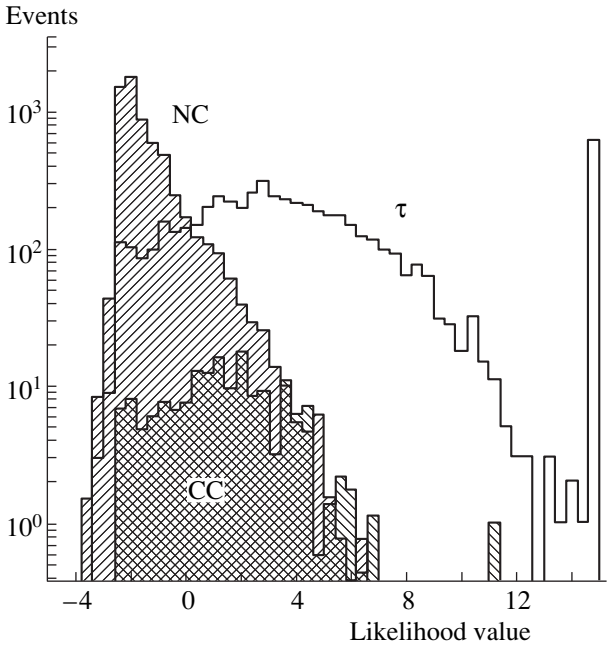

Fig. 9. Logarithm of the likelihood ratio for the $\tau^- \longrightarrow h^-$ analysis.

The total number of events remaining in the signal region is five, which is consistent with a background of 5.3 ± 0.8 distributed in the six bins as shown in Table 1 and in Fig. 7. If the oscillation probability had been equal to one, there would have been 4110 τ^- candidates; thus, there is no evidence for oscillations in this channel of τ^- decay.

5.2 $\tau^- \longrightarrow h^- + X$ Channel

The analysis of the hadronic one-prong decay of τ has also been performed with the full sample of data (collected from 1995 to 1998). The selection of a hadron candidate is achieved by imposing a veto on ν_μCC and ν_eCC events. All events with a primary muon or electron are rejected. In addition, events with a high-p_T track ($p_T > 0.8$ GeV/c) outside the acceptance of the lepton-identification detectors (for example, muon chambers and electromagnetic calorimeter) are also rejected to avoid CC events in which the lepton escapes identification. A hadron-decay candidate is selected as the track with the highest p_T or next-to-the-highest-p_T track in the event.

The rejection of NC and CC backgrounds is achieved by constructing a three-dimensional likelihood function involving the following variables: Q_T, the transverse mass M_T, and

$$\rho_m = \frac{|\mathbf{p}_T|}{|\mathbf{p}_T^h| + |\mathbf{p}_T^{\text{jet}}| + |\not{\mathbf{p}}_T|}.$$

The isolation of a hadron candidate is achieved by Q_T, and the separation of the NC and the signal populations

Table 3. Summary of $\nu_\mu \longleftrightarrow \nu_\tau$ search for the various channels

Channel	Data	Exp. background	N_{obs}	N_τ
$\tau \longrightarrow e^-\nu_\tau\bar{\nu}_e$ DIS	1995–1998	5.3 ± 0.8	5	4110
$\tau \longrightarrow e^-\nu_\tau\bar{\nu}_e$ LM	1995	$0.5^{+0.6}_{-0.2}$	0	218
$\tau^- \longrightarrow h^-(+n\pi^0)\nu_\tau$ DIS	1995–1998	6.8 ± 2.1	6	2232
$\tau^- \longrightarrow h^-(+n\pi^0)\nu_\tau$ LM	1995	$0.1^{+0.3}_{-0.1}$	1	198
$\tau^- \longrightarrow \rho^-\nu_\tau$ DIS	1995–1998	$7.3^{+2.2}_{-1.2}$	9	2547
$\tau^- \longrightarrow \pi^-\pi^-\pi^+\nu_\tau$ DIS	1995–1996	6.5 ± 1.1	5	1180
$\tau^- \longrightarrow \pi^-\pi^-\pi^+(+n\pi^0)\nu_\tau$ LM	1995	$0.4^{+0.6}_{-0.4}$	0	108

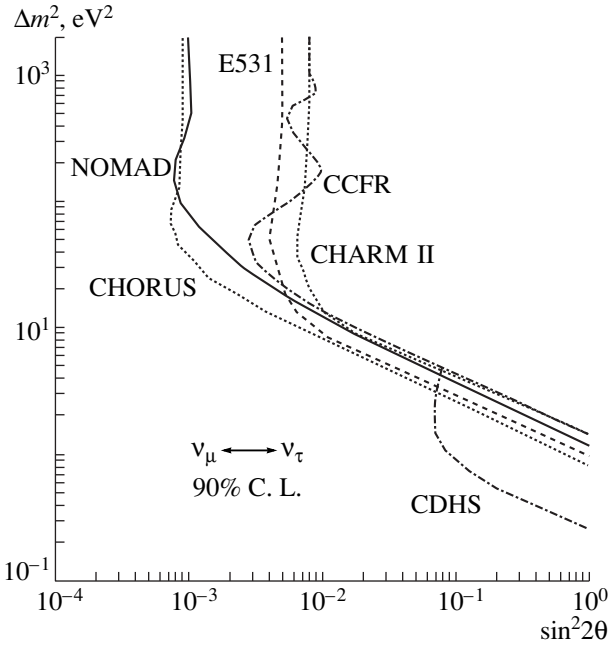

Fig. 10. NOMAD 90% C.L. exclusion plot for $\nu_\mu \longleftrightarrow \nu_\tau$ oscillations.

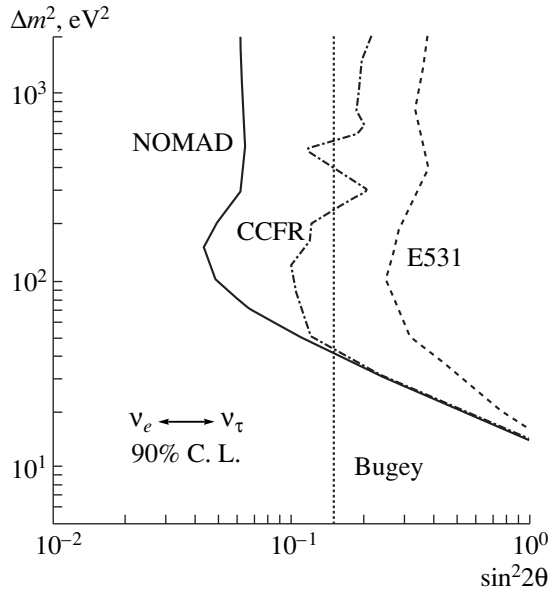

Fig. 11. NOMAD 90% C.L. exclusion plot for $\nu_e \longleftrightarrow \nu_\tau$ oscillations.

is obtained by the transverse-plane variables (M_T and ρ_m), as is shown in Fig. 8.

A further two variables, the ratio of the hadron-candidate momentum to the visible energy and the transverse momentum of the hadronic jet, complete the description of the global likelihood. Figure 9 displays the likelihood ratio for τ signals and the NC and CC backgrounds. Two bins above a likelihood of 7.2 make up the signal box. The total number of observed events inside this region is six, which is consistent with an estimated background of 6.8 ± 2.1 (see Table 2).

5.3. Other Channels of τ^- Decay

Other channels used in the analysis are the exclusive transition $\tau^- \longrightarrow \rho^-\nu_\tau$ in which the ρ^- meson decays into a $\pi^-\pi^0$ pair and $\tau^- \longrightarrow \pi^+\pi^-\pi^-\nu_\tau$. Both of these analyses use kinematical constraints associated with the intermediate resonance (a_1^- in the case of the 3π channel). All previous analyses were performed for the case where ν_τ undergoes deep-inelastic interaction and the data analyses encompass the runs from 1995 to 1998 (1995 to 1996 in the case of the 3π channel). In addition, we have low-multiplicity analyses that are rich in quasielastic and resonance events, but these have not been updated since our published result [1] using only 1995 data. The updated summary with all the channels studied up to now is included in Table 3.

6. RESULTS AND CONCLUSION

From Table 3, the background estimates are in good agreement with the number of events found in the data once the blind boxes are open. There is no evidence for an oscillation signal; therefore, NOMAD can set a new limit on the oscillation probability based on the unified approach that is now recommended by the Particle Data Group [10]: $P(\nu_\mu \longrightarrow \nu_\tau) < 0.5 \times 10^{-3}$ at a 90% C.L. This result is improved with respect to our result reported in [2]. This limit is comparable with that obtained by CHORUS [9]. A 90% C.L. exclusion plot in the (Δm^2, $\sin^2 2\theta$) plane can be derived, and this is shown in Fig. 10. At large Δm^2, the constraint on the angle is $\sin^2 2\theta_{\mu\tau} < 1.0 \times 10^{-3}$.

Owing to a 1% contamination of ν_e in the beam, one can also set a limit on the probability of $\nu_e \longleftrightarrow \nu_\tau$ oscillations, $P(\nu_e \longrightarrow \nu_\tau) < 3 \times 10^{-2}$ at a 90% C.L., and the corresponding exclusion plot is shown in Fig. 11. The resulting mixing angle would be $\sin^2 2\theta_{e\tau} < 6 \times 10^{-2}$ at large Δm^2.

NOMAD has set limits on $\nu_\mu \longleftrightarrow \nu_\tau$ oscillations on the basis of all data analyses (about 1.3×10^6 ν_μCC interactions from 1995 to 1998 runs for some of the τ-decay channels). The last year of NOMAD data taking was 1998. The quality of the event reconstruction and the analysis efficiencies are still being improved. Addition of the channels that have not been updated for the 1996, 1997, and 1998 data will hopefully provide further improvement in the sensitivity of the NOMAD analysis in the future.

REFERENCES

1. NOMAD Collab. (J. Altegoer *et al.*), Phys. Lett. B **431**, 219 (1998).

2. NOMAD Collab. (P. Astier *et al.*), Phys. Lett. B **453**, 169 (1999).
3. G. Acquistapace *et al.*, Preprint No. CERN-ECP 95-14, CERN (Geneva, 1995).
4. R. Brun *et al.*, GEANT: Detector Description and Simulation Tool, CERN Program Library Long Writeup W5013.
5. B. van de Vyver, Nucl. Instrum. Methods A **385**, 91 (1997); M. C. González-García and J. J. Gómez-Cadenas, Phys. Rev. D **55**, 1297 (1997).
6. NOMAD Collab. (J. Altegoer *et al.*), Nucl. Instrum. Methods A **404**, 96 (1998).
7. G. Bassompierre *et al*., Nucl. Instrum. Methods A **403**, 363 (1998); **411**, 63 (1998).
8. D. Autiero *et al.*, Nucl. Instrum. Methods A **373**, 358 (1996); **387**, 352 (1997); **411**, 285 (1998).
9. CHORUS Collab. (E. Eskut *et al*.), Nucl. Instrum. Methods A **401**, 7 (1997); Phys. Lett. B **424**, 202 (1998); CHORUS Collab. (M. Messina), in *Proceedings of XXXIV Rencontres de Moriond "Electroweak Interactions and Unified Theories," Les Arcs, March 13–20, 1999*.
10. G. J. Feldman and R. D. Cousins, Phys. Rev. D **57**, 3873 (1998); Particle Data Group (C. Caso *et al.*), Eur. Phys. J. C **3**, 172 (1998).

Physics of Atomic Nuclei, Vol. 63, No. 7, 2000, pp. 1119–1121. From Yadernaya Fizika, Vol. 63, No. 7, 2000, pp. 1196–1198.

NEUTRINO PHYSICS AT ACCELERATORS

Status of the Chorus Experiment*

M. Doucet
(for the CHORUS Collaboration)
CERN, Geneva, Switzerland

Abstract—The CHORUS experiment at CERN searches for $\nu_\mu \longleftrightarrow \nu_\tau$ oscillations by looking for τ decays from charged-current ν_τ interactions. The emulsion target of the detector, having a resolution of about a micron, enables the detection of the decay topology of the τ. After having analyzed a sample of 126000 events containing an identified muon and 7500 purely hadronic events, no ν_τ candidate has been found. This result translates in a limit on the mixing angle $\sin^2 2\theta_{\mu\tau} < 8 \times 10^{-4}$ at 90% C.L. for large $\Delta m^2_{\mu\tau}$. © *2000 MAIK "Nauka/Interperiodica".*

1. INTRODUCTION

The CHORUS experiment at CERN was designed to search for oscillations $\nu_\mu \longleftrightarrow \nu_\tau$ in appearance mode. This search is performed by looking for ν_τ charged-current interactions $\nu_\tau N \longrightarrow \tau^- X$ in a ν_μ beam. These interactions can be identified by the decay of the produced τ. For this purpose, CHORUS uses an emulsion target. Having a resolution of about a micron, emulsion enables the detection of the decay of the τ. CHORUS has studied the decay channels of the τ to a muon ($\tau \longrightarrow \mu\nu_\tau\bar{\nu}_\mu$) and to a single charged hadron ($\tau \longrightarrow h^-(nh^0)\nu_\tau$).

The ν_μ beam is provided by CERN's West Area Neutrino Facility. This beam contains mainly ν_μ neutrinos having an average energy of about 27 GeV. The contamination from other types of neutrinos is at the level of 5% for $\bar{\nu}_\mu$ and 1% for ν_e and $\bar{\nu}_e$. The prompt ν_τ contamination is of the order of $3.3 \times 10^{-6}\nu_\tau$ charged-current interaction per ν_μ charged-current interaction.

The experiment is positioned at about 820 m from the beam target. The flight length of the neutrinos is about 650 m. The combination of flight length and energy of the neutrinos enables CHORUS to probe neutrino mass differences above a few eV. This region of oscillation parameter space is interesting for cosmology. After having analyzed all its data, CHORUS expects to be sensitive to values of $\sin^2 2\theta_{\mu\tau}$ on the order of 10^{-4} for large $\Delta m^2_{\mu\tau}$ values.

The WANF neutrino beam was stopped in September 1998. The results presented here are based on a sample of the data taken between 1994 and 1997. No emulsion data was taken in 1998. Emulsion scanning is in progress.

* This article was submitted by the author in English.

2. THE CHORUS DETECTOR

The CHORUS detector consists of an 800-kg nuclear emulsion target preceded by a veto shield and followed by electronic detectors (Fig. 1). The emulsion target consists of four stacks of 36 plates of emulsion. Each plate has a 350-μm layer of emulsion on each side of a 90-μm-thick plastic base. Each emulsion stack is followed by three interface emulsion sheets consisting of an 800-μm base coated on each side with a 100-μm-thick emulsion layer.

Scintillating fiber trackers are placed between the emulsion stacks. They are used to extrapolate tracks in the emulsion. The target region of the detector is followed by a magnetic spectrometer, a lead/scintillating fiber calorimeter, and a muon spectrometer. More details about the CHORUS detector can be found elsewhere [1].

3. DECAY SEARCHES

For the search of muonic decays of τ's, events with one identified muon are selected (1μ sample) [2]. In the case of the single charged hadron decay channel of the τ, events without any muon are selected (0μ sample) [3]. In both cases, tracks (muon candidates or hadron candidates) are reconstructed in the fiber trackers and are used as predictions for the emulsion scanning. These predictions are then followed in the emulsion from plate to plate by automatic scanning until they disappear for two consecutive plates. The first plate where the prediction was lost is called the vertex plate. Once the vertex is found, the decay search is performed.

Due to the developments of the automatic scanning throughout the period of the analysis, different decay search algorithms were applied. Figure 2 shows the different decay topologies. The analysis performed on the 1994 data addressed two decay topologies: the short decay path (Fig. 2*a*) and the long decay path (Fig. 2*b* and 2*c*). These topologies are those for which the τ

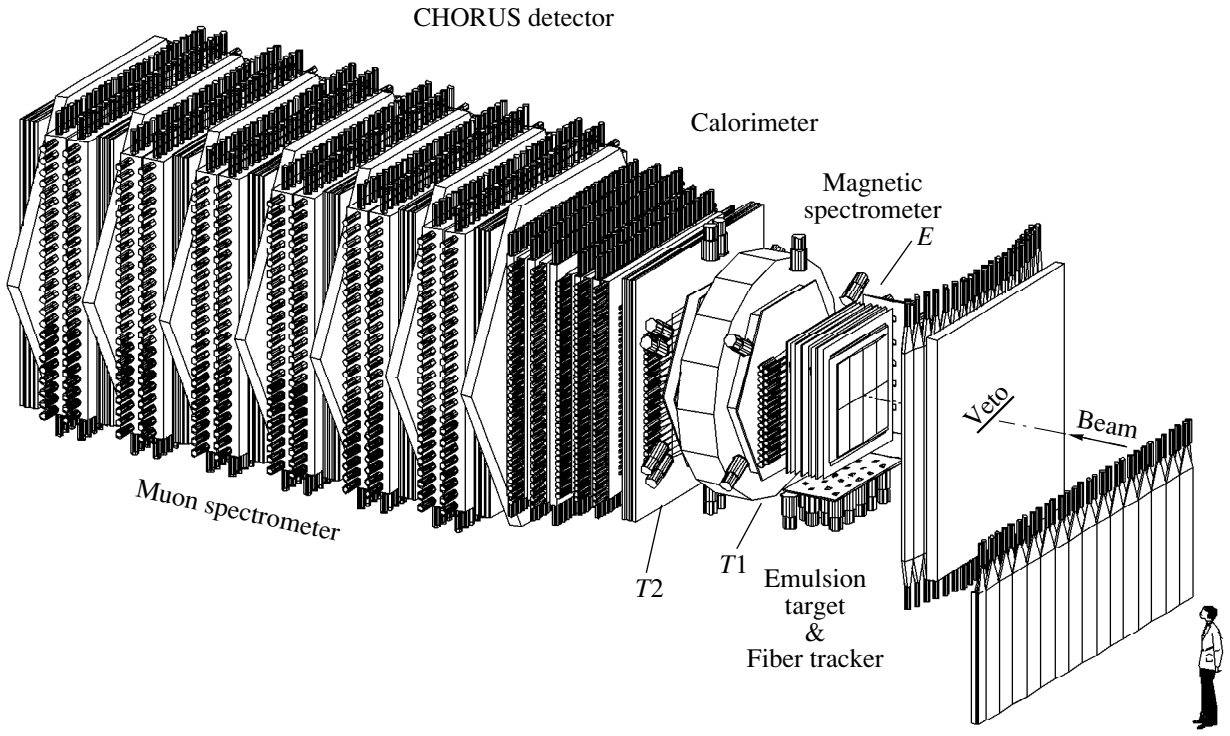

Fig. 1. The CHORUS detector.

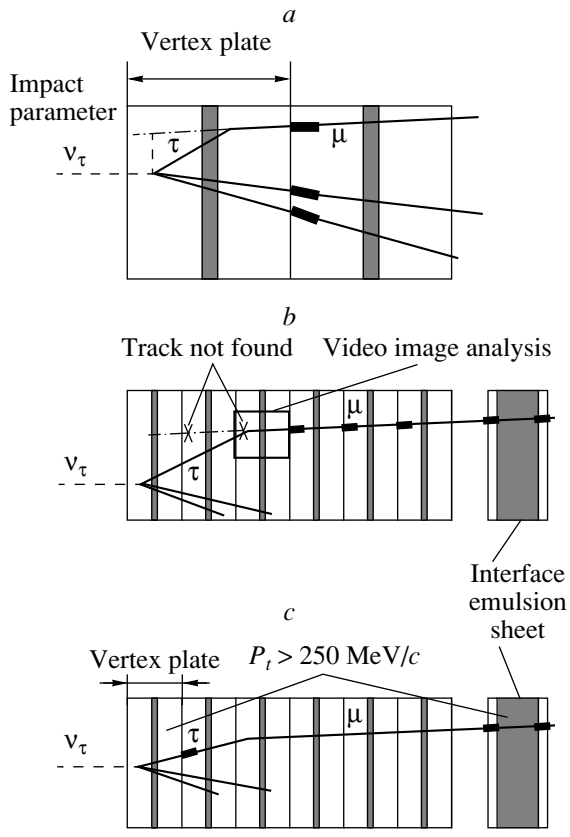

Fig. 2. Decay topologies.

decay is in the vertex plate and when it is in another plate further downstream, respectively. In the case of the short decay path topology, the decay is selected by the measurement of the impact parameter of the prediction candidate and two other tracks in the event. For the long decay path, a parent track is looked for within the angular acceptance of the scanning apparatus once the prediction is lost.

Starting with the data of 1995, the parent track search has been performed. Once the prediction is lost, other tracks are looked for in the vertex plate. If the minimal distance between a given track and the prediction is smaller than 15 μm, this track is considered to be the parent of the lost prediction.

For all decay searches, once a potential decay has been found, it is scanned by eye to study in more detail the possibility of a τ decay.

4. BACKGROUNDS

For the muonic decay search (1μ sample), the main source of background is charm production in charged-current interactions:

$$\nu_l(\bar{\nu}_l)N \longrightarrow l^{\mp}D^{\pm}X, \tag{1}$$

where $l = \mu$ or e, followed by

$$D^{\pm} \longrightarrow \mu^{\pm}X'. \tag{2}$$

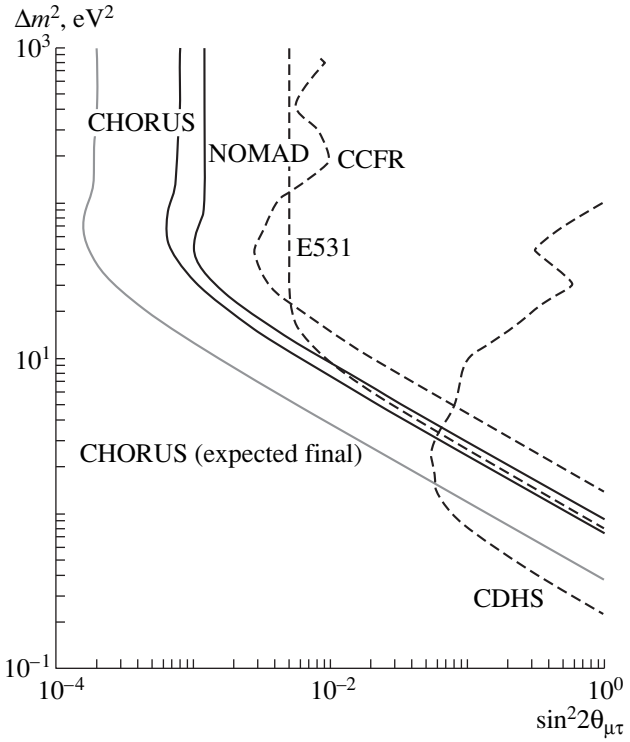

Fig. 3. Exclusion plot.

For the case of $\bar{\nu}_l$ interactions, the first muon must escape detection and identification. In the case of ν_l interactions, in addition, the charge of the muon produced by the charm meson decay must be misidentified. The expected background for the 1μ data sample is at the level of 10^{-6} event per 1μ event.

For the single charged hadron search (0μ sample), the main source of background is elastic hadron interactions in the emulsion. Hadrons produced by a neutrino interaction can mimic a τ decay when they interact elastically in the emulsion, without leaving any trace in addition to the outgoing hadron. The expected background for the 0μ data sample is at the level of 10^{-5} event per 1μ event. Charm production can also produce a background for 0μ events, at a level similar to the one described for the 1μ sample.

Status of the CHORUS emulsion scanning

Sample	To scan, k	Scanned, %	Located, k	Decay search, k
1μ, 1994–1997	459	66	126	126
0μ, 1994–1997	116	47	17	
1994–1995				7.5
1996–1997				To be done

5. OSCILLATION SENSITIVITY AND STATUS

A little more than half of the reconstructed events have been scanned so far. The table shows the current status of the emulsion scanning. The second column (to scan) shows the number of reconstructed events for which scanning is needed. The third column (scanned) shows the fraction of these events that was scanned. The fourth column (located) shows the number of events with a located vertex. The fifth column (decay search) shows the number of events for which the decay search was performed. For the 1μ sample, the decay analysis was done for the entire data sample scanned so far. For the 0μ sample, the decay analysis was done only for the data of 1994 and 1995. The 0μ data sample of 1996 and 1997 remains to be completely analyzed.

No τ candidate has been found. This result can be translated into a limit on the oscillation parameters for a given model. Figure 3 shows the 90% C.L. exclusion plot for the $\nu_\mu \longleftrightarrow \nu_\tau$ two-flavor mixing scheme. For large mass differences, CHORUS puts a 90% C.L. limit on $\sin^2 2\theta_{\mu\tau}$ at 8×10^{-4}.

6. CONCLUSION AND OUTLOOK

The CHORUS experiment has stopped taking data for its oscillation search in 1997. A little more than half of the emulsion scanning has been done so far. Having found no τ candidate, CHORUS can set a limit on $\sin^2 2\theta_{\mu\tau}$ for large $\Delta m^2_{\mu\tau}$ at $\sin^2 2\theta_{\mu\tau} < 8 \times 10^{-4}$ at 90% C.L.

CHORUS is now starting its second phase of emulsion scanning. Improvements of the reconstruction and of the scanning technique should provide a higher efficiency to find τ decays. After having scanned all its data, CHORUS expects to be able to probe the oscillation parameter space down to $\sin^2 2\theta_{\mu\tau} \simeq 2 \times 10^{-4}$ for large $\Delta m^2_{\mu\tau}$.

REFERENCES

1. E. Eskut *et al.*, Nucl. Instrum. Methods A **401**, 7 (1997).
2. E. Eskut *et al.*, Phys. Lett. B. **424**, 202 (1998).
3. E. Eskut *et al.*, Phys. Lett. B. **434**, 205 (1998).

Physics of Atomic Nuclei, Vol. 63, No. 7, 2000, pp. 1122–1128. From Yadernaya Fizika, Vol. 63, No. 7, 2000, pp. 1199–1204.

NEUTRINO PHYSICS AT ACCELERATORS

Latest Results on Atmospheric Neutrinos From Soudan 2 and the Status of MINOS*

D. A. Petyt**

Rutherford Appleton Laboratory, Chilton, Didcot, Oxfordshire, UK

Abstract—In this paper, the latest results on atmospheric neutrinos from the Soudan 2 iron calorimeter experiment are presented. The flavor ratio of ratios for a 4.2 fiducial kiloton year exposure of Soudan 2 is measured to be $0.66 \pm 0.11(\text{stat.}) \pm 0.06(\text{syst.})$. The region of parameter space in the oscillation mode $\nu_\mu \longrightarrow \nu_\tau$ allowed from a *L*/*E* analysis of Soudan 2 data is shown to be consistent with the results from the Super-Kamiokande experiment. The forthcoming long baseline experiment, MINOS, is also described. The current status of the experiment and its projected parameter measurement capabilities are discussed. © *2000 MAIK "Nauka/Interperiodica".*

1. THE ATMOSPHERIC NEUTRINO PROBLEM

The flux of atmospheric neutrinos has been measured by a number of large underground detectors [1–5]. These neutrinos are the decay products of pions, muons, and kaons, which are themselves products of interactions between primary cosmic rays (mostly protons) and atmospheric nuclei. The neutrino flux that results from these interactions is predicted by detailed Monte Carlo simulations [6]. The absolute fluxes of ν_μ and ν_e are uncertain to 20–30%, due to uncertainties in primary fluxes and hadronic cross sections, but the ratio of ν_μ to ν_e is known to better than 5%.

Experiments therefore quote their result in terms of the ratio of ν_μ to ν_e events, specifically, the double ratio, *R*, where

$$R = \frac{\nu_\mu/\nu_e|_{\text{data}}}{\nu_\mu/\nu_e|_{\text{MC}}}.$$

This ratio should be equal to unity if the data is correctly described by the Monte Carlo simulation. Several experiments have reported results on the flavor ratio. The water Cherenkov experiments, Kamiokande [1], IMB [2], and SuperKamiokande [3], have measured values of *R* that are significantly below unity. Results have also been presented from two iron calorimeter experiments, Frejus [4] and Nusex [5]. These are consistent with $R = 1$, although the experiments are much smaller and have accumulated much lower statistics than the water Cherenkov experiments. The Soudan 2 result of $R = 0.66 \pm 0.11(\text{stat.}) \pm 0.06(\text{syst.})$, measured in an iron calorimeter experiment, supports the water Cherenkov results in a detector with entirely different flavor identification techniques and systematic errors.

* This article was submitted by the author in English.

** e-mail: d.a.petyt@rl.ac.uk

2. THE SOUDAN 2 DETECTOR

The Soudan 2 detector [7] is a 963-t iron tracking calorimeter situated 731 m underground (2341 mwe) in the Soudan iron mine, northern Minnesota. The detector measures 8 m × 5.4 m × 14 m and is constructed of 224 identical modules with dimensions of 1 m × 1 m × 2.7 m, each weighing 4.3 t. Each module consists of corrugated sheets of 1.5-mm-thick steel arranged in a hexagonal honeycomb structure. Interleaved between the steel sheets are 1-m-long resistive Hytrel drift tubes, which are filled with an 85% CO_2, 15% Ar gas mixture. Ionization deposited within the tube volumes drifts to the tube ends under the influence of an applied electric field and is detected by means of vertical anode wires and horizontal cathode strips. The third coordinate is given by the drift time within the tubes. The Soudan 2 detector therefore provides three-dimensional images of events with excellent spatial resolution (vertex resolution ~1 cm) and good particle identification (including final state particles that are below Cherenkov threshold). The detector is surrounded by a 4π proportional tube veto counter, which is used to reject cosmic ray muons and background particles that originate in the rock volume surrounding the detector. The detector has been operational since 1989 and consistently runs with ~90% live time.

3. DATA REDUCTION AND FLAVOR CLASSIFICATION

The rate of triggers in Soudan 2 is 0.5 Hz; two-thirds of which are cosmic ray muons and one-third are due to radioactive noise. Neutrino events occur at the rate of one every three days. A computer filter and a two-stage physicist scan are used to reject this large background rate and to isolate a sample of interactions that are fully contained within the fiducial volume of the detector (defined to be greater than 20 cm from the outside faces of the detector). These contained events are expected to

1063-7788/00/6307-1122$20.00

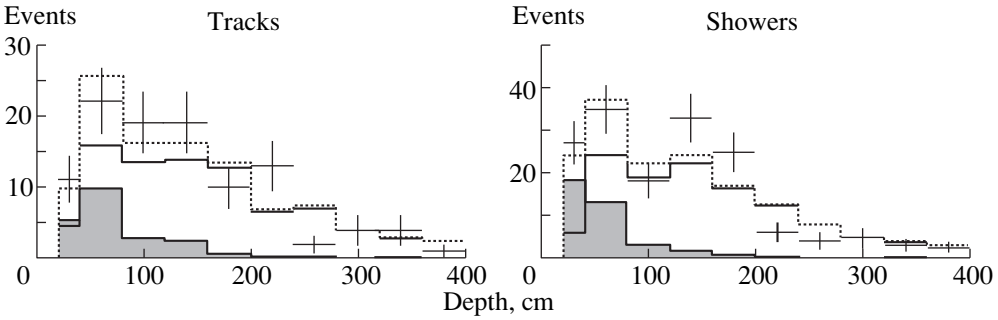

Fig. 1. Depth distributions for contained event data (crosses), neutrino Monte Carlo (solid histograms), shield tagged rock background events (shaded histograms) and the best-fit combination of rock and Monte Carlo distributions (dotted histograms).

be a pure source of neutrino interactions. The possible background contamination of this sample is explored in the next section.

Flavor classification of events is determined by physicist scanning. Monte Carlo events are inserted into the data stream, and the scanner has no a priori knowledge of the origin of a particular event. The events are classified into one of four classes [8]: single track (with recoil), single shower (with recoil), multiprong (multiple particles in the final state), and proton [9]. The classification matrix for Monte Carlo neutrino interactions is shown in Table 1. The track and shower classes are primarily composed of quasielastic interactions and are analogous to the single ring events in the water Cherenkov detectors. Only these two classes are currently used in the determination of the flavor ratio.

Background Contamination

Neutral particles (produced when a cosmic ray muon interacts in the rock surrounding the detector cavern) may pass undetected through the veto shield and produce interactions within the fiducial volume of the Soudan detector. These fake contained events will serve as a background to neutrino interactions. This particular source of background can be observed and measured in Soudan 2 by examining the depth distributions of data and Monte Carlo contained events. Here depth is defined as the closest perpendicular distance from the event vertex to the outside face of the detector. Data and Monte Carlo distributions are plotted for tracks and showers along with rock events. Rock events are contained events with associated shield activity, i.e., the charged particles that are also produced when the muon interacts with the rock pass through the shield and are detected. The presence of rock-induced background in the data is attested by the excess of data events at shallow depths over the neutrino Monte Carlo, as shown in Fig. 1. Background events that are induced by neutral particles should be distributed around the edges of the detector, with characteristic depths of 20 cm for photon-induced events and 80 cm for neutron-induced events. An extended maximum likelihood method is used to fit the shape of the data depth distribution to a linear combination of the rock and Monte Carlo distributions. Separate fits are performed for track and shower samples. The fits reveal that neutral-induced background exists in the data at the level of 20 to 30%. This contamination is accounted for in the final analysis.

4. RESULTS

Table 2 shows the steps that are necessary to calculate the flavor ratio of ratios in Soudan 2. The number of data tracks and showers corresponds to an exposure of 4.2 fiducial kt yr. These numbers are then corrected for the rock contamination to produce the final numbers of data tracks and showers. The Monte Carlo events correspond to an exposure that is 5.4 times the exposure of the data. Comparing the data to the normalized Monte Carlo reveals that the number of shower events in the data is consistent with the Monte Carlo (given the 20–30% error on the absolute flux), but there is a deficit

Table 1. Flavor classification matrix for Monte Carlo events

Interaction	Track	Shower	Multiprong	Proton
ν_μCC	765	22	312	26
ν_eCC	32	743	323	3
NC	50	40	135	60

Table 2. Data used in the calculation of the corrected flavor ratio (the Monte Carlo numbers in parentheses are normalized to the detector exposure; the error on the flavor ratio is statistical only)

Number of gold tracks	105
Number of gold showers	159
Number of MC tracks	847(155.4)
Number of MC showers	805(147.7)
Corrected number of ν tracks	83.6 ± 11.2
Corrected number of ν showers	119.7 ± 12.9
Raw value of R	0.63 ± 0.09
Corrected value of R	0.66 ± 0.11

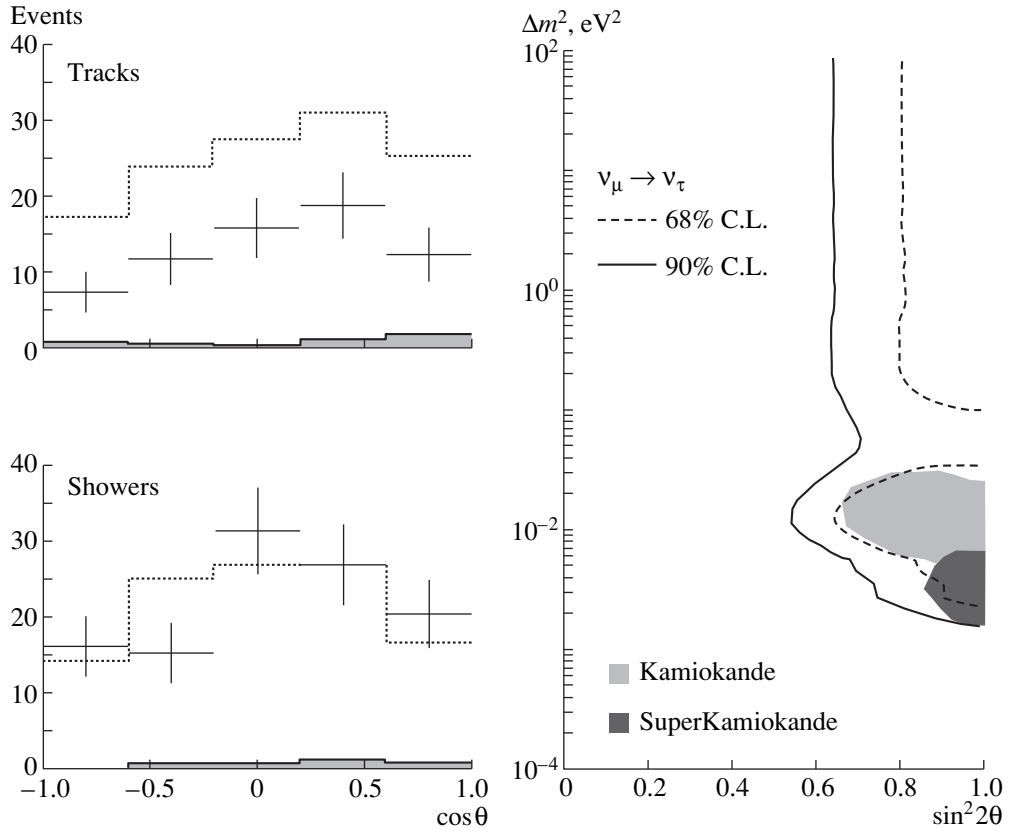

Fig. 2. Left-hand plots: zenith-angle distributions for tracks and showers. The data are denoted by crosses, Monte Carlo by the dotted histograms, and rock background by the shaded histograms. Right-hand plot: the 68 and 90% C.L. allowed regions from a fit to $\nu_\mu \longrightarrow \nu_\tau$ oscillations. The 90% C.L. allowed regions for the Kamiokande and SuperKamiokande analyses are also plotted.

in the data tracks of a factor of two. The flavor ratio of ratios is $0.66 \pm 0.11(\text{stat.}) \pm 0.06(\text{syst.})$. The probability that this result is a statistical fluctuation from $R = 1$ is 0.3%. The presence of rock-induced background does not significantly bias the flavor measurement. This can be seen by constructing the flavor ratio using the raw numbers of data tracks and showers, resulting in a value of $R = 0.63 \pm 0.09$, which is consistent with the background-corrected result.

L/E Analysis

A subset of the above data sample is used to test the hypothesis of neutrino oscillations. This "high resolution" data set is composed of high energy tracks, showers, and multiprong events with good pointing (the reconstructed neutrino direction is within 30° of the true direction) and low background contamination (< 5%). The rationale behind using this sample is to improve the angular resolution in order to discern any possible zenith-angle distortions and to reduce the prospect of any bias due to background subtraction.

The zenith-angle distributions for high resolution events are shown in the left-hand panel of Fig. 2. Tracks and showers are plotted separately. The data shower distribution is in agreement with the Monte Carlo. The data track distribution is suppressed, but the suppression is independent of zenith angle. This observation is not in conflict with the results from SuperKamiokande—which showed a strong zenith-angle-dependent suppression of ν_μ-like events—due to the lower energies and statistics of events in Soudan 2.

The region of parameter space allowed by this result is shown in the right-hand panel of Fig. 2. Neutrino oscillations in the mode $\nu_\mu \longrightarrow \nu_\tau$ are assumed, and the 68 and 90% C.L. allowed regions are plotted. One consequence of the lack of any significant zenith-angle distortion in the data is that the allowed region extends to large Δm^2. The best fit value of Δm^2 in Soudan 2 ($\Delta m^2 \sim 1 \times 10^{-2}$ eV^2) is slightly higher than that of SuperKamiokande [10], but the overlap between the Soudan 2 and SuperKamiokande allowed regions is good.

5. OUTLOOK FOR SOUDAN 2

The Soudan 2 experiment continues to take data at the rate of 0.7 fiducial kt yr per calendar year. The experiment will continue to operate into the MINOS era, upon which it will become part of the MINOS experiment. The goal of Soudan 2 is to reduce its cur-

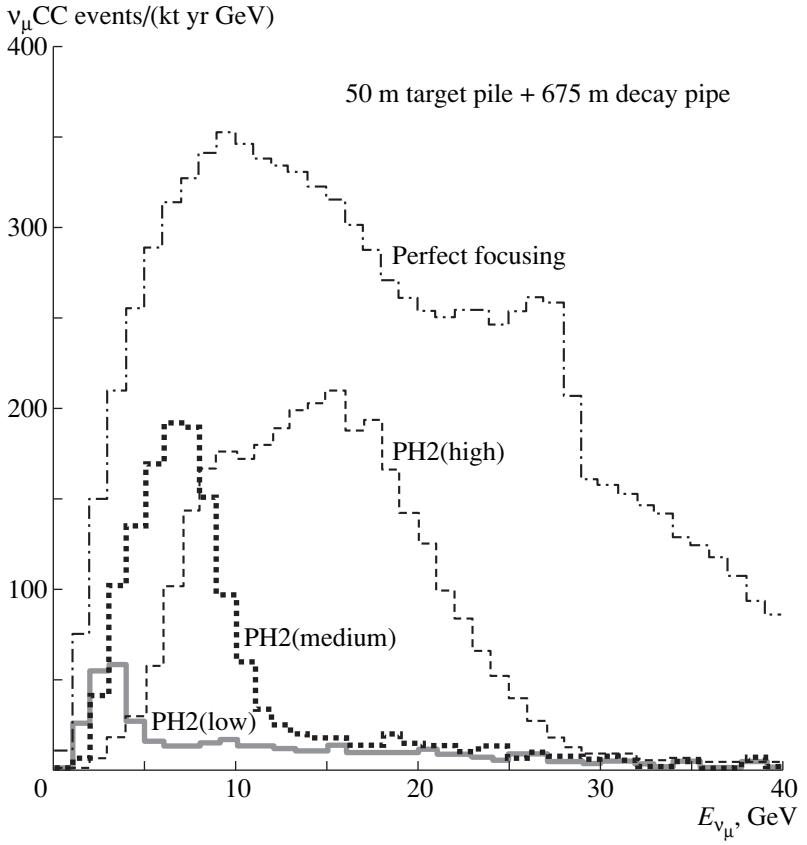

Fig. 3. The three NuMI beam options for MINOS. The ν_μCC energy spectra at the far detector for the three beams are shown, along with the spectrum that would be obtained if all secondary pions could be perfectly focused.

rent errors on the measurement of oscillation parameters, to check the results of SuperKamiokande, and to guide the running strategies of future long-baseline experiments. To help achieve this goal, work is underway to isolate a set of partially contained events in Soudan. These events have a clearly defined vertex in the fiducial volume of the detector along with an exiting final state lepton (typically a muon). Preliminary studies suggest that this sample could add an extra 50–60 high energy ν_μ events to the current data sample. The correlation between initial neutrino and final state lepton direction is very strong in these events, and they will therefore enhance our prospects of observing a zenith-angle distortion in Soudan.

6. THE MINOS EXPERIMENT

The MINOS[1)] experiment [11] is a logical successor to atmospheric neutrino experiments such as Soudan 2. It aims to probe the region of neutrino oscillation parameter space suggested by the atmospheric neutrino experiments with unprecedented statistical precision and low systematic uncertainties.

[1)]Main Injector Neutrino Oscillation Search.

A beam of ν_μ will be provided by the Fermilab Main Injector. The beam will be directed towards the Soudan Underground Laboratory, which is at a distance of 735 km from Fermilab. A large tracking calorimeter will be placed in a newly excavated cavern at Soudan to intercept the beam. In addition, a smaller, but closely similar, detector will be placed at the Fermilab site to measure the properties of the neutrino beam at production. A significant difference between the signals measured in the two detectors is indicative of neutrino oscillations.

6.1. The MINOS Beams

The current uncertainty on Δm^2 from the SuperKamiokande experiment is of the order of half a decade. An impressive degree of consistency has been demonstrated between the neutrino oscillation interpretation of low- and high-energy atmospheric neutrino data samples and up/through-going muons. However, the lower limit on Δm^2 from SuperKamiokande has increased by a factor of two in the previous year and the results from Soudan 2 and Kamiokande do appear to favor values of Δm^2 that are larger than the current indications from SuperKamiokande.

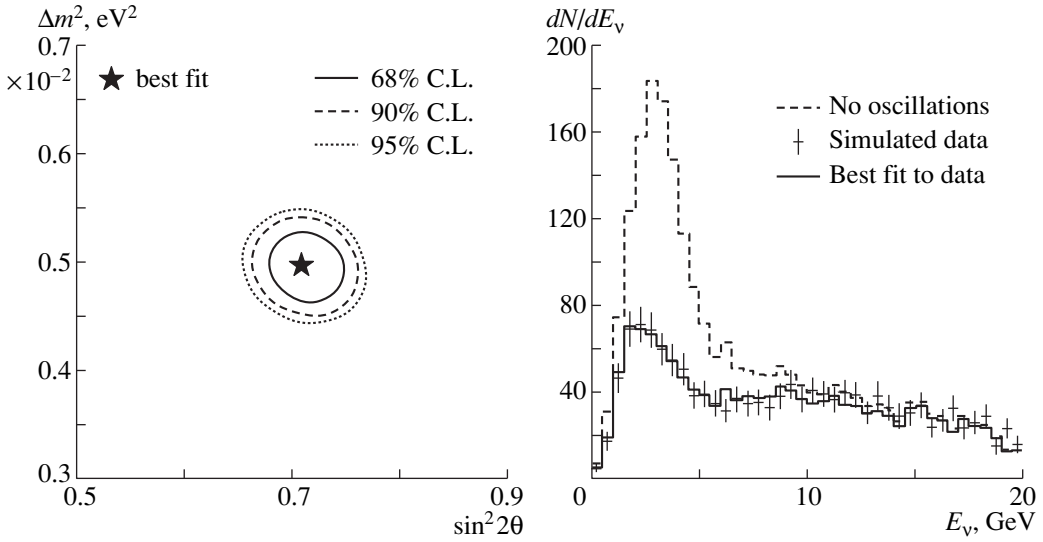

Fig. 4. Left-hand plot: parameter measurement errors for a signal with $\Delta m^2 = 0.005$ eV^2 and $\sin^2 2\theta = 0.7$. Right-hand plot: reconstructed neutrino energy distributions for oscillations with these parameters (crosses), no oscillations (dashed histogram), and the best-fit parameters (solid histogram).

Given this current level of uncertainty, it is vital to adopt a flexible approach in long-baseline running strategies. If the value of Δm^2 is of order 10^{-3} eV^2, then, for the MINOS baseline of 735 km, the oscillation probability is maximized at a neutrino energy of ~1 GeV. If $\Delta m^2 \sim 10^{-2}$ eV^2, then the oscillation probability is maximized at ~10 GeV. A long-baseline neutrino beam must have appreciable flux over at least one order of magnitude in order to cover the range of uncertainty in Δm^2. The method used to achieve this in MINOS is to have a beam line that can be tuned to accentuate low (~1–3 GeV), medium (~5 GeV), and high (~15 GeV) energy neutrinos by adjusting the relative positions of the target and the two focusing horns. The three resulting neutrino spectra are shown in Fig. 3, along with the beam that could be achieved if all secondary pions could be perfectly focused. The lower energy beams enhance the flux at low energies, at the expense of lower overall event rates. MINOS may initially start with the medium energy beam tune, but could switch to higher or lower energies, depending on the results of the initial run.

6.2. The MINOS Detectors

The detector at Soudan (the Far Detector) will be a large 5.4-kt device consisting of alternate planes of steel and plastic scintillator. The entire detector is 31 m in length. The steel sheets will be octagonal, 8 m in diameter and one inch thick, and will be magnetized with a mean field of 1.5 T. The field helps to contain and measure the momentum of muons in the detector. The plastic scintillator active detectors will take the form of extruded strips with a 1 cm × 4.1 cm cross section. The strips cover the entire face of the steel planes and will be up to 8 m in length. A wavelength shifting fiber, which is placed in a groove in the scintillator, transfers light that is deposited in the scintillator to individual pixels of a multianode photomultiplier tube. The light from eight 1.2 mm diameter fibers is deposited on one 4 × 4 mm pixel to reduce the number of electronics channels required.

The detector at Fermilab (the Near Detector) is functionally identical to the far detector. It is more compact in size (14 m in length, 6-m-diameter octagonal plates, and 1 kt) since the neutrino flux at the near detector site—which is 290 m downstream of the neutrino beam line—is a factor of 10^6 larger than at the far detector site. The active and passive detector technology is identical in the near and far detectors, although the degree of instrumentation is somewhat different. The neutrino beam spot is approximately one meter in diameter at the front face of the near detector. Therefore, only one quadrant of the first six meters of the near detector—the target region—is instrumented. The remaining 8 m—the muon spectrometer region—is fully instrumented. A current carrying coil provides a magnetic field that is closely similar to that of the far detector.

6.3. Physics Capabilities

The signature of neutrino oscillations in MINOS is the observation of differences in the characteristics of events in the near and far detectors. Two kinds of measurement are possible:

1. Disappearance tests: Fewer ν_μ events are observed in the far detector with respect to the number that would be predicted for no oscillations. If this suppression is observed to be a function of neutrino energy,

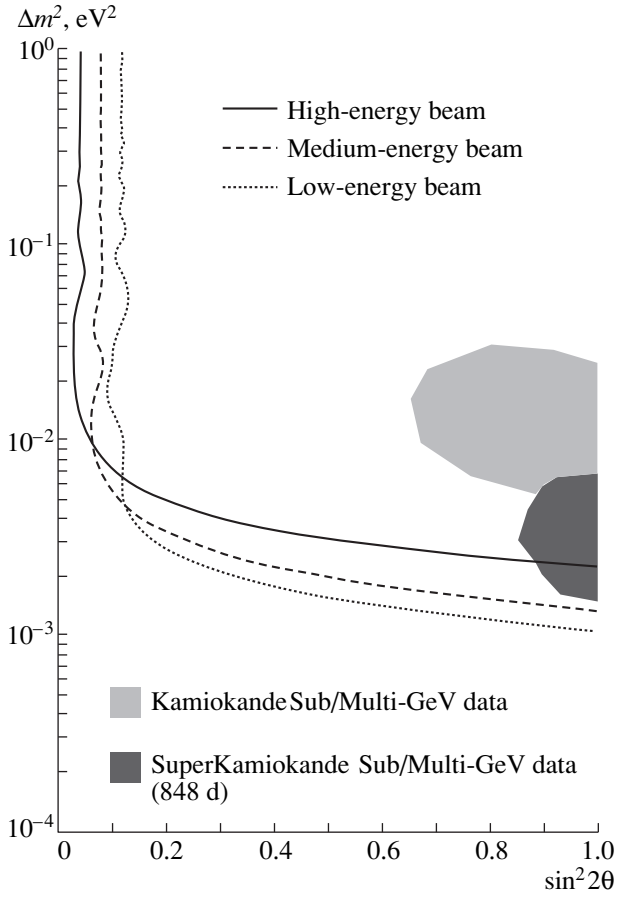

Fig. 5. Limits in parameter space for $\nu_\mu \longrightarrow \nu_\tau$ oscillations using the NC/CC ratio in MINOS. The limits that could be set with the three proposed beam designs are plotted and a two-year exposure is assumed.

then precise measurements of the oscillation parameters can be made. Figure 4 shows distributions of reconstructed neutrino energy (the sum of the observed muon and hadron energies) for ν_μ charged-current events with no oscillations and oscillations with $\Delta m^2 = 5 \times 10^{-3}$ eV^2 and $\sin^2 2\theta = 1$ in the low energy beam. An energy-dependent suppression of the neutrino event rate is clearly seen. Energy resolutions are obtained from a full GEANT simulation of the MINOS detector. The left-hand plot shows the results of an oscillation fit to these distributions, assuming the mode $\nu_\mu \longrightarrow \nu_\tau$. A two year run of MINOS with the low energy beam could measure Δm^2 and $\sin^2 2\theta$ to an accuracy of ~10% for oscillation parameters within the SuperKamiokande allowed region.

2. Appearance tests: The NuMI neutrino beam is a >99%-pure ν_μ and $\bar{\nu}_\mu$ source. Observation of ν_e or ν_τ events in the far detector is therefore a strong indication of neutrino oscillations. Electron neutrino events are identified by examining the longitudinal deposition of energy in the detector, and a series of cuts are applied to discriminate between ν_eCC events and neutral current events. The 0.6% $\nu_e + \bar{\nu}_e$ component of the beam will be measured in the near detector and a limit of $\sin^2 2\theta_{\mu e} < 3 \times 10^{-3}$ can be set at high Δm^2 in a 2 yr run with the high energy beam. The presence of tau-neutrino events can be deduced by examining the number and energy distributions of hadronic events (neutral currents and $\tau \longrightarrow$ hadron decays). An excess of events with energetic single pions (from $\tau \longrightarrow \pi$ decays) may be visible if $\Delta m^2 \sim 10^{-2}$ eV^2. It is also possible that an upgrade, in the form of an emulsion-based detector, may be placed in front of MINOS to allow the observation of tau-decay kinks. Finally, MINOS is also sensitive to $\nu_\mu \longrightarrow \nu_{\text{sterile}}$ oscillations via the ratio of the numbers of neutral-current to charged-current events.

Figure 5 shows a representative plot of the projected MINOS sensitivity to neutrino oscillations. MINOS will be sensitive to $\nu_\mu \longrightarrow \nu_\tau$ and $\nu_\mu \longrightarrow \nu_e$ oscillations down to $\sin^2 2\theta \simeq 10^{-2}$ at high Δm^2 and $\Delta m^2 \simeq 10^{-3}$ eV^2 at $\sin^2 2\theta = 1$.

7. OUTLOOK AND CONCLUSIONS

The MINOS experiment has been approved and funded. Excavation of the far detector cavern at Soudan is now underway and construction of the detectors will commence in the year 2001. The neutrino beam from the Main Injector is scheduled to reach Soudan in the year 2003, and the initial physics run will probably be with the medium energy PH2me beam. Further running with high or low energy beams, narrow band or antineutrino beams will depend on the results of the initial run.

The results of the atmospheric neutrino experiments have established that, in all probability, neutrino oscillations do occur in nature. However, the oscillation parameters are not precisely measured due to low statistics and uncertainties in the atmospheric neutrino flux. This situation is set to change in the next few years due to the advent of long-baseline experiments; MINOS, K2K [10], and the CERN-NGS proposals [12]. Large signals should be observed in these experiments if the atmospheric neutrino results are due to oscillations. The mixing parameters, which are elements of a CKM-like matrix for leptons, will therefore be far more precisely determined.

REFERENCES

1. Kamiokande Collab. (Y. Fukuda *et al.*), Phys. Lett. B **335**, 237 (1994).
2. The IMB Collab. (R. Becker-Szendy *et al.*), Phys. Rev. D **46**, 3720 (1992).
3. Super-Kamiokande Collab. (Y. Fukuda *et al.*), Phys. Rev. Lett. **81**, 1562 (1998).
4. Frejus Collab. (K. Daum *et al.*), Z. Phys. C **66**, 417 (1995).
5. Nusex Collab. (M. Aglietta *et al.*), Europhys. Lett. **8**, 611 (1989).

6. G. Barr, T. K. Gaisser, and T. Stanev, Phys. Rev. D **39**, 3532 (1989); M. Honda *et al*., Phys. Rev. D **52**, 4985 (1995).
7. Soudan 2 Collab. (W. W. M. Allison *et al*.), Nucl. Instrum. Methods A **376**, 36 (1996); W. W. M. Allison *et al*., Nucl. Instrum. Methods A **381**, 385 (1996).
8. H. Gallagher, *Neutrino Oscillation Searches with the Soundan 2 Detector*, PhD Thesis (University of Minnesota, 1996).
9. Suodan 2 Collab. (W. W. M. Allison *et al*.), Phys. Lett. B **449**, 137 (1999).
10. W. Gajewski, Yad. Fiz. **63**, 1010 (2000) [Phys. At. Nucl. **63**, 934 (2000)].
11. MINOS Collab., *The MINOS Detectors Technical Design Report*, Report No. NuMi-L-337, Fermilab (Batavia, 1998).
12. A. Guglielmi, Yad. Fiz. **63**, 1178 (2000) [Phys. At. Nucl. **63**, 1103 (2000)].

Physics of Atomic Nuclei, Vol. 63, No. 7, 2000, pp. 1129–1136. From Yadernaya Fizika, Vol. 63, No. 7, 2000, pp. 1205–1212.

NEUTRINO PHYSICS AT ACCELERATORS

Searches for *R*-Parity-Violating Supersymmetry at Colliders*

Y. Sirois**

LPNHE Ecole Polytechnique, Palaiseau, France

Abstract—The search for *R*-parity-violating supersymmetry at existing colliders is reviewed with emphasis on the sensitivity to the new Yukawa couplings λ, λ' (inducing lepton-number-violating interactions) and λ'' (inducing baryon-number-violating interactions). One dramatic consequence of the existence any such nonvanishing coupling is the instability of supersymmetric matter. The extent to which this affects the sensitivity to other free parameters of minimal supersymmetric models has been extensively studied at LEP and is briefly reviewed. Given that supersymmetric matter has not been observed yet, and since its existence still cannot be ruled out, we concentrate here on the important question of a possible "discovery" of supersymmetry (if it exists) through the *R*-parity-violating couplings. The case of resonant production of sleptons via λ' and squarks via λ'' at the Tevatron, as well as the case of resonant production of sneutrinos at LEP involving λ, is briefly discussed. A particular emphasis is then put on the case of resonant production of squarks through electron–quark fusion at HERA which involves λ'. © *2000 MAIK "Nauka/Interperiodica".*

1. INTRODUCTION

A likely ingredient of a true fundamental theory beyond the Standard Model (SM) is supersymmetry (SUSY) which connects elementary fermions and bosons. Traditionally, the possible consequences of SUSY at energy scales well below the SUSY-breaking scale have been analyzed mostly in the framework of either the Minimal Supersymmetric Standard Model (MSSM) [1] or of the more restrictive Minimal Supergravity [2] (SUGRA). Such theories offer predictive power given a finite and well-defined set of free parameters and have neither been proven nor disproven by experimental observations.

Gauge invariance and renormalizability does not ensure, in general, lepton- and baryon-number conservation in supersymmetric extensions of the SM. In the MSSM, lepton- and baryon-number-violating interactions are effectively avoided by imposing a strict conservation of the multiplicative *R*-parity (R_p) quantum number defined to be 1 for particles and –1 for sparticles. Thus, the theory is made minimal in terms of both field content and allowed couplings. Imposing this discrete symmetry is a somewhat *ad hoc* prescription which leads to the absolute stability of the lightest supersymmetric particle (LSP). But there might be reasons why SUSY matter should be unstable.

The essential instability of supersymmetric matter seems "natural" given that a most general SUSY superpotential allows for gauge-invariant trilinear terms with R_p-violating ($\not{R}_p$) Yukawa couplings. As an immediate result of such interactions, the LSP becomes unstable through virtual conversion to a fermion–sfermion pair followed by sfermion $\not{R}_p$ decay. This has dramatic consequences. An obvious one for cosmology is that the LSP does not qualify anymore as a candidate for Cold Dark Matter. At colliders, the LSP decay leads to event topologies requiring analyses differing strongly from the characteristic hunt for "missing energy" signals of the MSSM where the LSP escapes as a weakly interacting gaugino–higgsinos. Thus, it is mandatory to revisit specifically for $\not{R}_p$ models the direct constraints on sparticle masses and other MSSM or SUGRA model parameters. But the existence of $\not{R}_p$ interactions also has the obvious consequence that single production of sparticles becomes possible at colliders, opening new discovery windows.

2. TRILINEAR *R*-PARITY-ODD INTERACTIONS IN SUSY

2.1. The Superpotential for Yukawa-Type Interactions

Preserving the minimal field content of the MSSM, the most general Yukawa couplings allowed by the SM requirement of $SU(3)_C \times SU(2)_L \times U(1)_Y$ gauge invariance in a SUSY theory can be written [3, 4] in the compact formalism of the superpotential as $W_{\mathrm{SUSY}} = W_{\mathrm{MSSM}} + W_{\not{R}_p}$. The W_{MSSM} contains terms which are responsible for the Yukawa couplings of the Higgs fields to ordinary fermions. The additional $W_{\not{R}_p}$ terms violate *R* parity (and thus lepton and baryon numbers) defined as $R_p = (-1)^{3B+L+2S}$, where *S* denotes the spin, *B* the baryon number, and *L* the lepton number. These $\not{R}_p$ terms are not suppressed by any large mass scale and are given by

$$W_{\not{R}_p} = \lambda_{ijk} L_i L_j \bar{E}_k + \lambda'_{ijk} L_i Q_j \bar{D}_k + \lambda''_{ijk} \bar{U}_i \bar{D}_j \bar{D}_k, \quad (1)$$

* This article was submitted by the author in English.

** e-mail: sirois@polhp2.in2p3.fr

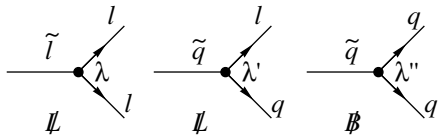

Fig. 1. Basic tree diagrams for trilinear $\not{R}_p$ interactions involving the Yukawa couplings λ or λ' ($\not{L}$), or λ" ($\not{B}$).

where a summation is implied over the generation indices *ijk* of the superfields *L*, *Q*, *E*, *D*, and *U*. The *L* and *Q* are left-handed doublets while *E*, *D*, and *U* are right-handed singlet superfields for charged leptons, down- and up-type quarks, respectively. A possible bilinear term [3] $\mu L_i H_2$ involving the Higgs doublet H_2, which will generally contribute to more mixing between the neutrinos and neutralinos after electroweak symmetry breaking [5], is assumed to be suppressed [6] and will not be considered further here.

The trilinear terms are permitted here given the presence of new scalars (sleptons and squarks). There are no equivalent terms in the SM, where triple fermion coupling is forbidden by Lorentz invariance. The λ and λ' terms induce $\not{L}$. The λ" terms induce $\not{B}$. The basic tree diagrams are illustrated in Fig. 1. The $\not{L}$ terms arise in a fundamental way from the fact that *SU*(2)-doublet lepton superfields and the Higgs H_1 superfield are identical when viewed from the SM gauge symmetry. The λ_{ijk} (λ''_{ijk}) couplings are antisymmetric under the interchange of the first (last) two generation indices, $\lambda_{ijk} = -\lambda_{jik}$ and $\lambda''_{ijk} = -\lambda''_{ikj}$. Hence, there are 9 (for each) independent λ and λ" couplings while 27 independent λ' couplings remain. Altogether 45 extra free parameters are grafted to minimal SUSY models.

In order to comply with the remarkable stability of the proton and the absence of n–$\bar{n}$ oscillations, it is mandatory to forbid somehow simultaneous presence of nonvanishing $\not{L}$ and $\not{B}$ couplings such that $\lambda \times \lambda'' \simeq 0$ and $\lambda' \times \lambda'' \simeq 0$. For this it is sufficient, for example, to impose the baryon-number conservation (*B* parity) as a viable [7] and less restrictive discrete symmetry. This implies λ" = 0 in (1).

This might be seen as a "natural" choice for cosmology where the observed matter/antimatter asymmetry imposes much more severe constraints [8] on λ" than on λ or λ'. On the contrary, $\not{L}$ terms do not unavoidably suffer from cosmological constraints [8] and are even required for baryon asymmetry genesis in some cosmological models with first-order electroweak phase transition [9]. Provided that baryon number is effectively conserved at low energy, sizable λ' couplings are consistent with GUT's, supergravity, and superstring theories [3, 7, 10].

2.2. The Lagrangian for R-Parity-Violating Interactions

Expanded in standard four-component Dirac notations, the Lagrangian of the theory corresponding to the λ, λ', and λ" scalar–spinor–spinor coupling terms of (1) can be written as

$$\mathcal{L}_{L_iL_j\bar{E}_k} = \lambda_{ijk}[\tilde{\nu}^i_L \bar{e}^k_R e^j_L + \tilde{e}^j_L \bar{e}^k_R \nu^i_L + (\tilde{e}^k_R)^* (\bar{\nu}^i_L)^c e^j_L - (i \longleftrightarrow j)] + \text{h.c.},$$

$$\mathcal{L}_{L_iQ_j\bar{D}_k} = \lambda'_{ijk}[-\tilde{e}^i_L u^j_L \bar{d}^k_R - e^i_L \tilde{u}^j_L \bar{d}^k_R - (\bar{e}^i_L)^c u^j_L \tilde{d}^{k*}_R + \tilde{\nu}^i_L d^j_L \bar{d}^k_R + \nu_L \tilde{d}^j_L \bar{d}^k_R + (\bar{\nu}^i_L)^c d^j_L \tilde{d}^{k*}_R] + \text{h.c.},$$

$$\mathcal{L}_{\bar{U}_i\bar{D}_j\bar{D}_k} = \lambda''_{ijk}\Big[(\bar{u}^i_R)^c d^j_R \tilde{d}^k_R + (\bar{u}^i_R)^c \tilde{d}^j_R d^k_R + \tilde{u}^i_R (\bar{d}^j_R)^c d^k_R\Big] + \text{h.c.},$$

where the superscripts *c* denote the charge-conjugate spinors and the asterisk labels the complex conjugate of scalar fields. The *R* and *L* chirality indices for the scalars distinguish independent fields corresponding to superpartners of right- and left-handed fermions, respectively.

Most of the searches carried out in collider experiments assume (for simplicity) a strong hierarchy among the Yukawa couplings such that the phenomenology is studied assuming the existence of only one sizable λ, λ', or λ" coupling. The search results are otherwise interpreted in the MSSM framework. The masses of the new squark and slepton scalars are treated as free parameters. In the gaugino–higgsino sector, there are four neutralino $\chi^0_{1,2,3,4}$ and two chargino $\chi^\pm_{1,2}$ mass eigenstates. The χ^0_m are mixed states of the photino $\tilde{\gamma}$, the zino $\tilde{Z}$, and the SUSY partners $\tilde{H}^0_1$ and $\tilde{H}^0_2$ of the two neutral Higgs fields. The $\chi^\pm_n$ are mixed states of the winos $\tilde{W}^\pm$ and of the SUSY partners of the charged Higgs fields. The masses and couplings of the χ^0 and $\chi^\pm$ are calculated in terms of the MSSM basic parameters:

M_1 and M_2, the *U*(1) and *SU*(2) soft-breaking gaugino mass terms;

μ, the mixing parameter associated to Higgs superfields;

$\tan\beta \equiv v_2/v_1$, the ratio of the vacuum expectation values of the two neutral Higgs fields.

The number of free parameters is reduced by assuming a relation at the Grand Unification (GUT) scale between M_1 and M_2, namely, $M_1 = (5/3)M_2 \tan^2\theta_W$,

where θ_W is the weak-mixing angle. No other GUT relations are used, and, in particular, the gluino ($\tilde{g}$) mass is left free. It is furthermore assumed for simplification that

all squarks (except the stop) are quasidegenerate in mass;

gluinos are heavier than the squarks such that real $\tilde{q} \longrightarrow q + \tilde{g}$ decays are kinematically forbidden;

the LSP is the lightest neutralino χ_1^0.

The latter is assumed notwithstanding the fact that there are no compelling cosmological constraint in $\not{R}_p$ models which imposes that the (generally) unstable LSP be neutral and colorless. It is nevertheless justified since other possible choices for the LSP (e.g., $\tilde{g}$ or $\chi^{\pm}$) would not significantly change the search and analysis strategy (e.g., at HERA). A possibly rich phenomenology emerges given even only one new nonvanishing lepton or baryon number Yukawa coupling.

3. *R*-PARITY-VIOLATING SUSY AT COLLIDERS

3.1. Searches in e^+e^- Collisions

Pair Production. Extensive searches for supersymmetric particles have been carried by the e^+e^- experiments at LEP collider under the assumption of $\not{R}_p$ via a single dominant $LL\bar{E}$, LQD, or $\bar{U}\bar{D}\bar{D}$ term for center-of-mass energies ranging from M_Z up to $\sqrt{s_{ee}} \simeq 183$ GeV [11]. Considering pair-produced sparticles through gauge couplings (e.g., gaugino and slepton pairs mediated by *s*-channel exchange of γ^* or Z^* boson), a major effort went into the investigation of the extent to which a $\not{R}_p$ coupling affects the experimental sensitivity to other MSSM parameters. The analyses are restricted to Yukawa coupling values $> \mathcal{O}(10^{-4})$ (assuming that the χ_1^0 is the LSP) so that the LSP decays within typically ~1 cm from the interaction point, but otherwise are not sensitive to specific values for a given coupling.

Essentially all possible direct and indirect decay modes of sparticles involving any given $\not{R}_p$ coupling have been considered in such studies. The existence of either a nonvanishing λ ($LL\bar{E}$), λ' (LQD), or λ'' ($\bar{U}\bar{D}\bar{D}$) can be readily distinguished. With $\lambda \neq 0$, the final states are characterized by a large number of charged leptons and escaping neutrinos. With $\lambda' \neq 0$, the final states are likely to contain multijets and multileptons (but slepton pair production would lead to four jet final states). Finally, $\lambda'' \neq 0$ leads to final states with very high jet multiplicities.

The broad conclusion which can be drawn from such analyses is that the sensitivity to MSSM parameters is generally at least as good as for the *R*-parity-conserving case, both for sfermion pair production and for the (μ, M_2) plane from the gaugino–higgsino sector. This implies restrictions on possible direct discoveries of SUSY through $\not{R}_p$ couplings that complements those derived from precision measurements of the Z total width Γ_Z which are applicable to any $\not{R}_p$ couplings.

Squark production processes at HERA (e^+ beam) via an *R*-parity-violating λ'_{1jk} coupling

λ'_{1jk}	Production process	
111	$e^+ + \bar{u} \longrightarrow \tilde{d}_R^*$	$e^+ + d \longrightarrow \tilde{u}_L$
112	$e^+ + \bar{u} \longrightarrow \tilde{s}_R^*$	$e^+ + s \longrightarrow \tilde{u}_L$
113	$e^+ + \bar{u} \longrightarrow \tilde{b}_R^*$	$e^+ + b \longrightarrow \tilde{u}_L$
121	$e^+ + \bar{c} \longrightarrow \tilde{d}_R^*$	$e^+ + d \longrightarrow \tilde{c}_L$
122	$e^+ + \bar{c} \longrightarrow \tilde{s}_R^*$	$e^+ + s \longrightarrow \tilde{c}_L$
123	$e^+ + \bar{c} \longrightarrow \tilde{b}_R^*$	$e^+ + b \longrightarrow \tilde{c}_L$
131	$e^+ + \bar{t} \longrightarrow \tilde{d}_R^*$	$e^+ + d \longrightarrow \tilde{t}_L$
132	$e^+ + \bar{t} \longrightarrow \tilde{s}_R^*$	$e^+ + s \longrightarrow \tilde{t}_L$
133	$e^+ + \bar{t} \longrightarrow \tilde{b}_R^*$	$e^+ + b \longrightarrow \tilde{t}_L$

Single Production. In e^+e^- collisions at LEP, the *s*-channel $\tilde{\nu}$ production via λ_{1j1} with $j = 1, 2$ is the only allowed resonant sparticle production. It was initially discussed in [4, 12], and searches were actually carried in the ALEPH and DELPHI experiments [13].

3.2. Searches in $e^{\pm}p$ Collisions

The $e^{\pm}p$ collider HERA, which provides both leptonic and baryonic quantum numbers in the initial state, is ideally suited for $\not{R}_p$-SUSY searches involving λ'.

Of particular interest for the $e^{\pm}p$ collider HERA are the terms $\lambda'_{ijk} L_i Q_j \bar{D}_k$ which allow for lepton-number-violating processes. This was first realized and investigated theoretically in [14], which motivated early experimental searches [15]. Among the 27 possible λ'_{ijk} couplings, the cases $i = 1$ can lead to direct squark resonant production through e–q fusion and are thus of special interest at HERA. In contrast to most indirect processes, HERA offers a high sensitivity to each of the nine λ'_{1jk} couplings as listed in the table for an e^+ beam. With an e^- beam, the corresponding charge conjugate processes are $e^- u_j \longrightarrow \tilde{d}_R^k$ ($e^- \bar{d}_k \longrightarrow \tilde{\bar{u}}_L^j$) for u-like (d-like) quarks of the jth (kth) generation. Squark pro-

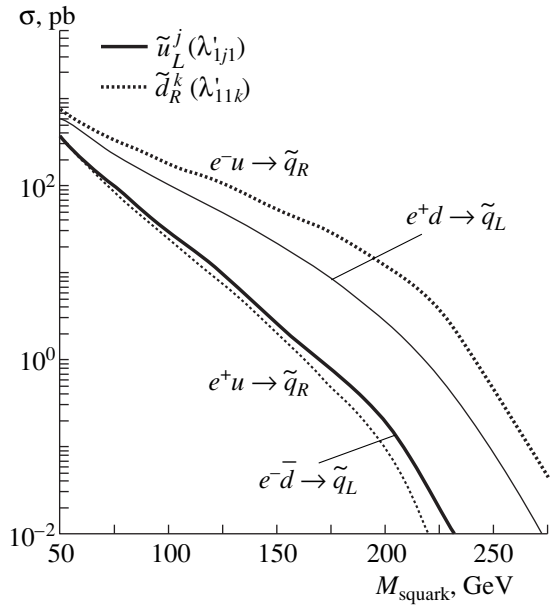

Fig. 2. Squark-production cross sections in *ep* collisions for a coupling $\lambda' = 0.1$.

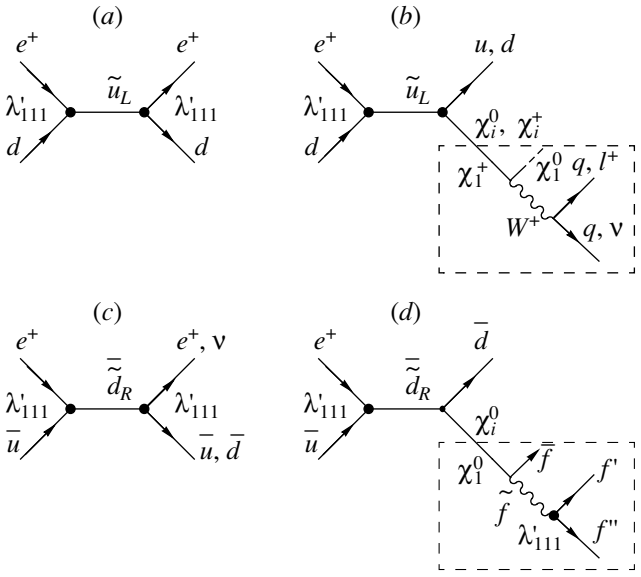

Fig. 3. Lowest order *s*-channel diagrams for first-generation-squark production at HERA followed by (*a*, *c*) $\not{R}_p$ decays and (*b*, *d*) gauge decays. In (*b*) and (*d*), the emerging neutralino or chargino might subsequently undergo $\not{R}_p$ decays, of which examples are shown in the dashed boxes for (*b*) the χ_1^+ and (*d*) the χ_1^0.

duction via λ'_{1j1} is especially interesting in e^+p collisions, as it involves a valence *d* quark, while λ'_{11k} are best probed with an e^- beam, since squark production then involves a valence *u* quark. This is seen in Fig. 2, which shows the production cross sections $\sigma_{\tilde{q}}$ for "up"-like squarks $\tilde{u}_L^j$ via λ'_{1j1} and for "down"-like squarks $\tilde{\bar{d}}_R^k$ via λ'_{11k}, each plotted for coupling values of $\lambda' = 0.1$. The *s*-channel diagrams for single squark production in *ep* collisions are illustrated in Fig. 3. By gauge symmetry, only $\tilde{u}_L$-like or $\tilde{d}_R$-like squarks (or their charge conjugates) can be produced in *ep* collisions. The production of "left" squarks is the dominating process if HERA delivers positrons, since the fusion occurs via a *d*-valence quark. On the contrary, with electrons in the initial state, mainly "right" squarks are produced. This dichotomy has important consequences since "left" and "right" squarks have different allowed or dominant decay modes. Recent investigations [16–18] have shown that a new and rich phenomenology (different for e^- and e^+ beams) emerges at HERA when considering the full complexity of the mixing in the gaugino–higgsino sector of the theory. In particular, new exotic final state topologies might have sizable contributions in e^+p collisions.

The squarks decay either via their λ' coupling into SM fermions or via their gauge couplings into a quark and a neutralino χ_m^0 or a chargino χ_n^+. The LSP decays via λ'_{1jk} into a quark, an antiquark, and a lepton. In cases where both production and decay occur through a λ'_{1jk} coupling (e.g., Figs. 3*a* and 3*c* for $\lambda'_{111} \neq 0$), the squarks behave as scalar LQs. The $\tilde{d}_R^{k*}$ can decay either into $e^+ + \bar{u}^j$ or $\nu_e + \bar{d}^j$. Gauge invariance forbids the $\tilde{u}_L^j \longrightarrow \nu q$ decay, and, hence, such squark type is left in the $\not{R}_p$ decay mode with $\tilde{u}_L^j \longrightarrow e^+ + d^k$. Hence, the final state signatures consist of a lepton and a jet and are, event-by-event, indistinguishable from the SM neutral and charged current DIS. In cases where the $\tilde{u}_L^j$ ($\tilde{d}_R^{k*}$) undergoes a gauge decay into a χ_α^0 or a χ_β^+ (χ_α^0) (e.g., Figs. 3*b* and 3*d*), the final state will depend on the subsequent decay of the χ. Neutralinos can undergo the $\not{R}_p$ decays $\chi_\alpha^0 \longrightarrow e^\pm q\bar{q}'$ or $\chi_\alpha^0 \longrightarrow \nu q\bar{q}$, the former (latter) being dominant if χ_α^0 is dominated by its photino (zino) component.

Overall, NC-like final states (from $\tilde{q}\not{R}_p$ decays) or $e^\pm$ + multijets final states (from squark gauge decays followed by gaugino–higgsino $\not{R}_p$ decays) are likely for a significant part of the Yukawa coupling–MSSM parameter space as discussed for HERA analysis in [18] and analyzed by H1 and ZEUS experiments [15, 19].

Apart from an excess of NC-like events at large Q_e^2 or large M_e observed in NC-like data, no significant

deviation from the SM expectations has been found in key topologies for squark $\not{R}_p$ and gauge decay channels. The rejection limits were derived as a function of the $\tilde{u}_L^j$ mass assuming that only one of the λ'_{1j1} is nonvanishing and combining all contributing channels. The masses of other sfermions were assumed to only influence weakly the branching ratios of the neutralinos and charginos [14, 20]. Rejection limits on λ'_{1j1} as a function of squark mass are shown in Fig. 4*a* for the $\tilde{u}_L^j$ when combining the relevant event topologies, taking into account either NC-like e^+ + jet only (*S*1), or NC-like e^+ + jet combined with e^+ + multijets (*S*3), or all three channels [including "wrong sign" e^- + multijets (*S*4)]. The MSSM parameters have been set here to $\mu = -200$ GeV, $M_2 = 70$ GeV, and $\tan\beta = 1.5$. With this choice of parameters, the lightest neutralino χ_1^0 is mainly dominated by its photino ($\tilde{\gamma}$) component and $M_{\chi_1^0} \simeq 40$ GeV, while the χ_1^+ and χ_2^0 are nearly degenerate around 90 GeV. Combining the three contributing channels improves the sensitivity on λ'_{1j1} by up to a factor of 5 at lowest mass compared to the one obtained using only the NC-like channel. The relative contributions of the three channels in the case where χ_1^0 is $\tilde{\gamma}$-like are plotted against the squark mass in Fig. 4*b* for λ' at the current sensitivity limit. It is seen that for masses up to $\simeq 230$ GeV, the channels e^+ + multijets and e^- + multijets have equal and dominant contributions. These channels play a decreasing role with increasing $M_{\tilde{q}}$ as squark decays into χ_1^+ and χ_2^0 become kinematically allowed. The χ_1^+ and χ_2^0 become dominated respectively by their wino and zino components [19, 18] and decay preferentially into $\nu q\bar{q}$ (a channel not covered in [19] except partly through CC-like analysis). In the very high mass domain, a large Yukawa coupling is necessary to allow squark production; hence, the relative contribution of e^+ + jet is largely enhanced. Another set of values for (μ, M_2, $\tan\beta$) leading to a 40 GeV χ_1^0 dominated by its zino ($\tilde{Z}$) component was considered in [19] to study the dependence of the rejection limits on the choice of MSSM parameters. In such a case, the χ_1^0 of the χ_1^+ decay preferably in $\nu q\bar{q}$ (rather than in eqq'), leading to multijets + $P_{T,\,\mathrm{miss}}^{\mathrm{vis}}$ topologies not easily separable from the SM background [19, 18] and, hence, not expected to contribute very much to the sensitivity to new physics. Since the gauge decay width of the squark does not depend on the Yukawa coupling λ'_{1j1}, the region of the plane (β_1, $M_{\tilde{q}}$) above the dotted line in Fig. 4*b* is excluded at 95% C.L.

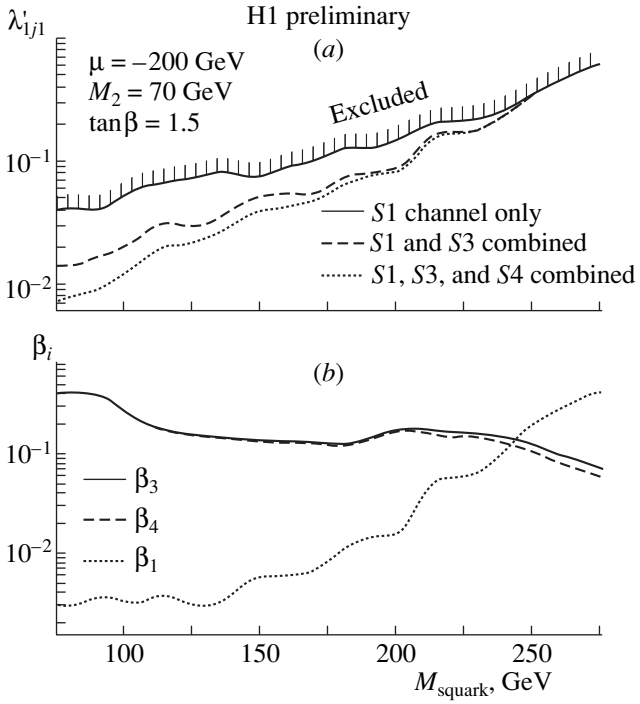

Fig. 4. (*a*) Exclusion upper limits at 95% C.L. for λ'_{1j1} as a function of the $M_{\tilde{q}}$, for a set of MSSM parameters leading to a 40 GeV χ_1^0 dominated by its $\tilde{\gamma}$ component. The limits are given for different possible combinations of the contributing channels. Regions above the curves are excluded. (*b*) The relative contributions of channels e^+ + jet, e^+ + multijets, and e^- + multijets versus $M_{\tilde{q}}$.

by H1 combined analysis. In particular the branching ratio of a 200 GeV $\tilde{u}_L^j$ squark into $e^+ + q$ is constrained to be smaller than $\simeq 1.5\%$ (Fig. 4*b*) for the MSSM parameter choice presented here. It should be noted, however, that other specific choices of (M_2, μ, $\tan\beta$) can allow for squarks at ~ 200 GeV to lead to NC-like topologies with $\beta_{eq} \gtrsim 10\%$.

Rejection limits obtained at HERA depending on the χ_1^0 mass and nature are compared in Fig. 5. The sensitivity to λ'_{1j1} for $M_{\tilde{q}} \lesssim 200$ GeV is better by a factor $\simeq 2$ for a $\tilde{\gamma}$-like χ_1^0 than for a χ_1^0 dominated by its $\tilde{Z}$ component, due to the highest part of total branching actually "seen" in the H1 analysis [19]. One can infer from previous $\not{R}_p$-SUSY searches at HERA [19] that the two cases presented here are somewhat "extreme" and in that sense quite representative of the sensitivity at HERA for any other choice of MSSM parameters leading to a $\simeq 40$ GeV χ_1^0. The sensitivity to λ'_{1j1} for $\tilde{\gamma}$-like χ_1^0 increases with $M_{\tilde{\gamma}}$ given the corresponding

increase of efficiency for the e + multijets channels. For $\lambda_{1j1} = \sqrt{4\pi\alpha_{em}}$, squark masses up to 262 GeV are excluded at 95% C.L. by this analysis, and up to 175 GeV for coupling strengths $\simeq 0.01\alpha_{em}$. For low masses, these limits represent an improvement of a factor $\simeq 3$ compared to H1 previously published results [19].

The rejection limits obtained at HERA are compared to the best indirect limits in Fig. 5. The most stringent indirect constraint comes from the nonobservation of neutrinoless double beta decay [21] but only concerns λ'_{111} coupling. The most severe indirect limits [22] on couplings λ'_{121} and λ'_{131}, which could allow for the production of squarks $\tilde{c}$ and $\tilde{t}$, respectively, come from APV [23]. It is seen that the sensitivity at HERA is better or comparable to the most stringent constraints on λ'_{121} and λ'_{131}. For large $M_{\chi_1^0}$ values, HERA limits improve the sensitivity on some λ' coupling by a factor up to $\simeq 4$.

LQ-like searches at the Tevatron imply stringent constraints on $\tilde{u}_L^j$ squark masses only if somehow β_{eq} can be made large. But as explained above, this is unlikely in $\not{R}_p$ SUSY for (say) $M_{\tilde{q}} \simeq 200$ GeV. Hence, LQ-like constraints from the Tevatron are easily evaded. The problem is that a small β_{eq} is so natural in $\not{R}_p$ SUSY [24] that, at first glance, only a minute portion of the MSSM parameter space is left if one would like to "explain" a NC-like signal at $M \simeq 200$ GeV in e^+p collisions via the production of a $\tilde{u}_L$-like squark (e.g., $\tilde{c}_L$ or $\tilde{t}_L$).

Actually, elegant solutions can be found as discussed below in the case of the $\tilde{t}_L$. Sizable branching ratios for both $\not{R}_p$ and gauge decay modes for a $\tilde{t}$ produced via λ'_{131} are very difficult to realize as argued in [25] when restricting to $\tilde{t}$ decays into $e + d$ and $b + \chi_1^+$. In particular, the conflicting requirements due to APV [23] constraints (implying a lower bound for β_{eq}) and to direct searches at the Tevatron (implying an upper bound on β_{eq}) are not easily accommodated. A special case occurs if there exists a very heavy χ_1^+ ($M_{\chi^+} > M_{\tilde{t}}$) and a light $\tilde{b}$ ($M_{\tilde{b}} < M_{\tilde{t}}$) such that the $\tilde{t}$ is left with the decay modes $\tilde{t} \longrightarrow e^+d$ and $\tilde{t} \longrightarrow \tilde{b}\,W^+$. This interesting possibility was first discussed in [26] as a way to "explain" simultaneously an excess in the NC-like channel and the striking observation [27] of LFV-like events with high $P_{T,\,\mathrm{miss}}^{\mathrm{vis}}$ containing a high P_T muon and jet(s). For a lightest $\tilde{b}$ mass $\simeq 100$ GeV, simultaneous sizable branching ratios β_{e^+d} and $\beta_{\tilde{b}W^+}$ become possible [17] for the $\tilde{t}$, thus extending the discovery potential at HERA for $M_{\tilde{t}} \simeq 200$–250 GeV.

3.3. Searches in $p\bar{p}$ Collisions

At the Tevatron, SUSY searches have been mainly carried out in the framework of SUGRA, which imposes mass relations between the sparticles and R-parity conservation. D0 [28] also considered squark pair production leading in $\not{R}_p$ SUGRA to like-sign dielectron events accompanied by jets and has ruled out $M_{\tilde{q}} < 252$ GeV (95% C.L.) when assuming five degenerate squark flavors. From a similar analysis by CDF [29] restricted to $\lambda'_{121} \neq 0$, one can infer that a cross section five times smaller would lead to a $M_{\tilde{q}}$ limit of ~150 GeV, depending on the gluino and χ^0 masses. The D0 analysis has been recently generalized [30] to cover all λ'_{1jk} couplings; CDF also considered separately [29, 31] the pair production of a light stop $\tilde{t}_1$, assuming a decay into $c\chi_1^0$, and excluded $M_{\tilde{t}} < 135$ GeV. To translate this constraint into that relevant to $\lambda'_{13k} \neq 0$, it should be noted that, in this latter case, $\not{R}_p$ decays of the $\tilde{t}$ would dominate over loop decays into $c\chi_1^0$. Moreover, $\not{R}_p$ decays would themselves be negligible compared to $\tilde{t} \longrightarrow b\chi_1^+$ decays as soon as this becomes allowed, i.e., if $M(\tilde{t}_1) > M(\chi_1^+)$ and if the $\tilde{t}_1$ eigenstate possesses a sizable admixture of $\tilde{t}_L$. The subsequent decays of the χ_1^+ would then lead to final states similar to those studied by CDF for $\tilde{t}_1 \longrightarrow c\chi_1^0$. Thus, 130–150 GeV appears to be a reasonable rough estimate of the Tevatron sensitivity to a light $\tilde{t}$ for $\lambda'_{13k} \neq 0$. In summary, Tevatron and HERA sensitivities are competitive in $\not{R}_p$-SUSY models with five degenerate squarks, but models predicting a light $\tilde{t}$ are better constrained at HERA provided that λ'_{13j} is not too small.

The λ'' coupling implies multijet final states for sparticle decays, which severely hampers the sensitivity in $p\bar{p}$ collisions at the Tevatron.

The lepton-number-violating couplings λ'_{ijk} allows for s-channel resonant production of sneutrinos ($\tilde{\nu}$) and charged sleptons ($\tilde{l}$) in hadronic collisions via $\bar{d}^j d^k \longrightarrow \tilde{\nu}^i$ and $\bar{u}^j d^k \longrightarrow \tilde{l}^{i+}$. The $\tilde{\nu}$ and $\tilde{l}^+$ will either decay back into quark–antiquark pairs through

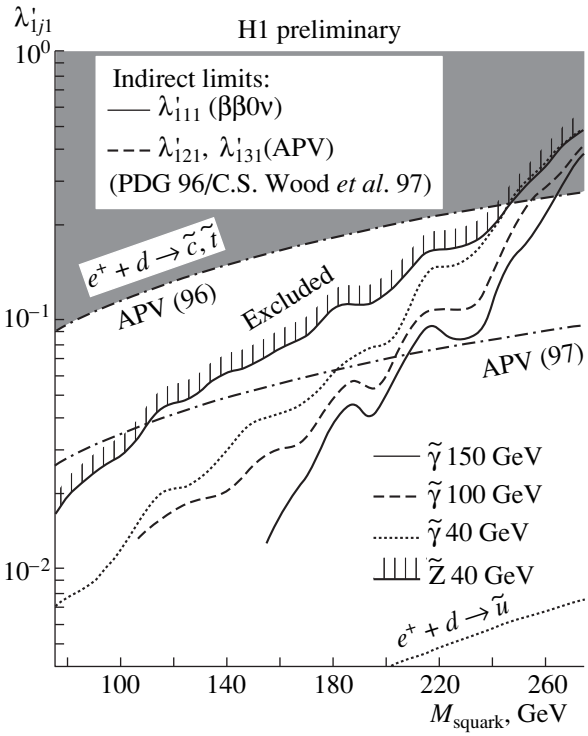

Fig. 5. Exclusion upper limits at 95% C.L. for the coupling λ'_{1j1} as a function of squark mass for various masses and mixtures of the χ^0_1; also represented are the most stringent indirect limits on λ'_{111} and λ'_{1j1}, $j = 2, 3$.

the same $\not{R}_p$ coupling or decay through gauge coupling as $\tilde{\nu}_i \longrightarrow \nu_i \chi^0_n$ and $\tilde{l}^{i+} \longrightarrow l^{i+} \chi^0_n$ where $n = 1, \ldots, 4$ is a neutralino mass eigenstate.

To my knowledge, the search for resonant slepton production via λ' has not been carried out yet in the D0 or CDF experiments at Tevatron. The feasibility was first discussed in [32], where relevant production cross sections and decays are presented together with an analysis of background sources. The topic has recently been extensively revisited in [33].

The baryon-number-violating couplings λ''_{ijk} allows for resonant production of squarks. In general the λ'' coupling implies multijet final states for sparticle decays, which severely hampers the sensitivity at the Tevatron. The case of the right-handed stop squark which proceeds via $\bar{d}^j \bar{d}^k \longrightarrow \tilde{t}_R$ is of particular interest since the lightest stop mass eigenstate $\tilde{t}_1$ could be the lightest squark. This *s*-channel production involves either λ''_{312}, λ''_{313}, or λ''_{323}. The $\tilde{t}_1$ will decay either back into antiquarks or, more favorably for experimental searches, via gauge decays as $\tilde{t}_1 \longrightarrow b\tilde{\chi}^+_n$ (or else if allowed via $\tilde{b}W^+$) with subsequent decay of the chargino, e.g., $\tilde{\chi}^+_1 \longrightarrow l^+ \nu \chi^0_1$. The search for resonant stop production via λ'' has not been explicitly carried through yet in the D0 or CDF experiments at Tevatron. An extensive prospective analysis in [33] has shown that, provided that the decay chain $\tilde{t}_1 \longrightarrow b\tilde{\chi}^+_1 \longrightarrow bl^+ \nu \chi^0_1$ is allowed, existing data at Tevatron could improve the sensitivity on λ'' by an order of magnitude compared to indirect constraints.

4. CONCLUSIONS

The observation by HERA experiments in their early Deep Inelastic Scattering data of possible deviations from Standard Model expectation in Neutral Current-like processes has considerably revived the interest in new theories requiring bosons with Yukawa couplings to lepton–quark pairs such as sfermions in *R*-parity-violating supersymmetry. Extensive searches carried out recently in collider experiments for manifestations of SUSY through *R*-parity-violating Yukawa couplings have been reviewed. Collider experiments are found to retain important discovery windows which shall be explored, in particular, in future high luminosity runs at HERA and at the Tevatron.

ACKNOWLEDGMENTS

I wish to thank the colleagues of the JINR in Dubna for their warm hospitality during the NANP'99 Conference. I thank the chairpersons of the organizing committee, Prof. V.B. Brudanin and Prof. S.G. Kovalenko, for providing me an opportunity to emphasize the complementarity between colliding and noncolliding experiments in the search for new physics involving the violation of leptonic or baryonic quantum numbers. Finally, I wish to thank members of the HERA Collider experiments H1 and ZEUS for their support.

REFERENCES

1. H. E. Haber and G. L. Kane, Phys. Rep. **117**, 75 (1985).
2. P. van Nieuwenhuizen, Phys. Rep. **68**, 189 (1981); H. P. Nilles, Phys. Rep. **110**, 1 (1984) and references therein.
3. L. J. Hall and M. Suzuki, Nucl. Phys. B **231**, 419 (1984).
4. S. Dawson, Nucl. Phys. B **261**, 297 (1985); S. Dimopoulos and L. J. Hall, Phys. Lett. B **207**, 210 (1988).
5. N. Polonsky, in *Proceedings of the 4th International Conference on Supersymmetries in Physics*, Ed. by R. Mohapatra (College Park, Maryland, 1996).
6. H. Dreiner, hep-ph/9707435.
7. L. E. Ibáñez and G. G. Ross, Nucl. Phys. B **368**, 3 (1992).
8. A. Nelson and S. Barr, Phys. Lett. B **246**, 141 (1990); H. Dreiner and G. G. Ross, Nucl. Phys. B **410**, 188 (1993).

9. A. Masiero and A. Riotto, Phys. Lett. B **289**, 73 (1992); U. Sarkar and R. Adhikari, hep-ph/9608209.
10. J. Ellis *et al.*, Phys. Lett. B **150**, 142 (1985); G. G. Ross and J. W. F. Valle, Phys. Lett. B **151**, 375 (1985); M. C. Bento, L. Hall, and G. G. Ross, Nucl. Phys. B **292**, 400 (1987); D. E. Brahm and L. J. Hall, Phys. Rev. D **40**, 2449 (1989); S. Lola and G. G. Ross, Phys. Lett. B **314**, 336 (1993); A. Yu. Smirnov and F. Vissani, Nucl. Phys. B **460**, 37 (1996); Phys. Lett. B **380**, 317 (1996).
11. ALEPH Collab. (D. Buskulic *et al.*), Phys. Lett. B **349**, 238 (1995); **384**, 461 (1996); R. Barate *et al.*, Eur. Phys. J. C **4**, 433 (1998); **7**, 383 (1999); Preprints Nos. CERN-EP/99-042, CERN-EP/99-033, CERN (Geneva, 1999); DELPHI Collab. (P. Abreu *et al.*), Preprint No. CERN-EP/99-049, CERN (Geneva, 1999); L3 Collab., Phys. Lett. B **414**, 373 (1997); **433**, 163 (1998); **459**, 354 (1999); OPAL Collab. (P. D. Acton *et al.*), Phys. Lett. B **313**, 333 (1993); Eur. Phys. J. C **6**, 1 (1999); G. Abbiendi *et al.*, Preprint No. CERN-EP/98-203, CERN (Geneva, 1998); 1999, Preprint Nos. CERN-EP/99-043, CERN-EP/99-097, CERN (Geneva, 1999).
12. V. Barger, G. F. Giudice, and T. Han, Phys. Rev. D **40**, 2987 (1989); H. Dreiner and S. Lola, hep-ph/9602207.
13. ALEPH Collab., Conference paper CONF 99-007 (March 1999); DELPHI Collab., Conference paper CONF 99-229 (March 1999).
14. J. Butterworth and H. Dreiner, Nucl. Phys. B **397**, 3 (1993).
15. H1 Collab. (T. Ahmed *et al.*), Z. Phys. C **64**, 545 (1994).
16. E. Perez and Y. Sirois, in *Proceedings of the Workshop on Supersymmetry and Unification of Fundamental Interactions, France, 1995* (Editions Frontiéres, Palaiseau, 1995), p. 21.
17. Y. Sirois, in *Proceedings of the 4th International Conference on Supersymmetries in Physics*, Ed. by R. Mohapatra (College Park, Maryland, 1996); hep-ph/9611457.
18. E. Perez and Y. Sirois, in *Proceedings of the Workshop on Dark Matter in Astro- and Particle Physics, 1997* (World Sci., Singapore, 1997), p. 615.
19. H1 Collab. (S. Aid *et al.*), Z. Phys. C **71**, 211 (1996); Contributed Paper 580, in *Proceedings of the 29th International Conference on High-Energy Physics, Vancouver, Canada, 1998*; H. C. Schultz-Coulon, Talk given at the 47th PRC Meeting at DESY, June 1999; ZEUS Collab., Contributed Paper 548, in *Proceedings of the International Europhysics Conference EPS 99, Tampere, Finland, July 1999.*
20. H. Dreiner and P. Morawitz, Nucl. Phys. B **428**, 31 (1994).
21. R. N. Mohapatra, Phys. Rev. D **34**, 3457 (1986); J. D. Vergados, Phys. Lett. B **184**, 55 (1987); M. Hirsch *et al.*, Phys. Lett. B **352**, 1 (1995); Phys. Rev. Lett. **75**, 17 (1995).
22. R. Barbier *et al.*, hep-ph/9810232.
23. P. Langacker, Phys. Lett. B **256**, 277 (1991); C. S. Wood *et al.*, Science **275**, 1759 (1997).
24. D. Choudhury and S. Raychaudhuri, Phys. Lett. B **401**, 54 (1997); H. Dreiner and P. Morawitz, Nucl. Phys. B **503**, 55 (1997); T. Kon and N. Kobayashi, Phys. Lett. B **409**, 265 (1997); G. Altarelli *et al.*, Nucl. Phys. B **506**, 29 (1997); J. Ellis *et al.*, Phys. Lett. B **408**, 252 (1997); J. E. Kim and P. Ko, Phys. Rev. D **57**, 489 (1998); R. Rückl and H. Spiesberger, in *Proceedings Workshop New Trends in HERA Physics, Hamburg, 1997* (DESY, Hamburg, 1997); A. S. Joshipura *et al.*, Phys. Rev. D **57**, 5327 (1998), and references therein.
25. G. Altarelli *et al.*, Nucl. Phys. B **506**, 3 (1997); **506**, 29 (1997).
26. T. Kon *et al.*, Mod. Phys. Lett. A **12**, 3143 (1997).
27. H1 Collab. (C. Adloff *et al.*), Eur. Phys. J. C **5**, 575 (1998).
28. D0 Collab., Contributed paper 588, in *Proceedings of the 29th International Conference on High Energy Physics, Vancouver, Canada, July 23–29, 1998.*
29. D0 and CDF Collab. (M. Chertok), in *Proceedings of the XXXIII Rencontres de Moriond, QCD and High Energy Hadronic Interactions, Les Arcs, France, 1998.*
30. D0 Collab. (B. Abbot *et al.*), hep-ex/9907019.
31. CDF Collab. (F. Abe *et al.*), Phys. Rev. Lett. **83**, 2133 (1999).
32. S. Dimopoulos *et al.*, Phys. Rev. D **41**, 2099 (1990).
33. B. Allanach *et al.*, hep-ph/9906224.

Physics of Atomic Nuclei, Vol. 63, No. 7, 2000, pp. 1137–1150. From Yadernaya Fizika, Vol. 63, No. 7, 2000, pp. 1213–1226.

NEW PHYSICS, NUCLEAR AND NUCLEON STRUCTURE IN RARE PROCESSES

Double-Beta Decay in Gauge Theories*

J. D. Vergados[1)]

Institut Theoretische Physik der Universität Tübingen, Germany

Abstract—Neutrinoless double-beta decay is a very important process both from the particle and nuclear physics point of view. From the elementary particle point of view, it pops up in almost every model, giving rise among others to the following mechanisms: (a) the traditional contributions like the light neutrino mass mechanism as well as the j_L–j_R leptonic interference (λ and η terms), (b) the exotic R-parity-violating supersymmetric (SUSY) contributions. Thus, its observation will severely constrain the existing models and will signal that the neutrinos are massive Majorana particles. From the nuclear physics point of view, it is challenging, because (1) the nuclei, which can undergo double-beta decay, have complicated nuclear structure; (2) the energetically allowed transitions are suppressed (exhaust a small part of all the strength); (3) since in some mechanisms the intermediate particles are very heavy one must cope with the short distance behavior of the transition operators (thus novel effects, like the double-beta decay of pions in flight between nucleons, have to be considered; in SUSY models, this mechanism is more important than the standard two-nucleon mechanism; and (4) the intermediate momenta involved are quite high (about 100 MeV/c). Thus one has to take into account possible momentum-dependent terms of the nucleon current, like modification of the axial current due to PCAC, weak magnetism terms, etc. We find that, for the mass mechanism, such modifications of the nucleon current for light neutrinos reduce the nuclear matrix elements by about 25%, almost regardless of the nuclear model. In the case of heavy neutrino, the effect is much larger and model-dependent. Taking the above effects into account, the needed nuclear matrix elements have been obtained for all the experimentally interesting nuclei A = 76, 82, 96, 100, 116, 128, 130, 136, and 150. Then, using the best presently available experimental limits on the half-life of the $0\nu\beta\beta$ decay, we have extracted new limits on the various lepton-violating parameters. In particular, we find $\langle m_\nu \rangle < 0.3$ eV/c^2, and, for reasonable choices of the parameters of SUSY models in the allowed SUSY parameter space, we get a stringent limit on the R-parity-violating parameter $\lambda'_{111} < 4.0 \times 10^{-4}$. © *2000 MAIK "Nauka/Interperiodica".*

1. INTRODUCTION

The nuclear double-beta decay can occur whenever the ordinary (single) beta decay is forbidden due to energy conservation or greatly suppressed due to angular momentum mismatch. The exotic neutrinoless double-beta decay ($0\nu\beta\beta$ decay) is the most interesting since it violates lepton number by two units. It is a very old process. It was first considered by Furry [1] exactly half a century ago as soon as it was realized that the neutrino might be a Majorana particle. It was continued with the work of Primakoff and Rosen [2] especially when it was recognized that kinematically it is favored by 10^8 compared to its nonexotic sister $2\nu\beta\beta$ decay. When the corresponding level of the 10^{15} yr lifetime was reached and the process was not seen, it was tempting to interpret this as an indication that the neutrino was a Dirac particle. The interest in it was resurrected with the advent of gauge theories which favor Majorana neutrinos, and through the pioneering work of Kotani and his group [3], it was brought again to the attention of the nuclear physics community. Today, fifty years later, $0\nu\beta\beta$ decay continues to be one of the most interesting processes.

From a theoretical point of view, it is the most likely, if not the only, process capable of deciding whether or not the neutrino is a Majorana particle; i.e., it coincides with its own antiparticle [4–9]. It is expected to occur whenever one has lepton-number-violating interactions. Lepton number, being a global quantity, is not sacred, but it is expected to be broken at some level. In short, this process pops up almost everywhere, in every theory.

From a nuclear physics point of view, calculating the relevant nuclear matrix elements is indeed a challenge. First, almost all nuclei that can undergo double-beta decay are far from closed shells, and some of them are even deformed. One thus faces a formidable task. Second, the nuclear matrix elements represent a small fraction of a canonical value (i.e., the matrix element to the energy nonallowed transition double Gamow–Teller resonance or some appropriate sum rule). Thus, effects which are normally negligible become important here. Third, in many models, the dominant mechanism for $0\nu\beta\beta$ decay does not involve intermediate light neutrinos, but very heavy particles, and one must be able to cope with the short-distance behavior of the relevant operators and wave functions.

* This article was submitted by the author in English.

[1)] Theoretical Physics Section, University of Ioannina, Greece; e-mail: vergados@cc.uoi.gr

1063-7788/00/6307-1137$20.00 © 2000 MAIK "Nauka/Interperiodica"

From the experimental point of view, it also very challenging to measure the slowest perhaps process accessible to observation, especially since it is realized that, even if one obtains only lower bounds on the lifetime for this decay, the extracted limits on the theoretical model parameters may be comparable, if not better, and complementary to those extracted from the most ambitious accelerator experiments.

The recent SuperKamiokande results have given the first evidence of physics beyond the Standard Model (SM) and, in particular, they indicate that the neutrinos are massive particles. It is important to proceed further and find out whether the neutrinos are Dirac or Majorana particles. As we have mentioned, there might be processes other than the conventional intermediate neutrino mechanism, which may dominate $0\nu\beta\beta$ decay. It has, however, been known that, whatever the lepton-violating process is, which gives rise to this decay, it can be used to generate a Majorana mass for the neutrino [10]. The study of the $0\nu\beta\beta$ decay is further stimulated by the development of Grand Unified Theories (GUTs) and Supersymmetric models (SUSY) representing extensions of the $SU(2)_L \otimes U(1)$ SM. The GUTs and SUSY offer a variety of mechanisms which allow the $0\nu\beta\beta$ decay to occur [11].

The best known possibility is via the exchange of a Majorana neutrino between the two decaying neutrons [4–9, 12]. Nuclear physics dictates that we study the light and heavy neutrino components separately. In the presence of only left-handed currents for light intermediate neutrinos, the obtained amplitude is proportional to a suitable average neutrino mass, which vanishes in the limit in which the neutrinos become Dirac particles. In the case of heavy Majorana neutrino components, the amplitude is proportional to the average inverse neutrino mass; i.e., it is again suppressed. In the presence of right-handed currents, one can have a contribution similar to the one above for heavy neutrinos but involving a different (larger) average inverse mass and some suppression due to the heaviness of W_R.

It is also possible to have, in addition, interference between the leptonic left and right currents, j_L–j_R interference. In this case, the amplitude in momentum space becomes proportional to the 4-momentum of the neutrino, and, as a result, only the light neutrino components become important. One now has two possibilities. First, the two hadronic currents have a chirality structure of the same kind J_L–J_R. Then, one can extract from the data a dimensionless parameter λ, which is proportional to the square of the ratio of the masses of the L and R gauge bosons, $\kappa = (m_L/m_R)^2$. Second, the two hadronic currents are left-handed, which can happen via the mixing of the two bosons. The relevant lepton-violating parameter η is now proportional to this mixing. Both of these parameters, however, involve the neutrino mixing, and they are proportional to the mixing between the light and heavy neutrinos.

In gauge theories, one has, of course, many more possibilities. Exotic intermediate scalars may mediate $0\nu\beta\beta$ decay [6]. These are not favored in current gauge theories and are not going to be further discussed. In superstring inspired models, one may have singlet fermions in addition to the usual right-handed neutrinos. Not much progress has been made on the phenomenological side of these models, and they are not going to be discussed further.

In recent years, supersymmetric models have been taken seriously, and semirealistic calculations are taking place. In standard calculations, one invokes universality at the GUT scale, employing all five parameters, and uses the renormalization-group (RG) equation to obtain all parameters (couplings and particle masses) at low energies. Hence, since such parameters are in principle calculable, one can use $0\nu\beta\beta$ decay to constrain some of the R-parity-violating couplings, which cannot be specified by the theory [13–19]. Recent review articles [8, 9] give a detailed account of the latest developments in this field.

From the above discussion, it is clear that one has to consider the case of heavy intermediate particles. One thus has to consider very short ranged operators in the presence of the nuclear repulsive core. If the interacting nucleons are pointlike, one gets negligible contributions. We know, however, that the nucleons are not pointlike and they have a structure described by a form-factor, which can be calculated in the quark model or parameterized in a dipole shape. This approach was first considered by Vergados [20], adopted later by almost everybody. The resulting effective operator has a range somewhat less than the proton mass (Section 4).

The other approach is to consider particles other than the nucleons present in the nuclear soup. For $0^+ \longrightarrow 0^+$, the most important such particles are the pions. One thus may consider the double-beta decay of pions in flight between nucleons, like

$$\pi^- \longrightarrow \pi^+, e^-, e^- \quad \text{and} \quad n \longrightarrow p, \pi^+, e^-, e^-. \qquad (1)$$

This contribution was first considered by Vergados [21] and was found to yield results of the same order as the nucleon mode with the above recipe for treating the short range behavior. It was revived by the Tübingen group [17, 18] in the context of R-parity-violating interactions, in which it appears to dominate.

One may explicitly consider six quark clusters in the nucleus. Then, there is no suppression due to the short nature of the operator, but the probability of finding these clusters in a nucleus must be estimated [22].

All the above approaches seem reasonable and lead to quite similar results. This gives us a great degree of confidence that the resulting matrix elements are sufficiently reliable, allowing double-beta decay to probe very important physics.

The other recent development is the better description of nucleon current by including momentum dependent terms, such as the modification of the axial current

due to PCAC and the inclusion of the weak magnetism terms. These contributions have been considered previously [12, 23], but only in connection with the extraction of the η parameter mentioned above. Indeed, these terms were very important in this case since they compete with the *p*-wave lepton wave function, which, with the usual currents, provides the lowest nonvanishing contribution. In the mass term, however, only slepton wave functions are relevant. So these terms have hitherto been neglected.

It was recently found [24] that for light neutrinos the inclusion of these momentum-dependent terms reduces the nuclear matrix element by about 25%, independently of the nuclear model employed. For the heavy neutrino, however, the effect can be larger and depends on the nuclear wave functions. The reason for expecting them to be relevant is that the average momentum $\langle q\rangle$ of the exchanged neutrino is expected to be large [25]. In the case of a light intermediate neutrino, the mean nucleon–nucleon separation is about 2 fm, which implies that the average momentum $\langle q\rangle$ is about 100 MeV. In the case of a heavy neutrino exchange, the mean internucleon distance is considerably smaller and the average momentum $\langle q\rangle$ is supposed to be considerably larger.

Since 0νββ decay is a two step process, one should in principle construct a sum over all the intermediate nuclear steps, a formidable job indeed in the case of the shell-model calculations (SMC). Since, however, the average neutrino momentum is much larger compared to the nuclear excitations, one can invoke closure using some average excitation energy (this does not apply in the case of 2νββ decays). Thus, one need construct only the initial and final 0^+ nuclear states. In the quasiparticle random phase approximation (QRPA), one must construct the intermediate states anyway. In any case, it was explicitly shown, taking advantage of the momentum-space formalism developed by Vergados [26], that this approximation is very good [27, 28]. The same conclusion was reached independently by others [29].

Granted that one takes into account all the above ingredients in order to obtain quantitative answers for the lepton-number-violating parameters from the results of 0νββ-decay experiments, it is necessary to evaluate the relevant nuclear matrix elements with high reliability. The methods used most extensively are the SMC (for a recent review, see [8]) and QRPA (for a recent review, see [8, 9]). The SMC is forced to use few single-particle orbitals, while this restriction does not apply in the case of QRPA. The latter suffers, of course, from the approximations inherent in the RPA method. So a direct comparison between them is not possible.

The SMC has a long history [30–36] in double-beta decay calculations. In recent years, it has led to large matrix calculations in traditional as well as Monte Carlo types of calculations [37–42] (for a more complete set of references, see [8]) and suitable effective interactions.

There have been a number of QRPA calculations covering almost all nuclear targets [43–53]. We also have seen some refinements of QRPA, like proton neutron pairing and inclusion of renormalization effects due to Pauli principle corrections [54, 55].

The above schemes, in conjunction with the other improvements mentioned above, offer some optimism in our efforts for obtaining nuclear matrix elements accurate enough to allow us to extract reliable values of the lepton-violating parameters from the data. We will review this in the case of most of the nuclear targets of experimental interest (^{76}Ge, ^{82}Se, ^{96}Zr, ^{100}Mo, ^{116}Cd, ^{128}Te, ^{130}Te, ^{136}Xe, ^{150}Nd).

2. THE INTERMEDIATE MAJORANA NEUTRINO MECHANISM

We shall consider the 0νββ-decay process assuming that the effective beta-decay Hamiltonian acquires the form

$$\mathcal{H}^{\beta} = \frac{G_F}{\sqrt{2}}[\bar{e}\gamma_\mu(1-\gamma_5)\nu^0_{eL}]J^{\mu\dagger}_L + [\bar{e}\gamma_\mu(1+\gamma_5)\nu^0_{eR}]J^{\mu\dagger}_R + \text{h.c.}, \quad (2)$$

where e and ν^0_{eL}, ν^0_{eR} are field operators representing the electron and the left-handed and the right-handed electron neutrinos in the weak-interaction basis, respectively. We suppose that neutrino mixing does take place according to

$$\nu^0_{eL} = \sum_{k=1}^{3} U^{(11)}_{ek}\nu_{kL} + \sum_{k=1}^{3} U^{(12)}_{ek}N_{kL}, \quad (3)$$

$$\nu^0_{eR} = \sum_{k=1}^{3} U^{(21)}_{ek}\nu_{kL} + \sum_{k=1}^{3} U^{(22)}_{ek}N_{kL}, \quad (4)$$

where ν_k (N_k) are fields of light (heavy) Majorana neutrinos with masses m_k ($m_k \ll 1$ MeV) and M_k ($M_k \gg 1$ GeV), respectively. The matrices $U^{(11)}_{ek}$ and $U^{(22)}_{ek}$ are approximately unitary, while the matrices $U^{(12)}_{ek}$ and $U^{(21)}_{ek}$ are very small (of order of the up quark divided by the heavy neutrino mass scales), so that the overall matrix is unitary. ν_k, N_k satisfy the Majorana condition: $\nu_k\xi_k = C\bar{\nu}^T_k$, $N_k\Xi_k = C\bar{N}^T_k$, where C denotes the charge conjugation and ξ, Ξ are phase factors (the eigenmasses are assumed positive).

2.1. The Majorana Neutrino Mass Mechanism

We will consider only $0^+_i \longrightarrow 0^+_f$ transitions. Then, both outgoing electrons are in the $s_{1/2}$ state. Thus, for the ground-state transition, restricting ourselves to the

mass mechanism, we obtain for the 0νββ-decay inverse half-life [4–9, 12],

$$[T^{0\nu}_{1/2}]^{-1} = G_{01}\left|\frac{\langle m_\nu\rangle}{m_e}M^{\text{light}}_{\langle m_\nu\rangle} + \eta^L_N M^{\text{heavy}}_{\eta_N}\right|^2 + \left|\eta^R_N M^{\text{heavy}}_{\eta_N}\right|^2. \quad (5)$$

The lepton-number nonconserving parameters, i.e., the effective neutrino mass $\langle m_\nu\rangle$ and η^L_N, η^R_N are given as follows:

$$\langle m_\nu\rangle = \sum_1^3 (U^{(11)}_{ek})^2 \xi_k m_k, \quad (6)$$

$$\eta^L_N = \sum_1^3 (U^{(12)}_{ek})^2 \Xi_k \frac{m_p}{M_k},$$
$$\eta^R_N = (\kappa^2+\epsilon^2)\sum_1^3 (U^{22}_{ek})^2 \Xi_k \frac{m_p}{M_k}, \quad (7)$$

where m_p (m_e) is the proton (electron) mass, κ is the mass squared ratio of W_L and W_R, and ϵ is their mixing. G_{01} is the integrated kinematical factor [5, 12]. The nuclear matrix elements associated with the exchange of light ($M^{\text{light}}_{\langle m_\nu\rangle}$) and heavy neutrino ($M^{\text{heavy}}_{\eta_N}$) must be computed in a nuclear model. Equation (5), however, applies to any intermediate particle.

At this point, we should stress that the main suppression in the mass terms comes from the smallness of neutrino masses. In the case of heavy neutrino, it is not only from the large values of neutrino masses but due to the small couplings, $U^{(12)}$ for the left-handed neutrinos and κ and ϵ for the right-handed ones.

2.2. The Leptonic Left–Right Interference Mechanism (λ and η Terms)

As we have already mentioned, in the presence of right-handed currents, one can have interference between the leptonic currents of opposite chirality. This leads to different kinematical functions and two new lepton violating parameters λ and η defined by

$$\eta = \epsilon\eta_{RL}, \quad \lambda = \kappa\eta_{RL},$$
$$\eta_{RL} = \sum_1^3 (U^{(21)}_{ek}U^{(11)}_{ek})\xi_k. \quad (8)$$

The parameters λ and η are small not only due to the smallness of the parameters κ and ϵ but in addition because of the smallness of $U^{(21)}$. All the above contributions vanish in the limit in which the neutrino is a Dirac particle.

Many nuclear matrix elements appear in this case, but they are fairly well known, and they are not going to be reviewed here (see, e.g., [4–9] and in our notation [12]). We only mention that in the case of the η we have additional contributions coming from the nucleon recoil term and the kinematically favored spin antisymmetric term. These dominate and lead to values of η much smaller than λ [12].

3. THE *R*-PARITY-VIOLATING CONTRIBUTION TO 0νββ DECAY

In SUSY theories, *R* parity is defined as

$$R = (-1)^{3B+L+2s} \quad (9)$$

with B = baryon, L = lepton numbers, and s being the spin. It is +1 for ordinary particles and –1 for their superpartners. *R*-parity violation has recently been seriously considered in SUSY models. It allows additional terms in the superpotential given by

$$W = \lambda_{ijk}L^a_i L^b_j E^c_k \epsilon_{ab} + \lambda'_{ijk}L^a_i U^b_j D^c_k \epsilon_{ab} + \lambda''_{ijk}U^c_i U^c_j D^c_k, \quad (10)$$

where a summation over the flavor indices i, j, k and the isospin indices a, b is understood (λ_{ijk} is antisymmetric in the indices i and j). The last term has no bearing in our discussion, but we will assume that it vanishes due to some discrete symmetry to avoid too fast a proton decay. The λ's are dimensionless couplings not predicted by the theory.

In the above notation L, Q are isodoublet and E^c, D^c isosinglet chiral superfields; i.e., they represent both the fermion and the scalar components. It was recognized quite sometime ago that the second term in the superpotential could lead to neutrinoless double-beta decay [13, 14] and was reexamined quite recently [17]. Typical diagrams at the quark level are shown in Fig. 1. Note that as intermediate states, in addition to the sleptons and squarks, one must consider the neutralinos, 4 states which are linear combinations of the gauginos and higgsinos, and the colored gluinos (supersymmetric partners of the gluons).

Whenever the process is mediated by gluons, a Fierz transformation is needed to lead to a colorless combination. The same thing is necessary whenever the fermion line connects a quark to a lepton. As a result, one gets at the quark level not only scalar (S) and pseudoscalar (PS) couplings, but tensor (T) couplings as well. This must be contrasted to the V and A structure of the traditional mechanisms. One, therefore, must consider how to transform these operators from the quark to the nucleon level.

3.1. The Lepton Violating Parameters with R-Parity Nonconservation

The effective lepton-violating parameter, assuming that pion exchange mode dominates, as the authors of

[9, 17] claim, is given by

$$\eta_{\rm SUSY} = (\lambda'_{111})^2 \frac{3}{8}(\chi_{PS}\eta_{PS} + \eta_T) \quad (11)$$

with η_{PS} (η_T) associated with the scalar and pseudoscalar (tensor) quark couplings given by

$$\eta_{PS} = \eta_{\tilde\chi,\tilde e} + \eta_{\tilde\chi,\tilde q} + \eta_{\tilde\chi,\tilde f} + \eta_{\tilde g} + 7\eta'_{\tilde g}, \quad (12)$$

$$\eta_T = \eta_{\tilde\chi,\tilde q} - \eta_{\tilde\chi,\tilde f} + \eta_{\tilde g} - \eta'_{\tilde g}. \quad (13)$$

They find $\chi_{PS} = 2/3$, but as we shall see it depends on ratios of nuclear matrix elements. For the diagram of Fig. 1*a*, one finds

$$\eta_{\tilde\chi,\tilde e} = \frac{2\pi\alpha}{(G_{\rm F}m_W^2)^2}(\kappa_{\tilde e})^2\left\langle\frac{m_p}{m_{\tilde\chi}}\right\rangle_{\tilde e\tilde e}. \quad (14)$$

For the diagram of Fig. 1*b*, one finds

$$\eta_{\tilde\chi,\tilde q} = \frac{\pi\alpha}{2(G_{\rm F}m_W^2)^2}\left[(\kappa_{\tilde d})^2\left\langle\frac{m_p}{m_{\tilde\chi}}\right\rangle_{\tilde d\tilde d} + (\kappa_{\tilde u})^2\left\langle\frac{m_p}{m_{\tilde\chi}}\right\rangle_{\tilde u\tilde u}\right], \quad (15)$$

$$\eta_{\tilde g} = \frac{\pi}{6}\alpha_s\frac{1}{(G_{\rm F}m_W^2)^2}[(\kappa_{\tilde d})^2 + (\kappa_{\tilde u})^2]\frac{m_p}{m_{\tilde g}}. \quad (16)$$

For the diagram of Fig. 1*c*, one finds

$$\eta_{\tilde\chi,\tilde f} = \frac{\pi\alpha}{2(G_{\rm F}m_W^2)^2}\left[\kappa_{\tilde e}\kappa_{\tilde d}\left\langle\frac{m_p}{m_{\tilde\chi}}\right\rangle_{\tilde e\tilde d} + \kappa_{\tilde e}\kappa_{\tilde u}\left\langle\frac{m_p}{m_{\tilde\chi}}\right\rangle_{\tilde e\tilde u} + \kappa_{\tilde d}\kappa_{\tilde u}\left\langle\frac{m_p}{m_{\tilde\chi}}\right\rangle_{\tilde d\tilde u}\right], \quad (17)$$

$$\eta'_{\tilde g} = \frac{\pi}{12}\alpha_s\frac{1}{(G_{\rm F}m_W^2)^2}\kappa_{\tilde d}\kappa_{\tilde u}\frac{m_p}{m_{\tilde g}}, \quad (18)$$

where

$$\kappa_X = \left(\frac{m_W}{m_X}\right)^2, \quad X = \tilde e_L, \tilde u_L, \quad \kappa_{\tilde d} = \left(\frac{m_W}{m_{\tilde d_R}}\right)^2, \quad (19)$$

$$\left\langle\frac{m_p}{m_{\tilde\chi}}\right\rangle_{\tilde f\tilde f'} = \sum_1^4 \epsilon_{\tilde\chi_i,\tilde f}\epsilon_{\tilde\chi_i,\tilde f'}\frac{m_p}{m_{\tilde\chi_i}}, \quad (20)$$

where $\epsilon_{\tilde\chi_i,\tilde f}$ and $\epsilon_{\tilde\chi_i,\tilde f'}$ are the couplings of the ith neutralino to the relevant fermion–sfermion, which are calculable [56]. Thus, ignoring the small Yukawa couplings coming via the higgsinos and taking into account only the gauge couplings, we find

$$\epsilon_{\tilde\chi_i,\tilde e} = \frac{Z_{2i} + \tan\theta_{\rm W}Z_{1i}}{\sin\theta_{\rm W}}, \quad (21)$$

$$\epsilon_{\tilde\chi_i,\tilde u} = \frac{Z_{2i} + (\tan\theta_{\rm W}/3)Z_{1i}}{\sin\theta_{\rm W}}, \quad (22)$$

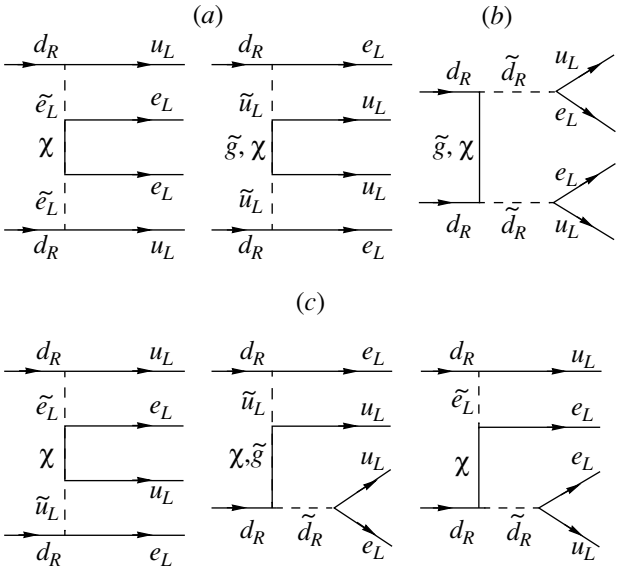

Fig. 1. The *R*-parity-violating contribution to 0νββ decay mediated by sfermions and neutralinos (gluinos).

$$\epsilon_{\tilde\chi_i,\tilde d} = -\frac{Z_{1i}}{3\cos\theta_{\rm W}}, \quad (23)$$

where Z_{1i}, Z_{2i} are the coefficients in the expansion of the $\tilde B$, $\tilde W_3$ in terms of the neutralino mass eigenstates. Note that in this convention some of the masses $m_{\tilde\chi_i}$ may be negative.

*3.2. The Pion Mode in R-Parity-Induced 0*νββ *Decay*

In this section we will elaborate a bit further on the *R*-parity-violating parameters. We will consider the pionic contribution (1). We will first attempt to evaluate the relevant amplitude using harmonic-oscillator wave functions, but adjusting the parameters to fit related experiments.

Let us begin with the second process of (1). This process involves a direct term and an exchange term. The direct term is nothing but a decay of the pion into two leptons with a simultaneous change of a neutron to a proton by the relevant nucleon current, which in this case can only be of the *PS* type. The tensor contribution cannot lead to a pseudoscalar coupling at the nucleon level, which is needed to be coupled to the usual pion–nucleon coupling in the other vertex to get the relevant operator for a $0^+ \longrightarrow 0^+$ decay. Thus, the amplitude involving the meson is related to π decay as

$$A_{1\pi}({\rm direct}) = 4\tilde\alpha_{1\pi}\frac{\boldsymbol\sigma_1\cdot\mathbf q}{(2m_N)}m_\pi^2. \quad (24)$$

The exchange contribution, in which the produced up quark of the meson is not produced from the "vacuum" but it comes from the initial nucleon, is a bit more

complicated. The harmonic-oscillator quark model, however, can be used to get its relative magnitude (including the sign) with respect to the direct term. In this his way, we find

$$A_{1\pi}(\text{exchange}) = -3\tilde{\alpha}_{1\pi}\frac{\boldsymbol{\sigma}_1\cdot\mathbf{q}}{(2m_N)}m_\pi^2 \tag{25}$$

with

$$\tilde{\alpha}_{1\pi} = (2\pi)^3\frac{m_N}{3m_q}\chi(0). \tag{26}$$

Thus, the effective two-body transition operator in the momentum space at the nucleon level becomes

$$\Omega_{1\pi}^{PS} = c_{1\pi}\left[\frac{(\boldsymbol{\sigma}_1\cdot\mathbf{q})(\boldsymbol{\sigma}_2\cdot\mathbf{q})}{(2m_N)^2}\exp\left(-\frac{(qb)^2}{6}\right)\right]\frac{m_\pi^2}{q^2+m_\pi^2} \tag{27}$$

with $c_{1\pi} = g_r\tilde{\alpha}_{1\pi}$, i.e.,

$$c_{1\pi} = (2\pi)^3\frac{m_N}{3m_q}q_r\chi(0), \tag{28}$$

where $g_r = 13.5$ is the pion–nucleon coupling and m_q is the constituent quark mass. We see that, in going from the quark to the nucleon level, the factor of three coming from the mass gain is lost due to the momentum being reduced by a factor of three. The quantity $\chi(0)$ is essentially the meson wave function at the origin given by

$$\chi(0) = \frac{\sqrt{6}}{2^{1/4}}m_\pi^{-3/2}\psi(0). \tag{29}$$

The quantity $\chi(0)$ can be obtained from the $\pi \longrightarrow \mu, \nu$ decay via the expression

$$\frac{1}{\tau} = \frac{1}{\pi}\left(\frac{G_F}{\sqrt{2}}\right)^2 m_\pi^2 m_\mu^2\left(1-\frac{m_\pi^2}{m_\mu^2}\right)^2\chi^2(0). \tag{30}$$

From the measured lifetime $\tau = 2.6\times10^{-8}$ s, we obtain $\chi(0) = 0.46$.

The first process of (1) is easier to handle. Now, both the *PS* and *T* terms contribute. We thus get

$$A_{2\pi}(T) = \frac{3}{8}\tilde{\alpha}_{2\pi}m^4, \quad A_{2\pi}(PS) = \frac{1}{8}\tilde{\alpha}_{2\pi}m^4, \tag{31}$$

$$\tilde{\alpha}_{2\pi} = 4(2\pi)^3\chi^2(0), \tag{32}$$

$$\Omega_{2\pi}^{T} = c_{2\pi}\frac{(\boldsymbol{\sigma}_1\cdot\mathbf{q})(\boldsymbol{\sigma}_2\cdot\mathbf{q})}{(2m_N)^2}\frac{m_\pi^4}{(q^2+m_\pi^2)^2}, \tag{33}$$

$$\Omega_{2\pi}^{PS} = \frac{2}{3}\Omega_{2\pi}^{T}, \tag{34}$$

with $c_{2\pi} = g_r^2\tilde{\alpha}_{2\pi}$, i.e.,

$$c_{2\pi} = 4(2\pi)^3 g_r^2\chi^2(0). \tag{35}$$

Using the above value of $\chi(0)$ and $g_r = 13.5$, we get $c_{1\pi} = 109$ and $c_{2\pi} = 198$, which are in good agreement with the values 132.4 and 170.3 respectively obtained by Faessler *et al*. [18]. It is now customary, but it can be avoided [26], to go to coordinate space and express the nuclear matrix elements in the same scale with the standard matrix elements involving only nucleons. Thus, we get

$$ME_k = \left(\frac{m_A}{m_p}\right)^2\alpha_{k\pi}\frac{m_p}{m_e}[M_{\text{GT}}^{k\pi} + M_T^{k\pi}], \tag{36}$$

where the two above matrix elements are the usual GT and *T* matrix elements with the additional radial dependence given by

$$F_{\text{GT}}^{1\pi} = e^{-x}, \quad F_T^{1\pi} = (3+3x+x^2)\frac{e^{-x}}{x}, \tag{37}$$

$$F_{\text{GT}}^{2\pi} = (x-2)e^{-x}, \quad F_T^{2\pi} = (1+x)e^{-x}, \tag{38}$$

$$\alpha_{1\pi} = -c_{1\pi}\rho, \quad \alpha_{2\pi} = c_{2\pi}\rho, \tag{39}$$

with

$$\rho = \frac{1}{48 f_A^2}\left(\frac{m_\pi}{m_p}\right)^4\left(\frac{m_p}{m_A}\right)^2. \tag{40}$$

In the above formulas, we have tried to stick to the definition of η_{SUSY} given above (11), but since the tensor (at the quark level) does not contribute to the 1π diagram the "effective" nuclear matrix element is not the sum of the two matrix elements of (36), but only ME_2, and χ_{PS} depends on the nuclear matrix elements, i.e.,

$$ME_{\text{eff}} = ME_2, \quad \chi_{PS} = \frac{2}{3}\left(4\frac{ME_1}{ME_2}+1\right). \tag{41}$$

There is no difference, of course, between the two expressions if ME_2 is dominant, as is actually the case.

Before proceeding further, we should remark that for the experimentally derived harmonic oscillator parameter for the π meson, $b = 1.8$ fm, $\alpha_{2\pi}$ is dominant and χ_{PS} approaches the value of 2/3. In fact we find $\alpha_{1\pi} = -1.2\times10^{-2}$ and $\tilde{\alpha}_{1\pi} = 0.15$, which are in good agreement with the values -4.4×10^{-2} and 0.20 respectively obtained by Faessler *et al.* [18]. Furthermore, from the nuclear matrix elements of [18], one can see that the $M^{2\pi}$ is favored, since, among other things, its tensor and Gamow–Teller components are the same magnitude and sign (in the 1π mode they are opposite). Thus, nuclear physics also favors the 2π mode.

4. THE EFFECTIVE NUCLEON CURRENT

As we have already mentioned, the operators are defined at the quark level, while the actual computations are done at the nucleon level. This procedure is very well understood for the usual one-step weak interactions, but in the case of neutrinoless double-beta

decay one has to be a bit careful. One has to tackle to problems. The first is the question of the correct treatment of short-range two-nucleon correlations, in particular, if the exchanged particles are heavy. The second involves the correct estimate of the momentum dependent corrections in the nucleon current.

4.1. The Correction to the Effective Nucleon Current for Short-Range Operators

The hadronic weak current at the quark level takes the form

$$j_L^{\mu\dagger} = \bar{q}\tau_+\gamma^\mu[1-\gamma_5]q. \quad (42)$$

Going to the nucleon level in the context of *V–A* theory is by now a straightforward procedure. One writes

$$J_L^{\mu\dagger} = \bar{\Psi}\tau^+\gamma^\mu[g_V(q^2) - g_A(q^2)\gamma_5]\Psi, \quad (43)$$

where $q^\mu = (p - p')_\mu$ is the momentum transferred from hadrons to leptons (p and p' are the four momenta of neutron and proton, respectively) and $g_V(q^2)$, $g_A(q^2)$ are real functions of a Lorentz scalar q^2, known as the vector and axial vector form factors. The values g_V and g_A of these form factors in the zero-momentum transfer limit are known as the vector and axial coupling constants, respectively, and take the values $g_V = 1$, $g_A = 1.254$. The needed form factors can be calculated in a given quark model. The nonrelativistic harmonic-oscillator quark model has certain advantages. One, e.g., can separate out the center of mass motions. Setting $g_V(q^2) = g_V(\mathbf{q}^2)$ and $g_A(q^2) = g_A(\mathbf{q}^2)$, one finds

$$\frac{g_A(\mathbf{q}^2)}{g_A} = \frac{g_V(\mathbf{q}^2)}{g_V} = \exp\left[-\frac{(|\mathbf{q}|b)^2}{6}\right]. \quad (44)$$

For momentum transfers that are not very large, we can approximate these form factors with a dipole shape: $g_V(\mathbf{q}^2) = g_V/(1 + \mathbf{q}^2/\Lambda_V^2)^2$ and $g_A(\mathbf{q}^2) = g_A/(1 + \mathbf{q}^2/\Lambda_A^2)^2$. In previous calculations, only one general cutoff $\Lambda_V = \Lambda_A = m_A \approx 0.85$ GeV was used (see below for a more up-to-date choice of the parameters). The above currents lead to the following two-body transition operator

$$\Omega_a = \tau_+(i)\tau_+(j)\omega_a\frac{R_0}{r_{ij}}F_a(r_{ij}), \quad a = V, \mathrm{GT}, \quad (45)$$

with

$$\omega_V = 1, \quad \omega_{\mathrm{GT}} = \boldsymbol{\sigma}(i)\cdot\boldsymbol{\sigma}(j). \quad (46)$$

If the mass of the exchanged particle between the two nucleons is much heavier than m_A, one finds ($x = m_A r_{ij}$)

$$F_V(r_{ij}) = F_{\mathrm{GT}}(r_{ij}) = \frac{m_A}{48m_e}F_N(x),$$
$$F_N(x) = x[x^2 + 3x + 3]e^{-x}. \quad (47)$$

Note that in the limit $m_A \longrightarrow \infty$, i.e., if the form factor is neglected, the radial functions become a δ function and the contribution of the heavy particles becomes zero in the presence of a hard core repulsion. In the presence of the form factor, however, the effective operator is characterized by a size if $1/m_A$ and gives a nonzero contribution even in the presence of a repulsive hard core. The form factor, however, causes some damping of the matrix elements compared to those without the form factor and without a hard core. The range of the effective operator is still large, compared to those resulting from pion exchange. As a result, the obtained matrix elements may be a bit more uncertain than the typical matrix elements encountered in the usual nuclear physics. In any case, one should calculate the resulting matrix elements as accurately as possible, even though the above uncertainties are typically much smaller than those of the underlying particle model, which gives rise to such mechanisms.

Before concluding this subsection, we should mention that the problem of form of the transition operator at short distances can be avoided if the $\beta\beta$ decay is induced by pions in flight between the two nucleons (see previous section). This is comparable to the contribution of the two-nucleon mode in the context of *V–A* theory [22] with $m_A = 0.85$ GeV. It can also be avoided if one employs the presence of six quark clusters inside the nucleus. In other words, the two-nucleon wave function at short distances, $r_{ij} < a_0$, is replaced by a colorless wave function of six quarks [22]. Then, the transition matrix element between the relative two-nucleon states (n, l) and (n', l') is proportional to $\sqrt{P_{nl}(a_0)P_{n'l'}(a_0)}$, where $P_{nl}P_{nl}$ is probability of finding the six quark clusters in the internal region of the relative two-nucleon wave function with quantum numbers (n, l). The results depend of course on the matching parameter a_0. Employing reasonable approximations, one finds [22] that this contribution is also comparable to the two-nucleon contribution with $m_A = 0.85$ GeV discussed above. Since in the above approaches the underlying physics is different, the obtained agreement allows one to have confidence in all of them.

4.2. Momentum-Dependent Corrections to the Effective Nucleon Current

As we have mentioned, the effective nucleon current in addition to the usual *V* and *A* terms (*PS*, *S*, *T* in SUSY contributions) contains momentum-dependent terms [24].

Within the impulse approximation, the nuclear current J_L^ρ in (2) expressed with nucleon fields Ψ takes the form

$$J_L^{\mu\dagger} = \bar{\Psi}\tau^+\left[g_V(q^2)\gamma^\mu - ig_M(q^2)\frac{\sigma^{\mu\nu}}{2m_p}q_\nu - g_A(q^2)\gamma^\mu\gamma_5 + g_P(q^2)q^\mu\gamma_5\right]\Psi, \quad (48)$$

where M is the nucleon mass and $\sigma^{\mu\nu} = (i/2)[\gamma^\mu, \gamma^\nu]$. $g_V(q^2)$, $g_M(q^2)$, $g_A(q^2)$, and $g_P(q^2)$ are the 4-nucleon form factors. The axial and vector form factors were discussed above. The values $g_M(q^2)$ and $g_P(q^2)$ in the zero-momentum transfer limit are known as weak-magnetism and induced pseudoscalar coupling constants, respectively.

For nuclear structure calculations, it is necessary to reduce the nucleon current to the nonrelativistic form. We shall neglect small energy transfers between nucleons in the nonrelativistic expansion. Then, the form of the nucleon current coincides with those in the Breit frame, and we arrive at [57],

$$J^\mu(\mathbf{x}) = \sum_{n=1}^{A} \tau_n^+ [g^{\mu 0} J^0(\mathbf{q}^2) + g^{\mu k} J_n^k(\mathbf{q}^2)]\delta(\mathbf{x} - \mathbf{r}_n), \quad k = 1, 2, 3, \tag{49}$$

with

$$J^0(\mathbf{q}^2) = g_V(q^2),$$
$$\mathbf{J}_n(\mathbf{q}^2) = g_M(\mathbf{q}^2) i\frac{\boldsymbol{\sigma}_n \times \mathbf{q}}{2M} + g_A(\mathbf{q}^2)\left[\boldsymbol{\sigma} - \frac{\mathbf{q}(\boldsymbol{\sigma}_n \cdot \mathbf{q})}{\mathbf{q}^2 + m_\pi^2}\right]. \tag{50}$$

Here, $\mathbf{r}_n$ is the coordinate of the nth nucleon. For the weak magnetism term, we shall use the following parametrization [24]:

$$g_M(\mathbf{q}^2) = (\mu_p - \mu_n) g_V(\mathbf{q}^2),$$

where $(\mu_p - \mu_n) = 3.70$, $\Lambda_V^2 = 0.71$ GeV^2 [58], and $\Lambda_A = 1.09$ GeV [59]. In previous calculations, only one general cutoff $\Lambda_V = \Lambda_A \approx 0.85$ GeV was used. In our discussion of the effects of the modified nucleon current, we take the empirical value of Λ_A deduced from the antineutrino quasielastic reaction $\bar{\nu}_\mu p \longrightarrow \mu^+ n$. A larger value of the cutoff Λ_A is expected to increase slightly the values of corresponding nuclear matrix elements. It worth noting that with these modifications of the nuclear current one gets a new contribution in the neutrino mass mechanism, namely, the tensor contribution. The two-body effective transition operator takes in momentum space the form

$$\Omega = \tau_+\tau_+(-h_F + h_{GT}\sigma_{12} - h_T S_{12}), \tag{51}$$

where the three terms correspond to Fermi (F), Gamow–Teller (GT), and tensor (T). One finds that

$$S_{12} = 3(\boldsymbol{\sigma}_1 \cdot \hat{q})(\boldsymbol{\sigma}_2 \cdot \hat{q}) - \sigma_{12},$$
$$\sigma_{12} = \boldsymbol{\sigma}_1 \cdot \boldsymbol{\sigma}_2, \tag{52}$$
$$h_F = g_V^2(\mathbf{q}^2),$$

$$h_{GT}(\mathbf{q}^2) = g_A^2(\mathbf{q}^2)\left[1 - \frac{2}{3}\frac{\mathbf{q}^2}{\mathbf{q}^2 + m_\pi^2} + \frac{1}{3}\left(\frac{\mathbf{q}^2}{\mathbf{q}^2 + m_\pi^2}\right)^2\right] + \frac{2}{3}\frac{g_M^2(\mathbf{q}^2)\mathbf{q}^2}{4m_p^2}, \tag{53}$$

$$h_T(\mathbf{q}^2) = g_A^2(\mathbf{q}^2)\left[\frac{2}{3}\frac{\mathbf{q}^2}{\mathbf{q}^2 + m_\pi^2} - \frac{1}{3}\left(\frac{\mathbf{q}^2}{\mathbf{q}^2 + m_\pi^2}\right)^2\right] + \frac{1}{3}\frac{g_M^2(\mathbf{q}^2)\mathbf{q}^2}{4m_p^2}.$$

The exact results will depend on the details of the nuclear model, since the new operators have different momentum (radial) dependence than the traditional ones and the tensor component is entirely new. We can get a crude idea of what is happening by taking the above average momentum $\langle q \rangle = 100$ MeV/c. Then, we find that the GT *ME* is reduced by 22%. Then, assuming, that T matrix element is about half the GT one, we find that the total reduction is 28%. This is in perfect agreement with the exact results for the $A = 76$ system, 29%, but a bit smaller than the 38% obtained for the $A = 130$ system. We will now summarize the results obtained with the above modifications of nucleon current. The details of our calculations will be given elsewhere [24]. A detailed study of Fermi, Gamow–Teller, and tensor contribution to the full nuclear matrix element $M^{\text{light}}_{\langle m_\nu \rangle}$ in (5) for the two representative $0\nu\beta\beta$-decay nuclei ^{76}Ge

Table 1. The Fermi, Gamow–Teller, and tensor nuclear matrix elements for the light Majorana neutrino exchange of the $0\nu\beta\beta$ decay of ^{76}Ge and ^{130}Te with (rows 2 and 4) and without (rows 1 and 3) short-range correlations

Transition	Gamow–Teller			Tensor		M_F^{light}	M_{GT}^{light}	M_T^{light}
	AA	*AP*	*PP*	*AP*	*PP*			
^{76}Ge	5.132	–1.392	0.302	–0.243	0.054	–2.059	4.042	–0.188
	2.797	–0.790	0.176	–0.246	0.055	–1.261	2.183	–0.190
^{130}Te	4.158	–1.173	0.258	–0.329	0.074	–1.837	3.243	–0.255
	1.841	–0.578	0.134	–0.333	0.075	–1.033	1.397	–0.258

Table 2. Nuclear matrix elements for the light and heavy Majorana neutrino exchange modes of the $0\nu\beta\beta$ decay for the nuclei studied in this work calculated within the renormalized *pn*-QRPA

M.E.	$(\beta\beta)_{0\nu}$ decay: $0^+ \longrightarrow 0^+$ transition								
	^{76}Ge	^{82}Se	^{96}Zr	^{100}Mo	^{116}Cd	^{128}Te	^{130}Te	^{136}Xe	^{150}Nd
	Light Majorana neutrino (I = light)								
M^I_{VV}	0.80	0.74	0.45	0.82	0.50	0.75	0.66	0.32	1.14
M^I_{AA}	2.80	2.66	1.54	3.30	2.08	2.21	1.84	0.70	3.37
M^I_{PP}	0.23	0.22	0.15	0.26	0.15	0.24	0.21	0.11	0.35
M^I_{AP}	–1.04	–0.98	–0.65	–1.17	–0.69	–1.04	–0.91	–0.48	–1.53
$M^I_{\langle m_\nu\rangle}$	2.80	2.64	1.49	3.21	2.05	2.17	1.80	0.66	3.33
	Heavy Majorana neutrino (I = heavy)								
M^I_{VV}	23.9	22.0	16.1	28.3	17.2	25.8	23.4	13.9	39.4
M^I_{MM}	–55.4	–51.6	–38.1	–67.3	–39.8	–60.4	–54.5	–31.3	–92.0
M^I_{AA}	106	98.3	68.4	123	74.0	111	100	58.3	167
M^I_{PP}	13.0	12.0	9.3	16.1	9.1	14.9	13.6	7.9	23.0
M^I_{AP}	–55.1	–50.7	–41.1	–70.1	–39.0	–64.9	–59.4	–34.8	–101
$M^I_{\eta_N}$	32.6	30.0	14.7	29.7	21.5	26.6	23.1	14.1	35.6

Table 3. The present state of the Majorana neutrino mass searches in $\beta\beta$-decay experiments. $T^{\exp-0\nu}_{1/2}$(present) is the best presently available lower limit on the half-life of the $0\nu\beta\beta$ decay for a given isotope. (The corresponding upper limits on lepton-number-nonconserving parameters $\langle m_\nu\rangle$ and η_N are presented. For the definition of the references and "best," see main body of the text)

Nucleus	^{76}Ge	^{82}Se	^{96}Zr	^{100}Mo	^{116}Cd
$T^{\exp-0\nu}_{1/2}$ (present), yr	1.1×10^{25}	2.7×10^{22}	3.9×10^{19}	5.2×10^{22}	2.9×10^{22}
Ref.	[Exp1]	[Exp2]	[Exp3]	[Exp4]	[Exp5]
$\langle m_\nu\rangle$, eV	0.62	6.3	203	2.9	5.9
$T^{\exp-0\nu}_{1/2}(\langle m_\nu\rangle^{\rm best})$, yr	1.1×10^{25}	2.8×10^{24}	4.2×10^{24}	1.2×10^{24}	2.6×10^{24}
η_N	1.0×10^{-7}	1.1×10^{-6}	4.0×10^{-5}	6.2×10^{-7}	1.1×10^{-6}
$T^{\exp-0\nu}_{1/2}(\eta_N^{\rm best})$, yr	1.1×10^{25}	2.9×10^{24}	5.8×10^{24}	1.8×10^{24}	3.2×10^{24}

Nucleus	^{128}Te	^{130}Te	^{136}Xe	^{150}Nd
$T^{\exp-0\nu}_{1/2}$ (present), yr	7.7×10^{24}	8.2×10^{21}	4.2×10^{23}	1.2×10^{21}
Ref.	[Exp6]	[Exp7]	[Exp8]	[Exp9]
$\langle m_\nu\rangle$, eV	1.8	13	4.9	8.5
$T^{\exp-0\nu}_{1/2}(\langle m_\nu\rangle^{\rm best})$, yr	6.6×10^{25}	3.8×10^{24}	2.7×10^{25}	2.3×10^{23}
η_N	2.9×10^{-7}	2.0×10^{-6}	4.5×10^{-7}	1.6×10^{-6}
$T^{\exp-0\nu}_{1/2}(\eta_N^{\rm best})$, yr	5.9×10^{25}	3.1×10^{24}	7.9×10^{24}	2.7×10^{23}

and ^{130}Te is presented in Table 1. One notices significant additional contributions to GT (*AP* and *PP*) and tensor (*AA* and *PP*) nuclear matrix elements coming from higher order nucleon current terms. *AP* and *PP* originate from the second (first) and third (second) terms in $h_{\rm GT}$ (h_T) of (53).

By glancing at the Table 1, we also see that, with proper treatment of short-range two-nucleon correla-

Table 4. The lifetimes predicted for $0^+ \longrightarrow 0^+$ $0\nu\beta\beta$ decay in various mechanisms (light neutrino, heavy neutrino, λ and η terms, and SUSY contribution) for suitable input of lepton-violating parameters and available nuclear calculations (for the definitions of the references see main body of the text)

Ref.	$(\beta\beta)_{0\nu}$ decay: $0^+ \longrightarrow 0^+$ transition $T_{1/2}^{\mathrm{theor}-0\nu}(\langle m_\nu\rangle, \langle\lambda\rangle, \langle\eta\rangle, \langle\eta_N\rangle, \langle\eta_{\mathrm{SUSY}}\rangle)$, yr									
	^{48}Ca	^{76}Ge	^{82}Se	^{96}Zr	^{100}Mo	^{116}Cd	^{128}Te	^{130}Te	^{136}Xe	^{150}Nd
	10^{24}	10^{24}	10^{24}	10^{24}	10^{24}	10^{24}	10^{25}	10^{24}	10^{24}	10^{22}
	$\langle m_\nu\rangle = 1$ eV, $\langle\lambda\rangle = 0$, $\langle\eta\rangle = 0$, $\langle\eta_N\rangle = 0$, $\langle\eta_{\mathrm{SUSY}}\rangle = 0$									
R	12.8	34.8	4.80						24.2	
H	6.34	3.36	1.16				0.80	0.32		
E1		4.60	1.84				0.90	0.48		
E2		28.0	11.2				3.00	1.32	6.60	
S		8.12	2.86				3.60	1.66		
M		4.66	1.20		2.54		1.54	0.98	4.42	6.74
T		4.32	1.22		0.52		1.96	1.08	2.80	8.90
P1	5.00	7.20	3.00	1.22	7.80	9.40	3.80	1.72	6.60	
P2	56.0	36.0	5.60	54.0		9.80	30.0	4.20	5.60	
S1		17.9			0.50	1.44	2.18		17.5	
P		4.22	1.08	1.61	0.46	0.99	2.53	1.46	10.1	8.78
	$\langle m_\nu\rangle = 0$, $\langle\lambda\rangle = 10^{-6}$, $\langle\eta\rangle = 0$, $\langle\eta_N\rangle = 0$, $\langle\eta_{\mathrm{SUSY}}\rangle = 0$									
R	7.45	50.2	3.25						22.2	
S		7.75	1.14				14.8	0.89		
M		7.35	0.99		0.95		13.5	0.95	4.90	3.73
T		8.02	1.07		0.55		21.1	1.18	3.47	6.71
P1	2.71	8.90	2.08	0.94	30.6	39.1	22.7	1.34	2.73	
P2	27.9	41.2	4.39	27.7	10.3	10.8	165	2.22	4.42	
	$\langle m_\nu\rangle = 0$, $\langle\lambda\rangle = 0$, $\langle\eta\rangle = 10^{-8}$, $\langle\eta_N\rangle = 0$, $\langle\eta_{\mathrm{SUSY}}\rangle = 0$									
R	6.42	27.2	6.24						22.2	
S		36.7	11.1				10.7	5.92		
M		7.35	0.99		0.95		13.5	0.95	4.90	3.73
T		2.25	0.65		0.28		0.67	0.44	1.21	3.39
P1	15.11	3.10	6.51	1.48	3.44	19.2	1.20	0.62	1.23	
P2	43.2	22.8	5.16	7.95	102	83.2	1.90	1.05	0.96	
	$\langle m_\nu\rangle = 0$, $\langle\lambda\rangle = 0$, $\langle\eta\rangle = 0$, $\langle\eta_N\rangle = 10^{-7}$, $\langle\eta_{\mathrm{SUSY}}\rangle = 0$									
P1	4.95	0.25	3.35	67.1	4.70	23.5	0.78	3.03	1.42	
P2	124	0.59	7.23	671	1.47	33.6	1.27	1.31	1.01	
P		15.4	4.10	8.10	0.97	8.40	8.51	4.54	3.94	40.6
	$\langle m_\nu\rangle = 0$, $\langle\lambda\rangle = 0$, $\langle\eta\rangle = 0$, $\langle\eta_N\rangle = 0$, $\langle\eta\rangle_{\mathrm{SUSY}} = 10^{-8}$									
F		3.3	0.86	0.71	0.30	0.85	0.93	0.45	1.2	3.2
P		4.5	1.0	1.4	0.59	1.4	1.5	0.71	2.0	5.2

Table 5. A sample of relevant parameters obtained by some choices in the allowed SUSY parameter space [it is clear that in all cases the neutralino-mediated mechanism is dominant (for definitions see main body of the text); the parameters C shown have been multiplied by 10^{-3}]

Input	Kane *et al.*			Ramond *et al.*					
	1	2	3	4	5	6	7	8	9
$\tan\beta$	10	1.5	5.0	5.4	2.7	2.7	5.2	2.6	6.3
$m_{\chi_1^0}$	124	26	96	83	124	58	34	34	50
$m_{\chi_2^0}$	237	65	173	150	204	108	66	74	92
$m_{\chi_3^0}$	455	219	310	391	445	336	170	191	208
$m_{\chi_4^0}$	471	263	342	409	472	361	208	236	244
$m_{\tilde{e}_L}$	328	124	211	426	472	310	90	94	109
$m_{\tilde{u}_L}$	700	283	570	590	664	449	251	275	319
$m_{\tilde{d}_R}$	676	276	550	577	638	441	246	268	310
$m_{\tilde{g}}$	718	292	610	483	706	371	280	304	350
$C_{\tilde{\chi}^0} \times 10^{-3}$	3.3	0.023	0.46	5.9	14	1.4	0.0068	0.0089	0.019
$C_{\tilde{g}} \times 10^{-3}$	14	1.6	54	56	110	13	0.97	1.5	3.1
$C_{\tilde{\chi}^0,\tilde{g}} \times 10^{-3}$	3.2	0.023	0.45	5.3	12	1.3	0.0068	0.0089	0.019

tions [6], all matrix elements are strongly suppressed. The effect is even stronger in the case of heavy intermediate particles. Detailed results [24] for various nuclei are presented in Table 2.

5. EXTRACTION OF THE LEPTON-VIOLATING PARAMETERS

The limits deduced for the lepton-number-violating parameters depend on the values of nuclear matrix element, of the kinematical factor, and of the current experimental limit for a given isotope [see (5)].

5.1. Traditional Lepton-Violating Parameters

Even though we expect the nuclear matrix elements entering the light neutrino mass mechanism to be decreased by about 30%, independently of the nuclear model, we will stick to the calculations as reported. Thus the present best experimental limits [60–70] can be converted to upper limits on $\langle m_\nu \rangle$ and η_N.

The results obtained are given in Table 3. The references of Table 3 are defined as follows: Exp1 = Heidelberg–Moscow Collaboration [60], Exp2 = Elliott *et al.* [61], Exp3 = Kawashima *et al.* [62], Exp4 = Ejiri *et al.* [63], Exp5 = Danevich *et al.* [64], Exp6 = Bernatovicz *et al.* [65], Exp7 = Alessandrello *et al.* [66], Exp8 = De Silva *et al.* [68], Exp9 = Busto *et al.* [67]. Thus, the most restrictive limits are as follows [24, 60]:

$$\langle m_\nu \rangle^{\text{best}} < 0.62 \text{ eV}, \tag{54}$$

$$\langle \eta_N \rangle^{\text{best}} < 1.0 \times 10^{-7}. \tag{55}$$

By assuming $\langle m_\nu \rangle = \langle m_\nu \rangle^{\text{best}}$ and $\eta_N = \eta_N^{\text{best}}$, we calculated half-lives (5) of the $0\nu\beta\beta$ decay $T_{1/2}^{\text{exp}-0\nu}(\langle m_\nu \rangle^{\text{best}})$ and $T_{1/2}^{\text{exp}-0\nu}(\eta_N^{\text{best}})$ for nuclear systems of interest using specific mechanisms with the "best" parameters. The thus obtained results are also given in Table 3. Since the quantities $\langle m_\nu \rangle$ and η_N depend only on particle theory parameters, these quantities indicate the experimental half-life limit for a given isotope, which the relevant experiments should reach in order to extract the best present bound on the corresponding lepton-number-violating parameter from their data. Some of them have a long way to go to reach the Ge target limit.

A summary involving most of the available nuclear matrix elements and taking into account what, at present, is a good guess as canonical values of the lepton-violating parameters is provided in Table 4. The references in this table are defined as follows: R = Retamosa *et al.* [37], H = Haxton *et al.* [31], E1 = Engel *et al.* [46], E2 = Engel *et al.* [43], S = Suhonen *et al.* [29], M = Muto *et al.* [45], T = Tomoda *et al.* [7], P1 = Pantis *et al.* [12], P2 = Pantis *et al.* [12] (*p*–*n* pairing), S1 = Šimkovic *et al.* [52] (and private communication), F = Faessler *et al.* [18, 19], P = present calculation (see Šimkovic *et al.* [24] for the nuclear matrix elements). Notice, in particular, that the present calculation, marked P in Table 4, involves not only renormalized QRPA [25, 55], but takes into account the corrections in the hadronic current [24] discussed above (Table 3).

Table 6. The limits for η_{SUSY} and λ'_{111} obtained: (a) for the pion mechanism using the values of $\alpha_{1\pi}$ and $\alpha_{2\pi}$ computed in this work and the nuclear *ME* of Faessler *et al.* (F) and (b) using the nuclear *ME* of the two nucleon mode of Wodecki *et al.* (in extracting the values of λ'_{111}, we used the SUSY data of case 7 of Table 5; the experimental lifetimes employed are those of Table 4)

(*A*, *Z*)	Pion mode				Only nucleons	
	η_{SUSY} (P)	λ'_{111} (P)	η_{SUSY} (F)	λ'_{111} (F)	η_{SUSY} (P)	λ'_{111} (P)
^{76}Ge	8.4×10^{-9}	6.0×10^{-4}	5.5×10^{-9}	4.8×10^{-4}	2.6×10^{-8}	1.1×10^{-3}
^{100}Mo	3.2×10^{-8}	1.8×10^{-3}	2.4×10^{-8}	1.1×10^{-3}	1.1×10^{-7}	2.2×10^{-3}
^{116}Cd	7.6×10^{-8}	1.8×10^{-3}	5.4×10^{-8}	1.5×10^{-3}	2.6×10^{-7}	3.3×10^{-3}
^{128}Te	1.6×10^{-8}	8.1×10^{-4}	1.1×10^{-8}	6.8×10^{-4}	5.6×10^{-8}	1.6×10^{-3}
^{130}Te	1.0×10^{-7}	1.8×10^{-3}	5.5×10^{-8}	1.5×10^{-3}	1.3×10^{-7}	6.5×10^{-3}
^{136}Xe	2.4×10^{-8}	9.4×10^{-4}	1.7×10^{-8}	7.8×10^{-4}	8.7×10^{-7}	2.2×10^{-3}
^{150}Nd	7.3×10^{-8}	2.3×10^{-3}	5.2×10^{-8}	1.4×10^{-3}	2.4×10^{-7}	3.0×10^{-3}

Table 7. Summary of the results presented in this work

(*A*, *Z*)	$\langle m_\nu\rangle$, eV	$\langle\lambda\rangle\times10^{-6}$	$\langle\eta\rangle\times10^{-8}$	$\langle\eta_N\rangle\times10^{-8}$	$\langle\eta_{SUSY}\rangle\times10^{-8}$	$\lambda'_{111}\times10^{-4}$
	P	P1	P1	P	P	P
^{76}Ge	0.27	0.56	0.32	0.44	0.31	4.0
^{100}Mo	2.9	26	8.8	6.2	3.2	18
^{116}Cd	5.9	37	26	11	7.6	18
^{128}Te	1.8	5.6	1.3	2.9	1.6	8.1
^{130}Te	13	7.6	5.2	20	10	18
^{136}Xe	49	2.1	1.4	45	2.4	9.4
^{150}Nd	8.5	5.6	5.3	16	7.3	23

5.2. R-Parity-Induced Lepton-Violating Parameters

With the above ingredients and using the nuclear matrix elements of [18], we can extract from the data values of η_{SUSY}. Then, one can use these values of η_{SUSY} in order to extract values for the *R*-parity-violating parameters λ'_{111}.

As we have already mentioned, one must start with five parameters in the allowed SUSY parameter space and solve the RG equations to obtain the values of the needed parameters at low energies [71–73]. For our purposes, it is adequate to utilize typical parameters, which have already appeared in the literature [71, 72]. One then finds

$$\lambda'_{111} = C_{\tilde\chi^0}(\eta_{SUSY})^{1/2}\ \text{(neutralinos only)}, \qquad (56)$$

$$\lambda'_{111} = C_{\tilde g}(\eta_{SUSY})^{1/2}\ \text{(gluino only)}. \qquad (57)$$

When both neutralinos and gluinos are included, we write

$$\lambda'_{111} = C_{\tilde\chi^0,\tilde g}(\eta_{SUSY})^{1/2}. \qquad (58)$$

The values of these coefficients are given in Table 5 for the nine SUSY models mentioned above.

From Table 5, we see that there is quite a spread in the quantities $C_{\tilde\chi^0}$, $C_{\tilde g}$, and $C_{\tilde\chi^0,\tilde g}$, depending on the SUSY parameter space. We will see that this is the largest uncertainty in estimating the SUSY contribution to $0\nu\beta\beta$ decay. In all of these cases, the intermediate selectron–neutralino mechanism appears to be the most dominant. The most favorable situation occurs in the case 7 of Table 5. And this is what we will consider in extracting the limits on λ'_{111}. Combining the above values of the couplings $\alpha_{k\pi}$, $k = 1, 2$, with the corresponding nuclear matrix elements of [18] (F) and the two nucleon *ME* of [73], we obtain the limits listed as P in Table 6. Thus, the most stringent limit is obtained from the ^{76}Ge data and is

$$\lambda'_{111} \le 4.8\times10^{-4}\ \text{(case 7)}. \qquad (59)$$

The above quantities are assumed positive. If not, the absolute value is understood.

6. CONCLUSION

We have seen that $0\nu\beta\beta$ decay pops up in almost any fashionable particle model. Thus, it can set useful limits

not only on the light neutrino mass (54), but in addition on other lepton violating parameters like $\langle\eta_N\rangle$ of (55) or the parameters λ and η (Section 2.2). Finally, we mention again the limit extracted on the *R*-parity-violating parameter (59). A set of limits, for our choice of nuclear matrix elements, derived from the various nuclear targets is given in Table 7. For ^{76}Ge, we have used here the unpublished new limit of the Heidelberg–Moscow experiment $T_{1/2} \geq 5.7 \times 10^{25}$ yr.

We see that limits are quite stringent, but they, of course, have uncertainties in them. They come from nuclear physics, especially for the short-range operators or from particle physics, as, e.g., in the case of supersymmetry.

It is clear that during the last year the interest of most people is being focused on the light neutrino mass mechanism. This due to the experimental indications for neutrino oscillations of solar (Homestake [74], Kamiokande [75], Gallex [76], and SAGE [77]), atmospheric (Kamiokande [78], IMB [79], and Soudan [80], SuperKamiokande [81]), and terrestrial (LSND [82]) experiments.

One can use the constraints imposed by the results of neutrino oscillation experiments on $\langle\Delta m_\nu^2\rangle$. These experiments, of course, cannot predict the scale of the masses or the Majorana phases. The predictions differ from each other due to the different input and structure of the neutrino mixing matrix and assumptions. Bilenky *et al.* [83] and others [84] have shown that under quite reasonable assumptions in a general scheme with three light Majorana neutrinos and mass hierarchy $|\langle m_\nu\rangle|$ is smaller than 10^{-2} eV. In another study outlined in [85], the authors end up with $|\langle m_\nu\rangle| \approx 0.14$ eV. Thus, one can see that the current limit on $\langle m_\nu\rangle$ in (54) is quite a bit higher than the neutrino oscillation data.

There is a new experimental proposal for measurement of the $0\nu\beta\beta$ decay of ^{76}Ge, which intends to use 1 t (in an extended version 10 t) of enriched ^{76}Ge and to reach the half-life limit $T_{1/2}^{\exp-0\nu} \geq 5.8 \times 10^{27}$ yr and $T_{1/2}^{\exp-0\nu} \geq 6.4 \times 10^{28}$ yr after 1 and 10 yr of measurements, respectively. From these half-life values, one can deduce [see (5) and Table 2] the possible future limits on the effective light neutrino mass 2.7×10^{-2} and 8.1×10^{-3} eV, respectively. From the comparison with limits advocated by the neutrino oscillation phenomenology, we conclude that GENIUS experiment [60, 86] would be able to measure this lepton-number-violating process, provided, of course, that the neutrinos are Majorana particles.

We must emphasize that the plethora of other $0\nu\beta\beta$-decay mechanisms predicted by GUT's and SUSY do not diminish the importance of this reaction in settling the outstanding neutrino properties. One can show that the presence of these exotic mechanisms implies that the neutrinos are massive Majorana particles, even if the mass mechanism is not the dominant one [10, 87].

Thus, one can say with certainty that the experimental detection of the $0\nu\beta\beta$-decay process would be a major achievement with important implications on the field of particle and nuclear physics as well as on cosmology.

ACKNOWLEDGMENTS

I would like to express my appreciation to the Humboldt Foundation for their award and my thanks to the Institute of Theoretical Physics at the University of Tübingen for its hospitality.

REFERENCES

1. W. Furry, Phys. Rev. **56**, 1184 (1939).
2. H. Primakoff, Phys. Rev. **85**, 888 (1952); H. Primakoff and S. P. Rosen, Phys. Rev. **184**, 1925 (1969); Proc. R. Soc. London **78**, 464 (1961).
3. M. Doi, T. Kotani, N. Nishiura, *et al.*, Phys. Lett. B **103**, 219 (1981); erratum: **113**, 513 (1982).
4. W. C. Haxton and G. S. Stephenson, Prog. Part. Nucl. Phys. **12**, 409 (1984).
5. M. Doi, T. Kotani, and E. Takasugi, Prog. Theor. Phys. Suppl. **83**, 1 (1985).
6. J. D. Vergados, Phys. Rep. **133**, 1 (1986).
7. T. Tomoda *et al.*, Rep. Prog. Phys. **54**, 53 (1991).
8. J. Suhonen and O. Civitarese, Phys. Rep. **300**, 123 (1998).
9. A. Faessler and F. Šimkovic, J. Phys. G **24**, 2139 (1998).
10. J. Schechter and J. W. F. Valle, Phys. Rev. D **25**, 2951 (1982).
11. R. N. Mohapatra, hep-ph/9808284.
12. G. Pantis, F. Šimkovic, J. D. Vergados, and A. Faessler, Phys. Rev. C **53**, 695 (1996).
13. R. N. Mohapatra, Phys. Rev. D **34**, 3457 (1986).
14. J. D. Vergados, Phys. Lett. B **184**, 55 (1987).
15. M. Hirsch, H. V. Klapdor-Kleingrothaus, and S. G. Kovalenko, Phys. Rev. Lett. **75**, 17 (1995); Phys. Rev. D **53**, 1329 (1996).
16. A. Wodecki, W. Kamiński, and S. Pagerka, Phys. Lett. B **413**, 342 (1997).
17. A. Faessler, S. Kovalenko, F. Šimkovic, and J. Schwieger, Phys. Rev. Lett. **78**, 183 (1997); Yad. Fiz. **61**, 1329 (1998) [Phys. At. Nucl. **61**, 1229 (1998)].
18. A. Faessler, S. Kovalenko, and F. Šimkovic, Phys. Rev. D **58**, 115004 (1998).
19. A. Faessler, S. Kovalenko, and F. Šimkovic, Phys. Rev. D **58**, 055004 (1998).
20. J. D. Vergados, Phys. Rev. C **24**, 640 (1981).
21. J. D. Vergados, Phys. Rev. D **25**, 914 (1982).
22. J. D. Vergados, Nucl. Phys. B **250**, 618 (1985).
23. T. Tomoda, F. Faessler, K. W. Schmidt, and F. Grümmer, Phys. Lett. B **157**, 4 (1985).
24. F. Šimkovic, G. Pantis, J. D. Vergados, and A. Faessler, Phys. Rev. C (in press).

25. F. Šimkovic, G. V. Efimov, M. A. Ivanov, and V. E. Lyubovitskij, Z. Phys. A **341**, 193 (1992).
26. J. D. Vergados, Nucl. Phys. A **506**, 842 (1990).
27. G. Pantis and J. D. Vergados, Phys. Lett. B **242**, 1 (1990).
28. A. Faessler, W. A. Kamiński, G. Pantis, and J. D. Vergados, Phys. Rev. C **43**, R21 (1991).
29. J. Suhonen, S. B. Khadkikar, and A. Faessler, Phys. Lett. B **237**, 8 (1990); Nucl. Phys. A **529**, 727 (1991).
30. J. D. Vergados, Phys. Rev. C **13**, 865 (1976).
31. W. C. Haxton, G. S. Stephenson, and D. Strottman, Phys. Rev. D **25**, 2360 (1982).
32. L. D. Skouras and J. D. Vergados, Phys. Rev. C **28**, 2122 (1983).
33. L. Zhao, B. A. Brown, and W. A. Richter, Phys. Rev. C **42**, 1120 (1990).
34. E. Caurier, A. Poves, and A. P. Zucker, Phys. Lett. B **252**, 13 (1990).
35. J. Sinatkas, L. D. Skouras, D. Strottman, and J. D. Vergados, J. Phys. G **18**, 1377 (1992).
36. L. Zhao and B. A. Brown, Phys. Rev. C **47**, 2641 (1993).
37. J. Retamosa, E. Caurier, and F. Novacki, Phys. Rev. C **51**, 371 (1995).
38. P. B. Radha *et al.*, Phys. Rev. Lett. **76**, 2642 (1996).
39. E. Caurier, F. Novacki, A. Poves, and J. Retamosa, Phys. Rev. Lett. **77**, 1954 (1996).
40. H. Nakada, T. Sebe, and K. Muto, Nucl. Phys. A **607**, 235 (1996).
41. J. Suhonen, P. C. Divari, L. D. Skouras, and I. D. Johnstone, Phys. Rev. D **55**, 714 (1997).
42. S. E. Koonin, D. J. Dean, and K. Langacke, Phys. Rep. **278**, 1 (1997).
43. P. Vogel and M. R. Zirnbauer, Phys. Rev. Lett. **57**, 3148 (1986); J. Engel, P. Vogel, and M. R. Zirnbauer, Phys. Rev. C **37**, 731 (1988).
44. O. Civitarese, A. Faessler, and N. Tomoda, Phys. Lett. B **194**, 11 (1987).
45. K. Muto, E. Bender, and H. V. Klapdor, Z. Phys. A **334**, 177 (1989); K. Muto and H. V. Klapdor, Phys. Lett. B **201**, 420 (1988).
46. J. Engel, P. Vogel, X. D. Ji, and S. Pittel, Phys. Lett. B **225**, 5 (1989).
47. A. A. Raduta, A. Faessler, S. Stoica, and W. A. Kamiński, Phys. Lett. B **254**, 7 (1991).
48. A. Griffiths and P. Vogel, Phys. Rev. C **46**, 181 (1992).
49. J. Suhonen and O. Civitarese, Phys. Lett. B **308**, 212 (1993).
50. O. Civitarese and J. Suhonen, Nucl. Phys. A **575**, 1111 (1994).
51. F. Šimkovic *et al.*, Phys. Lett. B **393**, 267 (1997); F. Šimkovic, J. Schwieger, G. Pantis, and A. Faessler, Found. Phys. **27**, 1275 (1997).
52. F. Šimkovic, G. Pantis, and A. Faessler, Yad. Fiz. **61**, 1318 (1998) [Phys. At. Nucl. **61**, 1218 (1998)]; Prog. Part. Nucl. Phys. **40**, 285 (1998).
53. M. K. Cheoun *et al.*, Nucl. Phys. A **561**, 74 (1993).
54. J. Toivanen and J. Suhonen, Phys. Rev. Lett. **75**, 410 (1995).
55. J. Schwieger, F. Šimkovic, and A. Faessler, Nucl. Phys. A **600**, 179 (1996).
56. J. D. Vergados, J. Phys. G **22**, 253 (1996).
57. T. Ericson and W. Weise, *Pions and Nuclei* (Clarendon Press, Oxford, 1988).
58. O. Dumbrajs *et al.*, Nucl. Phys. B **216**, 277 (1983).
59. I. S. Towner and J. S. Hardy, in *Symmetries and Fundamental Interactions in Nuclei*, Ed. by W. C. Haxton and E. M. Henley (World Sci., Singapore, 1995), p. 183; nucl-th/9504015.
60. Heidelberg–Moscow Collab. (L. Baudis *et al.*), Phys. Lett. B **407**, 219 (1997).
61. S. R. Elliot *et al.*, Phys. Rev. C **46**, 1535 (1992).
62. A. Kawashima, K. Takahashi, and A. Masuda, Phys. Rev. C **47**, 2452 (1993).
63. H. Ejiri *et al.*, Nucl. Phys. A **611**, 85 (1996).
64. F. A. Danevich *et al.*, Phys. Lett. B **344**, 72 (1995).
65. T. Bernatovicz *et al.*, Phys. Rev. Lett. **69**, 2341 (1992); Phys. Rev. C **47**, 806 (1993).
66. A. Alessandrello *et al.*, Nucl. Phys. B (Proc. Suppl.) **35**, 366 (1994).
67. J. Busto *et al.*, Nucl. Phys. B (Proc. Suppl.) **48**, 251 (1996).
68. A. De Silva, M. K. Moe, M. A. Nelson, and M. A. Vient, Phys. Rev. C **56**, 2451 (1997).
69. M. Günter *et al.*, Phys. Rev. D **55**, 54 (1997).
70. M. Moe and P. Vogel, Annu. Rev. Nucl. Part. Sci. **44**, 247 (1994).
71. G. L. Kane, G. Golda, L. Roszkowski, and J. D. Wells, Phys. Rev. D **49**, 6173 (1994).
72. D. J. Kastano, E. J. Piard, and P. Ramond, Phys. Rev. D **49**, 4882 (1994).
73. A. Wodecki, W. A. Kamiński, and F. Šimkovic, hep-ph/9902453.
74. B. T. Cleveland *et al.*, Nucl. Phys. B (Proc. Suppl.) **38**, 47 (1995).
75. K. S. Hirata *et al.*, Phys. Rev. D **44**, 2241 (1991).
76. Gallex Collab., Phys. Lett. B **357**, 237 (1995).
77. J. N. Abdurashitov *et al.*, Phys. Lett. B **328**, 234 (1994).
78. Y. Fukuda *et al.*, Phys. Lett. B **335**, 237 (1994).
79. R. Becker-Szendy *et al.*, Nucl. Phys. B (Proc. Suppl.) **38**, 331 (1995).
80. M. Goodman, Nucl. Phys. B (Proc. Suppl.) **38**, 337 (1995).
81. Y. Fukuda *et al.*, Phys. Lett. B **433**, 9 (1998).
82. C. Athanassopoulos *et al.*, Phys. Rev. Lett. **75**, 2650 (1995).
83. S. M. Bilenky, C. Giunti, and W. Grimus, hep-ph/9812360.
84. V. Bednyakov, A. Faessler, and S. Kovalenko, Phys. Lett. B **442**, 203 (1998).
85. G. Barenboim and F. Scheck, Phys. Lett. B **440**, 332 (1998).
86. J. Hellming and H. V. Klapdor-Kleingrothaus, Z. Phys. A **359**, 351 (1997); H. V. Klapdor-Kleingrothaus and M. Hirsch, Z. Phys. A **359**, 361 (1997); H. V. Klapdor-Kleingrothaus, hep-ex/9901021.
87. M. Hirsch, H. V. Klapdor-Kleingrothaus, and S. G. Kovalenko, Phys. Lett. B **398**, 311 (1997); **403**, 291 (1997).

Physics of Atomic Nuclei, Vol. 63, No. 7, 2000, pp. 1151–1157. From Yadernaya Fizika, Vol. 63, No. 7, 2000, pp. 1227–1233.

NEW PHYSICS, NUCLEAR AND NUCLEON STRUCTURE IN RARE PROCESSES

Grand Unification and B&L Conservation*

P. Nath and R. Arnowitt[1)]**

Department of Physics, Northeastern University, Boston, USA

Abstract—A brief summary of some of the recent developments in grand unification and B&L conservation is given. Proton stability in supergravity unified models is discussed. Also discussed are the effects of supersymmetric dark matter constraints and the constraints of proton lifetime on the SUSY spectrum. Other topics reviewed include Planck scale effects and p decay, effects of textures, and extension to nonminimal models including models with many Higgs triplets. Recent developments in GUTs and strings are also discussed. © *2000 MAIK "Nauka/Interperiodica".*

1. INTRODUCTION

In this paper, we give a brief review of some of the recent developments in grand unification and B&L conservation [1]. In Section 2, we give an introduction to SUSY grand unification. In Section 3, we discuss sources of baryon number violation in supersymmetric theories. In Section 4, we discuss in detail the dimension five operators and proton decay in supergravity grand unified theories. In Section 5, we discuss the effect of textures on proton lifetime. In Section 6, we discuss the effects of dark matter on proton lifetime. In Section 7, we discuss extension to nonminimal models. In Section 8, we discuss how p decay could be used to unmask Planck scale effects. In Section 9, we discuss proton decay models with gauge mediated breaking of supersymmetry. In Section 10, we discuss proton stability in the context of GUTs and strings. Future prospects and conclusions are discussed in Section 11.

2. SUSY GRAND UNIFICATION

As is well known, the LEP data on the gauge coupling constants extrapolated to high energy supports the idea of unification and supersymmetry [2, 3]. The minimal grand unification model where the unification of the LEP data occurs is the SUSY $SU(5)$ [3]. However, detailed analyses show that the unification occurs within (1–2)σ. This situation appears altogether reasonable as one expects Planck scale corrections to the predictions of grand unification which are typically $O\left(\frac{M_G}{M_{\rm Planck}}\right)$ [4–6]. Specific corrections of this nature can arise from the gauge kinetic energy function $f_{\alpha\beta}$ [4]:

$$\left[A\delta_{\alpha\beta} + \frac{c}{2M_{\rm Pl}} d_{\alpha\beta\gamma}\Sigma^{\gamma}\right] F^{\alpha}_{\mu\nu} F^{\beta\mu\nu}. \quad (1)$$

Values of $c \sim O(1)$ give agreement with the LEP data. In fact, using LEP data, one can put a limit on the range of c, and one has [5, 6]

$$-1 \le c \le 3. \quad (2)$$

The (1–2)σ deviation effects can also be gotten from other extensions of $SU(5)$, such as, for example, in the missing doublet model with a $U(1)$ symmetry [7].

3. SOURCES OF BARYON-NUMBER VIOLATION IN SUSY

There are several sources of B&L violation in superunifed theories [2]. First, as in any grand unified model, one has baryon- and lepton-number violation arising from leptoquark exchange. Additionally, in SUSY theories, one has B&L violation from dimension-4, dimension-5, and higher dimensional operators. The experiments for the detection of B&L violation of the type above are the nucleon stability experiments. We discuss below proton stability in the context of supersymmetric unification.

The dominant mode in leptoquark mediated p decay in $SU(5)$ is $p \longrightarrow e^+\pi^0$, and here the p lifetime is given by

$$\tau(p \longrightarrow e^+\pi^0) \approx \left(\frac{M_V}{3.5\times 10^{14}\ \text{GeV}}\right)^4 \times 10^{31\pm 1}\ \text{yr}. \quad (3)$$

In SUSY $SU(5)$, one estimates $\tau(p \longrightarrow e^+\pi^0)$ to be $1 \times 10^{35\pm 1}$ yr [8]. The current experimental limit on this decay model is [9]

$$\tau(p \longrightarrow e^+\pi^0) > 3.3\times 10^{33}\ \text{yr}\ \ (90\%\ \text{C.L.})\ (\text{current}), \quad (4)$$

and the limit that SuperKamiokande is expected to reach is [10]

$$\tau(p \longrightarrow e^+\pi^0) > 1\times 10^{34}\ \text{yr}\ \ (90\%\ \text{C.L.})\ (\text{SuperK}). \quad (5)$$

Thus, the $e^+\pi^0$ mode in SUSY $SU(5)$ via the leptoquark exchange may be on the edge of detection if SuperKamiokande and ICARUS reach their maximum sensitivity. As mentioned above, in addition to the B&L viola-

* This article was submitted by the authors in English.

** e-mail:nath@neuhep.hex.neu.edu

1) Center for Theoretical Physics, Department of Physics, Texas A&M University, College Station, TX, USA.

tion induced by leptoquark exchange, SUSY theories also contain other sources of B&L violation such as dimension-4, dimension-5, and higher dimensional operators. The dimension-4 operators have the following general form

$$W = \lambda_u Q u^c H_2 + \lambda_d Q d^c H_1 + \lambda_e L e^c H_1 + \mu H_1 H_2 + \left(\lambda'_B u^c d^c d^c + \lambda'_L Q d^c L + \lambda''_L L L e^c\right) \quad (6)$$

and lead to fast proton decay. Suppression of the fast p decay induced by these operators requires a very high degree of fine tuning

$$\lambda'_B \lambda'_L < \left(\frac{m^2_{\tilde{d}}}{10^{16}\ \mathrm{GeV}}\right)^2 \sim O(10^{-26\pm 1}). \quad (7)$$

In the MSSM, one eliminates fast p decay via a discrete R symmetry. However, R as a global symmetry is not preserved by gravitational interactions. For example, worm holes can generate dimension-4 operators and catalyze p decay [11]. For this reason, the R symmetry must be the remnant of a gauge symmetry [12].

While R-parity invariance suppresses dimension-4 operators, one still has B&L-violating dimension-5 operators which can induce the proton decay. In the MSSM, one can write many dimension-5 operators that violate B&L number, e.g., $QQQL$, $u^c u^c d^c e^c$, $QQQH_1$, $Qu^c e^c H_1$, LLH_2H_2, $LH_1H_2H_2$, etc. [13]. Dimension-5 and higher dimension operators can sometimes generate dangerous dimension-4 operators after spontaneous symmetry breaking. For example, dimension-5 operators of $SO(10)$ after VEV formation of ν^c ($M_{\mathrm{Pl}} = \langle \nu^c \rangle$) can generate dangerous operators, e.g., $(u^c d^c d^c \nu^c) \longrightarrow (M_{\mathrm{Pl}} u^c d^c d^c)$, and $(QLd^c\nu^c) \longrightarrow (M_{\mathrm{Pl}} QLd^c)$. Aside from this situation, the B&L violation of dimension-5 operators will exhibit p instability only at the loop level [14]. Most SUSY/string models do generate B&L-violating dimension-5 operators. Suppression of these operators can arise via discrete symmetries or via nonstandard embeddings. Most SUSY/string models, however, do not have a natural suppression, and a suppression requires a doublet–triplet splitting in the Higgs sector. Various mechanisms for doublet–triplet splitting have been discussed extensively in the literature.

4. PRECISION ANALYSES OF PROTON LIFETIME IN SUPERGRAVITY MODELS

Detailed analyses of the proton lifetime limits have been carried out in the framework of supergravity models [15–17] which are based on the idea of a hidden sector where supersymmetry breaks by a super-Higgs phenomenon and this breaking is communicated gravitationally to the physical sector [18, 19]. For the minimal supergravity model at scales much below the GUT scale, in scenarios where the breaking of the electroweak symmetry is triggered by radiative corrections, the low-energy theory can be parametrized by m_0, $m_{1/2}$, A_0, $\tan\beta$. Here, m_0 is the universal scalar mass, $m_{1/2}$ is the universal gaugino mass, A_0 is the universal trilinear coupling at the GUT scale, and $\tan\beta = \langle H_2\rangle/\langle H_1\rangle$, where H_2 gives mass to the up quarks and H_1 gives mass to the down quarks and to the leptons. For the more general case, where the Kahler potential at the GUT scale is not flat, the low energy mass scales can become nonuniversal [20–23]. The nonuniversal soft SUSY-breaking parameters have important implications for low-energy phenomenology.

Analyses of p decay via dimension-5 operators have been discussed in the literature for a variety of models such as $SU(5)$, $(SU(3))^3$, $SO(10)$, etc. [14, 15, 24–29]. We begin the discussion for the simplest case of $SU(5)$ unified model where the GUT interaction is governed by

$$W_Y = -\frac{1}{8} f_{1ij} \epsilon_{uvwxy} H^u_1 M^{vw}_i M^{xy}_j + f_{2ij} \bar{H}_{2u} \bar{M}_{iv} M^{uv}_j. \quad (8)$$

After breakdown of the GUT symmetry and integration over the Higgs triplet fields, the effective dimension-5 interactions below the GUT scale which governs p decay is given by

$$LLLL = \frac{\epsilon_{abc}}{M}(P f^u_1 V)_{ij}(f^d_2)_{kl} \times (\tilde{u}_{Lbi}\tilde{d}_{Lcj}(\bar{e}^c_{Lk}(Vu_L)_{al} - \nu^c_k d_{Lal}) + \ldots) + \mathrm{h.c.},$$

$$RRRR\ -\frac{\epsilon_{abc}}{M}(V^\dagger f^u)_{ij}(PV f^d)_{kl} \times (\bar{e}^c_{Ri} u_{Raj}\tilde{u}_{Rck}\tilde{d}_{Rbl} + \ldots) + \mathrm{h.c.},$$

where V is the CKM matrix and f_i are related to quark masses by $m^u_i = f^u_i(\sin 2\theta_W/e)M_Z \sin\beta$ and $m^d_i = f^d_i(\sin 2\theta_W/e)M_Z\sin\beta$ and P_i are generational phases which are given by $P_i = (e^{i\gamma_i})$, $\sum_i \gamma_i = 0$ ($i = 1, 2, 3$). The mass diagonal states $\tilde{u}_{i(1,2)}$ are mixtures of chiral states governed by the mixing matrix

$$\begin{pmatrix} m^2_{Ru} & m^u(A_u m_0 - \mu\cot\beta) \\ m^u(A_u m_0 - \mu\cot\beta) & m^2_{Lu} \end{pmatrix}, \quad (9)$$

where $\tilde{u}_{L(R)} = -(+)\cos\delta_u \tilde{u}_1 + \sin\delta_u \tilde{u}_2$ and $\sin 2\delta_u = -2m_u(A_u m_0 - \mu\cot\beta)/(\tilde{m}^2_{u1} - \tilde{m}^2_{u2})$. Dressing of these dimension-5 operators by chargino, gluino, and neutralino exchanges gives dimension-6 operators of the type $LLLL$, $LLRR$, $RRLL$, and $RRRR$. For certain regions of the parameter space, $LLRR$ interaction can be comparable to and may even dominate the $LLLL$ interaction

part. The decay branching ratios for $p \longrightarrow \bar{\nu}_i K^+$ is

$$\Gamma(p \longrightarrow \bar{\nu}_i K^+) = \left(\frac{\beta_p}{M_{H_3}}\right)^2 |A|^2 |B_i| C, \qquad (10)$$

where β_p is defined by $\beta_p U_L^\gamma = \epsilon_{abc}\epsilon_{\alpha\beta}\langle 0|d_{aL}^\alpha u_{bL}^\beta u_{cL}^\gamma|p\rangle$; from lattice gauge calculations, β_p has the value $\beta_p = (5.6 \pm 0.5) \times 10^{-3}$ GeV^3 [30].

The same B-violating dimension-6 quark operators that lead to the decay of the proton into lepton and pseudoscalar modes also lead to the decay modes with lepton and vector mesons. Although the vector mesons are considerably heavier than their corresponding pseudoscalar counterparts, the decay modes involving ρ, K^*, ω are allowed [31]; i.e., one has decay modes of the type

$$\begin{aligned} &\bar{\nu}_i K^*, \bar{\nu}_i \rho, \bar{\nu}_i \omega \ (i = e, \mu, \tau); \\ &eK^*, \mu K^*, e\rho, \mu\rho, e\omega, \mu\omega. \end{aligned} \qquad (11)$$

The branching ratios for the vector meson decay modes are typically smaller than the corresponding pseudoscalar decay modes.

$SO(10)$ grand unified models have several interesting features. One of these is that $SO(10)$ allows for the doublet–triplet splitting via VEV alignment [32]. For large $\tan\beta$, *LLRR* contributions can become dominant, and in this case the theory does lead to some distinguishing features compared to the small $\tan\beta$ models [26]. However, there is a potential problem in $SO(10)$ regarding proton stability vs. unification of gauge couplings using LEP data. The mass scale necessary to suppress p decay to the current experimental value is $(M^{-1})_{11} > \tan\beta(0.57 \times 10^{16})$ GeV, which for $\tan\beta \sim 50$ requires a GUT mass of 2.5×10^{17} GeV for suppression of p decay. A mass scale of this size upsets unification of couplings, and one needs large threshold corrections to get agreement with experiment [33]. The solution to these problems in the context of the model of [28] was discussed by Pati at this conference [34].

5. TEXTURES

GUT models give poor predictions for quark–lepton mass ratios. In $SU(5)$, m_b/m_τ is in good agreement with experiment, but m_s/m_μ and m_d/m_e are not. One needs textures which in the Higgs doublet sector can be written in the following form [35]

$$W_d = H_1 l A^E e^c + H_1 d^c A^D q + H_2 u^c A^U q, \qquad (12)$$

where A^E, A^D, and A^U are the texture matrices in the generation space and generation indices are suppressed. Textures involve a small ratio ϵ which typically lies in the range ~1/10–1/50. A possible origin of the parameter ϵ is from the ratio of mass scales, e.g., $\epsilon = M_{\rm str}/M_{\rm Planck}$ [36]. Another possibility is [37]

$$\epsilon = \frac{M_G}{M_{\rm str}}. \qquad (13)$$

In the context of supergravity unified models, ϵ can arise from higher dimensional operators. In the energy domain below the string scale, the effective theory that arises for scales $Q < M_{\rm str}$ after integration over the heavy modes of the string is of the type

$$W = W_3 + W_4 + W_5 + \dots . \qquad (14)$$

W_n ($n > 3$) are suppressed by the string (Planck) scale and in general contain the adjoints which develop VEVs ~ $O(M_G)$. After VEV formation of the heavy fields,

$$W_n \sim O\left(\frac{M_G}{M_{\rm str}}\right)^{n-3} \times \text{operators in } W_3. \qquad (15)$$

With the above, one can generate mass hierarchy with $\lambda_{yuk} \sim O(1)$. One can compute textures in the Higgs triplet sector [37]

$$\begin{aligned} W_t &= H_1 l B^E q + H_2 u^c B^U e^c \\ &+ \epsilon_{abc}(H_1 d_b^c B^D u_c^c + H_2^a u_b^c C^U d_c). \end{aligned} \qquad (16)$$

Because of the ambiguity in the choice of the higher dimensional operators, the textures in the Higgs triplet sector are not unique. There are a large number of higher dimensional operators one can add which give the same texture in the Higgs doublet sector but give different textures in the Higgs triplet sector. One needs a dynamical principle to constrain the Planck scale corrections. For example, an exotic sector with the exotic fields in the minimal vectorlike representation gives a minimal set of textures in the Higgs triplet sector. Inclusion of textures gives a moderate modification of p-decay branching ratios. A rough analysis shows that the proton lifetime for the $\bar{\nu} K^+$ mode is enhanced by a factor of $\sim \left(\frac{9}{8}\frac{m_s}{m_\mu}\right)^2$ [37]. The p-decay modes hold important information on GUT physics. For example, p-decay modes can be used to test texture theories. Further, textures affect in a differential way the various decay modes, which in turn can be used to provide a window on the textures at the GUT scale.

6. EFFECTS OF DARK MATTER CONSTRAINTS ON PROTON LIFETIME

As discussed in Section 3 the simplest procedure to eliminate fast proton decay from B&L-violating dimension-4 operators is by using R-parity invariance. This invariance then leads to the lowest supersymmetric particle (LSP) which is absolutely stable. Analyses in supergravity with radiative breaking of the elec-

troweak symmetry show that over most of the parameter space of the theory the LSP is the lightest neutralino. Thus, the lowest mass neutralino will be absolutely stable and hence a candidate for cold dark matter [38]. One constrains the relic density of the neutralino by constraining $\Omega_{\chi_1} h^2$. Here, $\Omega_{\chi_1} = \rho_{\chi_1}/\rho_c$, where ρ_{χ_1} is the mass density of the relic neutralinos in the universe and ρ_c is the critical relic density needed to close the universe, and h is defined so that $H = 100h$ km/(s Mpc), where H is the Hubble parameter. Current estimates for $\Omega_\chi h^2$ show that $\Omega_\chi h^2$ lies in the range $0.05 < \Omega_\chi h^2 < 0.3$. Imposition of the relic density constraint has an important effect on the proton lifetime and leads to an additional constraint on the neutralino mass from the experimental proton lifetime limit. In the minimal supergravity models, one then finds that within the usual naturalness constraints the gluino mass lies typically below about 500 GeV [39]. The spectrum of this model with p lifetime and relic density constraints would be accessible in RUNII at the Tevatron.

7. NONMINIMAL MODELS

One can also investigate models with a more complicated particle structure. For example, the Higgs triplet sector can be more complex involving many Higgs triplets [29, 40, 41]. In the basis where only $\bar{H}_1$ and H_1 couple with matter,

$$W_3^{\text{tripl}} = \bar{H}_1 J + \bar{J} H_1 + \bar{H}_i M_{ij} H_j. \qquad (17)$$

B&L-violating dimension-5 operators at low energy are given by

$$W_4^{\text{eff}} = -\bar{J}(M_{11}^{-1})J. \qquad (18)$$

A cancellation among the Higgs triplet couplings can lead to a factor ~3 or more suppression in amplitude and a factor ~10 or more suppression in the decay width. Including a factor of 2–3 uncertainty in the evaluation of proton-decay matrix elements, one can have an enhancement in p-decay lifetime of $\sim 10^2$.

Proton-decay modes discussed so far are all of the type where a proton decays into an antilepton and a meson, i.e., $p \longrightarrow e^+\pi^0$, $p \longrightarrow \bar{\nu} K^+(\pi^+)$, $p \longrightarrow \mu^+ K^0$. If there are interactions which violate $B - L$ conservation then new decay modes appear. Proton can then decay into a lepton and mesons [42]. For example, $5_M 5_M \overline{10}_H$ can generate $\Delta(B - L) = 2$ processes where a proton can decay into a lepton and mesons, i.e., $d + d + s \longrightarrow \mu^-$, $n \longrightarrow \mu^- K^+$, $p \longrightarrow \mu^- \pi^+ K^+$, …. Thus, p-decay selection rules can provide an important window to new physics in the desert and in the GUT scale region.

8. PLANCK SCALE EFFECTS ON GRAND UNIFICATION

In the RG analysis of α_i, there is an overlap of GUT threshold effects and of Planck scale effects (GUT–Planck confusion) [5, 6]. For $Q \sim M_G$,

$$\alpha_i^{-1}(Q) = \alpha_G^{-1} + C_{ia}\ln\left(\frac{M_a}{Q}\right) + \frac{cM}{2M_{\text{Pl}}}\alpha_G^{-1} n_i. \qquad (19)$$

The relation above shows that the Planck effects can be absorbed in the GUT thresholds by rescaling, e.g., in the minimal $SU(5)$ $\alpha_i^{-1}(Q) = (\alpha_G^{\text{eff}})^{-1} + C_{ia}\ln\left(\frac{M_a^{\text{eff}}}{Q}\right)$, where $M_a^{\text{eff}} = M_a e^{k_a C_{\text{P}}}$, $k_a = \left(-\frac{3}{5}(\Sigma), \frac{3}{10}(V), 5(H_3)\right)$, $(\alpha_G^{\text{eff}})^{-1} = \alpha_G^{-1} - \frac{15}{2\pi} C_{\text{P}}$, $C_{\text{P}} = \frac{\pi c M}{\alpha_G M_{\text{Pl}}}$. However, p decay depends on the unscaled GUT parameters. Thus p decay can unmask Planck effects and remove the GUT–Planck confusion. Thus, for the p decay modes $p \longrightarrow \bar{\nu} K^+$ and $p \longrightarrow e^+\pi^0$, one finds [5, 6]

$$p \longrightarrow \bar{\nu} K^+, \quad c = \frac{\alpha_G}{10}\frac{M_{\text{Pl}}}{\pi M_V}\ln\frac{M_{H_3}^{\text{eff}}}{M_{H_3}} \qquad (20)$$

and

$$p \longrightarrow e^+\pi^0, \quad c = \frac{100}{3}\sqrt{\frac{2}{3}}\alpha_G^{3/2}\frac{M_{\text{Pl}}}{M_V}\ln\frac{M_V}{M_V^{\text{eff}}}. \qquad (21)$$

Thus a knowledge of M_{H_3} and $M_{H_3}^{\text{eff}}$ and of M_V and of M_V^{eff} allow one to determine c and thus the presence of Planck correction. Proton decay can be used to test texture theories, since textures enter prominently in p decay amplitudes.

9. GAUGE-MEDIATED BREAKING (GMSB)

We discuss now p decay in the class of models where breaking of SUSY occurs via gauge mediation. In its simplest form, SUSY breaking in this mechanism arises from VEV formation of a chiral superfield $\hat{S} = (S, \tilde{S}, F)$ which couples to messenger chiral superfield $(\phi_i, \bar{\phi}_i)$ in vectorlike representation of the MSSM group with a superpotential of the form [43] $W = \sum C_i S \phi_i \bar{\phi}_i$. In $SU(5)$, $(\phi, \bar{\phi}) = (5, \bar{5})$, or $(10, \overline{10})$. Supersymmetry breaking is communicated to the visible sector by gauge interactions. Masses of gauginos arise at the one-loop level and of the scalars at the two-loop level:

$$M_a = \frac{\alpha_a}{4\pi}\Lambda, \quad \Lambda = \frac{\langle F\rangle}{\langle S\rangle} \sim 10^2 \text{ TeV}, \qquad (22)$$

$$\tilde{m}^2 = \sum_a 2C_F^a\left(\frac{\alpha_a}{4\pi}\right)^2\Lambda^2. \quad (23)$$

There are many extensions of this simplest GMSB version including models with incomplete multiplets. However, in these models, $\mu\&B\mu$ (where $B\mu$ is the Higgs mixing coefficient in the soft SUSY-breaking term, i.e., $B\mu H_1H_2$) have nongauge origin. Further, in this scenario, LSP is a gravitino with a mass constrained so that $m_{3/2} < 1$ keV and such a particle cannot constitute cold dark matter [44]. We discuss next p stability in these models. One class of models are those where the messenger fields lie in complete $SU(5)$ multiplets. Defining $\alpha_1(M_G) = \alpha_2(M_G) = \alpha_G$, $\alpha_3(M_G)$ then is given by

$$\alpha_3^{-1}(M_G) = \alpha_G^{-1} - \frac{1}{4\pi}\left[\frac{12}{5}\ln\frac{M_{H_3}}{M_G} + \Delta\right], \quad (24)$$

where $\Delta = \Delta_{\rm SUSY} + \Delta_{\rm messenger}$. Unification is not automatic in these models but requires fixing M_{H_3} so that $\alpha_3(M_G) = \alpha_G$. This gives a small value of M_{H_3}, leading to fast proton decay [45]. For models with incomplete multiplets [46], grand unification is also difficult. In one class of models, $\tan\beta$ is determined by the condition that the cubic (A) and the quadratic (B) soft SUSY-breaking terms vanish at the messenger scale [47]. Most of the models in this class appear to be eliminated by the current data.

10. GUTS AND STRINGS

In string theory, one has two possibilities regarding the way the standard model gauge group structure arises in the model. One possibility is that the standard model gauge group arises from a unified gauge group at the string scale, such as $SU(5)$, $SO(10)$, $E(6)$, etc., while the second possibility is that the $SU(3)\times SU(2)\times U(1)$ gauge group emerges directly at the string scale [48]. Since the LEP data seems to indicate that the gauge coupling constants unify with the MSSM spectrum at the GUT scale which lies below the Planck scale, it is very tempting to entertain the possibility of a string GUTs where a GUT model arises from a string model [49]. However, to achieve a GUT model from strings with the right attributes requires higher Kac–Moody levels k. Thus, while for $k = 1$ GUT groups such as $G = SU(5)$, $SO(10)$, $E(6)$, etc., are possible, there are no massless adjoints to break the unified symmetry with $N = 1$ SUSY and chiral fermions. For $k = 2$, massless adjoints exist, but there are no known examples of models with three massless generations. For $k = 3$, one can have massless adjoints and three light generations [50]. In this case, models with gauge groups $SU(5)$, $SO(10)$, $E(6)$ have been constructed. They contain $N = 1$ spacetime SUSY, three chiral families, massless adjoint Higgs, and a non-Abelian hidden sector. However, no viable model appears to have emerged thus far.

Regarding the second possibility, where the standard model gauge group arises directly at the string scale, the string models usually run into problems since a string scale close to the GUT would lead to a Newtonian constant much larger than the observed value. This is the situation that arises in the usual heterotic string framework. One possible solution arises in the M-theory framework where dualities play an important role. Thus, dualities relate the strongly coupled $E_8\times E_8$ heterotic string to an M theory on $R_{10}\times S^1/Z_2$. Here, gravitation propagates in the bulk on $R_{10}\times S^1/Z_2$, and the $E_8\times E_8$ gauge fields propagate on the hyperplanes, and compactification on $M_4\times CY\times S^1/Z_2$ gives [51]

$$\alpha_G = \frac{(4\pi\kappa^2)^{2/3}}{2V}, \quad G_{\rm N} = \frac{\kappa^2}{16\pi V\rho}, \quad (25)$$

where ρ is the S^1 radius, V is the volume of the Calabi–Yau compactified manifold with $V = (M_G)^{-6}$, $M_{11}\equiv\kappa^{-2/9}$, $M_5\equiv\rho^{-1}$, $\alpha_G = 1/24$, and $M_5 \simeq M_G/10$. This leads to the following simple picture where for scales $Q \le M_5$ the universe is $4D$, for scales $M_5 \le Q \le M_G$ the universe is $5D$, and for scales $Q \ge M_G$ the universe is $11D$. Some fine points remain to be worked out, e.g., in understanding the discrepancy $M_{11}/M_G \simeq 2$.

Most of the string model building as of two years ago was done in the framework of the weakly coupled heterotic string. However, recent advances in string duality mentioned above have made it possible to relate the strong coupling regime of one string theory to the weak coupling limit of another. One such duality conjectured is that the strongly coupled $SO(32)$ heterotic string with compactification on four dimensions is equivalent to a weakly coupled Type I string compactified on four dimensions. In scenarios of this type, the GUT/string scale can be very low, i.e., as low as few TeV, and the unification of the gauge couplings can occur in the TeV region consistent with the LEP data. The reason for low-scale unification is due to the effects of Kaluza–Klein states associated with extra dimensions opening up below the string scale $M_{\rm str}$ that give a power law behavior to the evolution of the gauge couplings. There are many phenomenological implications of scenarios of this type which have been investigated recently.

In models of this type, one will have in general rapid p decay from effective interactions of type $\frac{O^{(n+2)}}{M_S^n}$ ($n \ge 1$); $M_S = O$(few) TeV. There are several proposals to suppress such operators. These consist of $4D$ symmetries which kill such operators and higher D symmetries. More exotic proposals have also been made such as the one where the baryon number is gauged and the gauge symmetry is then broken on the "other wall" and this breaking communicated to "our wall" by messenger fields with Planck scale masses giving an effective B&L-

violating interaction [52] $L_{p\text{-decay}} \sim e^{(-Mr_n)} \frac{Q^\dagger U^c D^c L^\dagger}{M^2}$.

With $M \sim M_{\rm Pl}$, and $r_n \sim 1/(\text{TeV})$, p decay is exponentially suppressed by a huge power. However, it remains to be seen if any of the these models can arise from a realistic string model.

11. CONCLUSIONS

LEP data appears to support ideas of both grand unification and of supersymmetry. Thus, GUT may be an important checkpoint on way to the Planck scale where the unification of all interactions occurs. The B&L-violating dimension-5 operators of GUT models allow one to probe via the proton decay the parameter space of SUGRA models. SuperKamiokande with the expected sensitivity of 2×10^{34} yr for the $\bar{\nu} K^+$ mode and even more sensitive future experiments which may go up to limits of 10^{36} y will allow one to probe a majority of the parameter space of SUGRA models. Dark matter limits put further severe constraints on the analysis. Thus, future data from accelerator and nonaccelerator experiments will either observe a supersymmetric signal or severely constrain or even eliminate specific unified models.

ACKNOWLEDGMENTS

This research was supported in part by NSF grants PHY-9901057 and PHY-9722090.

REFERENCES

1. For a previous review see, P. Nath and R. Arnowitt, hep-ph/9808465; in *Proceedings of the International Symposium on Lepton and Baryon Number Violation, Trento, Italy, Inst. Phys. Publ., 1999*, p. 3.
2. For reviews of supersymmetric grand unification see, G. Ross, *Grand Unified Theories*, Frontiers in Physics (1984); R. Arnowitt and P. Nath, in *Proceedings of the VII J.A. Swieca Summer School*, Ed. by E. Eboli (World Sci., Singapore, 1994); R. Mohapatra, *TASI Lectures* (1997).
3. J. Ellis, S. Kelley, and D. V. Nanopoulos, Phys. Lett. B **249**, 441 (1990); **260**, 131 (1991); C. Ciunti, C. W. Kim, and U. W. Lee, Mod. Phys. Lett. A **6**, 1745 (1991); U. Amaldi, W. de Boer, and H. Furstenau, Phys. Lett. B **260**, 447 (1991); P. Langacker and M. Luo, Phys. Rev. D **44**, 817 (1991).
4. C. T. Hill, Phys. Lett. B **135**, 47 (1984); Q. Shafi and C. Wetterich, Phys. Rev. Lett. **52**, 875 (1984).
5. T. Dasgupta, P. Mamales, and P. Nath, Phys. Rev. D **52**, 5366 (1995).
6. D. Ring, S. Urano, and R. Arnowitt, Phys. Rev. D **52**, 6623 (1995).
7. A. Dedes and K. Tamvakis, IOA-05-97; J. Hisano, T. Moroi, K. Tobe, and T. Yanagida, Phys. Lett. B **342**, 138 (1995).
8. W. J. Marciano, in *Proceedings of SUSY-97, Philadelphia, 1997.*
9. Super-Kamiokande Collab., Yad. Fiz. **63**, 1010 (2000) [Phys. At. Nucl. **63**, 934 (2000)].
10. Y. Totsuka, in *Proceedings of the 24th Conference on High Energy Physics, Munich, 1989* (Springer-Verlag, Berlin, 1989).
11. G. Gilbert, Nucl. Phys. B **328**, 159 (1989).
12. L. Krauss and F. Wilczek, Phys. Lett. B **181**, 380 (1986).
13. L. E. Ibáñez and G. G. Ross, Phys. Lett. B **260**, 291 (1991).
14. S. Weinberg, Phys. Rev. D **26**, 287 (1982); N. Sakai and T. Yanagida, Nucl. Phys. B **197**, 533 (1982); S. Dimopoulos, S. Raby, and F. Wilczek, Phys. Lett. B **112**, 133 (1982); J. Ellis, D. V. Nanopoulos, and S. Rudaz, Nucl. Phys. B **202**, 43 (1982); S. Chadha, G. D. Coughlan, M. Daniel, and G. G. Ross, Phys. Lett. B **149**, 47 (1984).
15. P. Nath, R. Arnowitt, and A. H. Chamseddine, Phys. Rev. D **32**, 2348 (1985); J. Hisano, H. Murayama, and T. Yanagida, Nucl. Phys. B **402**, 46 (1993).
16. R. Arnowitt and P. Nath, Phys. Rev. D **49**, 1479 (1994).
17. T. Goto and T. Nihei, Phys. Rev. D **59**, 115009 (1999).
18. A. H. Chamseddine, R. Arnowitt, and P. Nath, Phys. Rev. Lett. **49**, 970 (1982).
19. For reviews, see P. Nath, R. Arnowitt, and A. H. Chamseddine, *Applied N = 1 Supergravity* (World Sci., Singapore, 1984); H. P. Nilles, Phys. Rep. **110**, 1 (1984); H. Haber and G. L. Kane, Phys. Rep. **117**, 195 (1985).
20. S. Soni and A. Weldon, Phys. Lett. B **126**, 215 (1983); V. S. Kaplunovsky and J. Louis, Phys. Lett. B **306**, 268 (1993).
21. D. Matalliotakis and H. P. Nilles, Nucl. Phys. B **435**, 115 (1995); M. Olechowski and S. Pokorski, Phys. Lett. B **344**, 201 (1995); N. Polonski and A. Pomerol, Phys. Rev. D **51**, 6532 (1995).
22. P. Nath and R. Arnowitt, Phys. Rev. D **56**, 2820 (1997).
23. A. Datta and M. K. Parida, Trieste Preprint No. IC/97/207 (Miramare, 1997).
24. B. R. Greene, K. H. Kirklin, P. J. Miron, and G. G. Ross, Nucl. Phys. B **292**, 606 (1987).
25. K. S. Babu and S. M. Barr, Phys. Lett. B **381**, 137 (1996).
26. V. Lucas and S. Raby, Phys. Rev. D **54**, 2261 (1996); **55**, 6986 (1997).
27. K. S. Babu and R. N. Mohapatra, hep-ph/9906271; Phys. Rev. Lett. **74**, 2418 (1995).
28. K. S. Babu, J. S. Pati, and F. Wilczek, Phys. Lett. B **423**, 337 (1998); hep-ph/9812538.
29. M. E. Gómez, J. Rizos, and K. Tamvakis, Phys. Rev. D **59**, 015015 (1999).
30. M. B. Gavela *et al.*, Nucl. Phys. B **312**, 269 (1989).
31. T. S. Yuan, Phys. Rev. D **33**, 1894 (1986).
32. S. Dimopoulos and F. Wilczek, Report No. NSF-ITP-82-07 (1981).
33. S. Urano and R. Arnowitt, hep-ph/9611389; S. M. Barr, Phys. Rev. D **59**, 015004 (1999).
34. J. S. Pati, Yad. Fiz. **63**, 1133 (2000) [Phys. At. Nucl. **63**, 1058 (2000)].

35. H. Georgi and C. Jarlskog, Phys. Lett. B **86**, 297 (1979); J. Harvey, P. Ramond, and D. Reiss, Phys. Lett. B **92**, 309 (1980).
36. V. Jain and R. Shrock, Phys. Lett. B **352**, 83 (1995).
37. P. Nath, Phys. Rev. Lett. **76**, 2218 (1996); Phys. Lett. B **381**, 147 (1996).
38. For a review, see P. Nath and R. Arnowitt, in *Proceedings of the International Workshop on Aspects of Dark Matter in Astrophysics and Particle Physics, Heidelberg, Germany, 1996* (World Sci., Singapore, 1997), p. 333; hep-ph/9610460.
39. R. Arnowitt and P. Nath, Phys. Lett. B **437**, 344 (1998).
40. R. Arnowitt and P. Nath, Phys. Rev. D **54**, 2374 (1996).
41. R. Arnowitt and P. Nath, Phys. Rev. D **60**, 044002 (1999).
42. F. Wilczek and A. Zee, Phys. Lett. B **88**, 311 (1979).
43. G. F. Giudice and R. Rattazzi, hep-ph/9801271.
44. H. Pagels and J. Primack, Phys. Rev. Lett. **48**, 223 (1982).
45. C. D. Carone and H. Murayama, Phys. Rev. D **53**, 1658 (1996); B. Blok, C.-D. Lu, and D.-X. Zhang, Phys. Lett. B **386**, 146 (1996).
46. P. Martin, Phys. Rev. D **56**, 4207 (1997).
47. H. Hamidian, K. Huitu, K. Puolamaki, and D.-X. Zhang, Phys. Lett. B **428**, 310 (1998).
48. For a discussion of proton stability in superstring derived standard-like models, see A. E. Farragi, Nucl. Phys. B **428**, 111 (1994).
49. D. C. Lewellen, Nucl. Phys. B **337**, 61 (1990); J. A. Schwarz, Phys. Rev. D **42**, 1777 (1990); S. Chaudhuri *et al.*, Nucl. Phys. B **452**, 89 (1995); G. B. Cleaver, Nucl. Phys. B **456**, 219 (1995).
50. Z. Kakushadze and S. H. H. Tye, Phys. Rev. D **55**, 7896 (1997); **56**, 7878 (1997); Phys. Lett. B **392**, 325 (1997); Z. Kakushadze *et al.*, Nucl. Phys. B **501**, 547 (1997).
51. E. Witten, Nucl. Phys. B **471**, 135 (1996); P. Horava and E. Witten, Nucl. Phys. B **460**, 506 (1996).
52. N. Arkani-Hamed and S. Dimopoulos, hep-ph/9811353.

Physics of Atomic Nuclei, Vol. 63, No. 7, 2000, pp. 1158–1164. From Yadernaya Fizika, Vol. 63, No. 7, 2000, pp. 1234–1239.

NEW PHYSICS, NUCLEAR AND NUCLEON STRUCTURE IN RARE PROCESSES

Lepton Flavor Violation: Constraints from the Exotic μ^-–$e\mu^-$ Conversion*

T. S. Kosmas[1)] and S. G. Kovalenko[1), **]

Division of Theoretical Physics, University of Ioannina, Greece

Abstract—The exotic neutrinoless $\mu^- \longrightarrow e^-$ conversion is studied within conventional extensions of the standard model as well as in minimal supersymmetric models with *R*-parity-conserving and *R*-parity-violating mechanisms. The dependence on the nucleon and nuclear structure of the μ–*e* conversion rates is consistently taken into account. From the available experimental data on the branching ratio $R_{\mu e^-}$ for the currently interesting nuclei ^{48}Ti and ^{208}Pb, and from the experimental sensitivity for ^{27}Al, which has been employed as a target in MECO experiment at Brookhaven, we extract very severe constraints for the flavor violation parameters with our calculated transition matrix elements. We especially emphasize the constraints resulting for SUSY *R*-parity-violating parameters. © *2000 MAIK "Nauka/Interperiodica".*

1. INTRODUCTION

The lepton-flavor-violating neutrinoless conversion of a bound 1*s*-muon to electron in the field of a nucleus [1–4],

$$(A, Z) + \mu_b^- \longrightarrow e^- + (A, Z)^*, \qquad (1)$$

has recently been established as one of the best probes to study the muon number nonconservation if it exists and to search for family lepton violation [1]. So far, the experiments [5–8] seeking μ–*e* conversion events have succeeded only to put upper bounds on the branching ratio $R_{\mu e^-} = \Gamma(\mu^- \longrightarrow e^-)/\Gamma(\mu^- \longrightarrow \nu_\mu)$—the ratio of the muon–electron conversion rate relative to the total rate of the ordinary muon capture. The best upper limits have been extracted at PSI by the SINDRUM II experiments (90% C.L.):

$$R_{\mu e^-} < 7.0 \times 10^{-13} \quad \text{for} \quad {}^{48}\text{Ti target [5]}, \qquad (2)$$

$$R_{\mu e^-} < 4.6 \times 10^{-11} \quad \text{for} \quad {}^{208}\text{Pb target [6]}. \qquad (3)$$

These limits are improvements over the previous limits set at TRIUMF [7] a decade ago with the same targets.

These days, two μ–*e* conversion experiments have been launched: the ongoing experiment at PSI with ^{48}Ti target [5] and the planned MECO experiment at Brookhaven [8] with ^{27}Al target. The expected sensitivity on $R_{\mu e^-}$ in the PSI experiment is 10^{-14}, while in the Brookhaven experiment it will be roughly [8]

$$R_{\mu e^-} < 2 \times 10^{-17} \quad \text{for} \quad {}^{27}\text{Al target}, \qquad (4)$$

which means an improvement over the existing limits by about four orders of magnitude.

The MECO experiment is going to be conducted in a new μ-beam line at the AGS, where the muons are produced with a pulsed proton beam [3]. The proton energy will be chosen in the range of 8–20 GeV to optimize the μ^- flux per unit time. Furthermore, the number of electrons with energy, which is equal to the energy for the coherent peak in ^{27}Al (E_e = 104 MeV), is very much suppressed. This is in contrast with $\mu^- \longrightarrow e^-\gamma$, where the electron flux from $\mu^- \longrightarrow e^-\nu\bar{\nu}$ decay is peaked at the energy of the electrons from $\mu^- \longrightarrow e^-\gamma$. For these experiments, the knowledge of nuclear transition matrix elements for all accessible $\mu^- \longrightarrow e^-$ channels of the targets employed are of significant importance [9—13].

In this work, we use the transition matrix elements calculated for the aforementioned isotopes in the coherent mode to constrain the lepton-flavor-violating parameters of various Lagrangians predicting this exotic process (e.g., couplings of scalar, vector, etc., current components; neutrino mixing angles and masses [11–14]; and supersymmetric *R*-parity-violating couplings [15–20]) by the recent experimental data and the expected sensitivity of the MECO experiment.

It is well known that only the coherent rate can be measured because it is free from background events from bound muon decay and radiative muon capture followed by a fully asymmetric e^+e^- pair creation [8]. On the other hand, previous studies of μ–*e* conversion rates [10–12] have shown that for all mechanisms the coherent mode dominates the process (1). Therefore, this is the most important channel. The incoherent reaction leading to excited nuclear states is suppressed due to Pauli blocking effects, and it is much harder to calculate, but its knowledge is also useful in order to deter-

* This article was submitted by the authors in English.

1) Joint Institute for Nuclear Research, Dubna, Moscow oblast, 141980 Russia

** e-mail: kovalen@nusun.jinr.ru

mine the experimentally interesting quantity of the ratio of the coherent to the total $\mu^- \longrightarrow e^-$ rate [9—13].

2. THE $\mu^- \longrightarrow e^-$ CONVERSION WITHIN COMMON EXTENSIONS OF THE STANDARD MODEL

The family quantum numbers L_e, L_μ, L_τ are conserved within the Standard Model (SM) in all orders of perturbation theory, but this is an accidental consequence of the SM field content and gauge invariance. Processes like μ–e conversion, which are forbidden in the standard model by muon and electron quantum number conservation, play an important role in the study of the flavor-changing neutral currents.

On the particle physics side [1, 2], there are many mechanisms leading to the μ–e conversion mediated by virtual photons, W-boson or Z-particle exchange, as well as mechanisms mediated by exotic particles like Higgs scalars, etc. [4], supersymmetric (SUSY) particles (sleptons, etc.) [11], or R-parity-violating mechanisms [15]. If one is emphasizing the nuclear structure aspects of the $\mu^- \longrightarrow e^-$, one could stay within the minimal extensions of the SM. Some Feynman diagrams which contribute to $\mu^- \longrightarrow e^-$ conversion in the lowest order of perturbation theory are shown in Fig. 1 (one-loop-level diagrams) and Fig. 2 (tree-level diagrams). In Fig. 1, mixing of intermediate neutrinos and gauge bosons or mixing of neutralinos and sleptons in SUSY models with R-parity conservation is involved [14].

In the SUSY extensions of SM, one can introduce a discrete symmetry known as R parity [19–21] defined as $R_p = (-1)^{3B+L+2S}$, where B, L, and S are the baryon, lepton, and spin quantum numbers. Up to now, there is no convincing theoretical motivation for such a symmetry of the low-energy Lagrangian. Therefore, SUSY models of both types "with" (R_p SUSY) and "without" ($\not{R}_p$ SUSY) R-parity conservation are "a priori" plausible. In the SUSY models, nontrivial contributions to the lepton-flavor-violating processes, like the $\mu^- \longrightarrow e^-$ conversion, are predicted (see recent discussion of $\not{R}_p$ SUSY in [15]).

In Fig. 2, we show some of the most important R-parity-violating mechanisms mediated by sneutrinos $\tilde{\nu}$, up $\tilde{u}_L$ and down $\tilde{d}_R$ squarks or by chargino–lepton mixing and Z bosons or squarks $\tilde{d}_L$. In the context of the above models, we construct below the effective (μ^-, e^-) conversion Hamiltonian by firstly writing down the hadronic and leptonic currents of these diagrams.

Hadronic $\mu^- \longrightarrow e^-$ Currents at the Nucleon Level

To write the hadronic $\mu^- \longrightarrow e^-$ currents at the nucleon level, one usually starts from the weak vector, axial vector, etc., quark currents. Then, assuming a specific nucleon model, one transforms these hadronic currents to the nucleon level. For the diagrams shown in Figs. 1 and 2, one gets the expressions given below.

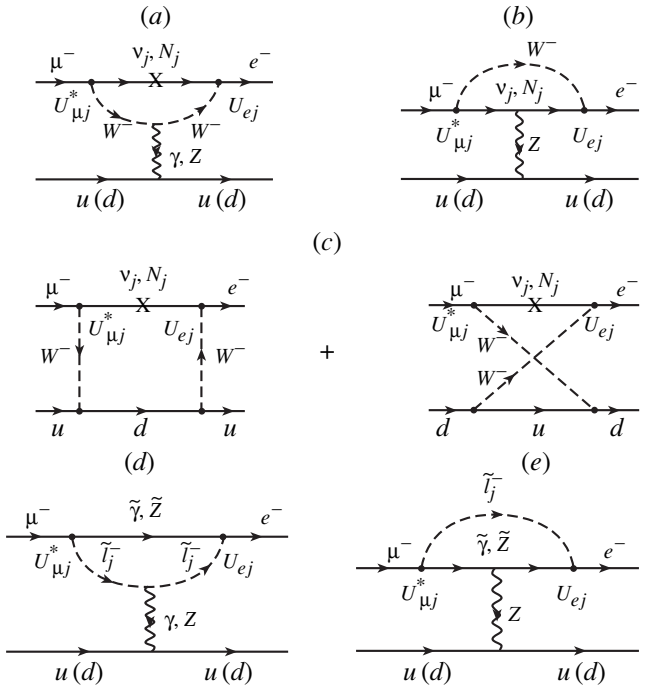

Fig. 1. Photonic and nonphotonic mechanisms exhibiting the $\mu^- \longrightarrow e^-$ process within the context of conventional extensions of the SM (*a*–*c*), as well as SUSY theories (*d*, *e*) with R-parity conservation. The hadronic vertex is mediated by photon exchange (*a*, *d*), Z-particle exchange (*a*, *b*, *d*, *e*), and W-boson exchange (*c*).

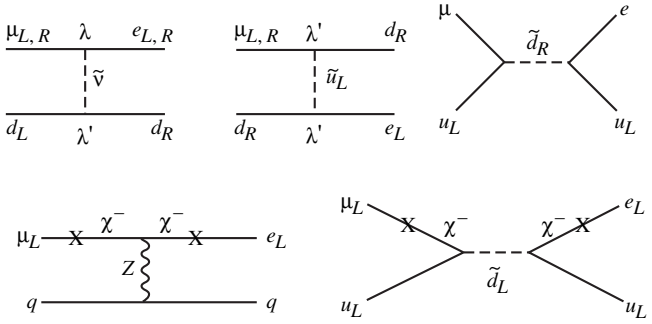

Fig. 2. Leading $\not{R}_p$ MSSM diagrams contributing to μ–e conversion at tree level. (i) (upper diagrams) Trilinear terms mediated by the sneutrino $\tilde{\nu}$, up $\tilde{u}_L$ and down $\tilde{d}_R$ squarks in the intermediate states. (ii) (lower diagrams) Bilinear terms mediated via the chargino–lepton mixing (schematically denoted by crosses (×) on the lepton lines). The intermediate states of the diagrams are Z bosons and squarks $\tilde{d}_R$.

(a) Gauge model and SUSY R-parity-conserving mechanisms

These mechanisms involve mixing of intermediate neutrinos and gauge bosons and mixing of intermediate

neutralinos and sleptons. In the photonic diagrams of Figs. 1*a* and 1*d*, the hadronic nucleon vertex is the usual electromagnetic current (photonic)

$$J_\lambda^{(1)} = \bar{N}_p \gamma_\lambda N_p = \bar{N}\gamma_\lambda \frac{1}{2}(1+\tau_3)N. \quad (5)$$

Here, N is the nucleon isospin doublet $N^T = (N_p, N_n)$ with $N_{p(n)}$ the proton (neutron) spinor.

In the case of the nonphotonic mechanisms, there are many diagrams contributing to the $\mu^- \longrightarrow e^-$ conversion. The nonphotonic hadronic current which includes contributions from Z-particle exchange (Figs. 1*a*, 1*b*, 1*d*, 1*e*) and the box diagrams (Fig. 1*c*) involving either massive neutrinos and W bosons or sleptons and neutralinos can be written as follows (nonphotonic):

$$J_\lambda^{(2)} = \bar{N}\gamma_\lambda \frac{1}{2}[(3 + f_V\beta\tau_3) - (f_V\beta'' + f_A\beta'\tau_3)\gamma_5]N, \quad (6)$$

where $f_{V(A)}$ represents the vector (axial-vector) static nucleon form factor ($f_A/f_V = 1.24$) and the parameters β, β' and β'' for the models adopted take the values given in [11]. The parameter β is defined as $\beta = \beta_1/\beta_0$, with β_0 (β_1) being the isoscalar (isovector) couplings at the quark level. We note that, in general, the parameters β, β', and β'' are functions of $\sin^2\theta_W$. For example, in the case of Z-exchange, we have $\beta' = 3/2\sin^2\theta_W = 6.90$.

The corresponding leptonic currents for the photonic and nonphotonic mechanism of Fig. 1 are given in [11].

(b) R-parity-violating mechanisms

In this work, we discuss all possible mechanisms for the $\mu^- \longrightarrow e^-$ process existing in the minimal SUSY model with a most general form of R-parity violation at the tree level. To write down the 4-fermion interaction Lagrangian for μ–e conversion, one starts from a most general gauge invariant form of the R-parity-violating superpotential at the quark level. For the diagrams of Fig. 2, this effective Lagrangian takes the form (first order of perturbation theory)

$$\mathcal{L}_{\text{eff}}^q = \frac{G_F}{\sqrt{2}} j_\mu [\eta_L^{ui} J_{uL(i)}^\mu + \eta_R^{ui} J_{uR(i)}^\mu + \eta_L^{di} J_{dL(i)}^\mu + \eta_R^{di} J_{dR(i)}^\mu] + \frac{G_F}{\sqrt{2}} [\bar{\eta}_R^{di} J_{dR(i)} j_L + \bar{\eta}_L^{di} J_{dL(i)} j_R], \quad (7)$$

where the coefficients η contain the R_p SUSY parameters [19–25] (i runs over generations so that $q_i = u_i, d_i$ with $u_i = u, c, t$ and $d_i = d, s, b$). The color singlet currents $J_{q_{L/R}(i)}^\mu$ and $J_{d_{L/R}(i)}$ at the quark level are written as

$$J_{q_{L/R}(i)}^\mu = \bar{q}_i \gamma^\mu P_{L/R} q_i, \quad J_{d_{L/R}(i)} = \bar{d}_i P_{L/R} d_i,$$

where $P_{L/R} = (1 \mp \gamma_5)/2$. The leptonic currents are written as

$$j^\mu = \bar{e}\gamma^\mu P_L \mu, \quad j_{L/R} = \bar{e} P_{L/R} \mu.$$

In the next step, to construct the R-parity-violating effective μ–e conversion Lagrangian, one rewrites (7), specified at the quark level, in terms of the nucleon degrees of freedom. This is usually achieved by utilizing the on-mass-shell matching condition [20] and gives

$$\mathcal{L}_{\text{eff}}^N = \frac{G_F}{\sqrt{2}} [\bar{e}\gamma_\mu(1-\gamma_5)\mu \cdot J^\mu + \bar{e}\mu \cdot J_+ + \bar{e}\gamma_5\mu \cdot J_-], \quad (8)$$

where the hadronic (nucleon) currents are

$$J^\mu = \bar{N}\gamma^\mu[(\alpha_V^{(0)} + \alpha_V^{(3)}\tau_3) + (\alpha_A^{(0)} + \alpha_A^{(3)}\tau_3)\gamma_5]N,$$
$$J_\pm = \bar{N}[(\alpha_{\pm S}^{(0)} + \alpha_{\pm S}^{(3)}\tau_3) + (\alpha_{\pm P}^{(0)} + \alpha_{\pm P}^{(3)}\tau_3)\gamma_5]N. \quad (9)$$

The coefficients α_K^τ, with $K = \pm S, V, A, P$, in (9) include the nucleon form factors (functions of the momentum transfer $\mathbf{q}^2$) for scalar, vector, axial-vector, and pseudoscalar contributions, respectively [15]. Since, however, the maximum momentum transfer $\mathbf{q}^2$ in μ–e conversion is much smaller than the typical scale of nucleon structure ($|\mathbf{q}| \approx m_\mu/c$, with $m_\mu = 105.6$ MeV being the muon mass), we can safely neglect the $\mathbf{q}^2$ dependence of the nucleon form factors.

3. NUCLEON AND NUCLEAR STRUCTURE DEPENDENCE OF THE $\mu^- \longrightarrow e^-$ CONVERSION BRANCHING RATIO

One of the most interesting quantities in $\mu^- \longrightarrow e^-$ conversion, both from theoretical and experimental point of view, is the branching ratio $R_{\mu e^-}$. The expression which gives $R_{\mu e^-}$ in the case of the dominant coherent channel has been written as [9]

$$R_{\mu e^-} = \rho\gamma, \quad (10)$$

where ρ is nearly independent of nuclear physics [11] and contains the flavor-violating parameters mentioned before. Byway of example, we indicate that, for photon exchange, ρ is given by

$$\rho = (4\pi\alpha)^2 \frac{|f_{M1} + f_{E0}|^2 + |f_{E1} + f_{M0}|^2}{(G_F m_\mu^2)^2}. \quad (11)$$

This expression contains four electromagnetic form factors f_{E0}, f_{E1}, f_{M0}, and f_{M1} parametrized in a specific elementary model [11].

The function $\gamma(A, Z)$ in (10) includes about all the nuclear information. Assuming that the total rate of the ordinary muon capture rate is described by the Goulard–Primakoff function f_{GP}, $\gamma(A, Z)$ is defined as

$$\gamma(A, Z) \equiv \gamma = \frac{E_e p_e}{m_\mu^2} \frac{M^2}{G^2 Z f_{GP}(A, Z)}, \quad (12)$$

where $G^2 \approx 6$. Thus, the nuclear aspects of the $\mu^- \longrightarrow e^-$ branching ratio $R_{\mu e^-}$ are mainly included in the matrix elements M^2 [4], which in the proton–neutron

representation, are written as

$$M^2 = (\mathcal{M}_p + Q(\beta)\mathcal{M}_n)^2 \langle \Phi_{1s} \rangle^2, \quad (13)$$

where $Q(\beta)$ is given in [11] and $\langle \Phi_{1s} \rangle^2$ is the square of the mean 1*s*-muon wave function [12].

In general, the transition matrix elements $\mathcal{M}_{p,n}$ in (13) depend on the final nuclear state populated during the μ–*e* conversion. For ground state to ground state transitions ($gs \longrightarrow gs$) in spherically symmetric nuclei, the following integral representation is valid:

$$\mathcal{M}_{p,n} = 4\pi \int j_0(p_e r)\Phi_\mu(r)\rho_{p,n}(r) r^2 dr, \quad (14)$$

where $j_0(x)$ is a zero-order spherical Bessel function and $\rho_{p(n)}$ is the proton (neutron) nuclear density normalized to the atomic number Z and neutron number N of the participating nucleus, respectively. The space dependent part of the muon wave function $\Phi_\mu(\mathbf{r})$ (a spherically symmetric function) can be obtained by solving numerically the Schrödinger and Dirac equations with the Coulomb potential.

The factorization approximation [10] is very good for light nuclei, and $M^2_{\rm coh}$ can be expressed in terms of the nuclear form factors $F_Z(q^2)$ (for protons) and $F_N(q^2)$ (for neutrons), which are easily estimated since for this channel only the ground state wave function is required. These form factors are defined as

$$F_Z = \frac{1}{Z}\sum_j \hat{j}(j\|j_0(qr)\|j)(V_j^p)^2, \quad (15)$$

$$F_N = \frac{1}{N}\sum_j \hat{j}(j\|j_0(qr)\|j)(V_j^n)^2, \quad (16)$$

and contain the single-particle orbit occupancies $(V_j)^2$, which one must evaluate with a nuclear model in the proton–neutron representation, e.g., QRPA in the case of ^{48}Ti and ^{208}Pb [11], or shell model in the case of ^{27}Al [26], etc.

With Lagrangian (8) for the μ–*e* conversion branching ratio, one can deduce an expression similar to (10) in the form

$$R_{\mu e^-} = \frac{G_F^2}{2\pi}\frac{p_e E_e (\mathcal{M}_p + \mathcal{M}_n)^2}{G^2 Z f_{\rm GP}(A,Z)}\mathcal{Q}, \quad (17)$$

where

$$\mathcal{Q} = 2\left|\alpha_V^{(0)} + \alpha_V^{(3)}\phi\right|^2 + \left|\alpha_{+S}^{(0)} + \alpha_{+S}^{(3)}\phi\right|^2 + \left|\alpha_{-S}^{(0)} + \alpha_{-S}^{(3)}\phi\right|^2 + 2\mathrm{Re}\{(\alpha_V^{(0)} + \alpha_V^{(3)}\phi) \times [\alpha_{+S}^{(0)} + \alpha_{-S}^{(0)} + (\alpha_{+S}^{(3)} + \alpha_{-S}^{(3)})\phi]\} \quad (18)$$

and

$$\phi = (\mathcal{M}_p - \mathcal{M}_n)/(\mathcal{M}_p + \mathcal{M}_n). \quad (19)$$

The quantity $\mathcal{Q}$ in (18) depends weakly on the nuclear parameters determining the factor ϕ. In fact, the terms depending on ϕ are small and in practice the nuclear dependence of $\mathcal{Q}$ can be neglected. Thus, the corresponding upper bounds on $\mathcal{Q}$ determine the sensitivity to the R_p SUSY signals arriving at the detector in various μ–*e* conversion experiments (see results below).

Table 1. Transition-matrix elements (muon–nucleus overlap integrals $\mathcal{M}_{p,n}$ (14)) evaluated with the exact muon wave function obtained via neural network techniques (other useful quantities, see text, are also included)

Nucleus	$\lvert\mathbf{p}_e\rvert$, fm^{-1}	ϵ_b, MeV	$\Gamma_{\mu c}$, 10^6 s^{-1}	$\mathcal{M}_p$, fm$^{-3/2}$	$\mathcal{M}_n$, fm$^{-3/2}$
^{27}Al	0.531	–0.470	0.71	0.047	0.045
^{48}Ti	0.529	–1.264	2.60	0.104	0.127
^{208}Pb	0.482	–10.516	13.45	0.414	0.566

A usual approximate expression for the ratio ϕ of (19), containing the nuclear parameters A (the atomic weight) and Z (the total charge of the nucleus), is the following:

$$\phi \approx \tilde{\phi} = (A - 2Z)/A. \quad (20)$$

This equation follows from the assumption that $\mathcal{M}_p \approx ZF_Z$ and $\mathcal{M}_n \approx NF_N$. For light and medium nuclei, $F_Z \approx F_N$ and (20) is a good approximation. For isoscalar nuclei, i.e., $A = 2Z$, $\phi \approx \tilde{\phi} = 0$ (see below).

4. RESULTS AND DISCUSSION

The pure nuclear physics calculations needed for the μ–*e* conversion studies refer to the integrals of (14). The results of $\mathcal{M}_p$ and $\mathcal{M}_n$ for the currently interesting nuclei Al, Ti, and Pb are shown in Table 1. They have been calculated with proton densities ρ_p from the electron scattering data [27] and neutron densities ρ_n from the analysis of pionic atom data [28]. We employed an analytic form for the muon wave function obtained by solving the Schrödinger equation with the Coulomb potential produced by the charge densities discussed before. In this way, the nucleon finite size was taken into consideration. Moreover, we included vacuum polarization corrections as in [12]. In solving the Schrödinger equation, we have used modern neural networks techniques [29] which give the wave function $\Phi_\mu(r)$ in the analytic form of a sum over sigmoid functions. Thus, in (14), only a simple numerical integration is finally required. To estimate the influence of the nonrelativistic approximation on the muon wave function $\Phi_\mu(\mathbf{r})$, we have also determined it by solving the Dirac equation. The results do not significantly differ from those of the Schrödinger picture.

In Table 1, we also show the muon binding energy ϵ_b (obtained as output of the Dirac and Schrödinger solution) and the experimental values for the total rate of the ordinary muon capture $\Gamma_{\mu c}$ taken from [30].

Table 2. The variation of the quantities ϕ (19) and its approximate expression $\tilde{\phi}$ (20) through the periodic table

A	Z	$\phi(A, Z)$	$\tilde{\phi}(A, Z)$
12	6	0.000	0.000
24	12	0.014	0.000
27	13	0.000	−0.037
32	16	0.023	0.000
40	20	0.037	0.000
44	20	−0.063	−0.091
48	22	−0.083	−0.083
63	29	−0.056	−0.079
90	40	−0.054	−0.111
112	48	−0.108	−0.143
208	82	−0.152	−0.212
238	92	−0.175	−0.227

Table 3. The limits on the elementary sector part of the exotic μ–e conversion branching ratio [quantity ρ (11) and quantity $\mathcal{Q}$ (18)] extracted from recent experimental data for the nuclear targets ^{48}Ti and ^{208}Pb [5, 6] and the sensitivity of the MECO experiment for the ^{27}Al target [8]

Mechanism	^{27}Al	^{48}Ti	^{208}Pb
Quantity ρ			
Photonic	$\leq 4.6\times10^{-18}$	$\leq 8.2\times10^{-14}$	$\leq 3.2\times10^{-12}$
W-boson exchange	$\leq 5.8\times10^{-19}$	$\leq 3.0\times10^{-14}$	$\leq 1.1\times10^{-12}$
SUSY sleptons	$\leq 1.8\times10^{-18}$	$\leq 3.0\times10^{-14}$	$\leq 1.1\times10^{-12}$
SUSY Z-exchange	$\leq 7.3\times10^{-19}$	$\leq 0.7\times10^{-14}$	$\leq 0.2\times10^{-12}$
Quantity $\mathcal{Q}$			
$\not{R}_p$ SUSY	$\leq 5.10\times10^{-19}$	$\leq 1.25\times10^{-14}$	$\leq 2.27\times10^{-13}$

Using the values for $\mathcal{M}_p$ and $\mathcal{M}_n$ for a set of nuclei throughout the periodic table [12], we can estimate the nuclear physics influence of the quantities ρ and $\mathcal{Q}$. In Table 2 we show the results obtained for the ratio ϕ (19) and its approximate expression $\tilde{\phi}$ (20). We see that ϕ is very small ($-0.17 \leq \phi \leq 0.04$) and, because the terms of the quantity $\mathcal{Q}$ which depend on ϕ are also small, we conclude that the nuclear dependence of the quantity $\mathcal{Q}$ can be ignored, as we have discussed before. Since there is at maximum ≈15% difference between ϕ and $\tilde{\phi}$ and because the isovector terms of the quantity $\mathcal{Q}$ are small, especially for light nuclear systems, one can use the explicit (A, Z) dependence of $\mathcal{Q}$.

The results of Table 1 can be exploited for setting constraints on the parameters of the specific gauge model predicting the μ–e process. In Table 3, we quote the bounds obtained for the quantities ρ and $\mathcal{Q}$ resulting from the use of the recent experimental data on the branching ratio $R_{\mu e^-}$ given in (2) and (3) and the expected experimental sensitivity of the Brookhaven experiment, $R_{\mu e^-} < 2\times10^{-17}$ (4). The limits of ρ and $\mathcal{Q}$ quoted in Table 3 are improvements by about four orders of magnitude over the existing ones.

We should stress that limits on the quantities ρ (11) and $\mathcal{Q}$ (18) are the only constraints imposed by the μ–e conversion on the underlying elementary particle physics. One can extract upper limits on the individual lepton-flavor-violation parameters (couplings of scalar, vector currents, neutrino masses, etc. [1, 4, 11, 15]) under certain assumptions like the commonly assumed dominance of only one component of the μ–e conversion Lagrangian, which is equivalent to constraining one parameter or product of the parameters at a time. For example, in the case of $\not{R}_p$ SUSY mechanisms, in order to learn about the size and the regularities of possible violation of R parity, one needs some information on the parameters λ, λ', and μ_i and the sneutrino vacuum expectation values $\langle\tilde{\nu}_i\rangle$ [31]. Using the upper limits for $\mathcal{Q}$ given in Table 3, we can derive under the above assumptions the constraints on $\alpha_K^{(\tau)}$ (18) and the products of various $\not{R}_p$ parameters. Thus, the bounds obtained for the scalar current couplings $\alpha_S^{(\tau)}$ in the R-parity-violating Lagrangian for the ^{27}Al target [26, 32] are $|\alpha_S^{(\tau)}| < 7\times10^{-10}$. The limit for $\alpha_S^{(\tau)}$ obtained with the data of Ti target [5] is $|\alpha_S^{(\tau)}| < 1.1\times10^{-7}$, i.e., more than two orders of magnitude weaker than the limit of ^{27}Al.

In Table 4, we list the constraints on the trilinear $\not{R}_p$ couplings obtained from the μ–e conversion in ^{48}Ti (the corresponding constraints for ^{208}Pb are significantly weaker, and those for ^{27}Al rely on the expected experimental sensitivity of the MECO detector). In this table, B denotes a scaling factor defined as

$$B = (R_{\mu e}^{\exp}/7.0\times10^{-13})^{1/2}.$$

From Table 4, we see that the limits on the products $\lambda\lambda'$ are very severe. In [15], we found that, except for a few cases, the constraints on $\lambda'\lambda'$, $\lambda\lambda'$, and $\lambda\lambda$ obtained from μ–e conversion are better than those derived from any other process [17].

As we have mentioned at the beginning, significantly better improvement on these limits is expected from the ongoing experiments at PSI [5] and even better from the MECO experiment at Brookhaven [8]. This would make the μ–e conversion constraints better than those from the other processes in all the cases.

Before closing, we should note that the last four limits for $\lambda'\lambda$ in Table 4 originate from the contribution of

Table 4. Upper bounds on $\lambda'_{ijk}\lambda_{lmn}$ obtained from the $\mu^- \longrightarrow e^-$ conversion in ^{48}Ti (they are given for scalar masses $\tilde{m}$ = 100 GeV; the scaling factor B is defined in the text)

Parameters	$(\mu\text{–}e) \times B$, 10^{-9}
$\lvert\lambda'_{211}\lambda_{212}\rvert$	4.1
$\lvert\lambda'_{311}\lambda_{312}\rvert$	4.1
$\lvert\lambda'_{111}\lambda_{121}\rvert$	4.1
$\lvert\lambda'_{311}\lambda_{321}\rvert$	4.1
$\lvert\lambda'_{222}\lambda_{212}\rvert$	7.7
$\lvert\lambda'_{322}\lambda_{312}\rvert$	7.7
$\lvert\lambda'_{122}\lambda_{121}\rvert$	7.7
$\lvert\lambda'_{322}\lambda_{321}\rvert$	7.7

the strange nucleon sea. These limits are comparable to the other μ–e constraints derived from the valence quarks contributions and significantly weaker than those derived in [31] from the SuperKamiokande atmospheric neutrino data.

5. SUMMARY AND CONCLUSIONS

The transition matrix elements of the flavor-violating $\mu^- \longrightarrow e^-$ conversion are of notable importance in computing accurately the corresponding rates for each accessible channel of this exotic process. Such calculations provide useful nuclear-physics inputs for the expected new data from the PSI and MECO experiments to put more severe bounds on the muon-number-changing parameters (isoscalar couplings, etc.) determining the effective currents in various models that predict the exotic $\mu^- \longrightarrow e^-$ process.

In the case of the R-parity-violating interactions discussed here, we have investigated all the possible tree-level contributions to the μ–e conversion in nuclei taking into account the nucleon and nuclear structure effects. We found a new important contribution to $\mu^- \longrightarrow e^-$ originating from the strange quark sea in the nucleon which is comparable with the usual contribution of the valence u, d quarks.

From the existing data on $R_{\mu e^-}$ in ^{48}Ti and ^{208}Pb and the expected sensitivity of the designed MECO experiment [8], we obtained stringent upper limits on the quantities ρ and $\mathcal{Q}$ introduced in (11) and (18). They can be considered as theoretical sensitivities of μ^-–e^- conversion experimental signals expected to be detected in various targets employed. Thus, these quantities are helpful for comparing different μ–e conversion experiments. In addition, limits for the products of the $\mathcal{R}_p$ parameters for ^{48}Ti show that the μ–e conversion constraints on all the products $\lambda\lambda$, $\lambda'\lambda$, and $\lambda'\lambda'$ would become more stringent than those from any other process. The importance of this conclusion is strengthened by the fact that no comparable improvements to that of the ongoing μ–e conversion experiments at PSI [5] and Brookhaven [8] is expected from other experiments in the next few years.

ACKNOWLEDGMENTS

T.S.K. would like to acknowledge partial support of this work by Ioannina University grants and the NANP'99 Conference Organizers for hospitality at Dubna.

REFERENCES

1. W. J. Marciano and A. I. Sanda, Phys. Rev. Lett. **38**, 1512 (1977); Phys. Lett. B **67**, 303 (1977).
2. J. D. Vergados, Phys. Rep. **133**, 1 (1986).
3. W. Molzon, Springer Tracts Mod. Phys. **163**, 105 (2000).
4. T. S. Kosmas, G. K. Leontaris, and J. D. Vergados, Prog. Part. Nucl. Phys. **33**, 397 (1994).
5. SINDRUM II Collab. (C. Dohmen *et al.*), Phys. Lett. B **317**, 631 (1993); H. K. Walter, Yad. Fiz. **61**, 1253 (1998) [Phys. At. Nucl. **61**, 1153 (1998)].
6. SINDRUM II Collab. (W. Honecker *et al.*), Phys. Rev. Lett. **76**, 200 (1996).
7. TRIUMF Collab. (S. Ahmad *et al.*), Phys. Rev. Lett. **59**, 970 (1987).
8. W. Molzon, Invited Talk at *International Conference on Symmetries in Physics at Intermediate and High Energies and Applications, Ioannina, Greece, 1998.*
9. T. S. Kosmas and J. D. Vergados, Nucl. Phys. A **510**, 641 (1990).
10. T. S. Kosmas, J. D. Vergados, and A. Faessler, Yad. Fiz. **61**, 1261 (1998) [Phys. At. Nucl. **61**, 1161 (1998)].
11. T. S. Kosmas, A. Faessler, and J. D. Vergados, J. Phys. G **23**, 693 (1997).
12. H. C. Chiang *et al.*, Nucl. Phys. A **559**, 526 (1993).
13. J. Schwieger, T. S. Kosmas, and A. Faessler, Phys. Lett. B **443**, 7 (1998).
14. R. Barbieri and L. Hall, Phys. Lett. B **338**, 212 (1994); R. Barbieri, L. Hall, and A. Strumia, Nucl. Phys. B **445**, 219 (1995).
15. A. Faessler, T. S. Kosmas, S. G. Kovalenko, and J. D. Vergados, hep-ph/9904335; submitted for publication in Nucl. Phys. B.
16. J. E. Kim, P. Ko, and D.-G. Lee, Phys. Rev. D **56**, 100 (1997); hep-ph/9701381.
17. K. Huitu, J. Maalampi, M. Raidal, and A. Santamaria, Phys. Lett. B **430**, 355 (1998); hep-ph/9712249.
18. M. Nowakowski and A. Pilaftsis, Nucl. Phys. B **461**, 19 (1996); A. Joshipura and M. Nowakowski, Phys. Rev. D **51**, 2421 (1995).
19. H.-P. Nilles, Phys. Rep. **110**, 1 (1984); H. Haber and G. Kane, Phys. Rep. **117**, 75 (1985).
20. A. Faessler, S. Kovalenko, F. Šimkovic, and J. Schwieger, Phys. Rev. Lett. **78**, 183 (1997).

21. EMC Collab. (J. Ashman *et al.*), Nucl. Phys. B **328**, 1 (1989).

22. G. Mallot, Nucl. Phys. B **441**, 12 (1995).

23. A. Manohar and R. Jaffe, Nucl. Phys. B **337**, 509 (1990).

24. M. A. Shifman, A. I. Vainshtein, and V. I. Zakharov, Phys. Lett. B **78**, 443 (1978).

25. T. P. Cheng, Phys. Rev. D **38**, 2869 (1988); H.-Y. Cheng, Phys. Lett. B **219**, 347 (1989); **317**, 631 (1993).

26. T. Siiskonen, J. Suhonen, and T. S. Kosmas, Phys. Rev. C (in press).

27. H. de Vries, C. V. de Jager, and C. de Vries, At. Data Nucl. Data Tables **36**, 495 (1987).

28. W. R. Gibbs and B. F. Gibson, Annu. Rev. Nucl. Part. Sci. **37**, 411 (1987); C. García-Recio, J. Nieves, and E. Oset, Nucl. Phys. A **547**, 473 (1992).

29. I. E. Lagaris, A. Likas, and D. I. Fotiadis, Comput. Phys. Commun. **104**, 1 (1997).

30. T. Suzuki *et al.*, Phys. Rev. C **35**, 2212 (1987).

31. V. Bednyakov, A. Faessler, and S. Kovalenko, Phys. Lett. B **442**, 203 (1998).

32. T. Siiskonen, T. S. Kosmas, and J. Suhonen, Phys. Rev. C (in press).

Physics of Atomic Nuclei, Vol. 63, No. 7, 2000, pp. 1165–1176. From Yadernaya Fizika, Vol. 63, No. 7, 2000, pp. 1240–1251.

NEW PHYSICS, NUCLEAR AND NUCLEON STRUCTURE IN RARE PROCESSES

Test of Physics beyond the Standard Model in Nuclei*

A. Faessler and F. Šimkovic[1)]

Institut für Theoretische Physik der Universität Tübingen, Germany

Abstract—The modern theories of Grand Unification (GUT) and SuperSymmetric (SUSY) extensions of Standard Model (SM) suppose that the conservation laws of the SM may be violated to some small degree. The nuclei are well-suited as a laboratory to test fundamental symmetries and fundamental interactions like lepton flavor (LF) and lepton number (LN) conservation. A prominent role between experiments looking for LF and total LN violation play not yet observed processes of neutrinoless double-beta decay ($0\nu\beta\beta$ decay). The GUT and SUSY models offer a variety of mechanisms that allow $0\nu\beta\beta$ decay to occur. They are based on mixing of Majorana neutrinos and/or *R*-parity-violation hypothesis. Although the $0\nu\beta\beta$-decay has not been seen, it is possible to extract from the lower limits of the lifetime upper limits for the effective electron Majorana neutrino mass, effective right-handed weak-interaction parameters, the effective Majoron coupling constant, *R*-parity-violating SUSY parameters, etc. A condition for obtaining reliable limits for these fundamental quantities is that the nuclear matrix elements governing this process can be calculated correctly. The nuclear structure wave functions can be tested by calculating the two-neutrino double-beta decay ($2\nu\beta\beta$ decay) for which we have experimental data and not only lower limits as for the $0\nu\beta\beta$ decay. For open-shell nuclei, the method of choice has been the quasiparticle random-phase approximation (QRPA), which treats Fermion pairs as bosons. It has been found that, by extending the QRPA including fermion commutation relations, better agreement with $2\nu\beta\beta$-decay experiments is achieved. This increases also the reliability of conclusions from the upper limits on the $0\nu\beta\beta$-decay transition probability. In this work, the limits on the LN-violating parameters extracted from current $0\nu\beta\beta$-decay experiments are listed. Studies in respect to future $0\nu\beta\beta$-decay experimental projects are also presented. © *2000 MAIK "Nauka/Interperiodica".*

1. INTRODUCTION

The Standard Model (SM) represents the simplest and most economical theory which describes jointly weak and electromagnetic interactions. It describes well all terrestrial experimental results known today. Nevertheless, the SM cannot be considered as the ultimative theory of nature and is likely to describe the effective interaction at low energy of an underlying more fundamental theory. The SuperSymmetry (SUSY), which is one of the fundamental new symmetries of nature, is believed to be next step beyond the successful SM. The supersymmetry is the symmetry between fermions and bosons, which has to be broken in order to explain the phenomenology of the elementary particles and their superpartners. It is the only known symmetry which can stabilize the elementary Higgs boson mass with respect to otherwise uncontrollable radiative corrections. The Minimal SuperSymmetric Model (MSSM), which leads to the SM at low energies, has been the subject of extensive investigations.

Both the SM and the MSSM lead to zero mass for the neutrinos. In view of the observed results on solar (Homestake [1], Kamiokande [2], Gallex [3], and SAGE [4]) and atmospheric neutrinos (IMB [5], Soudan 2 [6], MACRO [7], and SuperKamiokande [8]), it is more appropriate to consider the extensions of the SM and the MSSM that can lead to neutrino masses. Neutrino masses either require the existence of right-handed neutrinos or require violation of the lepton number (LN) so that Majorana masses are possible. So, one is forced to go beyond the minimal models again, whereby lepton flavor (LF) and/or LN violation can be allowed in the theory. A good candidate for such a theory is the left–right symmetric model of Grand Unification (GUT) inaugurated by Salam, Pati, Mohapatra, and Senjanović [9] (especially models based on $SO(10)$, which were first proposed by Fritzsch and Minkowski [10]) and its supersymmetric version [11]. The left–right symmetric models, representing generalization of the $SU(2)_L \otimes U(1)$ SM, predict not only that the neutrino is a Majorana particle, which means it is up to a phase identical with its antiparticle, but automatically predict the neutrino has a mass and a weak right-handed interaction. The basic idea behind grand unified models is an extension of the local gauge invariance from quantum chromodynamics [$SU(3)$] involving only the colored quarks also to electrons and neutrinos. We note that the nonsupersymmetric left–right models suffer from the hierarchy problem.

The expectations arising from GUTs and their SUSY versions are that the conservation laws of the SM, e.g., LN conservation, may be violated to some small degree. In the left–right symmetric models, the

* This article was submitted by the authors in English.

1) On leave from Department of Nuclear Physics, Comenius University, Bratislava, Slovakia; e-mail: Fedor.Simkovic uni-tuebingen.de

LN conservation is broken by the presence of the Majorana neutrino mass. The LN violation is also inbuilt in those SUSY theories where R parity, defined as $R_p = (-1)^{3B+L+2S}$ (S, B, and L are the spin, the baryon number, and the lepton number, respectively), is not a conserved quantity anymore. The conservation of LN is among the most stringently tested laws of physics nowadays. The nuclei are well-suited as a laboratory to test this fundamental symmetry due to the fact that a variety of quantum numbers is available as initial and final states. The neutrinoless double-beta decay ($0\nu\beta\beta$ decay),

$$(A, Z) \longrightarrow (A, Z+2) + 2e^-, \qquad (1)$$

which involves the emission of two electrons and no neutrinos, has been long recognized as a powerful tool to study the LN conservation. The $0\nu\beta\beta$ decay takes place only if the neutrino is a Majorana particle with non-zero mass [12]. The GUT and R-parity-violating SUSY models offer a plethora of the $0\nu\beta\beta$-decay mechanisms triggered by exchange of neutrinos, neutralinos, gluinos, leptoquarks, etc. [13, 14]. If one assumes that one mechanism at a time dominates, the half-life of the $0\nu\beta\beta$ decay can be written as

$$(T^{0\nu}_{1/2})^{-1} = |LNV|^2 \sum_i P^{0\nu}_i G^{0\nu}_i, \qquad (2)$$

where LNV is some effective LN-violating parameter, $P^{0\nu}_i$ is the real part of the product of two nuclear matrix elements governing the $0\nu\beta\beta$ decay, and $G^{0\nu}_i$ is the integrated kinematical factor. The sum over i runs over different phase-space integrals weighted by a corresponding product of nuclear matrix elements. There are different LNV parameters, e.g., the effective electron-neutrino mass, effective right-handed weak interaction parameters, effective Majoron coupling constant, and R-parity-violating SUSY parameters, which incorporate elements of the fundamental interaction of Majorana neutrinos and/or R-parity-violating interaction of SUSY particles (see, e.g., the recent review articles [13, 14]). The value of these parameters can be determined in two ways: (i) One can extract upper bound on the LNV parameter from the best presently available experimental lower limit on the half-life of the $0\nu\beta\beta$-decay $T^{0\nu-\exp}_{1/2}$ after calculating the corresponding nuclear matrix elements. (ii) One can use the phenomenological constraints imposed by other experiments, e.g., those looking for the neutrino oscillation, to evaluate the LNV parameter explicitly, which further can be compared with the extracted one. The $0\nu\beta\beta$-decay constraints on LNV parameters must be taken into account by the theoreticians when they build new theories of grand unification.

At present, the searches for $0\nu\beta\beta$ decay are pursued actively for different nuclear isotopes, e.g. ^{76}Ge (Heidelberg–Moscow [15] and IGEX [16]), ^{100}Mo (NEMO [17] and ELEGANT [18]), ^{116}Cd (INR [19] and NEMO [20]), ^{130}Te [21], and ^{136}Xe (Gotthard Xe [22]). The sensitivity of a given isotope to the different LN-violating signals is determined by the value of the corresponding nuclear matrix element connecting the ground state of the initial and final nuclei with $J = 0^+$ and the value of the kinematical factor determined by the energy release for this process. In order to correctly interpret the results of $0\nu\beta\beta$-decay experiment, i.e., to obtain qualitative answers for the LN-violating parameters, the mechanism of nuclear transitions has to be understood. The $0\nu\beta\beta$-decay nuclear systems of interest are medium and heavy open-shell nuclei with complicated nuclear structure. To test our ability to evaluate the nuclear matrix elements that govern the decay rate, it is desirable to describe the two-neutrino double-beta decay ($2\nu\beta\beta$ decay) allowed in the SM:

$$(A, Z) \longrightarrow (A, Z+2) + 2e^- + 2\bar{\nu}. \qquad (3)$$

We note that each mode of the double-beta decay requires the construction of the same many-body nuclear structure wave functions.

A variety of nuclear techniques has been used in attempts to calculate $2\nu\beta\beta$-decay matrix elements, which have been reviewed recently in [13, 14]. Especially, the Quasiparticle Random Phase Approximation (QRPA) and its extensions have been found to be powerful models, considering their simplicity, to describe nuclear matrix elements, which require the summation over a complete set of intermediate nuclear states. The recent $2\nu\beta\beta$-decay calculations [23–25] including the schematic ones [26, 27] manifest that the inclusion of the Pauli Exclusion Principle (PEP) in the QRPA improves the predictive power of the theory giving more reliable prediction of the $2\nu\beta\beta$-decay probability.

In this paper, we present the upper limits on some effective LN-violating parameters extracted from the current experimental limits of the $0\nu\beta\beta$-decay lifetime for A = 76, 82, 96, 100, 116, 128, 130, 136, and 150 isotopes, which are quantities of fundamental importance. A discussion in respect to the sensitivity of a given $0\nu\beta\beta$-decaying isotope to the different LN-violating signals is presented. Some related nuclear physical aspects, as well as studies in respect to future $0\nu\beta\beta$-decay experiments, are addressed.

2. NEUTRINOLESS DOUBLE-BETA DECAY

2.1. Majorana Neutrino Mixing Mechanisms

The presently favored models of grand unification are left–right symmetric models [9]. They contain left- and hypothetical right-handed vector bosons $W^{\pm}_L$ and $W^{\pm}_R$. These vector bosons mediating the left- and right-handed interaction are mixed if the mass eigenstates $W^{\pm}_1$ and $W^{\pm}_2$ are not identical with the weak eigen-

states, which have a definite handedness:

$$W_1^{\pm} = \cos\zeta \cdot W_L^{\pm} + \sin\zeta \cdot W_R^{\pm},$$
$$W_2^{\pm} = -\sin\zeta \cdot W_L^{\pm} + \cos\zeta \cdot W_R^{\pm}, \quad (4)$$

where ζ is the mixing angle of the vector bosons. The left–right symmetry is broken since the vector bosons $W_1^{\pm}$ and $W_2^{\pm}$ obtain different masses by the Higgs mechanism. Since we have not seen a right-handed weak interaction, the mass of the heavy, mainly "right-handed" vector boson must be much larger than the mass of the light (81 GeV) vector boson, which is responsible for the left-handed force. The weak-interaction Hamiltonian must now be generalized:

$$H_W \approx \frac{G_F}{\sqrt{2}}\Bigg[(J_L \cdot j_L) + \tan\zeta(J_R \cdot j_L) + \tan\zeta(J_L \cdot j_R) + \left(\frac{M_1^W}{M_2^W}\right)^2 (J_R \cdot j_R)\Bigg] + \text{h.c.}, \quad (5)$$

$$J_{L/R} = \bar{\Psi}_p \gamma_\mu (g_V \mp g_A \gamma_5)\Psi_n, \quad j_{L/R} = \bar{e}\gamma_\mu(1 \mp \gamma_5)\nu_{eL/R},$$

where $g_V = 1$ and $g_A = 1.25$, and M_1^W and M_2^W are the light and heavy vector boson masses, respectively. The J_L and J_R indicate the hadronic left- and right-handed currents changing a neutron into a proton, respectively. The j_L (j_R) is the left(right)-handed leptonic current which creates an electron (or annihilates a positron) and annihilates left(right)-handed current neutrino ν_{eL} (ν_{eR}). Weak interaction Hamiltonian (7) is given for $\zeta \ll 1$ and $M_2^W \gg M_1^W$ keeping only the lower order terms in expansion of ζ and M_1^W/M_2^W parameters.

The left–right symmetric models allow us to explain the smallness of the neutrino mass within the so-called seesaw mechanism in the most natural way. It is supposed that the neutrino mixing does take place according to

$$\nu_{eL} = \sum_{k\,=\,\text{light}} U_{ek}^L \chi_{kL} + \sum_{k\,=\,\text{heavy}} U_{ek}^L N_{kL},$$
$$\nu_{eR} = \sum_{k\,=\,\text{light}} U_{ek}^R \chi_{kR} + \sum_{k\,=\,\text{heavy}} U_{ek}^R N_{kR}, \quad (6)$$

where χ_k (N_k) are fields of light (heavy) Majorana neutrinos with masses m_k ($m_k \ll 1$ MeV) and M_k ($M_k \gg 100$ GeV), respectively, and U_{ek}^L and U_{ek}^R are unitary mixing matrices. In the most general lepton mixing originating from a Dirac–Majorana mass term in the Lagrangian, the flavor neutrino fields are superposition of three light and three heavy Majorana neutrinos with definite mass. The fields χ_k and N_k satisfy the Majorana condition: $\chi_k\xi_k = C\bar{\chi}_k^T$, $N_k\hat{\xi}_k = C\bar{N}_k^T$, where C denotes the charge conjugation and ξ and $\hat{\xi}$ are phase factors.

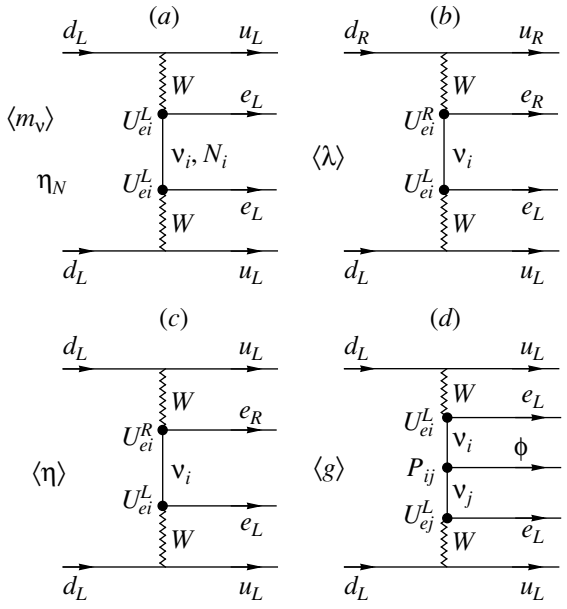

Fig. 1. Mechanisms for $0\nu\beta\beta$ decay associated with the exchange of a Majorana neutrino: (*a*) the light and the heavy neutrino mass mechanism, (*b*, *c*) right handed current mechanisms, (*d*) the Majoron mechanism. The following notation is used: $u_{L(R)}$, $d_{L(R)}$, and $e_{L(R)}$, are left(right)-handed *u*-quark, *d*-quark, and electron, respectively. *W* is vector boson (light or hypothetical heavy), and ν_i (i = 1, 2, …) is the Majorana neutrino.

The possible quark-level neutrino mixing mechanisms of $0\nu\beta\beta$ decay are displayed in Figs. 1*a*–1*c*. If the $0\nu\beta\beta$ decay is triggered by exchange of a light (heavy) left-handed Majorana neutrino (Fig. 1*a*), the corresponding amplitude of the process is proportional to the LN-violating parameter $\langle m_\nu \rangle$ (η_N):

$$\langle m_\nu \rangle = \sum_k^{\text{light}} (U_{ek}^L)^2 \xi_k m_k,$$
$$\eta_N = \sum_k^{\text{heavy}} (U_{ek}^L)^2 \hat{\xi}_k \frac{m_p}{M_k}, \quad (7)$$

where m_p is the proton mass. The difference between $\langle m_\nu \rangle$ and η_N comes from the fact that the neutrino propagator in the first and the second case shows different dependence on the mass of neutrinos [13]. We note that, even if the neutrino is a Majorana particle but massless (i.e., there is no mixing of neutrinos), the process in Fig. 1*a* can not happen since, for a pure left-handed weak interaction, the emitted neutrino must be right-handed (positive helicity), while the absorbed neutrino must be left-handed (negative helicity). With a finite mass, the neutrino no longer has a good helicity, and the

interference term between the leading helicity and the small admixtures allows the $0\nu\beta\beta$ decay.

The presence of the slight right-handed weak interaction in the GUT allows the mechanisms drawn in Figs. 1*b* and 1*c*. In these cases, there is no helicity matching problem. The emitted neutrino from the left-handed vertex is right-handed, and the absorbed neutrino is at the right-handed vertex. Assuming only light neutrinos, we distinguish two cases. (i) The chiralities of the quark hadronic currents are the same as those of the leptonic currents coupled through the *W*-boson propagator (Fig. 1*b*). Thus the $0\nu\beta\beta$-decay amplitude is proportional to

$$\langle\lambda\rangle = \left(\frac{M_1^W}{M_2^W}\right)^2 \sum_k^{\text{light}} U_{ek}^L U_{ek}^R \xi_k. \tag{8}$$

Recall that the *W*-boson propagator can be approximated by $1/M^2$ for $M = M_{1,2}^W$ [see (4)]. (ii) The chirality of the right-handed leptonic current is opposite to the coupled left-handed hadronic current (Fig. 1*c*). This is possible due to the *W*-boson mixing. The corresponding effective LN-violating parameter is

$$\langle\eta\rangle = \tan\zeta \sum_k^{\text{light}} U_{ek}^L U_{ek}^R \xi_k. \tag{9}$$

It is worthwhile to notice that the factor $\sum_k^{\text{light}} U_{ek}^L U_{ek}^R \xi_k$ in (10) and (11) is expected to be small and, if there are only light neutrinos, vanishes due to orthogonality condition [28]. It indicates that the values of $\langle\lambda\rangle$ and $\langle\eta\rangle$ might be strongly suppressed assuming the seesaw neutrino mixing mechanism.

2.2. Majoron Mechanism

The spontaneous breaking of the LN in the context of the seesaw model implies the existence of a physical Nambu–Goldstone boson [29], called Majoron [30], which is a light or massless boson with a very tiny coupling to the neutrinos

$$\mathcal{L}_{\phi\nu\nu} = \sum_{i\le j} \bar{\nu}_i \gamma_5 \nu_j (i\,\mathrm{Im}\phi) P_{ij},$$
$$P_{ij} = \sum_{\alpha,\beta = e,\mu,\tau} U_{i\alpha}^R U_{j\beta}^R g_{\alpha\beta}. \tag{10}$$

Here, ν_i denotes both light χ_i and heavy N_i Majorana neutrinos.

The Majoron ϕ might occur in the Majoron mode of the $0\nu\beta\beta$ decay ($0\nu\beta\beta\phi$ decay)

$$(A, Z) \longrightarrow (A, Z+2) + 2e^- + \phi, \tag{11}$$

and is offers a new possibility for looking for a signal of the new physics in the double-beta-decay experiments. The $0\nu\beta\beta\phi$-decay mode yields a continuous electron spectrum for the sum of electron energies like the $2\nu\beta\beta$-decay mode but differs from it by the position of the maximum due to different numbers of light particles are present in the final state. We remind that for the $0\nu\beta\beta$ decay the peak is expected to be at the end of the electron–electron coincidence spectra.

The mechanism leading to a $0\nu\beta\beta\phi$-decay mode is drawn in Fig. 1*d*. The experimental lower limits on the half-life of $0\nu\beta\beta\phi$-decay allow one to deduce the upper limit on the effective Majoron coupling constant $\langle g\rangle$:

$$\langle g\rangle = \sum_{ij}^{\text{light}} U_{ei}^L U_{ej}^L P_{ij}. \tag{12}$$

2.3. R-Parity-Violating SUSY Mechanism

Besides the simplest and the best known mechanism of the LN violation based on the mixing of the massive Majorana neutrinos advocated by different variants of the GUT, the *R*-parity violation proposed in the context of the MSSM is becoming the most popular scenario for the LN violation [31, 32]. The *R*-parity symmetry assigns even *R* parity to known particles of the SM and odd *R* parity to their superpartners, and the Lagrangian of the MSSM conserves *R* parity. The *R*-parity conservation is not required by gauge invariance or supersymmetry and might be broken at the Planck scale. The *R*-parity violation ($\not{R}_p$) is introduced in the effective Lagrangian (or superpotential) of the MSSM in terms of a certain set of hidden sector fields. The trilinear part of the $\not{R}_p$ superpotential takes the form

$$W_{\not R} = \lambda_{ijk} L_i L_j E_k^c + \lambda'_{ijk} L_i Q_j D_k^c + \lambda''_{ijk} U_i^c D_j^c D_k^c. \tag{13}$$

Here, L and Q stand for lepton and quark doublet left-handed superfields while E^c, U^c, and D^c stand for lepton and up and down quark singlet superfields. λ_{ijk}, λ'_{ijk}, and λ''_{ijk} are coupling constant and indices i, j, k denote generations. The λ'' terms cause baryon-number violation, and the remaining ones the LN violation. In fact, a combination of λ' and λ'' leads to the proton decay.

If the $\not{R}_p$ SUSY models are correct, the $0\nu\beta\beta$ decay is feasible. The nuclear $0\nu\beta\beta$ decay is triggered by the $0\nu\beta\beta$-decay quark transition $dd \longrightarrow uu + e^-e^-$. The relevant Feynman diagrams associated with gluino $\tilde{g}$ and neutralino χ trilinear $\not{R}_p$ SUSY contributions to the $0\nu\beta\beta$ decay are drawn in Fig. 1. The $\not{R}_p$ SUSY vertices are indicated with bold points. We see that the $0\nu\beta\beta$-decay amplitude is proportional to the λ'^2_{111} squared.

There are two possibilities of the hadronization, i.e., coming from the quark level to the nucleon level. One can place the four quark into the two initial neutrons and two final protons, what is just the conventional two-nucleon mechanism of $0\nu\beta\beta$ decay ($nn \longrightarrow pp + e^-e^-$). This mechanism is strongly suppressed by the nucleon-nucleon repulsion at short distances for the exchange of heavy SUSY particles and heavy Majorana neutrinos. Another possibility is to incorporate quarks involved in pions in flight between nucleons. This possibility was first pointed out by Pontecorvo [33]. It is the so-called pion exchange mechanism ($\pi^- \longrightarrow \pi^+ + e^- e^-$). The pion-exchange mode leads to a long-range nuclear interaction, which is significantly less sensitive to short-hand correlations effects. It was found that R_p SUSY pion-exchange contribution to the $0\nu\beta\beta$ decay absolutely dominates over the conventional two-nucleon mode [34–36].

The enhancement of the pion-exchange mode has also an origin in the bosonization of the $\pi^- \longrightarrow \pi^+ + e^-e^-$ vertex and is associated with the pseudoscalar $J_P J_P$ and tensor $J_T^{\mu\nu} J_{T\mu\nu}$ hadronic current structure of the effective R-parity-violating $0\nu\beta\beta$-decay Lagrangian on the quark level [34] ($J_P = \bar{u}\gamma_5 d$ and ($J_T^{\mu\nu} = \bar{u}\sigma^{\mu\nu}(1 + \gamma_5)d$). The corresponding hadronic matrix elements are

$$\langle \pi^+(q)|J_P J_P|\pi^-(q)\rangle \approx \frac{5}{3}\langle \pi^+(q)|J_P|0\rangle\langle 0|J_P|\pi^-(q)\rangle$$

$$= -\frac{10}{9} f_\pi^2 \frac{m_\pi^4}{(m_u + m_d)^2} = -m_\pi^4 c_P, \qquad (14)$$

$$\langle \pi^+(q)\big|J_T^{\mu\nu} J_{T\mu\nu}\big|\pi^-(q)\rangle \approx -4\langle \pi^+(q)|J_P|0\rangle\langle 0|J_P|\pi^-(q)\rangle.$$

Here, m_π is the pion mass, $f_\pi = 0.668\, m_\pi$. With the conventional values of the current quark masses m_u = 4.2 MeV and m_d = 7.4 MeV, one gets $c_P \approx 214$. For the exchange of a heavy Majorana neutrino, there is a vector and axial-vector hadronic current structure $J_{AV}^\mu J_{AV\mu}$ of the effective Lagrangian ($J_{AV}^\mu = \bar{u}^\alpha \gamma^\mu(1-\gamma_5)d_\alpha$). We have

$$\langle \pi^+(q)\big|J_A^\mu J_{A\mu}\big|\pi^-(q)\rangle \approx \frac{8}{3}\langle \pi^+(q)|J_P|0\rangle\langle 0|J_P|\pi^-(q)\rangle \qquad (15)$$

$$= -\frac{8}{3} f_\pi^2 q^2 = -m_\pi^4 c_A(q^2).$$

Assuming the average momentum of the exchanged pion to be about 100 MeV, we find $c_A \approx 0.61$. We note that $c_P \gg c_A$.

In order to derive a limit on the R-parity-violating first-generation Yukawa coupling λ'_{111} from the nonobservation of the $0\nu\beta\beta$ decay, it is necessary to use viable phenomenological assumptions about some of the fundamental parameters of the R_p MSSM. In [34], the ansatz of universal sparticle masses was assumed, and

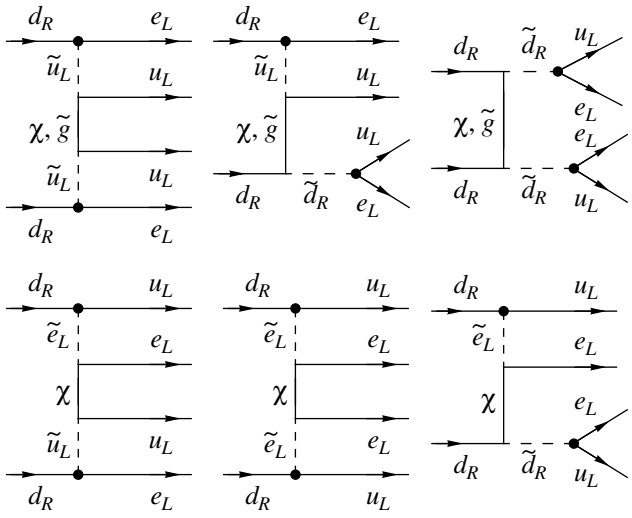

Fig. 2. Feynman graphs for the supersymmetric contributions to $0\nu\beta\beta$ decay. u_L, d_R, and e_L have the same meaning as in Fig. 1. $\tilde{u}_L$, $\tilde{d}_R$, and $\tilde{e}_L$ are left-handed u squark, right-handed d squark, and left-handed selectron, respectively. χ and $\tilde{g}$ are neutralinos and gauginos, respectively.

it was assumed that the lightest neutralino is bino-like. Within such phenomenological scenarios, it was found that the gluino and neutralino exchange mechanisms are of comparable importance [13, 34]. Another possibility is to implement relations among the weak-scale values of all parameters entering the superpotential and the soft SUSY-breaking Lagrangian and their values at the GUT scale. This scenario was outlined in [35, 37]. It was shown that there is no unique answer to the problem of the dominance of neutralino and gluino contribution to $0\nu\beta\beta$ decay. The dominance of any of them is bound with a different choice of the SUSY parameters m_0 and $m_{1/2}$. It is worthwhile to notice that in the extraction of λ'_{111} the main uncertainty comes from the parameters of supersymmetry and not from the nuclear physics side [35, 36].

3. $2\nu\beta\beta$ DECAY AND NUCLEAR STRUCTURE

Since there are measurements available for the $2\nu\beta\beta$ decay with the geochemical method (^{82}Se [38], ^{96}Zr [39], ^{128}Te, and ^{130}Te [40]) and with the radiochemical method (^{238}U [41]) and even laboratory measurements for seven nuclei (^{48}Ca [42], ^{76}Ge [43], ^{82}Se [44], ^{96}Zr [45–47], ^{100}Mo [48, 49], ^{116}Cd [19, 20], and ^{150}Nd [48]), one could try to calculate for a test of the theory the double-beta decay with two neutrinos and compare them with the data. We note that positive evidence for a $2\nu\beta\beta$-decay transition to the 0_1^+ excited state of final nucleus was observed for ^{100}Mo [50].

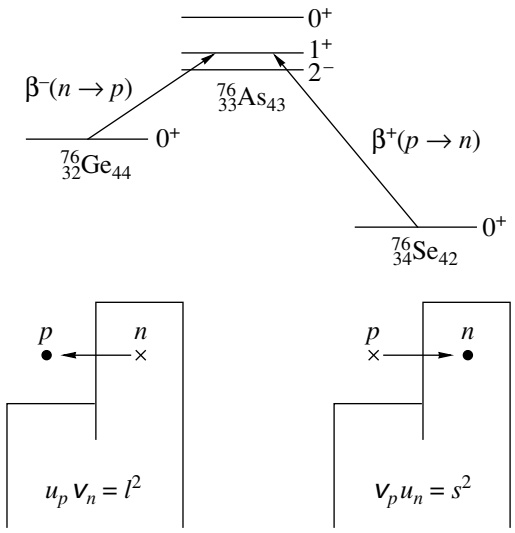

Fig. 3. The upper part shows the way how in the Random Phase Approximation (RPA) the 2νββ decay is calculated. For the Fermi transitions, the $\beta^-(n \longrightarrow p)$ amplitude moves just a neutron into the same proton level and the $\beta^+(p \longrightarrow n)$ amplitude moves a proton into the same neutron level. For the Gamow–Teller transitions, it can also involve a spin flip, but the orbital part remains the same. One immediately realizes that the occupation and nonoccupation amplitudes favor the β^- amplitude, but disfavor the β^+ amplitude. There, one has a transition from an unoccupied to an occupied single-particle state, which is twofold small (s^2) by the fact that first the occupation amplitude for the proton v_p and secondly the unoccupation amplitude for the neutron state u_n are both small. Therefore, the 2νββ is drastically reduced.

The inverse half-life of the 2νββ decay is free of unknown parameters on the particle physics and can be expressed as a product of a phase-space factor $G^{2\nu}$ and the Gamow–Teller transition matrix element $M_{\mathrm{GT}}^{2\nu}$ in second order:

$$[T_{1/2}^{2\nu}(0^+_{\mathrm{g.s.}} \longrightarrow 0^+_{\mathrm{g.s.}})]^{-1} = G^{2\nu}\left|M_{\mathrm{GT}}^{2\nu}\right|^2, \qquad (16)$$

where

$$M_{\mathrm{GT}}^{2\nu} = \sum_n \frac{\langle 0_f^+|A_k(0)|1_n^+\rangle\langle 1_n^+|A_k(0)|0_i^+\rangle}{E_n - E_i + \Delta}. \qquad (17)$$

$|0_i^+\rangle$, $|0_f^+\rangle$, and $|1_n^+\rangle$ are, respectively, the wave functions of the initial, final, and intermediate nuclei with corresponding energies E_i, E_f, and E_n. Δ denotes the average energy $\Delta = (E_i - E_f)/2$. A_k is the Gamow–Teller transition operator: $A_k = \sum_i \tau_i^+(\boldsymbol{\sigma}_i)_k$, $k = 1, 2, 3$.

The calculation of M_{GT} remains challenging and attracts specialists of different nuclear models. The computational complexity of M_{GT} consists in the reliable description of the complete set of the intermediate nuclear states. Recently, it has been shown the summation over the intermediate nuclear states in the present 2νββ-decay studies corresponds to a summation over a class of meson-exchange diagrams within the *S*-matrix approach [51].

The nuclear shell model gives a satisfactory description only of the low-lying excited states of nuclei. In the heavier nuclei, there are a large number of basis states in the shell model, which does not allow one to perform a realistic calculation without severe truncations. It is supposed to be the reason that the shell-model predictions of 2νββ-decay rate for heavier nuclei, especially those for the Te region, show deviations from the experimental data [52]. We note that the feasibility of shell-model calculations is growing with increasing computer facilities allowing one to handle much larger configuration spaces.

Many different nuclear structure aspects of the many-body Green's function M_{GT} have been discussed. It was suggested by Abad *et al*. [53] that M_{GT} could be dominated by the transitions through the lowest intermediate 1^+ state (so-called Single-State-Dominance-Hypothesis (SSDH)). The SSDH could be realized in two ways: (i) There is the true dominance of the first 1^+ state; i.e., the contribution from higher lying 1^+ states to M_{GT} is negligible. (ii) There are cancellations among the contributions of higher lying 1^+ states of the intermediate nucleus. The idea of SSDH has been outlined in [54] showing that some experimental and theoretical evidence supports it for a few 2νββ-decay systems.

The difficulty of the calculation of M_{GT} consists in the fact that the 2νββ-decay matrix elements are strongly suppressed. Its value is only a small fraction of the double Gamow–Teller sum rule that scales roughly like the number of pairs of unpaired neutrons [55],

$$\sum_f |\langle f|\mathbf{A}\cdot\mathbf{A}|i\rangle|^2 \approx (N-Z)(N-Z-1). \qquad (18)$$

The proton–neutron QRPA (*pn*-QRPA) has been found successful in describing the suppression mechanism for the 2νββ decay [56, 57]. Figure 3 explains why the 2νββ-decay amplitude is so drastically reduced. Therefore, the small effects which normally do not play a major role can affect the 2νββ-decay transition probability. If one looks to the second leg of the double-beta decay which is calculated backwards as a $\beta^+(p \longrightarrow n)$ decay from the final nucleus to the intermediate nucleus, one finds that the matrix elements involved in these diagrams are Pauli suppressed by a factor $(u_n v_p)^2 = (\mathrm{small})^4$. The neutron–particle proton–hole force in the isovector channel, which is usually included, is repulsive, while the particle–particle force usually neglected is attractive. Therefore, both excitations tend to cancel each other, and therefore the amplitude β^+ is drastically reduced. This cancellation for the second leg could be even complete; i.e., the backgoing amplitudes and thus ground-state correlations cancel the leading forward-going terms.

Although one can obtain agreement within *pn*-QRPA with the measured 2νββ data multiplying the particle–particle *G*-matrix elements of the nuclear Hamiltonian with a factor g_{pp} in a range of $0.8 \le g_{pp} \le 1.2$ (g_{pp} in principle should be equal to unity), two leaps of faith are usually quoted: (i) The extreme sensitivity of $M_{\rm GT}$ to the strength of particle–particle interaction, which does not allow a reliable prediction of the 2νββ-decay probability. We note that $M_{\rm GT}$ as a function of g_{pp} crosses zero. (ii) The collapse of the *pn*-QRPA solution within the physical range of g_{pp}, what is supposed to be a phase transition. The collapse is caused by the generation of too many ground state correlations with increasing strength of the attractive proton–neutron interaction.

The study of the QRPA approximation scheme for different model spaces manifest that the problems (i) and (ii) are related [58] with each other. The undesirable behavior of the *pn*-QRPA has its origin in the Quasiboson Approximation (QBA), violating the Pauli exclusion principle (PEP) and causing the QRPA excitation operators to behave like bosons. The renormalized QRPA, which considers the PEP in an approximate way, shifts the collapse of the QRPA outside the physical range of g_{pp} and shows a less sensitive dependence of $M^{2\nu}_{\rm GT}$ on g_{pp} [23, 24]. It allows us to predict more reliable values of the double-beta-decay matrix elements. The importance of the PEP for solving the problem of the QRPA collapse has been shown clearly within the schematic models, which are trying to simulate the realistic cases either by analytical solutions or by a minimal computational effort [26, 27]. In [27], to our knowledge, for the first time, the solution of the QRPA equation with full consideration of the PEP was presented. It was found that, restoring the PEP, the QRPA solutions are considerably stabilized and a better agreement with the exact solution is obtained. A new extension of the standard *pn*-QRPA "QRPA with PEP" was proposed, which considers the PEP in more appropriate way as the RQRPA and might work well also in the case of realistic calculations.

We note that the calculation of the 2νββ-decay nuclear transition continues to be a subject of interest, which stimulates the rapid development of the nuclear theory [27, 59–64].

4. LIMITS ON LN-VIOLATING PARAMETERS

The limits deduced for the LN-violating parameters depend on the values of nuclear matrix element $M^{0\nu}_i$, of the kinematical factor $G^{0\nu}_i$, and of the current experimental limit for a given isotope [see (2)]. Thus, it is useful to introduce sensitivity parameters for a given isotope to the different LN-violating parameters, which depend only on the characteristics of a given nuclear system. There are the following:

$$\begin{aligned}
\zeta_{\langle m_\nu\rangle}(Y) &= 10^7\left|M^{\rm light}_{\langle m_\nu\rangle}\right|\sqrt{G_{01}(\mathrm{yr})},\\
\zeta_{\eta_N}(Y) &= 10^6\left|M^{\rm heavy}_{\langle m_\nu\rangle}\right|\sqrt{G_{01}(\mathrm{yr})},\\
\zeta_{\langle\lambda\rangle}(Y) &= 10^7\left|M^{0\nu}_{\rm GT}\right|\sqrt{G_{\lambda\lambda}(\mathrm{yr})},\\
\zeta_{\langle\eta\rangle}(Y) &= 10^5\left|M^{0\nu}_{\rm GT}\right|\sqrt{G_{\eta\eta}(\mathrm{yr})},\\
\zeta_{\langle g\rangle}(Y) &= 10^8\left|M^{\rm light}_{\langle m_\nu\rangle}\right|\sqrt{G_B(\mathrm{yr})},\\
\zeta_{\lambda'_{111}}(Y) &= 10^5\left|M^{\pi N}\right|\sqrt{G_{01}(\mathrm{yr})}.
\end{aligned} \tag{19}$$

The explicit form of $M^{\rm light}_{\langle m_\nu\rangle}$, $M^{\rm heavy}_{\langle m_\nu\rangle}$, $M^{0\nu}_{\rm GT}$, $C_{\lambda\lambda}$, $C_{\eta\eta}$, G_B, and $M^{\pi N}$ can be found in [13, 35, 65].

Admittedly, there is a rather large spread between the calculated values of nuclear matrix elements within different nuclear theories (for ^{76}Ge the calculated rates differ by a factor of 3 [13, 14]). In principle, there are no exact criteria to decide which of them are correct. Nevertheless, one can argue the RQRPA method offers more reliable results than the QRPA as the ground state correlation is better under control due to the consideration of PEP.

The present limits on the LN-violating parameters $\langle m_\nu\rangle$, η_N, $\langle\lambda\rangle$, $\langle\eta\rangle$, and $\langle g\rangle$ are associated with the two-nucleon mechanism, for which the correct treatment of the weak nucleon current $J^{\mu\dagger}$ is crucial. We have

$$\begin{aligned}
J^{\mu\dagger}_L &= \bar{\Psi}\tau^+\Big[g_V(q^2)\gamma^\mu - ig_M(q^2)\frac{\sigma^{\mu\nu}}{2m_p}q_\nu\\
&\quad - g_A(q^2)\gamma^\mu\gamma_5 + g_P(q^2)q^\mu\gamma_5\Big]\Psi,
\end{aligned} \tag{20}$$

where $q^\mu = (p - p')_\mu$ is the momentum transferred from hadrons to leptons (p and p' are four momenta of neutron and proton, respectively) and $\sigma^{\mu\nu} = (i/2)[\gamma^\mu, \gamma^\nu]$; $g_V(q^2)$, $g_M(q^2)$, $g_A(q^2)$, and $g_P(q^2)$ are the vector, weak-magnetism, axial-vector, and induced pseudoscalar form factors, respectively, which are real functions of a Lorentz scalar q^2.

The matrix elements $M^{\rm light}_{\langle m_\nu\rangle}$ and $M^{\rm heavy}_{\langle m_\nu\rangle}$ have been calculated by neglecting the role of induced nucleon currents (weak magnetism and induced pseudoscalar terms). Recently, it has been shown that they contribute significantly to the 0νββ-decay amplitude [65]. They modify the Gamow–Teller contribution and create a new tensor contribution. Their contribution is as important as that of unchanged Fermi matrix element. It was found that indeed such corrections cause a more or less uniform reduction of the $M^{\rm light}_{\langle m_\nu\rangle}$ by approximately 30% throughout the periodic table. In the case of heavy-neutrino exchange ($M^{\rm heavy}_{\langle m_\nu\rangle}$), the effect is much larger (by a factor of 3) [65]. The nucleon finite size has been taken

Table 1. The present state of the Majorana neutrino mass (light and heavy), right-handed current, and Majoron and $\not{R}_p$ SUSY searches in 0νββ-decay experiments ($T^{0\nu-\exp}_{1/2}$ and $T^{0\nu\phi-\exp}_{1/2}$ are the best presently available lower limits on the half-lives of the 0νββ decay and 0νββφ decay for a given isotope, respectively; $\zeta_X(Y)$ denotes, according to (19), the sensitivity of a given nucleus Y to the LN-violating parameter X; the upper limits on $\langle m_\nu\rangle$, η_N, $\langle\lambda\rangle$, $\langle\eta\rangle$, $\langle g\rangle$, and λ'_{111} are presented; "gch." stands for geochemical data)

Nucleus	^{76}Ge	^{82}Se	^{96}Zr	^{100}Mo	^{116}Cd	^{128}Te	^{130}Te	^{136}Xe	^{150}Nd
$T^{0\nu-\exp}_{1/2}$ [yr]	1.6×10^{25}	1.4×10^{22}	1.0×10^{21}	2.8×10^{22}	2.9×10^{22}	7.7×10^{24}	5.6×10^{22}	4.4×10^{23}	1.2×10^{21}
C.L. [%]	90	90	90	90	90	gch.	90	90	90
Ref.	[15]	[67]	[47]	[18]	[19]	[40]	[21]	[22]	[48]
$T^{0\nu\phi-\exp}_{1/2}$ [yr]	7.9×10^{21}	2.4×10^{21}	3.9×10^{20}	3.1×10^{21}	1.2×10^{21}	7.7×10^{24}	2.7×10^{21}	7.2×10^{21}	2.8×10^{20}
C.L. [%]	90	90	90	90	90	gch.	gch.	90	90
Ref.	[43]	[44]	[47]	[18]	[20]	[40]	[40]	[22]	[48]
$\zeta_{\langle m_\nu\rangle}$	2.49	4.95	4.04	7.69	5.11	1.02	4.24	1.60	17.3
ζ_{η_N}	2.90	5.64	3.98	7.10	5.36	1.25	5.45	3.43	18.5
$\zeta_{\langle\lambda\rangle}$	3.35	6.92	10.3	1.81	1.60	0.66	8.62	6.06	27.6
$\zeta_{\langle\eta\rangle}$	5.67	3.91	8.20	5.39	2.28	2.86	12.7	9.00	40.9
$\zeta_{\langle g\rangle}$	2.41	6.59	5.93	10.5	6.60	0.53	5.08	1.90	26.7
$\zeta_{\lambda'_{111}}$	5.57	10.9	11.6	17.9	10.9	3.25	14.7	8.92	54.7
$\langle m_\nu\rangle$ [eV]	0.51	8.7	40	4.0	5.9	1.8	5.1	4.8	8.5
η_N [10^{-7}]	0.86	15	79	8.4	11	2.9	7.7	4.4	16
$\langle\lambda\rangle$ [10^{-6}]	0.75	12	31	33	36	5.5	4.9	2.5	10.4
$\langle\eta\rangle$ [10^{-8}]	0.44	22	38	11	26	1.3	3.3	1.7	7.1
$\langle g\rangle$ [10^{-4}]	4.7	3.1	8.5	1.7	4.4	0.69	3.8	6.2	2.2
λ'_{111} (100 GeV) [10^{-4}]	1.2	5.0	9.4	3.3	4.2	1.9	3.0	2.3	4.1
λ'_{111} (1 TeV) [10^{-2}]	3.8	16	30	10	13	6.0	9.6	7.4	13

into account through the phenomenological form factors and the PCAC hypothesis. We note that, in calculating the matrix elements involving the exchange of heavy neutrinos, the treatment of the short-range repulsion and nucleon finite size is crucial [66]. It is expected that the correct treatment of the induced pseudoscalar term (which is equivalent to a modification of the axial-vector current due to PCAC) might influence significantly also the amplitude of 0νββ decay in the case of the right-handed current mechanisms. It goes without saying that the validity of this argument can be ultimatively assessed by numerical calculations.

The numerical values of the sensitivity parameters $\zeta_X(Y)$ ($X = \langle m_\nu\rangle$, η_N, $\langle\lambda\rangle$, $\langle\eta\rangle$, $\langle g\rangle$, and λ'_{111}) are listed in Table 1. In their calculation, we used values of $M^{\text{light}}_{\langle m_\nu\rangle}$, $M^{\text{heavy}}_{\langle m_\nu\rangle}$, and $M^{\pi N}$ calculated within the *pn*-RQRPA [35, 65]. As there are no available *pn*-RQRPA results for $C_{\lambda\lambda}$, $C_{\eta\eta}$, we used those of [68]. The quantity $\zeta_X(Y)$ is an intrinsic characteristic of an isotope Y. The large numerical values of the sensitivity $\zeta_X(Y)$ correspond to those isotopes within the group of ββ-decaying nuclei which are the most promising candidates for searching for the LN-violating parameter X. However, we remind that there are also other microscopic and macroscopic properties of the isotope, which are important for building a 0νββ-decay detector. By glancing at Table 1, we see that the most sensitive isotope is ^{150}Nd. It is mostly due to the large phase space integral and partial due to the larger nuclear matrix element [35, 65]. We remark that the nucleus ^{150}Nd is deformed and that in the calculation of the corresponding nuclear matrix element the effects of nuclear deformation, which might be important, were not taken into account.

It is expected that the experimental constraints on the half-life of the 0νββ-decay are expected to be more stringent in future. Knowing the values of $\zeta_X(Y)$, there is a straightforward way to deduce limits on LN-violat-

ing parameters X from the experimental half-lives $T_{1/2}^{0\nu-\exp}$:

$$\frac{\langle m_\nu\rangle}{m_e} \le \frac{10^{-5}}{\zeta_{\langle m_\nu\rangle}}\sqrt{\frac{10^{24}\ \mathrm{yr}}{T_{1/2}^{0\nu-\exp}}}, \quad \eta_N \le \frac{10^{-6}}{\zeta_{\eta_N}}\sqrt{\frac{10^{24}\ \mathrm{yr}}{T_{1/2}^{0\nu-\exp}}},$$
$$\langle\lambda\rangle \le \frac{10^{-5}}{\zeta_{\langle\lambda\rangle}}\sqrt{\frac{10^{24}\ \mathrm{yr}}{T_{1/2}^{0\nu-\exp}}}, \quad \langle\eta\rangle \le \frac{10^{-7}}{\zeta_{\langle\eta\rangle}}\sqrt{\frac{10^{24}\ \mathrm{yr}}{T_{1/2}^{0\nu-\exp}}}, \tag{21}$$
$$\langle g\rangle \le \frac{10^{-4}}{\zeta_{\langle g\rangle}}\sqrt{\frac{10^{24}\ \mathrm{yr}}{T_{1/2}^{0\nu-\exp}}},$$
$$(\lambda'_{111})^2 \le \kappa^2\left(\frac{m_{\tilde q}}{100\ \mathrm{GeV}}\right)^4\left(\frac{m_{\tilde g}}{100\ \mathrm{GeV}}\right)\frac{10^{-7}}{\zeta_{\lambda'_{111}}}\sqrt{\frac{10^{24}\ \mathrm{yr}}{T_{1/2}^{0\nu-\exp}}}.$$

Here, κ is equal to 1.8 (gluino phenomenological scenario [13]). The normalization of 10^{24} yr was chosen so that the ζ's are of order unity.

The current experimental upper bounds on the $0\nu\beta\beta$-decay effective LN-violating parameters of interest for different isotopes are shown in Table 1. We see that the Heidelberg–Moscow experiment [15] (in Table 1 we give the sensitivity of the experiment for ^{76}Ge being $T_{1/2}^{0\nu-\exp} \ge 1.6\times10^{25}$ yr, as we want to compare this value with those from other experiments) offers the most restrictive limit for $\langle m_\nu\rangle$, η_N, $\langle\lambda\rangle$, and $\langle\eta\rangle$, and the ^{128}Te experiment [40] for $\langle g\rangle$. We note that, if the experimental data from another geochemical experiment on double-beta decay of ^{128}Te would be considered ($T_{1/2}^{\exp} = 1.5\times10^{24}$ yr [21]), one would get a less stringent limit on $\langle g\rangle$ ($\langle g\rangle \le 1.5\times10^{-4}$), which is comparable with the upper bound offered by the ^{100}Mo experiment [18] (Table 1).

At present, the largest attention is paid to the effective electron Majorana neutrino mass parameter $\langle m_\nu\rangle$ in light of the positive signals in favor of oscillations of solar, atmospheric, and terrestrial neutrinos. The masses and mixing angles can be determined from the available experimental data on neutrino oscillations and from astrophysical arguments by using some viable assumptions (hierarchical and nonhierarchical neutrino spectra, etc.). At present, the three and four neutrino mixing patterns are the most favorable ones [69, 70]. However, there is a discussion whether we really need the fourth sterile neutrino to fit the current experimental data. Knowing the elements of the neutrino mixing matrix, one can draw conclusions about the $0\nu\beta\beta$ decay, in particular, on $\langle m_\nu\rangle$, assuming neutrinos to be Majorana particles. From the study of different neutrino mixing schemes, it follows that the upper bound on effective Majorana neutrino mass $\langle m_\nu\rangle$ could range from 10^{-2} to 1 eV [69, 71, 72]. From Table 1, we see that the Heidelberg–Moscow $0\nu\beta\beta$ decay experiment [15] implies $\langle m_\nu\rangle$ to be less 0.5 eV. This fact allows us to make two important conclusions: (i) The $0\nu\beta\beta$ decay plays an important role in deciding among the alternative possibilities of neutrino mixing. (ii) The lepton-number violation is in reach of near future $0\nu\beta\beta$-decay experiments, if the neutrino is a Majorana particle. An issue which only $0\nu\beta\beta$ decay can decide. We remind that the discovery of the $0\nu\beta\beta$ decay, which would be a major achievement for particle physics and cosmology, will implies only the upper bound on $\langle m_\nu\rangle$ as a plethora of other $0\nu\beta\beta$-decay mechanisms is in the game. It is supposed that only further measurements of $0\nu\beta\beta$-decay transitions to the excited states of daughter nucleus together with inclusion of nuclear theory and study of different differential characteristics will allow us to decide which mechanism is the dominant one.

The present neutrino experiments do not provide us with useful information about the mixing of heavy Majorana neutrinos ($M_k \gg 100$ GeV). Therefore, it is difficult to extract the mass of heavy neutrinos from the current limit $\eta_N \le 8.6\times10^{-8}$ (Table 1). If one assumes the corresponding U_{ei} to be of the order of unity for the lightest heavy neutrino mass M_1 one gets $M_1 \ge 1.1\times10^4$ TeV. However, this element of the neutrino mixing matrix is expected to be rather small due to large differences in masses of light and heavy neutrinos within the seesaw mechanism. Therefore, the real limit on M_k is supposed to be much weaker. It is worthwhile to notice that the limit on η_N is extremely sensitive to the nucleon finite size and the short-range correlation effects [66]. The heavy neutrino exchange nuclear matrix elements evaluated without inclusion of the induced nucleon currents [73] are considerably overestimated [65] and should not be used in deducing the limit on η_N.

The present particle physics phenomenology does not allow us to deduce the magnitude of $\sum_k^{\mathrm{light}} U_{ek}^L U_{ek}^R \xi_k$ entering the expressions for the effective right-handed current parameters $\langle\lambda\rangle$ and $\langle\eta\rangle$. If we assume its value is about unity, then we get from the current limits on $|\langle\lambda\rangle| \le 7.5\times10^{-7}$ and $|\langle\eta\rangle| \le 4.4\times10^{-9}$ (Table 1) the corresponding bounds on the mass M_2^W of the heavy vector boson $W_2^\pm$ and the mixing angle ζ as follows: $M_2^W \ge 93$ TeV and $|\tan\zeta| \le 4.4\times10^{-9}$. Mohapatra has shown that in the left–right symmetric model with spontaneous R-parity violation there is an upper limit on M_{W_R} (in the limit $\tan\zeta \longrightarrow 0$ $M_{W_R} = M_2^W$) of at most 10 TeV [74]. By using this value for upper bound on M_2^W (for the lower limit on M_2^W we consider the value 100 GeV), we find

$$\left|\sum_k^{\mathrm{light}} U_{ek}^L U_{ek}^R \xi_k\right| \le 1.1\times10^{-6}\text{–}1.1\times10^{-2}, \tag{22}$$

$$|\tan\zeta| \le 3.8\times10^{-7}\text{–}3.8\times10^{-3}. \tag{23}$$

Table 2. The expected limits on LN-violating parameters of interest from the future 0νββ-decay experiments (the same notation as in Table 1 is used)

Experiments	Nucleus	$T_{1/2}^{0\nu-\mathrm{exp}}$, 10^{25} yr	$T_{1/2}^{0\nu\phi-\mathrm{exp}}$, 10^{23} yr	$\langle m_\nu \rangle$, eV	η_N, 10^{-8}	$\langle\lambda\rangle$, 10^{-7}	$\langle\eta\rangle$, 10^{-9}	$\langle g\rangle$, 10^{-5}	λ'_{111}, 10^{-5}
Current	^{76}Ge	1.6		0.51	8.6	7.5	4.4		12
	^{128}Te		77					6.9	
NEMO 3	^{82}Se	1	1	0.33	5.6	4.6	8.1	4.8	9.7
	^{96}Zr	1	1	0.40	7.9	3.1	3.8	5.3	9.4
	^{100}Mo	1	1	0.21	4.4	17	5.9	3.0	7.6
	^{116}Cd	1	1	0.32	5.9	20	14	4.8	9.7
	^{130}Te	1	1	0.38	5.8	3.7	2.5	6.2	8.3
	^{150}Nd	1	1	0.093	1.7	1.1	0.77	1.2	4.3
KAMLAND	^{136}Xe	5		0.45	4.1	2.3	1.6		7.2
CUORE	^{130}Te	10		0.12	1.8	1.2	0.79		4.7
GENIUS	^{76}Ge	580		0.027	0.45	0.39	0.23		2.8

Note that these limits could be modified after the pseudoscalar term of the nuclear current is properly taken into account.

The 0νββ-decay offers the most stringent limit on the *R*-parity-violating first-generation Yukawa coupling λ'_{111} [32]. Its value depends on the masses of SUSY particles [see (21)]. If the masses of squark $m_{\tilde{q}}$ and gluino $m_{\tilde{g}}$ would be at their present experimental lower bounds of 100 GeV, we deduce from the observed absence of the 0νββ decay $\lambda'_{111} \leq 1.2 \times 10^{-4}$ (phenomenological scenario). A conservative upper bound is obtained using the SUSY "naturalness" upper bound $m_{\tilde{q}}, m_{\tilde{g}} \approx 1$ TeV. It gives $\lambda'_{111} \leq 3.8 \times 10^{-2}$ (Table 1). We mention that the limits on λ'_{111} depend only weakly on the details of the nuclear structure, as λ'_{111} is proportional to the inverse square root of the nuclear matrix element. In addition, the corresponding nuclear matrix elements are changing only slightly within the physical range of parameters of the nuclear Hamiltonian [35]. However, λ'_{111} depends quadratically on the masses of SUSY particles. In the GUT-constrained SUSY scenario, there is a rather large SUSY parameter space. By using a different sample of relevant SUSY parameters, one ends up with significantly different limits on λ'_{111} [36]. Finally, we stress that the above limits are very strong and lie beyond the reach of near future accelerator experiments (HERA, TEVATRON) [34]. However, we note that the collider experiments are potentially sensitive to other couplings $\lambda'_{i,j,k}$, $\lambda''_{i,j,k}$, etc.

There are new experimental proposals for measurements of the 0νββ decay for different isotopes. A new NEMO 3 experiment is under construction, which is expected to reach a lower limit on the 0νββ-decay half-life of the order of 10^{25} yr for ^{82}Se, ^{96}Zr, ^{100}Mo, ^{116}Cd, ^{130}Te, and ^{150}Nd nuclei in a period of about 6 yr [46]. The KAMLAND [75], CUORE [76], and GENIUS [75] experiments are under consideration at the moment. The KAMLAND experiment is supposed to use as double-beta-decay emitter ^{136}Xe isotope in a liquid scintilator and measure a half-life limit of about 5×10^{25} yr. In the CUORE experiment, the cryogenic detector setup will be made with crystals of TeO_2. The expected half-life limit for the 0νββ decay of ^{130}Te could reach the value 1×10^{26} yr. The largest half-life limit of 5.8×10^{27} yr may be achieved in the future GENIUS experiment by using one ton of enriched ^{76}Ge and one year for the measurement [75]. If the above experiments could be realized, one would get considerably stronger limits on 0νββ-decay lepton-number-violating parameters. They are listed in Table 2. By glancing at this table, we see that NEMO 3 (^{150}Nd) and CUORE (^{130}Te) experiments have a chance to reach the value of 0.1 eV (^{150}Nd) for the effective neutrino mass and the GENIUS experiment could surpass this border to a lower value of 0.03 eV.

5. SUMMARY

We have discussed the problem of lepton-number violation in the context of rare nuclear processes, in particular, of the 0νββ decay, which has a broad potential for providing important information on modern particle physics. We have shown that the 0νββ decay has a strong impact on physics beyond the Standard Model in the way it constrains the parameters of other theories. The mechanism of the LN violation within the 0νββ decay has been discussed in the context of the problem of neutrino mixing and the *R*-parity-violating SUSY extensions of the Standard Model. The relevant LN-violating parameters have been the effective Majo-

rana neutrino mass $\langle m_\nu \rangle$, effective heavy neutrino mass parameter η_N, effective right-handed weak interaction parameters $\langle \lambda \rangle$ and $\langle \eta \rangle$, effective Majoron coupling constant $\langle g \rangle$, and the first generation trilinear *R*-parity-violating SUSY coupling λ'_{111}. The restrictions on the lepton-number-violating parameters have been deduced from the current experimental constraints on $0\nu\beta\beta$-decay half-life time for several isotopes of interest.

The present limit on the effective Majorana neutrino mass $\langle m_\nu \rangle \leq 0.5$ eV deduced from the $0\nu\beta\beta$-decay experiment has been discussed in connection with the different neutrino mixing scenarios advocated by current data of neutrino experiments. We conclude that the $0\nu\beta\beta$-decay experiment plays an important role in the determination of the character of the neutrino mass spectrum. Some analysis in respect to the heavy Majorana neutrino has been also presented. By using the upper and the lower limit on the mass of the heavy vector boson constrained by the left–right symmetric model with spontaneous *R*-parity violation, we have determined the allowed range for the mixing angle of vector bosons. It has been found that the current upper bound for the *R*-parity-violating SUSY interaction constant λ'_{111} is $\leq 1.2 \times 10^{-4}$ ($\leq 3.8 \times 10^{-2}$) assuming the masses of SUSY particle to be on the scale of 100 GeV (1 TeV). A discussion of the dominance of the pion-exchange *R*-parity-violating mode for the $0\nu\beta\beta$-decay process was also presented.

The interpretation of the LN-violating parameters involves some nuclear physics. It is necessary to explore the nuclear part of the $0\nu\beta\beta$-decay probability. The predictive power of different nuclear wave functions can be tested in the $2\nu\beta\beta$ decay. One needs a good description of the experimental data for the $2\nu\beta\beta$ probability. We have discussed the recent progress in the field of the calculation of double-beta-decay matrix elements associated with the inclusion of the Pauli exclusion principle in the QRPA. The reliability of the calculated $0\nu\beta\beta$-decay matrix elements was addressed.

We found it useful to introduce sensitivity parameters $\zeta_X(Y)$ for a given isotope *Y* associated with different LN-violating signals, which are free of influences from particle physics and relate simply the experimental half-lives with LN violating parameters. The largest value of $\zeta_X(Y)$ determines that isotope which is the most sensitive to a given lepton-number-violating parameter *X*. It is important information for planning new $0\nu\beta\beta$-decay experiments.

The $0\nu\beta\beta$ decay offers with both theoretical and experimental investigations a view to physics beyond the SM. New $0\nu\beta\beta$-decay experiments are in preparation or under consideration (NEMO 3, KAMLAND, CUORE, GENIUS). They could verify the validity of different mixing scheme of neutrinos. The expected limits on the LN-violating parameters which could be reached in these experiments are presented in Table 2. However, there is a possibility that the $0\nu\beta\beta$ decay could be detected in the forthcoming experiments. This would establish that the neutrino is a massive Majorana particle. The recent development in neutrino physics has triggered the hope that we could be close to this achievement.

ACKNOWLEDGMENTS

This work is partially supported (A.F.) by the European Union under the network contract CT93-0323 and the Deutsche Forschungsgemeinschaft Fa67/17-1 and Fa67/19-1.

REFERENCES

1. B. T. Cleveland *et al.*, Astrophys. J. **496**, 505 (1998).
2. K. S. Hirata *et al.*, Phys. Rev. Lett. **77**, 1683 (1996).
3. W. Hampel *et al.*, Phys. Lett. B **388**, 384 (1996).
4. J. N. Abdurashitov *et al.*, Phys. Rev. Lett. **77**, 4708 (1996).
5. R. Becker-Szendy *et al.*, Nucl. Phys. B (Proc. Suppl.) **38**, 331 (1995).
6. W. W. A. Alisson *et al.*, Phys. Lett. B **391**, 491 (1997).
7. M. Ambrosio *et al.*, Phys. Lett. B **434**, 451 (1998).
8. Y. Fukuda *et al.*, Phys. Lett. B **433**, 9 (1998); Phys. Rev. Lett. **81**, 1562 (1998).
9. J. C. Pati and A. Salam, Phys. Rev. D **10**, 275 (1974); R. N. Mohapatra and J. C. Pati, Phys. Rev. D **11**, 2558 (1975); R. N. Mohapatra and G. Senjanović, Phys. Rev. D **12**, 1502 (1975).
10. H. Fritzsch and R. Minkowski, Phys. Rep. **73**, 67 (1981).
11. R. Kuchimanchi and R. N. Mohapatra, Phys. Rev. D **48**, 4352 (1993); C. S. Aulakh, A. Melfo, A. Rasin, and G. Senjanović, Phys. Rev. D **58**, 115007 (1998); B. Dutta and R. N. Mohapatra, Phys. Rev. D **59**, 015018 (1999).
12. J. Schechter and J. W. F. Valle, Phys. Rev. D **25**, 2951 (1982); M. Hirsch, H. V. Klapdor-Kleingrothaus, and S. Kovalenko, Phys. Lett. B **372**, 8 (1996).
13. A. Faessler and F. Šimkovic, J. Phys. G: Nucl. Part. Phys. **24**, 2139 (1998).
14. J. Suhonen and O. Civitarese, Phys. Rep. **300**, 123 (1998).
15. Heidelberg–Moscow Collab. (L. Baudis *et al.*), Phys. Rev. Lett. **83**, 41 (1999).
16. C. E. Aalseth *et al.*, Phys. Rev. C **59**, 2108 (1999).
17. X. Sarazin *et al.*, Nucl. Phys. B (Proc. Suppl.) **70**, 239 (1999).
18. H. Ejiri *et al.*, Nucl. Phys. A **611**, 85 (1996).
19. F. A. Danevich *et al.*, Phys. Lett. B **344**, 72 (1995).
20. NEMO Collab. (R. Arnold *et al.*), Z. Phys. C **72**, 239 (1996).
21. A. Alessandrello *et al.*, Phys. Lett. B **433**, 156 (1998).
22. R. Luescher *et al.*, Phys. Lett. B **434**, 407 (1998).
23. J. Toivanen and J. Suhonen, Phys. Rev. Lett. **75**, 410 (1995); Phys. Rev. C **55**, 2314 (1997).
24. J. Schwieger, F. Šimkovic, and A. Faessler, Nucl. Phys. A **600**, 179 (1996).
25. F. Šimkovic *et al.*, Phys. Lett. B **393**, 267 (1997).

26. M. Sambataro and J. Suhonen, Phys. Rev. C **56**, 782 (1997).
27. F. Šimkovic, A. A. Raduta, M. Veselsky, and A. Faessler, nucl-th/9907113; Phys. Rev. C **61**, 044319 (2000).
28. S. M. Bilenky and S. T. Petcov, Rev. Mod. Phys. **59**, 671 (1987).
29. Y. Chikashige, R. N. Mohapatra, and R. Peccei, Phys. Rev. Lett. **45**, 1926 (1980).
30. G. Gelmini and M. Roncadelli, Phys. Lett. B **99**, 411 (1981); H. Georgi, S. Glashow, and H. Nusssinov, Nucl. Phys. B **193**, 297 (1981).
31. R. Barbier *et al.*, hep-ph/9810232.
32. V. Bednyakov, A. Faessler, and S. Kovalenko, hep-ph/9904414; Prog. Part. Nucl. Phys (in press).
33. B. Pontecorvo, Phys. Lett. B **26**, 630 (1968).
34. A. Faessler, S. Kovalenko, F. Šimkovic, and J. Schwieger, Phys. Rev. Lett. **78**, 183 (1997); Yad. Fiz. **61**, 1329 (1998) [Phys. At. Nucl. **61**, 1229 (1998)]; A. Faessler, S. Kovalenko, and F. Šimkovic, Phys. Rev. D **58**, 115004 (1998).
35. A. Wodecki, W. A. Kamiński, and F. Šimkovic, hep-ph/9902453; Phys. Rev. D **60**, 11507 (1999).
36. J. D. Vergados, hep-ph/9907316.
37. A. Wodecki and W. A. Kamiński, Phys. Rev. C **59**, 1232 (1999).
38. W. J. Lin *et al.*, Nucl. Phys. A **481**, 484 (1988).
39. A. Kawashima, K. Takahashi, and A. Masuda, Phys. Rev. C **47**, 2452 (1993).
40. T. Bernatovicz *et al.*, Phys. Rev. Lett. **69**, 2341 (1992); Phys. Rev. C **47**, 806 (1993).
41. A. L. Turkevich, T. E. Economou, and G. A. Gowan, Phys. Rev. Lett. **67**, 3211 (1991).
42. A. Balysh *et al.*, Phys. Rev. Lett. **77**, 5186 (1996).
43. M. Günter *et al.*, Phys. Rev. D **55**, 54 (1997).
44. NEMO Collab. (R. Arnold *et al.*), Nucl. Phys. A **636**, 209 (1998).
45. NEMO Collab. (A. S. Barabash), Nucl. Phys. A **629**, 517 (1998).
46. S. Julian, Talk presented at MEDEX 99, Prague, Czech Republic, Jul. 20–23, 1999; A. Barabash, private communications.
47. NEMO Collab. (R. Arnold *et al.*), Nucl. Phys. A (in press).
48. A. De Silva, M. K. Moe, M. A. Nelson, and M. A. Vient, Phys. Rev. C **56**, 2451 (1997).
49. NEMO Collab. (D. Dassié *et al.*), Phys. Rev. D **51**, 2090 (1995).
50. A. S. Barabash *et al.*, Phys. Lett. B **345**, 408 (1995).
51. F. Šimkovic and G. Pantis, Yad. Fiz. **62**, 632 (1999) [Phys. At. Nucl. **62**, 585 (1999)].
52. P. Vogel, nucl-th/9904065.
53. J. Abad, A. Morales, R. Núnez-Lagos, and A. F. Pacheco, Ann. Phys. (Leipzig) **80**, 9 (1984).
54. O. Civitarese and J. Suhonen, Phys. Rev. C **58**, 1535 (1998); Nucl. Phys. A **653**, 321 (1999).
55. P. Vogel, M. Ericson, and J. D. Vergados, Phys. Lett. B **212**, 259 (1988).
56. P. Vogel and M. R. Zirnbauer, Phys. Rev. Lett. **57**, 3148 (1986).
57. O. Civitarese, A. Faessler, and T. Tomoda, Phys. Lett. B **194**, 11 (1987).
58. F. Šimkovic, G. Pantis, and A. Faessler, Prog. Part. Nucl. Phys. **40**, 285 (1998); Yad. Fiz. **61**, 1318 (1998) [Phys. At. Nucl. **61**, 1218 (1998)].
59. M. Sambataro, Phys. Rev. C **59**, 2056 (1999).
60. O. Civitarese, P. O. Hess, J. G. Hess, and M. Reboiro, Phys. Rev. C **59**, 194 (1999).
61. E. J. V. de Passos, A. F. R. de Toledo Piza, and F. Krmpotić, Phys. Rev. C **58**, 1841 (1998).
62. A. Bobyk, W. A. Kamiński, and P. Zareba, Eur. Phys. J. A **5**, 385 (1999).
63. A. A. Raduta, C. V. Raduta, A. Faessler, and W. A. Kamiński, Nucl. Phys. A **634**, 497 (1998).
64. D. R. Bes, O. Civitarese, and N. N. Scoccola, Phys. Lett. B **446**, 93 (1999).
65. F. Šimkovic, G. Pantis, J. D. Vergados, and A. Faessler, hep-ph/9905509; Phys. Rev. C **60**, 055502 (1999).
66. F. Šimkovic, G. V. Efimov, M. A. Ivanov, and V. E. Lyubovitskij, Z. Phys. A **341**, 193 (1992).
67. S. R. Elliot *et al.*, Phys. Rev. C **46**, 1535 (1992).
68. G. Pantis, F. Šimkovic, J. D. Vergados, and A. Faessler, Phys. Rev. C **53**, 695 (1996).
69. S. M. Bilenky, G. Guinti, W. Grimus, *et al.*, hep-ph/9907234.
70. R. Adhikari and G. Omanović, Phys. Rev. D **59**, 073003 (1999).
71. F. Vissani, hep-ph/9906525.
72. V. Barger and K. Whisnant, Phys. Lett. B **456**, 194 (1999).
73. M. Hirsch, H. V. Klapdor-Kleingrothaus, and O. Panella, Phys. Lett. B **374**, 7 (1996).
74. R. N. Mohapatra, hep-ph/9806520.
75. J. Hellmig and H. V. Klapdor-Kleingrothaus, Z. Phys. A **359**, 351 (1997); H. V. Klapdor-Kleingrothaus, hep-ph/9907040.
76. O. Cremonesi, Talk presented at MEDEX 99, Prague, Czech Republic, Jul. 20–23, 1999.

Physics of Atomic Nuclei, Vol. 63, No. 7, 2000, pp. 1177–1181. From Yadernaya Fizika, Vol. 63, No. 7, 2000, pp. 1252–1256.

NEW PHYSICS, NUCLEAR AND NUCLEON STRUCTURE IN RARE PROCESSES

The Effect of Weak Magnetism and Induced Pseudoscalar Coupling in Neutrinoless Double-Beta Decay*

G. Pantis and F. Šimkovic[1)]

Department of Physics, University of Ioannina, Greece

Abstract—In calculating the amplitude of the Majorana neutrino–mass mechanism of neutrinoless double-beta decay (0νββ-decay), several approximations of the nucleon current have been done. For example, effects from induced current such as weak magnetism and pseudoscalar coupling have been neglected. We shall show in this work that, although such terms do not contribute significantly to the 2νββ-decay amplitude, they are important in the case of 0νββ decay. Performing calculations within the renormalized quasiparticle random phase approximation (*pn*-RQRPA) for all nuclei undergoing double-beta decay in the region $A = 76$ to $A = 150$, we have found that these additional contributions of the nucleon current reduce considerably the matrix elements in all cases for the light neutrino as well as for the heavy neutrino mass. In the light-neutrino mass, we find reductions up to thirty percent, while in the heavy-neutrino mass, up to almost a factor of five. These reductions make the limits on the lepton-number-violating parameters $\langle m_\nu \rangle$ and η_N less stringent. © *2000 MAIK "Nauka/Interperiodica".*

1. INTRODUCTION

In recent years, there has been considerable interest in the study of nuclear double-beta decay, both theoretically and experimentally. Recent review articles [1, 2] provide new developments in this field. Of particular interest is the neutrinoless double-beta decay (0νββ decay), which involves the emission of two electrons and no neutrinos, and the two-neutrino double-beta decay (2νββ decay) in which two electrons and two antineutrinos are emitted. The 0νββ decay, which has not yet been observed, violates the lepton-number conservation and has been predicted in some theories beyond the Standard Model [1, 2]. In order to deduce the lepton-number-violating parameters of interest from the experimental lower limits on the half-life of 0νββ decay, the corresponding nuclear transition should be calculated with good accuracy.

The Grand Unified Theories and supersymmetric models offer a variety of mechanisms for the 0νββ-decay process. So far, most attention is paid to the light Majorana neutrino mass mechanism, which allows us to deduce an important limit on the effective Majorana neutrino mass parameter $\langle m_\nu \rangle$. In the calculations of the corresponding nuclear transition so far, only the axial-vector and the vector parts of the nucleon current have been considered in detail, while an attempt has been made to estimate weak magnetism [3]. While the weak magnetism has been shown to be small, the induced pseudoscalar term is expected to play an important role. In fact, we find that such corrections are of the order $\mathbf{q}^2/(\mathbf{q}^2 + m_\pi^2)$; i.e. they are important if the average momentum $\langle q \rangle$ of the exchanged neutrino cannot be neglected in front of the pion mass. In the case of 0νββ decay, the neutrino is emitted by one nucleon and absorbed by another. The average momentum $\langle q \rangle$ of the exchanged neutrino is expected to be 100 MeV for a mean nucleon–nucleon separation of 2 fm. The situation is even clearer in the case of heavy Majorana neutrino exchange, as was shown in [4]. There, the mean internucleon distance is considerably smaller, and the average momentum $\langle q \rangle$ should be much larger. Thus, such large values of average momentum render it necessary to go beyond the usual approximation of the nucleon current at least for the 0νββ-decay matrix element for which in general so far only terms of axial-vector and vector contributions have been considered.

It is the motivation of this work to include induced current terms of the nuclear current in our calculations. In addition, we shall use the proton–neutron renormalized quasiparticle random-phase approximation (*pn*-RQRPA), which incorporates renormalization effects due to Pauli principle corrections. In this way we expect to obtain more reliable nuclear matrix elements.

2. THEORY

The Majorana neutrino mass mechanism of 0νββ decay has been discussed in many papers, see, for example, the recent review articles [1, 2, 5] and references cited there. We shall give here only some formulas necessary for this work. The effective beta-decay Hamiltonian is of the form,

$$\mathcal{H}^\beta = \frac{G_F}{\sqrt{2}}[\bar{e}\gamma_\mu(1-\gamma_5)\nu_{eL}]J_L^{\mu\dagger} + \text{h.c.}, \qquad (1)$$

* This article was submitted by the authors in English.

[1)] Department of Nuclear Physics, Comenius University, Bratislava, Slovakia.

where e and ν_{eL} are field operators representing the electron and the left-handed electron neutrino, respectively. We suppose that neutrino mixing does take place according to

$$\nu_{eL} = \sum_{k=\text{light}} U^L_{ek}\chi_{kL} + \sum_{k=\text{heavy}} U^L_{ek}N_{kL}, \quad (2)$$

where χ_k (N_k) are fields of light (heavy) Majorana neutrinos with masses m_k ($m_k \ll 1$ MeV) and M_k ($M_k \gg 1$ GeV), respectively, and U^L_{ek} is a unitary mixing matrix. In the first and second terms on the r.h.s. of (2), the summation is only over light and heavy neutrinos, respectively. The fields χ_k and N_k satisfy the Majorana condition: $\chi_k\xi_k = C\bar{\chi}_k^T$, $N_k\hat{\xi}_k = C\bar{N}_k^T$, where C denotes the charge conjugation and ξ, $\hat{\xi}$ are phase factors.

Within the impulse approximation, the nuclear current J^μ_L in (1) expressed with nucleon fields Ψ takes the form

$$J^{\mu\dagger}_L = \bar{\Psi}\tau^+\left[g_V(q^2)\gamma^\mu - g_M(q^2)\frac{i\sigma^{\mu\nu}}{2m_p}q_\nu - g_A(q^2)\gamma^\mu\gamma_5 + g_P(q^2)q^\mu\gamma_5\right]\Psi, \quad (3)$$

where m_p is the nucleon mass, $q^\mu = (p - p')_\mu$ is the momentum transferred from hadrons to leptons (p and p' are four momenta of neutron and proton, respectively), and $\sigma^{\mu\nu} = (i/2)[\gamma^\mu, \gamma^\nu]$. The functions $g_V(q^2)$, $g_M(q^2)$, $g_A(q^2)$, and $g_P(q^2)$ are real functions of the Lorentz scalar q^2.

In previous studies of the neutrino mass mechanism of $0\nu\beta\beta$ decay, the terms proportional to $g_M(q^2)$ and $g_P(q^2)$ of the nucleon current in (3) have been neglected, and the q^2 dependence of $g_V(q^2)$ and $g_A(q^2)$ was taken to be of dipole shape $(1 - q^2/\Lambda^2)^2$ with $\Lambda = 0.85$ GeV. In this work, we shall use the following parametrization of the form factors:

$$g_V(q^2) = \frac{g_V}{\left(1 - \frac{q^2}{\Lambda_V^2}\right)^2}, \quad g_M(q^2) = \frac{\mu_p - \mu_n}{\left(1 - \frac{q^2}{\Lambda_V^2}\right)^2},$$

$$\Lambda_V^2 = 0.71\ \text{GeV}^2, \quad (4)$$

$$g_A(q^2) = \frac{g_A}{\left(1 - \frac{q^2}{\Lambda_A^2}\right)^2}, \quad \Lambda_A = 1.086\ \text{GeV},$$

where Λ_V has been determined by Dumbrajs *et al.* [6] and Λ_A is the best fit of the axial-vector form factor for the neutrino reaction $\nu_\mu p \longrightarrow \mu^+ n$ by Amaldi *et al.* [7]. The vector, axial-vector, and weak-magnetism coupling constants have the following values: $g_V = 1$, $g_A = 1.254$, $(\mu_p - \mu_n) = 3.70$. The induced pseudoscalar form factor is determined by the pion pole, and its form within the partially conserved axial-vector current hypothesis (PCAC) is given [5] by

$$g_P(q^2) = \frac{2m_p g_A(q^2)}{m_\pi^2 - q^2}\left(1 - \frac{m_\pi^2}{\Lambda_A^2}\right). \quad (5)$$

In the nonrelativistic expansion, the form of the nucleon current coincides with that in Breit frame, and we get ($k = 1, 2, 3$),

$$J^\mu(\mathbf{x}) = \sum_{n=1}^{A}\tau_n^+[g^{\mu 0}J^0(q^2) + g^{\mu k}J_n^k(q^2)]\delta(\mathbf{x} - \mathbf{r}_n), \quad (6)$$

$$J^0(q^2) = g_V(q^2),$$

$$\mathbf{J}_n(q^2) = g_M(q^2)i\frac{\boldsymbol{\sigma}_n \times \mathbf{q}}{2m_p} + g_A(q^2)\boldsymbol{\sigma} - g_P(q^2)\frac{\mathbf{q}(\boldsymbol{\sigma}_n \cdot \mathbf{q})}{2m_p}. \quad (7)$$

In the case of $2\nu\beta\beta$ decay, the momentum transfer in the weak nucleon vertex is restricted by the Q value of the process, which is about a few MeV. It allows us to neglect safely terms proportional to $\mathbf{q}$ in (7). These terms have been ignored also in the Majorana neutrino–mass mechanism of $0\nu\beta\beta$ decay. We shall show in this work that one should take such terms into account. If we assume that both outgoing electrons are in the $s_{1/2}$-wave state and consider only the energetically most favored $0_i^+ \longrightarrow 0_f^+$ transition, we obtain, for the $0\nu\beta\beta$-decay half-life,

$$[T^{0\nu}_{1/2}]^{-1} = G_{01}\left|\frac{\langle m_\nu\rangle}{m_e}M^{\text{light}}_{\langle m_\nu\rangle} + \eta_N M^{\text{heavy}}_{\eta_N}\right|^2. \quad (8)$$

Here, m_e is the mass of electron, and G_{01} is the integrated kinematical factor. Its numerical values can be found, e.g., in [8, 9]. The lepton-number-violating parameters of interest $\langle m_\nu\rangle$ and η_N take the form

$$\langle m_\nu\rangle = \sum_k^{\text{light}}(U^L_{ek})^2\xi_k m_k,$$
$$\eta_N = \sum_k^{\text{heavy}}(U^L_{ek})^2\hat{\xi}_k\frac{m_p}{M_k}. \quad (9)$$

The nuclear matrix elements entering the half-life formula of $0\nu\beta\beta$-decay process in (8) with an obvious notation are

$$M^I_{\langle m_\nu\rangle,\,\eta_N} = M^I_{VV} + M^I_{MM} + M^I_{AA} + M^I_{PP} + M^I_{AP}, \quad I = \text{light, heavy}, \quad (10)$$

where M^I_{VV}, M^I_{MM}, M^I_{AA}, M^I_{PP}, and M^I_{AP} refer to the vector, weak-magnetism, axial-vector, induced pseudoscalar coupling, and the interference of the axial-vector and induced pseudoscalar coupling interaction, respec-

tively. Expressed in relative coordinates and using the second quantization formalism, they take the form

$$M^I_{\rm type} = \sum_{\substack{pnp'n' \\ J^\pi m_i m_f \mathcal{J}}} (-1)^{j_n + j_{p'} + J + \mathcal{J}} (2\mathcal{J}+1) \times \begin{Bmatrix} j_p & j_n & J \\ j_{n'} & j_{p'} & \mathcal{J} \end{Bmatrix} \langle p(1), p'(2); \mathcal{J} | f(r_{12}) \tau_1^+ \tau_2^+ \times \mathbb{O}^I_{\rm type}(12) f(r_{12}) | n(1), n'(2); \mathcal{J} \rangle \times \langle 0_f^+ \| \widetilde{[c^+_{p'} \tilde{c}_{n'}]_J} \| J^\pi m_f \rangle \langle J^\pi m_f | J^\pi m_i \rangle \times \langle J^\pi m_i \| [c^+_p \tilde{c}_n]_J \| 0_i^+ \rangle \quad (11)$$

with type = *VV*, *MM*, *AA*, *PP*, *AP*. The exact form of the one-body transition densities to excited states $|J^\pi m_i\rangle$ and $|J^\pi m_f\rangle$ generated from the initial (*A*, *Z*) and the final (*A*, *Z* + 2) ground states $|0_i^+\rangle$ and $|0_f^+\rangle$ within the *pn*-RQRPA can be found together with other details of the nuclear structure model in [2, 9–11]. The short-range correlation function $f(r) = 1 - e^{-\alpha r^2}(1 - br^2)$ (α = 1.1 fm^2 and b = 0.68 fm^2) takes into account the short-range repulsion of the nucleons. Here, $\mathbb{O}^I_{\rm type}(12)$ represents the coordinate- and spin-dependent part of the two body transition operators of the 0νββ-decay nuclear matrix elements in (11),

$$\mathbb{O}^I_{\rm type}(12) = H^I_{\rm type-F}(r_{12}) + H^I_{\rm type-GT}(r_{12})\sigma_{12} + H^I_{\rm type-T}(r_{12})\mathbf{S}_{12}. \quad (12)$$

The light-neutrino-exchange potential $H^{\rm light}_{{\rm type}-K}(r_{12})$ and the heavy-neutrino-exchange potential $H^{\rm heavy}_{{\rm type}-K}(r_{12})$ (K = F, GT, T) are of the following form:

$$H^{\rm light}_{{\rm type}-K}(r_{12}) = \frac{2}{\pi g_A^2} \frac{R}{r_{12}} \int_0^\infty \frac{\sin(qr_{12})}{q + E^m(J) - (E^i + E^f)/2} h_{{\rm type}-K}(q^2) dq, \quad (13)$$

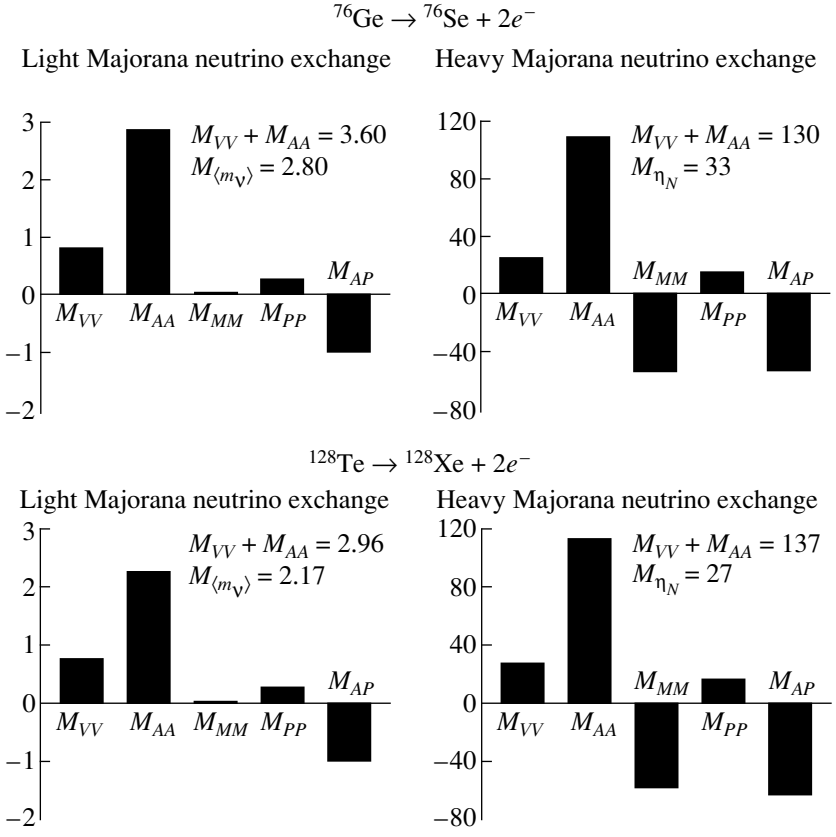

Fig. 1. Calculated light and heavy neutrino exchange 0νββ-decay nuclear matrix elements for A = 76 and 128 systems. The partial matrix elements M_{VV}, M_{AA}, M_{MM}, M_{PP}, and M_{AP} originate from vector, axial-vector, weak-magnetism, induced pseudoscalar coupling, and the interference of the axial-vector and induced pseudoscalar coupling interaction, respectively. $M_{\langle m_\nu \rangle}$ and M_{η_N} are 0νββ-decay matrix elements associated with $\langle m_\nu \rangle$ and η_N lepton-number-violating parameters, respectively.

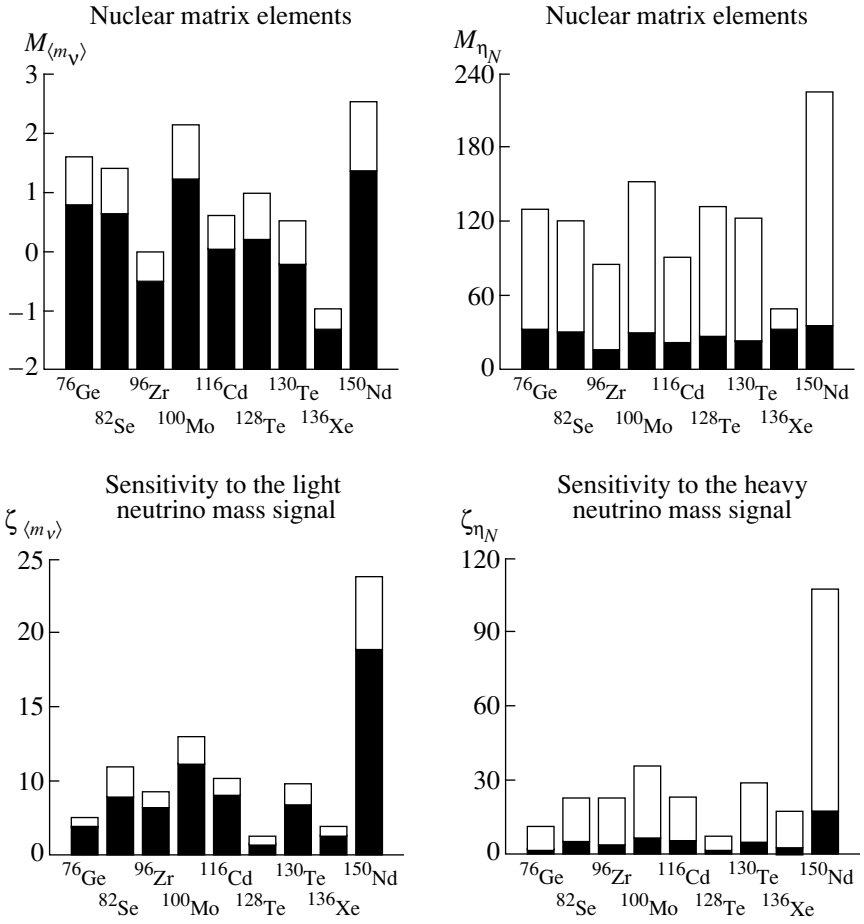

Fig. 2. Calculated nuclear matrix elements $M_{\langle m_\nu \rangle}$ and M_{η_N} and sensitivities $\zeta_{\langle m_\nu \rangle}$ and ζ_{η_N} for the experimentally interesting A = 76, 82, 96, 100, 116, 128, 130, 136, and 150 nuclear systems. The black bars show the results for the total interaction, and the open bars show the results without the induced pseudoscalar and weak-magnetism terms.

$$H^{\text{heavy}}_{\text{type}-K}(r) = \frac{1}{m_p m_e}\frac{2}{\pi g_A^2}\frac{R}{r_{12}}\int_0^\infty \sin(qr_{12})h_{\text{type}-K}(q^2)qdq$$

with

$$h_{VV-\text{F}}(q^2) = -g_V^2(q^2), \quad h_{VV-\text{GT}}(q^2) = 0,$$
$$h_{VV-T}(q^2) = 0,$$
$$h_{MM-\text{F}}(q^2) = 0, \quad h_{MM-\text{GT}}(q^2) = \frac{2}{3}\frac{g_M^2(q^2)q^2}{4m_p^2},$$
$$h_{MM-T}(q^2) = \frac{1}{3}\frac{g_M^2(q^2)q^2}{4m_p^2},$$
$$h_{AA-\text{F}}(q^2) = 0, \quad h_{AA-\text{GT}}(q^2) = g_A^2(q^2),$$
$$h_{AA-T}(q^2) = 0,$$
$$h_{PP-\text{F}}(q^2) = 0, \quad h_{PP-\text{GT}}(q^2) = \frac{1}{3}\frac{g_P^2(q^2)q^4}{4m_p^2},$$
$$h_{PP-T}(q^2) = -h_{PP-\text{GT}}(q^2),$$
$$h_{AP-\text{F}}(q^2) = 0, \quad h_{AP-\text{GT}}(q^2) = -\frac{2}{3}\frac{g_A(q^2)g_P(q^2)q^2}{2m_p},$$
$$h_{AP-T}(q^2) = -h_{AP-\text{GT}}(q^2).$$

Here, E^i, E^f, and $E^m(J)$ are, respectively, the energies of the initial, final, and intermediate nuclear state with angular momentum J, and $R = r_0 A^{1/3}$ is the mean nuclear radius, with r_0 = 1.1 fm.

3. DISCUSSION AND CONCLUSIONS

The nuclear matrix elements for the light and heavy Majorana neutrino exchange modes for the A = 76 and 128 systems have been calculated by the *pn*-RQRPA and are shown in the histogram on Fig. 1. For the light neutrino exchange the weak magnetism is very small. The other contributions are significant. In fact, the vector and the induced pseudoscalar parts together are almost equal to the interference term, which, however,

has opposite sign. The matrix elements with and without the induced current contributions are also shown. For the $A = 76$ system, we note a reduction of 22 percent in the case of light neutrino exchange and for the heavy neutrino exchange a reduction of a factor of 4. For the $A = 128$ system, the corresponding reductions are even larger, 27 percent and almost a factor of 5. The situation is also similar for the other nuclei as can be seen from the histogram of Fig. 2, where all nuclei are presented. We have reductions as high as 35 percent for the light neutrino mass. For the heavy neutrino mass, the reductions are much higher. Here, the weak magnetism contribution is much stronger and of opposite sign bringing down the matrix element by factors of 2 to 6. We have also studied the sensitivity of each nucleus to the light- and heavy-neutrino mass by introducing sensitivity parameters for a given isotope which depend only on the corresponding nuclear matrix element and the kinematical phase-space factor. These parameters are defined in the following way:

$$\begin{aligned} \zeta_{\langle m_\nu\rangle}(Y) &= 10^7 \left| M^{\text{light}}_{\langle m_\nu\rangle} \right| \sqrt{G_{01}(\text{yr})}, \\ \zeta_{\eta_N}(Y) &= 10^6 \left| M^{\text{heavy}}_{\langle m_\nu\rangle} \right| \sqrt{G_{01}(\text{yr})}. \end{aligned} \tag{14}$$

The numerical values of $\zeta_{\langle m_\nu\rangle}(Y)$ and $\zeta_{\eta_N}(Y)$ for all nuclear systems of interest are also shown in Fig. 2. Large numerical values of these parameters characterize those $0\nu\beta\beta$-decay isotopes, which are the most promising candidates for searching the lepton-number-violating signal. These sensitivity parameters can be used as a guide by the experimentalists in planning the $0\nu\beta\beta$-decay experiments. Our results show that the $A = 150$ system is the most sensitive by both the light and the heavy neutrino exchange. This should be taken into account together with other microscopic and macroscopic factors for building a $0\nu\beta\beta$ detector. So far, the best upper limit on the $\langle m_\nu\rangle$ and η_N parameters has been established by the Heidelberg–Moscow ^{76}Ge experiment ($T^{0\nu}_{1/2} \leq 1.1 \times 10^{25}$ yr) [12]. We denote these limits $\langle m_\nu\rangle^{\text{best}}$ and η_N^{best}, which take the values, $\langle m_\nu\rangle^{\text{best}} = 0.62$ and $\eta_N^{\text{best}} = 1.0 \times 10^{-7}$.

REFERENCES

1. J. Suhonen and O. Civitarese, Phys. Rep. **133**, 1 (1986).
2. A. Faessler and F. Šimkovic, J. Phys. G **24**, 2139 (1998).
3. J. Suhonen, S. B. Khadkikhar, and A. Faessler, Nucl. Phys. A **529**, 727 (1991); **535**, 509 (1991).
4. F. Šimkovic, G. V. Efimov, M. A. Ivanov, and V. E. Lyubovitskij, Z. Phys. A. **341**, 193 (1992).
5. F. Šimkovic, G. Pantis, J. D. Vergados, and A. Faessler, Phys. Rev. C **60**, 055502 (1999).
6. O. Dumbrajs *et al.*, Nucl. Phys. B **216**, 277 (1983).
7. E. Amaldi, S. Fubini, and G. Furlan, Springer Tracts Mod. Phys. **83**, 1 (1979).
8. M. Doi, T. Kotani, and E. Takasugi, Prog. Theor. Phys. Suppl. **83**, 1 (1985).
9. G. Pantis, F. Šimkovic, J. D. Vergados, and A. Faessler, Phys. Rev. C **53**, 695 (1996).
10. J. Toivanen and J. Suhonen, Phys. Rev. Lett. **75**, 410 (1995).
11. J. Schwieger, F. Šimkovic, and A. Faessler, Nucl. Phys. A **600**, 179 (1996).
12. L. Baudis *et al.*, Phys. Lett. B **407**, 219 (1997).

Physics of Atomic Nuclei, Vol. 63, No. 7, 2000, pp. 1182–1186. From Yadernaya Fizika, Vol. 63, No. 7, 2000, pp. 1257–1261.

NEW PHYSICS, NUCLEAR AND NUCLEON STRUCTURE IN RARE PROCESSES

Effective Shell-Model Transition Operators for Muon-Capture Calculations

T. Siiskonen, J. Suhonen, and M. Hjorth-Jensen[1)]

Department of Physics, University of Jyväskylä, Finland

Abstract—Recently many shell-model calculations have been performed in order to extract the value of the ratio C_P/C_A in light nuclei. Most of these calculations fail to reproduce the value given by the partially conserved axial vector hypothesis, roughly 7. We show that, with the effective transition operators calculated by the perturbative techniques, this discrepancy can be, at least partly, solved. New angular correlation data for ^{28}Si are used for the extraction of C_P/C_A. In the case of ^{20}Ne, the capture rate data are used for the extraction. © *2000 MAIK "Nauka/Interperiodica".*

1. INTRODUCTION

The calculations of the nuclear matrix elements involved in the ordinary (nonradiative) capture of stopped negative muons by atomic nuclei have been of considerable interest because they enable one to access the structure of the effective weak baryonic current. Due to the large mass of the captured muon, the process involves a large energy release (roughly 100 MeV) and thus surveys the baryonic current deeper than the ordinary beta decay. In particular, the role of the induced pseudoscalar coupling C_P becomes prominent, since its importance is proportional to Q/M, where Q is the energy release and M is the nucleon mass.

In the past, there have been many calculations of nuclear matrix elements involved in the muon-capture processes. These calculations have been either very schematic ones [1–3] or more realistic ones using various truncations of the nuclear shell model [2–4]. Ultimately, all these calculations have aimed at predicting the ratio C_P/C_A of the induced pseudoscalar and axial-vector coupling strengths of the weak baryonic current. These calculations seem to suggest wide ranges of values as can be seen from the table. For reference, we also give the nuclear-model independent Goldberger–Treiman value $C_P/C_A = 6.8$, which is obtained using the Partially Conserved Axial Current (PCAC) hypothesis. It should be reasonable to assume that this relation between the induced pseudoscalar and axial-vector coupling constants will survive in finite nuclei although corrections may occur, e.g., due to mesonic corrections in the weak vertices. In particular, this result should be roughly recovered using nuclear structure calculations assuming the impulse approximation. Renormalizations within the impulse approximation have been extensively discussed for the C_A coefficient in the context of beta decay and electron capture.

Recently, also the nuclear shell model has been used to calculate the needed nuclear matrix elements for muon capture [7–11]. In [9] and [10], no definitive conclusions about the C_P/C_A ratio could be reached on the basis of their computed matrix elements. In [7] and [8], the C_P/C_A ranges shown in the table were extracted from the available experimental muon capture rates. The angular correlation data, available for muon capture in ^{28}Si, have been in a key role in pointing out discrepancies in the shell-model calculations of C_P/C_A.

2. THEORETICAL FRAMEWORK

In [12, 13], we have proposed a method which, at least partly, lifts the above-mentioned discrepancy. This method is based on the use of effective transition operators in the shell-model formalism. Unfortunately, the anisotropy data are available only for ^{28}Si, and thus further testing of the effective operator method has to be done in the context of measured capture rates or future experiments on angular correlations in the capture of polarized muons. Very recently, two important measurements of correlation coefficients of γ-radiation anisotropy in the capture of a polarized negative muon

Experimental data and earlier estimates exploiting the measured muon-capture rates for the ratio C_P/C_A

Ref.	Value	Type of extraction
[1]	$4 \le C_P/C_A \le 39$	Schematic
[2, 3]	$3 \le C_P/C_A \le 20$	Schematic, realistic
[4]	$13 \le C_P/C_A$	Realistic
[5]	$6.8 \le C_P/C_A \le 10.6$	Exp.
[6]	$8.8 \le C_P/C_A \le 10.8$	Exp.
[7]	$4.1 \le C_P/C_A \le 8.9$	Shell model
[8]	$-3.0 \le C_P/C_A \le 2.5$	Shell model
	6.8	Goldberger–Treiman relation

* This article was submitted by the authors in English.

[1)] Department of Physics, University of Oslo, Norway.

1063-7788/00/6307-1182$20.00 © 2000 MAIK "Nauka/Interperiodica"

by ^{28}Si were reported [11, 14]. For the allowed muon capture, the angular correlation between the emitted γ radiation and the neutrino is scaled by the coefficient α [3, 11] which is related to the coefficient

$$x \equiv M_1(2)/M_1(-1) \tag{1}$$

of [14] by

$$\alpha = \frac{\sqrt{2}x - x^2/2}{1 + x^2}. \tag{2}$$

Here, the quantities $M_1(2)$ and $M_1(-1)$ are given by

$$M_1(-1) = \sqrt{\frac{2}{3}}\left\{\left(\frac{1}{3}G_P - G_A\right)[101] + G_P\frac{\sqrt{2}}{3}[121] - \frac{C_A}{M}[011p] + \frac{C_V}{M}\sqrt{\frac{2}{3}}[111p]\right\},$$

$$M_1(2) = \sqrt{\frac{2}{3}}\left\{\left(G_A - \frac{2}{3}G_P\right)[121] - G_P\frac{\sqrt{2}}{3}[101] + \frac{C_A}{M}\sqrt{2}[011p] + \frac{C_V}{M}\sqrt{\frac{2}{3}}[111p]\right\},$$

where M is the nucleon mass. The definitions of the involved reduced nuclear matrix elements are given in [1]. The constants G_P and G_A are defined as (with $C_T = C_S = 0$)

$$G_P = (C_P - C_A - C_V - C_M)\frac{E_\nu}{2M}, \qquad G_A = C_A - (C_V + C_M)\frac{E_\nu}{2M}. \tag{3}$$

The expressions of $M_1(2)$ and $M_1(-1)$ with (1) and (2) lead to rather contradictory results between different realistic nuclear models. In [14], the values $C_P/C_A = 3.4 \pm 1.0$ and $C_P/C_A = 2.0 \pm 1.6$ were extracted with the matrix elements of [15] and [16], respectively. In addition, the measurement of [11] gives $C_P/C_A = 5.3 \pm 2.0$ with the matrix elements of [15] and $C_P/C_A = 4.2 \pm 2.5$ with the matrix elements of [16]. The more realistic matrix elements, obtained from the full 1*s*0*d* shell calculation utilizing Wildenthal's USD interaction [17], yield the value of $C_P/C_A = 0.0 \pm 3.2$ [11, 18], far from $C_P/C_A \approx 7$ given by the nuclear-model-independent Goldberger–Treiman relation (see, e.g., [19]) obtained under the PCAC hypothesis. This anomaly present in the C_P/C_A predictions from state-of-the-art shell-model calculations is rather disturbing when contrasted with the experimental data. In this paper, we consider two capture reactions $^{28}_{14}\mathrm{Si}(0^+_{\mathrm{g.s}}) + \mu^-_b \longrightarrow {}^{28}_{13}\mathrm{Al}(1^+_3) + \nu_\mu$ and $^{20}_{10}\mathrm{Ne}(0^+_{\mathrm{g.s}}) + \mu^-_b \longrightarrow {}^{20}_{0}\mathrm{F}(1^+_1) + \nu_\mu$ [12, 13] within the full shell-model framework and try to evaluate the ratio C_P/C_A through the capture rates, the quantity x, and its measured values reviewed above. The needed muon-capture formalism is developed in [1] and reviewed in the case of shell-model calculations in [8, 10].

In the present shell-model calculation, we have employed three different two-body interactions. In addition to the USD interaction of Wildenthal [17], we have derived microscopic effective interactions and operators based on the recent CD-Bonn meson-exchange *NN* interaction model of Machleidt *et al*. [20] and the Nijm-I *NN* interaction model of the Nijmegen group [21]. These are the same interactions which were employed by us in [12, 13]. In order to obtain effective interactions [22] and operators for the muon capture studies, we use ^{16}O as a closed-shell nucleus and define the 1*s*0*d* shell as the shell-model space for which the effective interactions and operators are derived. In nuclear transitions, the quantity of interest is the transition matrix element between an initial state $|\Psi_i\rangle$ and a final state $|\Psi_f\rangle$ of an operator $\mathbb{O}$ defined as

$$\mathbb{O}_{fi} = \frac{\langle\Psi_f|\mathbb{O}|\Psi_i\rangle}{\sqrt{\langle\Psi_f|\Psi_f\rangle\langle\Psi_i|\Psi_i\rangle}}. \tag{4}$$

Since we perform the calculation in a reduced space, the exact wave functions $\Psi_{f,i}$ are not known, but only their projections $\Phi_{f,i}$ onto the model space are available. We are then confronted with the problem of how to evaluate $\mathbb{O}_{fi}$ when only the model space wave functions are known. In treating this problem, one usually introduces an effective operator $\mathbb{O}^{\mathrm{eff}}_{fi}$, defined by requiring

$$\mathbb{O}_{fi} = \left\langle \Phi_f \middle| \mathbb{O}^{\mathrm{eff}}_{fi} \middle| \Phi_i \right\rangle. \tag{5}$$

The standard scheme is then to employ a perturbative expansion for the effective operator [23, 24].

To obtain effective one-body transition operators for muon capture, we evaluate all effective operator diagrams through second-order in the *G*-matrix obtained with the CD-Bonn and Nijm-I interactions. Such diagrams are discussed in the reviews by Towner [23] and Ellis and Osnes [24]. Terms arising from meson-exchange currents have been neglected; similarly, the possibility of having isobars Δ as intermediate states is omitted too since here only the nucleonic degrees of freedom are relevant. Moreover, the nucleon–nucleon potentials we are employing do already contain such intermediate states. Intermediate-state excitations in each diagram up to $(6–8)\hbar\omega$ in oscillator energy were included in order to achieve a converged result.

3. RESULTS AND DISCUSSION

3.1. ^{28}Si

Our results for ^{28}Si are summarized in Fig. 1 with $C_A/C_V = -1.251$. The coefficient x is not sensitive to

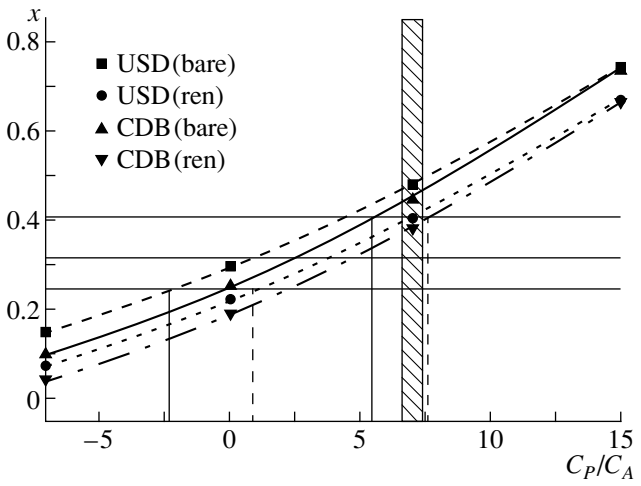

Fig. 1. The ratio $x = M(2)/M(-1)$ in ^{28}Si as a function of the ratio C_P/C_A. The experimental value [11] with the error limits is indicated by the horizontal lines.

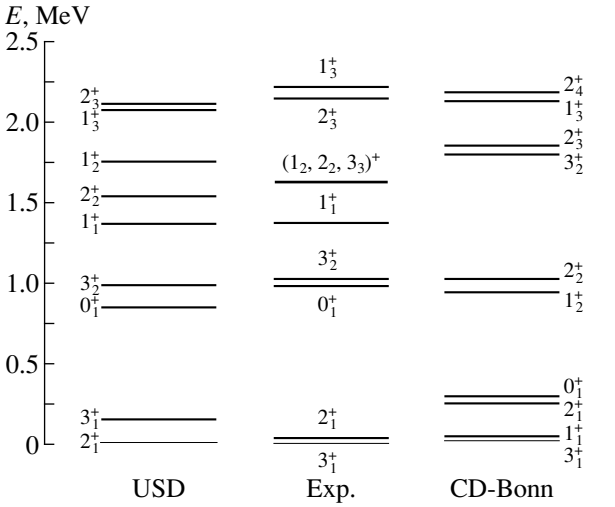

Fig. 2. Calculated and experimental [25] spectra of ^{28}Al.

changes in the ratio C_A/C_V. With the renormalized value $C_A/C_V = -1.0$, x changes only by a few percent for $C_P/C_A = 7$. In fact, using the renormalized axial vector coupling may lead to double counting, as the renormalization effects are already included in the renormalized single-particle matrix elements.

The experimental and theoretical spectra of ^{28}Al are shown in Fig. 2. One can see that although there are notable differences in the calculated results, the USD and the CD-Bonn predictions are very similar to each other for the muon capture observables. This is true also for the Gamow–Teller matrix elements B(GT), which are within 25% from each other for the 1_3^+ final state in ^{28}Al. The effects of renormalization are about 10% for the Gamow–Teller-type matrix element [101] and roughly 30% for 011p], [111p], and [121] matrix elements. In all cases, the magnitude of the matrix element reduces as compared to the bare interaction.

In spite of the different structures of the initial and final states of muon capture, emerging from the use of the two interactions, the renormalization of the muon capture matrix elements changes the value of x to the same direction in both cases. Thus, the renormalization effects on the value of x seem to be rather interaction-independent.

To extract an estimate for the ratio C_P/C_A, we have plotted x of (1) as a function of C_P/C_A. The experimental value $x = 0.315 \pm 0.08$ was taken from [11]. With this choice, we obtain from Fig. 1 the range $-2.3 \le C_P/C_A \le 5.5$ for the bare USD and CD-Bonn calculations in agreement with the USD result of [18] cited in [11]. Thus, for both of the adopted interactions, the bare result is almost the same, in spite of the basic difference in the origin of the used interactions, hinting to a strong suppression of the C_P/C_A ratio for the studied muon-capture transition in the framework of the nuclear shell-model. As discussed above, this contradicts the shell-model calculation of the partial capture rates in ^{23}Na (with a fitted C_P/C_A ratio) as well as experimental data on hydrogen.

Also the USD and CD-Bonn calculations with renormalized transition probabilities agree almost exactly and both yield a very different value for C_P/C_A than the calculation with bare operators. The renormalized result $0.9 \le C_P/C_A \le 7.6$ is closer to the PCAC value. This result encourages us to believe that the anomaly in the C_P/C_A ratio, inherent in the sophisticated shell-model calculations, has been lifted by introducing effective renormalized transitions operators acting in the muon-capture process.

3.2. ^{20}Ne

The energy spectrum of ^{20}F, emerging from our full 1s0d-shell calculation with ^{16}O as a closed-shell core, is shown in Fig. 3. The agreement with experiment is good. In particular, both the CD-Bonn and Nijm-I results are very close to the USD ones, and the energy of the 1_1^+ final state of the capture reaction is reproduced almost exactly.

The renormalization effects on the one-body transition matrix elements are of the order of 10–30% (as in ^{28}Si), and in almost all cases we get reduction in the absolute value. Again, the Gamow–Teller-type single-particle matrix elements are reduced roughly by 10%. However, it should be noted that the radial dependence in the [101] matrix element differs from the radial dependence of the pure Gamow–Teller matrix element.

Since the angular correlation data are not available for ^{20}Ne, the partial capture rates are the only source of information. The capture rates obtained with the formalism of [1] are shown in Fig. 4 together with the

experimental value of [26]. The capture rates W are calculated according to

$$W = 4P(\alpha Z m'_\mu)^3 \frac{2J_f+1}{2J_i+1}\left(1-\frac{Q}{m_\mu+AM}\right)Q^2, \quad (6)$$

where α is the fine-structure constant and m'_μ is the reduced muon mass. The reduced nuclear matrix elements are included in P (see [1] for further details). The calculations are performed with the bare value $C_A/C_V = -1.251$.

From Fig. 4, it can be seen that the renormalization increases the capture rate for all interactions, pushing it closer to the experimental value for both the USD, CD-Bonn, and Nijm-I interactions, when C_P/C_A is close to the PCAC value. The USD calculation with the bare operators yields an interval for C_P/C_A which lies far from a value that could be reasonably expected. Although the result with the renormalized operators does not overlap with experiment near the PCAC region, the correction shifts the values in the right direction. The ratio C_P/C_A calculated with the renormalized CD-Bonn and Nijm-I one-body operators agrees slightly better with the PCAC prediction. For the PCAC prediction $C_P/C_A \approx 7$, all these calculations yield capture rates below the experimental window.

As soon as the angular-correlation data on the muon capture in ^{20}Ne are published, our matrix elements [13] can be used for the extraction of the ratio C_P/C_A. If $C_P/C_A \approx 7$, as predicted by PCAC and as seen in the capture rate calculations, then $x \sim 0.35$ for all interactions employed [13]. The results from ^{28}Si indicate, however, that $C_P/C_A \sim 5$ [12, 27]. The latter value would yield $x \sim 0.30$ for the present reaction [13]. With $C_P/C_A \approx 5$, the capture rates depicted in Fig. 4 will clearly deviate from the experiment. How this deviation is related to the underlying one-body transition densities and their relative magnitudes is unclear. An experimental determination of x would clarify this point.

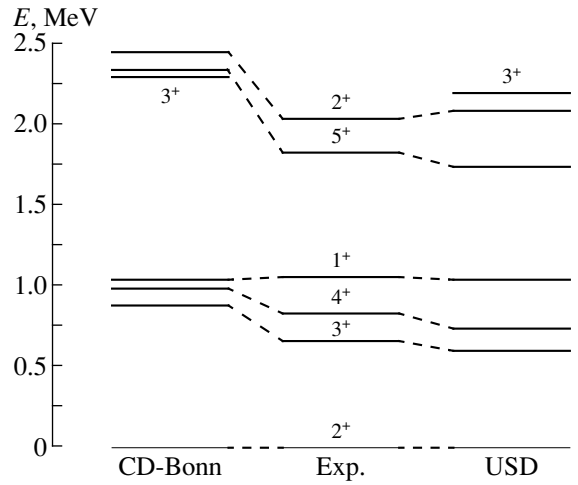

Fig. 3. Calculated and experimental [25] energy spectra of ^{20}F.

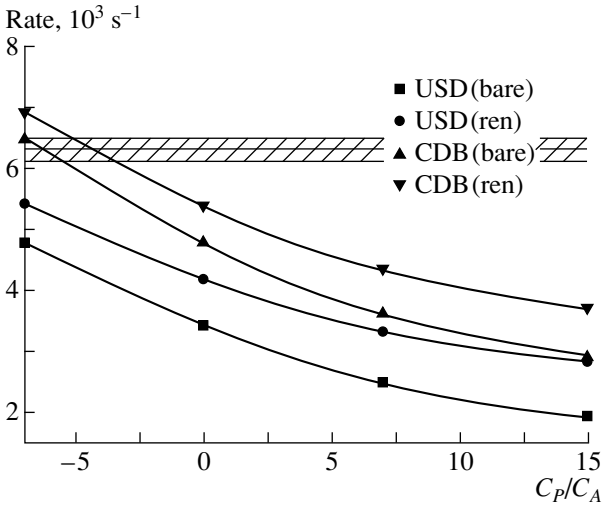

Fig. 4. Capture rates leading to the 1^+_1 (1.057 MeV) final state in ^{20}F. The experimental value with error bars is the cross-hatched region.

4. CONCLUSIONS

Our calculations support the nearly interaction independence of the effects of the renormalization of the one-body transition operators, involved in the shell-model calculation of the muon capture rates, and the angular correlation parameter x. This renormalization is introduced by replacing the bare transition operators of the full Hilbert space by effective ones calculated with the CD-Bonn and Nijm-I interactions and operating in the shell-model valence space. The renormalization has helped to reduce the C_P/C_A anomaly inherent in the shell-model calculations leading to C_P/C_A ratios closer to data coming from measurements of muon capture in hydrogen. For other nuclei of interest, the theoretical situation is more complicated than in ^{28}Si or ^{20}Ne since they are situated at the interface of either the 0p and 1s0d shells or the 1s0d and 1p0f shells, complicating thereby the evaluation of an effective interaction and increasing the dimensionality of the shell-model calculation. Research along such lines is in progress [28].

ACKNOWLEDGMENTS

J.S. thanks the Academy of Finland for financial support. This research has also been supported by the Nordic Academy of Advanced Studies (NorFA).

REFERENCES

1. M. Morita and A. Fujii, Phys. Rev. **118**, 606 (1960).
2. V. Gillet and D. Jenkins, Phys. Rev. B **140**, 32 (1965).

3. R. Parthasarathy and V. N. Sridhar, Phys. Rev. C **18**, 1796 (1978).
4. T. Ericson, J. C. Sens, and H. P. C. Rood, Nuovo Cimento **34**, 51 (1964).
5. G. Bardin *et al.*, Phys. Lett. B **104**, 320 (1981).
6. G. Jonkmans *et al.*, Phys. Rev. Lett. **77**, 4512 (1996).
7. B. L. Johnson *et al.*, Phys. Rev. C **54**, 2714 (1996).
8. T. Siiskonen, J. Suhonen, V. A. Kuz'min, and T. V. Tetereva, Nucl. Phys. A **635**, 446 (1998); **651**, 437 (1999).
9. M. Gmitro, S. S. Kamalov, F. Šimkovic, and A. A. Ovchinnikova, Nucl. Phys. A **507**, 707 (1990).
10. V. A. Kuz'min, A. A. Ovchinnikova, and T. V. Tetereva, Yad. Fiz. **57**, 1954 (1994) [Phys. At. Nucl. **57**, 1881 (1994)].
11. B. A. Moftah *et al.*, Phys. Lett. B **395**, 157 (1997).
12. T. Siiskonen, J. Suhonen, and M. Hjorth-Jensen, Phys. Rev. C **59**, R1839 (1999).
13. T. Siiskonen, J. Suhonen, and M. Hjorth-Jensen, J. Phys. G (in press).
14. V. Brudanin *et al.*, Nucl. Phys. A **587**, 577 (1995).
15. S. Ciechanowicz, Nucl. Phys. A **267**, 472 (1976).
16. R. Parthasarathy and V. N. Sridhar, Phys. Rev. C **23**, 861 (1981).
17. B. H. Wildenthal, Prog. Part. Nucl. Phys. **11**, 5 (1984).
18. K. Junker, V. A. Kuz'min, A. A. Ovichinnikova, and T. V. Tetereva, in *Proceedings of the IV International Symposium on Weak and Electromagnetic Interactions in Nuclei, WEIN'95*, Ed. by H. Ejiri, T. Kishimoto, and T. Sato (World Sci., Singapore, 1996), p. 394.
19. E. D. Commins and P. H. Bucksbaum, *Weak Interactions of Leptons and Quarks* (Cambridge Univ. Press, Cambridge, 1983), Chap. 4.11.
20. R. Machleidt, F. Sammarruca, and Y. Song, Phys. Rev. C **53**, R1483 (1996).
21. V. G. J. Stoks, R. A. M. Klomp, C. P. F. Terheggen, and J. J. de Swart, Phys. Rev. C **49**, 2950 (1994).
22. M. Hjorth-Jensen, T. T. S. Kuo, and E. Osnes, Phys. Rep. **260**, 125 (1995).
23. I. S. Towner, Phys. Rep. **155**, 263 (1987); B. Castel and I. S. Towner, *Modern Theories of Nuclear Moments* (Clarendon Press, Oxford, 1990), p. 55.
24. P. J. Ellis and E. Osnes, Rev. Mod. Phys. **49**, 777 (1977).
25. R. B. Firestone, V. S. Shirley, S. Y. F. Chu, C. M. Baglin, and J. Zipkin, *Table of Isotopes CD-ROM*, 8th ed. (Wiley, New York, 1996), Vers. 1.0.
26. T. Filipova, private communication.
27. V. Brudanin *et al.*, submitted to Nucl. Phys. A.
28. T. Siiskonen, J. Suhonen, and M. Hjorth-Jensen (unpublished).

Physics of Atomic Nuclei, Vol. 63, No. 7, 2000, pp. 1187–1192. From Yadernaya Fizika, Vol. 63, No. 7, 2000, pp. 1262–1267.

NEW PHYSICS, NUCLEAR AND NUCLEON STRUCTURE IN RARE PROCESSES

Second-Order Corrections to Correlations in Muon Capture*

A. L. Barabanov

Russian Research Centre Kurchatov Institute, pl. Kurchatova 1, Moscow, 123182 Russia

Abstract—Muon capture by a nucleus with an arbitrary spin is considered. Second-order terms in $1/M$ in the effective weak-interaction Hamiltonian are taken into account. New terms in the Hamiltonian associated with the nucleon–nucleus potential are found. A general expression for the angular distribution of neutrinos (recoil nuclei) is derived for polarized muons and oriented target nuclei. Second-order contributions to the amplitudes $M_u(k)$ are obtained. This allows one to calculate second-order corrections to any integral and correlation characteristics in muon capture that are expressed in terms of $M_u(k)$. *© 2000 MAIK "Nauka/Interperiodica".*

1. INTRODUCTION

Muon capture provides information about nucleon weak current at a relatively high momentum transfer (about $10^{-1}M$, where M is the nucleon mass). The weak current is of interest not only by itself but also for calculations of cross sections for neutrino-induced reactions. Note that the induced pseudoscalar term of the weak current, which is of importance just for high momentum transfers, is the least known. There is evidence for an anomalous suppression of the corresponding form factor g_P in muon-capture measurements on ^{6}Li [1] and ^{28}Si [2] nuclei, in disagreement with data obtained on ^{12}C [3] and ^{23}Na [4].

The hyperfine effect is one of the possible ways to measure the induced pseudoscalar coupling (see, for example, [4, 5]). The ratio of muon-capture rates, Λ_+/Λ_-, from different hyperfine sublevels is rather sensitive to g_P. In particular, if the Gamow–Teller matrix element dominates in the transition $|J\pi\rangle \longrightarrow |J-1\pi\rangle$, then the ratio

$$\frac{\Lambda_+}{\Lambda_-} = \frac{G_P^2}{\dfrac{3(2J+1)}{J}\left(G_A - \dfrac{1}{3}G_P\right)^2 + \dfrac{J-1}{3J}G_P^2} \qquad (1)$$

exhibits a high sensitivity to $G_P = (E_\nu/2M)(g_P - g_A - g_V - g_M)$—that is, to the form factor g_P. Here, E_ν is the emitted neutrino energy. However, it should be noted that the ratio Λ_+/Λ_- is proportional to $(1/M)^2$, whereas the description usually used for the hyperfine effect [6–9] is based on the nonrelativistic Hamiltonian, which is of the first order in $1/M$ [10, 11]. Thus, an analysis based on the second-order Hamiltonian seems desirable for a consistent description of the hyperfine effect.

Second-order corrections in $1/M$ to the nonrelativistic weak-interaction Hamiltonian for the free nucleon were first considered in [12, 13]. Later, they were discussed in [14, 15]. It was found that the contribution of these corrections to the integral muon-capture rate does not exceed a few percent; therefore, it is of little interest.

However, the nucleon inside a nucleus is not free. Thus, the nuclear potential should be substituted into the relativistic Hamiltonian, which results in new spin–orbit-like terms. Arguments for their possible considerable enhancement are adduced [16, 17]. Thus, an estimate of their contribution both to the integral and to the correlation characteristics of muon capture is of interest.

It is convenient to express the muon-capture rate and all correlation coefficients in terms of the amplitudes $M_u(k)$ [7] $\{T_J(k)$ in [11]$\}$. Explicit formulas for these amplitudes correct to the first order in $1/M$ were obtained in [6] by using the procedure proposed in [18]. In this paper, the second-order contributions to the amplitudes $M_u(k)$ are found. They allow one to estimate second-order corrections to any integral and correlation characteristics in muon capture.

In addition, the angular distribution of neutrinos (recoil nuclei) in muon capture by a target with nonzero spin J is considered. It is also very sensitive to g_P, provided that the initial mesic atom is aligned. However, the calculation of this angular distribution is a challenging task because of the hyperfine splitting in the initial mesic atom. Indeed, the interference of states with different angular momenta $F_\pm = J \pm 1/2$ makes no contribution to the differential probability of muon capture. Therefore, the angular distribution of neutrinos is given by

$$\frac{dw(\mathbf{n}_\nu)}{d\Omega} = \sum_F P(F)\frac{dw^F(\mathbf{n}_\nu)}{d\Omega}, \qquad (2)$$

where $P(F)$ is the population of the state $|F\rangle$. Thus, the angular distribution of neutrinos must be calculated separately for each state of the hyperfine structure.

Explicit expressions for the asymmetry of neutrino emission directions parallel and perpendicular to the direction $\mathbf{n}_\mu$ of mesic-atom polarization were obtained in [6, 8, 19]. However, the ensemble of the initial mesic atoms with spin $F > 1/2$ can be not only polarized but also aligned. This leads to anisotropy of neutrino emis-

* This article was submitted by the author in English.

sion in the directions parallel and orthogonal to the vector $\mathbf{n}_\mu$. The alignment effect was analyzed for $|1/2\pi\rangle \longrightarrow |1/2\pi\rangle$ and $|1\pi\rangle \longrightarrow |0\pi\rangle$ transitions in a model-independent (elementary-particle) approach in [15, 20] and for transitions $|J\pi\rangle \longrightarrow |J \pm 1\pi\rangle$ in the approximation of the dominating Gamow–Teller matrix element in [21]. It was pointed out that the alignment effect is linear in $1/M$ and is very sensitive to g_P. Nevertheless, a contribution of nonleading matrix elements—in particular, of velocity-dependent terms—is evidently of great interest.

Thus, an extended analysis of the alignment effect was performed in parallel with the investigation of the second-order corrections. This is the reason why a general expression for the neutrino angular distribution in muon capture is obtained with an accuracy of $(1/M)^2$.

2. SECOND-ORDER HAMILTONIAN

In the initial 1*s* state of the mesic atom, the captured muon is described by a 4-component wave function. It can be written in the nonrelativistic approximation as ($\hbar = c = 1$)

$$\psi_\mu(\sigma_\mu, \mathbf{r}_\mu, t) = \psi_{1s}(r_\mu)\begin{pmatrix}\varphi_\mu(\sigma_\mu)\\ 0\end{pmatrix}e^{-iE_\mu t}, \quad (3)$$

where E_μ is the total muon energy, including its binding energy in the atom; $\varphi_\mu(\sigma_\mu)$ is the two-component spinor; and σ_μ is the projection of the spin $s_\mu = 1/2$ onto the *z* axis. The final neutrino with the momentum $\mathbf{k}_\nu$ and projection σ_ν of the spin $s_\nu = 1/2$ onto the *z* axis is described by the wave function

$$\psi_\nu(\sigma_\nu, \mathbf{r}_\nu, t) = u_\nu(\mathbf{k}_\nu, \sigma_\nu)e^{i(\mathbf{k}_\nu \cdot \mathbf{r}_\nu - E_\nu t)}, \quad (4)$$

where $u_\nu(\mathbf{k}_\nu, \sigma_\nu)$ is a 4-spinor, and $E_\nu = k_\nu$ is the neutrino energy.

Assuming that the weak nucleon–lepton interaction is pointlike, we introduce the lepton current acting on the nucleon,

$$j_\lambda(\sigma_\mu, \sigma_\nu)e^{-i(\mathbf{k}_\nu \cdot \mathbf{r} + \omega t)} = i\psi_\nu^+(\sigma_\nu, \mathbf{r}, t)\gamma_4\gamma_\lambda(1+\gamma_5)\psi_\mu(\sigma_\mu, \mathbf{r}, t), \quad (5)$$

where $\omega = E_\mu - E_\nu$. Thus, the effective relativistic Hamiltonian for the nucleon inside the nucleus in muon capture is

$$\hat{H} = M\beta + \boldsymbol{\alpha}\cdot\hat{\mathbf{p}} + U(r) + \hat{H}_W, \quad (6)$$

$$\hat{H}_W = \frac{G\cos\theta_C}{\sqrt{2}}j_\lambda(\sigma_\mu, \sigma_\nu)e^{-i(\mathbf{k}_\nu \cdot \mathbf{r} + \omega t)}(i\Gamma_\lambda)\hat{\tau}_-, \quad (7)$$

where *G* is the weak-interaction coupling constant, and θ_C is the Cabibbo angle. The lowering operator $\hat{\tau}_-$ acts in isospin space and transforms a proton into a neutron. For the sake of simplicity, we take the nucleon–nucleus potential $U(r)$ in the central form. The operator of the weak nucleon current is given by

$$\Gamma_\lambda = \gamma_4\left(g_V\gamma_\lambda + \frac{g_M}{2M}\sigma_{\lambda\rho}k_\rho - g_A\gamma_\lambda\gamma_5 - i\frac{g_P}{m}k_\lambda\gamma_5\right). \quad (8)$$

It involves the matrices $\sigma_{\lambda\rho} = (\gamma_\lambda\gamma_\rho - \gamma_\rho\gamma_\lambda)/2i$; the muon mass *m*; and the 4-momentum transfer

$$k_\lambda = \nu_\lambda - \mu_\lambda = (\mathbf{k}_\nu, -i\omega), \quad (9)$$

where ν_λ and μ_λ are the 4-momenta of the neutrino and the muon, respectively. The form factors of vector interaction g_V, axial-vector interaction g_A, weak magnetism g_M, and induced pseudoscalar interaction g_P depend on $k^2 = k_\lambda k_\lambda$. We omit the contribution of second-class currents (that is, scalar and tensor terms).

To go over to the nonrelativistic description of the intranuclear nucleon, we perform the Foldy–Wouthuysen transformation of the relativistic Hamiltonian. Retaining the terms up to second order in $1/M$, we find the nonrelativistic Hamiltonian for the *j*th nucleon in the form

$$\hat{H} = M + \frac{\hat{\mathbf{p}}_j^2}{2M} + U(r_j) + \frac{\Delta U(r_j)}{8M^2} + \frac{U'(r_j)}{4M}\left(\boldsymbol{\sigma}\cdot\left[\mathbf{n}_j\times\frac{\hat{\mathbf{p}}_j}{M}\right]\right) + \hat{h}_j(\sigma_\mu, \sigma_\nu)e^{-i\omega t}, \quad (10)$$

$$\hat{h}_j = \frac{G\cos\theta_C}{\sqrt{2}}e^{-i\mathbf{k}_\nu\cdot\mathbf{r}_j}\left\{ij_4(\sigma_\mu, \sigma_\nu)\left[G_V' + G_P'(\boldsymbol{\sigma}_j\cdot\mathbf{n}_\nu) + g_A'\left(\boldsymbol{\sigma}_j\cdot\frac{\hat{\mathbf{p}}_j}{M}\right) + iG_1\left(\mathbf{n}_\nu\cdot\left[\boldsymbol{\sigma}_j\times\frac{\hat{\mathbf{p}}_j}{M}\right]\right)\right.\right.$$
$$\left.+ G_2\left(\mathbf{n}_\nu\cdot\frac{\hat{\mathbf{p}}_j}{M}\right) + ig_P\frac{U'(r_j)}{4M^2}(\boldsymbol{\sigma}_j\cdot\mathbf{n}_j)\right] \quad (11)$$
$$+ \mathbf{j}(\sigma_\mu, \sigma_\nu)\cdot\left[G_A'\boldsymbol{\sigma}_j + g_V'\frac{\hat{\mathbf{p}}_j}{M} + ig_1\left[\boldsymbol{\sigma}_j\times\frac{\hat{\mathbf{p}}_j}{M}\right]\right.$$
$$\left.\left.+ g_2\left[\left[\boldsymbol{\sigma}_j\times\frac{\hat{\mathbf{p}}_j}{M}\right]\times\frac{\hat{\mathbf{p}}_j}{M}\right] + g_3\boldsymbol{\sigma}_j\cdot\left(\mathbf{n}_\nu\cdot\frac{\hat{\mathbf{p}}_j}{M}\right) + g_V\frac{U'(r_j)}{4M^2}[\boldsymbol{\sigma}_j\times\mathbf{n}_j]\right]\right\}\hat{\tau}_{-j},$$

where $\mathbf{n}_\nu = \mathbf{k}_\nu/k_\nu$, $\mathbf{n}_j = \mathbf{r}_j/r_j$, and

$$G_V' = g_V\left(1 + \varepsilon - \frac{m}{4M}\varepsilon\right) - g_M\frac{m}{2M}\varepsilon,$$

$$G_A' = g_A\left(1 - \frac{\varepsilon^2}{2}\right) - \varepsilon\left(g_V\left(1 - \frac{\eta}{2}\right) + g_M(1-\eta)\right),$$

$$G'_P = \varepsilon\left((g_P - g_A - g_V)\left(1 - \frac{\eta}{2}\right) - g_M(1-\eta)\right),$$

$$g'_V = g_V - \frac{\varepsilon}{2}g_A,$$

$$g'_A = g_A\left(1 + \frac{\varepsilon}{2}\right) + g_P\frac{\eta}{2}, \quad (12)$$

$$G_1 = \frac{\varepsilon}{2}(g_V + g_A + 2g_M), \quad G_2 = -\frac{\varepsilon}{2}g_A,$$

$$g_1 = \frac{1}{2}(\varepsilon g_A - \eta(g_V + 2g_M)),$$

$$g_2 = \frac{1}{2}g_A, \quad g_3 = -\frac{\varepsilon}{2}g_A,$$

$$\varepsilon = \frac{E_\nu}{2M}, \quad \eta = \frac{\omega}{2M}. \quad (13)$$

We have already mentioned that the nonrelativistic Hamiltonian for muon capture by a free nucleon (that is, $U(r) = 0$) with second-order corrections was obtained earlier in [12][1)] and in another form in [13]. Additional terms for the bound nucleon contain $U'(r)$, as well as the spin–orbit coupling. Just these spin–orbit-like terms are of special interest, because they may be enhanced by the same mechanism as the nuclear spin–orbit interaction [17].

The zero-order and first-order terms are proportional to the operators $\hat{1}$, $\boldsymbol{\sigma}_j$, $\hat{\mathbf{p}}_j$, and $(\boldsymbol{\sigma}_j \cdot \hat{\mathbf{p}}_j)$. The second-order terms involve an additional set of operators: $[\boldsymbol{\sigma}_j \times \hat{\mathbf{p}}_j]$, $[[\boldsymbol{\sigma}_j \times \hat{\mathbf{p}}_j] \times \hat{\mathbf{p}}_j]$, $\boldsymbol{\sigma}_j(\mathbf{n}_\nu \cdot \hat{\mathbf{p}}_j)$, $(\boldsymbol{\sigma}_j \cdot \mathbf{n}_j)$, and $[\boldsymbol{\sigma}_j \times \mathbf{n}_j]$.

3. ANGULAR DISTRIBUTION OF NEUTRINOS

Let $|J_f M_f\rangle$ be the wave function that describes the internal state of the final nucleus with spin J_f and its projection M_f onto the z axis. At the same time, the initial state of the mesic atom having a total angular momentum F and involving a nucleus with spin J_i and a muon is represented as

$$|F\rangle = \sum_\xi a_\xi(F) \sum_{M_i\sigma_\mu} C^{F\xi}_{J_i M_i s_\mu \sigma_\mu} |J_i M_i\rangle \psi_\mu(\sigma_\mu). \quad (14)$$

The polarization and alignment of the ensemble of the mesic atoms with the given total angular momentum F are described by the density matrix

$$\rho_{\xi\xi'}(F) = \overline{a_\xi(F) a^*_{\xi'}(F)}, \quad \sum_\xi \rho_{\xi\xi}(F) = 1, \quad (15)$$

or by the spin–tensors

$$\tau_{Qq}(F) = \sum_{\xi\xi'} C^{F\xi'}_{F\xi Qq} \rho_{\xi\xi'}(F), \quad \tau_{00}(F) = 1. \quad (16)$$

The energy of the neutrino emitted in the fixed transition $|J_i\rangle \longrightarrow |J_f\rangle$ is

$$E_\nu = M_f\left[\left(1 + \frac{2Q_\mu}{M_f}\right)^{1/2} - 1\right] \simeq Q_\mu\left(1 - \frac{Q_\mu}{2M_f} + \ldots\right), \quad (17)$$

where $Q_\mu = M_i + E_\mu - M_f$, M_i and M_f being the masses of the initial and final nuclei, respectively. Using the Fermi rule, we find that the differential probability of muon capture per unit time from a given state $|F\rangle$ of the hyperfine structure has the form

$$\frac{dw^F(\mathbf{n}_\nu)}{d\Omega} = \frac{1}{(2\pi)^2}\frac{E_\nu^2}{1 + E_\nu/M_f} \times \sum_{\sigma_\nu M_f}\left|\sum_\xi a_\xi(F) \sum_{M_i\sigma_\mu} C^{F\xi}_{J_i M_i s_\mu \sigma_\mu} \sum_{j=1}^{A} \langle J_f M_f | \hat{h}_j | J_i M_i\rangle\right|^2. \quad (18)$$

It is useful to introduce the multipole expansions for the matrix elements of all operators appearing in the nonrelativistic Hamiltonian. Generalizing the definitions of [7] for the operators of the first-order Hamiltonian, we obtain the relevant matrix element of the scalar operator $\hat{a}_j$ in the form

$$\left\langle J_f M_f \left| \sum_{j=1}^{A} e^{-i\mathbf{k}_\nu \cdot \mathbf{r}_j} \hat{a}_j \hat{\tau}_{-j} \right| J_i M_i \right\rangle = (4\pi)^{3/2} \sum_{um} (-1)^u Y^*_{um}(\mathbf{n}_\nu) C^{J_f M_f}_{J_i M_i u m} [0uu, a], \quad (19)$$

where the reduced matrix elements $[0uu, a] = [0uu]$, $[0uu, p]$, and $[0uu, r]$ correspond to the operators $\hat{a}_j = \hat{1}$, $(\boldsymbol{\sigma}_j \cdot \hat{\mathbf{p}}_j)$, and $iU'(r_j)(\boldsymbol{\sigma}_j \cdot \mathbf{n}_j)$, respectively. For the qth spherical component of the vector operator $\hat{b}_{jq}$, we similarly have

$$\left\langle J_f M_f \left| \sum_{j=1}^{A} e^{-i\mathbf{k}_\nu \cdot \mathbf{r}_j} \hat{b}_{jq} \hat{\tau}_{-j} \right| J_i M_i \right\rangle = \frac{(4\pi)^{3/2}}{\sqrt{3}} \sum_{wm} (-1)^w Y^*_{wm}(\mathbf{n}_\nu) \sum_{uM} C^{uM}_{1qwm} C^{J_f M_f}_{J_i M_i u M} [1wu, b], \quad (20)$$

where $[1wu, b] = [1wu]$, $[1wu, p]$, $[1wu, \sigma p]$, $[1wu, \sigma p^2]$, $[1wu, r]$, and $\{1wu, \sigma p\}$ correspond to $\hat{b}_{jq} = \sigma_{jq}$, $\hat{p}_{jq}$, $i[\boldsymbol{\sigma}_j \times \hat{\mathbf{p}}_j]_q$, $[[\boldsymbol{\sigma}_j \times \hat{\mathbf{p}}_j] \times \hat{\mathbf{p}}_j]_q$, $U'(r_j)[\boldsymbol{\sigma}_j \times \mathbf{n}_j]_q$, and $\sigma_{jq}(\mathbf{n}_\nu \cdot \hat{\mathbf{p}}_j)$, respectively.

[1)] Our result differs by a factor of 1/4 in the term $m/(4M)\varepsilon$ in the definition of G'_V and by the sign of g_3.

The quantity $\{1wu, \sigma p\}$ is a linear combination of the reduced matrix elements $[kwu, \sigma p]$ ($k = 0$, 1 or 2),

$$\{1wu, \sigma p\} = (-1)^{w-u}\sum_k (-1)^k \sqrt{\frac{2k+1}{6(2u+1)}} \times (\sqrt{w}U(ww-11k, 1u)[kw-1u, \sigma p] - \sqrt{w+1}U(ww+11k, 1u)[kw+1u, \sigma p]), \quad (21)$$

defined by

$$C^{J_f M_f}_{J_i M_i uM}[kwu, \sigma p] = \sqrt{2}\langle J_f M_f|\sqrt{\frac{3}{4\pi}}\sum_{j=1}^{A} j_w(k_\nu r_j) \times \sum_{nm} C^{uM}_{knwm} i^w Y_{wm}(\mathbf{r}_j)\Big(\sum_{\lambda q} C^{kn}_{1\lambda 1q}\sigma_{j\lambda}\hat{p}_{jq}\Big)\hat{\tau}_{-j}|J_i M_i\rangle. \quad (22)$$

Note that $[0uu, \sigma p] = -\sqrt{2}\,[0uu, p]$. We use the normalized Racah function $U(abcd, ef) = \sqrt{(2e+1)(2f+1)}\,W(abcd, ef)$. All reduced matrix elements are real-valued quantities, provided that the nuclear wave functions are transformed under time reversal in the standard way [22]:

$$\hat{T}|JM\rangle = (-1)^{J+M}|J-M\rangle. \quad (23)$$

Let $\mathbf{n}_\mu$ be the unit vector along the z axis of the orientation of the ensemble of initial mesic atoms with a given spin F. After a straightforward calculation, we therefore find from (18) that the neutrino angular distribution can be expanded as a series in terms of Legendre polynomials $P_0(\theta) = 1$, $P_1(\theta) = \cos\theta$, $P_2(\theta) = (3\cos^2\theta - 1)/2$ …, as

$$\frac{dw^F(\mathbf{n}_\nu)}{d\Omega} = \frac{C_\mu}{4\pi}\frac{2J_f+1}{2J_i+1}\sum_K (2K+1)\tau_{K0}(F)B_K P_K(\theta), \quad (24)$$

where θ is the angle between $\mathbf{n}_\nu$ and $\mathbf{n}_\mu$. The constant is

$$C_\mu = 8(G\cos\theta_C)^2\Big(\frac{mZe^2}{1+m/M_i}\Big)^3\frac{R(Z)E_\nu^2}{1+E_\nu/M_f}, \quad (25)$$

where Z is the charge of the initial nucleus, and $R(Z)$ is a correction factor that takes into account its nonpointlikeness.

The explicit expressions for the coefficients B_K—they are rather cumbersome—are presented in [16]. They contain the amplitudes $V(u)$ and $A(wu)$, which, for the second-order Hamiltonian, are given by

$$V(u) = \begin{cases} G'_V[0uu] + G_1\dfrac{\{1u, \sigma p\}}{M} + G_2\dfrac{\{1u, p\}}{M} \\ \text{if} \quad \pi_i(-1)^u = \pi_f, \\ G'_P\{1u\} + g'_A\dfrac{[0uu, p]}{M} + g_P\dfrac{[0uu, r]}{4M^2} \\ \text{if} \quad \pi_i(-1)^u = -\pi_f, \end{cases} \quad (26)$$

$$A(wu) = \begin{cases} G'_A[1wu] + g_2\dfrac{[1wu, \sigma p^2]}{M^2} + g_3\dfrac{\{1wu, \sigma p\}}{M} \\ \text{if} \quad \pi_i(-1)^w = \pi_f \\ g'_V\dfrac{[1wu, p]}{M} + g_1\dfrac{[1wu, \sigma p]}{M} + g_V\dfrac{[1wu, r]}{4M^2} \\ \text{if} \quad \pi_i(-1)^w = -\pi_f, \end{cases} \quad (27)$$

where

$$\{1u\} = \sqrt{\frac{u+1}{3(2u+1)}}[1u+1u] - \sqrt{\frac{u}{3(2u+1)}}[1u-1u], \quad (28)$$

the quantities $\{1u, p\}$ and $\{1u, \sigma p\}$ are related to the reduced matrix elements $[1wu, p]$ and $[1wu, \sigma p]$ in the same way, and π_i and π_f are the parities of the initial and final nuclear states, respectively.

It can be seen from (24) that alignment of mesic atom $[\tau_{20}(F) \neq 0]$ leads to specific anisotropy $[\sim P_2(\theta)]$ of neutrino (recoil-nucleus) emission. The explicit expressions for the coefficients B_K in the approximation of the dominant Gamow–Teller matrix element [101] are presented in [21]. In particular, the alignment effect in this approximation is proportional to the induced pseudoscalar coupling: $B_2 \sim G'_A G'_P$. The general expression for B_2 allows one to estimate corrections for nonleading matrix elements.

4. HYPERFINE EFFECT

The rate of muon capture from the hyperfine state $|F_\pm\rangle$ ($F_\pm = J_i \pm 1/2$) of the mesic atom is given by the isotropic term of the differential probability (24); that is,

$$\Lambda_\pm = \oint\Big(\frac{dw^{F_\pm}(\mathbf{n}_\nu)}{d\Omega}\Big)d\Omega. \quad (29)$$

It can be represented in the form [9]

$$\Lambda_F = \bar{\Lambda} + \delta\Lambda_F, \quad (30)$$

where the statistically averaged muon-capture rate is given by

$$\bar{\Lambda} = \frac{C_\mu}{2}\frac{2J_f+1}{2J_i+1}\sum_u (x^2(u) + y^2(u)), \quad (31)$$

and the hyperfine increment takes the form

$$\delta\Lambda_F = \frac{C_\mu}{2}\frac{2J_f+1}{2J_i+1}\frac{J_i(J_i+1) + 3/4 - F(F+1)}{2J_i(J_i+1)} \times \sum_u\Big((J_i(J_i+1) + u(u+1) - J_f(J_f+1))$$

$$\times\left(\frac{x^2(u)}{u}-\frac{y^2(u)}{u+1}\right) \tag{32}$$
$$-2\sqrt{(J_i+J_f+u+2)(J_i-J_f+u+1)}$$
$$\times\sqrt{(J_i+J_f-u)(J_f-J_i+u+1)}\frac{x(u+1)y(u)}{u+1}\Bigg),$$

where

$$x(u) = \sqrt{\frac{2u}{2u+1}}V(u) \tag{33}$$
$$-\sqrt{\frac{2(u+1)}{3(2u+1)}}A(uu)+\sqrt{\frac{2}{3}}A(u-1u),$$

$$y(u) = \sqrt{\frac{2(u+1)}{2u+1}}V(u) \tag{34}$$
$$+\sqrt{\frac{2u}{3(2u+1)}}A(uu)-\sqrt{\frac{2}{3}}A(u+1u).$$

The muon-capture rates $\Lambda_\pm$ can also be reduced to the form

$$\Lambda_+ = \frac{C_\mu}{2}\frac{2J_f+1}{2J_i+1}\frac{1}{2(J_i+1)}\sum_u\frac{1}{u+1} \tag{35}$$
$$\times\left(\sqrt{(J_i+J_f-u)(J_f-J_i+u+1)}x(u+1)\right.$$
$$\left.+\sqrt{(J_i+J_f+u+2)(J_i-J_f+u+1)}y(u)\right)^2,$$

$$\Lambda_- = \frac{C_\mu}{2}\frac{2J_f+1}{2J_i+1}\frac{1}{2J_i}\sum_u\frac{1}{u+1} \tag{36}$$
$$\times\left(\sqrt{(J_i+J_f+u+2)(J_i-J_f+u+1)}x(u+1)\right.$$
$$\left.-\sqrt{(J_i+J_f-u)(J_f-J_i+u+1)}y(u)\right)^2.$$

Setting

$$x(u) = \begin{cases} M_u(u), & \text{if} \quad \pi_i(-1)^u = \pi_f \\ -M_u(-u), & \text{if} \quad \pi_i(-1)^u = -\pi_f, \end{cases} \tag{37}$$

$$y(u) = \begin{cases} M_u(-u-1), & \text{if} \quad \pi_i(-1)^u = \pi_f \\ M_u(u+1), & \text{if} \quad \pi_i(-1)^u = -\pi_f, \end{cases} \tag{38}$$

we obtain the formulas [6] for the muon-capture rates from various hyperfine states as expressed in terms of the amplitudes $M_u(k)$.

On the other hand, using (26), (27) and (33), (34), we obtain the required expressions for the amplitudes $M_u(k)$ correct to second-order terms in $1/M$. They are presented in the Appendix. Note that some first-order terms in (A.1)–(A.4) differ in sign from the analogous terms in [6]. This is because we fix the signs of the reduced matrix elements in (19) and (20) using the condition (23) for the wave functions.

5. SUMMARY

The effective nonrelativistic Hamiltonian of second-order in $1/M$ of muon capture has been obtained. New spin–orbit-like terms in the Hamiltonian that are associated with the nucleon–nucleus potential have been considered. Due to their possible enhancement, the second-order contribution to the muon-capture characteristics is of interest.

A general treatment of the hyperfine effect in the muon-capture rate with allowance for the second-order terms has been given. In particular, the generalized expressions for the amplitudes $M_u(k)$ have been presented. A general equation for the neutrino (recoil-nucleus) angular distribution in muon capture by a nucleus with nonzero spin involving alignment effect has been discussed.

Using the results obtained here—especially the equations for $M_u(k)$—one can calculate second-order corrections to any integral and correlation characteristics in muon capture.

ACKNOWLEDGMENTS

I am grateful to Prof. J.P. Deutsch for his interest in this study and stimulating discussions.

This work was supported by the Russian Foundation for Basic Research (project no. 96-15-96548).

APPENDIX

Explicit Expressions for the Amplitudes $M_u(k)$

$$M_u(u) = \sqrt{\frac{2}{2u+1}}\left\{\sqrt{u}G_V'[0uu]-\sqrt{\frac{u+1}{3}}G_A'[1uu]\right.$$
$$+\sqrt{\frac{2u+1}{3}}\left(g_V'-\frac{uG_2}{2u+1}\right)\frac{[1u-1u,p]}{M}$$
$$+\sqrt{\frac{u(u+1)}{3(2u+1)}}G_2\frac{[1u+1u,p]}{M}$$
$$-\sqrt{\frac{2u+1}{3}}\left(\frac{uG_1}{2u+1}-g_1-\frac{(u+1)g_3}{2(2u+1)}\right)$$
$$\times\frac{[1u-1u,\sigma p]}{M}+\sqrt{\frac{u(u+1)}{3(2u+1)}}\left(G_1+\frac{g_3}{2}\right) \tag{A.1}$$
$$\times\frac{[1u+1u,\sigma p]}{M}+\frac{1}{2}\sqrt{\frac{(u-1)(u+1)}{3(2u+1)}}g_3\frac{[2u-1u,\sigma p]}{M}$$
$$-\frac{1}{2}\sqrt{\frac{(u+1)(u+2)}{3(2u+1)}}g_3\frac{[2u+1u,\sigma p]}{M}$$
$$\left.-\sqrt{\frac{u+1}{3}}g_2\frac{[1uu,\sigma p^2]}{M^2}+\sqrt{\frac{2u+1}{3}}g_V\frac{[1u-1u,r]}{4M^2}\right\},$$

$$M_u(-u-1) = \sqrt{\frac{2}{2u+1}}$$
$$\times\Bigg\{\sqrt{u+1}G_V'[0uu] + \sqrt{\frac{u}{3}}G_A'[1uu]$$
$$-\sqrt{\frac{2u+1}{3}}\left(g_V' - \frac{(u+1)G_2}{2u+1}\right)\frac{[1u+1u,\,p]}{M}$$
$$-\sqrt{\frac{u(u+1)}{3(2u+1)}}G_2\frac{[1u-1u,\,p]}{M}$$
$$+\sqrt{\frac{2u+1}{3}}\left(\frac{(u+1)G_1}{2u+1} - g_1 - \frac{ug_3}{2(2u+1)}\right) \qquad \text{(A.2)}$$
$$\times\frac{[1u+1u,\,\sigma p]}{M} - \sqrt{\frac{u(u+1)}{3(2u+1)}}\left(G_1 + \frac{g_3}{2}\right)$$
$$\times\frac{[1u-1u,\,\sigma p]}{M} - \frac{1}{2}\sqrt{\frac{u(u-1)}{3(2u+1)}}g_3\frac{[2u-1u,\,\sigma p]}{M}$$
$$+\frac{1}{2}\sqrt{\frac{u(u+2)}{3(2u+1)}}g_3\frac{[2u+1u,\,\sigma p]}{M}$$
$$+\sqrt{\frac{u}{3}}g_2\frac{[1uu,\,\sigma p^2]}{M^2} - \sqrt{\frac{2u+1}{3}}g_V\frac{[1u+1u,\,r]}{4M^2}\Bigg\},$$

$$M_u(-u) = \sqrt{\frac{2}{2u+1}}$$
$$\times\Bigg\{-\sqrt{\frac{2u+1}{3}}\left(G_A' - \frac{uG_P'}{2u+1}\right)[1u-1u]$$
$$-\sqrt{\frac{u(u+1)}{3(2u+1)}}G_P'[1u+1u] - \sqrt{u}\left(g_A' + \frac{g_3}{3}\right)$$
$$\times\frac{[0uu,\,p]}{M} + \sqrt{\frac{u+1}{3}}g_V'\frac{[1uu,\,p]}{M}$$
$$+\sqrt{\frac{u+1}{3}}\left(g_1 + \frac{g_3}{2}\right)\frac{[1uu\sigma p]}{M} \qquad \text{(A.3)}$$
$$+\sqrt{\frac{(u-1)(2u+1)}{6(2u-1)}}g_3\frac{[2u-2u,\,\sigma p]}{M}$$
$$-\frac{1}{6}\sqrt{\frac{(u+1)(2u+3)}{2u-1}}g_3\frac{[2uu,\,\sigma p]}{M}$$
$$-\sqrt{\frac{2u+1}{3}}g_2\frac{[1u-1u,\,\sigma p^2]}{M^2} - \sqrt{u}g_P\frac{[0uu,\,r]}{4M^2}$$
$$+\sqrt{\frac{u+1}{3}}g_V\frac{[1uu,\,r]}{4M^2}\Bigg\},$$

$$M_u(u+1) = \sqrt{\frac{2}{2u+1}}$$
$$\times\Bigg\{-\sqrt{\frac{2u+1}{3}}\left(G_A' - \frac{(u+1)G_P'}{2u+1}\right)[1u+1u]$$
$$-\sqrt{\frac{u(u+1)}{3(2u+1)}}G_P'[1u-1u] + \sqrt{u+1}\left(g_A' - \frac{g_3}{3}\right)$$
$$\times\frac{[0uu,\,p]}{M} + \sqrt{\frac{u}{3}}g_V'\frac{[1uu,\,p]}{M} + \sqrt{\frac{u}{3}}\left(g_1 + \frac{g_3}{2}\right)$$
$$\times\frac{[1uu,\,\sigma p]}{M} - \sqrt{\frac{(u+2)(2u+1)}{6(2u+3)}}g_3\frac{[2u+2u,\,\sigma p]}{M} \qquad \text{(A.4)}$$
$$+\frac{1}{6}\sqrt{\frac{u(2u-1)}{2u+3}}g_3\frac{[2uu,\,\sigma p]}{M} - \sqrt{\frac{2u+1}{3}}$$
$$\times g_2\frac{[1u+1u,\,\sigma p^2]}{M^2} + \sqrt{u+1}$$
$$\times g_P\frac{[0uu,\,r]}{4M^2} + \sqrt{\frac{u}{3}}g_V\frac{[1uu,\,r]}{4M^2}\Bigg\}.$$

REFERENCES

1. J. P. Deutsch, L. Grenacs, P. Igo-Kemenes, *et al.*, Phys. Lett. B **26**, 315 (1968).
2. V. Brudanin, V. Egorov, T. Filipova, *et al.*, Nucl. Phys. A **587**, 577 (1995).
3. M. Fukui, K. Koshigiri, T. Sato, *et al.*, Prog. Theor. Phys. **78**, 343 (1987).
4. B. L. Johnson, T. P. Gorringe, D. S. Armstrong, *et al.*, Phys. Rev. C **54**, 2714 (1996).
5. V. Wiaux, J. Deutsch, J. Govaerts, *et al.*, Yad. Fiz. **61**, 1403 (1998) [Phys. At. Nucl. **61**, 1301 (1998)].
6. V. V. Balashov and R. A. Eramzhyan, At. Énerg. **5** (3), 3 (1967).
7. V. V. Balashov, G. Ya. Korenman, and R. A. Eramzhyan, *Meson Capture by Nuclei* (Atomizdat, Moscow, 1978).
8. A. Galindo and P. Pascual, Nucl. Phys. B **4**, 295 (1968).
9. J. D. Walecka, Nucl. Phys. A **258**, 397 (1976).
10. A. Fujii and H. Primakoff, Nuovo Cimento **12**, 327 (1959).
11. N. C. Mukhopadhyay, Phys. Rep. **30**, 1 (1977).
12. J. L. Friar, Nucl. Phys. **87**, 407 (1966).
13. H. Ohtsubo, Phys. Lett. **22**, 480 (1966).
14. B. D. Serot, Nucl. Phys. A **308**, 457 (1978).
15. J. G. Congleton and H. W. Fearing, Nucl. Phys. A **552**, 534 (1993).
16. A. L. Barabanov, Preprint No. IAE-6119/2, IAE (Russian Research Centre Kurchatov Institute, Moscow, 1999); nucl-th/9903054.
17. A. L. Barabanov, Eur. Phys. J. A **6**, 373 (1999).
18. M. Morita and A. Fujii, Phys. Rev. **118**, 606 (1960).
19. H. Primakoff, Rev. Mod. Phys. **31**, 802 (1959).
20. W.-Y. P. Hwang, Phys. Rev. C **17**, 1799 (1978); **18**, 1553 (1978).
21. A. L. Barabanov, Yu. V. Gaponov, B. V. Danilin, and N. B. Shul'gina, Yad. Fiz. **59**, 1940 (1996) [Phys. At. Nucl. **59**, 1871 (1996)].
22. A. Bohr and B. R. Mottelson, *Nuclear Structure, Vol. 1: Single-Particle Motion* (Benjamin, New York, 1969; Mir, Moscow; 1971).

Physics of Atomic Nuclei, Vol. 63, No. 7, 2000, pp. 1193–1195. From Yadernaya Fizika, Vol. 63, No. 7, 2000, pp. 1268–1270.

NEW PHYSICS, NUCLEAR AND NUCLEON STRUCTURE IN RARE PROCESSES

Estimation of Scalar and Tensor Weak-Interaction Constants on the Basis of Recent Neutron Experimental Data*

Yu. A. Mostovoĭ, Yu. V. Gaponov, and B. G. Yerozolimsky[1)]

Russian Research Centre Kurchatov Institute, pl. Kurchatova 1, Moscow, 123182 Russia

Abstract—The contributions of scalar and tensor interactions associated with right-handed neutrinos to the effective hadron–lepton Hamiltonian are estimated on the basis of modern measurements of the neutron lifetime and correlations in the beta decay of a free neutron. © *2000 MAIK "Nauka/Interperiodica".*

There are four invariant coupling constants in the effective Hamiltonian of allowed beta decay. These constants are usually denoted by various parameters C_i. The vector (C_V) and scalar (C_S) couplings describe Fermi transitions via the combination $G_F = + \sqrt{(C_V^2 + C_S^2)}$. The axial-vector ($C_A$) and tensor ($C_T$) couplings describe Gamow–Teller transitions by means of the combined parameter $G_{GT} = - \sqrt{(C_A^2 + C_T^2)}$. The most general form of the effective Hamiltonian (see, for example, [1]) also has some parameters denoted by C_i'. The prime here indicates the aforementioned coupling constant in the case of parity (P) violation. In this notation, the left-handed neutrino (right-handed antineutrino) corresponds to the relations $C_i = +C_i'$. There is experimental evidence that the scalar and tensor interactions with the standard, left-handed, neutrino do not contribute to the weak lepton–hadron processes. It is a consequence of the well-known fact that the so-called Fierz term b of the general theoretical formula for the beta spectrum does not manifest itself in the experimental shape of the spectra. This allows a very sensitive test of the scalar and tensor contributions owing to the interference terms for C_S–C_V and C_T–C_A mixings, which one can see from the following equation for real C_i and C_i':

$$b \sim (C_S C_V + C_S' C_V' + 3(C_T C_A + C_T' C_A')). \qquad (1)$$

When, however, $C_S = -C_S'$ and $C_T = -C_T'$, the Fierz term vanishes automatically, although the scalar and tensor couplings can be nonzero. From the physical point of view, this choice of signs means that the right-handed neutrino (left-handed antineutrino) is emitted when there are scalar and tensor contributions. This situation directly corresponds to the leptoquark hypothesis of Gaponov [2].

Let us investigate present experimental data on the beta decay of a free neutron under the following assumptions: $C_S = -C_S'$, $C_V = + C_V'$, $C_T = -C_T'$, and $C_A = + C_A'$. For this choice of signs, the main four experimental parameters of the beta decay of the free neutron (A, B, a, $f\tau_n$) are given by

$$A = -\frac{C_A^2 + C_T^2 + C_V C_A - C_S C_T}{C_V^2 + C_S^2 + 3(C_A^2 + C_T^2)}, \qquad (2)$$

$$B = -\frac{C_T^2 - C_A^2 + C_V C_A - C_S C_T}{C_V^2 + C_S^2 + 3(C_A^2 + C_T^2)}, \qquad (3)$$

$$a = \frac{C_V^2 - C_S^2 + C_T^2 - C_A^2}{C_V^2 + C_S^2 + 3(C_A^2 + C_T^2)}, \qquad (4)$$

$$f\tau_n = \frac{2\pi^3 \hbar^7}{m_e^5 c^4} \frac{1}{C_V^2 + C_S^2 + 3(C_A^2 + C_T^2)}. \qquad (5)$$

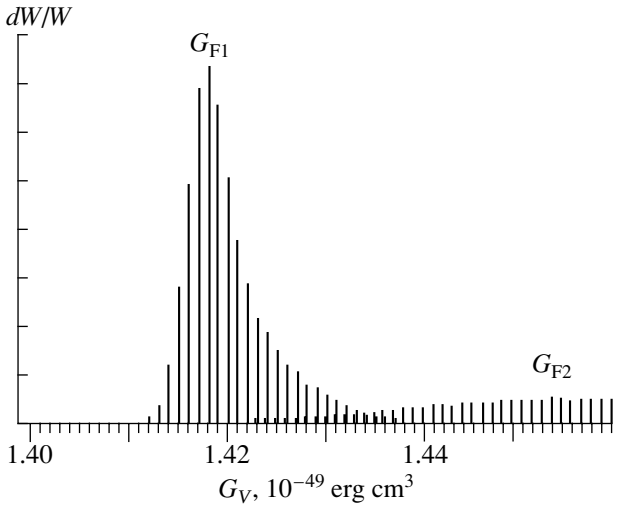

Fig. 1. Difference of the probability densities dW/W for two solutions G_{F1} and G_{F2} as a basic guideline for the solution type employed.

* This article was submitted by the authors in English.

[1)] Harvard University, 42 Oxford Street, Cambridge, MA 02138, USA.

1063-7788/00/6307-1193$20.00 © 2000 MAIK "Nauka/Interperiodica"

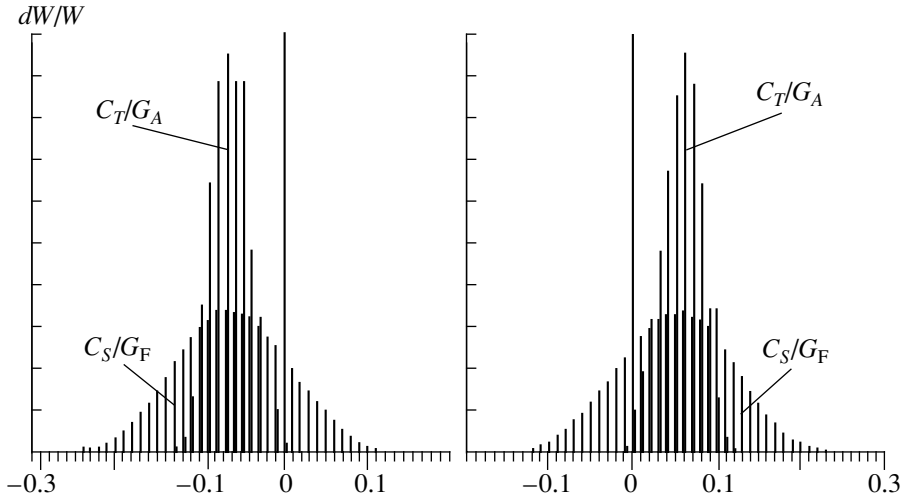

Fig. 2. Two versions with the sign reflection for the C_S/G_F and C_T/G_{GT} spectra.

By using experimental data for the aforementioned parameters, this set of four equations can be solved analytically for four coupling constants. The result is [3]

$$C_A = -\frac{k}{(1-A)}\sqrt{1+A+B+a}\times\{[(1+A)+(B-a)] \pm \sqrt{1+A-B-a}\sqrt{(1-A)^2-(B+a)^2-4A^2}\}, \quad (6)$$

$$C_V = \frac{k}{(1-A)}\sqrt{1+A+B+a}\times\{[3(1+A)-(B-a)] \mp \sqrt{1+A-B-a}\sqrt{(1-A)^2-(B+a)^2-4A^2}\}, \quad (7)$$

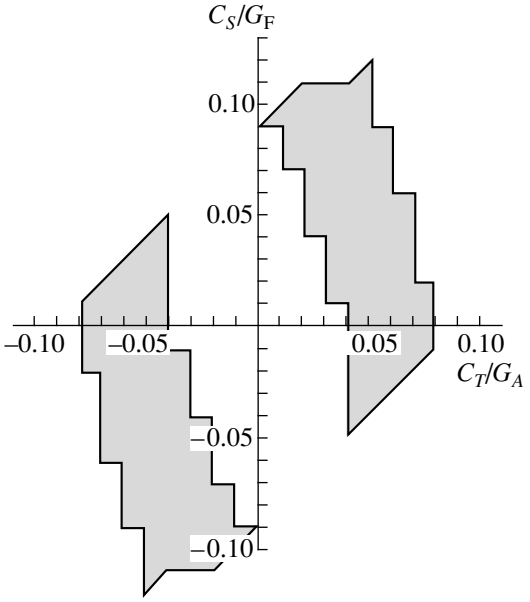

Fig. 3. Regions for the two-dimensional distribution C_S/G_F–C_T/G_{GT}.

$$C_S = -\frac{k}{(1-A)}\sqrt{1+A-B-a}\times\{[3(1+A)+(B-a)] \mp \sqrt{1+A+B+a}\sqrt{(1-A)^2-(B-a)^2-4A^2}\}, \quad (8)$$

$$C_T = \frac{k}{(1-A)}\sqrt{1+A-B-a}\times\{[(1+A)-(B-a)] \pm \sqrt{1+A+B+a}\sqrt{(1-A)^2-(B-a)^2-4A^2}\}, \quad (9)$$

where $k \simeq 6\times10^{-51}$ erg cm^3. The spectra for C_A, C_V, C_S, C_T, and $G_F = C_V/|C_V|\cdot\sqrt{(C_V^2+C_S^2)}$ were obtained by the Monte Carlo method (1000000 combinations) with the normal distribution of experimental data. These coupling constants were assumed to be real-valued. For the correlation coefficients, we used the values of $A = -0.1161 \pm 0.0007$, $B = +0.9820 \pm 0.0040$, and $a = -0.1017 \pm 0.0051$. The value of $\tau = 885.7$ s was used to calculate k [4].

Since we have two solutions to each quadratic equation [see (6)–(9)] with four combinations of the signs of the square roots, there are eight possible sets for C_i. By using similar signs and assuming that G_F is equal to the experimental value $G_F^{0\leftrightarrow0} = (+1.4173 \pm 0.0011)\times10^{-49}$ erg cm^3 extracted from data on 0^+–0^+ nuclear beta decays [5], we can reduce, however, this number to two. Figure 1 illustrates the criterion used to select the relevant solution of the quadratic equation. The remaining two versions have the same value for G_V, but the signs of C_S and C_T are simultaneously reversed. There is no reason to prefer one of them.

For these two versions, the spectra of C_S/G_F and C_T/G_{GT} (Fig. 2) were calculated with the additional constraint $(1.418 < G_F < 1.419)\times10^{-49}$ erg cm^3. Thus, the

final result is either $C_S/G_F = -0.065$ and $C_T/G_{GT} = -0.065$ or $C_S/G_F = +0.065$ and $C_T/G_{GT} = +0.065$.

By using the self-contained part for the analysis independently, B. Yerozolimsky arrived at the same conclusion [6]. He used formulas (2)–(4) and constructed the allowed region for the two-dimensional distribution C_S/G_F–C_T/G_{GT} by calculating all possible combinations of A, B, and a in the region of one standard deviation. Moreover, from the very beginning, he used only those combinations of signs that corresponded to the above value of $G_F^{0\leftrightarrow 0}$. It is interesting to note that the point {0, 0} lies beyond these distributions, but it is inside the allowed region of one standard error (Fig. 3).

In conclusion, we note that recent experimental data on angular correlations in the beta decay of a free neutron demonstrate the possible existence of the scalar and tensor terms of weak interactions if, simultaneously, the emission of right-handed neutrinos is assumed. For this case, the ratios $|C_S/G_F| = 0.065$ and $|C_T/G_{GT}| = 0.065$ are in agreement with their partial contribution to the full process of the beta decay of a free neutron (0.8%). These values provide a check of the lepton–quark hypothesis [1]. However, we cannot rule out the possibility that this effect results from the low accuracy of the antineutrino–electron correlation [the quantity a in (4)] experiments included in the above analysis.

ACKNOWLEDGMENTS

This work was supported in part by the Russian Foundation for Basic Research (project nos. 98-02-17706 and 97-02-16536).

REFERENCES

1. Yu. V. Gaponov, Usp. Fiz. Nauk **102**, 211 (1970) [Sov. Phys. Usp. **13**, 647 (1970)].
2. Yu. V. Gaponov, Yad. Fiz. **62**, 1281 (1999) [Phys. At. Nucl. **62**, 1206 (1999)]; **63** (2000) [**63** (2000)].
3. B. G. Erozolimskiĭ and Yu. A. Mostovoĭ, Yad. Fiz. **53**, 418 (1991) [Sov. J. Nucl. Phys. **53**, 260 (1991)]; Yu. A. Mostovoĭ and A. I. Frank, Pis'ma Zh. Éksp. Teor. Fiz. **24**, 43 (1976) [JETP Lett. **24**, 38 (1976)].
4. Yu. A. Mostovoy, Yad. Fiz. **61**, 1418 (1998) [Phys. At. Nucl. **61**, 1316 (1998)].
5. D. Wilkinson, Nucl. Instrum. Methods A **335**, 172 (1993).
6. B. G. Yerozolimsky, Nucl. Instrum. Methods A **440**, 491 (2000).

Physics of Atomic Nuclei, Vol. 63, No. 7, 2000, pp. 1196–1199. From Yadernaya Fizika, Vol. 63, No. 7, 2000, pp. 1271–1273.

NEW PHYSICS, NUCLEAR AND NUCLEON STRUCTURE IN RARE PROCESSES

Contribution of the Lowest 1^+ Intermediate State to the $2\nu\beta\beta$-Decay Amplitude*

S. V. Semenov, F. Šimkovic[1)], V. V. Khruschev, and P. Domin[1)]**

Russian Research Centre Kurchatov Institute, pl. Kurchatova 1, Moscow, 123182 Russia

Abstract—The half-life with respect to two-neutrino double-beta ($2\nu\beta\beta$) decay to the final ground state is calculated under the assumption of single-state dominance. To the best of our knowledge, the energy denominators of perturbation theory are considered for the first time without invoking any approximation. The results obtained for the experimentally interesting A = 100, 110, 114, 116, and 128 nuclear systems are presented. © *2000 MAIK "Nauka/Interperiodica".*

The inverse half-life with respect to two-neutrino double-beta ($2\nu2\beta$) decay can be represented as [1]

$$[t_{1/2}^{(2\nu)}(0^+ \longrightarrow 0^+)]^{-1} = \frac{(G_\beta g_A)^4 m_e^9}{32\pi^7 \ln 2} \times \int_1^{T+1} d\varepsilon_1 \int_1^{T+2-\varepsilon_1} d\varepsilon_2 \int_0^{T+2-\varepsilon_1-\varepsilon_2} d\omega_1 F(Z_f, \varepsilon_1) \times F(Z_f, \varepsilon_2) p_1\varepsilon_1 p_2\varepsilon_2 \omega_1^2 \omega_2^2 \left| \sum_m M_{\mathrm{GT}m}^{(2\nu)} \frac{K_m + L_m}{2} \right|^2, \quad (1)$$

where p_1, p_2 and ε_1, ε_2 are the electron momenta and energies, respectively; ω_1 and ω_2 are the antineutrino energies ($\omega_2 = T + 2 - \varepsilon_1 - \varepsilon_2 - \omega_1$); $T = M_i - M_f - 2 = Q_{\beta\beta}$ is the total kinetic energy of leptons in the final state; M_i (M_f) is the mass of the parent (daughter) nucleus; and $F(Z_f, \varepsilon)$ is the relativistic Coulomb function that corrects the electron plane waves for the distortion generated by the nuclear Coulomb field [1].

The factors K_m and L_m in (1) are expressed in terms of the energy denominators of second-order perturbation theory as

$$K_m = \frac{1}{\mu_m + (\varepsilon_1 + \omega_1 - \varepsilon_2 - \omega_2)/2} + \frac{1}{\mu_m - (\varepsilon_1 + \omega_1 - \varepsilon_2 - \omega_2)/2},$$
$$L_m = \frac{1}{\mu_m + (\varepsilon_1 + \omega_2 - \varepsilon_2 - \omega_1)/2} + \frac{1}{\mu_m - (\varepsilon_1 + \omega_2 - \varepsilon_2 - \omega_1)/2}, \quad (2)$$

where $\mu_m = E_m - (M_i + M_f)/2$, E_m being the energy of the mth 1^+ state of the intermediate nucleus.

In (1), the contribution from the double Fermi nuclear matrix element to $2\nu\beta\beta$-decay rate is neglected. The reduced matrix element $M_{\mathrm{GT}m}^{(2\nu)}$ of the double Gamow–Teller transition is given by

$$M_{\mathrm{GT}m}^{(2\nu)} = -\left\langle 0_f^+ \middle\| \hat{\beta}^- \middle\| N_m(1^+) \right\rangle \left\langle N_m(1^+) \middle\| \hat{\beta}^- \middle\| 0_i^+ \right\rangle. \quad (3)$$

It is worth noting that the $2\nu\beta\beta$-decay nuclear matrix element in (1) involves summation over all virtual intermediate 1^+ states.

The calculation of the half-life with respect to $2\nu\beta\beta$ decay is a complicated task because the factors K_m and L_m depend on the energies of the outgoing electrons and antineutrinos. Therefore, phase-space integration must be performed for each 1^+ state m of the intermediate odd–odd nucleus. The problem is usually simplified by assuming equal values for the kinetic energies of the outgoing leptons in the denominators entering into the expression for K_m and L_m—that is, $\varepsilon_1 - 1 \sim \varepsilon_2 - 1 \sim \omega_1 \sim \omega_2 = Q_{\beta\beta}/4$. As the result of this approximation, we obtain $K_m \cong L_m \cong 2/\mu_m$, and the inverse $2\nu\beta\beta$-decay half-life factorizes into the phase-space factor $G^{(2\nu)}$ and the relevant nuclear matrix element,

$$[t_{1/2}^{(2\nu)}]^{-1} = \left| \sum_m \frac{\left\langle 0_f^+ \middle\| \beta^- \middle\| N_m(1^+) \right\rangle \left\langle N_m(1^+) \middle\| \beta^- \middle\| 0_{f/}^+ \right\rangle}{Q_{\beta\beta}/2 + E_m - M_i + 1} \right|^2 G^{(2\nu)}, \quad (4)$$

where $Q_{\beta\beta}/2 + E_m - M_i + 1 = \mu_m$ and

$$G^{(2\nu)} = \frac{(G_\beta g_A)^4 m_e^9}{240\pi^7 \ln 2} \int_1^{T+1} d\varepsilon_1 \int_1^{T+2-\varepsilon_1} d\varepsilon_2 F(Z_f, \varepsilon_1) \times F(Z_f, \varepsilon_2) p_1\varepsilon_1 p_2\varepsilon_2 (T + 2 - \varepsilon_1 - \varepsilon_2)^5. \quad (5)$$

* This article was submitted by the authors in English.

** e-mail: semenov@post.imp.kiae.ru

1) Department of Nuclear Physics, Comensius University, Mlynská dolina, SK-84215 Bratislava, Slovak Republic.

The kinematical factor $G^{(2\nu)}$ is free from unknown parameters and can be directly evaluated [1–3].

In order to calculate the $2\nu\beta\beta$-decay half-life $t_{1/2}^{(2\nu)}$ in (4), it is necessary to know the nuclear matrix elements for both the initial branch, M_m^I $\left(M_m^I = \left\langle N_m(1^+)\middle\|\hat{\beta}^-\middle\|0_i^+\right\rangle\right)$, and the final branch, M_m^F $\left(M_m^F = \left\langle 0_f^+\middle\|\hat{\beta}^-\middle\|N_m(1^+)\right\rangle\right)$. These can be found theoretically—that is, in a model-dependent way [4].

In recent years, much attention has been given to the hypothesis of single-state dominance (SSD) [5, 6]; this hypothesis states that the $2\nu\beta\beta$-decay rates are governed by a virtual two-step transition connecting the initial and final ground state through the first m_0 1^+ state of the intermediate nucleus. We note that there is a similar dominance in the theory of induced $2\nu\beta\beta$ decay [7].

Within the SSD hypothesis, it is possible to calculate the matrix elements $M_{m_0}^I$ and $M_{m_0}^F$ corresponding to the single-β^- and electron-capture decays from the measured $\log ft$ values according to the relations [8]

$$M_{m_0}^I = \left\langle 1_{\mathrm{g.s}}^+\middle\|\hat{\beta}^-\middle\|0_i\right\rangle = \frac{1}{g_A}\sqrt{\frac{3D}{ft_{\mathrm{EC}}}},$$
$$M_{m_0}^F = \left\langle 0_f\middle\|\hat{\beta}^-\middle\|1_{\mathrm{g.s}}^+\right\rangle = \frac{1}{g_A}\sqrt{\frac{3D}{ft_{\beta^-}}}, \tag{6}$$

where $D = 2\pi^3\ln 2/G_\beta^2 m_e^5 = 6146.7$ s. By assuming that $K_{m_0} \simeq L_{m_0} \simeq 2/\mu_{m_0}$ we obtain

$$\left[t_{1/2}^{*(2\nu)}\right]^{-1} = \frac{9D^2}{g_A^2\mu_{m_0}^2 ft_{\mathrm{EC}} ft_{\beta^-}}G^{(2\nu)}, \tag{7}$$

where $\mu_{m_0} = (Q_{\mathrm{EC}} + Q_{\beta^-})/2$, Q_{EC} and Q_{β^-} being the Q values for electron capture and β^- decay, respectively. We note that, from (5) and (7), it follows that $t_{1/2}^{*(2\nu)}$ does not depend on g_A explicitly. Henceforth, we will assume that $g_A = 1.254$.

The effect of exactly taking into account K_m and L_m in (2) on the $2\nu\beta\beta$-decay half-life has not yet been investigated. In the case of the first $1_{m_0}^+$ state, however, the value of μ_{m_0} can be comparable with the maximum of the expressions $(\varepsilon_1 + \omega_1 - \varepsilon_2 - \omega_2)$ and $(\varepsilon_1 + \omega_2 - \varepsilon_2 - \omega_1)$—that is, with $Q_{\beta\beta}/2$. In this particular case, the value of the second denominator of K_{m_0} and L_{m_0} in (2) can be rather small. This fact might affect the results on $2\nu\beta\beta$-decay half-life considerably. The goal of this article is to deal with this problem.

If the exact form of the factors K_{m_0} and L_{m_0} is considered, the $2\nu\beta\beta$-decay half-life derived within the SSD hypothesis is given by

$$\left[t_{1/2}^{(2\nu)}\right]^{-1} = \left|M_{m_0}^I M_{m_0}^F\right|^2 \frac{(G_\beta g_A)^4 m_e^9}{32\pi^7\ln 2}$$
$$\times \int_1^{T+1} d\varepsilon_1 \int_1^{T+2-\varepsilon_1} d\varepsilon_2 \int_1^{T+2-\varepsilon_1-\varepsilon_2} d\omega_1 F(Z_f, \varepsilon_1)F(Z_f, \varepsilon_2) \tag{8}$$
$$\times p_1\varepsilon_1 p_2\varepsilon_2\omega_1^2(T + 2 - \varepsilon_1 - \varepsilon_2 - \omega_1)^2\left(\frac{K_{m_0} + L_{m_0}}{2}\right)^2.$$

The relativistic Coulomb correction factor $F_0(Z_f, \varepsilon)$ can be written as [1]

$$F_0(Z_f, \varepsilon) = \frac{4}{[\Gamma(2\gamma_1 + 1)]^2}(2pR_A)^{2(\gamma_1 - 1)}\left|\Gamma(\gamma_1 + iy)\right|^2 e^{\pi y}, \tag{9}$$
$$y = \frac{\alpha Z_f \varepsilon}{p}, \quad \gamma_1 = \sqrt{1 - (Z_f\alpha)^2}, \quad R_A = 1.2A^{1/3}\ \text{fm}.$$

The gamma function in (9) can be calculated by using of the Euler infinite-product formula:

$$\Gamma(z) = \lim_{n\to\infty}\frac{n!}{z(z+1)\cdots(z+n)}n^z,$$
$$\left|\Gamma(\gamma_1 + iy)\right|^2 \tag{10}$$
$$= \lim_{n\to\infty}\frac{(n!)^2 n^{2\gamma_1}}{(\gamma_1^2 + y^2)[(\gamma_1 + 1)^2 + y^2]\cdots[(\gamma_1 + n)^2 + y^2]}.$$

The above exact expression for the gamma function provides more reliable results than other common approximations [3]. The convergence of the integral in (8) at the lower boundary ($\varepsilon \longrightarrow 1$, $p \longrightarrow 0$, and $y \longrightarrow \infty$) is guaranteed by the following asymptotic property [9]:

$$\lim_{|y|\to\infty}\left|\Gamma(x + iy)\right|e^{\frac{\pi}{2}|y|}|y|^{1/2 - x} = \sqrt{2\pi}. \tag{11}$$

Thus, we have

$$\lim_{\varepsilon\to 1}\varepsilon pF(Z_f, \varepsilon) = \frac{8\pi}{[\Gamma(2\gamma_1 + 1)]^2}(2R_A/\lambda\!\!\!^{-}_{\mathrm{C}})^{2(\gamma_1 - 1)}(\alpha Z_f)^{2\gamma_1 - 1}, \tag{12}$$

where $\lambda\!\!\!^{-}_{\mathrm{C}}$ is the nuclear radius scaled by the Compton wavelength of the electron.

For the $2\nu\beta\beta$ decay of ^{100}Mo, ^{110}Pd, ^{114}Cd, ^{116}Cd, and ^{128}Te, the $2\nu\beta\beta$-decay half-lives calculated within

2νββ-decay half-lives calculated within the SSD hypothesis both with exact ($t_{1/2}^{(2\nu)}$) and with approximated ($t_{1/2}^{*(2\nu)}$) factors K_{m_0} and L_{m_0} (the parameters $Q_{\beta\beta}$ and μ_{m_0}, log*ft* values, and the corresponding nuclear matrix elements $M_{m_0}^I$ and $M_{m_0}^F$ are shown together with the kinematical factors $G^{(2\nu)}$. $\Delta = |t_{1/2}^{*(2\nu)} - t_{1/2}^{(2\nu)}|/t_{1/2}^{(2\nu)}$ and $t_{1/2}^{2\nu-\exp}$ is the experimental half-life or its lower limit)

Nucleus	^{100}Mo	^{110}Pd	^{114}Cd	^{116}Cd	^{128}Te
$Q_{\beta\beta}$	5.937	3.914	1.050	5.487	1.697
μ_{m_0}	3.3	3.697	3.35	3.66	3.31
logft_{EC}	4.45	4.08	4.9	4.39	5.05
logft_{β^-}	4.60	4.66	4.473	4.662	6.09
$M_{m_0}^I$	0.645	0.988	0.384	0.691	0.323
$M_{m_0}^F$	0.543	0.507	0.628	0.505	0.098
$G^{(2\nu)}$, yr^{-1}	9.417×10^{-18}	3.106×10^{-19}	1.463×10^{-23}	7.946×10^{-18}	8.401×10^{-22}
$t_{1/2}^{*(2\nu)}$, yr	9.44×10^{-18}	1.75×10^{20}	1.32×10^{25}	1.38×10^{19}	1.33×10^{25}
$t_{1/2}^{(2\nu)}$, yr	7.55×10^{-18}	1.64×10^{20}	1.31×10^{25}	1.2×10^{19}	1.3×10^{25}
Δ, %	25	7	0.5	15	1.5
$t_{1/2}^{2\nu-\exp}$, yr	$3.3^{+2.0}_{-1.0} \times 10^{18}$				
	$6.82^{+0.38}_{-0.53} \times 10^{18}$	$>6 \times 10^{16}$	$>9.2 \times 10^{16}$	$2.7^{+0.5}_{-0.4} \times 10^{19}$	2.0×10^{24}
	$11.5^{+3.0}_{-2.0} \times 10^{18}$			$2.6^{+0.9}_{-0.5} \times 10^{19}$	$7.7^{+0.4}_{-0.4} \times 10^{24}$
	$9.5^{+0.4}_{-0.4} \times 10^{19}$			$3.6^{+0.35}_{-0.35} \times 10^{19}$	
	$7.6^{+2.2}_{-1.4} \times 10^{18}$				

the SSD approach both with ($t_{1/2}^{*(2\nu)}$) and without ($t_{1/2}^{(2\nu)}$) the factorization of the nuclear matrix element and the integration over the phase space are listed in the table, along with associated parameters. We note that μ_{m_0} takes approximately the same value for all nuclear systems studied here. An exact consideration of the factors K_{m_0} and L_{m_0} is then expected to be important for 2νββ-decay nuclei with large $Q_{\beta\beta}$ values ($Q_{\beta\beta}/2 \approx \mu_{m_0}$). From the data in the table, we can see that an exact consideration of K_{m_0} and L_{m_0} reduces the theoretical half-life and that the largest effect is found for ^{100}Mo and ^{116}Cd isotopes with the largest $Q_{\beta\beta}$ value and is about 25 and 15% $\left(\Delta = \left|t_{1/2}^{*(2\nu)} - t_{1/2}^{(2\nu)}\right|/t_{1/2}^{(2\nu)}\right)$, respectively. By comparing the experimental half-lives [4, 10] with the theoretical values, we conclude that the mechanism based on the SSD hypothesis allows one to get reasonable estimates for the 2νββ-decay rate. In order to decide whether the SSD hypothesis is realized through a true dominance of the first intermediate 1^+ state or through cancellations of the contributions of higher lying 1^+ states of the intermediate nucleus, further theoretical and experimental studies are necessary. It is expected that the study of the energy and angular distributions of the outgoing electrons will be helpful in this respect. Such calculations are now in progress.

ACKNOWLEDGMENTS

The authors are grateful to Yu.V. Gaponov, L.V. Inzhechik, and V.I. Tretyak for stimulating discussions.

This work was supported by the Russian Foundation for Basic Research (project no. 98-02-17689) and the Grant Agency of the Czech Republic (grant no. 202/98/1216).

REFERENCES

1. M. Doi, T. Kotani, and E. Takasugi, Prog. Theor. Phys. Suppl. **83**, 1 (1985).

2. M. Doi and T. Kotani, Prog. Theor. Phys. **87**, 1207 (1992).
3. J. Suhonen and O. Civatarese, Phys. Rep. **300**, 123 (1998).
4. A. Faessler and F. Šimkovic, J. Phys. G **24**, 2139 (1998).
5. A. García *et al.*, Phys. Rev. C **47**, 2910 (1993); M. Bhattacharya *et al.*, Phys. Rev. C **58**, 1247 (1998).
6. O. Civatarese and J. Suhonen, Phys. Rev. C **58**, 1535 (1998); Nucl. Phys. A **653**, 321 (1999).
7. S. V. Semenov, Yu. V. Gaponov, and R. U. Khafizov, Yad. Fiz. **61**, 1379 (1998) [Phys. At. Nucl. **61**, 1277 (1998)]; L. V. Inzhechik, Yu. V. Gaponov, and S. V. Semenov, Yad. Fiz. **61**, 1384 (1998) [Phys. At. Nucl. **61**, 1282 (1998)].
8. K. Grotz and H. V. Klapdor-Kleingrothaus, *The Weak Interactions in Nuclear, Particle, and Astrophysics* (Adam Hilger, New York, 1990).
9. I. S. Gradshteyn and I. M. Ryzhik, *Table of Integrals, Series, and Products* (Nauka, Moscow, 1971, 5th ed.; Academic, New York, 1980, 4th ed.).
10. V. I. Tretyak and Yu. G. Zdesenko, At. Data Nucl. Data Tables **61**, 44 (1995).

Physics of Atomic Nuclei, Vol. 63, No. 7, 2000, pp. 1200–1205. From Yadernaya Fizika, Vol. 63, No. 7, 2000, pp. 1274–1279.

NEW PHYSICS, NUCLEAR AND NUCLEON STRUCTURE IN RARE PROCESSES

Possible Contribution of an Intermediate-Leptoquark-Boson Mechanism to Free-Neutron Beta Decay*

Yu. V. Gaponov**

Russian Research Centre Kurchatov Institute, pl. Kurchatova 1, Moscow, 123182 Russia

Abstract—A possible mechanism of the virtual intermediate-scalar-leptoquark-boson exchange associated with the contribution of right-handed nucleon currents to free-neutron beta decay is demonstrated. The hypothesis can be extended by considering the realization of the same mechanism in beta decay via the emission of right-handed neutrinos (left-handed antineutrinos). It is shown that a hypothesis of this kind leads to the appearance of scalar and tensor terms in the effective Hamiltonian of weak interaction and that these terms include the right-handed neutrinos. Relevant experimental data are discussed. © *2000 MAIK "Nauka/Interperiodica".*

Experimental investigation of free-neutron beta decay, one of the most accurate experiments in the physics of weak interaction, attracts much attention (for an overview, see, for example, [1–3]). Advances in experimental techniques allow the neutron lifetime and the correlation parameters to be considerably improved [4–6]. As the result of modern experiments, the effective low-energy Hamiltonian of nucleon–lepton weak interaction, which describes neutron beta decay, has the form

$$H_{\text{eff}} = (G_{V\beta}/\sqrt{2})(\overline{\Psi}_p\gamma_\mu(1-\lambda\gamma_5)\Psi_n) \times (\overline{\Psi}_e\gamma^\mu(1+\gamma_5)\Psi_{\nu e}). \quad (1)$$

It depends on two main constants:

$$\lambda = -1.2659(19),$$
$$G_{V\beta} = 1.4183(18)\times 10^{-62}\ \text{J m}^3. \quad (2)$$

These constants are usually extracted from two independent measurements of the neutron lifetime and the neutron spin–electron correlation. The second constant can be compared with a similar value that is extracted from data on the nuclear 0^+–0^+ beta transition

$$G_{V\ 0-0} = 1.4173(11)\times 10^{-62}\ \text{J m}^3 \quad (3)$$

and which follows from the latest analysis Towner [7]. This leads to the element $V_{ud} = 0.9740(5)$ of the Kobayashi–Maskawa matrix, which results in a small deviation of the sum rule for V_{ud}, V_{us}, and V_{ub},

$$V_{ud}^2 + V_{us}^2 + V_{ub}^2 = 0.9968(14), \quad (4)$$

from unity predicted in the Standard Model.

Previously, any search for effects beyond the Standard Model in free-neutron beta decay was mostly associated with a possible contribution of the right-handed lepton currents (right-handed neutrinos) to the standard $V-A$ version of the weak-interaction Hamiltonian [8, 9]. They were stimulated by the discrepancies between the experimental values of $G_{V\ 0-0}$ and $G_{V\beta}$ that existed for some years (the so-called "experimental neutron anomaly" [8]). However, modern experimental results on the neutron lifetime [4], the electron–spin correlation parameter [6, 10–12], and the neutrino–spin correlations [13, 14] changed substantially previous data by diminishing the limit on the expected contributions of right-handed current [6, 13, 14].

Moreover, the possibility of small (a few percent) additional contributions of the scalar (S) or tensor (T) "exotic" terms (or both) to the effective nucleon–lepton Hamiltonian was repeatedly discussed in the literature [2, 15–26]. It is useful to stress that the existing data restrict severely the possible contribution of these terms when the left-handed neutrinos take part in the process. However, the experimental constraint on these terms is relaxed significantly when the right-handed neutrinos contribute [15, 17, 19]. These contributions, which, from the physical point of view, can be compared with leptoquark interactions, have already been investigated in nuclear beta transitions or muon captures [18–26]. However, the experimental status of the contributions remains unclear.

Some months ago, a hypothesis of a new possible mechanism based on leptoquark boson exchange, which can exist in beta decay along with standard W-boson exchange, was proposed in [27]. The mechanism is a consequence of the alternative interpretation of the nucleon right-handed-current term of the effective nucleon–lepton weak interaction Hamiltonian, which can be recast by using the well-known Fierz transformation into a new form that can be interpreted in terms of a leptoquark heavy-boson exchange.

In the present article, it will be demonstrated that such a hypothesis does not contradict contemporary experimental data. Together with definite additional assumptions, it can lead to the appearance of some con-

* This article was submitted by the author in English.

** e-mail: gaponov@imp.kiae.ru

1063-7788/00/6307-1200$20.00

tributions to the effective Hamiltonian (1), which are equivalent to the scalar, pseudoscalar, and tensor terms of the weak interaction. While in [27] one could observe a proximity between the theoretical and experimental data on scalar and tensor terms, now, after more comprehensive analysis of the experimental data (performed by the author of [6]), the new results lead, however, to a contradiction between the data, which will be discussed below. In my opinion, the new situation is even more interesting than the previous. It pushes us to seek either new experimental check of the previous data on electron–neutrino correlation or new theoretical interpretations of the results. Therefore, it would be very useful to discuss these results.

In order to introduce the first leptoquark hypothesis, we transform the effective Hamiltonian (1) into a form where the left-handed and right-handed parts of the nucleon current appear separately. Note that, in describing the left- and right-handed nucleon states, it is more accurate to use the term "chirality" because the simple connection between the chirality and the left- and right-handed terms exists only for zero-mass particles. However, I will use the left- and right-handed terms, considering that all particles in the Standard Model are massless prior to spontaneous symmetry breaking. The aforementioned transformation leads to the Hamiltonian

$$H_{\text{eff}} = (G_{V\beta}/\sqrt{2})C[\alpha(\overline{\Psi}_p\gamma_\mu(1+\gamma_5)\Psi_n) + \beta(\overline{\Psi}_p\gamma_\mu(1-\gamma_5)\Psi_n)](\overline{\Psi}_e\gamma^\mu(1+\gamma_5)\Psi_{\nu e}). \quad (5)$$

The numerical values of the constants are ($\alpha^2 + \beta^2 = 1$)

$$C = \sqrt{1+\lambda^2} = 1.1407(11), \quad \alpha = 0.9932(18), \quad \beta = -0.1165(10). \quad (6)$$

The values of α and β fix the relative contribution of the left- and right-handed nucleon currents to the process of free-neutron decay, and C is a normalization factor. As can be seen from this form, the main contribution to neutron beta decay comes from the transition of the left-handed neutron to the left-handed proton. In the Standard Model, which holds the left weak-isospin doublets of leptons and quarks, the contribution can be naturally interpreted by considering the nucleon as a system of three left- and right-handed u and d quarks. In the case of the left-handed neutron, the left-handed d_L quark taking part in the interaction can either form a neutral-chiral pair together with a passive right-handed d_R or u_R quark or remain unpaired. The same is true for the left-handed proton state:

$$\Psi_{nL} = A(d_Rd_L)u'_L + B(u_Rd_L)d'_L + C(u'_Ld_R)d_L + D(u_Rd'_L)d_L;$$
$$\Psi_{pL} = A(d_Ru_L)u'_L + B(u_Ru_L)d'_L + C(u'_Ld_R)u_L + D(u_Rd'_L)u_L. \quad (7)$$

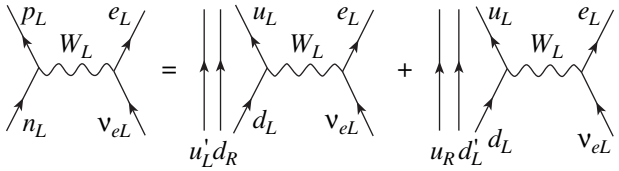

Fig. 1. Transition of a left-handed neutron into a left-handed proton in the Standard Model of free-neutron beta decay.

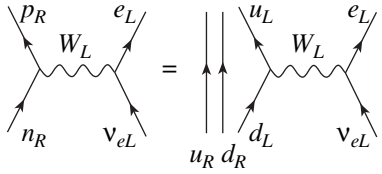

Fig. 2. Transition of a right-handed neutron into a right-handed proton in the Standard Model of neutron beta decay.

In the beta-decay process, the transformation of the active d_L quark into a u_L quark occurs without any change in the dynamical quark structure of the nucleon. In the Standard Model, the contribution of such a process can be described by the well-known Feynman diagram in Fig. 1.

Let us analyze the second term in (5). In the modern description of weak interaction, this term is interpreted as the transition of the left-handed d_L quark into the left-handed u_L quark with the emission of an intermediate W_L boson in perfect analogy with the first term (Fig. 2). In this case, the structure of the right-handed nucleons is as follows:

$$\Psi_{nR} = A'(d_Rd_L)u_R + B'(u_Rd_L)d_R,$$
$$\Psi_{pR} = A'(d_Ru_L)u_R + B'(u_Ru_L)d_R. \quad (8)$$

However, an alternative interpretation of this term is based on virtual intermediate-leptoquark-boson exchange [27]. It is clear that such a hypothesis means a step aside from the Standard Model.

Let us investigate the new physical hypothesis in detail. With the aid of the well-known Fierz transformation, the right-handed nucleon current can be represented in the form

$$\beta(\overline{\Psi}_p\gamma_\mu(1-\gamma_5)\Psi_n)(\overline{\Psi}_e\gamma^\mu(1+\gamma_5)\Psi_{\nu e}) = -2\beta(\overline{\Psi}_e(1-\gamma_5)\Psi_n)(\overline{\Psi}_p(1+\gamma_5)\Psi_{\nu e}) \quad (9)$$

(the opposite sign is associated with the transposition of the proton and the electron operators). By assuming the existence of the hypothetical heavy leptoquark (LQ) boson, one can interpret the term in terms of the diagram in Fig. 3. Note that the operation in (9), which recasts the term into the scalar–pseudoscalar form, is permitted for the right-handed nucleon current of (5) only owing to the invariance of the left-handed vector current under the Fierz transformation. In the case of

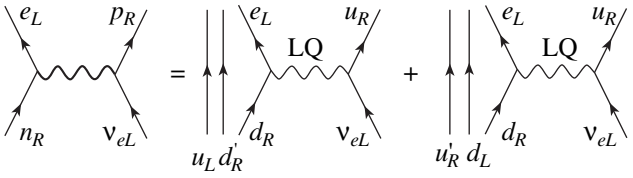

Fig. 3. Transition of a right-handed neutron into a right-handed proton in free-neutron beta decay within the new leptoquark mechanism of the decay process.

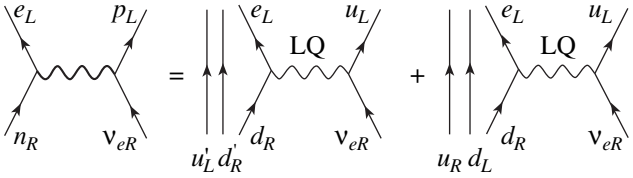

Fig. 4. New mechanism of neutron beta decay through a scalar leptoquark boson in the transition of a right-handed neutron into a left-handed proton with the result that scalar, pseudoscalar, and tensor terms with the emission of a right-handed neutrino appear in the effective weak-interaction lepton–nucleon Hamiltonian.

the right-handed nucleons, the active right-handed d_R quark taking part in the weak interaction can either form a neutral-chiral pair together with a left-handed passive u_L or d_L quark or remain unpaired:

$$\begin{aligned}\Psi_{nR} &= A''(d_R d_L)u'_R + B''(u_L d_R)d'_R \\ &+ C''(u'_R d_L)d_R + D''(u_L d'_R)d_R, \\ \Psi_{pR} &= A''(u_R d_L)u'_R + B''(u_L u_R)d'_R \\ &+ C''(u'_R d_L)u_R + D''(u_L d'_R)u_R.\end{aligned} \tag{10}$$

In this new interpretation, the LQ boson is a scalar particle, which has the electric charge of –2/3, zero color charge, and zero leptoquark quantum number ($N_L + N_Q = 0$). Because of a low momentum transfer in the process of LQ interaction (for intermediate bosons of large mass), the contribution of such a diagram will be determined by the LQ-interaction constant g_{LQ} and the boson mass M_{LQ}; that is,

$$-(G_{V\beta}/\sqrt{2})\cdot 2C\beta = N(g_{\mathrm{LQ}}^2/8M_{\mathrm{LQ}}^2), \tag{11}$$

where N is the characteristic constant of a specific theoretical model of LQ interaction. With fixed g_{LQ}, one can extract the LQ-boson mass from (11). The concept of the LQ boson ion is now used in some modern theoretical models generalizing the Standard Model based on $SU(3)_c \times SU(2)_L \times U(1)$ symmetry (see, for example, [18–20] and references therein). Comparing the experimental contribution of the LQ bosons and the W boson, one can obtain, however, the following estimate of the ratio β/α:

$$-2\beta/\alpha = N(g_{\mathrm{LQ}}^2/e^2)(M_W^2/M_{\mathrm{LQ}}^2) \approx 0.22. \tag{12}$$

Assuming the universality of the strength of the W-boson and LQ-boson interaction ($g_{\mathrm{LQ}}^2 = e^2$), one can estimate the LQ mass with an accuracy determined by the model constant N:

$$M_{\mathrm{LQ}} \approx 3M_W\sqrt{N/2} \approx 240\sqrt{N/2}\ (\mathrm{GeV}). \tag{13}$$

Within this hypothesis, the expected mass of the LQ boson is therefore about a few hundred GeV. The estimate in (13) for $N \geq 2$ does not contradict the restriction boundary for the similar bosons that follows from the latest experimental results obtained at HERA (>200–250 GeV) [28–30].

It is useful to compare the above scheme with others from the literature. As was demonstrated in [19], the most general form of the additional contribution from the scalar LQ boson to the effective weak-interaction Hamiltonian is as follows:

$$\begin{aligned}\Delta H &= \lambda_S^L \overline{u_R}\begin{pmatrix}e_L\\ \nu_L\end{pmatrix}S^+ + \lambda_S^{'L}\overline{d_R}\begin{pmatrix}e_L\\ \nu_L\end{pmatrix}S'^+ \\ &+ \lambda_S^R\overline{\begin{pmatrix}u_L\\ d_L\end{pmatrix}}i\tau_2 e_R S^+ + \lambda_S^{'R}\overline{\begin{pmatrix}u_L\\ d_L\end{pmatrix}}i\tau_2\nu_R S'^+.\end{aligned} \tag{14}$$

Comparing it with the above hypothesis, one can see that, in the scheme under discussion, the LQ bosons S and S' with a charge of –2/3, both being weak charge doublets, are the same particles. It is also important that only the first two terms in the general form exist in this scheme because both the right-handed electron and the neutrino are not included in the effective weak-interaction Hamiltonian (1). Thus, one can extract extra relations that reduce the general form (14):

$$(\lambda_S^L)^2 \approx e^2, \quad (\lambda_S^{'L}) \approx N(\lambda_S^L), \quad (\lambda_S^{'R}) = (\lambda_S^R) = 0. \tag{15}$$

The proposed hypothesis of an additional mechanism of free-neutron beta decay through an intermediate scalar LQ boson allows a new approach to the problem of the possible existence of small contributions of the scalar or tensor terms (or both) to the effective weak-interaction Hamiltonian. As was mentioned above, their existence at a level of a few percent is possible from the experimental point of view when right-handed neutrinos (not the standard left-handed ones!) take part in the process [15–17]. From the theoretical point of view, such a extension can be associated with the general form of the scalar LQ-boson Hamiltonian (14), where the strength $(\lambda_S^{'R})$ is nonzero. This extension of the standard scheme seems to be a very natural next step beyond the Standard Model.

Let us assume that these processes occur with the virtual exchange of the scalar LQ boson, right-handed neutrinos, and right-handed neutrons (Fig. 4). The existence of the mechanism should imply that, in addition to the LQ doublets of the $\begin{pmatrix} e_L \\ d_R \end{pmatrix}$ and $\begin{pmatrix} \nu_{eL} \\ u_R \end{pmatrix}$ types, which correspond to the previous mechanism (Fig. 3), the introduction of a new one of the $\begin{pmatrix} \nu_{eR} \\ u_L \end{pmatrix}$ type is necessary. If this is associated with the same scalar LQ boson with a charge of –2/3, the following additional contribution to Hamiltonian (1) appears:

$$(G_{V\beta}/\sqrt{2})C\gamma(\overline{\Psi}_e(1-\gamma_5)\Psi_n)(\overline{\Psi}_p(1-\gamma_5)\Psi_{\nu e}). \quad (16)$$

Here, γ is a new constant defined by the relations

$$\begin{aligned}(G_{V\beta}/\sqrt{2})C\gamma &\approx N''(g_{\mathrm{LQ}}g'_{\mathrm{LQ}}/(8M^2_{\mathrm{LQ}})) \\ &\approx N'(g^2_{\mathrm{LQ}}/8M^2_{\mathrm{LQ}}).\end{aligned} \quad (17)$$

By using the inverse Fierz transformation, one can find that expression (16) is equivalent to the contribution of the additional scalar, pseudoscalar, and tensor terms to the standard effective Hamiltonian (1). It describes the transitions of right-handed neutrons into left-handed protons with the emission of left-handed electrons and left-handed antineutrinos (antiparticles to right-handed neutrinos) and an LQ boson. The term has the form

$$\begin{aligned}&\gamma(\overline{\Psi}_e(1-\gamma_5)\Psi_n)(\overline{\Psi}_p(1-\gamma_5)\Psi_{\nu e}) \\ &= -(\gamma/2)[(\overline{\Psi}_p(1-\gamma_5)\Psi_n)(\overline{\Psi}_e(1-\gamma_5)\Psi_{\nu e}) \\ &\quad + (\overline{\Psi}_p\sigma_{\mu\nu}\Psi_n)(\overline{\Psi}_e\sigma^{\mu\nu}(1-\gamma_5)\Psi_{\nu e})].\end{aligned} \quad (18)$$

The expected value of the new contribution can be evaluated qualitatively at least with the already known parameter β:

$$\begin{aligned}-(G_{V\beta}/\sqrt{2})C\gamma/2 &\approx -N'(g^2_{\mathrm{LQ}}/8M^2_{\mathrm{LQ}}) \\ &= -(G_{V\beta}/\sqrt{2})C\beta(N'/N), \\ \gamma &\approx 2\beta(N'/N) \approx -0.22(N'/N).\end{aligned} \quad (19)$$

Thus, the hypothesis of the additional contribution of the mechanism employing a scalar LQ boson and involving the emission of right-handed neutrinos leads to the appearance of additional scalar (pseudoscalar) and tensor terms in the effective Hamiltonian (1). The new Hamiltonian has the form

$$\begin{aligned}H_{\mathrm{eff}} &= (G_{V\beta}/\sqrt{2})C'\{[\alpha(\overline{\Psi}_p\gamma_\mu(1+\gamma_5)\Psi_n) \\ &+ \beta(\overline{\Psi}_p\gamma_\mu(1-\gamma_5)\Psi_n)](\overline{\Psi}_e\gamma^\mu(1+\gamma_5)\Psi_{\nu e}) \\ &- (\gamma/2)[(\overline{\Psi}_p(1-\gamma_5)\Psi_n)(\overline{\Psi}_e(1-\gamma_5)\Psi_{\nu e}) \\ &- (\delta/2)(\overline{\Psi}_p\sigma_{\mu\nu}\Psi_n)(\overline{\Psi}_e\sigma^{\mu\nu}(1-\gamma_5)\Psi_{\nu e})\} \\ &= (G_{V\beta}/\sqrt{2})C'/C\{(\overline{\Psi}_p\gamma_\mu(1-\lambda\gamma_5)\Psi_n) \\ &\times(\overline{\Psi}_e\gamma^\mu(1+\gamma_5)\Psi_{\nu e}) - (\gamma/2)C(\overline{\Psi}_p(1-\gamma_5)\Psi_n) \\ &\times(\overline{\Psi}_e(1-\gamma_5)\Psi_{\nu e}) - (\delta/2)C(\overline{\Psi}_p\sigma_{\mu\nu}\Psi_n) \\ &\times(\overline{\Psi}_e\sigma^{\mu\nu}(1-\gamma_5)\Psi_{\nu e})\}.\end{aligned} \quad (20)$$

Here, γ is defined by relation (19), and δ is a new constant that must be close to γ ($\delta \approx \gamma$) in accordance with (18). However, it can generally differ from γ. The parameter C' is the changed normalization factor, which is defined by the condition

$$\begin{aligned}C^2(\alpha^2+\beta^2) &= C^2 = C'^2(\alpha^2+\beta^2+\gamma^2/4+\delta^2/4) \\ &= C'^2(1+\gamma^2/4+\delta^2/4).\end{aligned} \quad (21)$$

The possible contribution of the scalar and tensor terms to the Hamiltonian of beta decay for the neutron and nuclei was investigated experimentally in [6, 17–26]. In particular, Yerozolimsky [6] performed such an analysis for the contribution with the emission of right-handed neutrinos in free-neutron beta decay (this analysis was repeated and verified in [31]). He constructed the allowed regions of the relative contributions for the scalar (C_S/C_V) and tensor (C_T/C_A) that are allowed when the experimental data vary inside one standard deviation. This analysis employed the results of a global treatment of modern lifetime measurements and three correlation measurements (electron–neutron spin, neutrino–neutron spin, and electron–neutrino momenta). By assuming that the left-handed neutrinos contribute to the *V* and *A* terms of the effective Hamiltonian and that the right-handed neutrinos contribute to the *S* and *T* terms, these four experimental characteristics enabled a determination of the region of the allowed values [6] (see also [31]). In the analysis, the theoretical formulas from [7] were used. The probability distribution of the relative contributions of the *S* and *T* term inside this region has a nearly Gaussian form having a maximum around the points with coordinates $C_S/C_V = -0.055$ and $C_T/C_A = -0.066$ and the mean widths of 0.05 and 0.022, respectively. Assuming that the maximal values of C_S/C_V and C_T/C_A are in accord with the experimental mean values and that the widths determine the standard experimental error in the values, one can estimate γ and δ as follows:

$$\begin{aligned}-\gamma C/2 \approx C_S/C_V \approx -\beta C(N/N') \approx -0.055(50), \\ \gamma \approx 0.10(10), \\ -(\delta/2)(C/\gamma) \approx C_T/C_A \approx -0.066(22), \quad \delta \approx -0.15(5).\end{aligned} \quad (22)$$

Note that the values within the 3σ band include the origin of coordinates, so that the Standard Model is not excluded by the experimental analysis. By comparing

the first relation with the results presented in (19), one can estimate for N/N' as

$$N'/N \approx -1/2, \quad (N''g'_{\mathrm{LQ}})/(Ng_{\mathrm{LQ}}) \approx -1/2, \quad \gamma \approx -\beta. \tag{23}$$

This result can be interpreted by assuming that the constant of LQ-boson coupling to left-handed multiplets is twice as large as the constant of LQ-boson coupling to a right-handed multiplet and has an opposite sign. The relative contribution of the γ term to the full process is one-half as large as the contribution of the β term of the right-handed nucleon current. However, the experimental analysis leads to the crude equation $\gamma \approx -\delta$, in contradiction to (18).

Thus, it turns out that modern experimental data do not rule out existence of the additional contributions of scalar and tensor terms with the right-handed neutrino to the effective weak-interaction Hamiltonian. However, their interpretation in terms of the exchange of scalar LQ bosons leads to a contradiction because, in that interpretation, the relative sign of the experimental parameters γ and δ should be opposite to the results of the experimental analysis. This means that it is necessary either to conduct new experiments to improve experimental data (moreover, the modern data have great experimental errors and can change considerably upon future measurements) or to revise the theoretical model. The latter could be realized, for example, by introducing an additional intermediate tensorlike LQ boson, together with a scalar one. Alternatively, one can use another LQ model where the scalar leptoquark boson is of the Higgs boson type but not a gauge boson, as was supposed in the above constructions. Such a model was developed, for example, in [32] and will be analyzed additionally elsewhere. In any case, it is clear now that the conclusion concerning the second mechanism of LQ exchange with the emission of right-handed neutrinos requires additional experimental verification due to the estimations of the *S* and *T* contributions first of all.

Moreover, assuming that the general form of the effective nucleon–lepton weak-interaction Hamiltonian has the form (20) with γ and δ from (22), one must evaluate *C* by the equation

$$C'^2 = C^2(1 - \gamma^2/4 - \delta^2/4) \approx 0.992(5) \times C^2. \tag{24}$$

By virtue of this equation, the hypothesis under consideration leads to a slight effective reduction of the experimental constant $G^2_{V\beta}$. In the case of 0^+–0^+ transitions, it is even smaller because the tensor contribution is excluded. Therefore, the square of the matrix element V_{ud} of the Kobayashi–Maskawa matrix also decreases, which qualitatively agrees with the observed deviation in the sum rule (4). Thus, the result of Towner [7] can be associated with the appearance of the additional scalar term in the effective Hamiltonian. If the result of Towner is supported by new experiments, it will be possible to interpret the fact as an indirect argument in favor of the hypothesis discussed above.

It is obvious that, if the scalar and tensor terms with the right-handed-neutrino contribution to the effective Hamiltonian does exist, then they should manifest themselves in precision correlation experiments. A dedicated analysis shows that a consideration of these terms has to influence maximally the parameter of the electron–neutrino correlation both in free-neutron beta decay and in the allowed beta transitions of nuclei (see, for example, the review article of the present author [15]). Unfortunately, the current accuracy of the data from electron–neutrino correlation experiments is insufficient for an ultimate conclusion about the existence or the absence of the terms discussed in the effective Hamiltonian. The arrangement of new precise experiments aimed at verifying the hypothesis of the leptoquark mechanism in weak interaction is highly desirable. However, it is necessary to stress that the absence of the scalar and tensor contributions to the effective Hamiltonian does not disprove the whole hypothesis, but this only casts some doubt on the wider version of the hypothesis, that which includes the leptoquark doublet with the right-handed neutrino. The interpretation of the right-handed nucleon current (9) in terms of the LQ-boson exchange can be preserved independently of the additional scalar–tensor contribution.

ACKNOWLEDGMENTS

I am indebted to B.G. Yerozolimsky and Yu.A. Mostovoĭ for stimulating discussions on the possible scalar–tensor contributions to free-neutron decay. I am also grateful to J. Deutsch and J. Govard, who informed me about their publications and useful references. I would also like to thank the organizers of NANP'99 for the invitation to the this conference and especially Dr. S.G. Kovalenko, who helped me in seeking the latest literature on leptoquarks.

This work was supported by the Russian Foundation for Basic Research (project no. 98-02-17706).

REFERENCES

1. K. Schreckenbach and W. Mampe, J. Phys. G **18**, 1 (1992).
2. J. Deutsch and P. Quin, *Precision Tests of the Standard Electroweak Model* (World Sci., Singapore, 1993), p. 706.
3. Yu. A. Mostovoĭ *et al.*, Usp. Fiz. Nauk **166**, 987 (1996) [Phys. Usp. **39**, 925 (1996)].
4. S. Arzumanov *et al.*, in *Proceedings of ISINN-5, Dubna, 1997*, p. 53.
5. Yu. A. Mostovoy, Preprint No. 6040/2, IAE (Kurchatov Institute of Atomic Energy, Moscow, 1997).
6. B. G. Yerozolimsky, in *Proceedings of the International Workshop on Particle Physics with Slow Neutrons, ILL, Grenoble, France, 1998*; Nucl. Instrum. Methods A (2000) (in press).

7. I. S. Towner and J. C. Hardy, in *Proceedings of the International Conference WEIN-98, Santa Fe, USA* (World Sci., Singapore, 1999), p. 338.
8. Yu. V. Gaponov, P. E. Spivak, and N. B. Shulgina, Yad. Fiz. **52**, 1653 (1990) [Sov. J. Nucl. Phys. **52**, 1042 (1990)]; Phys. Lett. B **253**, 283 (1991).
9. A. S. Carnoy *et al.*, Phys. Rev. Lett. **65**, 3249 (1990); J. Phys. G **18**, 823 (1992).
10. B. G. Yerozolimsky *et al.*, Phys. Lett. B **412**, 240 (1997).
11. K. P. Schreckenbach *et al.*, Phys. Lett. B **349**, 427 (1995).
12. H. Abele *et al.*, Phys. Lett. B **407**, 202 (1997).
13. I. A. Kuznetzov *et al.*, Phys. Rev. Lett. **75**, 794 (1995).
14. A. P. Serebrov *et al.*, Zh. Éksp. Teor. Fiz. **113**, 1963 (1998) [JETP **86**, 1074 (1998)].
15. Yu. V. Gaponov, Usp. Fiz. Nauk **102**, 211 (1970) [Sov. Phys. Usp. **13**, 647 (1970)].
16. Yu. A. Mostovoĭ and A. I. Frank, Pis'ma Zh. Éksp. Teor. Fiz. **24**, 43 (1976) [JETP Lett. **24**, 38 (1976)].
17. B. G. Erozolimskiĭ and Yu. A. Mostovoĭ, Yad. Fiz. **53**, 418 (1991) [Sov. J. Nucl. Phys. **53**, 260 (1991)].
18. P. Herczeg, in *Proceedings of the International Conference WEIN-92, 1992* (World Sci., Singapore, 1992), p. 87.
19. R. N. Mohapatra *et al.*, Phys. Lett. B **145**, 433 (1984); W. Buchmüller *et al.*, Phys. Lett. B **191**, 442 (1987); S. Davidson *et al.*, Z. Phys. C **61**, 613 (1994); M. Leurer, Phys. Rev. D **50**, 536 (1994); J. L. Hewett, in *Proceedings of the Summer Study on High Energy Physics, Snowmass, 1991* (World Sci., Singapore, 1991).
20. P. Herczeg, *Precision Tests of the Standard Electroweak Model* (World Sci., Singapore, 1993), p. 786.
21. P. Quin, J. Deutsch, *et al.*, in *Proceedings of the 14th International Conference on Particles and Nuclei, Williamsburg, 1996*, p. 555.
22. J. Govaerts, in *Proceedings of the International European Conference on High Energy Physics, Jerusalem, 1997*.
23. P. Quin and T. A. Girard, Phys. Lett. B **229**, 29 (1989).
24. M. Allet *et al.*, Phys. Lett. B **383**, 139 (1996).
25. N. Severijns *et al.*, Phys. Rev. Lett. **70**, 4047 (1993); Erratum: **73**, 611 (1994).
26. J. Govaerts, Nucl. Instrum. Methods A **402**, 303 (1998).
27. Yu. V. Gaponov, Yad. Fiz. **62**, 1281 (1999) [Phys. At. Nucl. **62**, 1206 (1999)].
28. H1 Collab. (C. Adolff *et al.*), Preprint No. DESY 97-025, DESY (Hamburg, 1997).
29. G. Caso *et al.*, Eur. Phys. J. C **3**, 1 (1998).
30. H1 Collab. (P. Bruel *et al.*), in *Proceedings of Rencontres de Moriond: Electroweak Interaction and Unified Theory, Les Acrs, France, 1998.*
31. Yu. A. Mostovoĭ, Yu. A. Gaponov, and B. G. Yerozolimsky, Yad. Fiz. **63**, 1268 (2000) [Phys. At. Nucl. **63,** 1193 (2000)].
32. A. D. Smirnov, Yad. Fiz. **58**, 2252 (1995) [Phys. At. Nucl. **58**, 2137 (1995)]; Phys. Lett. B **346**, 297 (1995); **431**, 119 (1998).

Physics of Atomic Nuclei, Vol. 63, No. 7, 2000, pp. 1206–1209. From Yadernaya Fizika, Vol. 63, No. 7, 2000, pp. 1280–1283.

NEW PHYSICS, NUCLEAR AND NUCLEON STRUCTURE IN RARE PROCESSES

Real and Virtual Radiative Processes in the Beta Decay of the Free Neutron*

R. U. Khafizov and Yu. V. Gaponov*****

Russian Research Centre Kurchatov Institute, pl. Kurchatova 1, Moscow, 123182 Russia

Abstract—Theoretical investigation of as-yet-unobserved radiative neutron decay is performed. Experimental searches for this decay allow one to test directly part of radiative corrections whose contribution is presently estimated at 1.5% of the total probability of neutron beta decay. Descriptions of the neutron radiative decay and nuclear radiative beta decay are compared. The results of the theoretical evaluations of the radiative corrections given in the literature are discussed. © *2000 MAIK "Nauka/Interperiodica".*

It is well known that the decay of any elementary particle with charged particles in the final state has a rare decay branch—a radiative decay mode. This study aims at analyzing the radiative decay of the free neutron. As we can see from the Review of Particle Properties [1], there are no measurements of the branching ratio (Br) for this decay. On the other hand, this rare branch of decay is well investigated experimentally for other elementary particles.

An important question that can be solved by experimental research of the radiative neutron decay is the problem of radiative corrections to the neutron lifetime and correlation coefficients. Some part of these corrections can be estimated directly from the experiment studying the radiative decay of the free neutron.

The matrix element M of the radiative beta decay consists of two terms [2]; that is,

$$M = \frac{eg_V}{\sqrt{2}}\Big[\bar{u}_e\frac{2(p_e e)+\hat{e}\hat{K}}{2(p_e K)}\gamma_\rho(1+\gamma_5)u_\nu\bar{u}_p\gamma_\rho(1+\lambda\gamma_5)u_n$$

$$-\bar{u}_e\gamma_\rho(1+\gamma_5)u_\nu\bar{u}_p\frac{2(p_p e)+\hat{e}\hat{K}}{2(p_p K)}\gamma_\rho(1+\lambda\gamma_5)u_n\Big],$$

where $p_e(E_e, \mathbf{p}_e)$, $K(K, \mathbf{K})$, $p_\nu(E_\nu, \mathbf{p}_\nu)$, and $p_p(E_p, \mathbf{p}_p)$ are the 4-momenta of the electron, photon, neutrino, and proton, respectively, while e is the photon polarization. The first term describes photon emission from the electron, while the second term describes photon emission from the proton. Either term involves an infrared divergence, but this divergence will be canceled if photon-exchange diagrams are taken into account,. This cancellation was demonstrated by Sirlin [3] and Geshkenbeĭn and Popov [4], who used a Ward identity for this purpose. In contrast to ordinary muon decay, g_V is not equal here to g_A. Owing to photon exchange, the total radiative corrections therefore also depend on the ultraviolet cutoff parameter Λ. In the first order of perturbation theory, however, the radiative-beta-decay process does not depend on this parameter. In the radiative beta decay of the neutron, one can therefore measure only some part of these corrections, which is associated with the so-called outer radiative corrections.

After standard calculations, the differential cross section can be reduced to a form involving two terms:

$$\frac{d\Gamma}{dE_e dK} = \frac{1}{8\pi^4}\alpha g_V^2\frac{1}{12}\left(1-\frac{m_p^2}{Q_0^2}\right)^2$$

$$\times\int QdQ\Bigg\{Q_0^2\times 3\left(1+\frac{m_p^2}{Q_0^2}\right)(1+3\lambda^2)$$

$$\times\Bigg[\frac{1}{(p_e K)^2}[m_e^2(E_e+K)-(p_e K)K]+\frac{1}{K}$$

$$+\frac{E_e}{K^2}-\frac{2E_e(E_e+K)}{K(p_e K)}\Bigg]+(1-\lambda^2)\times 2Q_0\left(1+2\frac{m_p^2}{Q_0^2}\right)$$

$$\times\Bigg[\left(\frac{m_e^2}{(p_e K)^2}-\frac{1}{(p_e K)}\right)Q^2$$

$$-\frac{E_e}{(p_e K)K}[2(\mathbf{p}_e\cdot\mathbf{Q})+(\mathbf{K}\cdot\mathbf{Q})]$$

$$+\frac{1}{K^2}(\mathbf{p}_e\cdot\mathbf{Q})+\frac{1}{K}\times 4(Q_0-m_p)\Bigg]\Bigg\}.$$

Here, the momentum $\mathbf{Q} = \mathbf{p}_e + \mathbf{K}$, $Q = |\mathbf{Q}|$, is associated with the total energy $Q_0 = m_n - p_e - K$. The first term is proportional to $1 + 3\lambda^2$ and has a large value. The second term is proportional to $1 - \lambda^2$ and has a value of Q_0/m_N, which is very small. If one wants to investigate γ radiation directly from the weak-interaction vertex,

* This article was submitted by the authors in English.

** e-mail: rash@pretty.mbslab.kiae.ru

*** e-mail: gaponov@imp.kiae.ru

one should retain this small term. For the radiative beta decay of the neutron, one can take only the first term. To calculate the spectrum of electrons from radiative neutron decays, it is necessary to integrate the leading term over the energy of outgoing photons from the upper limit $m - E_e$ to a lower cutoff energy ω. This lower limit ω is the lower experimental cutoff for photons, which one can vary directly in experiments. Finally, one arrives at [5]

$$\frac{d\Gamma}{dE_e} \approx \frac{g_V^2}{2\pi^3}\frac{\alpha}{2\pi}(1+3\lambda^2)\int\limits_{\omega}^{\Delta m - E_e} dK(\Delta m - E_e - K)^2$$

$$\times 2\left[KN + 2E_e(N-\beta) + 2E_e^2\frac{(N-\beta)}{K}\right]$$

$$= \frac{g_V^2}{2\pi^3}\frac{\alpha}{2\pi}(1+3\lambda^2)w_0(E_e)(g_e(\beta)+g_p(\beta));$$

$$g_e(\beta) = \frac{N}{\beta}\frac{(E_{\mathrm{em}}-E_e)^2}{6E_e^2}$$

$$-2\left[\frac{E_{\mathrm{em}}-E_e}{3E_e} - \frac{3}{2} + \ln\frac{E_{\mathrm{em}}-E_e}{\omega}\right],$$

$$g_p(\beta) = 2\left(\frac{2N}{\beta}-1\right)\left[\frac{E_{\mathrm{em}}-E_e}{3E_e} - \frac{3}{2} + \ln\frac{E_{\mathrm{em}}-E_e}{\omega}\right].$$

Upon integration, one can compare these results with the previous ones and, first of all, with the results obtained by Christian and Kühnelt [6]. If we take Sirlin's function for total radiative corrections $g(\beta)$ [3],

$$r(E_e) = (\alpha/2\pi)g(\beta),\ \beta = |p_e|/E_e = v_e/c,$$

$$g(\beta) = 3\ln\frac{\Lambda}{m_e} - \frac{3}{4} + 4\left(\frac{N}{\beta}-1\right)$$

$$\times\left[\frac{E_{\mathrm{em}}-E_e}{3E_e} - \frac{3}{2} + \ln\frac{E_{\mathrm{em}}-E_e}{m_e/2}\right]$$

$$+\frac{4}{\beta}L\left(\frac{2\beta}{1+\beta}\right) + \frac{N}{\beta}$$

$$\times\left[2(1+\beta^2) - 4N + \frac{(E_{\mathrm{em}}-E_e)^2}{6E_e^2}\right],$$

$$N = \frac{1}{2}\ln\frac{1+\beta}{1-\beta},\ L(z) = \int\limits_0^z dt\frac{\ln|1-t|}{t},\ \frac{e^2}{4\pi} = \alpha \approx \frac{1}{137},$$

$$E_{\mathrm{em}} = \Delta - (\Delta^2 - m_e^2)/2m_n,\ \Delta = m_n - m_p,$$

and subtract our result, the rest of Sirlin's function will be identical to Christian and Kühnelt's one [6]. It is the so-called soft-photon approximation [6],

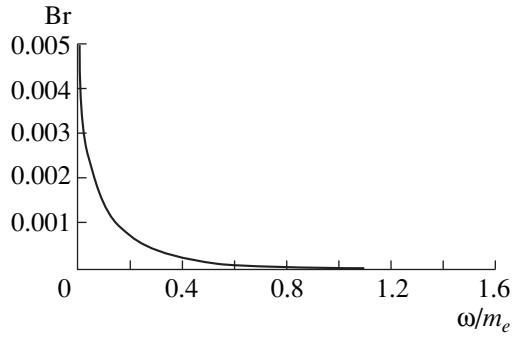

Fig. 1. Expected Standard Model branching ratio of the radiative beta decay of the neutron as a function of ω for the case where photons having energies in excess of the cutoff threshold ω are taken into account.

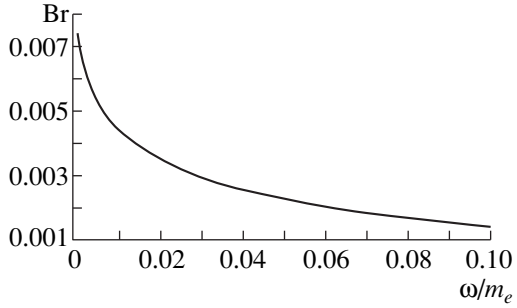

Fig. 2. As in Fig. 1, but for another region of the energy scale.

$$g(\beta,\omega) = 3\log\frac{\Lambda}{m_e} + \frac{4}{\beta}L\left(\frac{2\beta}{1+\beta}\right) - \frac{3}{4}$$

$$+2\frac{N}{\beta}(1+\beta^2-2N) + 4\left(\frac{N}{\beta}-1\right)\log\frac{2\omega}{m_p},$$

where $\Lambda = m_p$ is an ultraviolet cutoff parameter.

Another reference point is the so-called KUB approximation [7]. There are two directions in the problem under consideration. The first direction is connected with the radiative corrections, and the second one is connected with the radiative beta decay of nuclei. These two developed separately, and the KUB approximation is widely used in the field of radiative beta decays of nuclei. In the KUB approximation with the nuclear matrix element equal to $1 + 3\lambda^2$, one obtains the following leading term of the cross section:

$$\frac{d\Gamma}{dE_e dK} \approx \frac{g_V^2}{2\pi^3}\frac{\alpha}{2\pi}(Q_0 - m_p)^2$$

$$\times\left[2KN + 4E_e(N-\beta)\left(\frac{E_e}{K}+1\right)\right]|M|^2,$$

$$|M|^2 = 1 + 3\lambda^2.$$

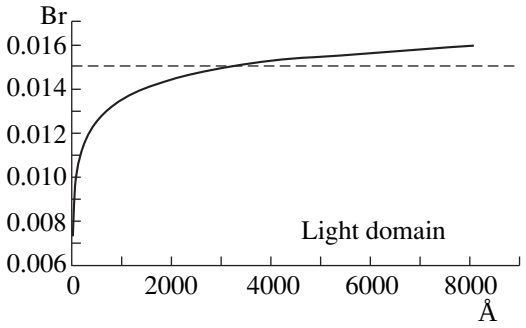

Fig. 3. As in Fig. 1, but for the ultraviolet and light regions (the cutoff threshold ω is indicated in angstroms.

Finally, we can calculate the dependence of the branching ratio for the radiative beta decay of the free neutron on the experimental cutoff parameter. One can see from Fig. 1 that this branching fraction has a large value for experimental cutoff parameter less than 100 keV. Figure 2 shows this region in more detail. Here, it is necessary to mention one experimental study [8], which we consider to be very important. In that study, the electron asymmetry was measured, and the electrons and protons from neutron β decay were recorded by the method of accidental coincidences. Along with the main proton peak, however, the authors of [8] observed a small peak of momentary, or, as they put it, false coincidences. The ratio of the number of false, events to the number of true decays was about 0.001. If one assumes that protons in this experiment were recorded with the aid of microchannel plates, which can also detect photons of very low energies (about 10 keV), and compares the ratio with the calculated branching ratio given in Fig. 2, one can arrive at a conclusion that, with a high probability, this false peak is due to the radiative neutron decays. Of course, this is only a hypothesis, and one should investigate the peak more carefully—for example, by means of a setup in a vacuum chamber with an extra γ detector installed together with proton and electron detectors.

The most interesting region is the so-called light domain. In Fig. 3, the x coordinate is expressed in angstroms, and the boundaries of this domain are indicated by arrows. One can see that the branching ratio for this light domain has a value of 1.09×10^{-3}. However, the main special feature of the light domain is as follows. As was mentioned earlier, the radiative decay of the neutron allows us to test the value of the outer corrections. At present, this correction is calculated with the experimental lifetime values for 0^+–0^+ β transitions of a number of nuclei and the neutron. For all of them, it has already been established with a high accuracy that the total outer radiative correction has the value of 1.5% for the neutron and oxygen and values in the range 1.45–1.42% for other nuclei [9]. The value of the outer radiative correction is shown in Fig. 3 by a dashed line. From a comparison of this line with the branching-ratio curve, it becomes obvious that the light domain is beyond the limits of the total outer correction. This fact renders the research of the light domain particularly important, because an experimental evaluation of the branching ratio in this region will make us reconsider substantially our knowledge of the total outer radiative correction. It will also allow us to obtain deeper insight into the neutron structure. In addition, there are the latest evaluations of the full outer radiative correction, already at a level of 1.2% [10], which renders the investigation of the branching ratio in the ultraviolet and light domains of photon energy especially important.

The radiative beta decay of the neutron also allows us to perform correlation experiments with different angles between the directions of the photon and beta-electron momenta (K and p_e). In terms of the angle θ between these momenta, the formula takes the form

$$\frac{d\Gamma}{dE_e dK d\Omega} = \frac{-\alpha}{4\pi^2}\frac{p_e}{f_0 K} \times \left[\frac{m_e^2(E_e+K)-(E_e-p_e\cos\theta)K^2}{(E_e-p_e\cos\theta)^2} + K + E_e - \frac{2E_e(E_e+K)}{(E_e-p_e\cos\theta)}\right](Q_0-m_p)^2,$$

where

$$f_0 = \int_{m_e}^{Q_0} p_e E_e (Q_0 - E_e)^2 dE_e.$$

It can be seen from this formula that as the angle θ increases, the probability of photon emission decreases. This phenomenon was observed in all experiments that studied the radiative beta decay of nuclei. In these investigations, a considerable excess of the experimental γ-radiation probabilities over the theoretical ones was obtained for large angles θ [11]. Moreover, as was mentioned by many authors, this difference remains considerable even if one takes into account the so-called detour transitions and the nuclear structure. Therefore, these correlation investigations of the radiative decay of the neutron will allow us to figure out what causes the excess: the nuclear structure or the structure of the nucleon.

Let us now proceed to another possibility of investigating the radiative beta decay of the neutron—namely, to the measurements of the polarization of the emitted photon. Since the weak-interaction vertex, which violates parity, occurs in this process, the photon is polarized. From this point of view, the radiative electron K capture in nuclei is the best investigated topic in the field of nuclear physics (the first theoretical and experimental study was performed in 1958 [12, 13]).

Even in the pioneering studies of Martin and Glauber, it was indicated that the degree of polarization depends on the constant of weak interaction. If we now take the model of right-handed currents as the "minimal" deviation from the standard "minimal" *V–A* model of weak interaction, then the degree of photon polarization will depend on the angle ζ of mixing of the left-handed W_L and right-handed W_R bosons,

$$W_1 = W_L\cos\zeta - W_R\sin\zeta,$$

$$W_2 = W_L\sin\zeta + W_R\cos\zeta,$$

and the ratio $\eta = m^2(W_1)/m^2(W_2)$ of the square of the masses of the two bosons W_1 and W_2. Provided that the absolute values of the polarization are determined experimentally with the accuracy $\varepsilon(P_\gamma)$, the limit on the parameters of right-handed currents is given by [14]

$$2\left(\zeta^2 + 2\frac{\lambda^2-1}{\lambda^2+1}\zeta\eta + \eta^2\right) \le \varepsilon(P_\gamma).$$

It can be seen from this limit that the boundary of the allowed region for the parameters of the right-handed-current model is a closed curve, an ellipse, as in the muon-decay case [15]. This result can easily be explained qualitatively if we consider muon decay from the viewpoint of nuclear physics. Actually, ordinary muon decay is a transition from one $1/2^+$ state to another $1/2^+$ state, and both allowed transitions (a Fermi and a Gamow–Teller one) contribute to this process. Therefore, absolute measurements of the circular polarization for any allowed j–j transition ($j \neq 0$) can yield results that are completely alternative to those of measurements of the asymmetry parameter of electron emission in ordinary muon decay [15].

Thus, from our point of view, the investigation of the radiative decay of the neutron is not only important but also experimentally possible. The most interesting investigations, from the modern point of view, are (i) research of the γ spectrum from radiative neutron beta decay—in particular, in the light region; (ii) research of the effects of correlation with measurement of the radiative photon momentum—first of all, in the e–γ correlations—and a comparison of the data with the corresponding data from nuclear beta decay; and (iii) measurement of circular photon polarization in radiative decay, which, in particular, would allow us to obtain new limits on the parameters of right-handed currents.

ACKNOWLEDGMENTS

We are grateful to F. Glück and B.G. Yerozolimsky and to our colleagues from the Kurchatov Institute L.N. Bondarenko, V.I. Morozov, and Yu.A. Mostovoĭ for stimulating discussions.

This work was supported in part by the Russian Foundation for Basic Research (project nos. 98-02-17706 and 00-02-17383).

REFERENCES

1. Particle Data Group, Phys. Rev. D **45**, VII.8 (1992).
2. A. I. Akhiezer and V. B. Berestetskiĭ, *Quantum Electrodynamics* (Wiley, New York, 1965; 3rd ed. Nauka, Moscow, 1969).
3. A. Sirlin, Phys. Rev. **164**, 1767 (1967); Rev. Mod. Phys. **50**, 573 (1978); Nucl. Phys. B **100**, 291 (1975); **71**, 29 (1974); **196**, 83 (1982).
4. B. V. Geshkenbeĭn and V. S. Popov, Zh. Éksp. Teor. Fiz. **41**, 199 (1961) [Sov. Phys. JETP **14**, 145 (1962)].
5. Yu. V. Gaponov and R. U. Khafizov, Phys. Lett. B **379**, 7 (1996).
6. R. Christian and H. Kühnelt, Acta Phys. Austriaca **49**, 229 (1978).
7. J. K. Knipp and G. E. Uhlenbeck, Physica **3**, 425 (1936); F. Bloch, Phys. Rev. **50**, 272 (1936).
8. B. G. Erozolimskiĭ, I. A. Kuznetsov, I. A. Kuida, *et al.*, Yad. Fiz. **52**, 1583 (1990) [Sov. J. Nucl. Phys. **52**, 999 (1990)].
9. J. Deutsch and P. Quin, in *Precision Tests of the Standard Electroweak Model* (World Sci., Singapore, 1994), p. 706.
10. I. S. Towner, Current Status of V_{ud} (in press).
11. I. S. Batkin and Yu. G. Smirnov, Fiz. Élem. Chastits At. Yadra **11**, 1421 (1980) [Sov. J. Part. Nucl. **11**, 564 (1980)].
12. P. C. Martin and R. J. Glauber, Phys. Rev. **109**, 31 (1958).
13. H. Schopper and S. Galter, Nucl. Phys. **6**, 295 (1958).
14. V. G. Tsinoev and R. U. Khafizov, Yad. Fiz. **58**, 785 (1995) [Phys. At. Nucl. **58**, 785 (1995)].
15. A. Jodidio *et al.*, Phys. Rev. D **34**, 1967 (1986).

Physics of Atomic Nuclei, Vol. 63, No. 7, 2000, pp. 1210–1213. From Yadernaya Fizika, Vol. 63, No. 7, 2000, pp. 1284–1287.

NEW PHYSICS, NUCLEAR AND NUCLEON STRUCTURE IN RARE PROCESSES

Possible Evidence for a Time Variation of the Weak-Interaction Constant from Double-Beta-Decay Experiments*

A. S. Barabash**

Institute of Theoretical and Experimental Physics, Bol'shaya Cheremushkinskaya ul. 25, Moscow, 117259 Russia

Abstract—The probabilities of the two-neutrino double-beta decay of ^{82}Se and ^{96}Zr in direct (counter) and geochemical experiments are compared. Relevant experimental data on ^{130}Te are also analyzed. It is shown that the probability is systematically lower in geochemical experiments, which characterize the probability of $\beta\beta(2\nu)$ decay about 10^9 yr ago. It is assumed that this can be due to a change in the weak-interaction constant with time. A series of new, precise measurements with the aid of counters and geochemical experiments is proposed. © *2000 MAIK "Nauka/Interperiodica".*

1. INTRODUCTION

The question of the time dependence of fundamental constants was formulated by Dirac in 1937 (so-called large-number hypothesis) [1]. This question was later discussed in [2–7]. Although Dirac's hypothesis was not confirmed in its initial form, interest in this problem gained new impetus in the 1980s, since coupling constants appear to be time-dependent in multidimensional Kaluza–Klein models [8, 9] and in superstring theories [10] (see also [11, 12]). These theories are formulated for a multidimensional space, which must then be compactified to the four observable dimensions of spacetime. In these theories, the fundamental coupling constants are associated with the radii of additional dimensions, and these additional dimensions can manifest themselves through the time dependence of the coupling constants. The radii can shrink, increase, or even oscillate. It is possible that the compactification process is continuing at present. Time dependence of the fundamental constants also arises in models with a massless dilaton, the scalar partner to the graviton [13]. Recently, a scheme with a time variation of the speed of light in a vacuum, c, and of the Newtonian gravitational constant G_N has been proposed as a solution to cosmological puzzles and as a possible alternative to inflationary cosmology [14, 15].

On the other hand, a clear regularity was discovered in the distribution of galaxies in the direction of the galactic north and south poles, with a characteristic scale of 128 h^{-1} Mpc (where $h \sim 0.5$–1; h is a constant characterizing the uncertainty in the value of the Hubble constant) [16]. This periodicity can be explained by oscillations of the gravitational constant G_N in time [17–20]. For example, a model with an oscillating massive scalar field, which is cosmological "dark matter" and which can be observed according to oscillations of the gravitational constant, is studied in [20]. This model explains well the periodicity in the distribution of galaxies that was observed in [16]. Variations in the solar year, which were discovered in the deposits of corals and sea mollusks, can also serve as indirect evidence for a change in G_N with time [21]. The value of the period of these variations (400–600 million years) is close to the values required to explain the periodicity in the distribution of the galaxies.

In addition, some indication that the fine-structure constant α was smaller at earlier epochs, $-\Delta\alpha/\alpha = (-1.9 \pm 0.5) \times 10^{-5}$ for redshifts of $z > 1$, was found in [22]. But, as was mentioned there, further work is required for exploring possible systematic errors in the data. Thus, one can conclude that there are theoretical and experimental motivations to seek time variations in the fundamental constants.

1.1. Present Limit on the Time Variation of the Weak-Interaction Constant

Modern limits on the possible variations in various fundamental constants with time can be found in [20–29]. For example, the most stringent limits on the weak-interaction constant were obtained from an analysis of the operation of the natural nuclear reactor in Oklo:[1)] $|\Delta G_F|/G_F < 0.02$ (where $\Delta G_F = G_F^{Oklo} - G_F^{now}$) or $|\dot{G}_F/G_F| < 10^{-11}$ yr^{-1} [29]. This value exceeds the limits obtained earlier from the analysis of nucleosynthesis processes ($|\Delta G_F|/G_F < 0.06$) [31] and the analysis of the beta decay of ^{40}K ($|\dot{G}_F/G_F| < 10^{-10}$ yr^{-1}) [32]. However, it should be borne in mind that these limits were obtained under the assumption that all other constants are constant, which renders estimates of this kind less reliable. It is possible that variations of the constants are interrelated and that the effect due to a change in

* This article was submitted by the author in English.

** e-mail: barabash@vitep5.itep.ru

[1)] The first analysis of the Oklo data for a possible change in the fundamental constants with time was performed in [30].

one constant can be compensated by a change in another constant.

2. ββ DECAY AND TIME VARIATION OF G_F

Double-beta decay is of interest in itself in the problem of the change in the fundamental constants with time. The probability of ordinary beta decay is proportional to G_F^2, while the probability of double-beta decay is proportional to G_F^4 (since ββ decay is of second order in the weak interaction). Here, G_F is the Fermi constant. For this reason, if, for example, in ordinary β decay the effect due to a change in G_F in time is compensated by a change in other fundamental constants, this effect could still manifest itself in ββ decay. Therefore, the study of the time dependence of the rate of ββ decay can give additional (and possibly unique) information about the possible change in G_F with time. We recall in this connection that the age of minerals and meteorites is determined by radioisotopic methods (β and α decay). For this reason, when attempts are made to observe the time dependence of the rate of β decay of ^{40}K, for example, then the change in G_F can be masked by incorrect dating of the sample under study.

3. COMPARISON OF THE "PRESENT" AND "PAST" RATES OF THE ββ DECAY OF ^{82}Se, ^{96}Zr, AND ^{130}Te

Let us compare the rate of ββ decay obtained in modern counter experiments with that obtained in geochemical experiments, which carry information about the rate of ββ decay in the past. Geochemical experiments are based on the separation of the ββ-decay products from ancient minerals followed by the isotopic analysis of the products. The observation of an excess quantity of a daughter isotope attests to the presence of ββ decay of the initial isotope and makes it possible to determine its half-life. Minerals containing tellurium, selenium, and zirconium were investigated, and the half-lives of ^{130}Te, ^{128}Te, ^{82}Se, and ^{96}Zr were measured. Since the age of the minerals investigated ranged from about 28 million years to 4.5 billion years, it is possible in principle to extract, from geochemical experiments, information about the values of G_F in the past—right back to the time when the solar system was formed (4.5 billion years ago). If the value of G_F oscillates with time, then these oscillations can be observed. Let us examine systematically all the existing experimental data.

3.1. ^{82}Se

The most accurate present-day value of the half-life of ^{82}Se with respect to the ββ(2ν) channel was obtained with the NEMO-2 track detector [33]: $T_{1/2} = [0.83 \pm 0.10(\text{stat.}) \pm 0.07(\text{syst.})] \times 10^{20}$ yr. The following most precise values were obtained in geochemical experiments: $T_{1/2} = (1.30 \pm 0.05) \times 10^{20}$ yr [34] (the average value for 17 independent measurements; the age of the samples ranged from 80 million years to 4.5 billion years) and $T_{1/2} = (1.2 \pm 0.1) \times 10^{20}$ yr [35] (the age of the sample was 1 billion years). These results show that the present-day value of the half-life of ^{82}Se is different from the half-life in the past (this effect is not less than 3σ). If this is due to a change in the value of the weak-interaction constant, then $\Delta G_F/G_F \approx -0.1$; with the errors taken into account, the possible range of values is approximately –(0.02–0.2). These values were obtained by using the dependence $T_{1/2} \sim G_F^{-4}$. However, if the G_F^{-2} law is assumed, which takes into account the possible "incorrect" dating of the sample, then the corresponding values will be approximately –(0.04–0.4). We note, however, that, in the case of oscillations, the interpretation of the experimental data becomes much more complicated and depends on the value of the period of the oscillations. It is interesting to note that the only experiment with a meteorite (age of about 4.5 billion years) gave the half-life value $T_{1/2} = (1.03^{+0.33}_{-0.42}) \times 10^{20}$ yr [36]. This value is equal, within an error of about 50%, to the present-day value. If G_F oscillates rather than changing with time linearly, then, for a fortuitous value of the period of the oscillations, the values of G_F at present can coincide exactly with the value it took 4.5 billion years ago, for example.

The accuracy of the present-day values of the half-life of ^{82}Se can be increased to a few percent, and such measurements will be performed with the NEMO-3 track detector [37]. The basic problem is to increase the accuracy of the results of geochemical measurements. Modern mass spectrometry makes it possible to perform such measurements with an accuracy of a few percent [38]. The age of the samples is also determined, as a rule, with an accuracy of a few percent. The main uncertainty in geochemical experiments with ^{82}Se is associated with the determination of the effective "retention" age of daughter ^{82}Kr in minerals. To solve this problem, it is necessary to pick samples that have a well-known geological history and for which the retention age of ^{82}Kr can be accurately determined.

3.2. ^{96}Zr

The present-day value of the half-life of ^{96}Zr with respect to the ββ(2ν) channel has been recently measured with the NEMO-2 detector. The result is $T_{1/2} = [2.1^{+0.8(\text{stat.})}_{-0.4(\text{stat.})} \pm 0.2\ (\text{syst.})] \times 10^{19}$ yr [39]. A geochemical experiment (the age of the sample was 1.7 billion years) gave the value of $T_{1/2} = (3.9 \pm 0.9) \times 10^{19}$ yr [40]. One can see that the present-day value of the half-life is approximately one-half as large as the value in the past. However, the errors in both experiments are quite large,

and it cannot be unambiguously concluded that the half-lives are different. New measurements with ^{96}Zr, where the half-life will be determined with an accuracy of 10% with the NEMO-3 detector [37], and new geochemical measurements with a good accuracy (10%) could clarify this situation. We note that, in the present case of the ββ decay of ^{96}Zr, it is a metal (^{96}Mo) that is formed, and not a gas as in the ββ decay of ^{130}Te, ^{128}Te, and ^{82}Se (^{130}Xe, ^{128}Xe, and ^{82}Kr, respectively). This gives hope that the problems involved in determining the retention age of the decay products will be considerably smaller in this case.

3.3. *^{130}Te and ^{128}Te*

Only data from geochemical measurements are available for these isotopes. Although the ratio of the half-lives of these isotopes has been determined to a high degree of accuracy (about 3%) [38], the absolute values of $T_{1/2}$ differ substantially in different experiments. One group of authors [35, 41–43] presents the value of $T_{1/2} \approx 0.8 \times 10^{21}$ yr for ^{130}Te and the value of $T_{1/2} \approx 2 \times 10^{24}$ yr for ^{128}Te, while another group [34, 38] gives about $(2.5–2.7) \times 10^{21}$ and about 2.7×10^{24} yr, respectively. Upon a closer examination, one can conclude that, as a rule, experiments with "young" minerals (of age less than 100 million years) give about $(0.7–0.9) \times 10^{21}$ yr for ^{130}Te, whereas experiments with "old" (of age not less than 1 billion years) minerals give about $(2.5–2.7) \times 10^{21}$ yr. It is interesting to note that even in the very carefully performed study of Varshalovich *et al.* [38] a half-life of about 0.9×10^{21} years was obtained for samples with an age of 28 million years (see Table VI in [38]), although the final result (2.7×10^{21} yr) was obtained by studying samples whose age was in excess of 1 billion years. Probably, this is mainly due to incorrectly estimating the retention age of xenon in old samples (see the discussion in [42]), but it is possible that, to some extent, this could also be due to a change in G_F. In this connection, it is very important to perform precise measurements of the present-day value of the half-life of ^{130}Te. Such measurements will be performed in the near future in an experiment with low-temperature TeO_2 detectors [44] and with the NEMO-3 track detector [37]. It is also obvious that new geochemical measurements with samples of different age and with an accuracy of about 10% are required. This problem can be solved only by carefully selecting experimental samples (with a well-known history and with a possibility of determining accurately the xenon retention age) and by using highly sensitive mass spectrometry. Unfortunately, a direct measurement of the half-life of ^{128}Te is virtually impossible because it is too long. In summary, the analysis has shown the following:

(I) There exists a discrepancy between the values of the half-life of ^{82}Se that were obtained in modern counter experiments and those from geochemical measurements.

(II) The ^{96}Zr data show the same tendency as the ^{82}Se data—the present-day value of $T_{1/2}$ is less than the value obtained in geochemical measurements. However, the measurement errors are too great to conclude unambiguously that the half-lives are unequal.

(III) Geochemical measurements with young minerals give lower values of $T_{1/2}$ (^{130}Te) than analogous measurements with old minerals, showing the same tendency as for ^{82}Se and ^{96}Zr.

These discrepancies can all be explained (at least partly) by a change in G_F with time. If this is indeed the case, this will have the most serious consequences for modern physics and astrophysics. Therefore, it is necessary to confirm (or refute) reliably the reality of these discrepancies. This can be done only by performing new and more accurate measurements. We propose the following:

(i) Precise laboratory measurements of the present-day values of the ββ2ν-decay half-lives of ^{82}Se, ^{96}Zr, and ^{130}Te should be performed.

(ii) New, precise measurements of the half-lives of ^{82}Se, ^{96}Zr, and ^{130}Te in geochemical experiments should be performed; for each isotope, it is desirable to perform measurements with minerals of different ages in order to follow the character of the time dependence of G_F.

(iii) The possibility of performing geochemical experiments with ^{100}Mo, ^{116}Cd, ^{124}Sn, ^{110}Pd, ^{150}Nd, and ^{76}Ge should be investigated; if these measurements are possible, they should be performed. This will make it possible to increase the range of isotopes investigated, since the half-lives of ^{100}Mo, ^{116}Cd, ^{150}Nd, and ^{76}Ge have already been measured in direct (counter) experiments [45–48], while the half-lives of ^{124}Sn and ^{110}Pd can be measured in the near future.

For all isotopes listed above, the products of ββ decay are not gases, so that problems associated with their escape from the minerals studied can be expected to be less serious. The best candidate is ^{100}Mo for the following reasons: (1) maximal ββ-decay rate; (2) high concentration in natural Mo (9.6%); and (3) ^{100}Ru (not gas!) as the final nucleus. One can see that the conditions of geochemical experiment with ^{100}Mo will be approximately 10 times better than in the experiment with ^{96}Zr, which has already been performed [40].

4. CONCLUSION

We have demonstrated that there are discrepancies between the results of the direct and geochemical ββ-decay experiments in ^{82}Se and ^{96}Zr and between the results obtained for ^{130}Te with "young" and "old" minerals of Te. One possible explanation of these discrepancies could be based on the hypothesis of time varia-

tion of G_F.[2)] To check this hypothesis, new direct and geochemical experiments are proposed.

ACKNOWLEDGMENTS

I am grateful to L.B. Okun for enlightening comments.

This work was supported by the Russian Foundation for Basic Research (project no. 97-02-17344) and INTAS (grant no. 96-0589).

REFERENCES

1. P. A. M. Dirac, Nature **139**, 323 (1937).
2. E. Teller, Phys. Rev. *73*, 801 (1948).
3. L. D. Landau, *Niels Bohr and the Development of Physics*, Ed. by W. Pauli (Pergamon, London, 1955).
4. C. Brans and R. H. Dicke, Phys. Rev. 124, 925 (1961).
5. B. S. DeWitt, Phys. Rev. Lett. **13**, 114 (1964).
6. G. Gamow, Phys. Rev. Lett. **19**, 759 (1967).
7. F. J. Dyson, *Aspects of Quantum Theory*, Ed. by A. Salam and E. P. Wigner (Cambridge Univ. Press, Cambridge, 1972).
8. A. Chodos and S. Detweiler, Phys. Rev. D **21**, 2167 (1980).
9. W. J. Marciano, Phys. Rev. Lett. **52**, 489 (1984).
10. Y.-S. Wu and Z. W. Wang, Phys. Rev. Lett. **52**, 489 (1984).
11. E. W. Kolb, M. J. Perry, and T. P. Walker, Phys. Rev. D **33**, 869 (1986).
12. J. Griego and H. Vucetich, Phys. Rev. D **40**, 1904 (1989).
13. T. Damour and A. M. Polyakov, Nucl. Phys. B **423**, 532 (1994).
14. A. Albrecht and J. Magueijo, Phys. Rev. D **59**, 043516 (1999).
15. J. D. Barrow, Phys. Rev. D **59**, 043515 (1999).
16. T. J. Broadhurst, R. S. Ellis, D. C. Koo, and A. S. Szalay, Nature **343**, 726 (1990).
17. T. C. Hill, P. J. Steinbardt, and M. S. Turner, Phys. Lett. B **252**, 343 (1990).
18. M. Morikawa, Astrophys. J. Lett. **362**, L37 (1990).
19. M. Salgado, D. Sudarsky, and H. Quevedo, Phys. Rev. D **53**, 6771 (1996).
20. M. Salgado, D. Sudarsky, and H. Quevedo, Phys. Lett. B **408**, 69 (1997).
21. P. D. Sisterna and H. Vucetich, Phys. Rev. Lett. **72**, 454 (1994).
22. J. K. Webb *et al.*, Phys. Rev. Lett. **82**, 884 (1999).
23. J. H. Irvine and L. Humphreys, Prog. Part. Nucl. Phys. **17**, 59 (1986).
24. J. Rich, O. D. Lloyd, and M. Spiro, Phys. Rep. **151**, 239 (1987).
25. H. V. Klapdor-Kleingrothaus and A. Staudt, *Non-Accelerator Physics* (IOP, Bristol, 1994).
26. P. Sisterna and H. Vucetich, Phys. Rev. D **41**, 1034 (1990).
27. D. A. Varshalovich, S. A. Levshakov, and A. Yu. Potekhin, Usp. Fiz. Nauk **163**, 111 (1993).
28. D. A. Varshalovich, V. E. Panchuk, and A. V. Ivanchick, Astron. Lett. **22**, 6 (1996).
29. T. Damour and F. Dyson, Nucl. Phys. B **480**, 37 (1996).
30. A. I. Shlyakhter, Nature **264**, 340 (1976).
31. H. Reeves, Rev. Mod. Phys. **66**, 193 (1994).
32. F. J. Dyson, in *Aspects of Quantum Theory*, Ed. by A. Salam and E. P. Wigner (Cambridge Univ. Press, Cambridge, 1972), p. 213.
33. R. Arnold *et al.*, Nucl. Phys. A **636**, 209 (1998).
34. T. Kirsten *et al.*, in *Proceedings of the International Symposium on Nuclear Beta Decay and Neutrino, Osaka, 1986*, Ed. by T. Kotani *et al.* (World Sci., Singapore, 1987), p. 81.
35. W. J. Lin *et al.*, Nucl. Phys. A **481**, 477 (1988).
36. S. V. S. Murty and K. Marti, Geochim. Cosmochim. Acta **51**, 163 (1987).
37. A. S. Barabash *et al.*, in *Proceedings of the International Conference "Neutrino'96,"* Ed. by K. Enqvist *et al.* (World Sci., Singapore, 1997), p. 374.
38. T. Bernatowicz *et al.*, Phys. Rev. C **47**, 806 (1993).
39. R. Arnold *et al.*, submitted to Nucl. Phys. A (1999).
40. A. Kawashima, K. Takahashi, and A. Masuda, Phys. Rev. C **47**, R2452 (1993).
41. N. Takaoka and K. Ogata, Z. Naturforsch. **21a**, 84 (1966).
42. O. K. Manuel, in *Proceedings of the International Symposium on Nuclear Beta Decay and Neutrino, Osaka, 1986*, Ed. by T. Kotani *et al.* (World Sci., Singapore, 1987), p. 71.
43. N. Takaoka, Y. Motomura, and K. Nagano, Phys. Rev. C **53**, 1557 (1996).
44. A. Alessandrello *et al.*, Nucl. Instrum. Methods A **370**, 241 (1996).
45. D. Dassie *et al.*, Phys. Rev. D **51**, 2090 (1995).
46. R. Arnold *et al.*, Z. Phys. C **72**, 239 (1996).
47. M. Gunther *et al.*, Phys. Rev. D **55**, 54 (1997).
48. A. De Silva *et al.*, Phys. Rev. C **56**, 2451 (1997).
49. L. B. Okun, *Leptons and Quarks*, 2nd ed. (Nauka, Moscow, 1990; North-Holland, Amsterdam, 1984).

[2)] In fact, G_F is not a "real" fundamental constant. Following, for example, [49], one can write the relation between the true gauge coupling constant of electroweak interaction g and G_F: $g^2/8m_W^2 = G_F/\sqrt{2}$ (where m_W is the mass of the W boson). Using expression $m_W^2 = 1/(4g^2\eta^2)$ (where η is the expectation value of the Higgs field), one can obtain $\eta \sim 1/\sqrt{G_F}$. This means that, if G_F increases with time, then η decreases.

Physics of Atomic Nuclei, Vol. 63, No. 7, 2000, pp. 1214–1217. From Yadernaya Fizika, Vol. 63, No. 7, 2000, pp. 1288–1291.

EXPERIMENTAL RESULTS, METHODS, AND FACILITIES

Measurement of the ββ-Decay Rate of ^{100}Mo to the First Excited 0^+ State in ^{100}Ru

L. De Braeckeleer, M. Hornish, A. S. Barabash[1)], and V. I. Umatov[1)]

Department of Physics, Duke University and Triangle Universities Nuclear Laboratory, Durham, North Carolina, USA

Abstract—A new and independent confirmation of ββ(2ν) decay of ^{100}Mo to the first 0^+ excited state in ^{100}Ru has been made. This was accomplished using a two-photon coincidence counting technique in which two HPGe detectors were used to observe the two emitted γ rays ($E_{\gamma 1}$ = 590.8 keV and $E_{\gamma 2}$ = 539.6 keV) from the daughter nucleus as it deexcites to the ground state ($0^+ \longrightarrow 2^+ \longrightarrow 0^+$). The half-life of this decay has been estimated as ~$(5–8) \times 10^{20}$ yr. © *2000 MAIK "Nauka/Interperiodica".*

1. INTRODUCTION

Although the main interest in double-beta (ββ) decay is related to the neutrinoless mode because of the promise of the discovery of elementary particle physics beyond the Standard Model, considerable efforts are made to investigate the ordinary allowed second-order weak decay (2νββ decay) [1–4]. Accumulation of experimental information for the 2νββ processes (transitions to the ground and excited states) promotes a better understanding of the nuclear part of double-beta decay and allows one to check theoretical schemes of nuclear matrix element calculations for the two-neutrino mode as well as for the neutrinoless one.

It is very important to note that in the framework of QRPA models, the behavior of nuclear matrix elements with the particle–particle strength parameter g_{pp} is completely different for transitions to the ground and excited states [3, 5]. This is why the decay to excited states probes different aspects of these calculations.

0νββ transitions to excited states of daughter nuclei have a very nice experimental signature: in addition to two electrons with a fixed energy, there is one ($0^+ \longrightarrow 2_1^+$ transition) or two ($0^+ \longrightarrow 0_1^+$ transition) photons which again have strictly fixed energy. If one can perform an experiment such that all decay products are detected with high efficiency and with good energy resolution, then the background can be totally suppressed.

The idea to detect the 2νββ($0^+ \longrightarrow 0_1^+$) decay in ^{100}Mo [6] initiated a few experiments to search for this decay using enriched molybdenum samples. In the experiment [7] with 310 g of ^{100}Mo and a surface-based 100-cm^3 HPGe detector, a lower limit of 4.2×10^{19} yr was obtained for the half-life. Then, the decay was detected using ~1 kg of ^{100}Mo and a low-background 114-cm^3 HPGe detector located in the Soudan mine in Minnesota (depth is 2090 mwe), yielding $T_{1/2} = (6.1^{+1.8}_{-1.1}) \times 10^{20}$ yr [8, 9]. At approximately the same time (the measurement was started a half-year after the beginning of the measurement in the Soudan mine), the experiment with another 1 kg sample of ^{100}Mo using a 100-cm^3 HPGe detector was done in the Modane Underground Laboratory (4800 mwe depth) [10]. However, only a lower limit was obtained because the measurement time was not long enough (a factor of ~4 in comparison with [8]) and a rather high level of background in this experiment (a factor of ~2 in comparison with [8]). A new positive result for 2νββ($0^+ \longrightarrow 0_1^+$) decay in ^{100}Mo was recently obtained [11]. The experiment was again performed in the Modane Underground Laboratory. A set of ^{100}Mo-enriched metal powder samples were measured by using low-background HPGe detectors with volumes of 100, 120, 380, and 400 cm^3. Data from 17 measurements were analyzed, the total spectrum was obtained, and a half-life value $T_{1/2} = (9.3^{+2.8}_{-1.7}) \times 10^{20}$ yr was produced. If the spectrum of [8] is added, one obtains $T_{1/2} = (7.6^{+1.8}_{-1.1}) \times 10^{20}$ yr [11].

This work presents a new positive result for 2νββ($0^+ \longrightarrow 0_1^+$) decay in ^{100}Mo using a new method with two HPGe detectors in a coincidence regime.

2. EXPERIMENT

Previous experiments have focused on a very low background detection system. This has been obtained by building the detectors with low-radioactivity materials and by operating the experiment in an underground laboratory which offers an efficient shielding against the cosmic-ray background. An alternative approach to background reduction is to operate in a coincidence mode, in which two separate detectors simultaneously detect the two emitted photons from the 2νββ($0^+ \longrightarrow$

* This article was submitted by the author in English.

[1)] ITEP, Moscow, Russia.

1063-7788/00/6307-1214$20.00 © 2000 MAIK "Nauka/Interperiodica"

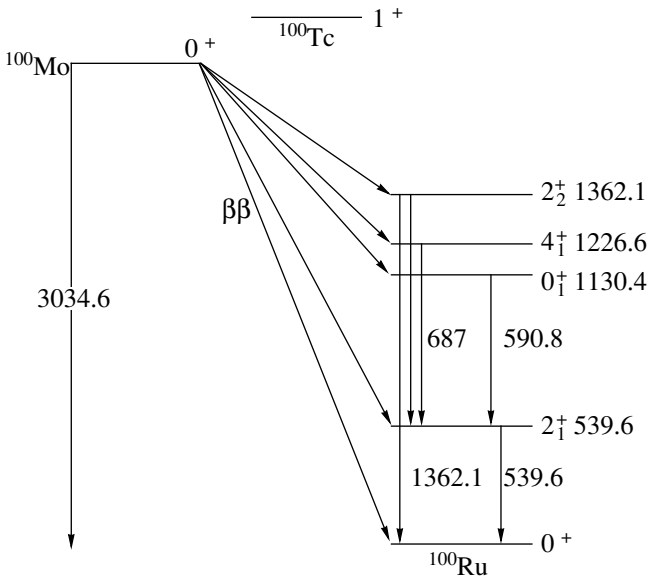

Fig. 1. Double-beta and γ-decay scheme of ^{100}Mo. Energies are given in keV.

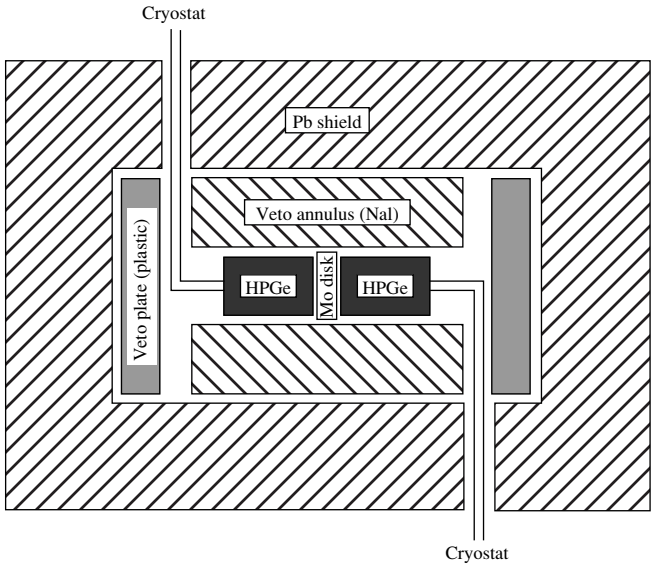

Fig. 2. Experimental setup including the molybdenum sample, HPGe detectors, active shielding (veto), and passive shielding (Pb).

0_1^+) decay in ^{100}Mo with $E_{\gamma 1}$ = 590.8 keV and $E_{\gamma 2}$ = 539.6 keV (Fig. 1). This was accomplished using two HPGe detectors (8.5 cm diameter, 5 cm width, 1.8 keV FWHM energy resolution at 1.33 MeV and 0.7 keV at 0.122 keV). A disk sample of molybdenum is sandwiched by these two γ-ray detectors, which are inserted in a NaI annulus (55.9 cm long, 35.6 cm in diameter and a 12.7 cm hole along the axis of symmetry) that acts as an active veto. Plastic plates on either side of the apparatus, 10.2 cm in thickness, act as a veto for the regions which are not covered by the NaI annulus. The entire apparatus is surrounded by a passive shielding made of lead bricks (Fig. 2). The experiment is conducted inside the Low Background Counting Facility of the Triangle Universities Nuclear Laboratory, a well-shielded room located in the basement of the Physics Department of Duke University.

It is necessary to understand and determine the efficiency of a two-photon coincidence apparatus in order to calculate the half-life of a given decay. To accomplish this, a ^{102m}Rh source was produced by (*p*, *n*) activation of a natural Ru target. This source was then used to measure the probability to detect the full energy of both photons. This radioactive isotope was chosen because it emits two photons having similar energy and the same angular distribution as the photons emitted in the ββ decay of ^{100}Mo. In addition, the lifetime of 206 d is quite convenient, and it decays to the first excited 0^+ state of the daughter nucleus via electron capture only; this implies no radiation from annihilation or bremsstrahlung and makes the measurement of the efficiency very simple. The source was used to measure the efficiency of the apparatus as a function of the distance from the center of the detectors. The source was also surrounded by disks of molybdenum to simulate the attenuation of the photons in the actual molybdenum sample. The efficiency was averaged over the whole volume of the sample, and it was determined that ϵ = 0.29%. The efficiency has also been studied with a Monte Carlo simulation. This calculation includes the effects of the extended geometry, the attenuation of the photons in the sample, the full-energy peak efficiency of the germanium detectors and the strongly anisotropic angular correlation between the γ rays. The results of this code agree with the above measured efficiency to within 10% (Fig. 3).

3. RESULTS

For a counting period of 180 d, a disk of natural molybdenum (1 kg, 10 cm diameter, 0.965 cm thickness, 9.6% ^{100}Mo) was studied. Four events of a 591 ± 2.5 keV photon in coincidence with a 540 ± 2.5 keV photon were detected. A measurement of the background rate yields 0.08 events/(keV^2 yr). Therefore, in a 5×5 keV^2 area, one expects one background event in a 180-d period.

A second sample, this time a ^{100}Mo sample (1.05 kg, 10.6-cm diameter, 1.1-cm thickness, 98.4% enrichment) was studied for 195 d. Eleven 540–591 coincidence events were detected, and Fig. 4 shows the γ-ray spectrum in coincidence with 540 ± 2.5 keV. The background rate is approximately the same as that of the natural molybdenum disk.

From this data, the half-life of the ββ decay of ^{100}Mo to the first excited 0^+ state in ^{100}Ru can be estimated. Ten events (having subtracted off one background count) in 195 d translates to a half-life of $\sim 5.7 \times 10^{20}$ yr.

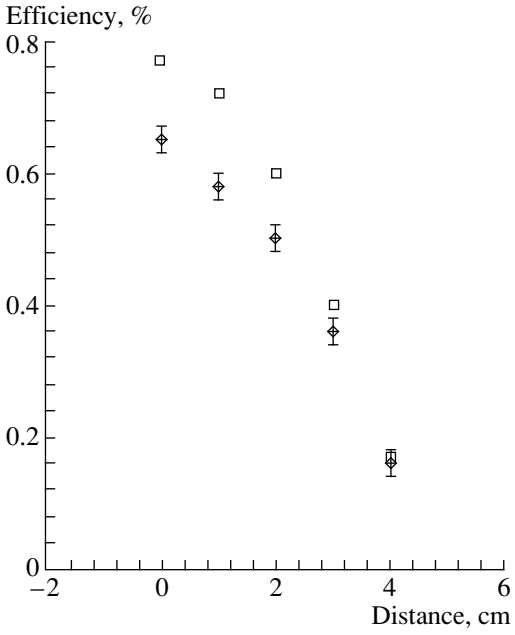

Fig. 3. Efficiency of measuring a two-photon coincidence as a function of distance from the axis of symmetry. Both experimental measurements (points with error bars) and Monte Carlo predictions (squares) are shown.

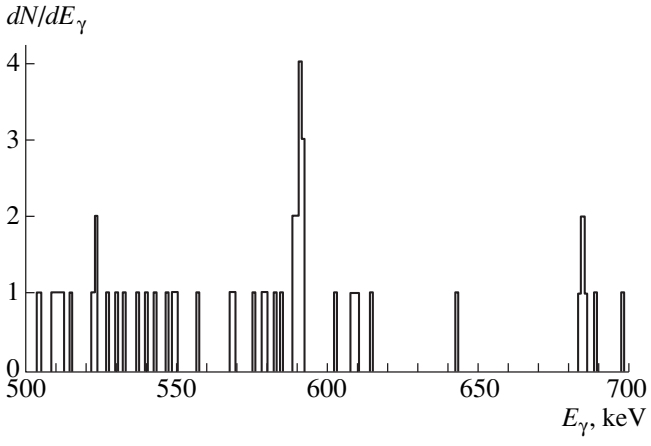

Fig. 4. γ-ray spectrum in coincidence with 540 ± 2.5 keV. Note the 11 events occurring at 591 ± 2.5 keV.

Because natural molybdenum was used as a blank, perhaps a more realistic case is to assume that seven of the 11 detected events are due to ββ decay, and thus seven events in 195 d leads to a half-life of $\sim 8.2 \times 10^{20}$ yr.

One must now investigate the possibility that the signal, or at least part of it, observed in the ^{100}Mo double-beta-decay experiment is due to ^{100}Mo(*p, n*) reactions. The ^{100}Mo(*p, n*) reactions to bound states in ^{100}Tc will produce, after prompt-gamma-ray deexcitation, the ground state of ^{100}Tc. The latter has a half-life of 15.8 s and a 6% branching ratio to the 0_1^+ state in ^{100}Ru, which decays to the ground state by emission of two photons (540 and 591 keV). It is worth noticing that the NaI veto is not acting against this process due to the 16-s half-life of the ^{100}Tc ground state. One way to estimate the magnitude of the ^{100}Mo(*p, n*) process is to seek the very similar ^{95}Mo(*p, n*) reactions. First, ^{95}Mo is an abundant isotope: 16% of natural Mo. One sample, weighing 1000 g, has been stored for 1 yr in the apparatus and subsequently investigated for 180 d. The production of the isomer ($9/2^+$, 20 h) of ^{95}Tc can proceed via the (*p, n*) reaction on ^{95}Mo and is very practical for this need. This element decays with large branching ratios to two excited states: 41% to the 786.2 keV and 32% to the 1039.2 keV. In both cases, these states decay to the first excited state at 204 keV with a branching ratio of 78 and 88%, respectively. Moreover, the first excited state has a short lifetime of 0.8 ns. One hundred eighty days' worth of data with the natural molybdenum sample were analyzed, and no such coincidence events were detected. Thus, it can be concluded that proton background does not contribute significantly to the ββ signal.

Another potential source of background would be neutrons which could contribute via neutron capture in the ^{100}Mo(*n*, γ) reaction. This happens because the decay of ^{101}Mo yields some photons with an energy very close to the one our experiment is looking for. However, this process should also produce other photons in coincidence with a probability 10^5 higher which are not being observed. This possible background is therefore completely ruled out.

This experimental method is incapable of distinguishing between 2ν and 0νββ decay because the energy of the two electrons is not measured. Nevertheless, ββ transitions of ^{100}Mo to the ground state of ^{100}Ru indicate that this experiment is observing the 2νββ mode instead of the neutrinoless one. Experimental measurements of ββ decay of the 0^+ ground state of ^{100}Mo to the 0^+ ground state of ^{100}Ru have resulted in $T_{1/2} = (9.5 \pm 0.4[\text{stat.}] \pm 0.9[\text{syst.}]) \times 10^{18}$ yr [12]. However, the neutrinoless mode of this decay is estimated to have $T_{1/2}^{0\nu} > 5.2 \times 10^{22}$ yr [13]. This indicates that less than 0.018% of ββ decays proceed via the neutrinoless mode. Thus, it is sensible to assume that the contribution of 0ν events in this set of data is negligible.

An important consideration in ββ decay is the comparison of decays to the ground state and those to excited states. For the decay of ^{100}Mo to the ground and 0_1^+ states, the nuclear matrix elements of these decays are dominated by transitions via the ground state (1^+) in the intermediate nucleus ^{100}Tc [14, 15]. Using this assumption, the matrix elements as calculated by the QRPA model are very similar for the ground state transition and the transition to the 0_1^+ state, and this similarity has also been observed experimentally.

4. CONCLUSION

Using the new method of two-photon coincidence counting, a new, independent confirmation of the ββ decay of ^{100}Mo to the first excited 0^+ state in ^{100}Ru has been made. The calculated half-life of this decay is consistent with previous measurements [8, 11]. If the efficiency of the apparatus can be increased, this experimental method of coincidence detection would enable analysis of ββ decay in many other isotopes, such as ^{150}Nd, ^{96}Zr, ^{82}Se, and ^{130}Te. This would also provide good perspectives on future experiments involving the search for neutrinoless ββ decay using a large mass detector.

REFERENCES

1. M. Moe and P. Vogel, Annu. Rev. Part. Sci. **44**, 247 (1994).
2. H. V. Klapdor-Kleingrothaus and A. Staudt, *Non-accelerator Particle Physics* (IOP Publ., Bristol, 1995).
3. J. Suhonen and O. Civitarese, Phys. Rep. **300**, 123 (1998).
4. A. Faessler and F. Šimkovic, J. Phys. G **24**, 2139 (1998).
5. M. Aunola and J. Suhonen, Nucl. Phys. A **602**, 133 (1996).
6. A. S. Barabash, Pis'ma Zh. Éksp. Teor. Fiz. **51**, 181 (1990) [JETP Lett. **51**, 207 (1990)].
7. A. S. Barabash, A. V. Kopylov, and V. I. Cherehovsky, Phys. Lett. B **249**, 186 (1990).
8. A. S. Barabash *et al.*, Phys. Lett. B **345**, 408 (1995).
9. A. S. Barabash *et al.*, in *Proceedings of the XXVI Rencontre de Moriond, 1991* (Editions Frontières, 1991), p. 77.
10. D. Blum *et al.*, Phys. Lett. B **275**, 506 (1992).
11. A. S. Barabash *et al.*, Yad. Fiz. **62**, 2211 (1999) [Phys. At. Nucl. **62**, 2039 (1999)].
12. D. Dassie *et al.*, Phys. Rev. D **51**, 2090 (1995).
13. H. Ejiri *et al.*, Nucl. Phys. A **611**, 85 (1996).
14. A. Griffiths and P. Vogel, Phys. Rev. C **46**, 181 (1992).
15. J. Suhonen and O. Civitaresse, Phys. Rev. C **49**, 3055 (1994).

Physics of Atomic Nuclei, Vol. 63, No. 7, 2000, pp. 1218–1221. From Yadernaya Fizika, Vol. 63, No. 7, 2000, pp. 1292–1295.

EXPERIMENTAL RESULTS, METHODS, AND FACILITIES

Double-Beta Decay of ^{48}Ca in the TGV Experiment*

V. B. Brudanin, N. I. Rukhadze, Ch. Briançon[1)], V. G. Egorov, V. E. Kovalenko, A. Kovalik, A. V. Salamatin, V. V. Tsoupko-Sitnikov, Ts. Vylov, and I. Štekl[2)]**

Joint Institute for Nuclear Research, Dubna, Moscow oblast, 141980 Russia

Abstract—The low-background, high-sensitivity Ge multidetector spectrometer TGV is used to study the double-beta decay of ^{48}Ca. Additional suppression of the recorded background is achieved with neutron shielding and a method for distinguishing β particles from γ rays by detector-pulse rise time. The estimates $T_{1/2}^{\beta\beta 2\nu} = (4.2 \pm 2.4) \times 10^{19}$ yr and $T_{1/2}^{\beta\beta 0\nu} > 1.5 \times 10^{21}$ yr (at a 90% C.L.) for the double-beta decay of ^{48}Ca are obtained.

1. INTRODUCTION

The most favorable isotope among all candidates for the investigation of double-beta decay is ^{48}Ca. According to the theory [1], this double-beta-decay candidate, being the lightest one, exhibits the simplest nuclear structure. Indeed, ^{48}Ca has only eight extra nucleons in relation to the doubly magic isotope ^{40}Ca ($Z = 20$, $N = 20$). On the other hand, the highest possible energy of $Q = 4271(4)$ keV is released in the double-beta decay $^{48}\text{Ca} \longrightarrow {}^{48}\text{Ti}$ (Fig. 1), resulting in the highest possibility for this ultrarare process. Another advantage of the largest Q is the increasing possibility of observing double-beta decay in the part of the spectrum with energy higher than the endpoint of the natural-background spectrum ($E = 2614.5$ keV). The single-beta decay $^{48}\text{Ca} \longrightarrow {}^{48}\text{Sc}$ is energetically allowed ($Q = 278$ keV), but it is strongly suppressed by a large difference of the angular momenta ($\Delta I = 6$) [2]. Therefore, the investigation of the double-beta decay of ^{48}Ca provides a good chance to test nuclear theories. Because of the low abundance of ^{48}Ca (only 0.187%), a large amount of this isotope is unavailable in practice for the experiment. This explains why only a few experimental results [3–5] were obtained in the investigations of the double-beta decay of ^{48}Ca. Unfortunately, the experimental results obtained so far could not completely solve the problems in the theoretical descriptions of the double-beta decay $^{48}\text{Ca} \longrightarrow {}^{48}\text{Ti}$. For example, theoretically predicted half-lives for the two-neutrino double-beta decay of ^{48}Ca (the simplest nuclear structure) vary within more than one order of magnitude: from $T_{1/2}^{\beta\beta 2\nu} = 1.9 \times 10^{19}$ yr [6] to $T_{1/2}^{\beta\beta 2\nu} = 5 \times 10^{20}$ yr [7].

The TGV experiment was planned as a practical test of the low-background, high-sensitivity Ge multidetector spectrometer TGV (telescope germanium vertical) [8, 9] and an original method for an extra suppression of the background by distinguishing β particles from γ rays [8, 9] in rare processes. The choice of ^{48}Ca was based on the permanent interest in this nuclide and on the ability of the spectrometer to seek rare processes with a small amount of the isotope. The TGV spectrometer, with advantages of so-called "passive-sources" experiments (identification of double-beta events and information about the energy of each beta particle, the energy of double-beta events, the time and place of detection, etc.), allows us to achieve not only a high energy resolution (previously inaccessible for ^{48}Ca), but also a high detection efficiency for double-beta events (as in "active-source" experiments) of about

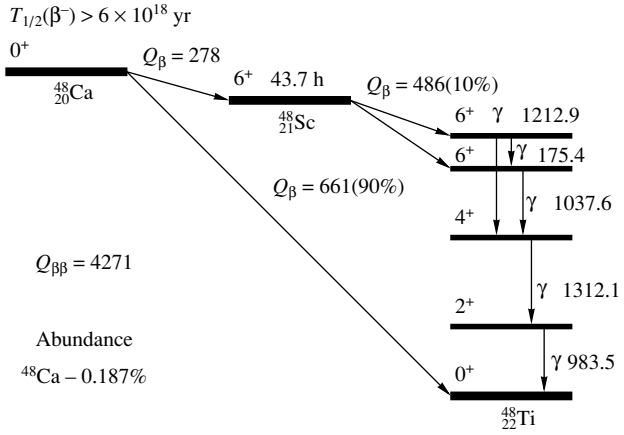

Fig. 1. Decay scheme of ^{48}Ca.

* This article was submitted by the authors in English.

** e-mail: rukhadze@nusun.jinr.ru

1) Centre de Spectrometrie Nucléaire et de Spectrometrie de Masse, F-91405 Orsay, France.

2) Faculty of Nuclear Science and Physical Engineering, Czech Technical University, CZ-11519 Prague, Czech Republic.

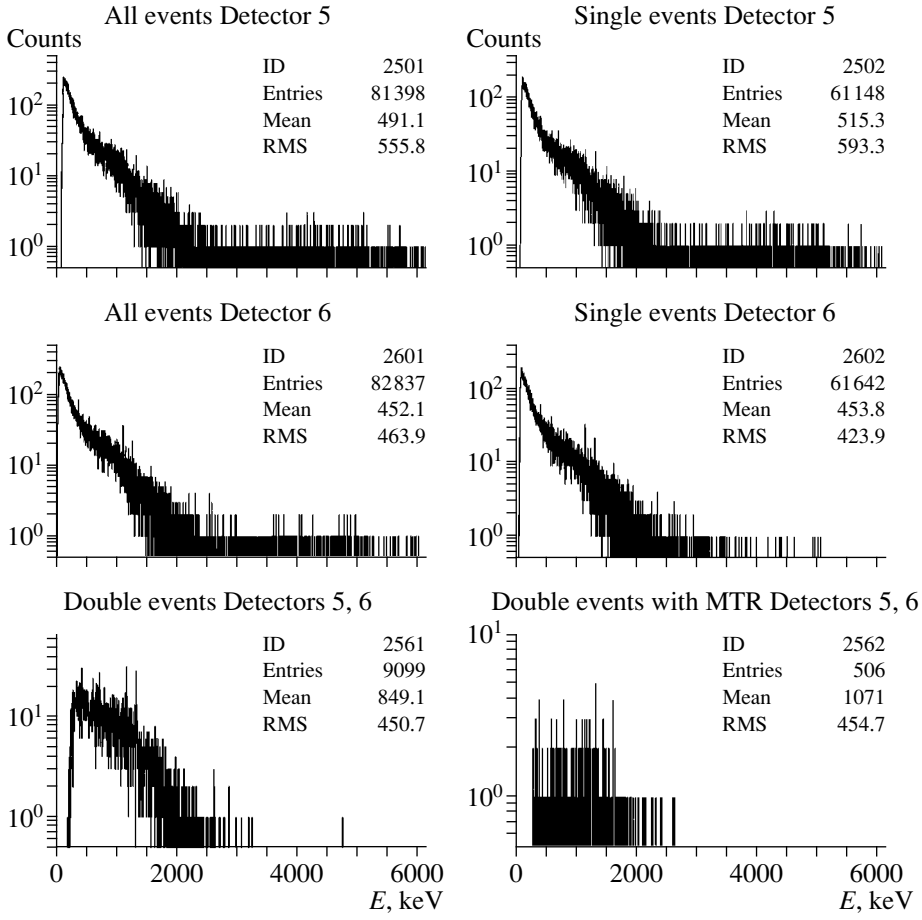

Fig. 2. Spectra of all, single, coincidence, and β–β events obtained with one pair of detectors 5 and 6.

50% for the two-neutrino mode and of about 63% for the neutrinoless mode.

2. DESCRIPTION OF THE EXPERIMENT

The TGV experiment was performed at the Modane underground laboratory, France (4000 mwe), between 1996 and 1999. The detector part of the TGV spectrometer was composed of 16 HPGe planar-type detectors with a sensitive volume of 1200 mm^2 × 6 mm each mounted vertically one over another in the same cryostat. Sources were placed into the cryostat between the neighboring detectors. The main suppression of the radioactive background was achieved due to (1) passive shielding (20 cm of copper and airtight box against radon), (2) deployment in an underground laboratory, (3) allowance for only double coincidences from neighboring HPGe detectors, and (4) discrimination of β particles from γ rays by different rise times of the detector pulses [8, 9]. The last two modes of the background suppression were used only at the stage of data processing (Fig. 2). Therefore, background γ peaks in the spectra of each detector were very useful as an additional test of stability of the spectrometer in long-term measurements.

For additional suppression of the radioactive background—especially in the high-energy region—neutron shielding from polyethylene, filled with boron up to 16 cm thick, was built around the detector part of the spectrometer. The average 20% suppression of the background (from 10 to 75% depending on the energy region) was observed in a 1070-h measurement (Fig. 3).

The square-shaped sources (32.5 × 32.5 mm) used in the TGV experiment were prepared from a mixture containing 80% calcium carbonate ($CaCO_3$) and 20% poly(vinyl formal) on a Mylar support. Eight of the sources contained ^{48}Ca (enrichment of 77.8%), and another eight contained natural Ca (for estimating source contributions to the recorded background). The total weight of the ^{48}Ca sources was 3.5(1) g, the total source area was about 84.5 cm^2, and the thickness of sources was 41(2) mg/cm^2. The total amount of ^{48}Ca was about 1.355×10^{22} atoms—that is, slightly more than 1 g of ^{48}Ca. The thickness of the sources from natural Ca was 45(1) mg/cm^2. In the main measurement (8700 h), fifteen sources were used. Eight of the

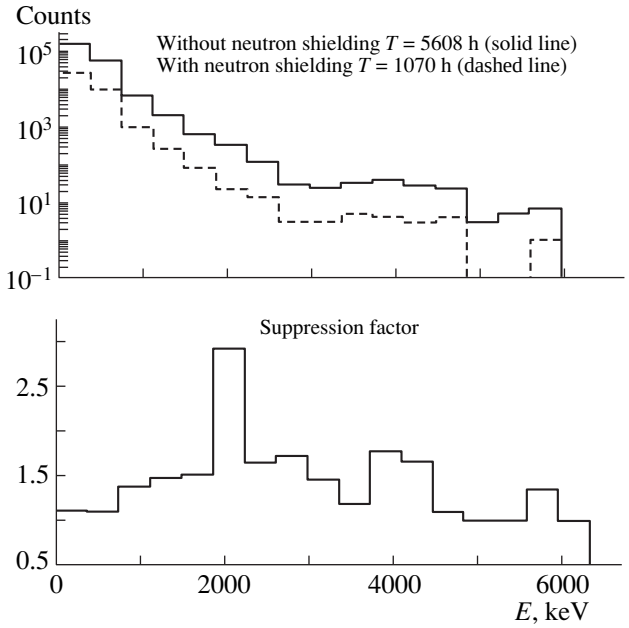

Fig. 3. Suppression of the background by the neutron shielding: (upper figure) spectra of the background (solid line) without and (dashed line) with neutron shielding; (lower figure) suppression of the background with neutron shielding.

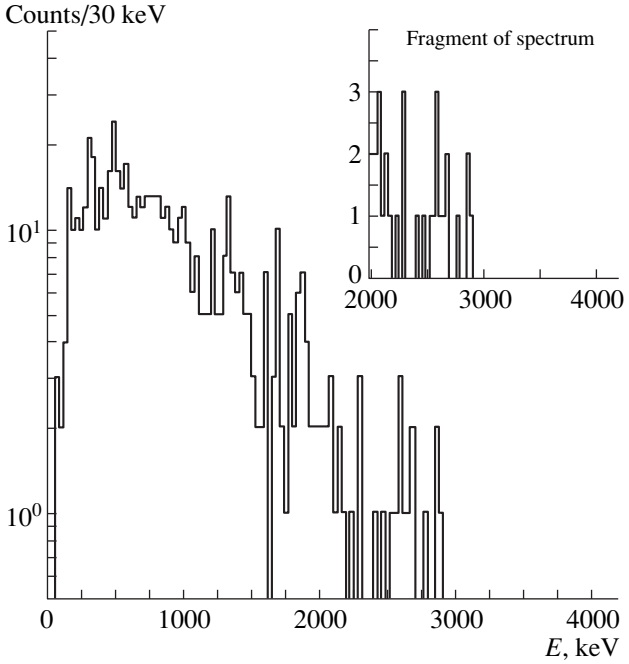

Fig. 4. Spectrum of a ^{214}Bi impurity in the ^{48}Ca sources simulated for 8700-h measurement and fragment of the spectrum.

sources (situated between the face sides of the detectors) were from ^{48}Ca, while the other seven sources (situated between the back sides of the detectors) were from natural Ca.

In order to identify reliably background events (which originated both from the natural background and from the pollution of the sources) in the final data evaluation, several additional runs were also performed. In the first run (of about the same exposure time as the main run), only eight sources from natural Ca were used. They were situated between the face sides of the detectors—that is, at the places of the ^{48}Ca sources in the main measurement. The second run was performed without any sources. Finally, a short run for testing the method for distinguishing β particles from γ rays by detector-pulse rise time [8, 9] was performed by using the sources from natural Ca with the known admixture of radioactive β (^{90}Sr) and α isotopes (^{148}Gd, ^{241}Am).

3. RESULTS

The radioactive background of the TGV spectrometer for the investigation of a small amount of isotopes (only about 1 g) was not sufficiently suppressed in the energy region below 2.7 MeV. But the energy spectrum of the double-beta decay of ^{48}Ca extends to almost 4.3 MeV. Since any double-beta background event with the total energy higher than 2.7 MeV was obtained in several long-term background measurements, it was decided to study the double-neutrino double-beta decay $^{48}\mathrm{Ca} \longrightarrow {}^{48}\mathrm{Ti}$ by analyzing the high-energy part of the final spectrum. According to the theoretical predictions from [6, 10], this region was expected to be sufficiently sensitive to the $\beta\beta2\nu$ decay of ^{48}Ca. The neutrinoless double-beta-decay mode was analyzed in the region of the expected peak of this process (4.27 MeV).

The experimental data was processed by the method of separation of β particles from γ rays [8, 9] and a Monte Carlo simulation. At the beginning, seven events obtained in the energy range from 2.7 to 3.5 MeV in an almost one year exposure (8700 h) were associated with the process being investigated. But later, it was figured out that some of them originated from impurities in the sources. The contamination of ^{48}Ca was negligible; nevertheless, the impurities of uranium, thorium, and their daughters [10(2) dpm/kg for ^{214}Bi, 10(2) dpm/kg for ^{214}Pb, less than 6 dpm/kg for ^{228}Ac, less than 1 dpm/kg for ^{208}Tl, etc.; 6(2) dpm/kg for ^{137}Cs, less than 4 dpm/kg for ^{60}Co, and less than 35 dpm/kg for ^{40}K] were found in the sources of ^{48}Ca. In the high-energy region, the contribution to the total double-beta spectrum comes from the ^{214}Bi impurity (Fig. 4).

In order to obtain a more reliable result for the double-beta double-neutrino decay of ^{48}Ca, we extended the region of data evaluation. The analysis was performed for double-beta events with energies higher than 2 MeV. There, we have less than 10% of all events of ^{48}Ca double-beta decay. Finally, with the data accumulated for ^{48}Ca, Ca natural (Fig. 5), and background measurements and with Monte Carlo simulations of the

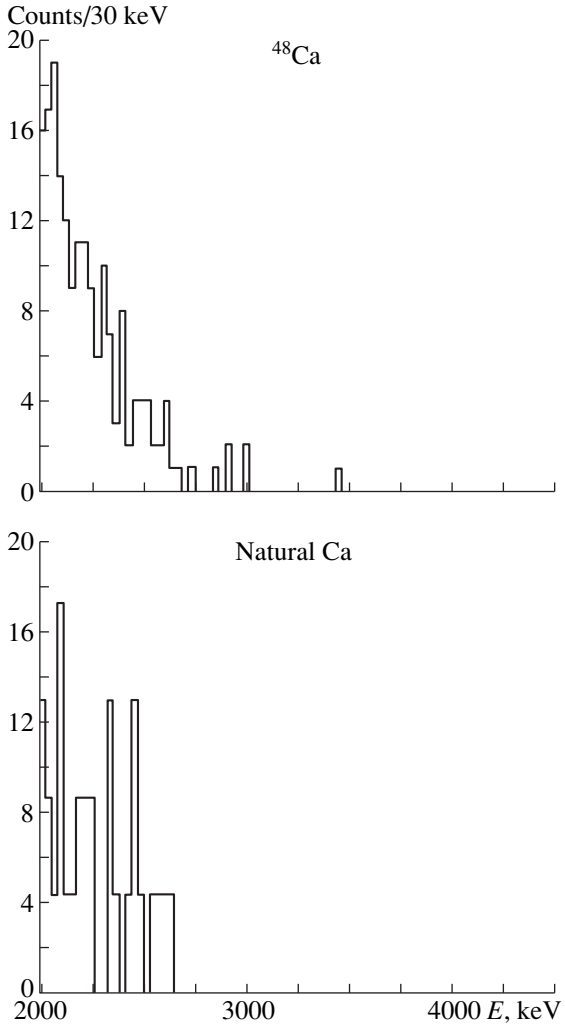

Fig. 5. High-energy part of the ^{48}Ca and natural Ca spectra accumulated for 8700 h.

impurity of the sources and the efficiency of the spectrometer in the region of interest, the half-life of ^{48}Ca with respect to two-neutrino double-beta decay was found to be

$$T_{1/2}^{\beta\beta 2\nu} = (4.2 \pm 2.4) \times 10^{19}\text{yr}.$$

The estimate for the neutrinoless double-beta decay of ^{48}Ca is

$$T_{1/2}^{\beta\beta 0\nu} > 1.5 \times 10^{21}\text{yr (90\% C.L.)},$$

which corresponds to $m_\nu < 20.9$ eV.

The present results, obtained in the test experiment TGV, are at the same level as previous results [4, 5]. It should be noted that the amount of isotopes investigated in the TGV experiment was one tenth of that in the experiments reported in [4, 5]. This observation is a good demonstration of the advantages of this spectrometer and of the method for additional background suppression by distinguishing β particles from γ rays by the detector-pulse rise time. With the experience gained with the HPGe multidetector TGV, the development of a new low-background spectrometer TGV-2 has been started. The TGV-2 spectrometer (like TGV) is intended for investigating ultrarare nuclear processes (double-beta decay, double-electron capture, etc.). The main advantages of TGV-2 will be a significantly greater sensitive volume (32 HPGe detectors of size 2000 mm^2 $\times$ 6 mm each) and a higher detection efficiency. Consequently, a higher mass of nuclides can be used (the amount of ^{48}Ca will be ten times larger). Some changes will be also made in the design of the cryostat and the detector holders in relation to TGV. We expect that TGV-2 will enable us to obtain more reliable and improved results both on the $\beta\beta$ decay of ^{48}Ca and on the EC/EC of ^{106}Cd.

ACKNOWLEDGMENTS

This work was supported in part by the Russian Foundation for Basic Research (project no. 00-02-16549).

REFERENCES

1. W. C. Haxton and G. J. Stephenson, Prog. Part. Nucl. Phys. **12**, 409 (1984).
2. D. E. Alburger and J. B. Cuming, Phys. Rev. C **32**, 1358 (1985).
3. R. K. Bardin *et al.*, Nucl. Phys. A **158**, 337 (1970).
4. Ke You *et al.*, Phys. Lett. B **265**, 53 (1991).
5. A. Balysh *et al.*, Phys. Rev. Lett. **77**, 5186 (1996).
6. Liang Zhao, B. A. Brown, and W. A. Richter, Phys. Rev. C **42**, 1120 (1990).
7. O. A. Rumyantsev and M. N. Urin, Pis'ma Zh. Éksp. Teor. Fiz. **61**, 356 (1995) [JETP Lett. **61**, 361 (1995)].
8. Ch. Briancon *et al.*, Nucl. Instrum. Methods A **372**, 222 (1996).
9. V. B. Brudanin *et al.*, Izv. Akad. Nauk, Ser. Fiz. **60**, 137 (1996).
10. E. Caurier, A. Powes, and A. P. Zuker, Phys. Lett. B **252**, 13 (1990).

Physics of Atomic Nuclei, Vol. 63, No. 7, 2000, pp. 1222–1224. From Yadernaya Fizika, Vol. 63, No. 7, 2000, pp. 1296–1298.

EXPERIMENTAL RESULTS, METHODS, AND FACILITIES

Double-Beta Decay with the Nemo Experiment: Status of the Nemo 3 Detector*

F. Piquemal
(for the NEMO Collaboration)[1)]

Centre d'Etudes Nucléaires de Bordeaux-Gradignan, France

Abstract—The NEMO 3 detector, devoted to search for the neutrinoless double-beta decay, will be able to reach the sensitivity to $\langle m_\nu \rangle$ of the order of 0.1 eV. The expected performance of the detector for signal detection and both internal and external background rejection is presented. A specific study of the neutron-induced background is given. The NEMO Collaboration is now mounting the detector in the Fréjus underground laboratory.

1. INTRODUCTION

Since 1988, the NEMO (Neutrinoless Experiment with Molybdenum) collaboration started a R& D program to build a detector able to lower the sensitivity of the effective neutrino mass down to about 0.1 eV by looking for the neutrinoless double-beta-decay process $\beta\beta(0\nu)$. The observation of such a process will prove the existence of a massive Majorana neutrino.

The guidelines to reach this goal are the following:

Several kilograms of $\beta\beta$ emitters to measure half-lives greater than 10^{24} yr.

Source and detector are independent, to allow the study of different $\beta\beta$ isotopes and to take into account nuclear matrix element uncertainties.

Full characterization of two electron decays by direct detection of the emitted electrons, including reconstruction of trajectories, time-of-flight and energy measurements.

All detector parts, including the shielding, are made of low radioactivity materials (selected with ultralow background γ-ray Ge spectrometers) to reduce background.

Stability and reliability of the used techniques to allow several years of running with full control from each laboratory of the collaboration.

α and γ detection, time-of-flight criteria, and magnetic field in order to reject the remaining background.

Two prototypes, NEMO 1 [1] and NEMO 2 [2], have proved the technical feasibility and have also permitted background studies (natural radioactivity, radon, cosmics, neutrons, etc.). In addition, the NEMO 2 prototype has shown enough sensitivity to measure $\beta\beta(2\nu)$ half-lives of ^{100}Mo [3, 4], ^{116}Cd [5], ^{82}Se [6], and ^{96}Zr [7]. The expected performance of the final detector NEMO 3 [8], which is under construction in the Fréjus underground laboratory, will be presented in this paper with a focus on the $\beta\beta(0\nu)$-neutron-induced background.

2. THE NEMO 3 DETECTOR

The NEMO 3 detector will house up to 10 kg of double-beta-decay isotopes. The detector is cylindrical in design and divided into 20 equal sectors. A thin (40–50 μm) cylindrical source foil will be constructed from either a metal film or powder bounded by an organic glue to Mylar strips.

The source will hang between two concentric cylindrical tracking volumes consisting of open octagonal drift cells operating in Geiger mode. These cells run vertically and are staged in a 4, 2, and 3 row patterns to optimize track reconstruction. The design of the drift cells calls for 50-μm stainless steel anode and cathode wires to have a good transparency of the detector. The tracking volumes are filled with a mixture of helium gas and 4% ethyl alcohol in order to minimize multiple scattering effects. The detector is able to track electrons with energy as low as 100 keV. The electronics of Geiger cells allows the possibility of detecting delayed alpha particles.

The external walls of these tracking volumes are covered by calorimeters made of large blocks of plastic scintillator coupled to very low radioactivity 3″ and 5″ Hammamatsu PMTs. At 1 MeV, the energy resolution, which depends on the scintillator shape and on the associated PMT, ranges from 11 to 15% (FWHM) and the time resolution is 250 ps (σ). The detection threshold is 30 keV. Time and energy calibrations will be checked daily by a laser and fiber optics system. The

* This article was submitted by the authors in English.

[1)] NEMO Collaboration: CEN—Bordeaux-Gradignan, France; CFR—Gif/Yvette, France; Charles University in Prague, Czech Republic; IReS—Strasbourg, France; Department of Physics, Jyväskylä, Finland; FNSPE—Prague, Czech Republic; INEEL—Idaho Falls, USA; INR—Kiev, Ukraine; ITEP—Moscow, Russia; JINR—Dubna, Russia; LAL—Orsay, France; LPC—Caen, France; MHC—South Hadley, USA.

complete detector contains 6180 Geiger cells and 1940 scintillators.

Additionally, a solenoid capable of producing a field of 30 Gs will surround the detector to reject pair-production events. An external shielding in the form of 20 cm of low activity iron will reduce gamma-ray flux. Finally an additional 20-cm polyethylene shielding will be introduced to suppress the contribution of neutrons. This will be detailed in Section 4.

The radioactivity of the materials which have gone into the construction of the detector has been measured with HPGe detectors at the Fréjus underground laboratory or at the CENBG laboratory in Bordeaux. The activities of the mechanical pieces which frame the detector are required to be less than 1 Bq/kg.

3. BACKGROUND INDUCED BY NATURAL RADIOACTIVITY INSIDE THE SOURCE

3.1. Description

In the NEMO detector, a signal from ^{100}Mo $\beta\beta(0\nu)$ decay is expected between 2.8 and 3.2 MeV depending on the energy resolution of the calorimeter as well as the energy loss by the electrons inside the source foil. In this energy range the only natural activities are from ^{214}Bi (Q_β = 3.2 MeV) and ^{208}Tl (Q_β = 5.0 MeV). These nuclei present in the source decay by β emission and a secondary electron can be produced by internal conversion, by the Compton effect from photons of the cascades, or by Möller scattering simulating a $\beta\beta(0\nu)$ emission. The $\beta\beta(2\nu)$ decays ultimately define the half-life limits to which the $\beta\beta(0\nu)$ decays can be studied. Indeed, the tail of the $\beta\beta(2\nu)$ decays contributes due to the energy resolution, which is the sum of two effects: energy resolution of the calorimeter and energy lost in the source foil.

3.2. Expected Contributions

To limit the contribution of $\beta\beta(2\nu)$ events in the energy range of neutrinoless double-beta decay, some improvements have been made to lower the energy resolution of the calorimeter. The actual performance is closed to the final limit imposed by the thickness of the source foil.

The internal component from ^{214}Bi and ^{208}Tl contaminations in the source foil are seriously minimized. The maximum acceptable activities of ^{214}Bi and ^{208}Tl in the source foil are calculated to be at the same contribution level as the $\beta\beta(2\nu)$-background events. To reach the required activities, several processes of both physical and chemical purification of the source foils have been developed.

The table summarizes the expected background for the considered $\beta\beta$ isotopes. For ^{100}Mo, it is believed that these limits can be reached, whereas, for ^{82}Se with a longer $\beta\beta(2\nu)$-decay half-life, more stringent levels are sought and will require some additional research.

NEMO 3 expected background rate and maximum acceptable activities (mBq/kg) in ^{214}Bi and ^{208}Tl

Isotope	Events/yr			mBq/kg	
	^{214}Bi	^{208}Tl	$\beta\beta2\nu$	^{214}Bi	^{208}Tl
^{100}Mo	0.4	0.4	1.1	0.3	0.02
^{82}Se	0.1	0.1	0.1	0.07	0.005
^{150}Nd	None	0.4	1.1	None	0.02

Note that the energetic decay of ^{150}Nd ($Q_{\beta\beta}$ = 3.368 MeV) removes the background from ^{214}Bi, but new techniques to enrich Nd will have to be developed for this to be realized.

4. EXTERNAL BACKGROUND

4.1. Description

The external background of a $\beta\beta(0\nu)$ signal is due to high-energy gamma rays (>2.6 MeV) crossing the source foil. Their origin is from neutron capture occurring inside the detector. The interactions of these photons in the foil can lead to the production of two electrons by e^+e^- pair creation, double Compton effect, or Compton effect following by a Möller scattering. To understand this background component, several tests with different types of shielding have been performed. The low-energy photon flux coming from photomultiplier tubes and other surrounding materials does not contribute to the background at the $\beta\beta(0\nu)$ energy.

4.2. Study of the Neutron-Induced Background

Most of the high-energy gamma rays produced by (n, γ) reactions interact in the scintillators and create Compton electrons crossing the detector ("one crossing electron" events). This has been proved by putting an AmBe source near the NEMO 2 prototype and comparing to the data with and without a neutron source. The number of events increases as shown in Fig. 1. A peak around 2 MeV can be noticed, due to 2.2 MeV gamma

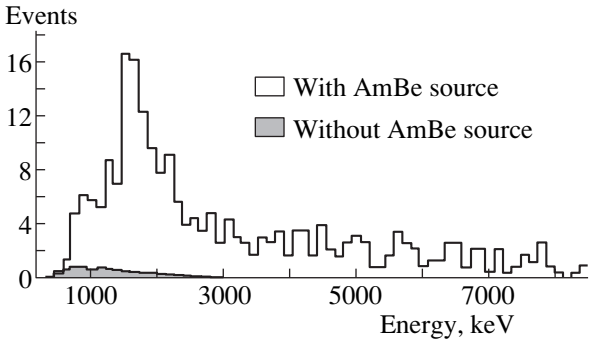

Fig. 1. Energy sum of "one crossing electron" events recorded with and without neutron source during 1 h.

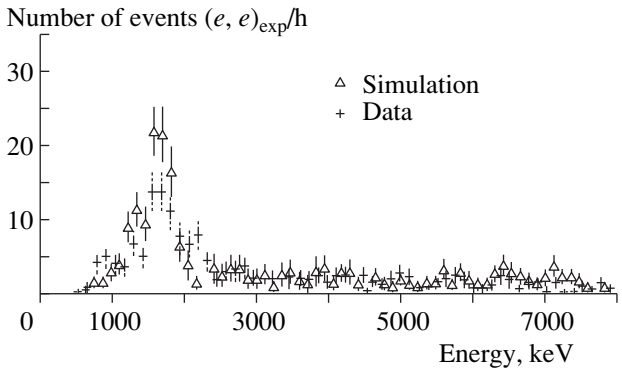

Fig. 2. Comparison of simulated and experimental energy spectrum of "one crossing electron" events for 1 h with the AmBe source located near the NEMO 2 prototype.

rays coming from neutron captures in hydrogen. High-energy events correspond to neutron captures in iron and copper frames of the detector.

The simulations based on the GEANT/MICAP code with a new photon library developed by the collaboration for γ rays emitted after (n, γ) captures and inelastic scattering reproduce well the number and the shape of the spectrum (Fig. 2) of the recorded events.

4.3. Expected Neutron Background in the NEMO 3 Detector

The simulations of the neutrons in the NEMO 3 detector achieved with 20 cm of iron shielding lead to a rate of 260 ± 110 (this error is due to the measured neutron flux uncertainty) for charged tracks events (similar to ββ(0ν) events) with an energy greater than 2.8 MeV for 5 yr of data taking and 10 kg of ^{100}Mo. The 30-Gs magnetic field permits one to reject 95% of (e^+, e^-) pairs. So, the number of remaining events becomes 50 ± 20.

An added neutron shielding of 20 cm of borated polyethylene placed outside the iron shielding allows us to reach 0.5 ± 0.3 events in 5 yr with an energy greater than 2.8 MeV corresponding to less than 0.1 event (at 90% C.L.) in the energy range of a ββ(0ν) signal (2.8–3.2 MeV for ^{100}Mo).

5. CONCLUSION

It has been shown that with 10 kg of ^{100}Mo and 5 yr of data acquisition, a total of 9.5 background events is expected in the NEMO 3 detector in the ββ(0ν)-energy region. This leads to a sensitivity of 2×10^{24} yr for a 5σ-ββ(0ν) signal effect corresponding to an effective neutrino mass between 0.4 and 0.9 eV, depending on the nuclear matrix elements. In terms of a limit, the sensitivity is of 5.5×10^{24} yr, which gives a limit in the range 0.2–0.6 eV for $\langle m_\nu \rangle$. More stringent limits could be reached with the NEMO 3 detector by replacing the ^{100}Mo with ^{82}Se or ^{150}Nd. In addition, the NEMO 3 detector will measure ββ(2ν)-energy spectrum and angular distribution with very high statistics (10^6 events/yr with 10 kg of ^{100}Mo). It will also be sensitive to the ββ(0ν) decay with Majoron emission at the level of 10^{23} yr and up to 10^{22} yr for double-beta decay to excited states.

Data taking with the full detector, now under construction in the Fréjus underground laboratory, is planned for summer 2000.

REFERENCES

1. D. Dassie *et al.*, Nucl. Instrum. Methods A **309**, 465 (1991).
2. R. Arnold *et al.*, Nucl. Instrum. Methods A **354**, 338 (1995).
3. R. Arnold *et al.*, Nucl. Instrum. Methods A **401**, 144 (1997).
4. D. Dassie *et al.*, Phys. Rev. D **51**, 2090 (1995).
5. R. Arnold *et al.*, Z. Phys. C **72**, 239 (1996).
6. R. Arnold *et al.*, Nucl. Phys. A **636**, 209 (1998).
7. NEMO Collab., submitted to Nucl. Phys. A.
8. NEMO 3 Proposal, Preprint No. 94-29, LAL (Orsay, 1994).

Physics of Atomic Nuclei, Vol. 63, No. 7, 2000, pp. 1225–1228. From Yadernaya Fizika, Vol. 63, No. 7, 2000, pp. 1299–1302.

EXPERIMENTAL RESULTS, METHODS, AND FACILITIES

Recent Results of the IGEX ^{76}Ge Double-Beta Decay Experiment*

C. E. Aalseth[1], F. T. Avignone III[1], R. L. Brodzinski[2], S. Cebrian, D. Gonzáles, E. García, W. K. Hensley[2], I. G. Irastorza, I. V. Kirpichnikov[3], A. A. Klimenko[4], H. S. Miley[2], A. Morales, J. Morales, A. Ortiz de Solórzano, S. B. Osetrov[4], V. S. Pogosov[5], J. Puimedón, J. H. Reeves[2], M. L. Sarsa, S. Scopel, A. A. Smolnikov[4], **, A. S. Starostin[3], A. G. Tamanyan[5], A. A. Vasenko[3], S. I. Vasiliev[4], and J. A. Villar

University of Zaragoza, Spain

Abstract—The International Germanium Experiment (IGEX) has now analyzed 117 mol yr of data from its isotopically enriched (86% ^{76}Ge) germanium detectors. Applying pulse shape discrimination (PSD) to the more recent data, the lower bound on the half-life for neutrinoless double-beta decay of ^{76}Ge is deduced: $T_{1/2}(0\nu) > 1.57 \times 10^{25}$ yr (90% C.L.). This corresponds to an upper bound on the Majorana neutrino mass parameter, $\langle m_\nu \rangle$, between 0.33 eV and 1.35 eV depending on the choice of theoretical nuclear matrix elements used in the analysis. © *2000 MAIK "Nauka/Interperiodica".*

1. INTRODUCTION

Data from the SuperKamiokande detector [1] confirm earlier evidence [2–4] that muon neutrinos created in the atmosphere oscillate to tau neutrinos (or sterile neutrinos). In addition, excess events from the reaction $p(\bar{\nu}_e, e^+)n$ in the LSND data have also been attributed to $\bar{\nu}_\mu \longrightarrow \bar{\nu}_e$ oscillations [5]. These data support the conclusion that the solar neutrino problem is due to neutrino oscillations and not some unforeseen subtle difficulty with the solar models [6, 7]. The KARMEN experiment was earlier thought to exclude the LSND signal [8]; however, more recent data and a new interpretation [9] lead to the conclusion that KARMEN will not be able to cover a large portion of the $\sin^2 2\theta$ vs. δm^2 parameter space allowed by the LSND signal. The CHOOZ reactor neutrino experiment result excludes this parameter space region where the positive SuperKamiokande signal exists [10], eliminating the possibility that ν_μ created in the atmosphere oscillate to ν_e. It is difficult to interpret all of these results in the same scenario of δm^2_{ij} and $\sin^2 2\theta_{ij}$ even using three neutrino families; nevertheless, it is clear that neutrinos likely have properties (mass and flavor mixing) outside the structure of the standard model. Accordingly, sensitive searches for neutrinoless double-beta ($0\nu\beta\beta$) decay are more important than ever. Experiments involving kilogram quantities of germanium, isotopically enriched in ^{76}Ge, have thus far proven to be the most sensitive, specifically IGEX [11] and the Heidelberg–Moscow experiments [12].

If one accepts the standard solar model of Bahcall and his coworkers, the deficit in the solar-ν_e flux on earth is explained by the Mikheyev–Smirnov–Wolfenstein (MSW) resonant oscillation. Until recently, the acceptable regions in the parameter space, δm^2 vs. $\sin^2 2\theta$, were not thought to be compatible with neutrino masses that would render $0\nu\beta\beta$ decay directly observable. A paper by Petcov and Smirnov [13] reconciles both the MSW and vacuum oscillation solutions of the solar neutrino problem with the possibility of $0\nu\beta\beta$ decay having an effective Majorana electron neutrino mass in the range 0.1 to 1.0 eV. This range may be observable in ^{76}Ge double-beta decay experiments. Isotopically enriched ^{76}Ge experiments are presently the most sensitive probe of $0\nu\beta\beta$ decay with electron emission only, which is predicted to leave a unique signal of 2038.56 keV. Present experiments each have ~100 moles of ^{76}Ge, efficiencies of ~95%, and energy resolutions of ~0.2%. These figures of merit make the choice of ^{76}Ge more advantageous than ^{100}Mo, ^{136}Xe, or ^{150}Nd, even though the latter have significantly larger predicted decay rates for the same effective Majorana neutrino mass. However, new cryogenic techniques could make ^{130}Te a competitive choice for next generation $\beta\beta$-decay experiments [14]. The analysis of 117 mol yr of data from the IGEX experiment is presented in this report.

* This article was submitted by the authors in English.

** e-mail: smolm@nusun.jinr.ru

[1] University of South Carolina, Columbia, USA.

[2] Pacific Northwest National Laboratory, Richland, USA.

[3] Institute for Theoretical and Experimental Physics, Moscow, Russia.

[4] Institute for Nuclear Research, Russian Academy of Sciences, Baksan Neutrino Observatory, and Joint Institute for Nuclear Research, Dubna, Russia.

[5] Yerevan Physical Institute, Armenia.

Table 1. Nuclear structure factors F_N and Majorana neutrino mass parameters $\langle m_\nu \rangle$ for $T^{0\nu}_{1/2} = 1.57 \times 10^{25}$ yr

F_N, yr^{-1}	Model	$\langle m_\nu \rangle$, eV
1.56×10^{-13}	Shell model [17]	0.33
9.67×10^{-15}	QRPA [19]	1.35
1.21×10^{-13}	QRPA [20]	0.38
1.12×10^{-13}	QRPA [22]	0.38
1.41×10^{-14}	Shell model [23]	1.09

Table 2. IGEX data after the partial application of PSD for 117 mol yr (the starting energy of each 2-keV bin is given)

Energy	Events	Energy	Events
2020	2.9	2042	5.5
2022	9.1	2044	6.0
2024	3.4	2046	1.7
2026	2.0	2048	5.3
2028	4.6	2050	3.4
2030	6.5	2052	4.6
2032	2.3	2054	5.0
2034	0.6	2056	0.6
2036	0.0	2058	0.1
2038	2.0	2060	4.3
2040	1.5		

2. DOUBLE-BETA DECAY

Double-beta decay is the only known way to determine if neutrinos are Majorana particles. According to Kayser, Petcov, and Rosen [15], the observation of $0\nu\beta\beta$ decay would constitute unambiguous proof that at least one neutrino eigenstate has nonzero mass, interpreted in the context of any gauge theory. This is similar to the black-box theorem of Schechter and Valle [16].

The decay rate for lepton-number-violating ($\Delta l = 2$) $\beta\beta$ decay driven by the Majorana neutrino mass can be written as

$$\lambda^{0\nu}_{\beta\beta} = G^{0\nu}(E_0, Z)\langle m_\nu \rangle^2 \left| M^{0\nu}_{\mathrm{F}} - (g_A/g_V) M^{0\nu}_{\mathrm{GT}} \right|^2. \quad (1)$$

Here, $G^{0\nu}$ is the two-body phase-space factor, including coupling constants; $M^{0\nu}_{\mathrm{F}}$ and $M^{0\nu}_{\mathrm{GT}}$ are the Fermi and Gamow–Teller nuclear matrix elements, respectively; and g_V and g_A are the vector and axial-vector weak coupling constants, respectively. The quantity $\langle m_\nu \rangle$ is a weighted mixture of eigenstate neutrino masses given by

$$\langle m_\nu \rangle \equiv \left| \sum_{k=1}^{2n} \lambda_k^{CP} (U^L_{ek})^2 m_{\nu_k} \right|, \quad (2)$$

where λ_k^{CP} is the kth CP eigenvalue (± 1 for CP conservation), U^L_{ek} are the elements of the matrix that diagonalizes the neutrino mass matrix, m_{ν_k} is the mass of the kth neutrino eigenstate, and n is the number of eigenstates. The virtual neutrinos exchanged must be Majorana particles to be absorbed on a vertex identical to that of emission, and have some right-handed helicity, due to finite mass.

3. NUCLEAR STRUCTURE CONSIDERATIONS

From (1), the sensitivity of a given experiment to the parameter $\langle m_\nu \rangle$ depends directly on nuclear matrix elements. In this regard, $2\nu\beta\beta$-decay experiments have some value in testing models, although $M^{2\nu}$ and $M^{0\nu}$ are completely different. The weak-coupling shell model calculations of Haxton, Stephenson, and Strottman [17] were an extensive effort to explain the geochemical $\beta\beta$-decay half-lives of ^{128}Te, ^{130}Te, and ^{82}Se, as well as to predict the half-life of ^{76}Ge. These early calculations used the value $(g_A/g_V) = 1.24$. It was later realized a value of unity is more appropriate for a neutron decaying in a complex nucleus. The shell model prediction then became $T^{2\nu}_{1/2}(^{82}\mathrm{Se}) = 0.8 \times 10^{20}$ yr [17], which is within 20% of the value measured by the Irvine group [18].

In 1986, the CalTech group [19] introduced the quasiparticle random phase approximation (QRPA) with three parameters to take into account pairing, particle–hole, and particle–particle interactions. Later, similar models were developed by the Tübingen [20] and Heidelberg groups [21]. In all of these models, the parameter g_{pp}, characterizing the short-range particle–particle correlations, had a single value near which the $2\nu\beta\beta$-matrix elements vanish; however, it is generally agreed that the $0\nu\beta\beta$-decay matrix elements have a much softer dependence on these parameters and are thus more stable. In 1994, Faessler concluded that the inclusion of neutron–proton pairing interactions reduces the dependence of $M^{2\nu}_{\mathrm{GT}}$ on g_{pp} [22]. Recently, however, new large-space shell-model calculations by Caurier *et al.* [23], yield significantly different results as shown in Table 1. The connection between the half-life and the neutrino mass parameter of (2) is made through a nuclear structure factor, F_N, as follows [24]:

$$\langle m_\nu \rangle = m_e (F_N T^{0\nu}_{1/2})^{-1/2} \ \text{(eV)}. \quad (3)$$

Values of F_N from five theoretical approaches are given in Table 1 along with corresponding values of $\langle m_\nu \rangle$ for a half-life of 1.57×10^{25} yr.

4. THE IGEX EXPERIMENT

A complete description of the IGEX experiment was recently published [11], along with the results from analyzing ~75 mol yr of data [24]. An additional

41.9 mol yr have been added and the totals are presented in Table 2 and Fig. 1. The darkened spectrum in Fig. 1 results from applying PSD to about 15% of the 75-mol-yr data set and to the entire 41.9-mol-yr data set.

Detailed models of the crystal and associated first stage preamplifier have been constructed, and pulse shapes from various sources of background are being simulated. Programs are also being written for determining whether fast pulses from a specially constructed preamplifier have a single- or multisite character, and for determining the probability of incorrect assignment. The PSD analysis leading to the results shown in Fig. 1 used a very conservative visual technique that compared experimental pulse shapes to computed single- and multisite pulses. Figures 2 and 3 show experimental pulses with features associated with multi- and single-site events, respectively.

Figure 4 shows a sample data set in the energy region of interest before and after removing events with multisite pulse shape characteristics.

Using standard statistical techniques, there are fewer than 3.1 candidate events (90% C.L.) under a peak having FWHM = 4 keV and centered at 2038.56 keV. This corresponds to

$$T_{1/2}^{0\nu}(^{76}\mathrm{Ge}) > \frac{4.87\times10^{25}\ \mathrm{yr}}{3.1} = 1.57\times10^{25}\ \mathrm{yr}. \quad (4)$$

With the values of F_N given in Table 1, one obtains $0.33 \le \langle m_\nu \rangle \le 1.35$ eV. The readers can interpret the data given in Table 2 as they wish.

Recently the Heidelberg–Moscow collaboration published a bound on the half-life [12], employing the statistical method of Feldman and Cousins [25], which had not previously been used in this type of experiment. We have failed to reproduce their analysis using Fig. 3 of [12] and Table V of [25]. Baudis *et al.* [12] reach their conclusion based on an expectation of 13 background events in the $\pm3\sigma$ peak interval and an observation of only 7 events in that interval. The data shown in Fig. 3 of [12] clearly show 13 real events in the $\pm3\sigma$ interval, and from Table V of [25] an expectation of 13 events and an observation of 13 events correspond to $T_{1/2}^{0\nu} \ge 1.7\times10^{25}$ yr. However, analysis of the data of [12] over a $\pm2\sigma$ interval, which would contain 95.7% of the events contained in a $\pm3\sigma$ interval, produces an expectation of 8.7 events and an observation of 7 events. Again, with Table V of [25], this would correspond to $T_{1/2}^{0\nu} \ge 3.1\times10^{25}$ yr, which makes the bound on the number of $0\nu\beta\beta$-decay events very sensitive to the energy interval chosen for the analysis [26].

We conclude that the statistical method of [25] should be applied with great care in this type of experiment, in which the energy distribution of background events is very different from that of the hypothesized real events. As further proof of this conclusion, we subject our data from Table 2 above to the same analysis

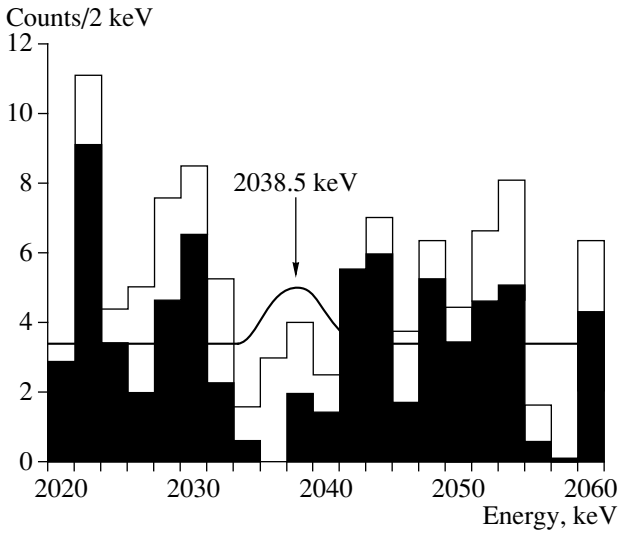

Fig. 1. Histograms from 117 effective mole years of IGEX data. Energy bins are labeled on the left edge. The darkened spectrum results from the application of PSD to ~45% of the total data set. The Gaussian curve represents the 90% C.L. constraint of ≤3.1 $0\nu\beta\beta$-decay events and has a FWHM of ~4 keV, corresponding to the energy resolution of the entire experiment.

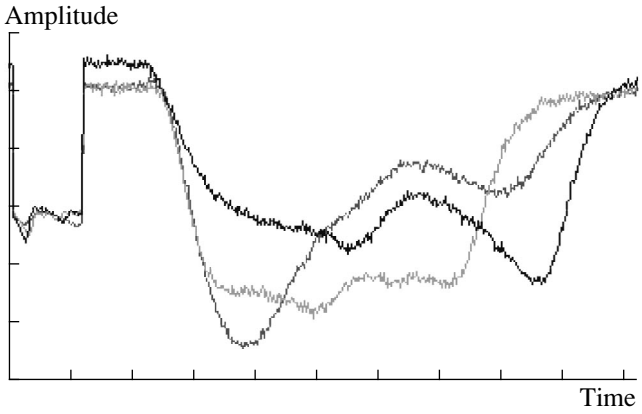

Fig. 2. Examples of fast pulses from a specially constructed preamplifier that are interpreted as resulting from multisite interactions in the crystal.

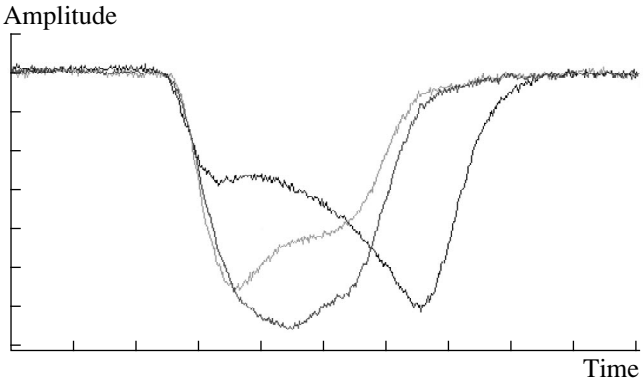

Fig. 3. Examples of fast pulses that do not have the obvious characteristics of multisite interactions in the crystal.

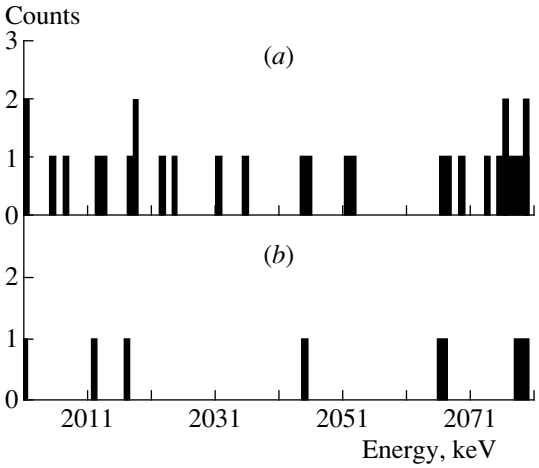

Fig. 4. A 237-d sample of data (*a*) without applying PSD and (*b*) after the application of PSD.

procedure. Based on a $\pm 3\sigma$ interval, $T_{1/2}^{0\nu} \geq 2.4 \times 10^{25}$ yr, and based on a $\pm 2\sigma$ interval, $T_{1/2}^{0\nu} \geq 3.7 \times 10^{25}$ yr, both of which are more stringent than the corresponding results from [12]. However, since the number of mole years of accumulated data in [12] is greater than in our data, and since the background in [12] is even lower than in our data, it is not plausible that our data should produce more sensitive results.

Pulse-shape-discrimination methods are under development to provide an effective, objective method for eliminating spectral background with a well-characterized efficacy. These methods exploit the unique high-bandwidth signal recovered from a modified preamplifier.

One method consists of a precise simulation of energy transport, charge deposition, and pulse formation to construct the optimum algorithm for pulse selection. This method requires an accurate model of the electric fields in the germanium crystal and a complete functional description of the preamplifier. One benefit of this approach is that a potential pulse selection algorithm can be evaluated against a contrived ensemble of pulses.

Other approaches are being pursued in parallel, including model-independent reconstruction of the detector displacement current. This will allow development of discrimination techniques based on the physics of the detector and the charge collection process. These techniques are currently being evaluated and are expected to be available for application to IGEX data by the end of 1999.

ACKNOWLEDGMENTS

The Canfranc Astroparticle Underground Laboratory is operated by the University of Zaragoza under contract AEN96-1657. The research is partially funded by the Spanish Commission for Science and Technology (CICYT), the US National Science Foundation, and the U.S. Department of Energy. The isotopically enriched ^{76}Ge was supplied by the Institute for Nuclear Research (INR), Moscow, and the Institute for Theoretical and Experimental Physics (ITEP), Moscow.

REFERENCES

1. Y. Fukuda *et al.*, Phys. Rev. Lett. **81**, 1562 (1998); **82**, 2644 (1999).
2. Y. Fukuda *et al.*, Phys. Lett. B **335**, 237 (1994).
3. M. C. Goodman *et al.*, in *Proceedings of International Conference "Neutrino-94"*; Nucl. Phys. B (Proc. Suppl.) **38**, 337 (1995).
4. S. Ahlen *et al.*, Phys. Rev. Lett. **72**, 608 (1994).
5. C. Athanassopolous *et al.*, Phys. Rev. Lett. **77**, 3082 (1996).
6. S. Nussinov, in *Proceedings of International Conference "Neutrino-94"*; Nucl. Phys. B (Proc. Suppl.) **38**, 497 (1995).
7. J. Bahcall, S. Basu, and N. H. Pinsonneault, Phys. Lett. B **433**, 1 (1998).
8. B. Zeitnitz, in *Proceedings of International Conference "Neutrino-98"*; Nucl. Phys. B (Proc. Suppl.) **77**, 212 (1999).
9. C. Giunti, hep-ph/9808405.
10. M. Apollonio *et al.*, Phys. Lett. B **420**, 397 (1998).
11. C. E. Aalseth *et al.*, Phys. Rev. C **59**, 2108 (1999).
12. L. Baudis *et al.*, Phys. Rev. Lett. **83**, 41 (1999).
13. S. Petcov and Yu. Smirnov, Phys. Lett. B **322**, 109 (1994).
14. E. Fiorini, Yad. Fiz. **61**, 1243 (1998) [Phys. At. Nucl. **61**, 1137 (1998)].
15. B. Kayser, in *Proceedings of the 23th International Conference on High Energy Physics, 1987*, Ed. by S. C. Loken (World Sci., Singapore, 1987), p. 945; S. P. Rosen, *Symmetries and Fundamental Interaction in Nuclei*, Ed. by W. C. Haxton and E. M. Henley (World Sci., Singapore, 1995), p. 251.
16. J. Schechter and J. W. F. Valle, Phys. Rev. D **25**, 2951 (1982).
17. W. C. Haxton, G. J. Stephenson, Jr., and D. Strottman, Phys. Rev. D **25**, 2360 (1981).
18. S. R. Elliott *et al.*, J. Phys. G: Nucl. Part. Phys. **17**, S145 (1991); Phys. Rev. C **46**, 1535 (1992).
19. P. Vogel and M. R. Zirnbauer, Phys. Rev. Lett. **57**, 3148 (1986).
20. O. Civitarese, A. Faessler, and T. Tomoda, Phys. Lett. B **194**, 11 (1987); T. Tomoda and A. Faessler, Phys. Lett. B **199**, 475 (1987).
21. K. Muto, E. Bender, and H. V. Klapdor, Z. Phys. A **334**, 177 (1989); the matrix elements used in Table 1 are from A. Staudt, K. Muto, and H. V. Klapdor, Europhys. Lett. **13**, 31 (1990).
22. A. Faessler, Prog. Part. Nucl. Phys. **32**, 1 (1994).
23. E. Caurier *et al.*, Phys. Rev. Lett. **77**, 1954 (1996).
24. A. Morales, Nucl. Phys. B (Proc. Suppl.) **77**, 335 (1999).
25. J. G. Feldman and R. D. Cousins, Phys. Rev. D **57**, 3873 (1998).
26. F. T. Avignone III, C. E. Aalseth, and R. L. Brodzinski, submitted to Phys. Rev. Lett. (1999).

Physics of Atomic Nuclei, Vol. 63, No. 7, 2000, pp. 1229–1237. From Yadernaya Fizika, Vol. 63, No. 7, 2000, pp. 1303–1311.

EXPERIMENTAL RESULTS, METHODS, AND FACILITIES

New Phase of the ^{116}Cd 2β-Decay Experiment with $^{116}CdWO_4$ Scintillators*

F. A. Danevich, V. V. Kobychev, B. N. Kropivyansky, A. S. Nikolaiko, O. A. Ponkratenko, V. I. Tretyak, Yu. G. Zdesenko, P. G. Bizzeti[1)], T. F. Fazzini[1)], and P. R. Maurenzig[1)]

Institute for Nuclear Research, National Academy of Sciences of Ukraine, pr. Nauki 47, MSP 04680 Kiev, Ukraine

Abstract—A new step of the ^{116}Cd 2β-decay experiment is in progress at the Solotvina Underground Laboratory. The upgraded setup consists of four enriched $^{116}CdWO_4$ crystal scintillators of total mass 339 g. As an active shield, 15 $CdWO_4$ crystals (20.6 kg) are used. The background rate (in the energy interval 2.7–2.9 MeV) is 0.06 count/(yr kg keV), one order of magnitude lower than in the previous apparatus. Combined with results of preceding measurements, the half-life limit for the neutrinoless 2β decay of ^{116}Cd to the ground state of ^{116}Sn is determined as $T_{1/2}(0\nu) \geq 5.1 \times 10^{22}$ yr with 90% C.L. The limits on $T_{1/2}$ for transitions to the excited 2_1^+ and 0_1^+ levels of ^{116}Sn are 8.6×10^{21} and 4.1×10^{21} yr, respectively (at a 90% C.L.). For 0ν2β decay accompanied by the emission of one and two Majorons, the constraints on the half-life are $T_{1/2}(0\nu M1) \geq 1.4 \times 10^{21}$ yr and $T_{1/2}(0\nu M2) \geq 4.1 \times 10^{20}$ yr (at a 90% C.L.). The corresponding constraints on the neutrino mass and the neutrino–Majoron coupling constant are $\langle m_\nu \rangle \leq 3.1$ eV and $\langle g_M \rangle \leq 1.9 \times 10^{-4}$, respectively. © *2000 MAIK "Nauka/Interperiodica".*

1. INTRODUCTION

With the aim of extending the number of 2β-decay candidate nuclides studied at a sensitivity comparable with that for ^{76}Ge and ^{136}Xe (a neutrino-mass limit of 1–3 eV [1]), scintillators made of cadmium tungstate crystal and enriched in ^{116}Cd to 83% were used in ^{116}Cd research [2, 3]. The measurements were performed in the Solotvina Underground Laboratory (SUL) in a salt mine 430 m below sea level (about 1000 mwe) [4]. The $^{116}CdWO_4$ crystal (15.2 cm^3) viewed by a FEU-110 photomultiplier tube (PMT) through a light guide 51 cm long was placed inside a plastic scintillator (∅38 × 115 cm) that served as a veto detector. Passive shield of high-purity copper (5 cm), lead (23 cm), and polyethylene (16 cm) surrounded the plastic counter with the main detector. The detector background rate in the vicinity of energy release in the 2β decay of ^{116}Cd ($Q_{2\beta}$ = 2805(4) keV [5]) was reduced to a level of 0.6 count/(yr kg keV) [2, 3]. On the basis of total statistics collected over 19175 h ($Nt = 3.63 \times 10^{23}$ nucleus yr, where N is the number of ^{116}Cd nuclei and t is the measurement time), the half-life limit for the neutrinoless 2β decay of ^{116}Cd was found to be given by $T_{1/2}(0\nu) \geq 3.2 \times 10^{22}$ yr (at a 90% C.L.) [3]. Calculations revealed that [6] this value corresponds to the following limits on the neutrino mass and right-handed admixtures in weak interaction: $\langle m_\nu \rangle \leq 4.4$ eV, $\langle \eta \rangle \leq 5.7 \times 10^{-8}$, and $\langle \lambda \rangle \leq 5.0 \times 10^{-6}$; neglecting the right-handed contribution, we arrive at $\langle m_\nu \rangle \leq 3.9$ eV. The calculations from [7] lead to a similar result: $\langle m_\nu \rangle \leq 3.5$ eV. In accordance with [8], the R-parity-violating parameter of the minimal SUSY Standard Model is restricted by our $T_{1/2}$ limit as $\varepsilon \leq 1.1 \times 10^{-3}$. Also, limits on 0ν2β-decay modes involving the emission of one (M1) or two (M2) Majorons were established: $T_{1/2}(0\nu M1) \geq 1.2 \times 10^{21}$ yr and $T_{1/2}(0\nu M2) \geq 2.6 \times 10^{20}$ yr (at a 90% C.L.) [9]. By using the calculated nuclear matrix elements and the phase-space integral for ^{116}Cd [10], the limit on the Majoron–neutrino coupling constant was determined as $\langle g_M \rangle \leq 2.1 \times 10^{-4}$, at a level compared with the best results obtained for other nuclei [1].

2. NEW SETUP WITH FOUR $^{116}CdWO_4$ DETECTORS

2.1. New Setup and Measurements

In order to enhance the sensitivity of the ^{116}Cd experiment, the following improvements were scheduled: an increase in the number of ^{116}Cd nuclei, a reduction of the background, and an advance in the data taking and processing [3]. With this aim, the upgraded setup with four enriched $^{116}CdWO_4$ crystals (total mass of 339 g) was mounted at the SUL in August 1998. All the materials used in the apparatus were previously tested and selected for low radioactive impurities in order to avoid their contributions to the background.

* This article was submitted by the authors in English.

[1)] Dipartimento di Fisica, Universitá di Firenze, and Istituto Nazionale di Fisica Nucleare, Sezione di Firenze, Largo E. Fermi 2, I-50125 Firenze, Italy.

In the new apparatus, enriched crystals were viewed by the PMT (EMI9390KFLB53) through a light guide 10 cm in diameter and 55 cm long, which is composed of two glued parts: quartz 25 cm long and plastic scintillator (Bicron BC-412) 30 cm long. The enriched crystals are surrounded by an active shield made from fifteen natural $CdWO_4$ scintillators of large volume (about 200 cm^3 each) with a total mass of 20.6 kg. This active shield provides an effective suppression of background in the energy region of interest owing to the large density (8 g/cm^3) and the high purity of $CdWO_4$ crystals [11]. The later are viewed by a low-background PMT (FEU-125) through an active plastic light guide (17 cm in diameter and 49 cm long). In turn, the entire array of $CdWO_4$ detectors is placed within the additional active shield made from polystyrene-based plastic scintillator of dimensions $40 \times 40 \times 95$ cm^3. Together with active light guides (connected to enriched and natural $CdWO_4$ crystals), a complete 4π active shield of the main $^{116}CdWO_4$ detectors is therefore provided.

The outer passive shield surrounds plastic scintillators and consists of high-purity copper (thickness 3–6 cm), lead (22.5–30 cm), and polyethylene (16 cm). Two plastic scintillators ($120 \times 130 \times 3$ cm^3) are installed above the passive shield to ensure cosmic-muon veto. Because the air in the SUL contains radon (about 30 Bq/m^3), the setup is isolated carefully to avoid any penetration of the air into the detectors. All cavities inside the shield were filled with pieces of Plexiglas, and a high-purity Cu shield was sealed with the aid of silicon glue and enclosed inside a tight Mylar envelope.

The new event-by-event data acquisition is based on two IBM PCs and a CAMAC crate with electronic units. The system allows one to carry out measurements with up to 16 independent channels. For each event, the following information is stored on the hard disk of the first computer: the amplitude (energy) of a signal, its arrival time, and additional tags (coincidence between different detectors and signal of a radionoise-detection system; and triggers for the light-emitting diode and the pulse-shape digitizer). The second computer allows one to record the pulse shape of the $^{116}CdWO_4$ scintillators in the energy range 0.25–5 MeV. This complementary system is developed on the basis of a fast 12-bit ADC (Analog Devices AD9022) and is connected to a computer by a parallel digital I/O board (PC-DIO-24 from National Instruments) [12]. Two additional PC-DIO-24 boards are used to link both computers and to establish (with the aid of the corresponding software) a one-to-one dependence between information stored in the first PC and the pulse-shape data recorded by the second computer.

The energy calibration is performed weekly by using a ^{207}Bi source (γ rays with energies of 570, 1064, and 1770 keV) and once per two weeks by using ^{232}Th (2615 keV). The resolution of the main detector (four enriched crystals taken as a whole) was 14.5% at 1064 keV and 11% at 2615 keV. During measurements, the dead time of the spectrometer and data acquisition is monitored permanently with the aid of a light-emitting diode optically connected to the PMT of the enriched $^{116}CdWO_4$ scintillators. The background spectrum of the four $^{116}CdWO_4$ crystals measured over 4056 h in the new apparatus is shown in Fig. 1, which also displays, for the sake of comparison, the data obtained with the old apparatus using one $^{116}CdWO_4$ crystal of mass 121 g. As can be seen from this figure, the background is decreased over the entire energy range owing to the improved shielding and the pulse-shape analysis of the data (see below). The only exception is the β spectrum of ^{113}Cd ($Q_\beta = 316$ keV), which is present in the $^{116}CdWO_4$ crystals with an abundance of 2.15% [2]. The background rate in the energy region of interest (2.7–2.9 MeV), where we expect the peak corresponding to the $0\nu2\beta$ decay of ^{116}Cd, is reduced to 0.06 count/(yr kg keV) (2 events over 4056 h), which is one order of magnitude lower than that in the previous apparatus.

2.2. Time–Amplitude Analysis

As was shown previously [13], information about the arrival time for each event can be used to analyze and select some decay chains in ^{232}Th, ^{235}U, and ^{238}U families like ^{214}Bi ($Q_\beta = 3.3$ MeV) $\longrightarrow$ ^{214}Po ($Q_\alpha = 7.8$ MeV, $T_{1/2} = 164.3$ μs) $\longrightarrow$ ^{210}Pb or ^{220}Rn ($Q_\alpha = 6.4$ MeV) $\longrightarrow$ ^{216}Po ($Q_\alpha = 6.9$ MeV, $T_{1/2} = 0.145$ s) $\longrightarrow$ ^{212}Pb. The energies of the first and second decays and the time interval between events are used to enhance sensitivity and to reach higher accuracy in determining the trace radioactive contaminants in the detector. By way of example (important in the following for the analysis of the background in the region of the $0\nu2\beta$ decay of ^{116}Cd), the events in the decay chain $^{220}Rn \longrightarrow ^{216}Po \longrightarrow ^{212}Pb$, which were selected from a 2822.7-h run, are shown in Fig. 2. Taking into account the contribution from accidental coincidences (4 pairs from 107 selected), we found that the activity of ^{228}Ac (^{232}Th family) inside the $^{116}CdWO_4$ crystals is as low as 39(4) μBq/kg.

The relative light yield for α and β particles and the energy resolution of the detector for α particles were also determined from the time–amplitude analysis. The results are $\alpha/\beta = 0.148 + 0.0072E_\alpha$ (E_α is measured in MeV) and $\mathrm{FWHM}_\alpha\,(E_\alpha) = 0.0444E_\alpha$.

2.3. Pulse-Shape Discrimination

The shape of the pulse in the $^{116}CdWO_4$ scintillators in the energy region 0.25–5 MeV is digitized by the 12-bit ADC and stored in 2048 channels with a channel width of 50 ns. On the basis of the optimal digital filter, the method of pulse-shape (PS) discrimination was developed [12] to process scintillation pulses from the

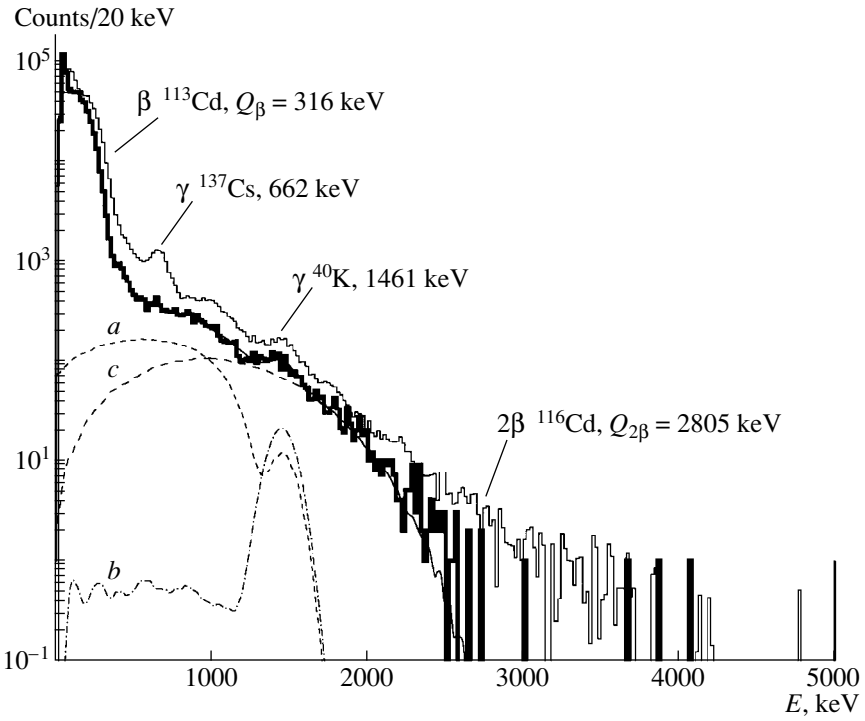

Fig. 1. Background spectrum of $^{116}CdWO_4$ detectors (339 g) measured in the new setup over 4056 h (thick histogram). The old data obtained with 121-g $^{116}CdWO_4$ crystal over 19986 h are shown for the sake of comparison (thin histogram; the data are normalized to the time of measurements and the mass of the new detector). The background components used for fitting in the energy region 950–2900 keV are (curve *a*) ^{40}K inside the $^{116}CdWO_4$ detector [activity value from the fit is 1.7(2) mBq/kg], (curve *b*) ^{40}K in the shielding of $CdWO_4$ crystals [1.7(4) mBq/kg], and (curve *c*) 2ν2β decay of ^{116}Cd ($T_{1/2}(2\nu2\beta) = 2.3(2) \times 10^{19}$ yr].

$CdWO_4$ crystals. Owing to the different shapes of the scintillation signals for different kinds of sources (α particles, protons, photons, and cosmic muons were investigated), a clear discrimination between γ rays and γ particles was achieved [12]. A numerical characteristic of the shape (shape indicator, further abbreviated as SI) has a slight dependence on the particle energy (with the slope of about –1%/1 MeV) and lies in the region $SI_\gamma = 20.0 \pm 2.8$ for photons and $SI_\alpha = 28.5 \pm 3.2$ for α particles (the values are given for 0.9-MeV photons and 4.8-MeV α particles). The technique of pulse-shape selection ensures the very important possibility of discriminating "illegal" events, such as double pulses and α events, and thereby suppressing the background. The example of a double pulse is shown in Fig. 3*a*. The value of the shape indicator for the full signal is SI = 12.0; for the first pulse, it is $SI_1 = 20.2$ (hence, it corresponds to a γ or a β particle). For the second pulse, we have $SI_2 = 27.8$ (α particle). The energy release is 2.99 MeV, and, without a PS analysis, it would be a candidate event for the 0ν2β decay of ^{116}Cd. By way of illustration, Fig. 4 displays the spectra of the $^{116}CdWO_4$ scintillators in the energy region 1.2–5 MeV that were collected over 4056 h in anticoincidence with the active shield. Figure 4*a* presents the initial spectrum without pulse-shape selection, while Fig. 4*b* shows this spectrum after a PS selection of events whose SI lies in the interval $SI_\gamma \pm 2.58\sigma$ (SI_γ) (it contains 99% of γ/β events). From these figures, the background reduction due to pulse-shape analysis is obvious. Further, Fig. 4*c* shows the distribution of events with $SI \geq SI_\gamma + 2.58\sigma(SI_\gamma)$. These events, at least for energies in excess of 2 MeV, can be produced by the ^{228}Ac activity from the intrinsic contamination of the $^{116}CdWO_4$ crystals (measured by the time–amplitude analysis as described above). Indeed, two decays in the fast chain ^{212}Bi (Q_β = 2.3 MeV) ⟶ ^{212}Po (Q_α = 9.0 MeV, $T_{1/2}$ = 0.3 μs) ⟶ ^{208}Pb cannot be time-resolved in the $CdWO_4$ scintillator (decay time is about 15 μs [11, 12]) and will result in one event. The response function of the $^{116}CdWO_4$ detectors for the ^{228}Ac chain was simulated with the aid of the GEANT3.21 package [14]; the initial kinematics of events (how many particles are emitted, their types, energies, and directions and times of emission) was determined with the event generator DECAY4 [15]. One can see from Fig. 4*c* that the high-energy tail of the experimental spectrum is well reproduced by the expected response for ^{212}Bi ⟶ ^{212}Po ⟶ ^{208}Pb decays. The corresponding activity of ^{228}Ac inside the $^{116}CdWO_4$ crystals, as obtained from the fit in the energy range between 2.6 and 3.6 MeV, is 34(5) μBq/kg, in

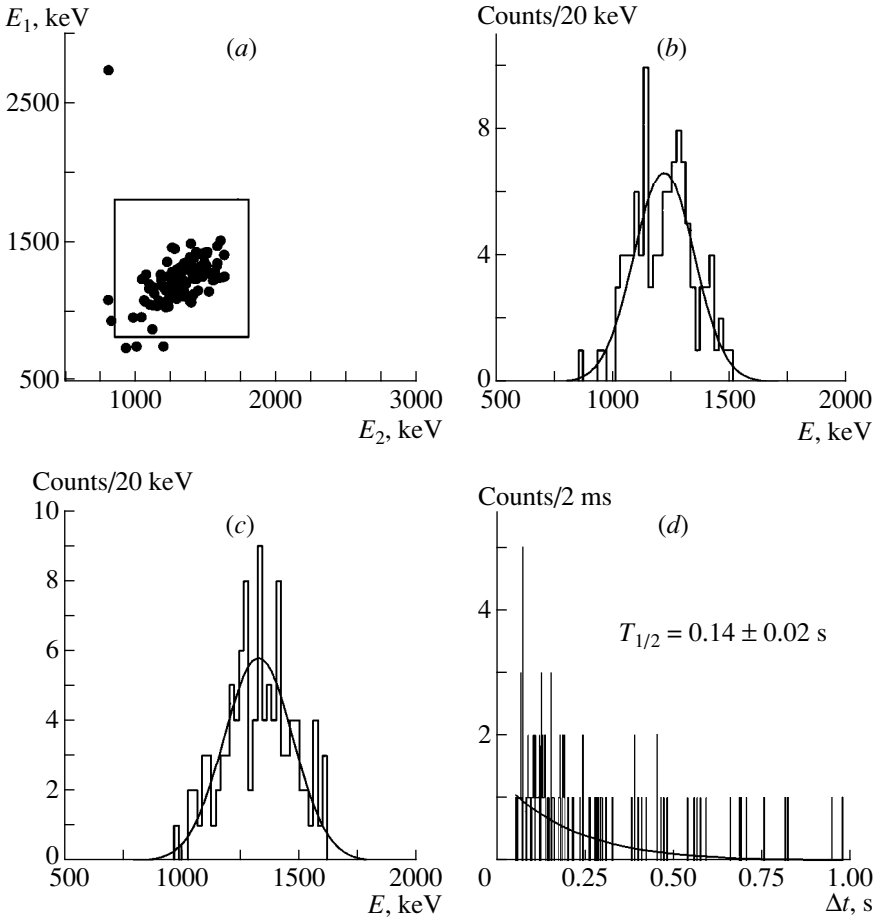

Fig. 2. (*a*) Two-dimensional and (*b* and *c*) one-dimensional energy spectra of first and second α particles in the decay chain ^{220}Rn (Q_α = 6.4 MeV) ⟶ ^{216}Po (Q_α = 6.9 MeV, $T_{1/2}$ = 0.145 s) ⟶ ^{212}Pb ($^{116}CdWO_4$ 339 g, 2822.7 h). Because α/β ratio is less than unity, the equivalent energy on the scale of photon energies is nearly 5 times smaller. The inset in Fig 2 *a* shows events used for a further analysis. (*d*) Distribution of times between the first and second events, together with the fitting exponent. The fitted value of $T_{1/2} = 0.14 \pm 0.02$ s is in agreement with the tabular value of $T_{1/2}$ = 0.145(2) s from [17].

good agreement with the value determined by the time–amplitude analysis.

Apart from the shape indicator, which characterizes the full signal, it is also useful to examine the pulse front edge (Fig. 3*b*). By way of example, we indicate that, from the analysis of 42 events with energies 2.0–3.8 MeV presented in Fig. 4*c*, the half-life of the second part of the signal was determined as $T_{1/2}$ = 0.29(7) μs, in agreement with the tabular value for ^{212}Po $T_{1/2}$ = 0.299(2) μs [17].

3.RESULTS AND DISCUSSION

3.1. Two-Neutrino Double-Beta Decay of ^{116}Cd

In order to determine the half-life of ^{116}Cd with respect to its two-neutrino 2β decay, the background in the energy interval 950–2900 keV was simulated with the aid of the GEANT3.21 package [14] and the event generator DECAY4 [15]. Only three components were used to construct the background model: a ^{40}K contamination of the enriched and natural $CdWO_4$ scintillators, whose activity limits of less than 4 mBq/kg were established earlier [11], and the two-neutrino 2β decay of ^{116}Cd. This simple background model describes experimental data in the chosen energy interval 950–2900 keV reasonably well (χ^2 = 1.4) and yields the following results: the activities of ^{40}K inside the enriched and natural $CdWO_4$ crystals are, respectively, 1.7(2) and 1.7(4) mBq/kg (only statistical uncertainties are given); the half-life of ^{116}Cd with respect to two-neutrino 2β decay is $T_{1/2}(2\nu2\beta) = 2.3(2) \times 10^{19}$ yr. These components are depicted in Fig. 1.

The 2ν2β Curie plot determined as $K(\varepsilon) = [S(\varepsilon)/((\varepsilon^4 + 10\varepsilon^3 + 40\varepsilon^2 + 60\varepsilon + 30)\varepsilon)]^{1/5}$, where S is the number of events in the experimental spectrum with energy ε (in electron-mass units) is presented in Fig. 5*a*. For actual 2ν2β-decay events, the Curie plot should be the straight line $K(\varepsilon) \sim Q_{2\beta} - \varepsilon$, where $Q_{2\beta}$ is the energy release in the 2β decay of ^{116}Cd. From Fig. 5*a*, one can see that, in the region 1.6–2.4 MeV (it is chosen to avoid the

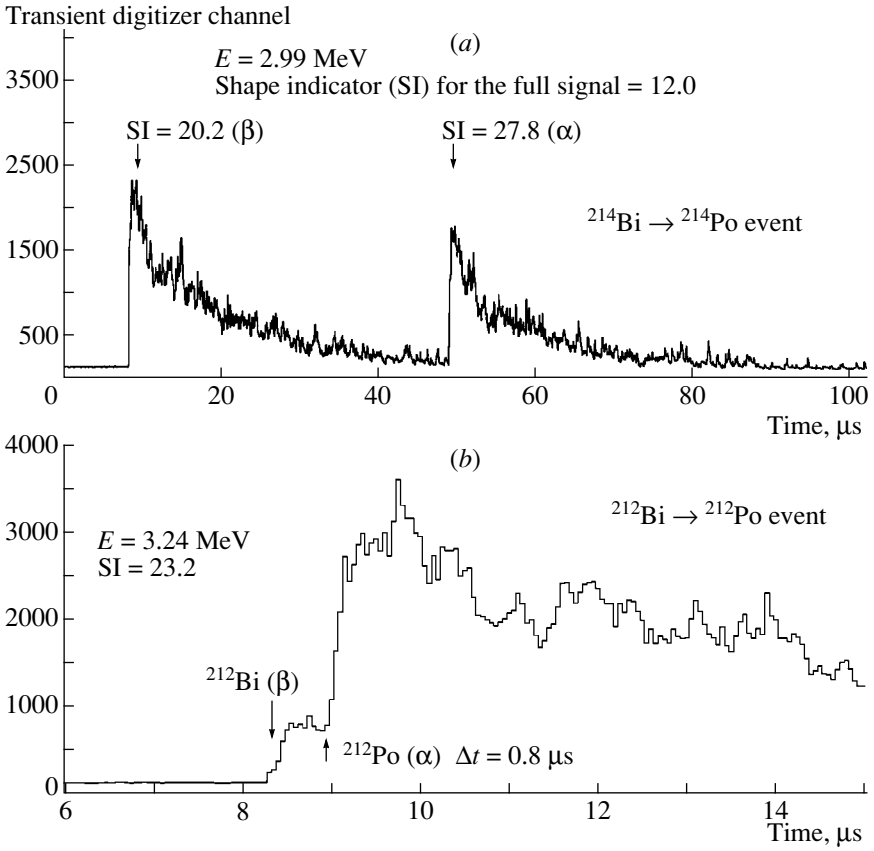

Fig. 3. (*a*) Example of a double pulse with the energy release in the region of ^{116}Cd 0ν2β decay (E = 2.99 MeV). The shape indicators for the full signal and separately for its first and second parts are SI_{full} = 12.0, SI_1 = 20.2 (close to SI_γ), and SI_2 = 27.8 (close to SI_α). Most probably, it is the event of the successive decays ^{214}Bi (β) ⟶ ^{214}Po (α; $T_{1/2}$ = 164.3 μs) ⟶ ^{210}Pb. (*b*) Probable event of the chain ^{212}Bi (β) ⟶ ^{212}Po (α; $T_{1/2}$ = 0.3 μs) ⟶ ^{208}Pb.

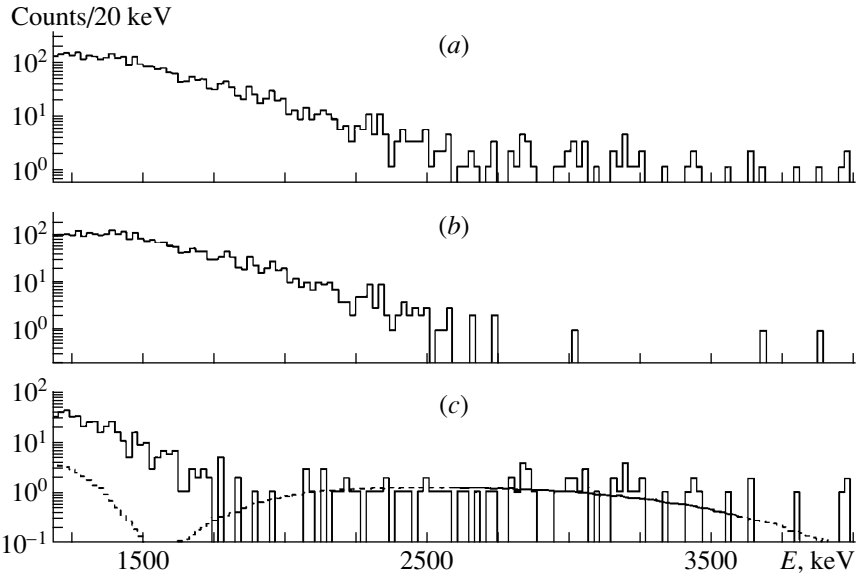

Fig. 4. (*a*) Initial spectrum of the $^{116}CdWO_4$ crystals (339 g, 4056 h) in anticoincidence with shielding detectors without pulse-shape discrimination; (*b*) pulse-shape-selected γ events with $SI = SI_\gamma \pm 2.58\sigma(SI_\gamma)$; (*c*) events with $SI \geq SI_\gamma + 2.58\sigma\ (SI_\gamma)$, together with the fit by the response function for the ^{212}Bi ⟶ ^{212}Po ⟶ ^{208}Pb decay chain. The fitted (in the range 2.6–3.6 MeV) activity of ^{228}Ac inside the $^{116}CdWO_4$ crystals is 34(5) μBq/kg.

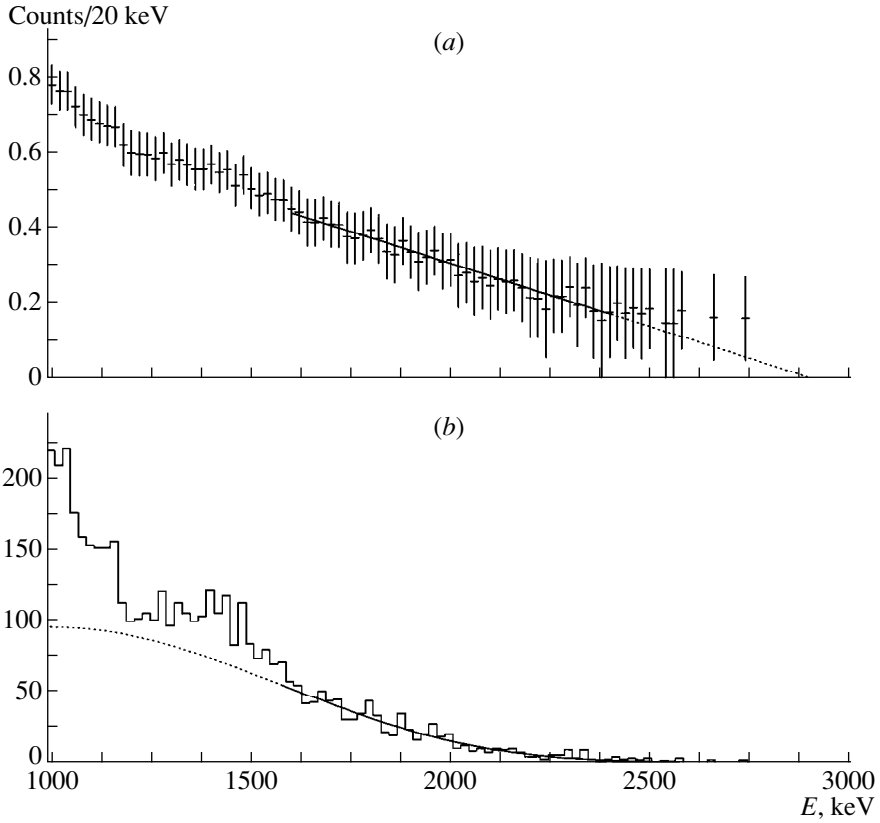

Fig. 5. (*a*) 2ν2β-decay Curie plot and its fit by a straight line in the range 1600–2400 keV; (*b*) experimental spectrum of the $^{116}CdWO_4$ scintillators (339 g, 4056 h, anticoincidence with the shielding detectors) and its fit by the convolution of the theoretical 2ν2β distribution with the detector resolution function.

influence of ^{40}K), the experimental Curie plot is well fitted by the straight line with $Q_{2\beta} = 2908(211)$ keV (the latter is in reasonable agreement with the theoretical value of $Q_{2\beta} = 2805(4)$ keV [5]). In this approach, however, the energy resolution of the $^{116}CdWO_4$ scintillators was not taken into account; the latter does not distort significantly the continuous 2ν2β curve but effectively shifts it to higher energies (recall that, for four $^{116}CdWO_4$ crystals, FWHM $\simeq$290 keV at the energy 2615 keV) and results in an overestimated $Q_{2\beta}$ value. To take into account this effect, the experimental spectrum was fitted to the convolution of the theoretical 2ν2β distribution $\rho(\varepsilon) = A\varepsilon(\varepsilon^4 + 10\varepsilon^3 + 40\varepsilon^2 + 60\varepsilon + 30)(Q_{2\beta\nu} - \varepsilon)^5$ [1] with the detector resolution function (a Gaussian function with a FWHM determined in the measurements with calibration sources as $\mathrm{FWHM}(E) = \sqrt{-226.0 + 16.6E + 6.42 \times 10^{-3}E^2}$, energy E and FWHM being given in keV). The amplitude A of the theoretical distribution and the $Q_{2\beta}$ value are the parameters of the fit. The result of the fit in the energy region 1.6–3.0 MeV is shown in Fig. 5*b*. The resulting value of $Q_{2\beta} = 2807(29)$ keV is in a good agreement with the theoretical result $Q_{2\beta} = 2805(4)$ keV [5], thus justifying greatly our assumption that experimental data in the region above 1.6 MeV are associated primarily with the 2ν2β decay of ^{116}Cd. The amplitude A corresponds to the half-life of $T_{1/2}(2\nu2\beta) = 2.4 \times 10^{19}$ yr.

The systematic uncertainties in the determined $T_{1/2}(2\nu2\beta)$ value were estimated in a way similar to that adopted [2]. The result, $T_{1/2}(2\nu2\beta) = [2.3 \pm 0.2(\mathrm{stat.})^{+1.0}_{-0.3}(\mathrm{syst.})] \times 10^{19}$ yr is in a good agreement with the measured half-lives of $T_{1/2}(2\nu2\beta) = 2.6^{+0.9}_{-0.5} \times 10^{19}$ yr [16] and $T_{1/2}(2\nu2\beta) = 2.7^{+0.5}_{-0.4}(\mathrm{stat.})^{+0.9}_{-0.6}(\mathrm{syst.}) \times 10^{19}$ yr [2] and disagrees to some extent with the value of $T_{1/2}(2\nu2\beta) = [3.75 \pm 0.35(\mathrm{stat.}) \pm 0.21(\mathrm{syst.})] \times 10^{19}$ yr [7]. It should be noted, however, that, in the last experiment, the detection efficiency η was quite small ($\eta = 0.0173$) and was only calculated by the Monte Carlo method (without experimental verification); therefore, the systematic error could be significantly higher than the quoted value.

In addition to the determined value of $T_{1/2}(2\nu2\beta)$, it seems useful (for comparison with theoretical predictions) to set a lower limit on the ^{116}Cd 2ν2β half-life from our data. It could be obtained in the simplest and very conservative way by just demanding that, in any energy region, the theoretical 2ν2β distribution not

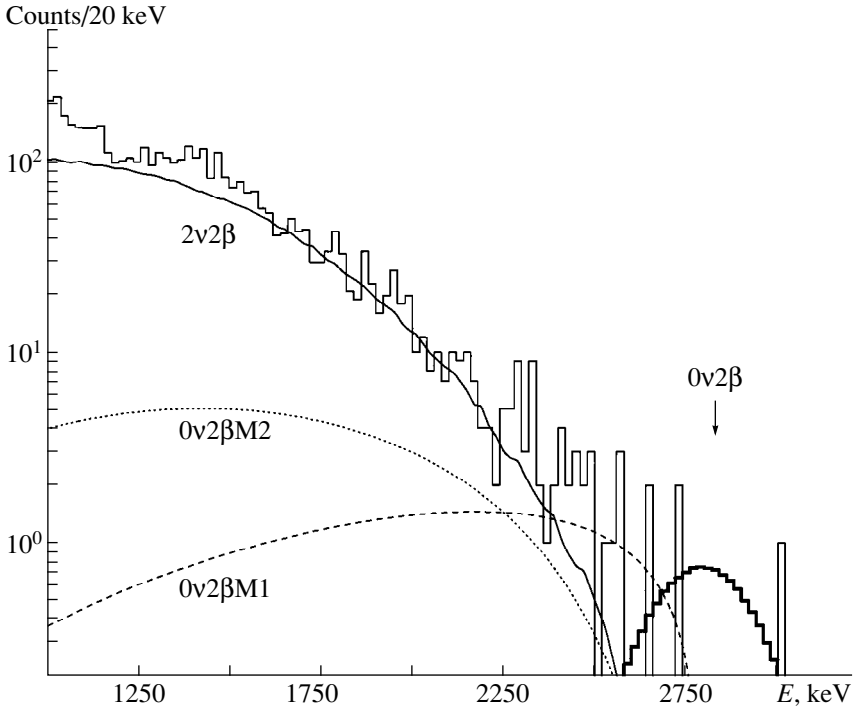

Fig. 6. Section of the experimental spectrum of the $^{116}CdWO_4$ detectors measured over 4056 h (histogram), together with the fit by 2ν2β contribution ($T_{1/2}(2\nu) = 2.3 \times 10^{19}$ yr) and excluded (at a 90% C.L.) distributions of 0νM1 and 0νM2 decays of ^{116}Cd with $T_{1/2}(0\nu M1) = 1.4 \times 10^{21}$ yr and $T_{1/2}(0\nu M2) = 4.1 \times 10^{20}$ yr, respectively. Expected distribution from ^{116}Cd 0ν2β decay with $T_{1/2}(0\nu) = 1.0 \times 10^{22}$ yr is also shown.

exceed the experimental spectrum. There are 729 events in the region 1600–2200 keV, which gives a 99.5% C.L. limit for the number of events $S \leq 7562$ under the full 2ν2β curve. Using the relation $T_{1/2} = N\eta t \ln 2/S$, where N is number of ^{116}Cd nuclei ($N = 4.66 \times 10^{23}$), t is the time of the measurements ($t = 4056$ h), and η is efficiency for 2η2β decay in anticoincidence with the shielding detectors (η = 0.962), we obtain $T_{1/2}(2\nu2\beta) \geq 1.9 \times 10^{19}$ yr at a 99.5% C.L.

3.2. New Limit for 0ν2β Decay of ^{116}Cd to the Ground State of ^{116}Sn

To estimate the half-life limit for the neutrinoless decay mode, the simple background model was used. In fact, only two background contributions are important for the 0ν2β-decay energy region: the tail of the 2ν2β spectrum and the expected distribution from the $^{212}Bi \longrightarrow {}^{212}Po \longrightarrow {}^{208}Pb$ decay (^{228}Ac chain). As was shown above, two decays in the fast chain $^{212}Bi \longrightarrow {}^{212}Po \longrightarrow {}^{208}Pb$ create the background in the region of 0ν2β decay (Fig. 4*c*). For the activity of ^{228}Ac inside the $^{116}CdWO_4$ crystals, two values were obtained: 39(4) μBq/kg (time–amplitude method) and 34(5) μBq/kg (pulse-shape analysis). Hence, we can conclude that, with the current code used for the pulse-shape analysis, there is a residual ^{228}Ac activity of 5(6) μBq/kg in our resulting pulse-shape-selected spectrum (Fig. 4*b*). The experimental data are in agreement with this calculation: for example, five events presented in the region 2600–3600 keV of the pulse-shape-selected spectrum correspond to 3.8 μBq/kg of ^{228}Ac.

The high-energy part of the experimental spectrum of $^{116}CdWO_4$ crystals (339 g, 4056 h) measured in anticoincidence with the shielding detectors and after the pulse-shape discrimination is shown in Fig. 6. The peak of 0ν2β decay is absent, and the data were used to obtain a lower limit on the half-life: $\lim T_{1/2} = N\eta t \ln 2/\lim S$, where $N = 4.66 \times 10^{23}$ is the number of ^{116}Cd nuclei, t = 4056 h, and $\lim S$ is the number of events in the peak that can be excluded at a given confidence level. The value of η = 0.828 was calculated by the DECAY4 [15] and GEANT3.21 [14] codes. To obtain the value of $\lim S$, the section of the spectrum in region 1.9–3.8 MeV was fitted in terms of the sum of three functions: the 2ν2β tail and the expected distribution from the $^{212}Bi \longrightarrow {}^{212}Po \longrightarrow {}^{208}Pb$ decay, which represent the background, and the simulated ^{116}Cd 0ν2β peak. This procedure yields the value of $S = -2.0 \pm 2.5$ and, thus, $\lim S = 3.1$ at a 90% C.L. It corresponds to $T_{1/2}(0\nu2\beta) \geq 4.0 \times 10^{22}$ yr (at a 90% C.L.), which is higher than the value of 3.2×10^{22} yr obtained in the previous experiment with one $^{116}CdWO_4$ crystal over 19986 h [3].

Using the calculations from [6], we can obtain the following limits on the neutrino mass and the right-handed admixtures in the weak interaction: $\langle m_\nu \rangle \leq 3.9$ eV, $\langle \eta \rangle \leq 5.1 \times 10^{-8}$, and $\langle \lambda \rangle \leq 4.5 \times 10^{-6}$; neglecting the right-handed contribution, we have $\langle m_\nu \rangle \leq 3.5$ eV.

Finally, the limits obtained in the previous experiment (with one crystal) and current measurements (with four crystals) can be combined in the following way: $\lim T_{1/2} = \ln 2 \sum_{i=1}^{2} N_i \eta_i t_i / \lim S$. To derive the value of combined $\lim S$, the numbers of events in the 0ν2β peak have been simply added: $S = S_1 + S_2$; their error were added quadratically: $\sigma^2 = \sigma_1^2 + \sigma_2^2$. With $S_1 = -5.0 \pm 5.5$ (previous result) and $S_2 = -2.0 \pm 2.5$, we arrive at $S = -7.0 \pm 6.2$; thus, we have $\lim S = 6.8$ at a 90% C.L. Considering that $N_1 = 1.66 \times 10^{23}$, $t_1 = 19986$ h, and $\eta_1 = 0.835$, we obtain the combined limit $T_{1/2}(0\nu2\beta) \geq 5.1 \times 10^{22}$ yr (at a 90% C.L.). The corresponding constraints on the neutrino mass and right-handed admixtures are $\langle m_\nu \rangle \leq 3.5$ eV, $\eta \leq 4.5 \times 10^{-8}$, and $\lambda \leq 3.9 \times 10^{-6}$; neglecting the right-handed contribution, we obtain $\langle m_\nu \rangle \leq 3.1$ eV.

3.3. 0ν2β Decay of ^{116}Cd to Excited Levels of ^{116}Sn

Not only ground state (g.s.) but also excited levels of ^{116}Sn with $E_{lev} \leq Q_{2\beta}$ can be populated in the ^{116}Cd 2β decay. In this case, one or a few photons, conversion electrons, and e^+e^- pairs will be emitted in a deexcitation process, in addition to two electrons emitted in the 2β-decay process. The response functions of the $^{116}CdWO_4$ detectors for ^{116}Cd 0ν2β decay to the first and second excited levels of ^{116}Sn (2_1^+ with $E_{lev} = 1294$ keV and 0_1^+ with $E_{lev} = 1757$ keV) were simulated with the aid of the DECAY4 and GEANT3.21 codes. The full absorption of all emitted particles should result in the peak at $E = Q_{2\beta}$ (the same peak as that which is expected for the 0ν2β decay of ^{116}Cd to the g.s. of ^{116}Sn). The calculated full peak efficiencies are $\eta(2_1^+) = 0.137$ and $\eta(0_1^+) = 0.065$. These numbers and the value of $\lim S = 3.1$ (determined for the g.s. ⟶ g.s. transition) give the following restrictions on $T_{1/2}$ of ^{116}Cd with respect to 0ν2β decay to the excited levels of ^{116}Sn: $T_{1/2}(0\nu2\beta, \text{g.s.} \longrightarrow 2_1^+) \geq 6.6 \times 10^{21}$ yr and $T_{1/2}(0\nu2\beta, \text{g.s.} \longrightarrow 0_1^+) \geq 3.1 \times 10^{21}$ yr at a 90% C.L.

These limits can be slightly improved by combining them with the old data, as was described above for the g.s. ⟶ g.s. transition. Taking into account the efficiency values for the 121-g $^{116}CdWO_4$ crystal used in the previous run [$\eta(2_1^+) = 0.144$ and $\eta(0_1^+) = 0.069$] and using the already determined combined value of $\lim S = 6.8$, we arrive at $T_{1/2}(0\nu2\beta, \text{g.s.} \longrightarrow 2_1^+) \geq 8.6 \times 10^{21}$ yr and $T_{1/2}(0\nu2\beta, \text{g.s.} \longrightarrow 0_1^+) \geq 4.1 \times 10^{21}$ yr (at a 90% C.L.).

3.4. Neutrinoless 2β Decay with Majoron(s) Emission

Because it is obvious that the contributions of ^{40}K are negligible above the energy of 1600 keV, the fitting procedure to obtain half-life limits for 0ν2β decay with the emission of one (two) Majoron(s) was performed as follows. The data were fitted in the energy range 1600–2500 keV by using only two theoretical distributions: the two-neutrino 2β decay of ^{116}Cd as a background, and 0ν2β decay with the emission of one (two) Majoron(s) as the effect. The χ^2 value was equal to 1.1 both for 0νM1 and for 0νM2 fits. As a result, the number of events under the theoretical 0νM1 curve was determined to be 47 ± 35, giving no statistical evidence for the effect. It leads to an upper limit of 94 events, which corresponds to the following half-life limit of 0νM1 2β decay of ^{116}Cd: $T_{1/2}(0\nu M1) \geq 1.4 \times 10^{21}$ yr at a 90% C.L. (the efficiency in anticoincidence mode is $\eta = 0.905$). A similar procedure for 0ν2β decay accompanied by the emission of two Majorons leads to $T_{1/2}(0\nu M2) \geq 4.1 \times 10^{20}$ yr (at a 90% C.L.). A section of the experimental spectrum with the excluded 0νM1 and 0νM2 distributions is shown in Fig. 6. Either of the half-life limits presented above is better than that established in the previous experiment over 19986 h [9] and in the NEMO experiment [7].

The probability of 2β decay with Majoron emission is $T_{1/2}^{-1}(0\nu M1) = \langle g_M \rangle^2 |\text{NME}|^2 G$, where $\langle g_M \rangle$ is the effective Majoron–neutrino coupling constant, NME is the nuclear matrix element, and G is a kinematical factor. By using our result $T_{1/2}(0\nu M1) \geq 1.4 \times 10^{21}$ yr and the G and NME values as calculated within the model relying on the quasiparticle random-phase approximation and taking into account proton–neutron pairing [10], we obtain $\langle g_M \rangle \leq 1.9 \times 10^{-4}$ (in the approach used in [7], $\langle g_M \rangle \leq 1.1 \times 10^{-4}$), which is one of the most stringent constraints obtained so far in direct 2β-decay experiments [1].

4. CONCLUSION

The experiment to seek for ^{116}Cd 2β decay with enriched $^{116}CdWO_4$ scintillators entered into a new phase, now in collaboration with the group from the University of Firenze and INFN (Firenze). A new setup with four $^{116}CdWO_4$ crystals (339 g) has been running since October 1998. In addition to the active shield of plastic scintillators, a new active shield made from fifteen pure $^{nat}CdWO_4$ crystals (full weight of 20.6 kg) was installed. The passive shield was improved too. The new data-acquisition system makes it possible to apply the time–amplitude analysis and pulse-shape dis-

crimination to experimental data. All these measures resulted in reducing the background in the range 2.7–2.9 MeV to 0.06 count/(yr kg keV), which is nearly one order of magnitude less than that in the previous apparatus.

Together with increased number of ^{116}Cd nuclei (by a factor of 3), this leads to a substantial improvement of the sensitivity of the ^{116}Cd experiment by about one order of magnitude. In the first run of duration 4056 h, the half-life of ^{116}Cd with the respect to 2ν2β decay was determined to be $T_{1/2}(2\nu2\beta) = [2.3 \pm 0.2(\text{stat.})^{+1.0}_{-0.3}(\text{syst.})] \times 10^{19}$ yr, and improved limits for neutrinoless modes of 2β decays were obtained to be $T_{1/2}$ $(0\nu2\beta) \geq 4.0 \times 10^{22}$ yr, $T_{1/2}(0\nu\text{M1}) \geq 1.4 \times 10^{21}$ yr, and $T_{1/2}(0\nu\text{M2}) \geq 4.1 \times 10^{20}$ yr (all at a 90% C.L.). The combined (with old data) constraint for 0ν2β decay was also derived: $T_{1/2}(0\nu2\beta) \geq 5.1 \times 10^{22}$ yr (at a 90% C.L.). The half-life limits for 2β transitions to first two excited levels of ^{116}Sn were determined: $T_{1/2}(0\nu2\beta, \text{g.s.} \longrightarrow 2^+_1) \geq 8.6 \times 10^{21}$ yr and $T_{1/2}(0\nu2\beta, \text{g.s.} \longrightarrow 0^+_1) \geq 4.1 \times 10^{21}$ yr (at a 90% C.L.). The following constraints on the neutrino mass, the right-handed admixtures in the weak current, and the Majoron–neutrino coupling constant were calculated: $\langle m_\nu \rangle \leq 3.5$ eV, $\langle \eta \rangle \leq 4.5 \times 10^{-8}$, $\langle \lambda \rangle \leq 3.9 \times 10^{-6}$ (neglecting the right-handed contribution, we have $\langle m_\nu \rangle \leq 3.1$ eV), and $\langle g_M \rangle \leq 1.9 \times 10^{-4}$.

In August 1999, one of $^{116}CdWO_4$ crystals used (with the poorest spectrometric characteristics) was additionally annealed (for about 100 h at high temperature), and its light output was improved on about 13%. The PMT of the main $^{116}CdWO_4$ detectors was replaced by a special low-background EMI tube (5 inches in diameter) with an RbCs photocathode, whose spectral response better fits the $CdWO_4$ scintillation light. As a result, spectrometric parameters of four crystals taken as a whole were improved. In particular, the energy resolution of the main detector is equal now 11.4% at 1064 keV and 8.6% at 2615 keV (Those before upgrading were 14.5 and 11%, respectively).

It is expected that, after approximately three years of measurements, the limit $T_{1/2}(0\nu2\beta) \geq 2 \times 10^{23}$ yr will be reached, which corresponds to $\langle m_\nu \rangle \leq 1.5$ eV. The $T_{1/2}$ limits for neutrinoless modes of ^{116}Cd 2β decay accompanied by Majoron emission; 2β transitions to the excited levels of ^{116}Sn; and 2β processes in ^{106}Cd, ^{108}Cd, ^{114}Cd, ^{180}W, and ^{186}W can also be improved.

ACKNOWLEDGMENTS

The present research was supported in 1996–1998 by the Science and Technology Center in Ukraine (project no. 411).

REFERENCES

1. M. Moe and P. Vogel, Annu. Rev. Nucl. Part. Sci. **44**, 247 (1994); V. I. Tretyak and Yu. G. Zdesenko, At. Data Nucl. Data Tables **61**, 43 (1995); J. Suhonen and O. Civitarese, Phys. Rep. **300**, 123 (1998).
2. F. A. Danevich *et al.*, Phys. Lett. B **344**, 72 (1995); A. Sh. Georgadze *et al.*, Yad. Fiz. **58**, 1170 (1995) [Phys. At. Nucl. **58**, 1093 (1995)].
3. F. A. Danevich *et al.*, Nucl. Phys. B (Proc. Suppl.) **70**, 246 (1999).
4. Yu. G. Zdesenko *et al.*, in *Proceedings of the 2nd International Symposium on Underground Physics, Baksan Valley, 1988* (Nauka, Moscow, 1988), p. 291.
5. G. Audi and A. H. Wapstra, Nucl. Phys. A **595**, 409 (1995).
6. A. Staudt *et al.*, Europhys. Lett. **13**, 31 (1990).
7. R. Arnold *et al.*, Z. Phys. C **72**, 239 (1996).
8. M. Hirsch *et al.*, Phys. Rev. D **53**, 1329 (1996).
9. F. A. Danevich *et al.*, Nucl. Phys. A **643**, 317 (1998).
10. M. Hirsch *et al.*, Phys. Lett. B **372**, 8 (1996).
11. A. Sh. Georgadze *et al.*, Instrum. Exp. Tech. **39**, 191 (1996); S. Ph. Burachas *et al.*, Nucl. Instrum. Methods A **369**, 164 (1996).
12. T. Fazzini *et al.*, Nucl. Instrum. Methods A **410**, 213 (1998).
13. F. A. Danevich *et al.*, Nucl. Phys. B (Proc. Suppl.) **48**, 235 (1996).
14. GEANT, *CERN Program Library Long Write-up W5013* (CERN, Geneva, 1994).
15. Yu. G. Zdesenko *et al.*, Preprint No. 89-7, KINR (Kiev Institute for Nuclear Research, Kiev, 1989); V. I. Tretyak, Preprint No. 92-8, KINR (Kiev Institute for Nuclear Research, Kiev, 1992); O. A. Ponkratenko *et al.*, Yad. Fiz. **63**, 1355 (2000) [Phys. At. Nucl. **63**, 1282 (2000)].
16. H. Ejiri *et al.*, J. Phys. Soc. Jpn. **64**, 339 (1995).
17. R. B. Firestone, in *Table of Isotopes*, Ed. by V. S. Shirley (Wiley, New York, 1996, 8th ed.).

Physics of Atomic Nuclei, Vol. 63, No. 7, 2000, pp. 1238–1241. From Yadernaya Fizika, Vol. 63, No. 7, 2000, pp. 1312–1314.

EXPERIMENTAL RESULTS, METHODS, AND FACILITIES

Present Status of the ITEP Tracking Experiment Devoted to the Double-Beta Decay Search*

V. A. Artemiev, E. V. Brakchman, M. A. Ivanovskiĭ, A. K. Karelin, V. V. Kirichenko, O. M. Kozodaeva, A. V. Kuchenkov, V. A. Lubimov, A. I. Mitin, T. N. Tsvetkova, and O. Ya. Zeldovich**

Institute of Theoretical and Experimental Physics, Bol'shaya Cheremushkinskaya ul. 25, Moscow, 117259 Russia

Abstract—A large time-projection-chamber detector in a magnetic field for studying the double-beta decay of various isotopes begins to operate. © *2000 MAIK "Nauka/Interperiodica".*

1. INTRODUCTION

Searches for the neutrinoless double-beta decay are popular now, as many years ago, due to a unique possibility of investigating many phenomena beyond the Standard Model—for example, the origin of the neutrino mass. The best limit on the neutrino mass was obtained in an experiment with ^{76}Ge semiconductor detectors ($m_\nu \le 0.4$ eV) [1]. Other results are not so impressive [2]. Changes in the neutrino-mass limit that are associated with uncertainties in the calculation of the nuclear matrix elements can be as large as one order of magnitude [3]. Therefore, investigations with various isotopes are still important if they can reach the level of the Ge experiment.

Over many years, we have been developing a large track setup to seek the neutrinoless double-beta decay of various isotopes. The main problem in studying rare processes is the background, which is many orders of magnitude larger than the expected effect. The track method has a large advantage in selecting 2β-decay events [4]. The method was tested by a time-projection chamber (TPC) ($V = 0.3$ m^3) in a magnetic field. This TPC is a prototype of our large chamber of volume $V = 13$ m^3. A background-rejection coefficient of $K \ge 10^7$ was obtained under the conditions of the ordinary Earth laboratory owing to measurement of all kinematical parameters for both electrons and a full visualization of relevant events. Investigations with ^{136}Xe (210 g) [5] and ^{150}Nd (50 g) [6] were performed. Some new results were obtained for 2β2ν decay.

2. DESCRIPTION OF TPC DETECTOR

A schematic view of the setup is presented in Fig. 1. Electrons from the 2β decay of ^{136}Xe, which enter the central part of the TPC, are recorded in two adjacent volumes, separated by a thin Mylar (50 μm) film. These two volumes are filled with methane in order to reduce the multiple scattering of low-energy (0.3–2.0 MeV) electrons. The TPC is positioned in a magnetic field for increasing the acceptance and measuring the energy. The coordinates are measured with multiwire proportional detectors arranged at the center of the TPC. There are three separate detectors for each gas volume. The number of the cell (sense wire) gives the coordinate along the magnetic field, while the drift time gives the coordinate along the electric field. The analysis of the helix-trajectory parameters gives the momentum of the electrons. The third projection is formed by cathode

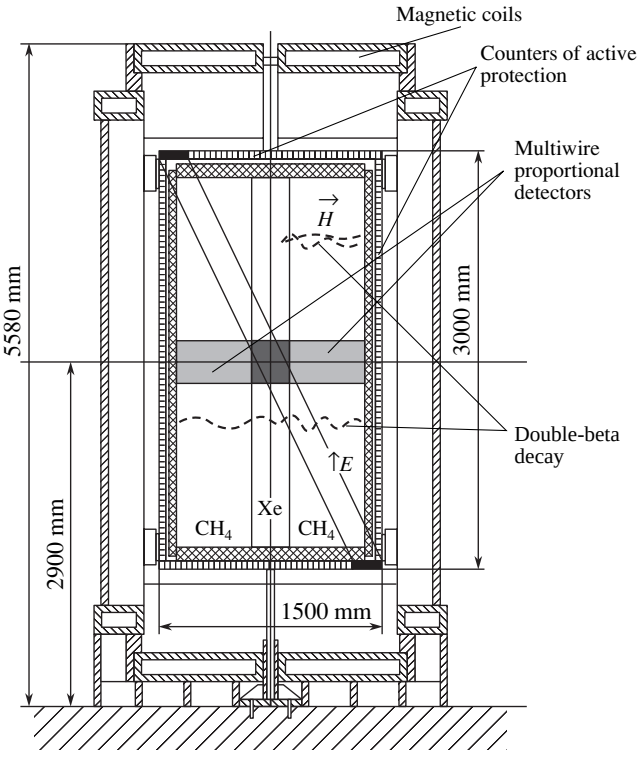

Fig. 1. Schematic view of the TPC in a magnetic field. Coincidence between the top and bottom counters (black ones) gives a cosmic trigger.

* This article was submitted by the authors in English.

** e-mail: zeldovich@vxitep.itep.ru

Comparison of two TPCs

	Small TPC, $V = 0.3$ m^3	Large TPC, $V = 13$ m^3
Number of gas volumes	2	3
Number of drift gaps	1	2
Maximal drift length	0.75 m	1.5 m
Magnetic field	0.7 kGs	1.0 kGs
Number anode wires	40, $l = 1.0$ m	260, $l = 3.0$ m
Number cathode strips	44	980
Number of TDC blocks	80	340
Cosmic shielding	Prop. gas count. 2 m^2	40 m^2
Amount of isotopes	500 g—^{136}Xe, 50 g—^{150}Nd	7.5 kg—^{136}Xe, 5 kg—^{150}Nd
Energy resolution	100 keV, 1 MeV	3–4%, 2.5 MeV, MC cal.
Efficiency	2.8% $2\beta2\nu$, cal., exper.	20–30%, MC cal.
Results and sensitivity	^{136}Xe, $T^{2\nu}_{1/2} > 9.3 \times 10^{19}$ yr	$T^{0\nu}_{1/2} \geq (2\text{–}4) \times 10^{24}$ yr
	^{150}Nd, $T^{2\nu}_{1/2} = 1.9 \times 10^{19}$ yr	(expected)

strips, forming an angle of 45° with respect to the direction of the sensing wire. Using the strip projection, we can determine the direction of particle motion (the sign of the particle charge). Also, ionization losses in Xe must be measured.

The TPC size is $3 \times 3 \times 1.5$ m^3. It operates at atmospheric pressure and can utilize up to 10 kg of Xe. In the case of the ^{150}Nd isotope, the solid source will be located on the Mylar film separating two gas volumes. The TPC is surrounded by proportional counters of the active shield from cosmic radiation. The features of both TPCs (prototype and full-size one) are presented in the table.

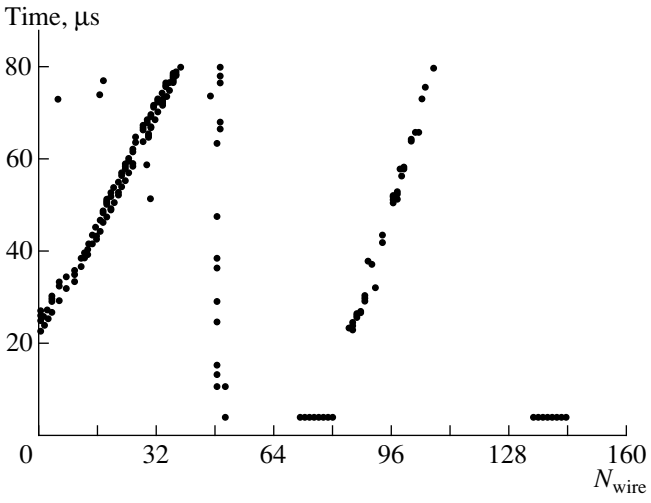

Fig. 2. Example of the cosmic muon, wire, and strip projections. Maximal drift time is 80 μs.

3. GAS SYSTEM

It is necessary to have a very pure gas in the TPC detector in order to obtain high-quality tracks from the drift length of up to 1.5 m. A powerful gas system was developed to fill and to purify working gases. The filling of the TPC is not very easy, because TPC volumes cannot be pumped [4].

We performed some time and amplitude measurements, using a cosmic trigger. The coincidence between two cosmic counters (up and bottom ones,

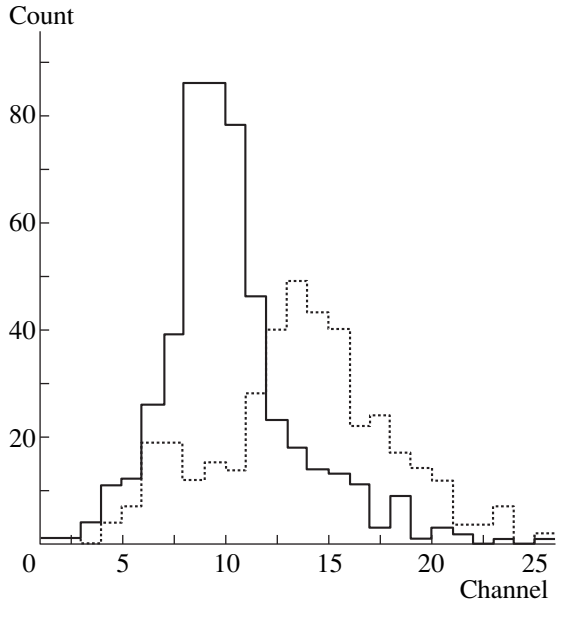

Fig. 3. Amplitude distributions of the ionization losses collected from the drift passes in two ranges: (dotted line) L = (20–80) cm and (solid line) L = (115–145) cm.

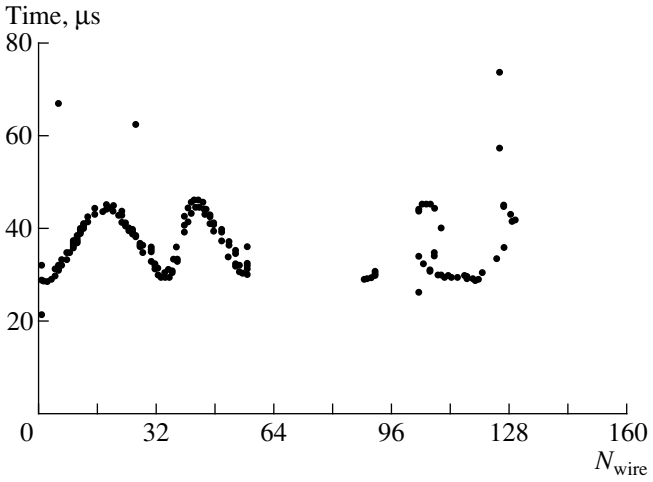

Fig. 4. Example of the background electron in the magnetic field: NN (1–56) wire projection, sine-shaped, and NN (100–128) strip projection, cycloid-shaped.

Fig. 1) selects μ mesons that traversed the TPC with different drift times for the all sensing wires and strips. An example of the cosmic track is presented in Fig. 2. Using this trigger as a "start" for time-to-digital converter (TDC) blocks, we studied the dependence of the drift velocity on the high-voltage drift potential. This dependence is linear in our range of electric drift fields (0.1–0.4 kV/cm) and agrees well with other measurements [7]. We also examined the dependences of ionization losses, collected in the cells, on the electric field and the drift length. We did not observe any noticeable change in the amplitude from the electric field, due to a large width of the distributions. The amplitude distributions of the ionization losses, collected from the drift passes in two ranges, are presented in Fig. 3 for L = 20–80 and L = 115–145 cm. The measurements were performed at 30 kV (E = 0.2 kV/cm). With aid of these distributions and the formula from [7], we estimated the attenuation length for ionization electrons and the concentration of the negatively charged admixture in our gas as $\lambda_e \simeq 147$ cm (mean pass for electron attachment). It corresponds to the concentration of electronegative impurities that is equal to $p \simeq 16$ ppm (equivalent O_2). Our purification system gives gas of purity higher than that of high-purity balloon CH_4 gas.

4. MAGNET

The magnet used consists of two halves 30 t each, which can be moved to permit operation with the TPC and the cosmic counters inside the magnet. Each half has eight coils 5.5 m in diameter, two coils 4.2 m in diameter, and an iron disk 4.0 m in diameter. The magnet is cooled with water. The calculations on the basis of the POISCR code (CERN library) showed that the magnetic field must be uniform over the TPC volume to within 1.5%. The magnetic measurements were performed and confirmed that the field has a high uniformity: about 1.5% for $R \le 1.5$ m and about 4.5% at the angles of the TPC ($R \le 4.5$ m). An example of the background electron event is presented in Fig. 4.

5. EXPECTED BACKGROUND

We expect two main types of the background from our experience gained with the prototype. One is the external background due to the external radiation flux. Photons can mimic 2β events through double Compton or Compton–Möller scattering in the Xe target. The radiation flux was measured at the center of the magnet with the NaI detector. The mass of NaI was equal to 4 kg. The measured spectrum was used for Monte Carlo calculations of the expected two-electron event background with the vertex in the central volume, which contains 6 kg of Xe. If the background were only external, we could estimate the sensitivity to ^{136}Xe 2β 2ν decay as $T_{1/2} > 10^{21}$ yr for 1000 h of the measured time. The best limit for this decay is $T^{2\nu}_{1/2} > 3.3 \times 10^{20}$ yr [2].

The other type of the background is the internal one, which is caused by radioactive isotopes, such as ^{214}Bi and ^{208}Tl, appearing in the Xe volume due to the diffusion of ^{220}Rn and ^{222}Rn from the elements of the gas-purification system. We eliminate this background and control the Rn admixture in the volumes on a very low level of 10^{-20}–10^{-21} atom/atom by means of tagging the events by a delayed α particle. New measurements are necessary.

The rate of the TPC (1/4 part) is equal to 140 event/s, as was expected on the basis of the work with the prototype. The twofold coincidence between the sensing wires in some time gate means that a particle passes the CH_4 volume in the horizontal direction. The coincidence is the main part of our trigger.

The active shielding from cosmic radiation reduces the rate only to (120–110)/s, the dead time being not more than 5%. A small reduction of the rate due to the cosmic shield is because our trigger selects a horizontal particle itself.

6. STATUS AND CONCLUSIONS

The large TPC with the maximal drift pass of 1.5 m starts to operate. All systems work sufficiently well, including the active shield from cosmic radiation. The magnetic field is uniform to a good accuracy. We have 10 kg of ^{136}Xe with enrichment of 95%. We have finished some repairs and corrections of all systems. We hope to start background measurements with natural Xe in the near future.

ACKNOWLEDGMENTS

We are very grateful to M.V. Danilov for his support.

This work was supported by the Russian Foundation for Basic Research (project no. 99-02-18930).

REFERENCES

1. L. Baudis *et al.*, hep-ex/9902014.
2. R. Luescher *et al.*, Phys. Lett. B **434**, 407 (1998).
3. A. Faessler and F. Šimkovic, hep-ph/9901215 (1999).
4. V. Artemiev *et al.*, Nucl. Instrum. Methods A **303**, 309 (1991).
5. V. Artemiev *et al.*, Phys. Lett. B **280**, 159 (1992).
6. V. Artemiev *et al.*, Phys. Lett. B **345**, 564 (1995).
7. F. Sauli, Preprint No. CERN 77-09, CERN (Geneva, 1977).

Physics of Atomic Nuclei, Vol. 63, No. 7, 2000, pp. 1242–1248. From Yadernaya Fizika, Vol. 63, No. 7, 2000, pp. 1315–1321.

EXPERIMENTAL RESULTS, METHODS, AND FACILITIES

The CRESST Dark Matter Search*

W. Seidel, M. Bravin, M. Bruckmayer[2], C. Bucci[3], S. Cooper[2], P. DiStefano, F. V. Feilitzsch[1], T. Frank, J. Jochum[1], R. Keeling[2], H. Kraus[2], M. Loidl, J. Marchese[2], O. Meier, P. Meunier, U. Nagel*, D. Pergolesi, F. Pröbst, Y. Ramachers[2], J. Schnagl[1], I. Sergeyev[4], M. Sisti, L. Stodolsky, S. Uchaikin[4], and L. Zerle

Max-Planck-Institut für Physik, Munich, Germany

Abstract—We discuss the short- and long-term perspectives of the CRESST (Cryogenic Rare Event Search using Superconducting Thermometers) project and present the current status of the experiment and new results concerning detector development. In the search for elementary particle dark matter, CRESST is presently the most advanced deep underground, low-background, cryogenic facility. The basic technique involved is to search for WIMPs (Weakly Interacting Massive Particles) by the measurement of nonthermal phonons, as created by WIMP-induced nuclear recoils. Combined with our newly developed method for the simultaneous measurement of scintillation light, strong background discrimination is possible, resulting in a substantial increase in WIMP detection sensitivity. This will allow a test of the reported positive evidence for a WIMP signal by the DAMA Collaboration in the near future. In the long term, the present CRESST setup permits the installation of a detector mass up to 100 kg. In contrast to other projects, CRESST technology allows the employment of a large variety of detection materials. This offers a powerful tool in establishing a WIMP signal and in investigating WIMP properties in the event of a positive signal. *© 2000 MAIK "Nauka/Interperiodica".*

1. INTRODUCTION

The goal of the CRESST project is the direct detection of elementary particle dark matter and the elucidation of its nature. The search for dark matter and the understanding of its nature remains one of the central and most fascinating problems of our time in physics, astronomy, and cosmology. There is strong evidence for it on all scales, ranging from dwarf galaxies, through spiral galaxies like our own, to large-scale structures. The history of the universe is difficult to reconstruct without it, be it big bang nucleosynthesis [1] or the formation of structure [2]. The importance of the search for dark matter in the form of elementary particles, created in the early stages of the universe, is underlined by the recent weakening of the case for other forms such as MACHOs, faint stars, and black holes [3]. Particle physics provides a well-motivated candidate through the assumption that the lightest supersymmetric (SUSY) particle, the "neutralino," is some combination of neutral particles arising in the theory and it is possible to find many candidates obeying cosmological and particle physics constraints. Indeed, SUSY models contain many parameters and many assumptions, and by relaxing various simplifying assumptions one can find candidates in a wide mass range [4]. Generically, such particles are called WIMPs (Weakly Interacting Massive Particles) and are to be distinguished from proposals involving very light quanta such as axions. WIMPs are expected to interact with ordinary matter by elastic scattering on nuclei, and all direct detection schemes have focused on this possibility.

Conventional methods for direct detection rely on the ionization or scintillation caused by the recoiling nucleus. This leads to certain limitations connected with the relatively high energy involved in producing electron–ion or electron–hole pairs and with the sharply decreasing efficiency of ionization by slow nuclei. Cryogenic detectors use the much lower energy excitations, such as phonons, and while conventional methods are probably close to their limits, cryogenic technology can still make great improvements. Since the principal physical effect of a WIMP nuclear recoil is the generation of phonons, cryogenic calorimeters are well suited for WIMP detection, and, indeed, the first proposals to search for dark matter particles were inspired by early work on cryogenic detectors [5]. Further, as we shall discuss below, when this technology is combined with charge or light detection, the resulting background suppression leads to a powerful technique to search for the rare nuclear recoils due to WIMP scatterings.

The detectors developed by the CRESST Collaboration consist of a dielectric crystal (target or absorber) with a small superconducting film (thermometer) evap-

* This article was submitted by the authors in English.

[1] Technische Universität München, Physik Department, Germany.
[2] University of Oxford, Physics Department, UK.
[3] Laboratori Nazionali del Gran Sasso, Italy.
[4] Permanent Address: Joint Institute for Nuclear Research, Dubna, Russia.

1063-7788/00/6307-1242$20.00 © 2000 MAIK "Nauka/Interperiodica"

orated onto the surface. When this film is held at a temperature in the middle of its superconducting to normal conducting phase transition, it functions as a highly sensitive thermometer. The detectors presently employed in Gran Sasso use tungsten (W) films and sapphire (Al_2O_3) absorbers, running near 15 mK. It is important for the following, however, to realize that the technique can also be applied to a variety of other materials. The small change in temperature of the superconducting film resulting from an energy deposit in the absorber leads to a relatively large change in the film's resistance. This change in resistance is measured with a SQUID. To a good approximation, the high-frequency phonons created by an event do not thermalize in the crystal before being directly absorbed in the superconducting film [6]. Thus the energy resolution is only moderately dependent on the size of the crystal, and scaling up to large detectors of some hundred grams or even kilograms per channel is feasible. The high sensitivity of this system also allows us to use a small separate detector of the same type to see the light emitted when the absorber is a scintillating crystal.

2. PRESENT STATUS OF CRESST

The task set for the first stage of CRESST was to show the operation of 1 kg of sapphire in the millikelvin range, with a threshold of 500 eV under low-background conditions [7]. Meeting this goal involved two major tasks:

the setting up of a low-background, large-volume, cryogenic installation and

the development of massive, low-background detectors with low-energy thresholds.

2.1. CRESST Installation in the Gran Sasso Laboratory (LNGS)

The central part of the CRESST low-background facility at the LNGS is the cryostat. The design of this cryostat had to combine the requirements of low temperatures with those of a low background. The first generation cryostats in this field were conventional dilution refrigerators where some of the materials were screened for radioactivity. Because due to cryogenic requirements some non-radiopure materials, for example, stainless steel, cannot be completely avoided in a dilution refrigerator, a design was chosen in which a well-separated "cold box" houses the experimental volume at some distance from the cryostat. The cold box is constructed entirely of low-background materials, without any compromise. It is surrounded by shielding consisting of 20 cm of lead and 14 cm of copper. The cooling power of the dilution refrigerator is transferred to the cold box by a 1.5-m-long cold finger protected by thermal radiation shields, all of low-background copper. The experimental volume can house up to 100 kg of target mass. The cold box and shielding are installed in a clean room area with a measured clean room class of 100. This design type of a cryostat in a high quality clean room, deep underground in the LNGS, presently makes this instrument unique in the world. The installation is now complete and entering into full operation. At present four 262-g detectors are in the experimental volume, performing the first measurements under low-background conditions. The first results of this run have shown that, at energies above 30 keV, the counting rate is on the order of a few counts/(kg keV d) and above 100 keV below 1 count/(kg keV d). There are strong indications that the low-energy part of the spectrum was dominated by external disturbances such as mechanical vibrations or electromagnetic interference. We are working to correct this in future runs.

2.2. Detector Development

Present CRESST detectors have by far the highest sensitivity per unit mass of any cryogenic device now in use. Figure 1 shows the spectrum of an X-ray fluorescence source measured with a 262-g CRESST sapphire detector, as presently being used, showing an energy resolution of 133 eV at 1.5 keV. These 262-g detectors were developed by scaling up a 32-g sapphire detector [8]. Due to optimized design and because of the nonthermalization of the phonons as explained in the introduction, this scaling-up could be achieved without loss in sensitivity. Further developments for the next detector generation are in progress.

In order to improve linearity, dynamic range and time response, a mode of operation with thermal feedback was developed and successfully operated with the present CRESST detectors.

For another thermometer type, the iridium–gold proximity sandwich, fabrication improvements now allow the application of these thermometers with a wide choice of absorber materials, even for low-melting point materials such as germanium. A germanium detector with a mass of 342 g is in preparation.

Passive techniques of background reduction—radiopure materials and a low-background environment—are of course imperative in work of this type. However, there is a remaining background dominated by β and γ emissions from nearby radioactive contaminants. These produce exclusively electron recoils in the detector. In contrast, WIMPs and also neutrons lead to nuclear recoils. Therefore, dramatic improvements in sensitivity are to be expected if, in addition to the usual passive shielding, the detector itself is capable of distinguishing electrons from nuclear recoils and rejecting them.

2.3. Simultaneous Phonon and Light Measurement

We have recently developed a system, presently using $CaWO_4$ crystals as the absorber, where a measurement of scintillation light is carried out in parallel to the phonon detection. We find that these devices

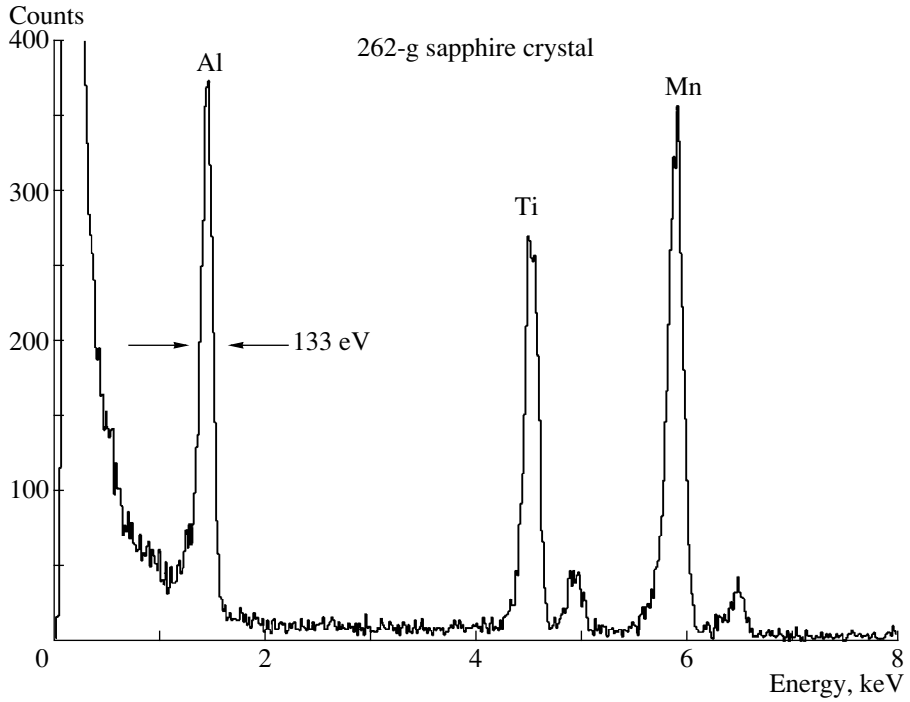

Fig. 1. Pulse height spectrum of a 262-g detector operated with thermal feedback and an X-ray fluorescence source [8] installed inside the cryostat to provide the X-ray lines of Al, Ti, and Mn. The large background towards lower energies, which was not present in our earlier spectra [9], is attributed to damage later noticed to the thin Al sheet meant to absorb Auger electrons from the source.

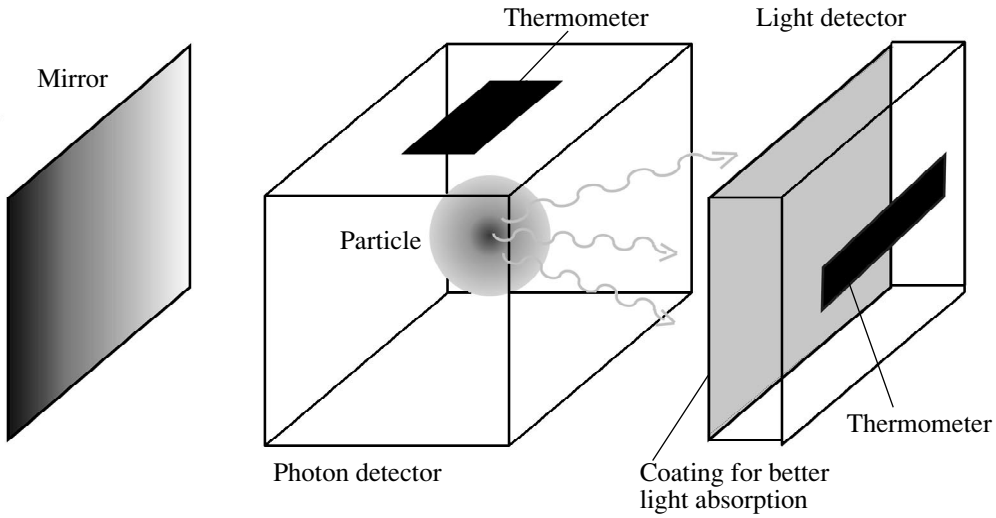

Fig. 2. Schematic view of the arrangement used for the simultaneous light and phonon detection.

clearly discriminate nuclear recoils from electron recoils.

The system is shown schematically in Fig. 2. It consists of two independent detectors, each of the CRESST type: a scintillating absorber with a tungsten superconducting phase transition thermometer on it, and a similar but smaller detector placed next to it to detect the scintillation light from the first detector. A detailed description is given in [10]. Both detectors were made by standard CRESST techniques and were operated at about 12 mK. The $CaWO_4$ crystal was irradiated with photons and simultaneously with electrons. The left plot in Fig. 3 shows a scatter plot of the pulse heights observed in the light detector versus the pulse height observed in the phonon detector. A clear correlation between the light and phonon signals is observed. The right-hand plot shows the result of an additional irradiation with neutrons from an Am–Be source. A second

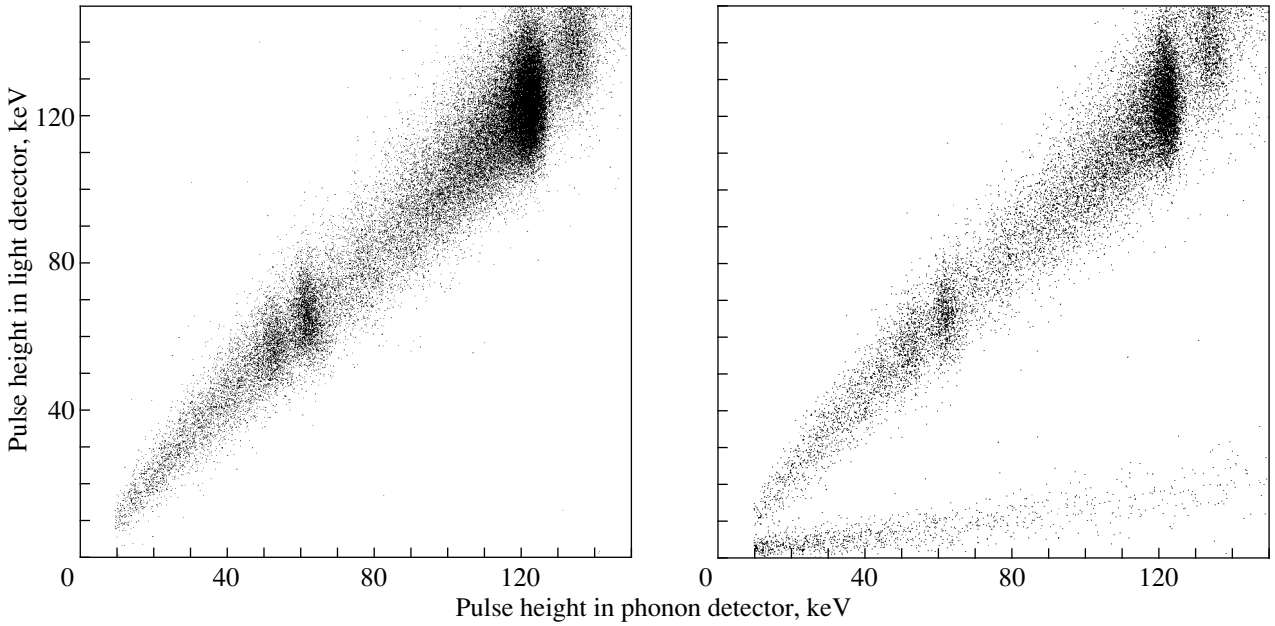

Fig. 3. Pulse height in the light detector versus pulse height in the phonon detector. The scatter plot on the left side has been measured with an electron and a photon source, while a neutron source was added on the right.

line can be seen due to neutron-induced nuclear recoils. It is to be observed that electron and nuclear recoils can be clearly distinguished down to a threshold of 10 keV. The leakage of some electron recoils into the nuclear recoil line gives the electron recoil rejection according to the quality factor of [11]. A detailed evaluation yields a rejection factor of 98% in the energy range between 10 and 20 keV, 99.7% in the range between 15 and 25 keV, and better than 99.9% above 20 keV.

3. NEXT STEPS FOR CRESST

All our detectors, including those measuring scintillation light, use superconducting phase transition thermometers with SQUID readout and can be run in the present setup. The CRESST cold box is designed to house detectors of various types, up to a total mass of about 100 kg. Due to the complementary detector concepts of low-threshold calorimeters, on the one hand, and detectors with the simultaneous measurement of light and phonons, on the other, CRESST can cover a very wide range of WIMP masses.

3.1. Low-Mass WIMPs

The present sapphire detectors, with their extremely low-energy thresholds and a low-mass target nucleus with high spin (Al), cover the low WIMP mass range from 1 to 10 GeV in the sense that they are presently the only detectors able to explore this mass range effectively for noncoherent interactions. The sensitivity for WIMPs with spin-dependent interactions, an expected threshold of 0.5 keV, a background of 1 count/(kg keV d), and an exposure of 0.1 and 1 kg yr is shown in Fig. 4. For comparison, the present limits from the DAMA [12] and UKDMC [13] NaI experiments are also shown.

Data taking with the present sapphire (Al_2O_3) detectors (262 g each) will continue during 1999.

3.2. Medium- and High-Mass WIMPs

In the second half of 1999, we intend to start the installation of the next detector generation with back-

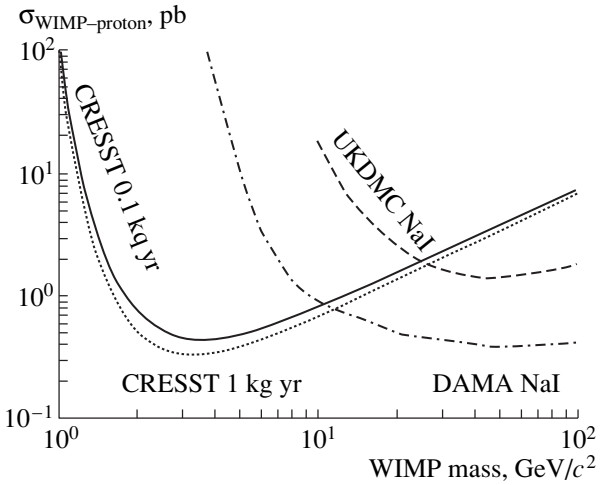

Fig. 4. Equivalent WIMP–proton cross-section limits (at a 90% C.L.) for spin dependent interactions as a function of the WIMP mass, as expected for the present CRESST sapphire detectors with a total mass of 1 kg. The expectation is based on a threshold of 0.5 keV, a background of 1 count/(kg keV d), and an exposure of 0.1 and 1 kg yr. For comparison, the present limits from the DAMA [12] and UKDMC [13] NaI experiments are also shown.

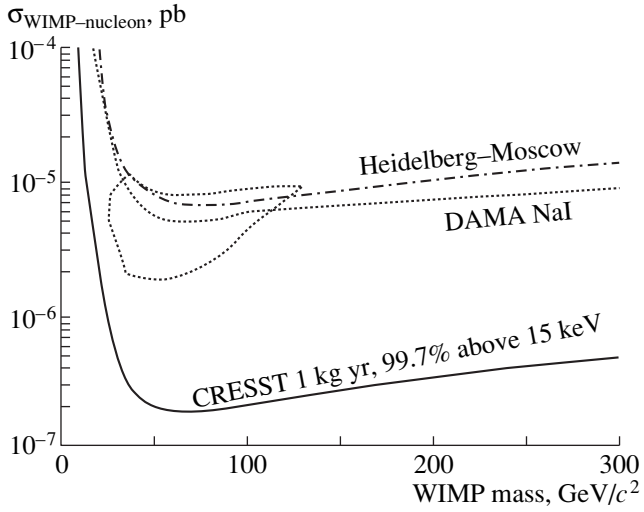

Fig. 5. WIMP–nucleon cross-section limits (at a 90% C.L.) for scalar (coherent) interactions as a function of the WIMP mass, expected for a 1 kg $CaWO_4$ detector with a background rejection of 99.7% above a threshold of 15 keV detector and 1 yr of measurement time in the CRESST set-up in Gran Sasso. For comparison, the recently updated limit from the Heidelberg–Moscow ^{76}Ge experiment [14] and the DAMA NaI limits [12] (with the contour for positive evidence [15]) are also shown.

ground suppression using the simultaneous measurement of scintillation light and phonons. These detectors will have target nuclei of large atomic number, such as tungsten, making them particularly sensitive to WIMPs with coherent interactions. Here the WIMP cross section profits from a large coherence factor of the order A^2 (where A is number of nucleons). Combined with the strong background rejection, this means these detectors can be sensitive to low WIMP cross sections. Figure 5 shows the anticipated sensitivity obtained with a $CaWO_4$ detector in the present CRESST setup in Gran Sasso. The CRESST $CaWO_4$ curve is based on a background rate of 1 count/(kg keV d), an intrinsic background rejection of 99.7% above a recoil threshold of 15 keV, and an exposure of 1 kg yr.

For comparison, the recently updated limits of the Heidelberg–Moscow ^{76}Ge-diode experiment [14] and the DAMA NaI experiment [12] are also shown. A 60-GeV WIMP with the cross section claimed in [15] would give about 55 counts between 15 and 25 keV in 1 kg $CaWO_4$ within 1 yr. A background of 1 count/(kg keV d) suppressed with 99.7% would leave 11 background counts in the same energy range. A 1-kg $CaWO_4$ detector with 1 yr of measuring time in the present set-up of CRESST should allow a comfortable test of the recently reported positive signal.

4. LONG-TERM PERSPECTIVES

The sensitivity reached by a system that simply relies passively on radiopure materials, but lacks active intrinsic background suppression, saturates at some point and cannot be improved with more mass (M) and measuring time (t). On the other hand, in a system with a precisely determined background suppression factor, the sensitivity continues to improve as $\sigma \propto 1/\sqrt{Mt}$ [11], as is possible with the CRESST scintillation light method.

Beginning in the year 2000, we intend to upgrade the multichannel SQUID readout and systematically increase the detector mass, which can go up to about 100 kg before reaching the full capacity of the present installation.

With a 100-kg $CaWO_4$ detector, the sensitivity shown in Fig. 6 can be reached in one year of measuring time. If we wish to cover most of the MSSM parameter space of SUSY with neutralino dark matter, the exposure would have to be increased to about 300 kg yr, the background suppression improved to about 99.99% above 15 keV, and the background lowered to 0.1 count/(kg keV d). The recent tests in Munich with $CaWO_4$, which were limited by ambient neutrons, suggest that a suppression factor of this order should be within reach underground, with the neutrons well shielded and employing a muon veto.

The excellent background suppression of cryodetectors with active background rejection makes them much less susceptible to systematic uncertainties than conventional detectors, which must rely heavily on a subtraction of radioactive backgrounds. Since this kind of systematic uncertainty cannot be compensated by an increase of detector mass, even moderate sized cryogenic detectors can achieve much better sensitivity than large mass conventional detectors. Note that the excellent levels shown in Fig. 6 can be achieved with the rather moderate assumptions of background at 1 count/(kg keV d) and 0.1 count/(kg keV d). To a large extent, even higher background levels can be compensated with increased exposure. On the other hand, dark matter searches with conventional detectors require a scaling of the presently reached best background levels of 0.057 counts/(kg keV d) [19] by a factor of 2000 to reach the same sensitivity level.

If WIMPs are not found, at some point the neutron flux, which also gives nuclear recoils, will begin to limit further improvement. With careful shielding, the neutron flux in Gran Sasso should not limit the sensitivity within the exposures assumed for the upper CRESST curve in Fig. 6. With still larger exposures, the neutron background may still be discriminated against large-mass WIMPs. This can be done by comparing different target materials, which is possible with the CRESST technology, since different variations with nuclear number for the recoil spectra are to be expected with different mass projectiles.

The phase of the project with large increased total detector mass will necessitate certain improvements and innovations in the technology, particularly involving background rejection, optimization of the neutron

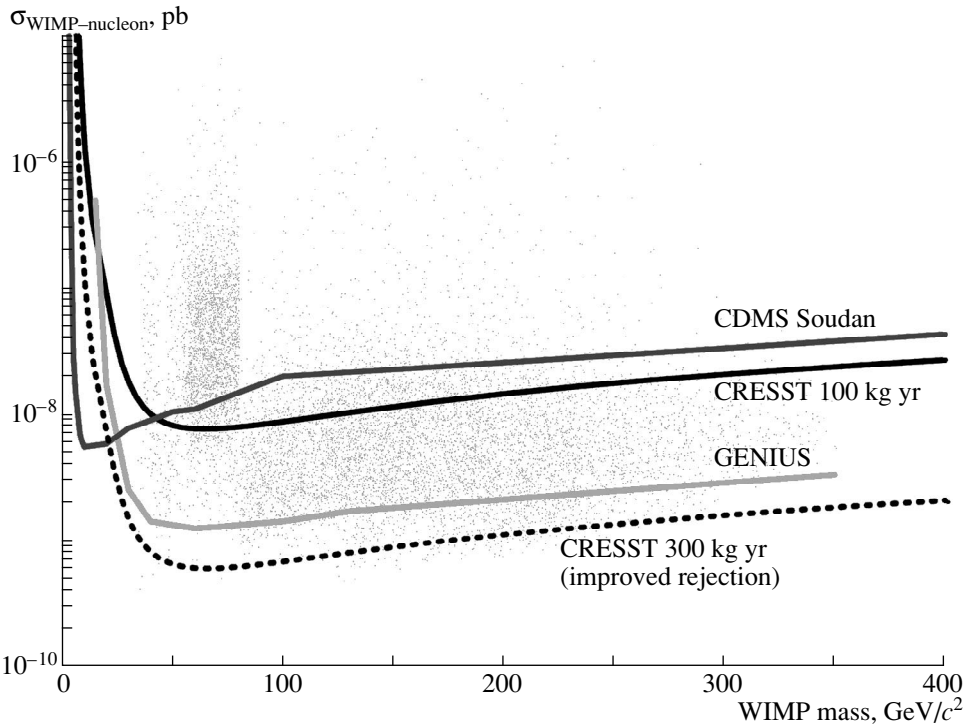

Fig. 6. WIMP–nucleon cross-section limits (at a 90% C.L.) for scalar (coherent) interactions, as a function of the WIMP mass, expected for a $CaWO_4$ detector with a background of 1 count/(keV kg d), a background suppression of 99.9% above a threshold of 15 keV, and an exposure of 100 kg yr in the CRESST setup. With a suppression of 99.99% above 15 keV, a reduced background of 0.1 count/(kg keV d), and an increased exposure of 300 kg yr most of the MSSM parameter space would be covered. For comparison, the projected sensitivity of CDMS at Soudan [16], and the limits of the proposed GENIUS experiment [17] are also shown. For comparison, all sensitivities are scaled to a galactic WIMP density of 0.3 GeV/cm^3. The dots (scatter plot) represent expectations for WIMP-neutralinos calculated in the MSSM framework with non-universal scalar mass unification [18].

shielding, and muon vetoing. As described above, if a positive dark matter signal exists, increased mass and improved background rejection will be important in verifying and elucidating the effect. A large target mass, such as 100 kg, is of importance to reach the high statistics needed to study the annual modulation effect.

5. CONCLUSIONS

The installation of the large-volume, low-background, cryogenic facility of CRESST at the Gran Sasso Laboratory is completed. The highly sensitive CRESST sapphire detectors are up to now the only technology available to reasonably explore the low-mass WIMP range. The new detectors with the simultaneous measurement of phonons and scintillation light allow one to distinguish the nuclear recoils very effectively from the electron recoils caused by background radioactivity. For medium- and high-mass WIMPs, this results in one of the highest sensitivities possible with today's technology.

This will allow a test of the reported positive evidence for a WIMP signal by the DAMA Collaboration in the near future. In the long term, the present CRESST setup permits the installation of a detector mass up to 100 kg. In contrast to other projects, CRESST detectors allow the employment of a large variety of target materials. This offers a powerful tool in establishing a WIMP signal and in investigating WIMP properties in the event of a positive signal.

By its combination of detection technologies, CRESST is over the whole WIMP mass range one of the best options for direct particle dark matter detection.

REFERENCES

1. J. Audouze, Nucl. Phys. News **8**, 22 (1998).
2. S. Dodelson, E. I. Gates, and M. S. Turner, Science **274**, 69 (1996).
3. *Proceedings of the Workshop on Dark Matter in Astro- and Particle Physics, Heidelberg, 1998*, Ed. by H. V. Klapdor-Kleingrothaus, L. Baudis, and S. Kolb; *Proceedings of the Workshop on the Identification of Dark Matter, Buxton, England, 1998*, Ed. by N. Spooner.
4. A. Gabutti *et al.*, Astropart. Phys. **6**, 1 (1996).
5. M. Goodman and E. Witten, Phys. Rev. D **31**, 3059 (1985).
6. F. Pröbst *et al.*, J. Low Temp. Phys. **100**, 69 (1995).
7. S. Cooper *et al.*, Preprint No. MPI-PhE/93-29, MPI (Munich, 1993).

8. P. Colling *et al.*, Nucl. Instrum. Methods A **354**, 408 (1995).
9. M. Sisti *et al.*, in *Proceedings of the VII International Workshop on Low Temperature Detectors, Munich, Max-Planck-Institute of Physics, 1997.*
10. P. Meunier *et al.*, submitted to Appl. Phys. Lett.
11. R. J. Gaitskell, P. D. Barnes, A. DaSilva, *et al.*, Nucl. Phys. B (Proc. Suppl.) **51**, 279 (1996).
12. R. Bernabei *et al.*, Phys. Lett. B **389**, 757 (1996).
13. P. F. Smith *et al.*, Phys. Lett. B **379**, 299 (1996).
14. L. Baudis *et al.*, submitted to Phys. Rev. D.
15. R. Bernabei, P. Belli, and F. Montecchia, Preprint No. ROM2F/98/34, Roma (Roma, 1998).
16. S. W. Nam *et al.*, in *Proceedings of the VII International Workshop on Low Temperature Detectors, Munich, Max-Planck-Institute of Physics, 1997.*
17. H. V. Klapdor-Kleingrothaus, J. Hellmig, and M. Hirsch, J. Phys. G **24**, 85 (1998).
18. V. Bednyakov, H. V. Klapdor-Kleingrothaus, S. Kovalenko, and Y. Ramachers, Z. Phys. A **357**, 339 (1997).
19. L. Baudis *et al.*, hep-ex/9811040.

Physics of Atomic Nuclei, Vol. 63, No. 7, 2000, pp. 1249–1258. From Yadernaya Fizika, Vol. 63, No. 7, 2000, pp. 1322–1331.

EXPERIMENTAL RESULTS, METHODS, AND FACILITIES

Neutrinoless Double-Beta Decay and Dark Matter Search with GENIUS*

H. V. Klapdor-Kleingrothaus and St. Kolb**

Max-Planck-Institut für Kernphysik, Heidelberg, Germany

Abstract—The potential of the GENIUS (GErmanium in liquid NItrogen Underground Setup) experiment, proposed as the successor of the Heidelberg–Moscow experiment, for the search for neutrinoless double-beta decay, the direct search for neutralino Cold Dark Matter, and for other physics beyond the Standard Model will be presented. The current status of the Heidelberg–Moscow experiment will be reviewed. © *2000 MAIK "Nauka/Interperiodica".*

1. INTRODUCTION

Neutrinoless double-beta-decay ($0\nu\beta\beta$) experiments are one of the key experiments in order to establish the nature of the neutrino since they are the only experiments able to decide if the neutrino is a Majorana or a Dirac particle: a nonvanishing $0\nu\beta\beta$-decay amplitude pins the neutrino down to be a massive Majorana particle. From a theoretical point of view currently, this seems to be the most natural solution since most models going beyond the Standard Model (SM) are based on the idea of Grand Unification, which in turn frequently predict the neutrino to be massive and of the Majorana type [1–4]. The most sensitive of the operating $0\nu\beta\beta$-decay experiments, the Heidelberg–Moscow experiment, restricts the effective Majorana mass of the neutrino to be [5]

$$\langle m_\nu \rangle < 0.2 \text{ eV} \quad (90\% \text{ C.L.}). \tag{1}$$

This limit already tests some of the neutrino mass models constructed in order to explain the solar neutrino deficit, the atmospheric neutrino deficit, the need for a Hot component of Dark Matter (HDM) in the Universe and the LSND result [6–12].

In addition to the hunt for a nonvanishing Majorana neutrino mass which may represent (at least a fraction of) the HDM of the universe, the Heidelberg–Moscow experiment yields stringent limits on the parameters of the cold component of the dark matter in the Universe [13].

In order to increase the sensitivity of the $0\nu\beta\beta$-decay experiments significantly, a new setup is mandatory. Of the proposals currently at hand, the most far reaching and also most realistic one is the GENIUS proposal [6, 14, 15], whose aim is to test the effective neutrino mass down to $\langle m_\nu \rangle < 10^{-2}$ eV or even 10^{-3} eV. If the neutrino is a Majorana particle, the final GENIUS setup would be superior to current and highly competitive to future dedicated accelerator neutrino oscillation experiments.

On the other hand, the GENIUS setup in a first phase already would be in a position to cover almost the full parameter space of the MSSM for predictions of neutralinos as Cold Dark Matter (CDM).

Besides the search for neutrino masses and dark matter, the nonobservation of $0\nu\beta\beta$ decay poses very stringent constraints on extensions of the SM which incorporate lepton-number violation. In case of the Heidelberg–Moscow experiment, limits from $0\nu\beta\beta$ decay are often more restrictive than those which can be obtained at currently operating collider facilities [16]. In the case of GENIUS, the constraints will become more restrictive and in some cases competitive to the sensitivity of future collider projects such as the Large Hadron Collider (LHC) and the Next Linear Collider (NLC) [6].

Due to its projected extremely low background, the GENIUS setup could be able to measure for the first time the flux of the lowest energy solar neutrinos (*pp* neutrinos) in real time [17].

The following chapters are dedicated to some of the details of the GENIUS proposal, the current status of the Heidelberg–Moscow experiment, and the discussion of some of the impacts on non-Standard Model physics originating from these setups.

2. $0\nu\beta\beta$ DECAY AND NEUTRINO MASS, THE HEIDELBERG–MOSCOW EXPERIMENT

Double-beta decay is a nuclear process which takes place in the SM allowed 2ν mode, or possibly in the 0ν mode

$$^{A}_{Z}X \longrightarrow {}^{A}_{Z+2}X + 2e^- + 2\bar{\nu} \quad \text{(allowed in the SM)},$$

$$^{A}_{Z}X \longrightarrow {}^{A}_{Z+2}X + 2e^- \quad \text{(not allowed in the SM)}.$$

Furthermore, other modes involving Majorons exist. The SM allowed decay is observed for a couple of isotopes with half lives of order 10^{20} yr. The by far more

* This article was submitted by the authors in English.

** e-mail: kolb@gustav.mpi-hd.mpg.de

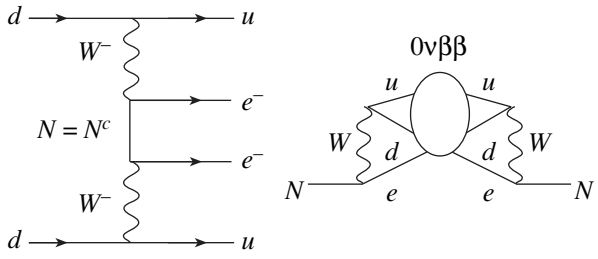

Fig. 1. The neutrino mass mode of 0νββ decay induced by a massive Majorana neutrino $N = N^c$ (left), contribution to the Majorana neutrino mass induced by any nonvanishing 0νββ graph (right).

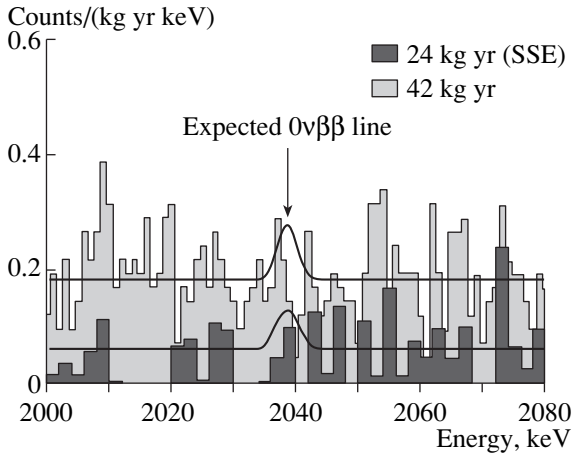

Fig. 2. Sum spectrum of the Heidelberg–Moscow experiment after 42 kg yr of data taking. 24 kg yr have been analyzed applying pulse shape analysis which allows one to identify Single Site Events (SSE) and reduces the very low background further [5]. The lower (upper) solid line denotes the excluded signal $T_{1/2}^{0\nu\beta\beta} > 1.6 \times 10^{25}$ (1.3×10^{25}) yr (90% C.L.) with (without) pulse shape analysis. The resulting half-life limit on 0νββ decay applying the method is $T_{1/2}^{0\nu\beta\beta} > 5.7 \times 10^{25}$ yr (90% C.L.) [22].

interesting mode is the neutrinoless one, which, if observed, indicates the existence of non-SM physics since lepton number is violated by two units. So far, this mode has not been observed.

The 0νββ mode may be induced by different mechanisms in models which incorporate lepton-number violation, the "classical" one being the neutrino mass mechanism (Fig. 1). Some examples for contributions to the 0νββ mode in other models will be presented later. The most general (low-energy) neutrino mass term is [18]

$$\mathcal{L} = -\frac{1}{2}(\overline{(\nu_L)^c}, \overline{\nu_R})\mathcal{M}\begin{pmatrix}\nu_L \\ (\nu_R)^c\end{pmatrix} + \text{h.c.},$$
$$\mathcal{M} = \begin{pmatrix} m_L^M & (m^D)^T \\ m^D & m_R^M \end{pmatrix}. \qquad (2)$$

If either m_L^M or m_R^M or both are different from zero, the mass states N which are obtained after diagonalization of $\mathcal{M}$ by means of a unitary rotation U satisfy the Majorana condition $N = N^c$, indicating the breakdown of lepton number, and a contribution to the 0νββ is induced (Fig. 1). For light ($m_i < 10$ MeV) and heavy ($M_i > 10$ GeV) N_i, 0νββ measures effective masses

$$\langle m_\nu \rangle = \sum{}' U_{ei}^2 m_i, \quad \langle M_\nu^{-1} \rangle = \sum{}'' U_{ei}^2 \frac{1}{M_i}, \qquad (3)$$

respectively. The prime (double prime) indicates summation over the light (heavy) neutrino states only. This is simply due to the propagator structure of the Majorana neutrino mode (for details see [18]). The limit on the half-life of the decaying nucleus can be converted into a limit on the masses. This procedure requires knowledge of some nuclear matrix elements [19]. The results for the bounds on the neutrino masses are usually reliable up to a factor of two and can to some extent be cross-checked with the predictions for the actually observed 2ν decay modes.

The relation between 0νββ decay and the Majorana mass of the neutrino is a very intimate one by virtue of a theorem established in [20]: any contribution to 0νββ, regardless of its origin, induces a nonvanishing Majorana mass for the neutrino (Fig. 1). This theorem has been extended to the supersymmetric case in [21].

The most stringent limits on the 0νββ mode of double-beta decay are obtained from the Heidelberg–Moscow experiment, which operates five enriched germanium crystals of total mass 11.5 kg containing 86% of the double-beta emitter ^{76}Ge. This corresponds to about 1.2 t of natural Ge and represents the strongest source strength of double-beta experiments, which, together with the very good energy resolution of 3 keV at 2000 keV (the region, where the 0νββ peak is situated), results in the most sensitive double-beta-decay experiment so far. The experiment is set up in the Gran Sasso Underground Laboratory in Italy and, with pulse shape discrimination, has a background of 0.06 counts/(kg yr keV) in the energy range of 0νββ decay.

At present, after 42 kg yr of measurement, of which 24 kg yr are analyzed applying pulse shape discrimination, applying the procedure suggested by the Particle Data Group [22], the following limits on the 0νββ-decay mode are deduced (see Fig. 2 and [5])

$$T_{1/2}^{0\nu\beta\beta} > 5.7 \times 10^{25} \text{ yr} \ (90\% \text{ C.L.}),$$
$$T_{1/2}^{0\nu\beta\beta} > 2.5 \times 10^{26} \text{ yr} \ (68\% \text{ C.L.}). \qquad (4)$$

This translates into a constraint on the Majorana neutrino mass of

$$\langle m_\nu \rangle < 0.2 \text{ eV} \ (90\% \text{ C.L.}),$$
$$\langle m_\nu \rangle < 0.1 \text{ eV} \ (68\% \text{ C.L.}). \qquad (5)$$

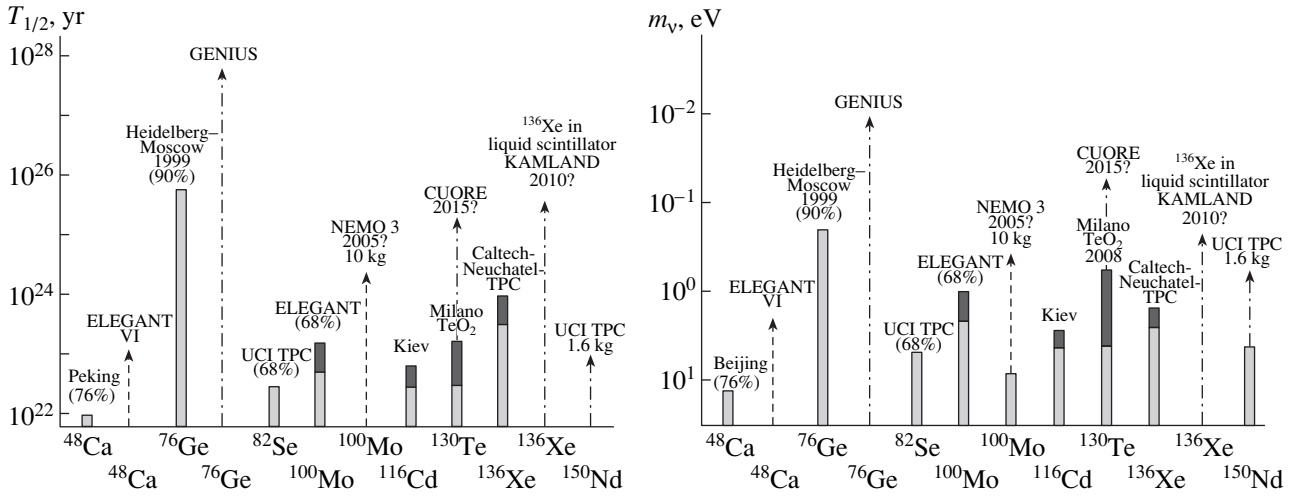

Fig. 3. Comparison of present and future half-life limits (left) and neutrino mass bounds (right) of currently operating and projected double-beta decay experiments. Light (dark) shaded bars correspond to present status (expectations) for running setups, dashed lines to experiments under construction, and dash-dotted lines to proposed facilities [6, 14, 15].

The experimental situation in the field of double-beta decay search is shown in Fig. 3.

The limit on $\langle m_\nu \rangle$ has a deep impact on neutrino mass models [6]. There is growing confidence that the neutrino is massive especially due to the observation of the solar and atmospheric neutrino deficits. The result of the LSND Collaboration [23] points to nonvanishing neutrino masses too but awaits confirmation. The Chooz experiment did not find evidence for neutrino oscillations. Furthermore, a massive neutrino is still the only candidate for the HDM in the universe. It is a formidable task to accommodate all the existing hints on neutrino masses in a compelling model for neutrino masses and a lot of activity is taking place in this field. Schemes containing three neutrinos and being compatible with the small angle MSW solution to the solar neutrino problem and the atmospheric neutrino problem and neutrino HDM are excluded by the limit (5) [7]. If the Chooz result is included and if the cosmological constant vanishes, the large angle MSW to the solar neutrino deficit is excluded too by (5) with 68% C.L. (without unnatural fine tuning) [8]. Three-neutrino models compatible with solutions to the solar and atmospheric neutrino deficits, LSND and Chooz (and no neutrino HDM), are ruled out by (5) according to [24] both in the degenerate and hierarchical case.

Models mixing four neutrinos exhibit the general mass pattern $m_1 < m_2 \ll m_3 < m_4$ in order to account for all four experiments on neutrino oscillations. Taking into account both the limit (5) and the limit on the number of active neutrino species from Big Bang Nucleosynthesis, the case where solar neutrinos oscillate between m_3, m_4 and atmospheric neutrinos oscillate between m_1, m_2 is ruled out [9, 25–27]. In the opposite case (solar neutrinos oscillate between m_1, m_2 and atmospheric neutrinos oscillate between m_3, m_4), an effective Majorana mass $7 \times 10^{-4} < |\langle m_{ee} \rangle| < 2 \times 10^{-2}$ eV is suggested by the operating oscillation experiments [12]. This mass range is not accessible by the currently operating $0\nu\beta\beta$-decay experiments, and a new approach is mandatory.

In addition, later on it will be argued that, if the neutrino is a Majorana particle, improving the sensitivity of double-beta experiments on the neutrino mass by one or two orders of magnitude would make them competitive and even superior to running or projected neutrino oscillation experiments. The most realistic next generation double-beta-decay setup designed to reach these goals is the GENIUS proposal [6, 14, 15], the proposed successor of the Heidelberg–Moscow experiment. Some of the characteristics of this project will be presented in the next chapter.

In respect to other models incorporating lepton-number violation, the constraints on their parameters currently set by the Heidelberg–Moscow experiment are summarized in the table. Some of the models mentioned will be discussed in more detail later when the expected impact of the GENIUS experiment will be compared to the sensitivity of future collider searches for new physics.

3. THE FUTURE OF DOUBLE-BETA DECAY: GENIUS

According to

$$T_{1/2} \sim 10^{25} \frac{a}{\mathrm{kg}} \sqrt{\frac{Mt}{\Delta E B}} \qquad (6)$$

(a enrichment factor, M active detector mass, t time of measurement, B background, ΔE energy resolution), to improve the sensitivity of $0\nu\beta\beta$ decay, one has to reduce the background and increase the active detector mass. The basic idea of the GENIUS setup is to operate

Current bounds on models incorporating lepton-number violation deduced from the current limit (4) on the half-life of 0νββ decay from the Heidelberg–Moscow experiment (most of the listed limits are superior to constraints which can be obtained from presently operating high- or low-energy experiments)

	Bound	Ref.
Light neutrino mass	$\langle m_\nu \rangle < 0.2$ eV	[5]
Heavy left-handed neutrino mass	$\langle m_\nu^{\text{heavy}} \rangle > 1.6 \times 10^8$ GeV	[28, 29]
W coupling to right-handed current (absolute lower limit)	$m_{W_R} > 1.6$ TeV	[30]
SUSY without R_P violation (for SUSY particle masses 100 GeV)	$\lambda'_{111} < 3.9 \times 10^{-4}$	[31]
	$\lambda'_{112}\,\lambda'_{121} < 5.0 \times 10^{-6}$, $\lambda'_{113}\,\lambda'_{131} < 1.6 \times 10^{-7}$	[32, 33]
SUSY with R_P violation, L-violating sneutrino mass	$\tilde{m}_{\not L} < 14$ MeV	[34]
Composite excited Majorana neutrino N^*	$m_{N^*} > 3.4 m_W$ (for N^*–e–W coupling $\sigma(1)$ and compositeness scale $\Lambda_C \approx m_{N^*}$)	[35, 36]
Constraints on leptoquarks–Higgs couplings		[37]
Test of Lorentz invariance and equivalence principle		[38]

enriched Germanium crystals of the Heidelberg–Moscow type directly in liquid nitrogen, thus avoiding any problematic contamination stemming from materials in the vicinity of the crystals. The feasibility of exposing the Ge crystals to liquid N has been tested in the Heidelberg low-level laboratory [39, 40]. Furthermore, the liquid nitrogen acts as shielding from ambient radiation. This leads to a reduction of the background by about a factor of 1000 to 0.04 counts/(t yr keV) in the region of interest for 0νββ decay. Below 100 keV (the region of interest for the direct search for CDM), the expected background is 10 counts/(t yr keV). The vessel has dimensions of height 12 m and diameter 12 m and will contain 100 kg of natural Ge for dark matter search, and 1 t and perhaps in a later step 10 t of enriched ^{76}Ge for 0νββ search. Some of the results of the Monte Carlo background simulations are shown in Fig. 4 (for details see [6, 14, 15, 40]).

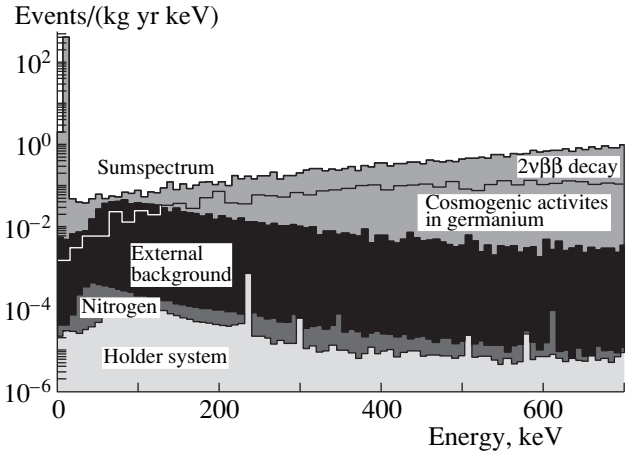

Fig. 4. Monte Carlo simulation of the background of GENIUS [40]. The dominant contribution below the expected 0νββ peak comes from the 2νββ-decay mode and can be subtracted, yielding a background of order 10 counts/(t yr keV) at energies below 100 keV [40]. In the region of the 0νββ peak, the background is on the 10^{-1} counts/(t yr keV) level (see also [6, 14, 15]).

For these parameters the 1-t GENIUS setup would explore the half-life of the 0νββ mode up to

$$T_{1/2}^{0\nu\beta\beta} > 5.8 \times 10^{27} \text{ yr} \quad (68\% \text{ C.L.})$$

after one year of measurement. Applying the same procedure as for the derivation of (5), the resulting limit on the neutrino mass is

$$\langle m_\nu \rangle < 0.02 \text{ eV} \quad (68\% \text{ C.L.}). \tag{7}$$

The final sensitivity (ten years of measurement, zero background) for the 1-t setup is

$$\begin{aligned} T_{1/2}^{0\nu\beta\beta} &> 6.4 \times 10^{28} \text{ yr} \quad (68\% \text{ C.L.}), \\ \langle m_\nu \rangle &< 6 \times 10^{-3} \text{ eV} \quad (68\% \text{ C.L.}), \end{aligned} \tag{8}$$

and the ultimate 10-t setup yields

$$\begin{aligned} T_{1/2}^{0\nu\beta\beta} &> 5.7 \times 10^{29} \text{ yr} \quad (68\% \text{ C.L.}), \\ \langle m_\nu \rangle &< 2 \times 10^{-3} \text{ eV} \quad (68\% \text{ C.L.}). \end{aligned} \tag{9}$$

4. GENIUS COMPARED TO THE LHC, NLC

In this section, the consequences of the expected limit on the half-life of the 0νββ mode set by GENIUS for some selected scenarios of non-SM physics will be discussed and compared to the expected results of next generation collider experiments, the LHC and the NLC.

The impact of GENIUS on neutrino oscillations will be presented in the next chapter.

4.1. GENIUS and Compositeness

If the ordinary fermions possess a substructure ("preons") which manifests itself at energies of the order of a compositeness scale Λ_C, there will be excited states of the SM fermions with masses of order or bigger than Λ_C. In particular, if the neutrino is of Majorana type, excited neutrino states yield contributions to $0\nu\beta\beta$ decay. Current conservation restricts the effective ν^*–*e*–*W* interaction (the asterisk denotes an excited fermion state) to be of magnetic-moment type

$$\mathcal{L}_{\text{eff}} = \frac{gf}{\sqrt{2}\Lambda_C}(\overline{\nu^*}\sigma^{\mu\nu}P_L e)\partial_\nu W_\mu^- + \text{h.c.},$$

where f is the coupling strength of the ν^*–*e*–*W* vertex. Nonobservation of $0\nu\beta\beta$ decay results in the limit [35, 36]

$$\left|\frac{f}{\Lambda_C}\right| \le m_{\nu^*}^{1/2}\left(\frac{m_e^2}{m_A^8}\right)^{1/4}\frac{1}{G_{01}^{1/4}(T_{1/2}^{0\nu\beta\beta})^{1/4}|M_{FI}|^{1/2}},$$

where G_{01} is a phase space integral and m_A, M_{FI} are input from nuclear physics (for details see [35, 36, 41]).

On the other hand, at the LHC, if operated in the proton–proton mode, the exchange of a Majorana composite neutrino gives rise to a like-sign dilepton signature [41]

$$pp \longrightarrow 2 \text{ jets} + \text{like-sign dilepton}, \quad \Delta L = 2.$$

A comparison of the discovery potential for the ν^*-induced $0\nu\beta\beta$ and for the like sign dilepton signal at the LHC (together with the current bound from the Heidelberg–Moscow experiment) is shown in Fig. 5 demonstrating that the two approaches are complementary, GENIUS for low ν^* masses being slightly more sensitive than LHC.

4.2. GENIUS and Left–Right Symmetry

In left–right-symmetric models, the SM gauge group is enlarged by a factor $SU(2)_R$. Below the scale at which the additional symmetry is broken, heavy Majorana neutrinos coupling to right-handed currents are present and trigger $0\nu\beta\beta$ decay (Fig. 6). The symmetry-breaking scale of the right-handed sector is a free parameter (but of course bigger than $\mathcal{O}$(1 TeV)). It was shown in [42] that the requirement of unitarity preservation in inverse $0\nu\beta\beta$ decay implies the presence of two Higgs triplets $\Delta_{L/R} = (\Delta^{--}, \Delta^-, \Delta^0)_{L/R}$ in the theory inducing itself contributions to $0\nu\beta\beta$ decay (Fig. 6). An analysis of both types of contributions has been carried out in [30].

Neglecting mixing between the left- and right-handed gauge bosons and Higgs scalars, the most conservative (lower) bounds on the masses of the right-handed *W* bosons and heavy neutrinos from nonobser-

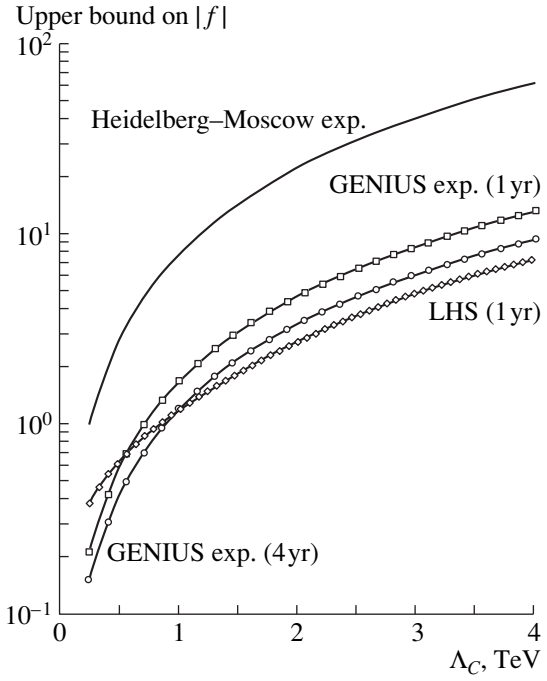

Fig. 5. GENIUS compared to the sensitivity of the LHC on the like-sign dilepton signal induced by a composite Majorana neutrino. The two facilities are complementary [41].

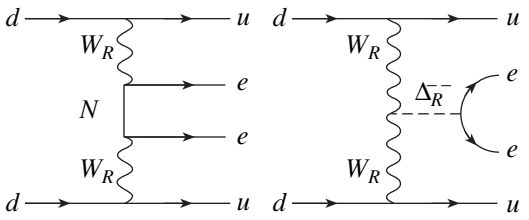

Fig. 6. Contribution to $0\nu\beta\beta$ decay in a left–right scenario via heavy Majorana neutrino (left) and doubly charged Higgs (right) [30].

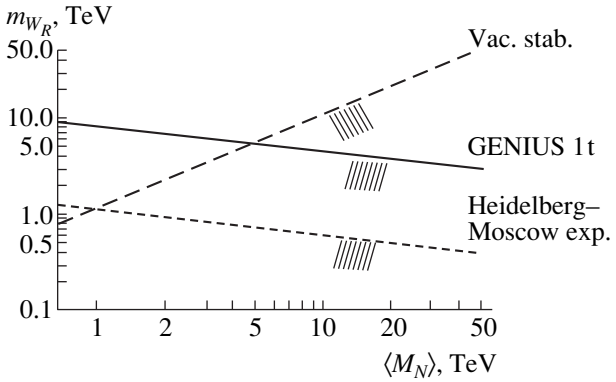

Fig. 7. The bounds on the m_{W_R}–M_N parameter space from $0\nu\beta\beta$ decay from the Heidelberg–Moscow experiment (short-dashed line) and GENIUS (solid line) together with the bounds from vacuum stability (long-dashed line). The region beneath the lines is excluded. The intercept of the lines is the absolute lower bound on m_{W_R}.

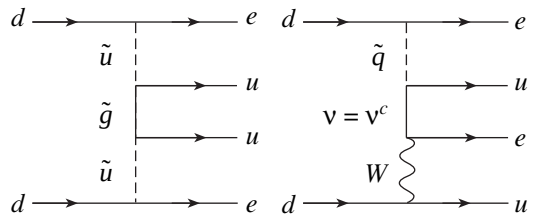

Fig. 8. Examples of contributions to 0νββ decay in SUSY models with R_P violation. The diagram on the left-hand side is generation diagonal in the coupling λ'_{111} [31], the diagram on the right-hand side involves a product of different couplings [33].

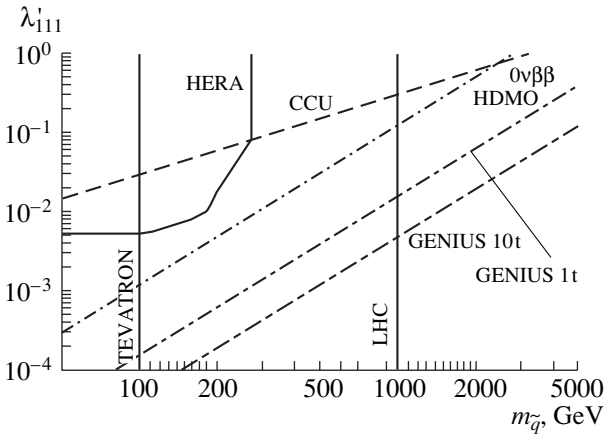

Fig. 9. Bounds on the $\lambda'_{111} - m_{\tilde{q}}$ parameter space for operating and planned low- and high-energy experiments. "CCU" is the limit from charged current universality (from [6, 14, 15]). Areas beyond and left of the contour lines are excluded.

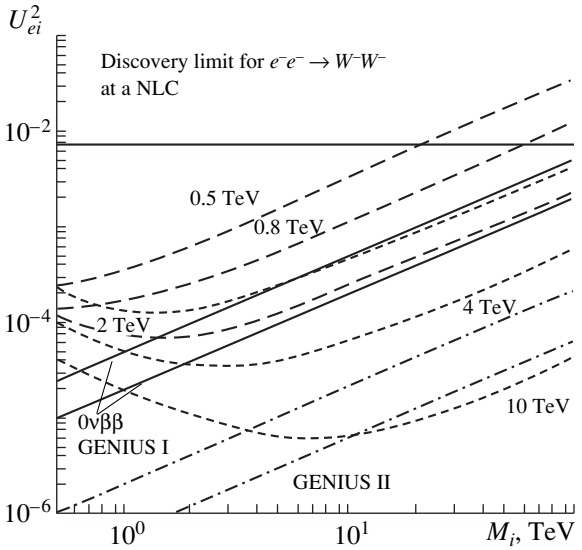

Fig. 10. The sensitivity of the GENIUS setup in the mixing angle–mass plane, compared to the sensitivity reachable at a NLC for several cms energies. GENIUS would exclude inverse 0νββ to be observed for any realistic NLC facility [28, 29].

vation of 0νββ decay are obtained for the mass of the doubly charged Higgs tending to infinity, reducing the bounds on the three-dimensional parameter space M_N–m_{W_R}–$m_{\Delta_R^{--}}$ into constraints on the M_N–m_{W_R} plane [30]. For the 1 t (10 t) GENIUS setup and for a neutrino mass $\langle M_N \rangle = 1$ TeV, the lower limit on m_{W_R} is [6, 14, 15]

$$m_{W_R} > 8 \ \ (18 \text{ TeV}). \qquad (10)$$

On the other hand, the LHC reaches a sensitivity of $m_{W_R} \approx 6$ TeV after 100 fb^{-1} of statistics.

In addition to the constraints from 0νββ decay, vacuum stability sets limits on the m_{W_R}–M_N parameter space too [43]. The two bounds together are shown in Fig. 13.

4.3. GENIUS and R_P-Violating SUSY

In SUSY models containing R_P-violating parts in the superpotential, 0νββ receives contributions from diagrams involving either the coupling λ'_{111} only [31] or products of couplings λ_{ijk}, λ'_{ijk}, (*ijk* are generation indices) [33]. Two examples of such graphs are depicted in Fig. 8. The Heidelberg–Moscow experiment yields the so far most restrictive bound on a R_P-violating coupling

$$|\lambda'_{111}| \le 3.9 \times 10^{-4} \left(\frac{m_{\tilde{q}}}{100 \text{ GeV}}\right)^2 \left(\frac{m_{\tilde{g}}}{100 \text{ GeV}}\right)^{1/2}. \qquad (11)$$

This bound is plotted together with the bounds from the 1-t and 10-t versions of GENIUS in Fig. 9. The current limit is superior to the ones at HERA and TEVATRON. GENIUS is more sensitive than the LHC for SUSY particle masses above 1 TeV. However, since SUSY masses are expected to be not significantly bigger than 1 TeV, LHC may do better than 0νββ, although only after several years of data taking.

4.4. GENIUS and Inverse 0νββ Decay at the NLC

The *L*-violating process $e^-e^- \longrightarrow W^-W^-$ is usually referred to as "Inverse Neutrinoless Double-Beta Decay" and has been investigated, e.g., in [28, 29], in the case that it is mediated by heavy Majorana neutrinos ν_i with masses M_i (its SUSY counterpart $e^-e^- \longrightarrow \chi^-\chi^-$ has been discussed in [44]). The cross section for this process for center of mass energies $s \gg M_i^2$ is unobservably small, whereas for heavy neutrino states $M_i^2 \gg s$ the cross section grows like $(\sum_i M_i (U_{ei})^2)^2 = (M_{ee}^*)^2$ in the limit $s \longrightarrow \infty$. This requires either this sum to be zero or the presence of a left-handed Higgs triplet whose contributions would restore unitarity. The presence of such a Higgs triplet is disfavored phenom-

enologically (see the discussion in [28, 29]). On the other hand, the absence of a left-handed Higgs triplet automatically guarantees the sum over masses and mixing angles to be zero since only a nonvanishing vacuum expectation value (vev) of a Higgs triplet generates $M_{ee} \neq 0$ (note that in the section about left–right symmetry the contribution of the right-handed Higgs triplet was discussed, which is unaffected by these considerations).

On the other hand, according to (3), 0νββ decay sets limits on the masses and mixing angles of the heavy neutrino states. The bounds for GENIUS and for the Heidelberg–Moscow experiment are plotted together with the discovery limits for the inverse 0νββ decay in Fig. 10 for a next generation linear collider assuming different values for the luminosity and $\sqrt{s}$. The GENIUS setup is more sensitive than any realistic NLC proposal.

5. GENIUS AND NEUTRINO OSCILLATIONS

If the neutrino is a Majorana particle, GENIUS will compete with or surpass the sensitivity of current or planned dedicated neutrino oscillation experiments. In order to understand the impact of 0νββ search on the Δm^2–$\sin^2 2\theta$ oscillation parameter space, remember that 0νββ measures the effective neutrino mass $\langle m_\nu \rangle$ as defined in (3). Since we are interested in oscillations between the light neutrino states, the small admixtures of the heavy neutrino states to the light states may be neglected, which then mix via a 3×3 mixing matrix in generation space. In contrast to the CKM matrix, the light Majorana neutrino mixing matrix can be parameterized by three angles and three phases [18]. The effective Majorana neutrino mass measured by 0νββ decay in this case is

$$\langle m_\nu \rangle = \left| c_{12}^2 c_{13}^2 m_1 + s_{12} c_{13} e^{-i\delta_{12}} m_2 + s_{13} e^{-i\delta_{13}} m_3 \right|, \quad (12)$$

where $c_{12} = \cos\theta_{12}$, etc. In order to compare 0νββ to the results of neutrino oscillation experiments, we consider, as a simple example, the two generation case and *CP* conservation. Then,

$$\langle m_\nu \rangle = \left| c_{12}^2 m_1 + s_{12}^2 m_2 e^{2i\delta_{12}} \right|, \quad e^{2i\delta_{12}} = \pm 1,$$
$$\Delta m_{21}^2 = m_2^2 - m_1^2 = m_2^2 \left(1 - \left(\frac{m_1}{m_2} \right)^2 \right). \quad (13)$$

Together with

$$m_2 = \frac{\langle m_\nu \rangle}{\left| \frac{m_1}{m_2} + \frac{1}{2}(1 - \sqrt{1 - \sin^2 2\theta}) \left(\pm 1 - \frac{m_1}{m_2} \right) \right|},$$

the result of 0νββ decay can be plotted in the Δm^2–$\sin^2 2\theta$ parameter space, once an assumption on the mass ratio $R = m_1/m_2$ of the two mass eigenstates under question is made. The worst case for the 0νββ case is

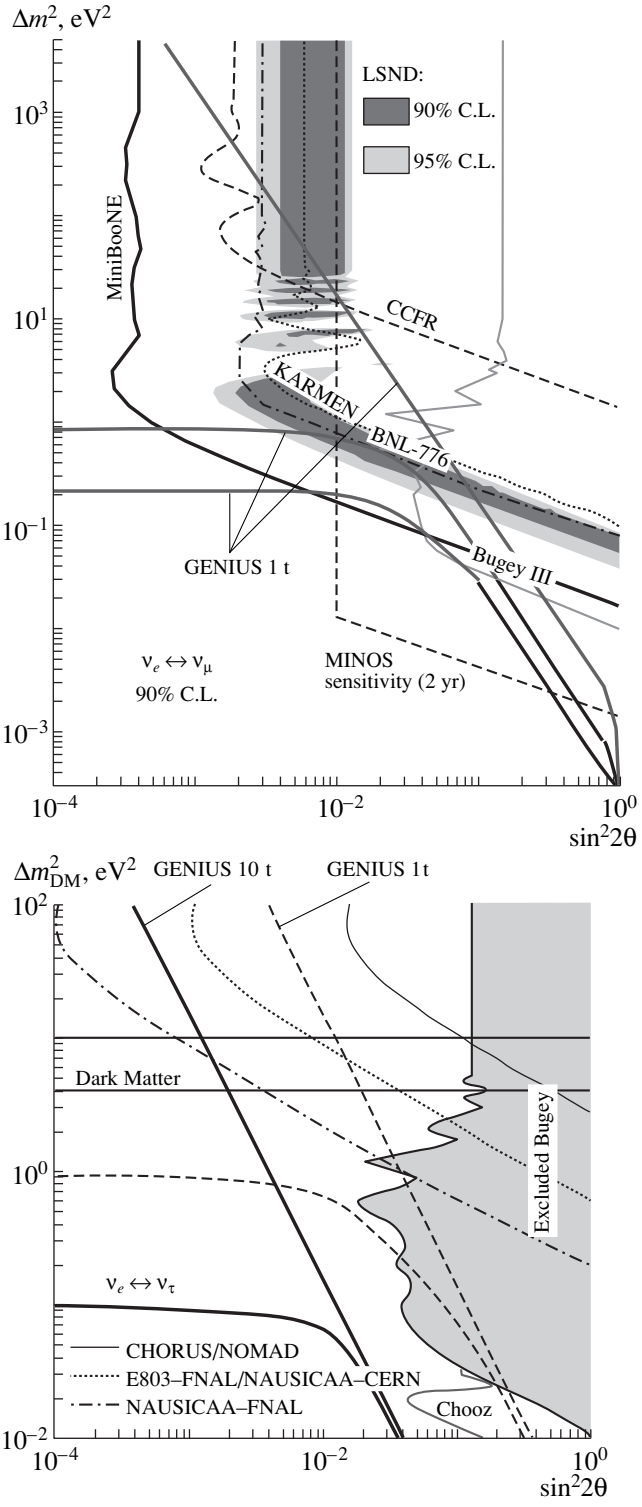

Fig. 11. The sensitivity of the GENIUS setup together with the results from running or projected reactor and accelerator experiments for neutrino oscillations in the $\nu_e \longleftrightarrow \nu_\mu$ (left) and $\nu_e \longleftrightarrow \nu_\tau$ (right) channels. The sensitivity of GENIUS is depicted for the cases $R = 0$, 0.01 (from top to bottom, for the $\nu_e \longleftrightarrow \nu_\mu$ channel, the curve for $R = 0.1$ is shown as well). GENIUS will cover a large new area of the parameter space unaccessible by the remaining approaches. In particular, GENIUS will definitely decide on the LSND result if R is not much smaller than 0.01 [6, 14, 15].

the case of strong hierarchy $m_1 \ll m_2$, while for the degenerate case $m_1 \approx m_2$ $0\nu\beta\beta$ is extremely sensitive. In particular, nonobservation of $0\nu\beta\beta$ by the 1-t GENIUS setup rules out degenerate neutrino mass textures which are able to account for neutrino HDM. Furthermore, for R not much smaller than 0.01 and a positive CP eigenvalue, GENIUS 1 t tests the LSND result (Fig. 11). The large-angle MSW solution to the solar neutrino problem is tested by the 10-t setup for any ratio R; the small angle solution would be tested by the 10-t version for a ratio R not much smaller than 0.5 (Fig. 12).

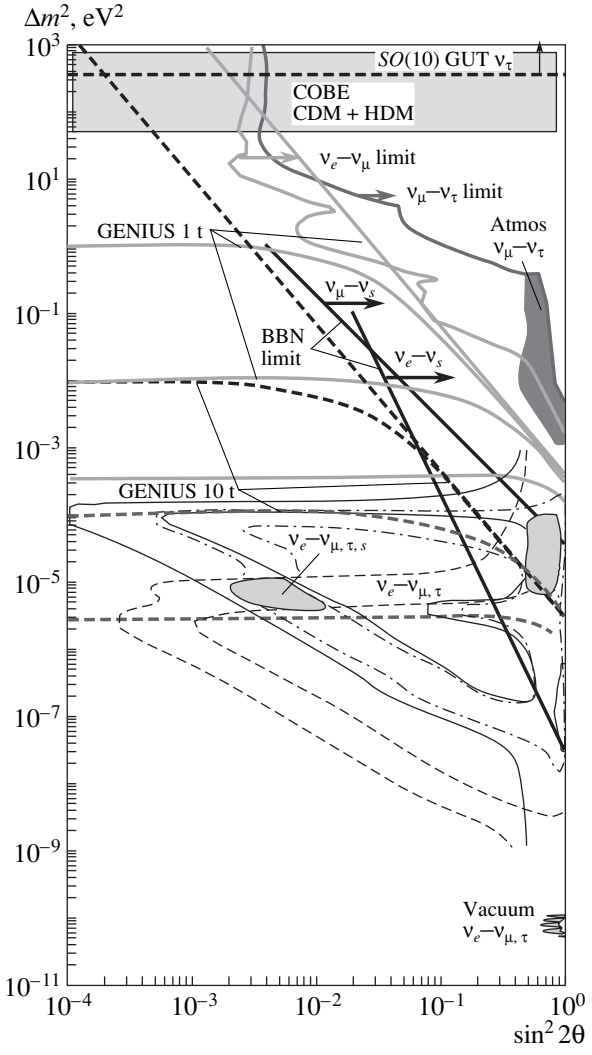

Fig. 12. Summary of currently available data on neutrino oscillations together with the expected results from GENIUS (from [6, 14, 15]). Solutions to the solar and atmospheric neutrino problems are depicted together with limits from reactor and accelerator oscillation searches. Furthermore, the mass range for cosmologically relevant neutrino HDM and the limit from Big Bang Nucleosynthesis for oscillations into sterile states are shown. The lines for GENIUS correspond to the ratios R = 0, 0.01, 0.1 (from top to bottom), and for the 10-t setup an additional curve for R = 0.5 is shown. The 1-t version excludes neutrino HDM (the neutrinos in this case usually being almost degenerate), although for the case of neutrino HDM neutrinos have to be degenerate [8]. The 10-t version even tests the small angle MSW solution to the solar neutrino problem for R not much smaller than 0.5 [16].

6. DARK MATTER SEARCH WITH GENIUS

In addition to the search for neutrino masses, i.e., the search for a hot component for the dark matter in the universe, the GENIUS setup, as the Heidelberg–Moscow experiment (Fig. 13 and [13]), will be used to search for CDM. In Fig. 13, the sensitivity of current and planned experiments for the scalar nucleon-WIMP (Weakly Interacting Massive Particle) cross section in dependence of the WIMP mass is shown. In the case of GENIUS, the line corresponds to a setup employing 100 kg of natural germanium and a measuring time of 3 yr. Furthermore, the expected cross sections in the case of neutralino CDM, being at present the best motivated candidate, are depicted (so-called scatter plot) for the MSSM with nonuniversal scalar mass unification [45]. For further references on the various approaches, see, e.g., [16]. In order to reach the sensitivity necessary to cover almost the full neutralino parameter space, GENIUS using 100 kg of natural germanium would be sufficient.

Both the currently running and the other proposed experiments cover a part of the relevant parameter space only. The Heidelberg Dark Matter Search setup (HDMS) [46, 47], which will start data taking in autumn 1999, will be sensitive to the parameter space compatible with the positive annual modulation signal claimed by the DAMA Collaboration [48].

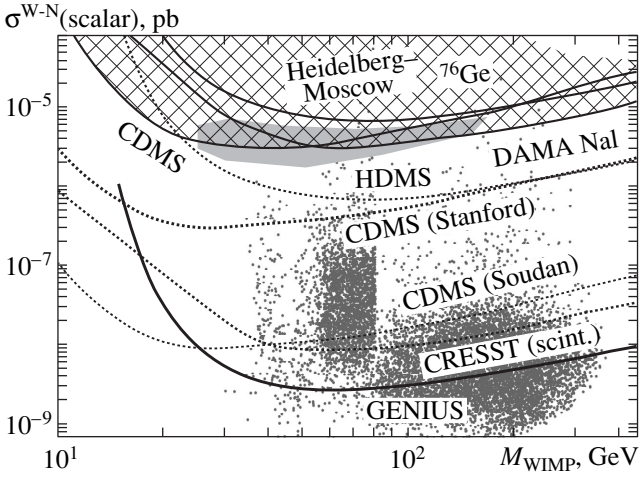

Fig. 13. The sensitivity of various operating and planned setups for scalar WIMP-nucleon interactions together with the scatter plot for neutralino CDM. The GENIUS version operating 100 kg of natural germanium is capable of testing the whole parameter space relevant for neutralino CDM [6, 14, 15].

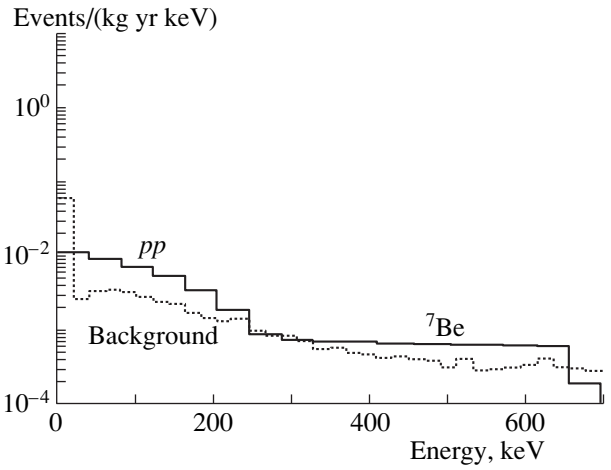

Fig. 14. Expected counts from *pp* and ^{7}Be neutrinos for a GENIUS setup operating 1 t of natural germanium. The excellent energy resolution and low background allow one to distinguish the edge of the highest energy ^{7}Be neutrinos. As a consequence, the day–night difference of the neutrino flux may be used to test the MSW solution; the seasonal flux variation may be explored to test the vacuum-oscillation hypothesis to the solar-neutrino problem [17].

7. LOWEST ENERGY SOLAR-NEUTRINO DETECTION WITH GENIUS

The extremely low background, low threshold (11 keV in the worst case) and high energy resolution (1 keV at 300 keV) of the GENIUS setup will allow one to measure the spectrum of lowest energy *pp* and ^{7}Be solar neutrinos [6, 17] in real time. For a version operating 1 t of natural germanium, the expected event rates in the absence of neutrino oscillations (via both neutral and charged current elastic scattering) in the Standard Solar Model are [6] 1.8 events/d for the *pp* neutrinos and 0.6 events/d for the ^{7}Be neutrinos (Fig. 14). On the other hand, for a full conversion $\nu_e \longrightarrow \nu_\mu$, the expected event rates are 0.48 events/d for *pp* neutrinos and 0.14 events/d for ^{7}Be neutrinos.

The very good energy resolution of the germanium detectors for detecting the recoiling electrons will allow one to determine for the first time the 1.3-keV predicted shift of the average energy of the beryllium neutrino lines. This shift is a direct measure of the central temperature of the sun. GENIUS will be able to test the "Low" MSW solution via the day–night modulation of the neutrino flux and the vacuum oscillation solution via the seasonal flux variation.

8. CONCLUSION

The Heidelberg–Moscow $0\nu\beta\beta$ search sets stringent limits on the Majorana neutrino mass and on other physics beyond the Standard Model, being in many cases the most sensitive ones up to date. Its proposed successor, the GENIUS setup operating one and in its extended version 10 t of enriched ^{76}Ge, will be competitive to next generation collider experiments in respect to, e.g., left–right-symmetric scenarios, compositeness, etc. Furthermore, due to its increased sensitivity to the neutrino Majorana mass by one and in an extended version two orders of magnitude, it will compete with and in many cases surpass dedicated neutrino oscillation searches if the neutrino is of Majorana type. In a less ambitious approach employing 100 kg of natural Ge, the sensitivity for the search for WIMPs will be superior to any other operating or projected approach and, in particular, will cover almost the entire parameter space relevant for neutralino CDM. A version running 1 t of natural germanium would be capable of measuring the fluxes of lowest energy solar neutrinos in real time and test the vacuum oscillation solution and the low MSW solution to the solar neutrino problem.

REFERENCES

1. K. Grotz and H. V. Klapdor, *The Weak Interaction in Nuclear, Particle and Astrophysics* (Adam Hilger, Bristol and Philadelphia, 1990).
2. R. N. Mohapatra and P. B. Pal, *Massive Neutrinos in Physics and Astrophysics* (World Sci., Singapore, 1991).
3. H. V. Klapdor-Kleingrothaus and A. Staudt, *Non-accelerator Particle Physics* (IOP Publ., Bristol and Philadelphia, 1995).
4. H. V. Klapdor-Kleingrothaus and K. Zuber, *Particle Astrophysics* (IOP Publ., Bristol and Philadelphia, 1997).
5. Heidelberg–Moscow Collab. (L. Baudis *et al.*), Phys. Rev. Lett. **83**, 41 (1999).
6. H. V. Klapdor-Kleingrothaus, L. Baudis, B. Majorovits, and H. Päs, hep-ph/9910205; MPI Report MPI-H-V26-1999.
7. R. Adhikari and G. Rajasekaran, hep-ph/9812361v3.
8. H. Minakata and O. Yasuda, Nucl. Phys. B **523**, 597 (1998).
9. C. Giunti, hep-ph/9906275.
10. E. Ma, hep-ph/9902392.
11. F. Vissani, hep-ph/9906525.
12. S. M. Bilenky *et al.*, hep-ph/9907234.
13. Heidelberg–Moscow Collab. (L. Baudis *et al.*), Phys. Rev. D **59**, 022001 (1999).
14. H. V. Klapdor-Kleingrothaus, Int. J. Mod. Phys. A **13**, 3953 (1998).
15. H. V. Klapdor-Kleingrothaus, in *Beyond the Desert, 1997, Accelerator and Non-accelerator Approaches, Castle Ringberg/Tegernsee, Germany, July 1997*, Ed. by H. V. Klapdor-Kleingrothaus and H. Päs (IOP, Bristol, 1998), p. 485.
16. H. V. Klapdor-Kleingrothaus, in *Proceedings of the 1st International Symposium on Lepton and Baryon Number Violation, Trento (Italy), Apr. 1998*, Ed. by H. V. Klapdor-Kleingrothaus and I. Krivosheina (IOP, Bristol, 1999), p. 251.
17. L. Baudis and H. V. Klapdor-Kleingrothaus, Eur. Phys. J. A **5**, 441 (1999).
18. M. Doi, T. Kotani, and E. Takasugi, Prog. Theor. Phys. Suppl. **83**, 1 (1985).

19. K. Muto and H. V. Klapdor, in *Neutrinos*, Ed. by H. V. Klapdor (Springer, Heidelberg, 1988), p. 183.
20. J. Schechter and J. W. F. Valle, Phys. Rev. D **25**, 2951 (1982).
21. M. Hirsch, H. V. Klapdor-Kleingrothaus, and S. Kovalenko, Phys. Lett. B **403**, 291 (1997).
22. C. Caso *et al.*, Eur. Phys. J. C **3**, 1 (1998).
23. W. C. Louis, in *Beyond the Desert, 1997, Accelerator and Non-accelerator Approaches, Castle Ringberg/Tegernsee, Germany, July 1997*, Ed. by H. V. Klapdor-Kleingrothaus and H. Päs (IOP, Bristol, 1998), p. 923.
24. G. Barenboim and F. Scheck, hep-ph/9808327.
25. S. Burles, K. M. Nollet, J. M. Truram, and M. S. Turner, astro-ph/9901157.
26. Y. Fukuda *et al.*, Phys. Rev. Lett. **82**, 1810 (1999).
27. J. H. Bahcall, P. I. Krastev, and A. Yu. Smirnov, Phys. Rev. D **58**, 096016 (1998).
28. G. Belanger, F. Boudjema, D. London, and H. Nadeau, Phys. Rev. D **53**, 6292 (1996).
29. G. Belanger, in *Proceedings of the 1st International Symposium on Lepton and Baryon Number Violation, Trento (Italy), Apr. 1998*, Ed. by H. V. Klapdor-Kleingrothaus and I. Krivosheina (IOP, Bristol, 1999), p. 605.
30. M. Hirsch, H. V. Klapdor-Kleingrothaus, and O. Panella, Phys. Lett. B **374**, 7 (1996).
31. M. Hirsch, H. V. Klapdor-Kleingrothaus, and S. Kovalenko, Phys. Rev. Lett. **75**, 17 (1995); Phys. Rev. D **53**, 1329 (1996).
32. H. Päs, M. Hirsch, and H. V. Klapdor-Kleingrothaus, Phys. Lett. B **459**, 450 (1999).
33. M. Hirsch, H. V. Klapdor-Kleingrothaus, and S. Kovalenko, Phys. Lett. B **372**, 181 (1996); Erratum: **381**, 488 (1996).
34. M. Hirsch, H. V. Klapdor-Kleingrothaus, and S. Kovalenko, Phys. Rev. D **57**, 1947 (1998).
35. O. Panella *et al.*, in *Beyond the Desert, 1997, Accelerator and Non-accelerator Approaches, Castle Ringberg/Tegernsee, Germany, July 1997*, Ed. by H. V. Klapdor-Kleingrothaus and H. Päs (IOP, Bristol, 1998), p. 339.
36. O. Panella, C. Carimalo, Y. N. Srivastava, and A. Widom, Phys. Rev. D **56**, 5766 (1997).
37. M. Hirsch, H. V. Klapdor-Kleingrothaus, and S. Kovalenko, Phys. Lett. B **378**, 17 (1996); Phys. Rev. D **54**, 4207 (1996).
38. H. V. Klapdor-Kleingrothaus, H. Päs, and U. Sarkar, Eur. Phys. J. A **5**, 3 (1999).
39. J. Hellmig and H. V. Klapdor-Kleingrothaus, Z. Phys. A **359**, 351 (1997).
40. L. Baudis *et al.*, Nucl. Instrum. Methods A **426**, 425 (1999).
41. O. Panella, C. Carimalo, and Y. N. Srivastava, hep-ph/9903253.
42. T. Rizzo, Phys. Lett. B **116**, 23 (1982).
43. R. N. Mohapatra, Phys. Rev. D **34**, 909 (1986).
44. M. Hirsch, H. V. Klapdor-Kleingrothaus, St. Kolb, and S. Kovalenko, Phys. Rev. D **57**, 2020 (1998).
45. V. Bednyakov, H. V. Klapdor-Kleingrothaus, S. Kovalenko, and Y. Ramachers, Z. Phys. A **357**, 339 (1997).
46. L. Baudis *et al.*, Nucl. Instrum. Methods A **385**, 265 (1997).
47. H. V. Klapdor-Kleingrothaus and Y. Ramachers, in *Proceedings of the International Workshop on Dark Matter in Astro- and Particle-Physics, Heidelberg, Sept. 1996*, Ed. by H. V. Klapdor-Kleingrothaus and Y. Ramachers (World Sci., Singapore, 1997), p. 459.
48. R. Bernabei, in *Proceedings of the Second International Conference on Dark Matter "Dark 98," Heidelberg, Germany, July 1998*, Ed. by H. V. Klapdor-Kleingrothaus and L. Baudis (IOP, Bristol, 1999), p. 711.

Physics of Atomic Nuclei, Vol. 63, No. 7, 2000, pp. 1259–1263. From Yadernaya Fizika, Vol. 63, No. 7, 2000, pp. 1332–1336.

EXPERIMENTAL RESULTS, METHODS, AND FACILITIES

The CUORE/CUORICINO Project: Preliminary Studies*

C. Brofferio**
(for the CUORE Collaboration)
Dipartimento di Fisica dell'Universitá di Milano-Bicocca and Sezione di Milano dell'INFN, Italy

Abstract—A 1-t bolometer detector, aiming at the search for neutrinoless double-beta decay, cold dark matter, and solar axions with extremely high sensitivity, has been proposed (CUORE project). At the moment, the construction of a 42-kg array of 56 TeO_2 bolometers (CUORICINO project) has been approved and is financed. CUORICINO will be a feasibility test for CUORE, while increasing the present sensitivity on $0\nu\beta\beta$ half-life of ^{130}Te (1×10^{23} yr, 90% C.L.). The state of the art of CUORICINO, together with the physical motivations and the technical feasibility of the CUORE project, is briefly discussed. © *2000 MAIK "Nauka/Interperiodica".*

1. INTRODUCTION

Most of the interest in underground physics is presently devoted to the search for rare events [1]. Typical examples are radioactive processes like single- and double-beta decay, nuclear exotic decays emitting alpha particles or other complex nuclei, and interactions of solar neutrinos, axions, and weakly interacting massive particles (WIMPs). Underground experiments with "artificial" neutrinos have already been carried out to test the performance of solar neutrino detectors and are now proposed to search for a nonzero neutrino magnetic moment. At higher energies, a long baseline underground experiment with neutrinos from accelerators is already taking data, and others are planned for the future.

In all these experiments, the overburden of rock present in underground laboratories is essential to reduce the background due to cosmic rays, while the investigation and reduction of radioactive environmental background goes through a strict selection of all the materials surrounding and composing the detector itself. Other requirements are a good energy resolution, low threshold, and, in some cases, as in the search for WIMPs, a specific good detection efficiency for nuclear recoils. A very useful, even if not compulsory, tool in rare event detection is the capability to distinguish between interactions with high-ionizing (typically β and γ) and low-ionizing particles.

Low-temperature detectors can match all these requirements and have therefore been developed since 1984 [2] for underground physics, as well as for many other fields of scientific research, ranging from biology to material science and from nuclear to astroparticle physics [3]. At the moment, four large cryogenic experiments are running underground to search for double-beta decay (DBD) and cold dark matter (CDM) [4]. It is on the wake of the good results already achieved by these experiments that the CUORE project has been proposed, as the natural future development in underground physics with bolometers.

2. LOW-TEMPERATURE DETECTORS (LTD)

At the basis of the phonon-mediated particle detection, there is a very simple idea: the specific heat C of a dielectric and diamagnetic crystal cooled down in the millikelvin (or tens of millikelvin) region can be so low (being proportional to the cube of the ratio between the operating and the Debye temperature of the crystal) that appreciable temperature increases can be induced in macroscopic amounts of material even by the tiny energy released by a single particle interaction. In a very naive approach, a LTD can be sketched as a device consisting of a particle absorber and a thermometer in good thermal contact with it. A weak thermal link (of conductance G) between the detector and a heat sink kept at constant temperature must also be present to restore the original temperature after the impinging of the particle, with a characteristic time τ given by C/G. It can be shown that the fluctuations of the internal energy of a system are given by $\Delta E_{\mathrm{rms}} \approx \sqrt{k_b T^2 C}$. This expression gives the order of magnitude of the intrinsic energy resolution of LTD and can be as low as a few eV even for masses of the order of 1 kg, provided that the temperatures are low enough. Of course, this schematization is sufficiently correct only if the energy released in the absorber is fully thermalized.

In a different approach, the thermometer can be replaced by a phonon sensor which detects directly the high-energy phonons produced out of equilibrium just after the energy is released in the absorber: typical examples are superconducting tunnel junctions (STJ) and superconducting films kept at the transition edge (TES), where they are sensitive. In this case, the energy resolution is not given by the above formula, but depends on the statistical fluctuation of the produced

* This article was submitted by the author in English.
** WEB site: http://hpbbgs.lngs.infn.it/halla/index_CUORE.html

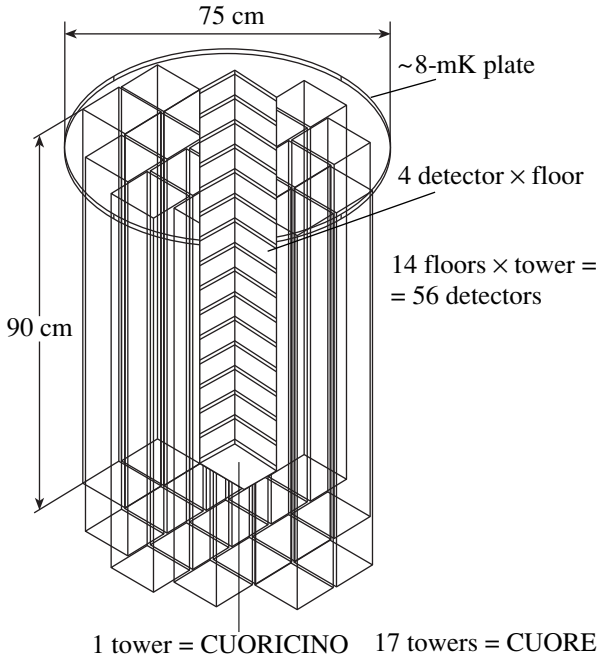

Fig. 1. Schematic CUORE setup.

quasiparticles in STJ and on the heat capacity of the sensor in TES, thus not depending anymore on the mass of the absorber.

LTDs offer remarkable advantages over conventional nuclear detectors: apart from their intrinsic energy resolution, there is a large freedom in the choice of the absorbing material, and the sensitivity to ionizing and nonionizing (like nuclear recoils induced by WIMPs) events is equivalent. Hybrid detectors, consisting of both conventional and low-temperature detectors, have been proposed and tested, showing their great advantage in the discrimination on the type of interacting quantum.

3. THE CUORE PROJECT

The present proposed configuration for the CUORE project is a nearly straightforward extension of the Milano–Gran Sasso 20-detector array now running in Gran Sasso Underground Laboratories [5], which is performing an experiment on DBD of ^{130}Te with nearly 7 kg of TeO_2 crystals. CUORE should be composed of 255 identical copper structures (the elementary module), each fastening (by means of two PTFE frames) four TeO_2 cubic crystals of 5-cm side, 750 g each, stacked in 17 towers of 15 floors (Fig. 1). The detector will therefore be a close-packed, high-granularity, 1020 crystal array, working at 10 mK inside a single dilution refrigerator.

In the present configuration, the heat pulses are thought to be registered via NTD Ge thermistors glued on the crystals, because they have demonstrated to be very reliable and reproducible, easy to handle, well matched to the already developed Milano front-end electronics, and not too expensive. But alternative options, like TES combined with DC_SQUID readout, could be taken into account for their already demonstrated better energy resolution, even if these sensors are much more critical, delicate, expensive, and limited in energy spanning (the temperature range in which they are sensitive is small). Nevertheless, crystals operated contemporarily with NTD thermistors and TES, to investigate the high and low energy regions of the spectrum, respectively, could also be considered, if this solution should prove to be technically and financially viable. The first goal (even if not the only one) of CUORE should be to test the $\langle m_{\nu_e} \rangle$, derived from $0\nu\beta\beta$, in the 10^{-2}-eV energy range (for a general introduction on DBD, see, for instance, [6]). In fact, the present technology, thanks to the experiments which study $0\nu\beta\beta$ of ^{76}Ge [7, 8], has already pushed the limit on $\langle m_{\nu_e} \rangle$ below 1 eV and will reach the 0.1-eV energy range in the future. To improve further, a new concept experiment must be designed. The study of ^{130}Te using the bolometric technique is a very promising approach for new generation DBD experiments. By comparing CUORE with the only other future proposed project, GENIUS [9], based on ^{76}Ge, we can observe that ^{130}Te transition energy (2528 keV) gives a phase space three times larger than that of ^{76}Ge and it should have (some disagreements in calculations are still present) a more favorable nuclear matrix element [10, 11]. Moreover, CUORE will contain 10^{27} ^{130}Te nuclei without enrichment (which is often economically prohibitive for large quantities), thanks to ^{130}Te high natural abundance (34%). Taking into account both isotopic abundance and decay rate, the CUORE 765 kg of TeO_2 (more than 200 kg of ^{130}Te) are equivalent to the effectiveness of 700–1000 kg (depending on the nuclear matrix elements) of Ge detectors isotopically enriched to 86% in ^{76}Ge. The total cost of CUORE, in this configuration, should not exceed \$10 M, to be compared with the S130 M needed for GENIUS.

Different scenarios for CUORE are also possible, thanks to the unique flexibility of LTD in the choice of the absorber material. Other crystals have already been tested, like Si, Ge, LiF, CaF_2, Al_2O_3, $CdWO_4$, and $PbWO_4$, so CUORE could also be composed of a core of 5500-cm^3 Compton-suppressed detectors (44 crystals) with absorbers optimum for, for instance, CDM search or solar axions interactions, or any other kind of interesting physics requiring low-background counting rates and feasible with bolometers. The external layer of 956 TeO_2 detectors would then be used for $0\nu\beta\beta$ of ^{130}Te, while acting as a live shield for the internal detectors. The potentials of CUORE have already been presented in other conferences (see for instance [12]). The most stringent requirements are of course energy resolution, energy threshold, and background counting rate. The present mean values for the 20 detectors running in

Gran Sasso are a baseline ΔE_{FWHM} of 3 keV and a ΔE_{FWHM} of 8 keV at 2.6 MeV, with a background counting rate of 0.5 counts/(keV kg yr) [13]. A 20-keV threshold with a 100% efficiency has been reached on all detectors, with a background of 5 counts/(keV kg d), while work is in progress in noise discrimination to reach a 100%-efficient 5-keV threshold (which should be feasible, looking to the energy resolution). In the following sections, the realistic expectations for CUORE will be discussed.

4. TECHNICAL CHALLENGES IN THE CUORE PROJECT

The operation of bolometric detectors with large sensitive volumes requires high-sensitivity thermistors, very low temperatures (~10 mK), long-term stability and single detector reproducibility. Many years of work of the Milano group has shown that the bolometric technique is mature in all these aspects and that a large channel multiplication is now viable. Reliability and reproducibility of NTD Ge thermistors have been proven by several groups all over the world and do not require further studies. Optimization of resistivity, geometry, and thermal conductances versus crystal and heat sink are under study. The cryogenics required to cool down and maintain a 1-t detector at 10 mK are complex (you need a huge, powerful, dilution refrigerator), but already studied for the GRAIL project [14] and tested in the NAUTILUS experiment, where 2.35 t of Al are cooled down to less than 100 mK and kept at low temperatures for very long time [15]. At first sight, one would expect that the increase in mass of the absorber (750 g instead of 340 g) should imply a worsening of the energy resolution, since the heat capacity should increase. The experimental evidence is, however, the opposite: the Milano group started to develop TeO_2 LTD in 1991 with a 6-g crystal reaching a FWHM energy resolution of only 50 keV for γ rays of 2.6 MeV (^{208}Tl), while in the present experiment less than 5 keV are obtained at the same energy with crystals of 340 g. The possible explanations for this behavior are that there has been an improvement in base temperature and sensitivity, together with microphonic noise reduction, and that there could be a nonthermal component of the signal, not scaling with C. In both cases, there is still room for improvements, since the intrinsic energy resolution is still insufficient, being only a few tens of eV for crystals of 750 g, working around 10 mK.

Cryogenic setups exhibit instabilities which can affect bolometer performances: an active mechanism to stabilize detector response is therefore necessary. The solution adopted in the Milano–Gran Sasso 20-detector array has proven to be satisfactory and will be used also for CUORE. A doped silicon resistance, with a metallic behavior, is glued directly on each crystal and acts as a heater, delivering calibrated energy amounts to the absorber through joule power. The heater pulses are very similar to particle pulses; therefore, once the correlation between the heater pulse height and the detector instantaneous operation point (sometimes varying several percent from the set one, due to unavoidable cryostat instabilities) is obtained, it is possible to correct the amplitude of all physical pulses in a very effective way, as explained in [16]. Single detector reproducibility is, with the present technical knowledge, feasible, as has been demonstrated with the 20-detector array [13]. An important step for CUORE will nevertheless be the "industrialization" of the construction and mounting of 1000 detectors, therefore requiring ad hoc studies. But many other collaborations have already shown that this can always be achieved.

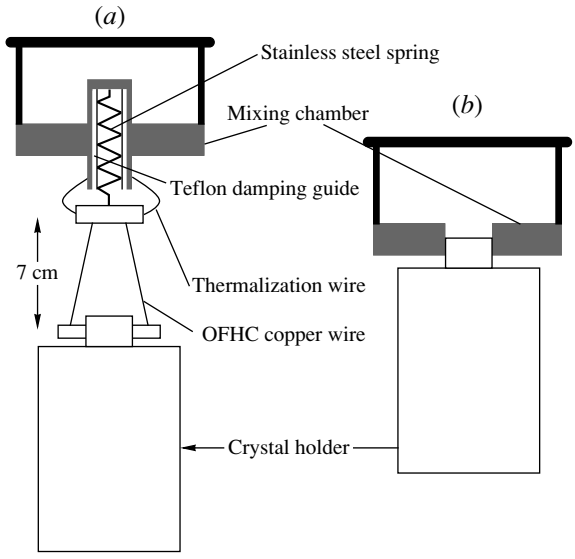

Fig. 2. Adopted detector holding methods: (*a*) crystal holder suspended from the mixing chamber; (*b*) crystal holder screwed under the mixing chamber.

Background reduction is a crucial point in all rare event experiments. As far as CUORE is concerned, Monte Carlo simulations are under study. It is, however, important to notice that the present background level in the Milano experiment is a factor 5–10 times better, depending on the energy region, than the best previous result obtained with a single TeO_2 detector. This improvement has come from very simple care on material selection and crystal mounting, which can certainly still be improved, thanks also to the worldwide recognized expertise in low radioactive contamination of some of the CUORE collaborators. Nevertheless, to be more convincing on this and on the other technical challenges discussed up to now, we have proposed a pilot experiment: CUORICINO.

5. THE CUORICINO PROJECT AND SOME PRELIMINARY RESULTS

As a first step toward CUORE, CUORICINO will be housed in the Milano dilution refrigerator, which is located in hall A of Gran Sasso Underground Laborato-

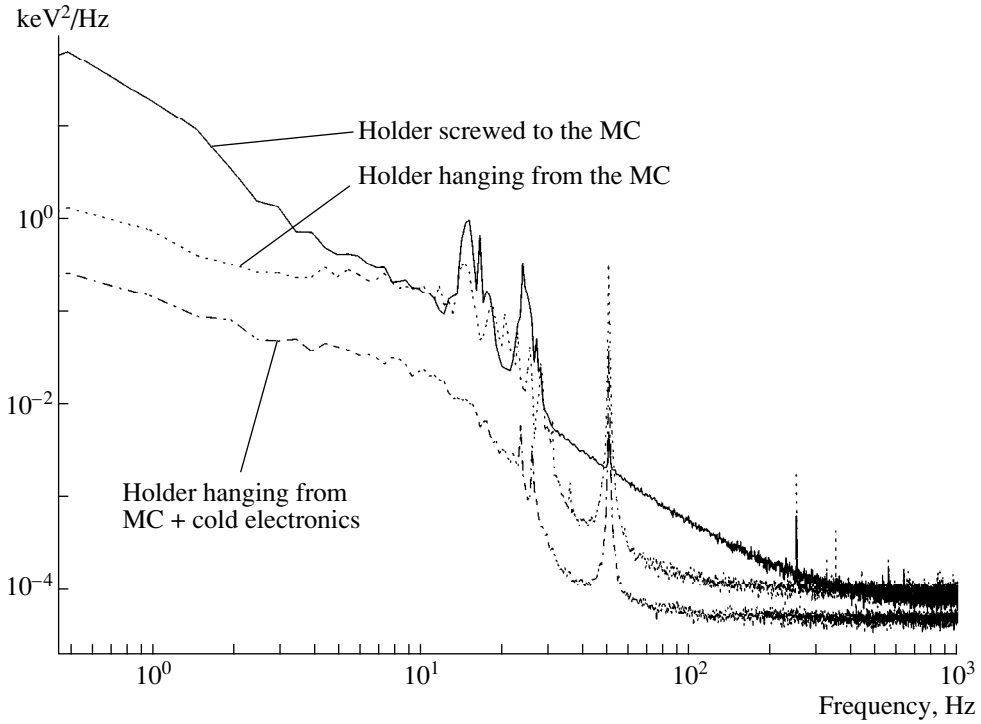

Fig. 3. Energy noise spectra obtained with the same detector in different runs. The electronics has a 4-pole 12-Hz Bessel filter.

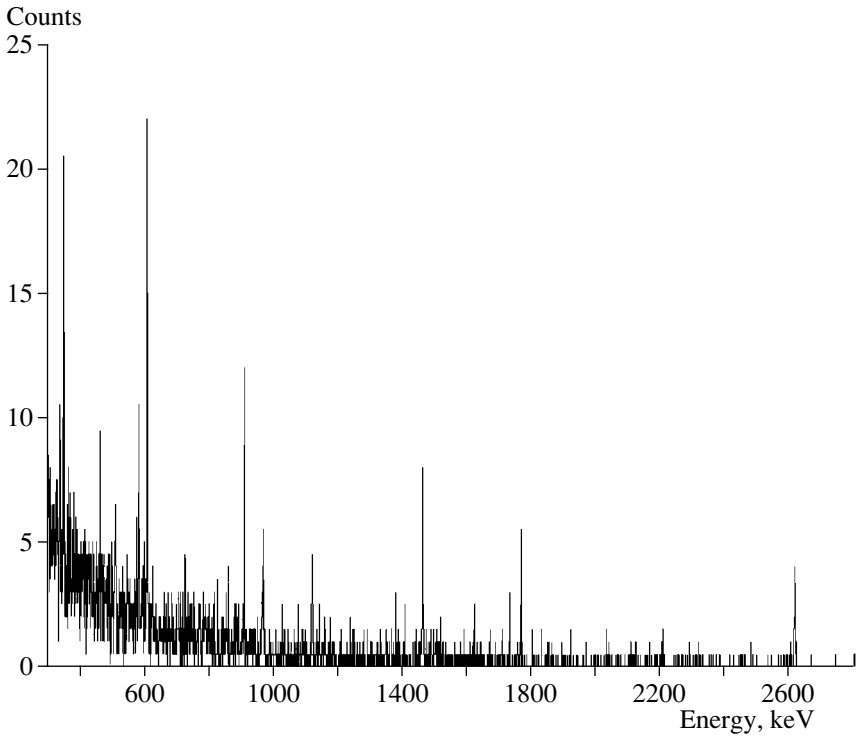

Fig. 4. ^{232}Th + ^{238}U calibration spectrum obtained with the single 750 g TeO_2 detector.

ries and where presently the Milano experiment is running. This will limit cost and save space in the Laboratories, which are always "overbooked." It will consist of 56 crystals, stacked in a single tower, identical to those proposed for CUORE (except for the number of crystals, due to room limitation in the existing dilution refrigerator), therefore being a real test for many aspects of the CUORE project, but also a powerful self-

consistent rare-event detector (42-kg total mass, more than 6 times bigger than the present array). The entire tower will be surrounded by several electrolytic Cu coaxial cylinders, corresponding to the main thermal shieldings and vessels of the dilution refrigerator, and will be topped with a Roman lead disk of 10-cm height and 15-cm diameter to shield it from the dilution unit, where some minor, but unavoidable, components could contain a residual intrinsic radioactive contamination. The refrigerator itself will be shielded by 2-cm-thick Roman lead coaxial cylinder and by two layers of 10 + 10-cm-thick modern lead, of respectively 16- and 150-Bq/kg ^{210}Pb activity. A sealed plexiglas box, with continuous N_2 gas flushing, will reduce the ^{222}Rn contamination. A passive or active neutron shield is also under study.

Since the CUORICINO Project has been approved and financed by the different international committees, supervising the CUORE Collaboration, we are now testing the performance of the elementary module using the dilution refrigerator located in hall C. The preliminary tests were realized with a single 750-g crystal mounted in a structure similar to that of the 20-detector array [17, 18]. To increase the signal amplitude, some changes were performed on the thermistor, with respect to those used in the 20-detector array. To reduce vibrations of the structure, the crystal holder was hanging from the mixing chamber, forming a mechanical system equivalent to a damped pendulum (Fig. 2), while, to reduce readout wire microphonic noise and electronic intrinsic noise, the load resistors and first stage JFETs were operated at ≈120 K in a special box, at only few tens of cm from the detector (instead of the nearly 3-m distance of the room temperature electronics). The noise reduction can be observed in Fig. 3, while the FWHM energy resolution, spanning from 1.5 keV at 238 keV to 3.9 keV at 2.6 MeV, can be appreciated in the calibration spectrum reported in Fig. 4. These results are 2 times better than the mean energy resolution obtained with the 20 340-g crystals, despite a more than double mass of the absorber, reaching values very similar to Ge-diode detectors. Furthermore, an excellent energy resolution of 4 keV was obtained on the ^{210}Po α line at 5.4 MeV, which is the best energy resolution for α particles ever obtained with any type of detector. We hope now to confirm these beautiful results also with the CUORE/CUORICINO elementary module, presently running in Gran Sasso.

6. CONCLUSIONS

As discussed in this paper, CUORE can be foreseen as the medium-term goal of large mass cryogenic detectors. Some of the positive aspects of this project are as follows.

It is a renewable detector. One can choose the absorber material according to the physics one wants to study: one can start with one configuration and then switch to a completely or partially different one.

Its costs and logistics requirements are reasonable.

It will be tested on a smaller scale by CUORICINO, therefore getting free from a complete dependence on difficult Monte Carlo simulations for the final approval, even if Monte Carlo will certainly help to understand the residual background sources.

CUORICINO is an approved experiment, for which technical R&D is already going on, with very promising preliminary results. Data taking should start before the end of 2001 and, depending on the energy resolution, threshold, and background counting rates, could already make some good underground physics.

ACKNOWLEDGMENTS

This work is partially supported by the European Community (contract FRMX-CT98-0167).

REFERENCES

1. Many contributions at this conference were dealing with this subject.
2. E. Fiorini and T. O. Niinikoski, Nucl. Instrum. Methods **224**, 83 (1984).
3. For recent reviews on cryogenic detectors, see D. Twerenbold, Rep. Prog. Phys. **59**, 349 (1996); N. Booth, B. Cabrera, and E. Fiorini, Annu. Rev. Nucl. Sci. **46**, 471 (1996).
4. The present status of these experiments has been presented at the *VIII International Workshop on "Low Temperature Detectors," Dalfsen, Netherlands, Aug. 1999*, Nucl. Instrum. Methods A (in press).
5. A. Alessandrello *et al.*, Phys. Lett. B **433**, 156 (1998).
6. M. K. Moe and P. Vogel, Annu. Rev. Nucl. Sci. **44**, 247 (1994).
7. S. Kolb *et al.*, Yad. Fiz. **63** (2000) [Phys. At. Nucl. **63** (2000)].
8. I. V. Kirpichnikov *et al.*, Yad. Fiz. **63** (2000) [Phys. At. Nucl. **63** (2000)].
9. J. Hellmig and H. V. Klapdor-Kleingrothaus, Z. Phys. A **359**, 361 (1997).
10. J. Suhonen and O. Civitarese, Phys. Rep. **300**, 123 (1998) and references therein.
11. A. Faessler, Yad. Fiz. **63** (2000) [Phys. At. Nucl. **63** (2000)].
12. A. Alessandrello *et al.*, in *Proceedings of VI International Symposium on "Particles, Strings and Cosmology (PASCOS)," Boston, 1998* (World Sci., 1998).
13. A. Alessandrello *et al.*, in *Proceedings of VIII International Workshop on "Low Temperature Detectors," Dalfsen, Aug. 1999*, Nucl. Instrum. Methods A (in press).
14. G. Frossati and E. Coccia, Cryogenics **34**, 9 (1994).
15. P. Astone *et al.*, Astropart. Phys. **7**, 231 (1997).
16. A. Alessandrello *et al.*, Nucl. Instrum. Methods A **412**, 454 (1998).
17. A. Alessandrello *et al.*, in *Proceedings of VIII International Workshop on "Low Temperature Detectors," Dalfsen, Aug. 1999*, Nucl. Instrum. Methods A (in press).
18. A. Alessandrello *et al.*, Nucl. Instrum. Methods A **440**, 397 (2000).

Physics of Atomic Nuclei, Vol. 63, No. 7, 2000, pp. 1264–1267. From Yadernaya Fizika, Vol. 63, No. 7, 2000, pp. 1337–1340.

EXPERIMENTAL RESULTS, METHODS, AND FACILITIES

Results of the Pilot Experiment to Search for Inelastic Interactions of WIMPs with ^{73}Ge*

F. T. Avignone III[1)], R. L. Brodzinski[2)], A. A. Klimenko, H. S. Miley[2)], S. B. Osetrov, J. H. Reeves[2)], A. A. Smolnikov, and S. I. Vasiliev**

Institute for Nuclear Research, Russian Academy of Sciences, pr. Shestidesyatiletiya Oktyabrya 7a, Moscow, 117312 Russia and Joint Institute for Nuclear Research, Dubna, Moscow oblast, 141980 Russia

Abstract—A pilot search for the excitation of ^{73}Ge to the first excited state at 13.26 keV by spin-dependent interactions of Weakly Interacting Massive Particles (WIMPs) was performed. The first experimental results have been analyzed with a new method. The background for these reactions is ≤0.0012 events/(keV kg(^{73}Ge) d). Although there is no theory for *E*2 excitations by WIMPs, this very large suppression of the background may promise an enlarged version of this experiment to be competitive. It is appropriate to propose an experiment with several kg of enriched ^{73}Ge detectors based on these results. © *2000 MAIK "Nauka/Interperiodica".*

1. INTRODUCTION

There is compelling evidence from rotation curves that galactic halos contain about 10 times more mass in the form of dark matter than the total mass of the galaxy contains in ordinary visible matter. This is also found on larger scales to explain the dynamics of galaxy clusters, as well as fluctuations in the ≈3 K background radiation [1].

Until recently, cosmological models that best explained the present state of the Universe have contained about 90% nonbaryonic Dark Matter (DM), of which ≈70% is nonrelativistic Cold Dark Matter (CDM) that played a key role in the formation of stars and galaxies, and most of the rest in the form of relativistic "free streaming," Hot Dark Matter (HDM). The HDM component was needed to yield the large-scale structure compatible with astronomical observations up to a few years ago. In addition, most of the cosmological models that yielded the best results had an average mass density parameter, $\Omega \equiv \rho/\rho_{crit} = 1$, where ρ_{crit} is that which just closes the Universe. A comprehensive review of the subject is given in [1]. The most popular candidates for the CDM are weakly interacting massive particles (WIMPs), the lightest supersymmetric particles (neutralinos), or perhaps axions. Popular candidates for HDM are massive neutrinos. However, recent observations have shown that the Universe expansion is accelerating, which favors the existence of a nonzero Einstein cosmological constant, Λ, and $\Omega = \Omega(\mathrm{CDM}) + \Omega(\Lambda) = 1$. In this scenario, $\Omega(\mathrm{CDM}) \approx 0.3$ and $\Omega(\Lambda) \approx 0.7$.

Recent papers have even introduced new hypothesized CDM scenarios, namely superheavy [2], new sources of "clumpiness" of CDM [3], and new WIMP populations in the Solar System due to scattering in the Sun and trapping in planetary elliptical orbits [4]. The CDM problem appears to be in a state of flux.

In the experimental realm, since the first experiment with an ionization detector [5], a dozen years of continuous improvement have followed [6–10], with the most sensitive bounds set by the DAMA experiment [11]. In fact, the DAMA collaboration has claimed a positive result, although it has been seriously questioned [12]. A very recent paper by Baudis *et al.* [13] gives new results from a large Ge detector as well as expected sensitivities of several present and future experiments. They also propose a large germanium array, inserted directly in a large tank of liquid nitrogen, that they claimed will cover almost completely the range of CDM particle masses and interaction cross sections of current theories.

2. EXPERIMENT

In this article, we report the results of a pilot experiment designed to detect the excitation of ^{73}Ge by inelastic spin-dependent scattering of WIMPs on the 7.73%-abundant ^{73}Ge in an ultralow background Ge detector. The energy spectrum of the recoil nuclei resulting from elastic interaction of WIMPs with a target detector is a continuous, exponentially decaying spectrum, a large portion of which lies in the region of several keV. The relative ionization efficiency factor, for example, for Ge recoil nuclei, at 10 keV equals 0.25. For such a response function it is virtually impossible to distinguish the desired WIMP spectrum from the spectrum of background events by means of only the shape of the spectrum. In order to make an unequivocal claim that WIMPs have been detected, it is necessary to use a method which makes it possible to distin-

* This article was submitted by the authors in English.

** e-mail: smoln@nusun.jinr.ru

1) University of South Carolina, Columbia, South Carolina, USA.

2) Pacific Northwest National Laboratory, Richland, USA.

guish, with a high probability, the true interaction of WIMPs from the background interaction, according to structure. In our paper [14], a unique scheme of long-lived excited levels of ^{73}Ge in the case of inelastic scattering of WIMPs by a target detector was proposed for use. This nucleus possesses two low-lying levels with energies 13.26 and 66.73 keV (metastable) and half-lives of 2.95 μs and 0.50 s, respectively [15]. The level scheme of ^{73}Ge is displayed in Fig. 1.

The method employs simultaneously amplitude analysis and temporal analysis of events together with the trace of the pulse shape. A true event should consist of a sequence of several signals: first a signal from the recoil nucleus as a result of inelastic scattering of WIMPs (continuous spectrum) and then, over a period of several half-lives, a complicated signal due to deexcitation. In the case of excitation of the first excited state, the second signal will be due to internal conversion or a γ ray ($e_c/\gamma = 325$) with a fixed energy of 13.26 keV. Essentially, the only possible background in such an experiment is the interaction of neutrons with excitation of the above-indicated levels. However, computational and experimental estimates show that the contribution from neutrons can be made negligibly small by performing the experiment in a deep underground laboratory with sufficiently thick neutron shielding.

In the present work, a low-background germanium detector is employed, consisting of material having natural isotopic composition of Ge, with an active mass of 0.952 kg and thus containing 74 g of ^{73}Ge.

In order to have sufficient kinetic energy to excite the first level of ^{73}Ge, the WIMPs must have mass $M \geq 9$ GeV. Such excitations can be produced by particles of the photino or higgsino type, with spin-dependent interaction. The shape of the pulse for inelastic scattering of WIMPs with excitation of the 13.26-keV level is a superposition of the energy releases of the recoil nucleus and electrons and (or) γ rays (Fig. 2*b*). In Fig. 2*a*, the first component (E_1) of the ionization pulse belongs to the recoil nucleus, while the second component (E_2) belongs to conversion electrons or γ rays with detected energy 13.26 keV with an accuracy to within the resolution of the detector. The time interval T between the two maxima lies in the range from zero to several lifetimes of the excited level.

To search for events with the above-described signature of the signal, data collected for 810 d of lifetime (59.9 kg d in terms of the ^{73}Ge) in an underground low-background laboratory at a depth of 660 m of water equivalent (mwe) were used [16].

To select double events, a superposition of two standard pulses (Fig. 2*a*) with the positions (T_1, T_2) of the maxima and the amplitudes (E_1, E_2) as free parameters was fit to the shape of the detector pulses. Double events with low values of the amplitude of the first component (E_1) and of the time interval (T) can be mimicked by an instability of the slope of the leading edge of the pulse and by noise; therefore, it is necessary to determine the time resolution and the energy threshold for the first component.

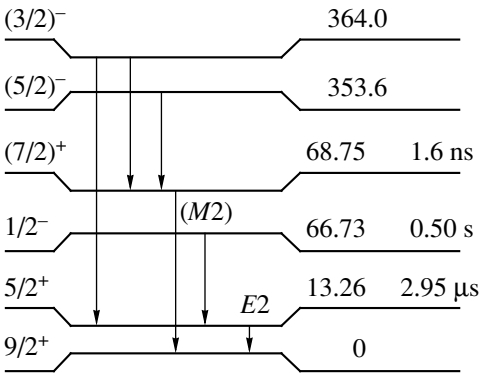

Fig. 1. Scheme of low-energy levels of ^{73}Ge (the level energies are given in keV).

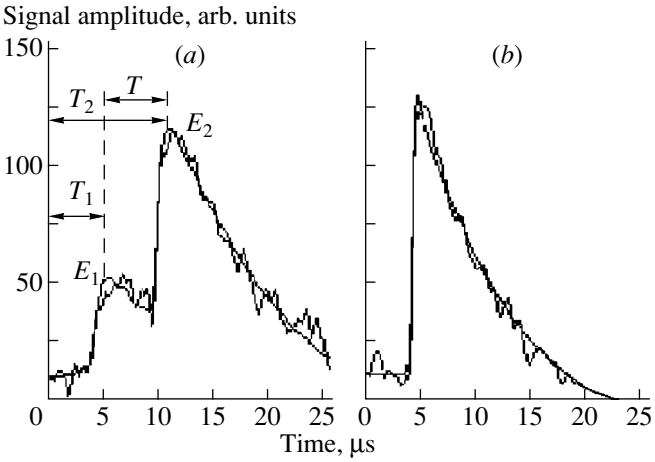

Fig. 2. (*a*) Example of the shape of a double-event pulse. The first component of the pulse E_1 can be produced by the recoil nucleus and the second component E_2 can be produced by conversion electrons or γ rays with energy 13.26 keV. (*b*) Example of the standard shape of a pulse produced by a γ or electrons. The smooth solid curve shows the result of fit.

Information about the energy release in each component of double events can only be obtained from the pulse shape on a digital oscilloscope, and the energy resolution in this case is worse than when spectrometric analog-to-digital converters (ADCs) are used. By using ^{60}Co calibration source and by comparing the amplitudes of the signals obtained from a spectrometric ADC and computed from the shape of the pulse, the energy resolution on the digital oscilloscope was determined to be 2 keV near 13.26 keV. The temporal resolution for double events (in the case of excitation of the 13.26-keV level), equal to 2 μs, and the energy threshold for the first component, equal to 2.5 keV, were determined by analyzing data from a ^{60}Co source. The distribution of the time intervals in the events that had been selected as

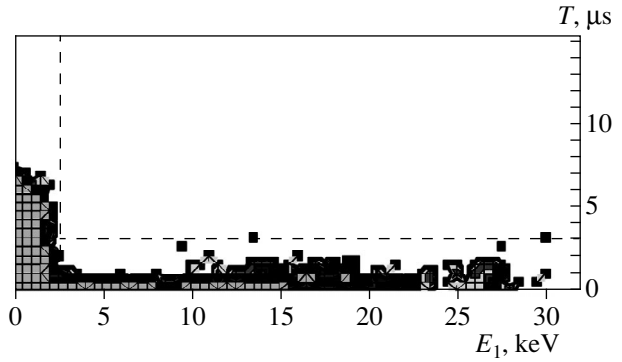

Fig. 3. Distribution in the (E, T) plane of events selected as double events in the case of a ^{60}Co source (E_1 is the energy of the first component, and T is the interval between maxima).

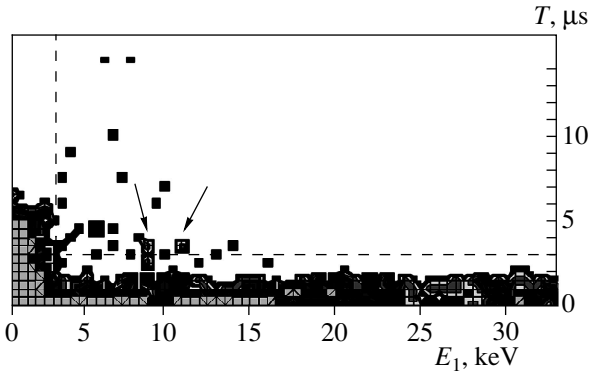

Fig. 4. Distribution in the (E, T) plane of background double events collected in a period 810 d (E_1 is the energy of the first component, and T is the interval between maxima).

double events (Fig. 3) for which the energy of the second component lay in interval $9.3 \le E_2 \le 17.3$ keV. Double events with a ^{60}Co source can be imitated on account of the spread in rise times (0.75 ± 0.22 μs for the 9- to 35-keV range), superposition of detector and amplifier noise on the real signal, and the random pileup of pulses. A total of 17116 events with a ^{60}Co source were analyzed. With a counting rate of 20 events/s, the probability of random pileup of pulses in a 15 μs window equals 3×10^{-4}, which for our case comprises five of the 17116 events. In the measurements with ^{60}Co source only one event was detected above the time-resolution threshold of 2.95 μs (horizontal dashed line in Fig. 3) and above the energy threshold for detection of the first component (to the right of the vertical dashed line); this agrees with the number of random pileups. Therefore, we can confidently detect double events with the time interval $2.95 \le T \le 15$ μs between the maxima E_1 and E_2. The upper limit is due to the pulse tracking time of 25 μs of the digital oscilloscope, with allowance for 5 μs in front of the leading edge and 5 μs on the trailing edge of the pulse. The detection efficiency for the desired events, equal 0.47, was determined by comparing this time interval with the decay curve for $T_{1/2} = 2.95$ μs.

Figure 4 shows a similar distribution obtained by analyzing background events accumulated for a period of 810 d (40762 events in total). Thirty-two events fall into the range above the threshold (dashed lines). Eight of them are shown in Fig. 5 as examples with corresponding values of E_1, E_2 (keV), T (μs), and delay time between veto and detector signals.

Thirty are in coincidence with the active shielding; i.e., they are due to the cosmic-ray neutron background. Taking into account the inefficiency of the active shield (7%) two events can be rejected as produced by cosmic ray neutrons too. As a result, we have no events as candidates for WIMPs for 810 d after the selection procedure, and that yields a limitation of the background level 0.0012 events/(keV kg(^{73}Ge) d).

The background level of the same detector for elastic scattering in the energy range 2.5–35 keV equals 0.51 events/(keV kg d); i.e., the relative reduction of the background is greater than 400. Comparison of the number of double events in coincidence (30) and that in anticoincidence (2) with the active shielding shows that main source of the background for the detector at the depth the apparatus is now located is from cosmic-ray-generating neutrons in the vicinity of the detector. A much greater decrease in the background can be

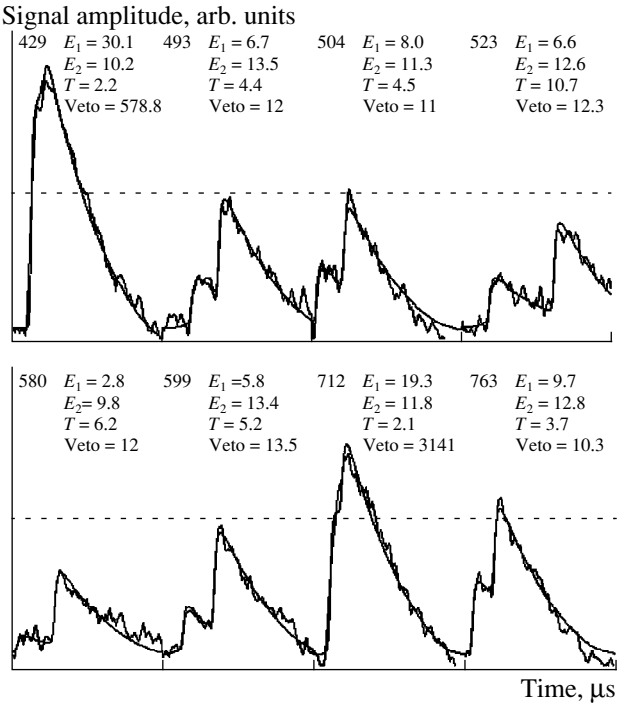

Fig. 5. Examples of the background double event pulses (8 from 32 events accumulated for 810 d) with corresponding values of E_1, E_2 (keV), T (μs), and delay time between veto and detector signals. $T_{\text{Veto}} < 15$ corresponds to a direct coincidence.

achieved by performing these experiments at a greater depth with enriched ^{73}Ge detectors and with a faster digital oscilloscope. To check the correctness of the program selecting the double events and to estimate the probability of random generation of events of this type, a search for double events with same selection criteria but with the energy of the second component $17.3 \leq E_2 \leq 25.3$ keV was performed. No one double event satisfying these criteria was found.

Only two experiments of this type have been reported since the original theoretical treatment of Ellis, Flores, and Lewin [17]. For comparison, we can consider the background levels from two previous experiments devoted to the search for WIMP-nucleus inelastic scattering. Inelastic scattering on ^{127}I was studied in [18]. A rate of about 600 counts/(kg d) in the region of the first excited state of ^{127}I (57.6 keV) was measured. The contribution of standard contaminants was simulated by the Monte Carlo method and subtracted from the experimental spectrum. This procedure gives a subtracted rate of less than 0.0979 counts/(kg d) at a 2σ C.L. The background index of about 0.2 counts/(keV kg d) in the region of the excited state of ^{129}Xe at 39.6 keV was achieved in the experiment with the liquid-xenon scintillator at the Gran Sasso Laboratory [19]. It is evident that the present experiment has no background in an extended running time (810 d) with total mass natural Ge of almost 1 kg. Accordingly, it seems that one or more detectors of this size, but isotopically enriched to 90% in ^{73}Ge, would be competitive in such a search. While the transition to the first excited state may be significantly suppressed by the details of nucleon structure, the background of less than 0.0012 counts/(keV kg(^{73}Ge) d) at a peak less than 2-keV-wide 0.0024 counts/(keV kg d) compares very well to the 600 counts/(kg d) of the full peak of [18].

We propose an experiment with several kg of enriched ^{73}Ge to be performed in a deep-underground laboratory to further reduce background from cosmic ray neutrons. This would increase the sensitivity of this search by a factor of the mass of ^{73}Ge.

The fact that there are no theoretical calculations for the $E2$ excitation of nuclei by spin-dependent WIMP interactions prevents us from calculating an exclusion plot. We hope that the promise of this technique shown by the present data will stimulate the needed theoretical activity.

ACKNOWLEDGMENTS

The detectors used in this experiment were fabricated in the framework of the IGEX collaboration. We are grateful to the Zaragoza and ITEP IGEX teams for their kind permission to use data coming from the detectors. The authors thank Petr Vogel, John Vergados, and H. Ejiri for helpful discussions. One of us (F.T.A.) was supported by the US National Science Foundation. The PNNL collaborators were supported by the US Department of Energy. This work was supported by the Russian Foundation of Basic Research (project no. 98-02-17973).

REFERENCES

1. G. Jungman, M. Kamionkovski, and K. Griest, Phys. Rep. **267**, 195 (1996).
2. D. J. H. Chung, E. W. Kolb, and A. Riotto, Phys. Rev. Lett. **81**, 4048 (1998).
3. L. Bergstron *et al.*, Phys. Rev. D **59**, 043506 (1999).
4. T. Damour and L. M. Krauss, Phys. Rev. D **59**, 063509 (1999).
5. S. P. Ahlen *et al.*, Phys. Lett. B **195**, 603 (1987).
6. D. A. Caldwell *et al.*, Phys. Rev. Lett. **61**, 510 (1988).
7. M. Beck *et al.*, Phys. Lett. B **336**, 141 (1994).
8. E. García *et al.*, Phys. Rev. D **51**, 1458 (1995).
9. D. Abriola *et al.*, Astropart. Phys. **10**, 133 (1999).
10. D. S. Akerib *et al.*, Nucl. Phys. B (Proc. Suppl.) **70**, 64 (1999).
11. R. Bernabei *et al.*, Phys. Lett. B **389**, 757 (1996); **424**, 195 (1998).
12. G. Gerbier *et al.*, astro-ph/9902194.
13. L. Baudis *et al.*, Phys. Rev. D **59**, 022001 (1999).
14. A. A. Klimenko, S. B. Osetrov, A. A. Smolnikov, and S. I. Vasil'ev, Pis'ma Zh. Éksp. Teor. Fiz. **67**, 835 (1998) [JETP Lett. **67**, 875 (1998)].
15. *Table of Isotopes*, Ed. by C. M. Lederer and V. S. Shirly (Wiley, New York, 1987).
16. A. A. Klimenko, A. A. Pomansky, and A. A. Smolnikov, Nucl. Instrum. Methods B **17**, 445 (1986).
17. J. Ellis, R. Flores, and J. D. Lewin, Phys. Lett. B **211**, 375 (1988).
18. E. Ejiri, K. Fushimi, and O. Ohsumi, Phys. Lett. B **317**, 14 (1993).
19. P. Belli *et al.*, in *Proceedings of the 2nd Workshop on the Dark Side of the Universe, 1996* (World Sci., Singapore, 1996), p. 177; P. Belli *et al.*, Phys. Lett. B **317**, 14 (1993).

Physics of Atomic Nuclei, Vol. 63, No. 7, 2000, pp. 1268–1271. From Yadernaya Fizika, Vol. 63, No. 7, 2000, pp. 1341–1344.

EXPERIMENTAL RESULTS, METHODS, AND FACILITIES

New Results of the WIMP Search with the First IGEX Ge Detectors*

C. E. Aalseth[1)], F. T. Avignone III[1)], R. L. Brodzinski[2)], S. Cebrian, D. Gonzáles, E. García, W. K. Hensley[2)], I. G. Irastorza, I. V. Kirpichnikov[3)], A. A. Klimenko[4)], H. S. Miley[2)], A. Morales, J. Morales, A. Ortiz de Solórzano, S. B. Osetrov[4)], V. S. Pogosov[5)], J. Puimedón, J. H. Reeves[2)], M. L. Sarsa, S. Scopel, A. A. Smolnikov[4), **], A. S. Starostin[3)], A. G. Tamanyan[5)], A. A. Vasenko[3)], S. I. Vasiliev[4)], and J. A. Villar

Institute for Nuclear Research, Russian Academy of Sciences, pr. Shestidesyatiletiya Oktyabrya 7a, Moscow, 117312 Russia
Joint Institute for Nuclear Research, Dubna, Moscow oblast, 141980 Russia

Abstract—To search for cold dark matter (CDM) particles, the data from two (Ge-76 and Ge-natural) detectors, fabricated in the first phase of the IGEX collaboration, were accumulated and analyzed for a period from May 1995 to May 1999. The use of effective passive and active shielding together with pulse shape discrimination allowed us to perform long-term measurements with an energy threshold of 2 keV at a level of the residual background 0.1 counts/(kg keV d). New restrictions on masses of weakly interacting massive particles and the cross section of their elastic scattering on nuclei have been obtained from the data corresponding to 810 d of live time. The derived exclusion plots compete with the best bounds obtained so far. Annual modulations of the CDM signal have been also investigated. It is shown that the planned operation of all IGEX detectors (at Canfranc and Baksan) with the recently achieved low-energy thresholds gives a chance to achieve the DAMA annual modulation sensitivity region in a nearest future. *© 2000 MAIK "Nauka/Interperiodica".*

1. INTRODUCTION

Much evidence and well-founded arguments point out that the missing mass of the Universe may well consist of a suitable mixture of cold dark matter (CDM), hot dark matter (HDM), and baryons [1]. Weakly Interacting Massive Particles (WIMP), possible candidates for CDM particles, have been extensively searched for by various detectors and methods. The reduction of the background in the low-energy part of the recoil-energy spectrum and the search for distinctive signatures of DM signal, such as its annual modulation, are the most important issues in the experimental search for cold dark matter [2]. Annual modulation originates from the annual variation of the Earth velocity with respect to the Galactic halo due to the orbital motion of the Earth around the Sun [3]. Recent results from the DAMA collaboration [4] obtained with a set of 87.3 kg of NaI(Tl), supposedly showing a periodic variation in the count rate, have been interpreted as due to a relic neutralino with mass of 59^{+17}_{-14} GeV and a proton cross section of $7.0^{+0.4}_{-1.2} \times 10^{-6}$ pb. This intriguing result has stimulated the making of other experiments that can achieve the same level of sensitivity.

2. EXPERIMENT

A detailed description of the experimental setup was published earlier [5], and the preliminary results from the 525 d of analyzed data were published in the previous NANP conference proceedings [6]. The data from two low-background HPGe detectors (^{76}Ge and Ge-natural), fabricated in the first phase of the IGEX collaboration [7], were accumulated and analyzed for a period from May 1995 to May 1999. One of them has an active mass of 0.95 kg and is made of natural Ge and the other has an active mass of 0.70 kg and is made of germanium isotopically enriched in ^{76}Ge to 87%. Both detectors are placed in a common passive shielding, which consists of 12 cm of copper, 6 cm of lead sheets (these materials were kept underground for about 20 yr), 15 cm of lead bricks, and 8 cm of borated polyethylene. The passive shielding is surrounded with an active shielding, which consists of five Plexiglas containers filled with liquid scintillator. This setup is placed in a low-background chamber of the Baksan underground laboratory at a depth of 660 mw.e. The low-background chamber walls consist of 50 cm of low-radioactive concrete, 50 cm of dunite, and 8 mm of steel. Only amplifiers are placed in this chamber near the detectors. The other "noisy" parts of the electronics (ADCs, high-voltage supply, computer) are located in another room of

* Thia article was submitted by the authors in English.

** e-mail: smoln@nusun.jinr.ru
1) University of South Carolina, Columbia, USA.
2) Pacific Northwest National Laboratory, Richland, USA.
3) University of Zaragoza, Spain.
4) Institute for Theoretical and Experimental Physics, Bol'shaya Cheremushkinskaya ul. 25, Moscow, 117259 Russia.
5) Yerevan Physical Institute, Armenia.

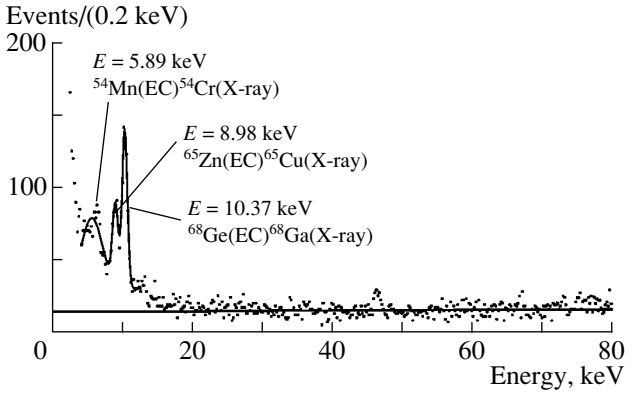

Fig. 1. Low-energy part of the background spectrum of the nonenriched Ge detector accumulated for 810.7 d of measurements. Results of fitting of the cosmogenic peaks and approximation of the spectrum by line in the energy region from 30 to 70 keV are shown.

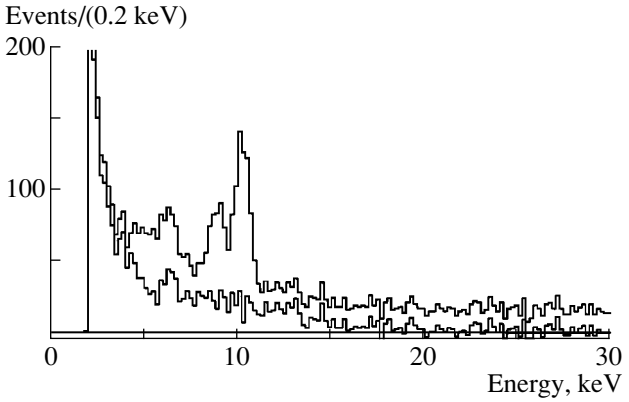

Fig. 2. The nonenriched Ge detector spectra in the region from 2 to 30 keV before and after subtraction of the cosmogenic peaks and baseline.

the laboratory. Both detectors have an energy resolution of 0.9 keV at an energy of 59.5 keV and high stability of calibration during 3 yr (better than 0.2%).

The active shielding with 93% efficiency reduces the cosmic-ray background. The use of a digital oscilloscope and pulse shape discrimination reduces microphonic and electronic noises [8].

3. RESULTS

3.1. Low-Energy Spectra

The low-energy parts of the background spectrum of the Ge-natural detector, collected during 810.7 d, are presented in Fig. 1. The nonenriched detector has a 2-keV threshold and achieved a figure of 0.26 counts/(keV kg d) of background counting rate in the energy region 12–22 keV. One can see the 5.89, 8.98, and 10.37 keV peaks from the decays of cosmogenically produced ^{54}Mn, ^{65}Zn, and ^{68}Ge, respectively. These peaks confirm the proper procedure of the pulse shape discrimination and the stability of our calibration. On the other hand, the enriched Ge-76 detector achieved a 6-keV threshold and 0.26-counts/(keV kg d) background counting rate in the interval 12–22 keV. There are no visible 8.98- and 10.37-keV peaks in this case because the cosmogenic isotope contamination is negligible.

The cosmogenic peaks, identified in the nonenriched detector spectrum can be subtracted. Moreover, the background spectrum of the detector in the energy region above 30 keV is approximated by a line with a small positive slope. The background counting rate in this region can be attributed essentially to radioactive impurities and not to WIMPs because WIMPs with masses less than 25 GeV are not able to produce nuclear recoil energies that yield ionization energies higher than 30 keV in Ge. Therefore, one could subtract the "radioactive baseline" from the detector spectrum below 30 keV. This method, which implicitly assumes that the radioactive background usually increases with decreasing energy and which involves subtraction of a fraction of the background counts recorded below a certain energy value, which depends obviously on the WIMPs, was first applied in [9]. The result of subtraction the cosmogenic peaks and the "radioactive baseline" from the accumulated spectrum of the nonenriched detector is shown in Fig. 2. The residual spectrum produces a background figure of 0.09 counts/(keV kg d) in the region from 10 to 30 keV.

To obtain exclusion plots for the WIMP masses and cross sections, both spectra with and without subtraction of a "radioactive baseline" were used, and so the reader could choose his own option. The method followed to draw the spin-independent exclusion plots was the standard procedure of comparing for each m and σ the predicted rate with the observed one including the statistical uncertainties. In the exclusion plot of WIMPs the cross section is normalized to the nucleon under the assumption of a scalar-type interaction. The theoretical recoil spectra were calculated under the assumption that the whole density of the dark halo (0.3 GeV/cm^3) is in the form of WIMPs with fixed mass, which are distributed according to the Maxwell–Boltzmann velocity distribution with mean velocity v_{rms} = 270 km/s and an escape velocity v_{esc} = 650 km/s. To calculate the distribution in the vicinity of the Earth, we used v_{Earth} = 232 km/s. The relative ionization efficiency $f(E_{rec})$ or quenching factor for Ge was taken to be 0.25. The loss of coherence for interacting WIMPs is taken into account with a nuclear form factor. Figure 3 shows the excluded cross section as a function of the WIMP mass obtained in our analysis.

3.2. Search for Annual Counting Rate Modulations

Detailed analysis of the detector counting rates and time distributions show the presence of annual count rate variations in a wide energy region with the same

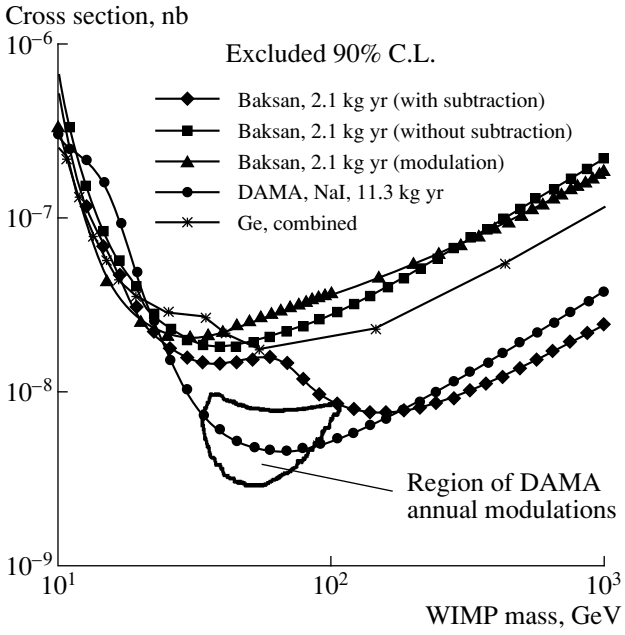

Fig. 3. Exclusion plots of WIMP masses and cross sections obtained from considering the detector background spectra and from considering the limits on annual modulations of the detector counting rate. Exclusion plot obtained by DAMA experiment [5] is shown for comparison too.

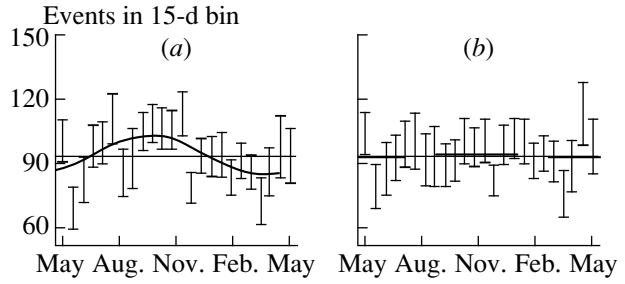

Fig. 4. Results of the data correction in the low-energy region by using the correlation with data from energy region 200–2700 keV and with data rejected by PSD within low-energy region. (The enriched detector, 7–30 keV.) (*a*) Input data. Fitting by sinusoid indicates variations with amplitude 9.6% (3σ). (*b*) Input data after correction. Fitting by sinusoid indicates variations with amplitude 1.1% (0.3σ).

phase. These variations are produced by fluctuations of the noise counting rate in the low-energy part, fluctuation of radon contamination, and instability of the active shield operation. A strong correlation was found between the counting rate of the detectors in certain low-energy regions and the counting rate in the energy region 200–2700 keV, as well as a correlation between low-energy data selected with PSD and the same data rejected by PSD. Counting rate fluctuations in the energy region 200–2700 keV are produced by the radon contamination fluctuation and the instability of the active shielding operation. There are the same fluctuations in the low-energy region too. Fluctuations of the noise counting rate in the low-energy part of the spectrum persist in the counting rate selected with PSD due to non-100% rejection efficiency of the PSD. These fluctuations should not be periodic themselves but can produce sine-like variations in annual periodicity of the count rate. Thus, the input data, collected for searching for the annual modulations, must be corrected for the above-mentioned factors, and this correction has been performed with help of the data taken from the energy region 200–2700 keV and the data rejected by PSD. The correction procedure is described in detail in our previous papers [6]. No modulations with a significant amplitude were found in the data represented for both enriched and nonenriched detectors in the low-energy region after the correction procedure. For example, the sensitivity to annual modulation of the enriched detector in the energy region 7–30 keV is 7.3% at 95% C.L. (Fig. 4).

We used the obtained limits on the annual modulations counting rate to derive exclusion plots of the WIMP masses and cross sections which are presented in Fig. 3 too. For the calculation of the recoil nuclear spectra, the same kinematic parameters of the Earth and WIMPs were used as for the calculation of the above-mentioned exclusion plot by considering the shape of the detector background spectra presented in Fig. 2. Variation in the relative velocity of the WIMPs and the Earth during one year was taken to be 13.2 km/s. The cross section was taken as a free parameter with a given WIMP mass and was changed until the amplitude of the modulation became detectable (more than 2σ) in the considered energy region. For comparison, the DAMA exclusion plots obtained from the 11.3-kg-yr data are shown in Fig. 3 too. One can see that our result obtained with only two Ge detectors is close enough to a region of the DAMA annual modulation effect. Recently, all other IGEX detectors with a total active mass of about 9 kg started to operate with low energy thresholds. It gives a chance to achieve the DAMA sensitivity level in the nearest future.

4. CONCLUSION

The (810.7 d of live time) information is collected and analyzed from May 1995 to May 1999 for two low-background HPGe detectors, fabricated in the first phase of the IGEX collaboration. New exclusion limits for the WIMP cross sections and masses are obtained. The result is close enough to the region of the DAMA positive effect. It is shown that the planned operation of all IGEX detectors with low-energy thresholds gives a chance to achieve the DAMA sensitivity level in the nearest future.

ACKNOWLEDGMENTS

This work is supported in part by the Russian Foundation for Basic Research (project no. 98-02-17973).

The authors would especially like to thank V.I. Volchenko for his help in the electronics optimization.

REFERENCES

1. G. F. Smoot *et al.*, Astrophys. J. Lett. **396**, L1 (1992); E. L. Wright *et al.*, Astrophys. J. Lett. **396**, L13 (1992).
2. S. P. Ahlen *et al.*, Phys. Lett. B **195**, 603 (1987); D. O. Caldwell *et al.*, Phys. Rev. Lett. **61**, 510 (1988); A. Morales, Nucl. Phys. B (Proc. Suppl.) **77**, 335 (1999).
3. A. K. Drukier, K. Freese, and D. N. Spergel, Phys. Rev. D **33**, 3495 (1986); J. I. Collar and F. T. Avignone, Phys. Lett. B **275**, 181 (1992).
4. R. Bernabei *et al.*, Phys. Lett. B **389**, 757 (1996); **424**, 195 (1998).
5. A. A. Klimenko *et al.*, in *Proceedings of the International School "Particles and Cosmology," Baksan Valley, 1995* (World Sci., Singapore, 1996), p. 108; A. A. Klimenko *et al.*, Preprint No. INR-0948/97 (Institute for Nuclear Research, Moscow, 1997).
6. A. A. Klimenko *et al.*, Yad. Fiz. **61**, 1129 (1998) [Phys. At. Nucl. **61**, 1129 (1998)].
7. F. T. Avignone *et al.*, Nucl. Phys. B (Proc. Suppl.) **48**, 223 (1996); C. E. Aalseth *et al.*, Phys. Rev. C **59**, 2108 (1999).
8. I. R. Sagdeev *et al.*, Nucl. Phys. B (Proc. Suppl.) **35**, 175 (1994).
9. E. García *et al.*, Nucl. Phys. B (Proc. Suppl.) **28**, 286 (1992); M. Beck *et al.*, Phys. Lett. B **336**, 141 (1994).

Physics of Atomic Nuclei, Vol. 63, No. 7, 2000, pp. 1272–1275. From Yadernaya Fizika, Vol. 63, No. 7, 2000, pp. 1345–1348.

EXPERIMENTAL RESULTS, METHODS, AND FACILITIES

pep Neutrino Detection by a Lithium Detector as a Direct Way to Seek Oscillations of Solar Neutrinos*

A. Kopylov
(for the LESNE Collaboration)

Institute for Nuclear Research, Russian Academy of Sciences, pr. Shestidesyatiletiya Oktyabrya 7a, Moscow, 117312 Russia

Abstract—The high sensitivity of a lithium detector to *pep* and ^{7}Be neutrinos renders a radiochemical lithium detector a powerful tool for seeking solar-neutrino oscillations. The first phase of the lithium experiment with an apparatus involving 10 t of metallic lithium will allow collecting data within 1 yr of measurements to provide very definite information about a MSW SMA solution. The second phase with ten modules 10 t each will measure the semiannual variations of the signal, whereby the contributions of *pep* and ^{7}Be lines will be weighted, which will give "smoking-gun" evidence for the "just-so" solution for large mixing angles and Δm^2 about 10^{-10}–10^{-9} eV^2. If both regions are not confirmed, the results of the lithium detector can be interpreted in favor of the MSW LMA solution. © *2000 MAIK "Nauka/Interperiodica".*

1. INTRODUCTION

The recent results obtained by SuperKamiokande (SK) [1], compared with the earlier results of four solar-neutrino experiments [2], reveal three possible regions for the oscillation of solar neutrinos: MSW SMA, MSW LMA, and the "just-so" region of vacuum oscillations with a large mixing angle. So far, experimental data have not provided "smoking-gun" evidence that would allow us to select one of the three regions. A further collection of statistics will hardly give a breakthrough in this direction—some ambiguities will remain, especially when the neglect of a systematic error in at least one of the previous experiments cannot be completely excluded. Thus, any experiment that can distinguish, with high reliability, between these three possibilities is now very valuable. Great expectations are connected with other experiments to be carried out soon with the SNO detector in Canada [3] and with BOREXINO in Italy [4]. The potentials of these detectors are great, but experimental difficulties associated with the methods chosen are great too. So far, it is rather difficult to predict what will be the result and whether the ambiguities due to the systematic errors will be reduced to the extent required for solving the solar-neutrino problem. Another possibility is the LENS project [5], and it is highly desirable to get the results from the pilot LENS setup to understand the real potential of this project. The HELLAZ project [6] as a solar-neutrino spectrometer with a high energy resolution and a very low threshold also holds promise. But, as for any other electron detector, the question of the background is very crucial there. R. Davis, who opened this world of solar-neutrino research, used to point out that, although a radiochemical detector is not ideal (it does not give a signature of the event, the time resolution is not high, etc.), it has several substantial advantages: the sources of the background are very limited, so that the background can be predicted with a high accuracy; the threshold is determined by the neutrino-capture reaction, and not by the equipment used. When people discuss radiochemical detectors, they usually say that a substantial limitation of these detectors is that the integral effect over all neutrinos with energies higher than a threshold is measured, so that the contribution of different sources cannot be found. It will be shown in this paper that this statement is not always true and that, in a certain case (or cases), what seems to be impossible is in fact possible. It will also be shown that a radiochemical lithium detector can give very definite information that will enable one to distinguish between three possible regions of the solar-neutrino oscillations. Moreover, we will see that accumulation of adequate statistics will take only a few years. To perform this complex task, the efforts of several institutions and the close cooperation of several laboratories on a variety of chemical and physical problems, from a metal technology to cryogenics, are needed. Luckily, the lithium project is not very expensive.

2. WHAT IS A LITHIUM DETECTOR?

A lithium detector was proposed by Bahcall [7]. The main advantage of lithium as a target is that the neutrino-capture cross section for the ground state of ^{7}Be,

$$^7\mathrm{Li} + \nu_e \longrightarrow {}^7\mathrm{Be} + e^-, \quad (1)$$

and for the first excited state of ^{7}Be,

$$^7\mathrm{Li} + \nu_e \longrightarrow {}^7\mathrm{Be}^* + e^-, \quad (2)$$

is guaranteed by well-established isospin connections between mirror nuclei. The threshold for the neutrino-capture reaction on lithium is 0.862 MeV. Both transi-

* This article was submitted by the author in English.

tions (to the ground state and to the first excited state) are superallowed. A precise calculation of the cross section for neutrino capture on ^{7}Li was performed by Bahcall [8, 9]. The relative contributions of transitions to the first excited state of ^{7}Be are about 5% for the ^{15}O and ^{65}Zn spectra [^{65}Zn neutrino source (E_ν = 1.343 MeV) proposed by L. Alvarez is planned to be used for calibrating a lithium detector], 7% for *pep* neutrinos, and about 21% for the average ^{8}B spectrum (^{13}N neutrinos do not have sufficient energy to populate the excited state). The contribution of the excited states above the first one to the total cross section for solar neutrinos is negligible. Because both transitions are superallowed, the cross section for neutrino capture is relatively high: $\sigma = 6 \times 10^{-44}$ cm^2 for *pep* neutrinos (E_ν = 1.44 MeV) and $\sigma = 2.25 \times 10^{-44}$ cm^2 for ^{65}Zn source (E_ν = 1.343 MeV). It is clear from these values that lithium is a highly sensitive detector of solar neutrinos and that the threshold is exactly that which one needs: it is sufficiently high to cut off *pp* neutrinos and sufficiently low to see the entire intermediate energy range. In fact, as will be shown later, with only ten tons of lithium in metallic form, a 6.5% accuracy can be achieved within one year of measurements. And what renders a lithium detector very attractive is the selectively high sensitivity to *pep* neutrinos. It is explained by the following. As one can see from the table, the intensity of the ^{7}Be line in the solar-neutrino spectrum is nearly 35 times higher than the intensity of the *pep* line. For a lithium target, neutrinos from the decay of ^{7}Be have precisely the threshold energy if one neglects electron screening in terrestrial atoms and thermal energy in the Sun. In fact, if one considers electron screening in terrestrial atoms and neglects thermal energy, neutrinos from ^{7}Be in the Sun will be below the threshold, so that the absorption cross section will be zero. It was first shown by Domogatskiĭ [10] that thermal averaging over the energy distribution of the electrons captured in the Sun is important for ^{7}Be neutrinos incident on ^{7}Li. The differential cross section for the electron-capture process with the production of a neutrino of energy q, $d\sigma/dq$, must be computed by taking into account the thermal motion of both the ^{7}Be ions and the electrons. (We use the lithium cross sections here from a private communication of J. Bahcall, since he has recently made improvements in his calculations over the past 20 years.) Because of this effect, the lithium detector is also sensitive to ^{7}Be neutrinos, and according to the predictions of the standard solar model (SSM), the weights of these neutrinos and of the *pep* neutrinos are comparable (see table).

A comparison of the results of the chlorine [2] and SK [1] experiments shows that there is a deficit of ^{7}Be neutrinos (this is in good agreement with the results of gallium experiments [2] as well). This means that the expected contribution of these neutrinos in lithium is substantially lower. But, since the flux of ^{7}Be neutrinos is model-dependent, we do not know precisely what the explanation is for this deficit—whether it is due to some unknown character of the processes inside the Sun, or it is a manifestation of neutrino oscillations. In order to clarify this point with a high reliability, we need some "standard" line, which is directly connected with the luminosity of the Sun, and the only possibility here is *pep* neutrinos.

3. WHAT IS LITHIUM EXPERIMENT AIMED AT?

There are two phases of the lithium experiment that we are planning now. The first phase is that with one module of 10 t of metallic lithium, while the second phase is with ten modules 10 t each. The second phase will start only if the first phase is a success. The primary aim of the first phase is to measure the flux of the intermediate-energy solar neutrinos. The contribution of boron neutrinos is just a background known with a good accuracy from the results of SK (see table). The minimal signal of the lithium detector is composed of three parts: 9.5 SNU from boron neutrinos, 9.1 SNU from *pep* neutrinos, and some contribution from the ^{7}Be line. If one compares the results provided by the chlorine detector and SK, one can deduce that the flux of beryllium neutrinos is by no means more than 20% of the SSM predictions. Here, we will accept as an extreme case that the in-Sun-generated flux of the ^{7}Be line as low as 20% of SSM is not excluded, assuming that one needs direct experimental evidence to reject this possibility. Thus, the total minimal signal is about 20 SNU. If the experiment observes a signal less than 20 SNU—say, 10 SNU—this will be evidence for a strong attenuation of intermediate-energy neutrinos from the Sun, which conforms to the MSW SMA solution. If we get more, it will be necessary to find the way to distinguish between the MSW LMA and "just-so" regions. The presence of two lines in the spectrum of solar neutrinos with different energies (0.862 MeV for the ^{7}Be line and 1.44 MeV for the *pep* line) with equal capture rates (according to the SSM) on a lithium target gives a good opportunity for the lithium detector to distinguish between these solutions. For the "just-so" case, semiannual variations of the signal with the characteristic harmonics should in fact be observed for each of these lines, and the modulation will be very deep for large mixing angles (there will be of course some smearing by boron and CNO neutrinos with continuous spectra). Just to illustrate this possibility, the figure shows the curves for *pep*, ^{7}Be lines, and their sum for the "just-so" case following the expression

$$P(\nu_e \longrightarrow \nu_e) = 1 - \sin^2 2\theta \sin^2(1.9 \times 10^{11} \Delta m^2 R(t)/E),$$

where $R(t) = 1 + 0.01675\cos\pi t$ and t varies from –1 to +1, $t = 0$ corresponding to perihelion. One can see from the figure that the curves corresponding to *pep* and ^{7}Be lines have very different harmonics, so that it is possible to weight the contributions of these neutrino sources in the radiochemical lithium detector if one has good statistics. This opens up excellent possibilities for the lithium detector. Not only is it possible to confirm

Standard Model predictions: solar-neutrino fluxes and neutrino-capture rates for Li, with 1σ uncertainty (the fluxes of *pp* and *pep* neutrinos are predicted with an uncertainty of 1%; the contribution of the CNO cycle to the total energy generation in the Sun is strictly limited by the results of helioseismology)

Source	Flux, 10^{10} cm^{-2} s^{-1}	Rate of capture on ^{7}Li, SNU
pp	$5.94 \times (1 + 0.01/-0.01)$	
pep	1.39×10^{-2} (1 + 0.01/–0.01)	9.1
^{7}Be	4.80×10^{-1} (1 + 0.09/–0.09)	9.1
^{8}B	2.44×10^{-4} (1 + 0.03/–0.03)*	9.5
^{13}N	6.05×10^{-2} (1 + 0.19/–0.13)	2.6
^{15}O	5.32×10^{-2} (1 + 0.22/–0.15)	13.1
Total		43.4

Note: The value labeled with the asterisk represents the flux measured by SuperKamiokande for the case where all neutrinos are of the electron type.

or reject the "just-so" region and find $\sin^2 2\theta$ and Δm^2, but we will also get very valuable information about the generation intensity of ^{7}Be line, which is very important for solving the solar-neutrino problem in a pure astrophysical aspect (an interesting possibility of this is discussed in [11]). Having the flux of boron neutrinos from the results of SK, we can find the contribution of each neutrino source detected by the lithium detector: *pep*, ^{7}Be, and CNO. At certain $\sin^2 2\theta$ and Δm^2, it will probably be even possible to detect the effect of smearing of the signal because of the large radius of the active zone of the Sun, where neutrinos are generated. If so, it will give direct information about the structure of the Sun. Because we need vast statistics in this case, this will be the aim of the second phase of the lithium of experiment with ten modules 10 t each. It does not look fantastical at all. If the cost of gallium were as low as the cost of lithium, the GNO experiment would work on a 300- to 400-t scale now.

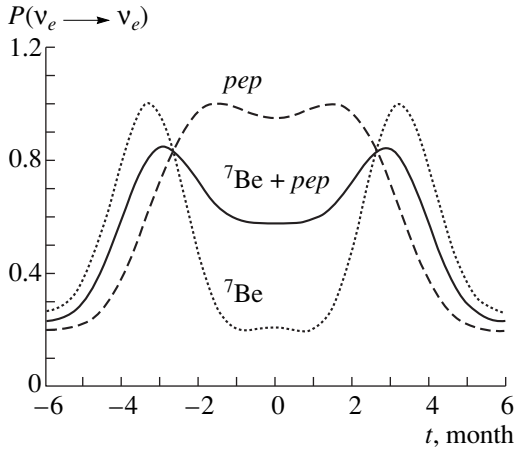

Semiannual variations of the signal for *pep*, ^{7}Be, and *pep* + ^{7}Be neutrinos ($\Delta m^2 = 4 \times 10^{-10}$ eV^2, $\sin^2 2\theta = 0.8$).

If neither the MSW SMA nor the "just-so" region is observed, the results of the lithium detector will be interpreted in favor of the MSW LMA solution. Thus, the results of the lithium detector will furnish valuable information for all three possible regions.

The statistics of the lithium detector is of course very different for phase I and phase II.

The characteristics of phase I are the following: 10 tons of lithium at 20 SNU; one year of measurements; one year for calibration with the ^{65}Zn neutrino source; time of exposure of three months; extraction efficiency of 90%; counting efficiency of 95%; counting within five half-lives; statistical accuracy (1σ) of 13% in one run; four runs per year; and total accuracy of 6.5% for one year of measurements.

The characteristics of phase II are the following: ten modules 10 t each at 20 SNU; the exposure time of two months; six runs per year; accuracy of 4.5% in each run; and a 2% accuracy of each two-month point for 5 yr of measurements. If the modulation of the signal is deep, positive evidence can be obtained within 1 to 2 yr.

4. PRESENT STATUS OF LITHIUM DETECTOR

The work on radiochemistry of the lithium detector started quite a long time ago [12, 13]. It was shown that beryllium can be efficiently extracted both from an aqueous solution of lithium chloride [12] and from metallic lithium [13]. For many years, the main difficulty in implementing this project was the problem of counting the extracted atoms of ^{7}Be. For a solar-neutrino experiment, it is necessary to have the counting system with an efficiency close to 100%, and this is very difficult to implement with conventional detectors because the energy of the Auger electron during *e* capture of ^{7}Be is only 55 eV. The major breakthrough came after the success of counting ^{7}Be by means of a cryogenic detector, which was achieved in collaboration with the Genoa group in Italy [14, 15]. After this, it became clear that the lithium program can be implemented, although a lot of efforts should be made to have a working detector. Now, the R&D work is in progress on the basis of the prototype lithium detector with 300 kg of metallic lithium at the Institute of Nuclear Research in Troitsk, together with the Institute of Physics and Power Engineering in Obninsk. The present status of this work is discussed in a number of articles [16]. The main obstacle is the lack of financial support. The participation of other laboratories interested in this program is vital for the success of the whole experiment. We hope that people will join the program, considering the importance of the task and good prospects for this detector.

ACKNOWLEDGMENTS

I am grateful to the organizing committee for the possibility of attending the NANP'99 conference and to G. Zatsepin, J. Bahcall, and to all my colleagues for stimulating discussions. I appreciate very much the help of V. Petukhov in writing the manuscript.

REFERENCES

1. W. Gajewski, Yad. Fiz. **63**, 1010 (2000) [Phys. At. Nucl. **63**, 934 (2000)].
2. K. Lande, V. Gavrin, and T. Kirsten, in *Proceedings of the International Conference Neutrino 98, Takayama, 1998.*
3. S. R. Elliot, in *Proceedings of the Satellite Symposium on New Era in Neutrino Physics, Tokyo, Tokyo Metropolitan University, 1998*, Frontiers Science Series, No. 25, Ed. by H. Minakata and O. Yasuda.
4. G. Ranucci, in *Proceedings of the Satellite Symposium on New Era in Neutrino Physics, Tokyo, Tokyo Metropolitan University, 1998*, Frontiers Science Series, No. 25, Ed. by H. Minakata and O. Yasuda.
5. R. Raghavan, in *Proceedings of the International Conference Neutrino 98, Takayama, 1998.*
6. P. Gorodetsky, in *Proceedings of the Satellite Symposium on New Era in Neutrino Physics, Tokyo, Tokyo Metropolitan University, 1998*, Frontiers Science Series, No. 25, Ed. by H. Minakata and O. Yasuda.
7. J. N. Bahcall, Phys. Rev. Lett. **23**, 251 (1969).
8. J. N. Bahcall, Rev. Mod. Phys. **50**, 881 (1978).
9. J. N. Bahcall, Annu. Rev. Astron. Astrophys. **16**, 241 (1978).
10. G. V. Domogatskiĭ, Preprint No. 153, FIAN (Lebedev Institute of Physics, Academy of Sciences of USSR, 1969).
11. J. N. Bahcall, Preprint No. IASSNS-AST 93/41 (1993).
12. J. K. Rowly, in *Proceedings of the Conference on Status and Future of Solar Neutrino Research, BNL, 1978*, p. 265.
13. E. Veretenkin, V. Gavrin, and E. Yanovich, At. Énerg. **58**, 65 (1985); V. Gavrin and E. Yanovich, Izv. Akad. Nauk SSSR, Ser. Fiz., No. 6, 51 (1987).
14. M. Galeazzi *et al.*, Nucl. Instrum. Methods A **401**, 317 (1997).
15. M. Galeazzi *et al.*, Phys. Lett. B **398**, 187 (1997).
16. S. N. Danshin, G. T. Zatsepin, A. V. Kopylov, *et al.*, Fiz. Élem. Chastits At. Yadra **28**, 3 (1997) [Phys. Part. Nucl. **28**, 1 (1997)]; A. Kopylov, in *Proceedings of the International Solar Neutrino Conference, Heidelberg, 1997*, Ed. by W. Hampel (MPI für Kernphysik, Heidelberg, 1997), p. 263; M. N. Arnoldov, A. V. Kopylov, I. V. Orekhov, *et al.*, Izv. Vyssh. Uchebn. Zaved.: At. Énerg. **3** (1999); G. Y. Novikova and V. V. Petukhov, Izv. Vyssh. Uchebn. Zaved.: At. Énerg. **3** (1999).

Physics of Atomic Nuclei, Vol. 63, No. 7, 2000, pp. 1276–1281. From Yadernaya Fizika, Vol. 63, No. 7, 2000, pp. 1349–1354.

EXPERIMENTAL RESULTS, METHODS, AND FACILITIES

Fast-Neutron-Flux Measurements in the Underground Facilities at Baksan*

J. N. Abdurashitov, V. N. Gavrin, A. V. Kalikhov, A. A. Klimenko[1)], S. B. Osetrov[1)], A. A. Shikhin, A. A. Smolnikov[1), **], S. I. Vasiliev[1)], V. E. Yantz, and O. S. Zaborskaya

Institute for Nuclear Research, Russian Academy of Sciences, pr. Shestidesyatiletiya Oktyabrya 7a, Moscow, 117312 Russia

Abstract—The fast-neutron flux in one of the deep underground facilities situated at a depth of 4900 mwe in the Baksan Neutrino Observatory are measured. The relative neutron-shielding properties of several commonly available natural materials are also investigated. Preliminary results obtained with a highly sensitive fast-neutron spectrometer at a sensitivity level of about 10^{-7} neutron cm^{-2} s^{-1} are presented and discussed. © *2000 MAIK "Nauka/Interperiodica".*

1. INTRODUCTION

It is well known that one of the main sources of background in underground physics experiments (such as those that are aimed at investigating the solar-neutrino flux, neutrino oscillations, and neutrinoless double-beta decay and at seeking annual and daily modulations in the flux of cold-dark-matter particles) is fast neutrons originating from surrounding rocks. Several research groups have investigated the neutron background at various underground laboratories [1–3]. Some of them relied on the technique employing ^{6}Li-doped liquid scintillator [3]; the others used liquid scintillators without loading elements, but they invoked the technique of pulse-shape discrimination [1].

The measurements of fast-neutron flux in the deep-underground low-background laboratory of the Baksan neutrino observatory (DULB BNO) were performed with a dedicated fast-neutron spectrometer characterized by a high sensitivity [4]. This laboratory is located under Mt. Andyrchy (Northern Caucasus Mountains, Russia) in a tunnel that penetrates 4.5 km into the mountain at a depth of 4900 mwe.

The results of these measurements lead to the conclusion that a neutron background places a severe limitation on the sensitivity of current and planned experiments. Because of this fact, the development of new cost-effective, high-strength radiation shielding against neutrons becomes a very important task for modern nonaccelerator physics experiments. For such purposes, the relative neutron-shielding properties of several commonly available natural materials were investigated too. Specially, these materials are planned for use in the construction of large-volume underground facilities that will be covered with suitable shielding materials and are situated in the DULB Laboratory at Baksan.

2. NEUTRON DETECTOR

This spectrometer was constructed to measure low-background neutron fluxes at a level of up to 10^{-7} cm^{-2} s^{-1} in the presence of intense gamma-ray background.

The detector consists of liquid organic scintillator viewed by photomultipliers with 19 neutron counters (^{3}He proportional counters) uniformly distributed over the scintillator volume. The main sources of fast neutrons originating from the surrounding rocks are (α, n) reactions on light elements contained in the rock (C, O, F, Na, Mg, Al, Si). Neutrons from the spontaneous fission of ^{238}U make an additional contribution to the total fast-neutron flux of about 15–20%.

Fast neutrons with $E_n > 1$ MeV that enter the liquid scintillator (LS) are moderated down to thermal energy, producing an LS signal. After that, they diffuse through the detector volume to be captured in ^{3}He counters or on protons in the scintillator. The LS signal starts the recording system. After this triggering, the system waits for a signal from any of the helium counters for a specific time. This time window corresponds to the delay time between correlated events in the scintillator and in the helium counters. This is one of specific features of the detector. The signal from the LS is "labeled" as that which is coincident with a neutron capture in the ^{3}He counters only if a single counter is triggered during the waiting period. The amplitude of the "labeled" LS signal corresponds to the initial neutron energy. This method allows us to suppress the natural γ-ray background considerably.

The described event-discriminating procedure allows us to measure extremely low neutron fluxes at a level of up to 10^{-7} cm^{-2} s^{-1} reliably even if the LS counting rate is as large as a few hundred per second. The

* This article was submitted by the authors in English.

** e-mail: smoln@nusun.jinr.ru

1) Joint Institute for Nuclear Research, Dubna, Moscow oblast, 141980 Russia.

1063-7788/00/6307-1276$20.00 © 2000 MAIK "Nauka/Interperiodica"

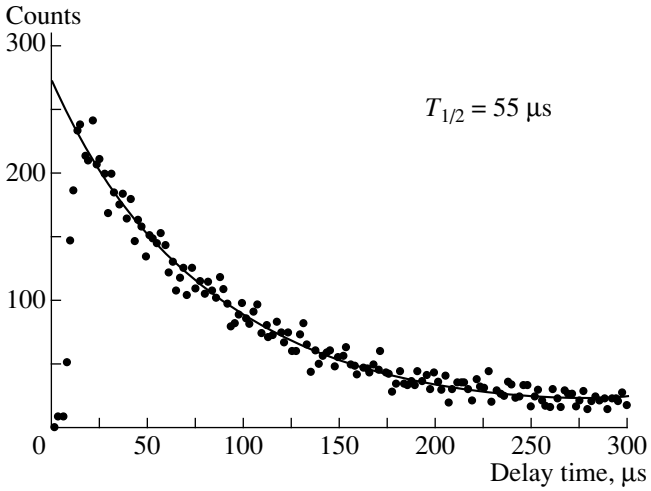

Fig. 1. Delay-time distribution for neutron events accumulated with Pu–Be source.

dead time of the detector is equal to the delay time (a variable value, but generally about 120 μs) plus about 400 μs, which is needed to analyze an LS event to be positive as to whether it corresponds to a neutron or not.

The detection efficiency depends, in a complicated manner, on the response function of the detector. As a rough estimate, we use the efficiency value equal to 0.04 ± 0.02 in the energy range from 1 to 15 MeV. This is based on preliminary measurements performed with a Pu–Be source. Owing to this fact, absolute values of the neutron fluxes can be estimated with an uncertainty of 50% on the basis of available calibration data. The delay time is a specific feature of the detector and depends on the detector design. The acquisition system allows us to measure the delay time for neutron events directly. Such measurements were carried out by using a Pu–Be source with a time window selected to be equal to 300 μs. A typical delay-time distribution is shown in Fig. 1. A fitting procedure leads to a time constant of $T_{1/2} \sim 55$ μs. According to this result, it is sufficient to select the time window to be equal 120 μs for an actual measurement.

3. MEASUREMENTS

3.1. Geometry of Measurements

It was mentioned above that, so far, we have no precise information about the detection efficiency; for this

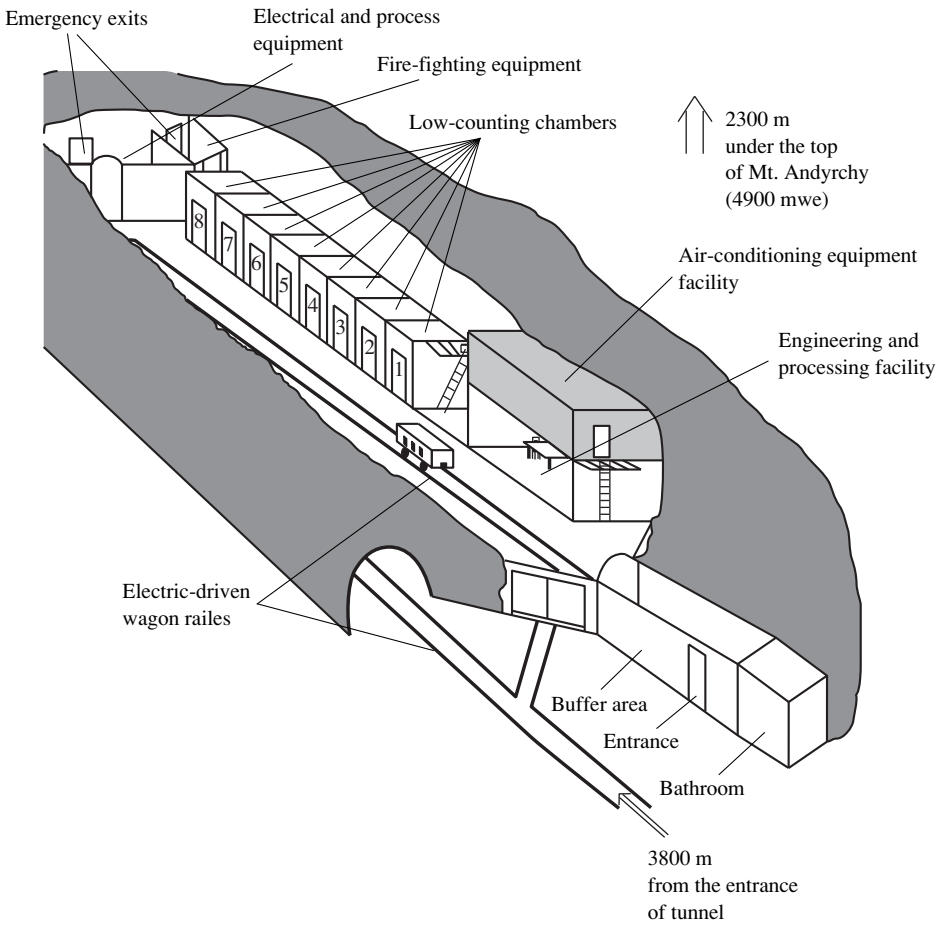

Fig. 2. Cutaway view of the DULB BNO Laboratory.

Table 1. Concentration of U, Th, and K in rock samples

	^{238}U, g/g	^{232}Th, g/g	^{40}K, g/g
Quartzite	$(1.1 \pm 0.1) \times 10^{-7}$	$(4.3 \pm 0.1) \times 10^{-7}$	$(1.9 \pm 0.03) \times 10^{-7}$
Serpentine	$(2.2 \pm 0.5) \times 10^{-8}$	$(2.0 \pm 0.9) \times 10^{-8}$	$<1.2 \times 10^{-8}$
Surrounding mine rock	$(1.6 \pm 0.3) \times 10^{-6}$	$(4.0 \pm 0.1) \times 10^{-6}$	$(1.6 \pm 0.1) \times 10^{-6}$

reason, one can calculate the absolute value of neutron fluxes only with a 50% certainty. However, it is possible to measure the relative neutron-absorption abilities of various shields with a high precision. This information will be very useful for developing new low-background experiments and for seeking cost-effective neutron-absorption shields. Such measurements were performed in the DULB BNO with the neutron spectrometer described above. This new laboratory, which consists of eight separate counting facilities, is located under Mt. Andyrchy in a tunnel penetrating 4.3 km into the mountain at a depth of 4900 mwe. The laboratory has a total floor area of about 370 m^2 and a total volume of 2200 m^3. Eight separate counting facilities with sizes of $3 \times 4 \times 3$ m^3 each are being constructed in the laboratory for performing several independent experiments simultaneously. A cutaway view of the DULB BNO Laboratory is shown in Fig. 2.

Quartzite and serpentine were selected as materials to be tested because of comparatively low concentrations of uranium- and thorium-bearing compounds contained in these rocks. For instance, the measured concentrations of uranium and thorium in ultrabasic rock serpentine are about 10^{-8} g(Th/U)/g(sample) to be compared with 10^{-6} g(Th/U)/g(sample) for the surrounding rock. As to potassium (^{40}K) contained in serpentine, it was found to be less than 10^{-8} g(^{40}K)/g(sample) to be compared with 10^{-6} g(^{40}K)/g(sample) for the surrounding rock. Measurements of the gamma activity of various rock samples were performed with a well-type NaI gamma spectrometer that had a sensitivity level of about 10^{-9} g(Th/U)/g(sample) and which operated in one of the underground low-counting facilities at BNO [5]. The measured Th, U, and K concentrations in various rock samples are given in Table 1.

Four series of measurements were performed with the neutron spectrometer surrounded by various radiation shields. In the first series, the spectrometer was surrounded by a lead shield 4 cm thick (in order to reduce the natural-gamma-ray counting rate), and the natural neutron-background radiation field existing in the open experimental site was measured. In the second and third series, the spectrometer was surrounded by shields of quartzite and serpentine, respectively. The rock shields consisted of broken pieces of various sizes ranging from 1 to 15 cm with an effective shield thickness of 35 cm in all directions. The mean relaxation length of fast neutrons in these shields is about 15 cm (25 g/cm^2 for quartzite and 21 g/cm^2 for serpentine). In the fourth series, we measured the internal background of the detector using a neutron-absorbing shield consisting of a 40-cm-thick section of polyethylene containing an admixture of boron and water about 30 cm thick.

3.2. Calibration

In order to calibrate the LS channel, a ^{60}Co γ source has been used. The energy of the middle of the Compton edge was assumed to be 1 MeV on the electron-energy scale, which corresponds to 3 MeV on the neutron-energy scale. In order to calibrate the NC channel of ^{3}He counters, a Pu–Be source was used. The spectrum produced by the Pu–Be source in the ^{3}He counters has a specific shape owing to a wall effect distorting the counter event spectrum. Despite this distortion, the range of energies observed for true neutron events is narrower than the broad background spectrum produced by internal alphas. The use of only events from the neutron window as triggered signals makes it possible to suppress the internal background of the detector.

3.3. Conditions of Measurements

The main conditions for all series of measurements, such as the measurement times and the LS- and NC-counting rates, are given in Table 2. The typical exposure time for each series was a few weeks. The gamma-ray background in the open experimental site is sufficiently high, which leads to a γ-counting rate in the LS channel of about 700 s^{-1}. Due to this fact, the following values of dead time were determined for the different series: 12% of the total exposure time for the measurements with the lead shield, 4.3% for the quartzite series, 2.7% for the serpentine series, and 1.5% for the measurements with the polyethylene/water shield. In order to calculate the true neutron-counting rates, a correction for the proper dead time was introduced.

4. DATA TREATMENT AND RESULTS

A contamination of the ^{222}Rn gas inside the experimental site can make a considerable contribution (up to 20%) to the background γ-counting rate, which can affect the results of our measurements because ^{222}Rn activity can vary significantly over the period of a measurement.

In order to suppress the counting-rate-variation effect, we used a special procedure for experimental-data treatment. It consists of the following steps.

Table 2. Main conditions of the measurements

	No shielding (5 cm lead)	Quartzite	Serpentine	Water+ polyethylene
The measurement time, h	400	290	950	605
Dead time, % of overall measurement time	12	4.3	2.7	1.5
Total LS-counting rate, s^{-1}	202	83	62	21
Total NC-counting rate, h^{-1}	123 ± 0.6	103 ± 0.6	92 ± 0.3	95 ± 0.4
R_{meas}, NC-counting rate in neutron window, h^{-1}	58 ± 0.4	37 ± 0.4	27 ± 0.2	27 ± 0.2 (R_{bkg})
R_{rnd}, random coincidence rate, h^{-1}	1.41 ± 0.005	0.38 ± 0.002	0.19 ± 0.001	0.07 ± 0.001
R_n, neutron counting rate, h^{-1}	29.6 ± 0.5	9.6 ± 0.5	-0.2 ± 0.3	–

Two types of data files are stored as the result of a measurement. One of them contains information about neutron-energy losses (LS-signal amplitudes), the amplitudes of signals from the ^{3}He counters, and the delay time for each "neutron" event. Data accumulation was stopped every half-hour, and the overall numbers of NC counts, LS counts, LS counts above 1 MeV, and elapsed time were saved in a file. The total background

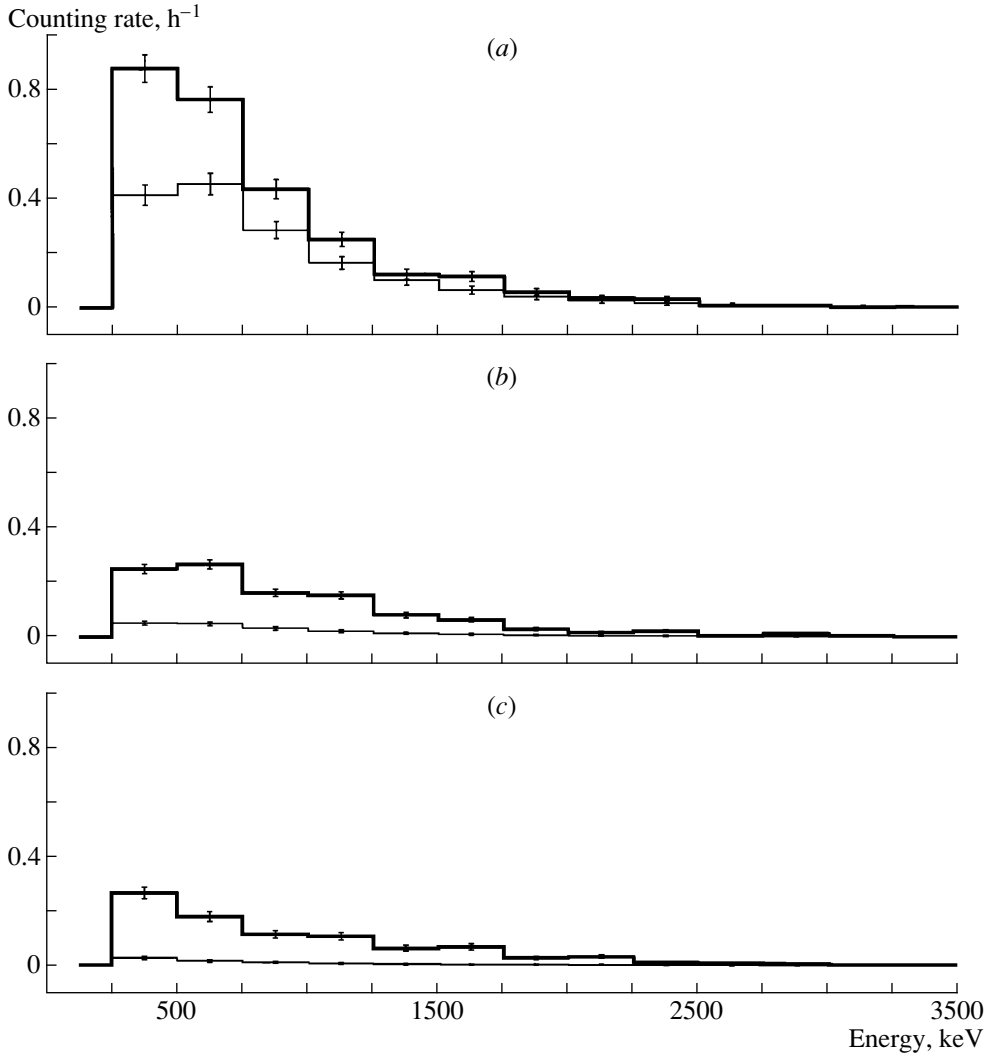

Fig. 3. Accumulated LS spectra of all coincident events (R_{meas}, thick lines) and the rescaled spectra of random coincidences (R_{rnd}, thin lines) for the series (*a*) without any shield and with (*b*) a serpentine and (*c*) a water shield.

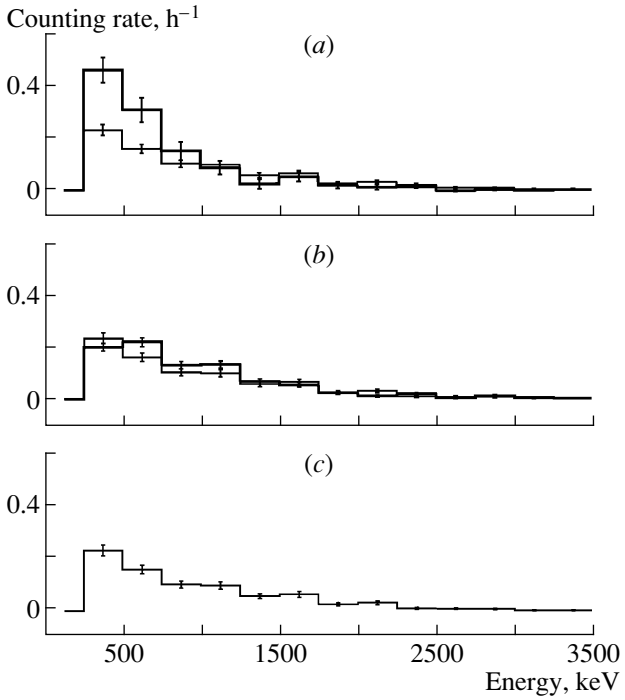

Fig. 4. Residual LS spectra ($R_{meas} - R_{rnd}$, thick lines) along with the internal-background LS spectrum (R_{bkg}, thin lines) for the series (*a*) without any shield and with (*b*) a serpentine and (*c*) a water shield.

γ spectra for every half-hour run were measured simultaneously and saved in the second file to make it possible to take into account the time variation in the background γ-counting rate.

We consider three contributions to the experimentally measured counting rate R_{meas}: the random-coincidence rate R_{rnd}, the internal-detector-background-counting rate R_{bkg}, and the "neutron"-counting rate R_n, so that

$$R_n = R_{meas} - R_{rnd} - R_{bkg}. \quad (1)$$

We obviously made the assumption that the total background γ spectrum and the random-coincidence spectrum have the identical shapes. In order to obtain the random-coincidence spectrum for a further subtraction procedure, the total background γ spectrum was normalized with a factor corresponding to the calculated random-coincidence rate. The maximal evaluation for the random-coincidence rate, if LS and NC events are absolutely independent, can be calculated as

$$R_{rnd} = r_\gamma r_n^w \Delta t, \quad (2)$$

where r_γ is the γ rate, r_n^w is the counting rate in ^{3}He counters within the determined neutron energy window, and Δt is the time window. In the case of the measurements performed ($R_{LS} \gg R_{He}$), this evaluation is very close to the real counting rate for random coincidences. Due to a variation in time of the ^{222}Rn activity, the current value of r_γ^i depends on time too. Owing to this fact, we applied the described subtraction procedure to each half-hour run with the corresponding current value of R_{rnd}^i and then summed the resulting neutron spectra into a total serial spectrum. The accumulated LS spectra of all coincident events (R_{meas}) and the rescaled spectra of random coincidences (R_{rnd}) for the no-shield, quartzite, and serpentine series are presented in Fig. 3.

The internal-detector-background spectrum R_{bkg} was accumulated inside the neutron-absorbing shield consisting of polyethylene and water. The counting rate obtained for the internal-background correlated (neutron-type, but non-neutron) events was measured as 27 counts per hour, which, in terms of the neutron flux, corresponds to $(8.1 \pm 0.5) \times 10^{-7}$ cm^{-2} s^{-1}. The residual LS spectra ($R_{meas} - R_{rnd}$) are presented in Fig. 4, along with the internal-background LS spectrum (R_{bkg}).

Performing the total subtraction procedure in accordance with (1), we obtain values of the neutron-counting rate R_n for the no-shield, quartzite, and serpentine series. Taking into account the uncertainty in the detection efficiency ($\varepsilon = 0.04 \pm 0.02$), we the present the values obtained for the fast-neutron fluxes (above 700 keV of neutron energy) as

$$a(3.5 \pm 1.1) \times 10^{-7} \text{ cm}^{-2} \text{ s}^{-1}$$
for the no-shield measurement,

$$a(2.9 \pm 1.1) \times 10^{-7} \text{ cm}^{-2} \text{ s}^{-1} \text{ for the quartzite shield,}$$

$$a(0.6 \pm 0.7) \times 10^{-7} \text{ cm}^{-2} \text{ s}^{-1} \text{ for the serpentine shield,}$$

where $a = (\varepsilon + \Delta\varepsilon)/\varepsilon$. One can see that the resulting neutron flux measured when the serpentine shield was used is at about the minimum sensitivity level of the spectrometer. This means that the neutron background inside the serpentine shield is consistent with a neuron flux less than 0.7×10^{-7} cm^{-2} s^{-1}. This indicates that serpentine is indeed clear from uranium and thorium and is therefore the most appropriate candidate for a cost-effective neutron-shield-material for large-scale low-background experiments.

An analysis of the delay-time distribution was performed to understand the origin of a high level of the internal detector background.

4.1. Delay-Time Distributions

The decays of Bi and Po radioactive isotopes, such as

$$^{214}\text{Bi}(e, \tilde{\nu}) \xrightarrow{164\ \mu\text{s}} {}^{214}\text{Po}(\alpha) \longrightarrow \ldots, \quad (3)$$

which can occur in the helium-counter walls, have been considered as main possible sources of the significant internal background. To imitate an actual neutron event, the beta decay of ^{214}Bi can fire the liquid scintillator, followed by a delayed capture α signal from Po decay in helium counters. The delay-time distribution

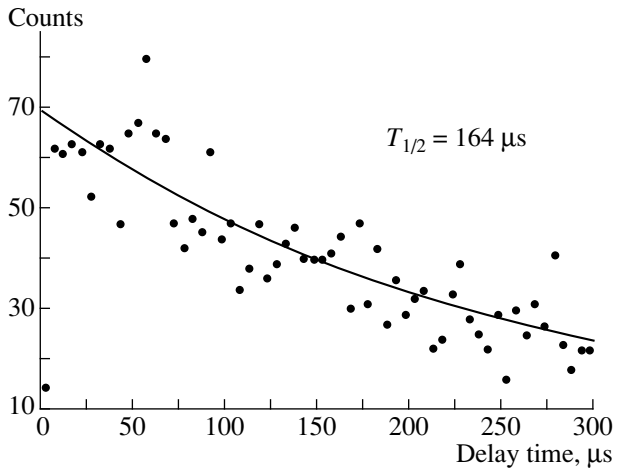

Fig. 5. Delay-time distribution for the coincident events, R_{meas} (R_{bkg}), accumulated in the series with a water shield.

of the neutron-type coincident events obtained for the series in the water shield is shown in Fig. 5. The fitting procedure leads to the time constant $T_{1/2}$ = 164 μs. This means that, as was assumed, the origin of the internal background of our detector is mostly due to the contamination of ^{214}Bi in the ^{3}He-counter walls.

To analyze these distributions, we used the fitting function (t should be expressed in μs)

$$A + Be^{-t\ln 2/55} + Ce^{-t\ln 2/164}, \quad (4)$$

where A is a constant, B is an amplitude corresponding to neutrons, and C corresponds to the internal background. The ratio B/C, which was obtained in this manner, decreases from measurements in the lead shield to the measurements in the serpentine shield.

5. CONCLUSIONS

The main results of the measurements can be summarized as follows.

(i) The preliminary results obtained from the fast-neutron spectrum accumulated in the open experimental site of the DULB Laboratory at Baksan are consistent with a neutron flux (for neutrons with energies above 700 keV) estimated to be between 5.3×10^{-7} and 1.8×10^{-7} cm^{-2} s^{-1}, a specific value being dependent on the current uncertainty in the determination of the detection efficiency.

(ii) The neutron-spectrometer sensitivity in a shielded experimental site is estimated at 0.5×10^{-7} cm^{-2} s^{-1} for a measurement time of about 1000 h.

(iii) It is shown that the main source of the limitation on the detection sensitivity is not random coincidences but the internal spectrometer background, which is mostly due to the presence of α-particle emitters (^{214}Bi–^{214}Po decays) in the walls of the ^{3}He counters.

(iv) The achieved neutron background inside the serpentine shield is consistent with a neutron flux less than 0.7×10^{-7} cm^{-2} s^{-1}. This indicates that serpentine is one of the most appropriate candidates for a cost-effective neutron-shield material for large-scale low background experiments.

We have obtained the present results using a simple event-discrimination procedure and have not used pulse-shape discrimination yet. Nevertheless, this enables us to measure extremely low neutron fluxes up to 10^{-7} cm^{-2} s^{-1} even when the external γ-counting rate is more than 200 s^{-1}.

ACKNOWLEDGMENTS

We are grateful to I.I. Pyanzin for the management in proving reserves and quarrying domestic ultrabasic rock samples. We thank P.S. Wildenhain for carefully reading the manuscript and for his critical remarks.

This work was supported in part by the Russian Foundation for Basic Research (project nos. 98-02 16962 and 98-02-17973).

REFERENCES

1. V. Chazal *et al.*, Astropart. Phys. **9**, 163 (1998).
2. F. Arneodo *et al.*, Preprint No. INFN/AE-97/52, INFN (1997).
3. R. Alexan *et al.*, Nucl. Instrum. Methods A **274**, 203 (1989).
4. J. N. Abdurashitov *et al.*, Instrum. Exp. Tech. **40**, 741 (1997).
5. A. A. Klimenko, A. A. Pomansky, and A. A. Smolnikov, Nucl. Instrum. Methods B **17**, 445 (1986).

Physics of Atomic Nuclei, Vol. 63, No. 7, 2000, pp. 1282–1287. From Yadernaya Fizika, Vol. 63, No. 7, 2000, pp. 1355–1360.

EXPERIMENTAL RESULTS, METHODS, AND FACILITIES

Event Generator DECAY4 for Simulating Double-Beta Processes and Decays of Radioactive Nuclei*

O. A. Ponkratenko, V. I. Tretyak, and Yu. G. Zdesenko

Institute for Nuclear Research, National Academy of Sciences of Ukraine, pr. Nauki 47, MSP 04680 Kiev, Ukraine

Abstract—The computer code DECAY4 is developed to generate initial-energy, time, and angular distributions of particles emitted in radioactive decays of nuclides and in nuclear (atomic) deexcitations. Data for describing nuclear- and atomic-decay schemes are taken from the ENSDF and EADL database libraries. By way of example, the DECAY4 code is applied to describing several underground experiments. *© 2000 MAIK "Nauka/Interperiodica".*

1. INTRODUCTION AND DESCRIPTION OF THE DECAY4 CODE

Although the effect-to-background ratio is a key problem in all realms of experimental physics, there is a certain class of experiments where this problem is so crucial that even the very possibility of performing them strongly depends on the background level of the detectors used. These are so-called underground experiments devoted to investigating extremely rare or forbidden decays and processes like double-beta decay, proton decay, dark-matter-particle searches, and solar-neutrino studies. The ultimate sensitivity of such experiments is determined primarily (the strengths of available sources apart) by the detector background. The background due to cosmic rays can be eliminated by choosing a proper underground site for the setup. Yet, the background exerting the strongest effect on the sensitivity arises from the decays of the nuclides of radioactive impurities in a detector material, in the materials used to install the detector mounting and to shield it, and in the surroundings. Therefore, it is obvious that a simulation of the background—and, in particular, a simulation of the nuclide decays—is an overwhelmingly important part of this kind of research, which can allow one (i) to understand and determine the sources of the background and, hence, to find certain methods for eliminating or suppressing the background contributions and (ii) to construct the background model and response functions of the detector for the effect to be sought (together with the detector energy and efficiency calibrations, resolution, source activities, etc.) and thus to extract and evaluate the sought effect (or to exclude it) more precisely.

There are several general programs that are commonly used to simulate particle interactions in the experimental setup—for example, the GEANT package [1] or the EGS4 code [2]. In any such program, the user should describe the initial kinematics of events by using the so-called event generator. The latter is an important part of the simulation program providing information as to what particles are emitted and how many of them, what their energies are, and what the directions of their motion and the times of their emission are. The existing computer codes RADLST [3] and IMRDEC [4] determine only the radiation spectra associated with the decay of nuclides; therefore, they cannot be used for further particle tracking.

In an attempt at filling this gap, the code DECAY4 was developed for generating events in low-energy nuclear and particle physics (double-beta decay and decay of radioactive nuclides). This code was elaborated over the last decade, mainly for 2β-decay research [5].

This article is organized as follows. First, the overall features of the DECAY4 generator and databases used are considered; then, the parts associated with the double-beta decay of atomic nuclei and the decays of natural and artificial radioactive nuclides are described in detail. In the last section, several examples illustrating the use of the DECAY4 generator in actual underground experiments are given.

The program DECAY4 makes it possible to generate events of the 2β decay of atomic nuclei and events of the radioactive decays (α, $\beta^{\pm}$, p, n decay, electron capture) of all known unstable isotopes. It is divided into two main parts: (a) INIT performs search and reading of all parameters of the nucleus and its decay needed for a decay simulation from the ENSDF [6] (or NuDat [7]), EADL [8], and other libraries in order to construct the nuclear- and atomic-decay schemes; (b) GENDEC is a Monte Carlo event generator.

The ENSDF database library includes the following information about 2500 isotopes used to generate radioactive decays: (a) decay modes, their probabilities and energy releases, and isotope half-lives; (b) radiation type and particle energies and intensities; (c) parameters of nuclear levels (half-life, spin, parity, and excitation energy); (d) parameters of nuclear transitions

* This article was submitted by the authors in English.

1063-7788/00/6307-1282$20.00

(branching ratios, multipolarities, coefficients of internal conversion, and mixing ratios).

The DECAY4 code also uses tables listing data on the atomic properties of isotopes [electron binding energies, electron-capture (EC) subshell ratios, and x-ray and Auger electron intensities) from the EADL database [8] (as well as from [9]) and tables quoting theoretical Hager–Seltzer conversion coefficients [10].

The GENDEC part of the DECAY4 generates the energy, the time of emission, and the direction and polarization for the following emitted particles: (i) electrons and positrons from the single- and double-beta decays; (ii) α particles from the α decay, protons and neutrons from the *p* and *n* decays; (iii) photons from the nuclear deexcitation process; (iv) conversion electrons; (v) e^-e^+ pairs from internal-pair conversion; (vi) bremsstrahlung photons from beta decay and EC; (vii) neutrinos (antineutrinos) from EC or beta (double-beta) decay; and (viii) x-rays and Auger electrons from the atomic deexcitation processes.

2. DOUBLE-BETA-DECAY PROCESSES

DECAY4 describes double-beta processes ($2\beta^-$ and $2\beta^+$ decays; electron capture followed by positron emission, $\varepsilon\beta^+$ and double electron capture 2ε) for all nuclides. Double-beta transitions to the ground state, as well as to the excited 0^+ and 2^+ levels, of the daughter nucleus are allowed. If the 2β-decay process occurs to an excited level of a nucleus, the electromagnetic deexcitation process follows. The energy release $Q_{\beta\beta}$ for the double-beta processes is taken from the table of atomic masses [11]. For each transition to the ground or an excited level, various modes (with the emission of two neutrinos or a Majoron, neutrinoless decays due to nonzero neutrino mass or right-handed admixture in the weak interaction, etc.) and mechanisms (two-nucleon $2n$ and Δ-isobar N^*) of double-beta decay are possible. Below, we list double-beta processes that can be simulated on the basis of DECAY4:

(I) $0\nu2\beta^\pm$ decay with a nonzero neutrino mass, 0^+–0^+ transition, $2n$ mechanism;

(II) $0\nu2\beta^\pm$ decay with right-handed currents, 0^+–0^+ transition, $2n$ mechanism;

(III) $0\nu2\beta^\pm$ decay with right-handed currents, 0^+–0^+ and 0^+–2^+ transitions, N^* mechanism;

(IV) $2\nu2\beta^\pm$ decay, 0^+–0^+ transition, $2n$ mechanism;

(V) $0\nu2\beta^\pm$ decay with Majoron emission, 0^+–0^+ transition, $2n$ mechanism;

(VI) $0\nu2\beta^\pm$ decay with double Majoron emission, 0^+–0^+ transition, $2n$-mechanism; decay involving a charged $L = -2$ Majoron or a massive vector Majoron;

(VII) $0\nu2\beta^\pm$ decay with right-handed currents, 0^+–2^+ transition, $2n$ mechanism;

(VIII) $2\nu2\beta^\pm$ decay, 0^+–2^+ transition, $2n$ and N^* mechanisms;

(IX) $0\nu\varepsilon\beta^+$ decay;

(X) $2\nu\varepsilon\beta^+$ decay, 0^+–0^+ and 0^+–2^+ transitions;

(XI) $0\nu2\varepsilon$ decay;

(XII) $2\nu2\varepsilon$ decay, 0^+–0^+ and 0^+–2^+ transitions.

Theoretical formulas for the energy and for the angular distribution $\rho(E_1, E_2, \cos\theta)$ of emitted electrons (positrons) were taken from [12–16]. For example, the above angular distribution for the first process has the form

$$\rho(E_1, E_2, \cos\theta) = p_1(E_1 + 1)F(E_1, Z)p_2(E_2 + 1) \times F(E_2, Z)\delta(E_0 - E_1 - E_2)(1 - \beta_1\beta_2\cos\theta), \quad (1)$$

where E_i is the kinetic energy of the ith $e^\pm$ (in units of the electron mass m_ec^2), p_i is its momentum (in units of m_ec), $F(E_i, Z)$ is the Fermi function, Z is the atomic number of the daughter nucleus ($Z > 0$ for $2\beta^-$ decay and $Z < 0$ for $2\beta^+$ decay), θ is the angle between the particle momenta, E_0 is the energy available for the particles ($E_0 = Q_{\beta\beta} - E_j^{ex}$ for $2\beta^-$ decay and $E_0 = Q_{\beta\beta} - 4 - E_j^{ex}$ for $2\beta^+$ decay, E_j^{ex} being the energy of the populated level of the daughter nucleus), and $\beta_i = p_i/(E_i + 1)$.

3. RADIOACTIVE DECAYS OF NUCLIDES

The DECAY4 describes six decay modes: β^-, α, *p*, and *n* decays; electron capture and β^+ decay (EC); and isomeric transition (IT). The modes *d* ($d = \beta^-$, α, *p*, *n*, EC, IT), their probabilities p^d, the available decay energies Q^d, and the isotope half-lives $T_{1/2}$ were taken from the ENSDF [6] or NuDat [7] databases. The decay mode *d* was sampled according to the probabilities p^d.

β^- decay. The endpoint energies in the β^- decay E_i^0 are related to the energy release Q^{β^-} and the level energies E_i^{exc} of the daughter nucleus by the equation

$$Q^{\beta^-} = E_i^0 + E_i^{exc}. \quad (2)$$

The kinetic energy of the β particle *E* is sampled in accordance with the distribution

$$\rho(E) = p(E + 1)(E_i^0 - E)^2F(E, Z)S_k(E), \quad (3)$$

where $S_k(E)$ is the forbiddenness factor. The probability of the internal bremsstrahlung in β decay and the energy–angular distribution of bremsstrahlung photons are calculated as in [17].

α, *p*, *n* decays. The particle energies E_i^k ($k = \alpha$, *p*, *n*) are related to the level energies E_i^{ex} of the daughter nucleus as

$$E_i^k = A_d/A_p \cdot (Q^k - E_i^{exc}), \quad (4)$$

where A_p and A_d are the mass numbers of the parent and daughter nuclei, respectively.

EC (electron capture and β⁺ decay). The ENSDF database includes information about the probabilities p_i^{EC} (for EC) and $p_i^{\beta^+}$ (for β^+ decay) for the ith level of the daughter nucleus. If the level is populated in the β^+ decay process, the positron energy is sampled according to (3), where

$$E_i^0 = Q^{\mathrm{EC}} - 2 - E_i^{\mathrm{exc}}. \quad (5)$$

If the ith nuclear level was populated in the electron-capture process, the number x of the atomic subshell ($x = K, L_1, L_2, L_3, M_1, M_2, \ldots, M_5, N_1, N_2, \ldots, N_7, O_1, O_2, \ldots, O_7$) where the primary electron vacancy is created is sampled according to probabilities P_x^{EC} [9],

$$P_x^{\mathrm{EC}}(Z, q_x) = \mathrm{const}\frac{n_x p_x^{2(k_x-1)} q_x^{2(L-k_x+1)} \beta_x^2 B_x}{[(2k_x-1)!(2L-2k_x+1)!]}, \quad (6)$$

where L is the angular momentum of the electron-capture transition; n_x is the relative occupation number for partially filled subshells x ($n_x = N_x / N_x^{\max}$; here, N_x is the number of electrons in the subshell x, while $N_x^{\max}$ is the maximal number of electrons in the subshell); $q_x = Q^{\mathrm{EC}} - E_i^{\mathrm{exc}} - E_x$ is the neutrino energy, E_x being the electron binding energy in the parent atom; and k_x is the angular momentum of the x subshell. The amplitudes squared $\beta_x^2 B_x p_x^{2(k_x-1)}$ of the radial wave functions for the bound-state electron and the electron binding energy E_x were taken from [9, 18]. The internal-bremsstrahlung probability and the spectra of bremsstrahlung photons in an allowed electron-capture transition from the atomic subshell x are calculated in accordance with [18].

Nuclear deexcitation process. This process occurs if a daughter nucleus is in the ith excited level with energy E_i^{exc}. The electromagnetic transition from the ith to the jth level is sampled according to probabilities

$$p_{ij} = J_{ij} / \sum_j J_{ij}, \quad (7)$$

where J_{ij} is the branching ratio of electromagnetic transition from the ith level to the jth one taken from the NuDat or ENSDF database. There are three possible electromagnetic-transition modes involving the emission of (i) a photon with energy $E^\gamma = E_i^{\mathrm{exc}} - E_j^{\mathrm{exc}}$; (ii) a conversion electron with energy $E_x^{\mathrm{ce}} = E_i^{\mathrm{exc}} - E_j^{\mathrm{exc}} - E_x$ (the condition $E_x^{\mathrm{ce}} > 0$ should be fulfilled), E_x being the electron binding energy in the x subshell; or (iii) a conversion electron–positron pair with total energy $E^{\mathrm{cp}} = E_i^{\mathrm{exc}} - E_j^{\mathrm{exc}} - 2$ (if $E^{\mathrm{cp}} > 0$). To sample the mode, the respective probabilities p_{ij}^γ, p_{ij}^{ce}, and p_{ij}^{cp} are used, where

$$p_{ij}^\gamma = 1/(1 + \alpha_{ij}^{\mathrm{ce}} + \alpha_{ij}^{\mathrm{cp}}),$$
$$p_{ij}^{\mathrm{ce}} = \alpha_{ij}^{\mathrm{ce}} p_{ij}^\gamma, \quad p_{ij}^{\mathrm{cp}} = \alpha_{ij}^{\mathrm{cp}} p_{ij}^\gamma \quad (8)$$

for all transitions, with the exception of $E0$, and

$$p_{ij}^\gamma = 0, \quad p_{ij}^{\mathrm{ce}} = 1/(1 + I_{ij}^{\mathrm{cp}}/I_{ij}^{\mathrm{ce}}), \quad p_{ij}^{\mathrm{cp}} = I_{ij}^{\mathrm{cp}}/I_{ij}^{\mathrm{ce}} \cdot p_{ij}^{\mathrm{ce}} \quad (9)$$

for the $E0$ transition. Here, $\alpha_{ij}^{\mathrm{ce}}$ and $\alpha_{ij}^{\mathrm{cp}}$ are the coefficients of internal electron and pair conversion, respectively, while I_{ij}^{ce} and I_{ij}^{cp} are the intensities of internal electron and pair conversion, respectively.

The total, partial subshell, and shell coefficients of internal electron conversion [$\alpha_{ij}^{\mathrm{ce}}$, $\alpha_{ij}^{\mathrm{ce}}(s_m)$, and $\alpha_{ij}^{\mathrm{ce}}(s)$, respectively] are related by the equations

$$\alpha_{ij}^{\mathrm{ce}} = \sum_s \alpha_{ij}^{\mathrm{ce}}(s); \quad \alpha_{ij}^{\mathrm{ce}}(s) = \sum_m \alpha_{ij}^{\mathrm{ce}}(s_m), \quad (10)$$

where s is the shell index, while m is the subshell index of the s shell ($s_m \equiv x$). The coefficients $\alpha_{ij}^{\mathrm{ce}}$ and $\alpha_{ij}^{\mathrm{ce}}(s)$ were taken from the NuDat or ENSDF databases. If their values are not known, the coefficients are calculated as

$$\alpha_{ij}^{\mathrm{ce}}(s_m) = [\alpha_{ij}^{\mathrm{ce}}(s_m, E^\gamma, \pi_1\lambda_1, Z) + \delta_{ij}\alpha_{ij}^{\mathrm{ce}}(s_m, E^\gamma, \pi_2\lambda_2, Z)]/(1 + \delta_{ij}^2), \quad (11)$$

where the values of the partial coefficients $\alpha^{\mathrm{ce}}(s_m, E^\gamma, \pi\lambda, Z)$ were taken from [10]. Here, $\pi\lambda$ is the multipolarity of the transition, and δ_{ij} is the mixing ratio of different multipolarities in the $i \longrightarrow j$ transition. For pure $E0$ transitions, the electron-conversion coefficients are calculated according to the formulas from [9]. The coefficient of internal pair conversion, $\alpha_{ij}^{\mathrm{cp}}$, is given by formulas similar to (11), while the partial coefficients $\alpha^{\mathrm{cp}}(E^\gamma, \pi\lambda, Z)$ and the electron–positron energy and angular distributions are calculated according to the formulas from [9, 19].

x rays and Auger electrons. The vacancies in the atomic shells result from electron capture or internal electron conversion. An ionized atom is deexcited via filling the vacancies by electrons from higher atomic shells, x rays and Auger electrons being emitted in this process. In order to sample an atomic deexcitation process, the electron binding energies and occupation numbers and the radiative and radiationless partial widths were taken from the EADL library [8]. The type of process (radiation or Auger electron emission) is sampled according to the values of the radiative and radiationless partial widths. For the vacancy in the s_i subshell, the x-ray energy for the radiative process

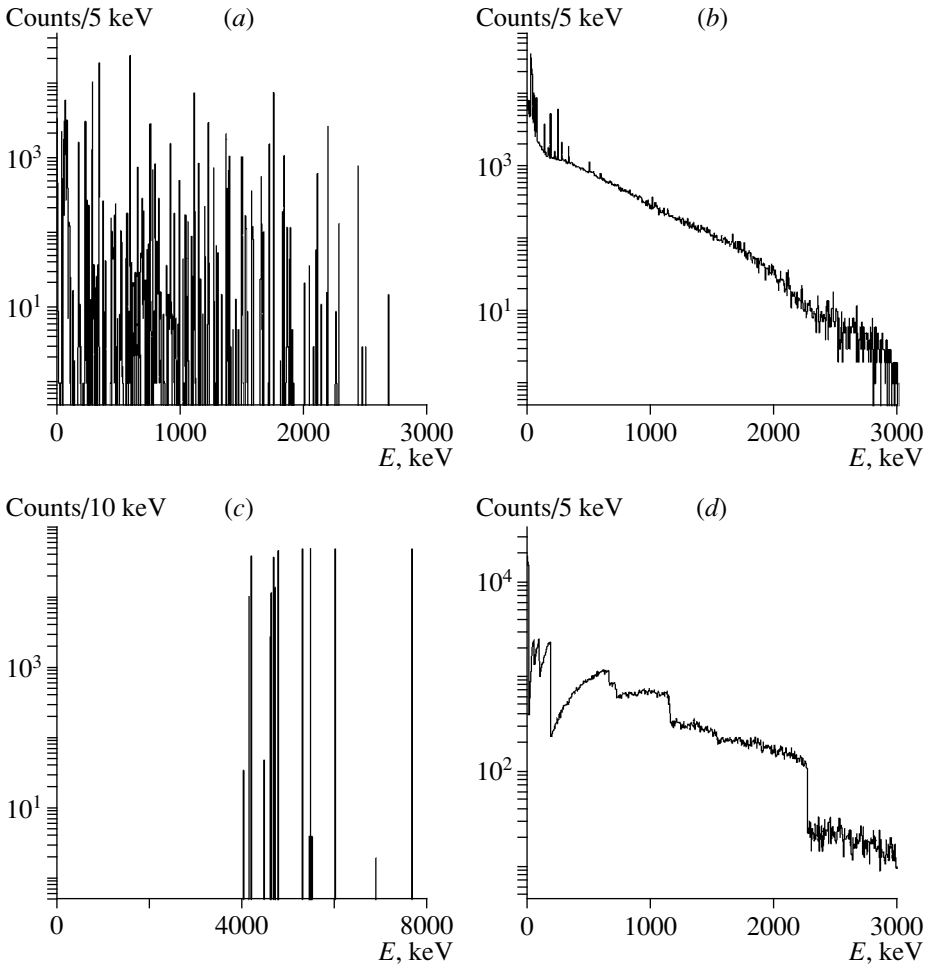

Fig. 1. Generated initial-energy spectra of particles emitted in the ^{238}U decay chain (in equilibrium): (*a*) photons, (*b*) electrons, (*c*) α particles, and (*d*) antineutrinos.

where a higher vacancy q_j is created and the Auger electron energy for a nonradiative process (vacancies q_j and t_l are created) are given by

$$E^{\mathrm{X}}_{s_i-q_j} = E_{s_i}(Z) - E_{q_j}(Z);$$
$$E^{\mathrm{A}}_{s_i-q_jt_l} = E_{s_i}(Z) - E_{q_j}(Z) - E_{t_l}(Z) - \Delta E_{q_jt_l}. \quad (12)$$

The correction $\Delta E_{q_jt_l}$ is found on the basis of equations presented in [20]. Multivacancy corrections for energies and partial widths are also included. The x-ray and Auger electron energy spreading is taken into account according to the Lorentzian distribution function [20].

Decay chains and time characteristics. The time interval T^k between the appearance of the unstable state k of a nucleus or an atom and its decay with the emission of a particle is sampled in accordance with the relation

$$T^k = -T^k_{1/2}\ln\eta/\ln 2, \quad (13)$$

where η is a random number uniformly distributed in the range (0, 1) and $T^k_{1/2}$ is the half-life of the unstable state. DECAY4 can also simulate the full decay chain for the parent nuclide together with its daughters. By way of example, the generated spectra of particles emitted in the decay of nuclides from the full chain of ^{238}U are shown in the figure. The activities of all daughter nuclei were calculated by the DECAY4.

Angular correlations between emitted particles. The direction (polar and azimuthal angles θ_i and φ_i) of the particle i is taken to be isotropic if one of the following conditions is satisfied: (1) the particle is the first in the decay of an unoriented parent nuclear state i; (2) $I_i < 1$ (I_i is the nuclear spin before the emission of the particle i); (3) $T^i > \tau_{\max}$ [T^i is the time given by (13), while $\tau_{\max}$ is a parameter (time) that is defined by the user to take into account the influence of external fields violating the angular correlation]; (4) $\lambda_i = 0$ or $\lambda_{i-1} = 0$ (λ_i and λ_{i-1} are the angular momenta of the particles i and $i-1$ if the particle $i-1$ exists); and (5) one of the quan-

tities I_{i-1}, I_i, I_{i+1}, λ_i, and λ_{i-1} is unknown and cannot be evaluated. If the particle $i+1$ does not satisfy any of the above conditions, while the particle i satisfies one of them, the polar angle θ^i_{i+1} of the particle $i+1$ in the coordinate frame associated with the particle i is sampled according to the correlation function [21]

$$W(\theta^i_{i+1}) = \sum_{k_{i+1}=0}^{k^{\max}_{i+1}} A^-_{k_{i+1}}(\lambda_i\lambda'_i I_{i+1}I_i, x_i) \times A^+_{k_{i+1}}(\lambda_{i+1}\lambda'_{i+1} I_{i+2}I_{i+1}, x_{i+1}) P_{k_{i+1}}(\cos\theta^i_{i+1}), \quad (14)$$

where $\lambda'_i = \lambda_i \pm 1$ is the second possible angular momentum of the particle (for the mixture of multipolarities), x_i is the type of the particle i ($x_i = \gamma, \beta, \alpha, e$), $A^\pm_{k_{i+1}}(\lambda_i\lambda'_i I_{i+1}I_i, x_i)$ are functions of the angular momenta, and k is even. In this case, the correlation function is independent of the azimuthal angle φ^i_{i+1}. If the next emitted particle $i+2$ exists and if does not satisfy any of the condition in (1)–(5), its direction is determined by a more complicated correlation function depending on the directions of preceding particles. The correlation of linear photon polarizations is also taken into account [21].

4. CONCLUSION

The code DECAY4 was successfully used in several underground experiments to design and optimize detectors, to simulate backgrounds (with the aid of the GEANT package), and to evaluate results. Some examples are listed below.

(i) Kiev 2β-decay experiments performed at the Solotvina Underground Laboratory in a salt mine 430 m underground (about 1000 mwe).

Scintillators made from a cadmium tungstate crystal (enriched in ^{116}Cd to 83%) were used to study ^{116}Cd [22, 23]. The background of a $^{116}CdWO_4$ crystal (15.2 cm^3) in the energy region of interest ($Q_{\beta\beta}$ = 2805 keV) was equal to about 0.6 count/(yr kg keV). With statistics collected for 19175 h, a half-life limit for the neutrinoless 2β decay of ^{116}Cd was obtained: $T^{0\nu}_{1/2} \geq 3.2 \times 10^{22}$ yr (at a 90% C.L.) [23]. Limits on 0ν modes with emission of one (M1) or two (M2) Majorons were also established: $T^{0\nu M1}_{1/2} \geq 1.2 \times 10^{21}$ yr and $T^{0\nu M2}_{1/2} \geq 2.6 \times 10^{20}$ yr (at a 90% C.L.) [24]. A comparison of these limits with theoretical results constrains the neutrino mass as $\langle m_\nu \rangle \leq 3.9$ eV and the Majoron–neutrino coupling constant as $g \leq 2.1 \times 10^{-4}$, which are among the most sensitive results for other nuclei [16].

The 2β decay of ^{160}Gd was studied by using a Gd_2SiO_5 : Ce crystal scintillator of dimensions 95 cm^3. The background was reduced to about 1.0 count/(keV kg) in the vicinity of the $Q_{\beta\beta}$ energy (approximately 1.73 MeV). An improved half-life limit was obtained for 0ν2β decay of ^{160}Gd: $T^{0\nu}_{1/2} \geq 1.2 \times 10^{21}$ yr at a 68% C.L. [25].

(ii) Deep underground DAMA collaboration experiments performed at the Gran Sasso National Laboratory.

Two radiopure CaF_2 : Eu crystal scintillators (370 g each) were used to study the 2β decay of ^{46}Ca and the double electron capture of ^{40}Ca and to seek dark matter. The highest up-to-date half-life limits were reached for 0ν and 2ν double electron capture of ^{40}Ca: $T^{0\nu}_{1/2} \geq 4.9 \times 10^{21}$ yr and $T^{2\nu}_{1/2} \geq 9.9 \times 10^{21}$ yr (at a 68% C.L.) [26].

The 2β$^+$ decay of ^{106}Cd was studied with the aid of two low-background NaI(Tl) crystals and enriched (to 68%) ^{106}Cd samples (about 154 g). New $T_{1/2}$ limits for the β$^+$ β$^+$, β$^+$/EC, and EC/EC decay of ^{106}Cd were obtained in the range $(0.3–4) \times 10^{20}$ yr at a 90% C.L. [27].

(iii) NEMO collaboration experiment performed at the Frejus Underground Laboratory to study the 2β decay of ^{100}Mo [28]. The first version of the DECAY4 code [29] was used to simulate the corresponding background. A clear two-neutrino 2β signal (1433 events over 6140 h) was observed, which leads to a half-life of $T_{1/2} = (0.95 \pm 0.04(\text{stat.}) \pm 0.09(\text{syst.})) \times 10^{19}$ yr [28].

(iv) Heidelberg–Kiev collaboration. Background simulations were performed for the GENIUS project aimed at improving the present sensitivity of searches for 2β decay and dark matter. Contributions from the cosmogenic activity produced in the Ge detectors used and from their radioactive impurities, as well as from the contamination of liquid nitrogen and other materials, were calculated. External γ, μ, and neutron backgrounds were also considered. The results of the calculations clearly show the feasibility of the GENIUS experiment [30].

Therefore, the DECAY4 code is a powerful tool for simulating radionuclide decays in a wide range of decays, emitted particles, etc.; it can be connected easily with the codes that simulate particle propagation like GEANT or EGS4.

The code includes the most advanced databases: ENSDF, NuDat, EADL, and others. The event generator DECAY4 was successfully used in many underground experiments (Kiev, Roma–Kiev, DAMA, NEMO, GENIUS collaborations).

ACKNOWLEDGMENTS

This work was supported in part by the Science and Technology Center of Ukraine (project no. 411).

REFERENCES

1. GEANT, *CERN Program Library Long Write-up W5013* (CERN, Geneva, 1994).
2. W. R. Nelson *et al.*, Preprint No. 265, SLAC (Stanford, 1985).
3. T. W. Burrows, Preprint No. BNL-NCS-52142, BNL (Brookhaven, 1988).
4. J. Stepanek, Comput. Phys. Commun. **106**, 237 (1997).
5. Yu. G. Zdesenko *et al.*, Preprint No. 89-7, KINR (Kiev Institute for Nuclear Research, Kiev, 1989); V. I. Tretyak, Preprint No. 92-8, KINR (Kiev Institute for Nuclear Research, Kiev, 1992).
6. J. K. Tuli, Preprint No. BNL-NCS-51655-Rev, BNL (Brookhaven, 1987).
7. C. L. Dunford and T. W. Burrows, Preprint No. BNL-NNDC/ONL-95/10, BNL (Brookhaven, 1995).
8. S. T. Perkins *et al.*, Lawrence Livermore Lab. Rep. UCRL-50400, Vol. 30 (1991).
9. R. B. Firestone, *Table of Isotopes*, Ed. by V. S. Shirley (Wiley, New York, 1996, 8th ed.).
10. Obtained from the NNDC (BNL, USA) as part of the ENSDF Analysis and Checking Codes for MS-DOS.
11. G. Audi and A. H. Wapstra, Nucl. Phys. A **595**, 409 (1995).
12. M. Doi *et al.*, Prog. Theor. Phys. **66**, 1739 (1981); **66**, 1765 (1981).
13. R. N. Mohapatra and E. Takasugi, Phys. Lett. B **211**, 192 (1988).
14. C. P. Burgess and J. M. Cline, Phys. Lett. B **298**, 141 (1993).
15. C. D. Carone, Phys. Lett. B **308**, 85 (1993).
16. V. I. Tretyak and Yu. G. Zdesenko, At. Data Nucl. Data Tables **61**, 43 (1995).
17. B. G. Pettersson, in *Alpha-, Beta- and Gamma-ray Spectroscopy*, Ed. by K. Siegbahn (North-Holland, Amsterdam, 1965).
18. W. Bambynek *et al.*, Rev. Mod. Phys. **49**, 77 (1977).
19. M. E. Rose, Phys. Rev. **76**, 678 (1949).
20. E. H. S. Burhop and W. N. Asaad, Adv. At. Mol. Phys. **8**, 163 (1972).
21. L. C. Biendenharn and M. E. Rose, Rev. Mod. Phys. **25**, 729 (1953).
22. F. A. Danevich *et al.*, Phys. Lett. B **344**, 72 (1995).
23. F. A. Danevich *et al.*, Nucl. Phys. B (Proc. Suppl.) **70**, 246 (1999).
24. F. A. Danevich *et al.*, Nucl. Phys. A **643**, 317 (1998).
25. F. A. Danevich *et al.*, Nucl. Phys. B (Proc. Suppl.) **48**, 235 (1996).
26. P. Belli *et al.*, Nucl. Phys. B **563**, 97 (1999).
27. P. Belli *et al.*, Astropart. Phys. **10**, 115 (1999).
28. D. Dassie *et al.*, Phys. Rev. D **51**, 2090 (1995).
29. V. I. Tretyak, NEMO note 2/92 (Orsay, 1992); NEMO note 6/93 (Orsay, 1993).
30. O. A. Ponkratenko, V. I. Tretyak, and Yu. G. Zdesenko, in *Proceedings of Workshop on Dark Matter in Astro- and Particle Physics, 1998* (IOP, London, 1999), p. 738.

Physics of Atomic Nuclei, Vol. 63, No. 7, 2000, pp. 1288–1291. From Yadernaya Fizika, Vol. 63, No. 7, 2000, pp. 1361–1364.

EXPERIMENTAL RESULTS, METHODS, AND FACILITIES

Powerful Dynamical Neutrino Source with a Hard Spectrum*

Yu. S. Lutostansky[1)] and V. I. Lyashuk**

Institute of Theoretical and Experimental Physics, Bol'shaya Cheremushkinskaya ul. 25, Moscow, 117259 Russia

Abstract—A powerful dynamical neutrino source with a hard spectrum obtained via the (n, γ) activation of ^{7}Li and a subsequent β^- decay ($T_{1/2}$ =0.84 s) of ^{8}Li with the emission of high-energy $\tilde{\nu}_e$ (up to 13 MeV) is discussed. In the dynamical system, lithium is pumped over in a closed cycle through a converter near the reactor core and further to a remote $\tilde{\nu}_e$ detector. It is shown that, owing to a large growth of the hardness of the total $\tilde{\nu}_e$ spectrum, the cross section for the interaction with a deuteron can strongly increase both in the neutral ($\tilde{\nu}_e + d \longrightarrow n + p + \tilde{\nu}_e$) and in the charged ($\tilde{\nu}_e + d \longrightarrow n + n + e^+$) channel in relation to the analogous cross sections in the reactor $\tilde{\nu}_e$ spectrum. © *2000 MAIK "Nauka/Interperiodica".*

1. INTRODUCTION

Presently, nuclear reactors provide the most powerful artificial source for neutrino investigations. But the spectrum of reactor antineutrinos is soft and its hardness decreases fast with increasing energy $E_{\tilde{\nu}_e}$. Moreover, the $\tilde{\nu}_e$ spectrum is not well defined for energies $E_{\tilde{\nu}_e} > 6$ MeV.

2. STATIC REGIME OF NEUTRON-TO-ANTINEUTRINO CONVERTER

An intense antineutrino source that is alternative to a reactor and which possesses a well-defined hard spectrum can be based on a special nuclear reactor with a core surrounded by a converter of neutrons to antineutrinos. In such a converter, neutrons outgoing from the reactor core (abbreviated in the figure and in the subscripts as RC) will be absorbed with the subsequent production of short-lived β^--active isotopes in a converter material. Decaying, these isotopes emit antineutrinos with a well-defined hard spectrum. Therefore, the resulting $\tilde{\nu}_e$ spectrum will appear to be a superposition of the soft reactor spectrum and the hard spectrum of the converter.

Let $F_{\mathrm{Li}}(\mathbf{r})$ and $F_{\mathrm{AZ}}(\mathbf{r})$ be, respectively, the density of lithium antineutrino flux and the density of the antineutrino flux from the reactor core; the number of the reactor antineutrinos emitted per fission event in the reactor core is $\bar{n}_\nu$ = 6.13–6.14. We assume that the hardness of the total $\tilde{\nu}_e$ spectrum at the point $\mathbf{r}$ is equal to one unit of hardness if $F_{\mathrm{Li}}(\mathbf{r})/F_{\mathrm{AZ}}(\mathbf{r}) = 1/\bar{n}_\nu$. The hardness of the total spectrum is then given by

$$H(\mathbf{r}) = \bar{n}_\nu \frac{F_{\mathrm{Li}}(\mathbf{r})}{F_{\mathrm{AZ}}(\mathbf{r})}. \quad (1)$$

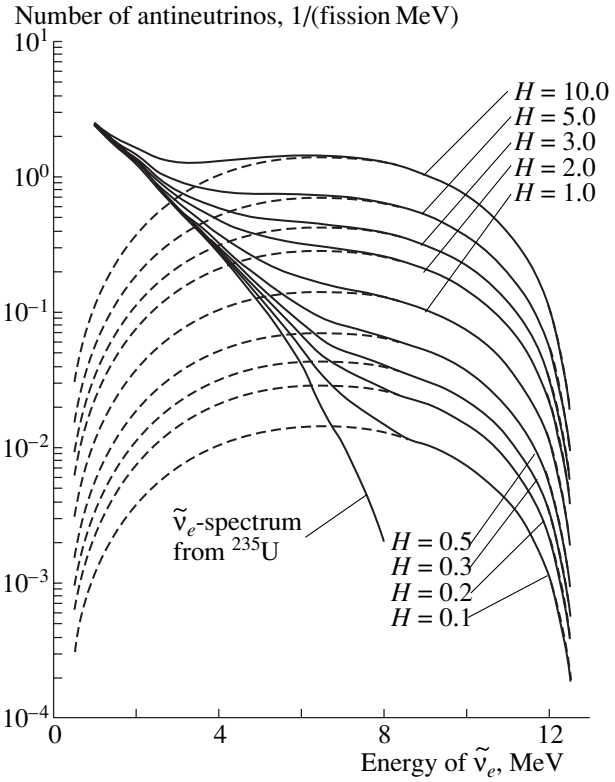

Fig. 1. Spectrum of antineutrinos from ^{235}U, total antineutrino spectra from the reactor core and lithium converter, and spectra of antineutrinos from the lithium converter (dashed curves) for various values of the hardness H.

* This article was submitted by the authors in English.

** e-mail: Lyashuk@alpha.itep.ru

1) Moscow State Engineering Physics Institute (Technical University), Kashirskoe sh. 31, Moscow, 115409 Russia.

The total $\tilde{\nu}_e$ spectra for various values of the hardness H are presented in Fig. 1.

The problem of isotope choice for a converter material was discussed in [1]. The requirements for such β^--active isotopes are as follows: (a) hard $\tilde{\nu}_e$ spectrum, (b) high production rate at the neutron absorption, (c) small half-life $T_{1/2}$, (d) adaptability to manufacture (i.e., the possibility to obtain the required mass of the starting isotopes with necessary purity), and (e) safety. The ^{7}Li isotope is the most suitable one. The idea of a neutrino source based on ^{7}Li was first proposed by Mikaelian *et al.* [2]. The possibility of using ^{7}Li for neutron-to-antineutrino conversion in a pulsed reactor was discussed in [3], and the characteristics of a lithium converter for the stationary-mode reactor were estimated in [1, 4, 5]. Some estimates for a converter based on E_n =14.1 MeV neutrons from thermonuclear devices were obtained in [4].

Owing to (anti)neutrino–nucleus interaction—the cross section is proportional to $E^2_{\tilde{\nu}_e}$—the new hard-spectrum $\tilde{\nu}_e$ source will have a serious advantage in experiments where ($\tilde{\nu}_e$, d) reactions are used to detect $\tilde{\nu}_e \longleftrightarrow \tilde{\nu}_{\mu,\tau}$ oscillations [1].

The converter efficiency κ (the number of ^{8}Li nuclei produced per neutron escaping from the reactor core) was calculated (by the MAMONT code [1, 6]) for spherically layered geometries A and B (Fig. 2) as a function of the ^{7}Li isotope purity P_7 and geometric parameters. It was assumed that one fission-spectrum neutron escapes from the reactor core per fission event. It is important that, in the case of the static regime, the hardness of the total $\tilde{\nu}_e$ spectrum is estimated by the value of the converter efficiency κ according to definition (1).

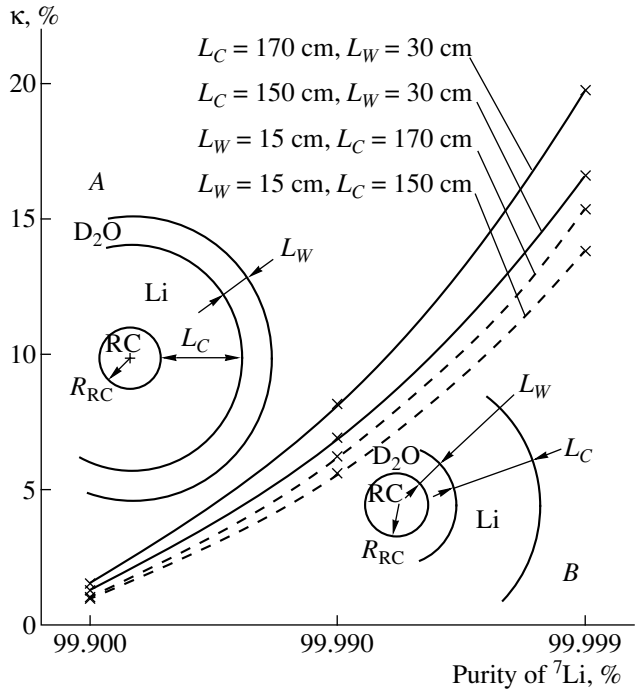

Fig. 2. Converter efficiency κ as a function of the purity of ^{7}Li isotope in (solid curves) geometry A and (dashed curves) geometry B for a converter thickness L_C and a heavy-water layer L_W at the reactor-core radius R_{RC} = 23 cm (51-l volume similar to high-flux PIK reactor [7]). The D_2O layer acts as a reflector in geometry A and as an effective moderator in geometry B. The layers of thicknesses L_W = 30 and 15 cm are optimal for the κ value in A and B geometries, respectively. The purity of P_7 = 99.99% is technologically feasible. Geometry A is preferable because of greater κ values at a smaller ^{7}Li volume: at L_C = 150 cm and L_W = 15 cm, the total volumes of ^{7}Li are 22.01 and 28.03 m^3 in A and B geometries, respectively.

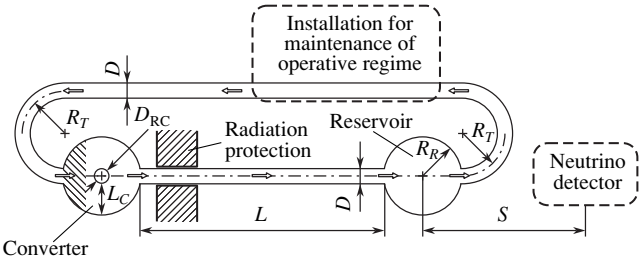

Fig. 3. Scheme of the neutrino-source facility operating in the dynamical mode. The geometry chosen for a computation has the following parameters: the thickness of the spherical converter is L_C = 1 m; the diameter of the reactor core is D_{RC} = 46 cm [7]; the channel diameter is D = 0.40 cm; and the radius of turn is R_T = 1.35 m. This converter on the basis of heavy-water solution of LiOD with a lithium concentration not less than 5.66% and a purity of P_7 = 99.99% possesses the efficiency of $\kappa \geq 0.10$.

3. DYNAMICAL SCHEME

All the converters that were discussed above and which operate in the static regime have a general demerit: the total $\tilde{\nu}_e$ flux has a significant soft $\tilde{\nu}_e$ component from the reactor core. It is possible to exclude this soft component and provide a harder $\tilde{\nu}_e$ spectrum by using a dynamical scheme (see [8]) where liquid lithium (or a chemical compound containing lithium) is pumped over in closed cycle through a converter and further to a large reservoir positioned in close proximity to a detector (Fig. 3). Such a facility will ensure not only a harder $\tilde{\nu}_e$ spectrum near the detector but also an opportunity to investigate $\tilde{\nu}_e$ interactions at various values of the spectrum hardness by varying the rate at which lithium is pumped.

The construction of this facility will be much more complicated than those in the static version (Fig. 2), but its advantages are obvious: (i) Owing to the reduction of the influence of soft $\tilde{\nu}_e$ from the reactor core, hard lithium $\tilde{\nu}_e$-component will be increased strongly, and

this may solve the old problem of uncertainty in the shape of the reactor $\tilde{\nu}_e$ spectrum. (ii) Owing to the cross-section dependence $\sigma_\nu \sim E_{\nu_e}^2$ and the hard lithium $\tilde{\nu}_e$ spectrum, the rate of $(\tilde{\nu}_e + p)$ and $(\tilde{\nu}_e + d)$ interactions will also increase greatly. (iii) The dynamical scheme permits one to increase the efficiency of experimental investigations of $\tilde{\nu}_e \longleftrightarrow \tilde{\nu}_{\mu,\tau}$ and $\tilde{\nu}_e \longleftrightarrow \nu_e$ oscillations in relation to the static regime.

The main requirements for the dynamical system are the following: (i) The converter must have the maximum possible efficiency κ. (ii) The reservoir with an optimally large volume must be located near the detector to ensure a high hardness of the total $\tilde{\nu}_e$ spectrum and a high event rate. (iii) A rapid delivery of a sufficient volume of lithium from the converter to the reservoir is necessary for reducing the delivery time t_d. (iv) The distance L between the converter and reservoir must be as large as possible in order to minimize the soft reactor-core component in the total $\tilde{\nu}_e$ spectrum.

In order to describe the dynamical regime of operation for the facility in question, we must solve the following set of equations for the production of the ^{8}Li isotope in the reaction $^7\mathrm{Li}(n,\gamma)^8\mathrm{Li}$:

$$\begin{aligned} \dot{N}_7(t) &= -\lambda_{n,\gamma} N_7(t), \\ \dot{N}_8(t) &= \lambda_{n,\gamma} N_7(t) - \lambda_\beta N_8(t). \end{aligned} \tag{2}$$

Here, $N_7(t)$ and $N_8(t)$ are the numbers of, respectively, ^{7}Li and ^{8}Li nuclei at the instant t; $\lambda_{n,\gamma}$ is the rate of the relevant (n,γ) reaction; and λ_β is the rate of the β^- decay of ^{8}Li. We assume that, at $t = 0$, the initial conditions are the following: $N_7(0) = N_7^0$ and $N_8(0) = 0$.

The quantity $\lambda_{n,\gamma} N_7^0$ (that is, the number of ^{8}Li nuclei produced per unit time) is the converter efficiency κ in view of the accepted normalization per fission event in the reactor core. Knowledge of $\lambda_{n,\gamma} N_7^0$ makes it possible to calculate fluxes of lithium $\tilde{\nu}_e$ from any part of the dynamical system (including the converter, the reservoir, and the channel of delivery) and the total hardness of the $\tilde{\nu}_e$ spectrum at the neutrino-detector position.

The set of equations (2) for $\tilde{\nu}_e$ fluxes from the converter, the reservoir, or the delivery channel can be solved analytically [8]. For example, the integrated (with respect to time) flux of lithium $\tilde{\nu}_e$ from the converter is

$$N_C(t) = (t/t_p)\{S_1 + S_2/\varphi(V_0)\}, \tag{3}$$

where w is a volume pumped in a time unit (i.e., circulation rate), $t_p = V_C/w$ is the time of pumping of the converter volume V_C, V_0 is the volume of lithium in the dynamical system, $\varphi(y) = 1 - \exp[-(\lambda_\beta/w)y]$, and

$$S_1 = \lambda_{n,\gamma} N_7^0 t_p - (\lambda_{n,\gamma} N_7^0/\lambda_\beta)\varphi(V_C),$$

$$S_2 = \frac{\lambda_{n,\gamma} N_7^0}{\lambda_\beta}\varphi(V_C) \times \exp\left(-\frac{\lambda_\beta}{w}V_0\right)\left[\exp\left(\frac{\lambda_\beta}{w}V_C\right) - 1\right].$$

The integrated flux of lithium $\tilde{\nu}_e$ from the reservoir is

$$\begin{aligned} &N_r(t) \\ &= [\lambda_{n,\gamma} N_7^0 t \varphi(V_C)\varphi(V_r)\exp(-\lambda_\beta t_d)]/[\lambda_\beta t_p \varphi(V_0)], \end{aligned} \tag{4}$$

where V_r is the volume of the pumped reservoir, and t_d is the time of lithium delivery from the converter to the pumped reservoir. The construction of this facility operating in the dynamical mode meets serious problems associated with the need for temperature-regime maintenance (t_{melt}(Li) =180.5°C) and a large mass of highly pure lithium. For a converter layer of thickness L_C = 150 cm, 11.9 t of ^{7}Li with a purity a P_7 = 99.99% are required for reaching the efficiency of κ = 0.077. In order to implement a dynamical mode, we need amounts of ^{7}Li greater by a factor of 2 to 4 [8].

For a facility operating in a dynamical mode, a heavy-water solution of lithium hydroxide LiOD is a promising substance (with high a moderating power $\bar{\xi}\bar{\Sigma}_S$ and very small absorption cross sections) [9]. At a LiOD mass concentration of 5.66%, the efficiency κ of such converters is about 0.10 for a layer thickness of L_C = 100 cm and about 0.108 for L_C = 150 cm. In order to achieve κ = 0.077 at a concentration of 9.46%, it is necessary to have 300 times smaller amounts of ^{7}Li than for a converter filled only with lithium. For the total spectrum hardness at the neutrino-detector position (at the distance S from the center of the reservoir—see Fig. 3) to be maximal, we must ensure as many β^- decays in the reservoir as possible. This can be achieved by increasing the circulation rate w. Figure 4 shows the dynamics of the behavior of the total hardness and cross sections for the channels of the $(\tilde{\nu}_e, d)$ reaction versus the flow rate for detectors positioned at the distances of S =2.5–6.0 m.

Now, it is possible to ensure a very high flow rate w and linear speed V of motion in the channel. These serious technical problems can be successfully resolved, for example, with the aid of the ATR reactor (Idaho, USA) having the flow rate of the water coolant in the range 170–200 m^3/min, the GHFR reactor (Grenoble, France) with a linear speed of the D_2O coolant about 15.5 m/s, and the SRHFD reactor (Savannah River, USA) with the flow rate of the D_2O coolant equal to 5.65 m^3/s at a linear speed of 19.8 m/s.

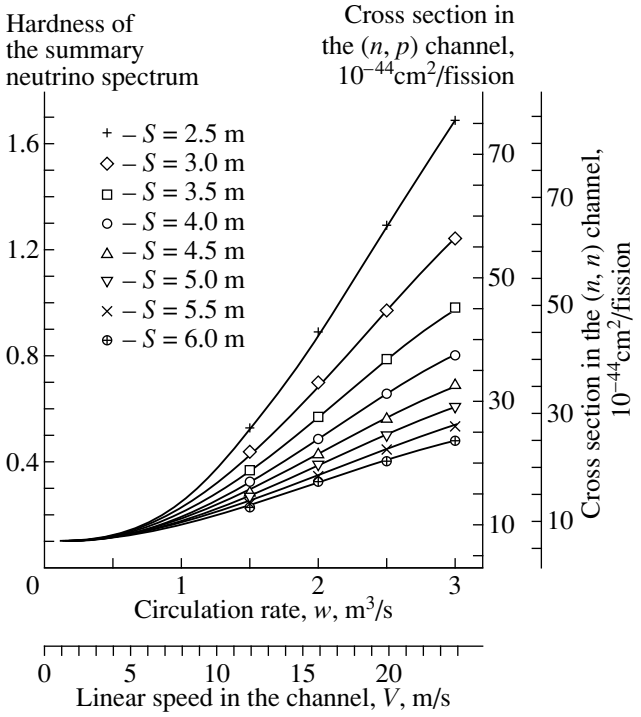

Fig. 4. Hardness H of the total $\tilde{\nu}_e$ fluxes and cross sections for the ($\tilde{\nu}_e$, d) interactions in the (n, p) and (n, n) channels as functions of the circulation rate w. Curves are presented for detectors positioned at distances S of 2.5 to 6.0 m from the reservoir center and at the fixed length of delivery channel (L = 17.90 m) corresponding to the delivery time of t_p = 1 s in the case of the flow rate of w = 2.25 m^3/s. The construction of this facility requires 22.0 m^3 of a 5.66% heavy-water solution of LiOD (412.8 kg of ^{7}Li isotope with purity P_7 = 99.99%). Linear speeds V correspond to flow rates w and are plotted along the lower axis.

The greatest effect is reached at small distances S from the reservoir, a maximum flow rate w, and larger distances L. In this way, it is possible to increase the cross sections in the (n, p) and (n, n) channels of the ($\tilde{\nu}_e$, d) reaction by more than one order of magnitude in relation to the cross sections at $H \approx 0.10$ in the static mode of converter operation. As compared to the cross sections for these reactions in the case of purely reactor $\tilde{\nu}_e$, the cross section in the neutral channel grows by a factor of a few tens, and the cross section in the charged channel grows by two orders of magnitude.

ACKNOWLEDGMENTS

We are indebted to Yu.G. Abov, A.A. Borovoĭ, L.A. Mikaélian, and Yu.V. Gaponov for stimulating discussions and their interest in this study.

REFERENCES

1. Yu. S. Lyutostansky and V. I. Lyashuk, Nucl. Sci. Eng. **117**, 77 (1994).
2. L. A. Mikaelian, P. E. Spivak, and V. G. Tsinoev, Nucl. Phys. **70**, 574 (1965).
3. S. M. Feinberg and Y. Y. Shevelev, in *Proceedings of the International Conference on Peaceful Uses of Atomic Energy, 1964* (United Nations, New York, 1964), Vol. 7, p. 455.
4. Yu. S. Lyutostansky and V. I. Lyashuk, in *Proceedings of the Interenational Conference on Neutron Physics, Kiev, 1987* (Atominform, Moscow, 1988), Vol. 4, p. 182.
5. L. A. Mikaelian and S. V. Tolokonnikov, Yad. Fiz. **50**, 111 (1989) [Sov. J. Nucl. Phys. **50**, 70 (1989)].
6. B. E. Lukhminsky *et al.*, Vopr. At. Nauki Tekh., Ser. Fiz. Reaktorov **2**, 23 (1989).
7. A. N. Yerikalov *et al.*, *Physics and Technology of Reactors* (LINP, Leningrad, 1986), p. 31; D. E. Bartine and J. W. Cable, DOE/NBM-4007547, ORNL (1984).
8. Yu. S. Lyutostansky and V. I. Lyashuk, Preprint No. ITEP-38, ITEP (Institute of Theoretical and Experimental Physics, Moscow, 1997).
9. Yu. S. Lyutostansky and V. I. Lyashuk, At. Énerg. **69**, 120 (1990) [Sov. J. At. Energ. **69**, 696 (1991)].

Physics of Atomic Nuclei, Vol. 63, No. 7, 2000, pp. 1292–1296. From Yadernaya Fizika, Vol. 63, No. 7, 2000, pp. 1365–1369.

EXPERIMENTAL RESULTS, METHODS, AND FACILITIES

Precise Measurement of ^{14}C Beta Spectrum by Using a Wall-less Proportional Counter*

V. V. Kuzminov[1)] and N. Ja. Osetrova

Joint Institute for Nuclear Research, Dubna, Moscow oblast, 141980 Russia

Abstract—The technique and results of a precise measurement of the ^{14}C beta spectrum in the energy range 10–160 keV by using a wall-less proportional counter are presented. The results of analysis and the inclusion of possible factors that distort the spectrum in the calculation of the detector response function are reported. Considerable deviations from the distribution expected for an allowed transition are found. © *2000 MAIK "Nauka/Interperiodica".*

1. INTRODUCTION

The beta decay of ^{14}C into ^{14}N is an allowed ground-state-to-ground-state ($0^+ \longrightarrow 1^+$) transition according to the Gamow–Teller rules with the endpoint energy of E_0 = 156 keV and a half-life of 5730 yr. The Gamow–Teller matrix element is anomalously small ($\langle \mathrm{GT} \rangle \approx 2 \times 10^{-3}$). The observed comparative half-life $\log(f_t)$ = 9.04 exceeds the average value for a pure allowed transition by a factor of about 4 and suggests empirical classification among second-forbidden transitions. The beta decay of ^{14}C was investigated by many groups, but some unsatisfactory features remain. Over almost 50 years, there have been discussions on possible deviations in the shape of the ^{14}C beta spectrum from that which is expected for a pure allowed transition. The beta energy spectrum with a massless neutrino can be written as [1]

$$\frac{dN(E)}{dE} = \frac{1}{2\pi^3}\xi C(E)F(Z,E)pE(E_0 - E)^2, \qquad (1)$$

where E and p are the electron energy and momentum; E_0 is the total decay energy; the Fermi function $F(Z, E)$ takes into account the final-state interaction between the electron and the daughter nucleus; ξ is the energy-independent part of $\langle \mathrm{GT} \rangle$; and $C(E)$ is the spectral-shape factor, which contains deviations from the allowed shape. This is the energy-dependent part of spectrum. It was shown in [2] that, in a typical allowed Gamow–Teller transition, this shape factor is dominated by the contributions from the GT-axial-matrix element and its interference with the weak-magnetism vector matrix element:

$$C(E) \cong 1 + \frac{4}{3M}\frac{\langle \mathrm{WM} \rangle}{\langle \mathrm{GT} \rangle}\left(E - \frac{E_0}{2} - \frac{m_e^2}{E}\right). \qquad (2)$$

Here, $\langle \mathrm{GT} \rangle$ and $\langle \mathrm{WM} \rangle$ are the GT and WM matrix elements, m_e is the electron mass, and M is mass of the nucleus. Assuming the conservation of vector currents (CVC) and charge independence of nuclear interactions ($\langle \mathrm{WM} \rangle = \langle M1 \rangle$), one can deduce the WM matrix element from the strength of the analogous electromagnetic $M1$ transition [3]:

$$\Gamma_{M1} = \frac{1}{6}\alpha E_\gamma \frac{\langle M1 \rangle^2}{M^2}. \qquad (3)$$

The GT matrix element can be deduced from the beta-decay half-life. In the case of ^{14}C, the matrix element is anomalously small, and the approximation of (2) that the shape factor is dominated by the interference of $\langle \mathrm{GT} \rangle$ with $\langle \mathrm{WM} \rangle$ may be violated. Behrens *et al.* [4] presented the complete expressions for the shape factor, allowing one to obtain a numerical result if one knows the necessary matrix elements or, equivalently, the wave functions,

$$C(E) = 1 + aE + \mu_1\gamma_1 b/E + cE^2. \qquad (4)$$

Here, $\gamma_1 = [1 + (\alpha Z)^2]^{1/2}$, where α is the fine-structure constant and Z is the charge number of the daughter nucleus; μ_1 is a special Coulomb function; and E stands for the total electron energy. The expressions for the coefficients a, b, and c can be found [4].

For a long time, the anomalously long lifetime of ^{14}C with respect to beta decay has been the subject of considerable interest. The beta spectrum of ^{14}C was studied carefully by many investigators, and, while there exists general agreement on the endpoint energy, the question of its shape still remains open. The studies of Cook *et al.* [5], Warshaw [6], and Angus *et al.* [7], along with the results of Mize and Zaffarano [8], show a deviation from the straight line of Fermi plot. In contradiction to the above results, Feldman and Wu [9] and Wu and Schwarzschild [10] have presented experimental evidence that the Kurie plot is straight to 25 keV. Moljk and Curran [11] showed that experimental data

* This article was submitted by the authors in English.

[1)] Institute for Nuclear Research, Russian Academy of Sciences, pr. Shestidesyatiletiya Oktyabrya 7a, Moscow, 117312 Russia.

1063-7788/00/6307-1292$20.00

were found to follow the theoretical shape for the allowed transition to within 1% at energies above about 3 keV. Rose *et al.* [12] found that the f_t value and other mass-14 β- and γ-ray data were consistently explained by the inclusion of a tensor component in the effective interaction. By calling attention to second-order correction terms, Zweifel [13] hoped to show that the concave shape observed by Mize [8] is consistent with beta-decay theory.

The accidental cancellation in the Gamow–Teller matrix element provides the possibility that higher order corrections to allowed beta-decay processes may become significant and may cause a nonstatistical shape of the ^{14}C beta spectrum. Garcia and Brown [3] proposed shell-model wave functions to calculate the matrix elements and the spectral-shape factor. The main conclusion is that, with respect to the magnetic matrix element, one should not expect very large charge-symmetry-breaking effects in the A = 14 system. They showed that the assumption that the axial and vector $\langle GT \rangle$ matrix elements are equal, as was previously done by Genz *et al.* [14], can lead to a very large charge-symmetry-breaking effect on the magnetic matrix element. The results of their calculation are in good agreement with the theoretical prediction of Calaprice [2] and with the experimental result of Weitfeldt *et al.* [15]. But the theoretical prediction of Genz for the values of the spectral-shape factor is in good agreement with the Commins prediction [16] and with the experimental results of Sur *et al.* [17] and Alimonti *et al.* [18]. Moreover, the theoretical prediction of Genz for the values of the spectral-shape factor is in good agreement with experimental studies of ^{14}O β^+ decay by Sidhu and Gerhart [19], of ^{20}F β^- decay [20], and β decays in the A = 12 systems (^{12}B–^{12}N) and in the A = 24 systems (^{24}Na–^{24}Al) [4]. The experimental result obtained by Sonntag *et al.* [21] with the aid of proportional counters is in strong disagreement with all theoretical predictions. The experimental results and various theoretical predictions for different interaction mechanisms and the amplitudes of the shell-model wave functions are presented in Table 1, where Δ is the absolute difference in fitting data for the kinetic energy region E_k = 0–156 keV.

One observes a considerable distinction between the values of the spectral factor $C(E)$, which we want to address in this study. In particular, we hope that our result could be useful for experiments with detectors employing large amounts of liquid scintillator. These detectors will be used in forthcoming experiments that will seek rare events with low energy deposition. These experiments include the spectroscopy of solar neutrinos, searches for a neutrino moment, and searches for nonbaryonic dark matter. The feasibility of these experiments depends on a low-background counting rate at energies below a few hundred keV. Since organic liquid scintillators are predominantly composed of carbon, the intrinsic concentration of the radioisotope ^{14}C can constitute the main background at low energies and, hence, can restrict the sensitivity of these experiments.

Table 1. Experimental results and theoretical predictions for the shape factor of the ^{14}C spectrum

References	Detector	Searching method $C(E)$, (E in MeV)	Δ, %
		Experimental results	
[5]	Magnetic spectrometer	Kurie plot	≈30
[7]	Proportional counter	Kurie plot	>30
[6]	Magnetic spectrometer	Kurie plot	≈25
[8]	Proportional counter	Kurie plot	>25
[21]	Proportional counter	$C(E) = 1 - 4.67E + 3/E + 2E^2$	≈65
[17]	^{14}C-doped germanium detector	$C(E) = 1 + \beta(E_0 - E)$ $\beta = 1.1 \pm 0.05$ MeV^{-1}	17.16 ± 0.78
[15]		$C(E) = 1 + aE$ $a = -0.45 \pm 0.04$ MeV^{-1}	7.02 ± 0.6
[18]	BOREXINO	$C(E) = 1 + aE$ $a < -0.72$ MeV^{-1}	>11.2
		Theoretical predictions	
[13]		Second-order correction terms	~25
[2]		$C(E) = 1 + aE$ $a = -0.38$ MeV^{-1}	~6
[16]		$C(E) = 1 + \beta(E_0 - E)$ $\beta \approx 1.2$ MeV^{-1}	≈18.7
[14]		$C(E) = 1 + aE$ $a = -1.179$ MeV^{-1}	≈18
[3]		$C(E) = 1 + aE$ $a = -0.37 \pm 0.04$ MeV^{-1}	≈6

2. EXPERIMENTAL PROCEDURE

We have studied the beta spectrum of ^{14}C using a wall-less proportional counter filled with a gaseous mixture of xenon and 0.05% (CO_2 + $^{14}CO_2$). The cross section of the detector is shown in Fig. 1. The central main counter (CMC) is surrounded by a near-wall guard ring counter (GRC). The anticoincidence mode of the central counter and guard allows one to eliminate beta-spectrum distortions associated with wall effects, since the crossing of the border between the counters by an electron gives a signal in both detectors. This mode also ensures a suppression of the background from the charged cosmic particles and electrons produced in the wall of the counter. The counter has the following technical characteristics: the inner diameter of the housing is 59 mm, while the diameters of the guard-counter anode grid and inner cathode grid are 51

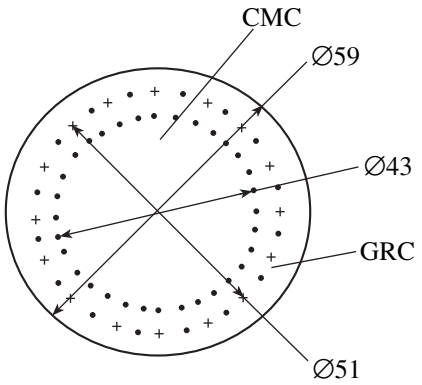

Fig. 1. Cross section of the counter; the central main counter and the guard ring counter are connected in the anticoincidence mode.

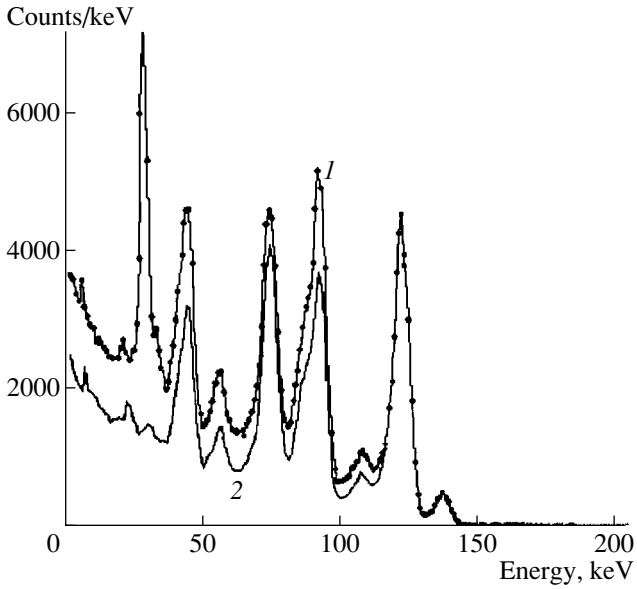

Fig. 2. Spectra of pulses derived from the central main counter and initiated by a ^{57}Co γ-ray source when the anticoincidence mode is disabled (*1*) and enabled (*2*).

and 43 mm, respectively. The grids of the central-counter anode and of the cathodes are made from a Nichrome wire 0.024 and 0.050 mm in diameter, respectively. The anode of the central counter is made from a gold-plated tungsten wire 0.010 mm in diameter manufactured by the Fine Wire Company (US) and has an average length of 280 mm. The total volume of the counter is 1083 cm^3, the volumes of the central counter and of the guard ring counter being 465 and 300 cm^3, respectively. The output insulators were adapted from automobile spark plugs. The insulator thickness was kept as small as possible in order to improve the degassing conditions during the vacuum conditioning of the counter and to stabilize the performance characteristics of the detector during measurements. The voltage applied to the CMC and GRC anodes is 2133 and 2370 V, respectively. The gas-amplification coefficients for the CMC and the GRC are 180 and 210, respectively. The operating characteristics and stability of the detector were investigated in the xenon–pressure range P = 5–15 atm. The pressure of P = 5 atm was chosen for work because of a comparatively good detection efficiency for electrons from the ^{14}C β decay and a sufficiently high energy resolution. An AI 1024-95 multichannel analyzer with a channel width of 0.2 keV (so that the 200-keV range covered 1000 channels) was used in the experiment. To suppress the background from natural radioactivity, the counter was enclosed in a lead shield 10 cm thick.

The data in Fig. 2 show the performance of the central counter (CC) connected in the anticoincidence mode to the GRC. The spectra of the CC pulses initiated by a collimated ^{57}Co γ-ray source (for Xe, P = 5 atm) are shown in Fig. 2. The upper spectrum (*1*) was obtained without enabling the anticoincidence mode, and the lower one (*2*) was measured in the anticoincidence mode. The spectrum represented by curve *1* includes the lines at 136.3 (^{57}Co), 122.0 (^{57}Co), 106.5 [136.3–29.8(K_αXe)], 92.2 (122.0–29.8), 75.0 (K_αPb), 57.5 ($K_{\beta 2}$Pb–K_αXe), 45.2 (K_αPb–K_αXe), and 29.8 keV (K_αXe). The average background-counting rate with the anticoincidence mode on and off was 0.57 and 2.66 s^{-1}, respectively. The 29.8-keV line is virtually completely suppressed in the spectrum obtained in the anticoincidence mode. The technique of a precise determination of the ^{14}C beta spectrum in the energy region 10–160 keV by using this proportional counter was described in detail elsewhere [22].

3. EXPERIMENTAL DATA

The experimental beta spectrum of ^{14}C with an average counting rate of 350 s^{-1} was measured for 602 h and is shown in Fig. 3. This spectrum was obtained by summing the data acquired over 24-h runs. The sum included only the runs where a shift of the 122.0-keV line from the 610th channel was not greater than ±2 channels. The calibration was checked after each run. There is a total of about 8×10^8 events of ^{14}C beta decay in the energy range 1–200 keV. The statistical accuracy is 0.03% at E = 30 keV and 0.17% at E = 140 keV (in the region near the endpoint energy).

Prior to comparing the experimental data with the theoretical spectrum, it is necessary to remove, from the experimental data, the components associated with nonideality of the detector and the recording apparatus. This procedure involves calculating the detector response function. The main distortion factors are the following: (i) the random coincidence of pulses in the CMC [two-pulse pileups (10.347%) (Fig. 3) and three-pulse pileups (1.145%) (Fig. 4)]; (ii) the random coincidence of CMC pulses with AC operating pulses (0.729%) [Fig. 4 (*2*)]; (iii) the background (0.049%) [Fig. 4 (*3*)]; (iv) the dependence of gas amplification on

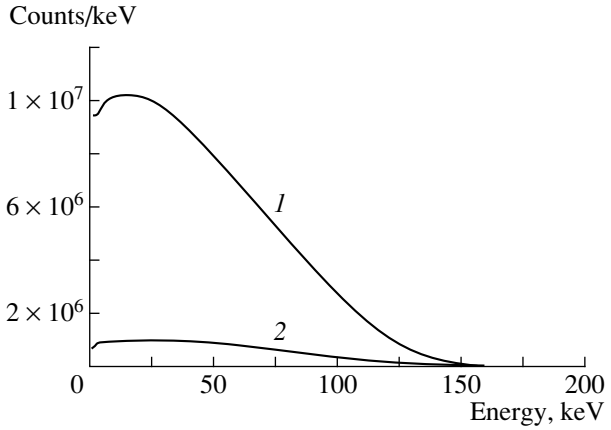

Fig. 3. ^{14}C experimental spectrum for the acquisition time of 602 h (*1*) and spectrum of two-pulse pileups (10.347%) (*2*).

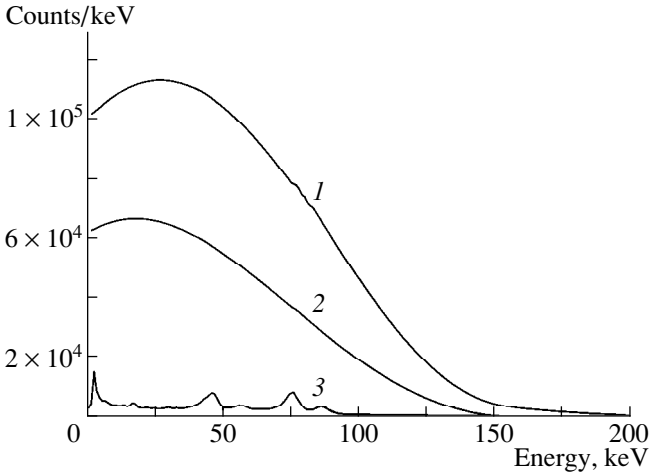

Fig. 4. Spectra of three-pulse pileups (1.145%) (*1*), of the random coincidence of CMC pulses and AC operating pulses (0.729%) (*2*), and of the background (0.049%) (*3*).

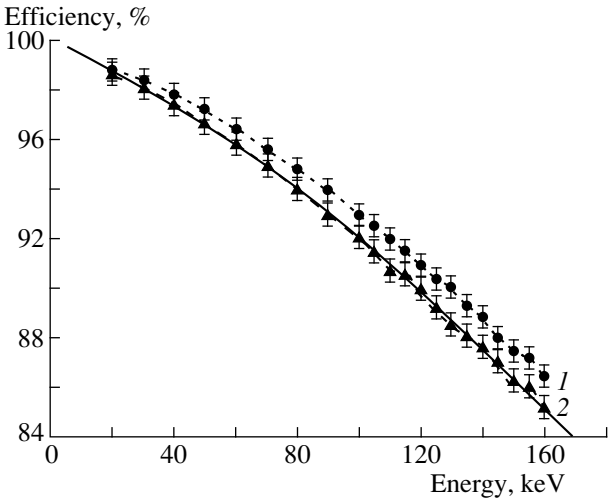

Fig. 5. Efficiencies of electron-energy detection for two shapes of the (*1*) circular and (*2*) curvilinear boundary between the CMC and the GRC.

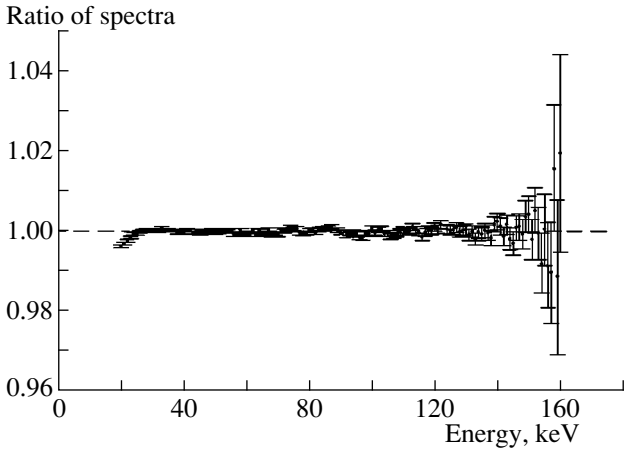

Fig. 6. Ratio of the experimental spectrum free from distortions to the theoretical amplitude spectrum after the introduction of the spectral-shape factor $C(E) = 1 + \beta(E_0 - E)$.

$M/\overline{M}$ and the distribution of the energy resolution R along the anode wire; (v) end effects associated with the reduction of the electric-field strength in the vicinity of the anode wire as the result of the influence of the surface charge on the end insulators; and (vi) the reduction of the detection efficiency for electrons from the ^{14}C beta decay because of the electric-boundary distortion between the CMC and the GRC due to the effect of the anode and cathode wires on each other.

With exception of the background, all distortion factors were taken into account in the calculation of the amplitude spectrum by using the theoretical spectrum for the allowed beta transition. The theoretical spectrum was calculated via a Monte Carlo simulation of electron trajectories on the basis of the GEANT code [23]. The statistical accuracy of the calculated spectrum is 0.12% (0.7×10^6 events/keV). The energy release from electrons was rescaled according to the distributions of the gas-amplification coefficients and the energy resolution of the detector and the boundary distortion between the CMC and the GRC. Our calculation of the boundary distortion was based on the method proposed in [24]. The real boundary between the CMC and the GRC is a curvilinear line with the maximal deflection of 1.5 mm inside the central counter. A comparison of the electron-detection efficiencies for two shapes (circular and curvilinear) of the boundary is illustrated in Fig. 5.

The theoretical amplitude spectrum of the ^{14}C beta decay for the allowed transition was compared with the experimental spectrum free from distortions. The ratio of the spectra normalized in the region of the endpoint

Table 2. Fit results for ^{14}C

ΔE, keV	χ^2/n
20–160	459.308/140 = 3.2808
30–160	159.445/130 = 1.2265
70–160	90.351/90 = 1.0039
95–145	49.975/50 = 0.9995
70–145	83.268/75 = 1.1102
95–160	60.274/65 = 0.9273

energy is a linear function of energy. The deviation is 10% for the energy of 70 keV and 17% for 20 keV. We have thoroughly analyzed the measurement technique and failed to identify any additional mechanism of distortion apart from those mentioned above. Therefore, we have to assume that the shape of the experimental beta spectrum does not correspond to the shape of the theoretical spectrum for the allowed transition. The observed discrepancy can be eliminated by introducing the spectral-shape factor in the form

$$C(E) = 1 + \beta(E_0 - E). \quad (5)$$

After that, the experimental data were compared with the theoretical amplitude spectrum multiplied by the shape factor. In doing this, we relied on a least squares fitting procedure in which the overall normalization factor A of the spectrum, the coefficient β, and the endpoint energy E_0 were allowed to vary simultaneously. The best fit was achieved with $\beta = (1.24 \pm 0.04) \times 10^{-3}$ keV^{-1} and $E_0 = 156.27 \pm 0.03(\text{stat.}) \pm 0.14(\text{syst.})$ keV. The result of the analysis is presented in Fig. 6 and in Table 2.

Our examination of the shape of the ^{14}C beta spectrum yielded results that are consistent with the theoretical predictions of Genz [14] and Commins [16], but which contradict the predictions of Calaprice [2] and Garcia [3]. The present result for the endpoint energy agrees with the results of the previous measurements of beta endpoint energy.

REFERENCES

1. M. Morita, *Beta Decay and Muon Capture* (Benjamin, Reading, 1973), p. 33.
2. F. P. Calaprice and B. R. Holstein, Nucl. Phys. A **273**, 301 (1976).
3. A. García and B. A. Brown, Phys. Rev. C **52**, 3416 (1995).
4. H. Behrens, H. Genz, M. Conze, *et al.*, Ann. Phys. (N.Y.) **115**, 276 (1978).
5. C. S. Cook, L. M. Langer, and H. C. Price, Phys. Rev. **74**, 548 (1948).
6. S. D. Warshaw, Phys. Rev. **80**, 111 (1950).
7. J. Angus, A. L. Cockroft, and S. C. Curran, Philos. Mag. **40**, 552 (1949).
8. J. P. Mize and D. J. Zaffarano, Phys. Rev. **91**, 210 (1953).
9. L. Feldman and C. S. Wu, Phys. Rev. **75**, 1286 (1949).
10. C. S. Wu and M. Schwarzschild, Phys. Rev. **91**, 483 (1953).
11. A. Moljk and S. C. Curran, Phys. Rev. **96**, 395 (1954).
12. H. J. Rose, O. Hausser, and E. K. Warburton, Rev. Mod. Phys. **40**, 591 (1968).
13. P. F. Zweifel, Phys. Rev. **95**, 112 (1954).
14. H. Genz, G. Kuhner, A. Richter, and H. Behrens, Z. Phys. A **341**, 9 (1991).
15. F. E. Weitfeldt, E. B. Norman, Y. D. Chan, *et al.*, Phys. Rev. C **52**, 1028 (1995).
16. E. Commins, private communication.
17. B. Sur, E. B. Norman, K. T. Lesko, *et al.*, Phys. Rev. Lett. **66**, 2444 (1991).
18. G. Alimonti, G. Angloher, C. Arpesell, *et al.*, Phys. Lett. B **422**, 349 (1998).
19. G. S. Sidhu and J. B. Gerhart, Phys. Rev. **148**, 1024 (1966).
20. H. Genz, A. Richter, B. M. Schmitz, and H. Behrens, Nucl. Phys. A **267**, 13 (1976).
21. Ch. Sonntag, H. Rebel, B. Ribbat, *et al.*, Lett. Nuovo Cimento **4**, 717 (1970).
22. V. V. Kuzminov, N. Ya. Osetrova, and A. M. Shalagin, Prib. Tekh. Éksp. **39**, 654 (1996) [Instrum. Exp. Tech. **5**, 38 (1996)].
23. GEANT3, *Detector Description and Simulation Tool* (CERN, Geneva, 1994).
24. J. Szarka, P. Povinec, and V. Hlinka, Nucl. Instrum. Methods **164**, 463 (1979).

Physics of Atomic Nuclei, Vol. 63, No. 7, 2000, pp. 1297–1300. From Yadernaya Fizika, Vol. 63, No. 7, 2000, pp. 1370–1373.

EXPERIMENTAL RESULTS, METHODS, AND FACILITIES

Germanium Detector with an Internal Amplification for Investigating Rare Processes*

A. S. Starostin ** **and A. G. Beda**

Institute of Theoretical and Experimental Physics, Bol'shaya Cheremushkinskaya ul. 25, Moscow, 117259 Russia

Abstract—A device of a new type—a germanium detector with an internal amplification—is proposed. Having the effective threshold of about 10 eV, the detector opens up a fresh opportunity for investigating dark matter, measuring the neutrino magnetic moment, exploring coherent neutrino scattering off nuclei, and studying the solar-neutrino problem. The design of the germanium detector with an internal amplification and prospects for its use are described. © *2000 MAIK "Nauka/Interperiodica".*

1. INTRODUCTION

Detectors with a low background and a low energy threshold are required for investigating rare processes that involve low-energy neutrinos and weakly interacting particles. These detectors can be effectively used to seek dark matter, to measure the neutrino magnetic moment and coherent neutrino scattering off nuclei, and to investigate the solar-neutrino problem. For these purposes, one needs a low-background detector with a mass of a few kg and with a threshold energy less than 1000 eV. Cryogenic and germanium detectors comply partly with these requirements. A drawback of cryogenic detectors is the complexity of their production and use. A drawback of germanium detectors is a rather high threshold of 2–10-keV, which is due to a leakage current and electronic and microphonic noises. It would be very attractive to provide an effective decrease in the detector threshold by an internal proportional amplification of the signal. An internal proportional amplification in semiconductor detectors (SD) is realized now in silicon avalanche photodiodes (APD) [1, 2], where a gain of about 10^2–10^4 is achieved by an avalanche multiplication of electrons at the electric field of (5–6) $\times$ 10^5 V/cm in a narrow *p–n* junction with a sensitive volume of a few mm^3. Below, we demonstrate the possibility of implementing a germanium detector with internal amplification (GDA) and present its design.

2. PRINCIPLES OF A GDA AND ITS DESIGN

There are conditions for an internal proportional amplification of electrons in semiconductor detectors as well as in a gas proportional counter (PC) or a multiwire proportional chamber (MWPC). It is well known that, in an APD, the critical electric field E_{cr}, which provides the multiplication of electrons at room temperature, is equal to (5–6) $\times$ 10^5 V/cm. The field E_{cr} for germanium at liquid-nitrogen temperature can be found from the dependence of the electron drift velocity on the electric field and on the energy of the production of electron–hole pairs and photons [3]. For germanium at 77 K, E_{cr} derived in this way is 9×10^4 V/cm. In an APD and a gas PC, the critical electric field is produced in a different way. In the first case, E_{cr} is achieved by a high concentration of impurities in a narrow junction. As a result, the sensitive volume of the APD is about a few mm^3. In the gas PC, E_{cr} can be achieved by a special configuration of the electric field due to a large difference between the sizes of the cathode and the anode. In high-purity germanium (HPGe) with a sensitive volume of about 100 cm^3, E_{cr} can be obtained in the same way. The electric field in a cylindrical gas PC is

$$E(r) = \frac{V}{r\ln(R_2/R_1)}, \quad (1)$$

where V is the applied voltage; R_1 and R_2 are the radii of the cathode and the anode, respectively; and r is the distance from the anode. One can see from (1) that, at $V = 10^3$ V, $R_1 = 0.001$ cm, and $R_2 = 1$ cm, $E(r)$ is about 10^5 V/cm near the anode.

In contrast to the case of a gas PC, the electric field in a coaxial HPGe detector is determined not only by V, R_1, and R_2, but also by the concentration of donor (n type) or acceptor (p type) impurities. The magnitude of the volume charge in the sensitive volume of the crystal depends on these impurities. The electric field in an HPGe coaxial detector with regards to the impurities is [4]

$$E(r) = \frac{Ne}{2\epsilon}r - \frac{[V + (Ne/4\epsilon)(R_2^2 - R_1^2)]}{r\ln(R_2/R_1)}, \quad (2)$$

where N is the impurity concentration, e is the electron charge, and ϵ is the dielectric constant of the germanium. The electric field (2) can be expressed in terms of the depletion voltage V_d, which is a minimum voltage necessary for neutralizing the volume charge and to provide the sensitive region in the entire crystal vol-

* This article was submitted by the authors in English.

** e-mail: starostin@vitep5.itep.ru

1063-7788/00/6307-1297$20.00

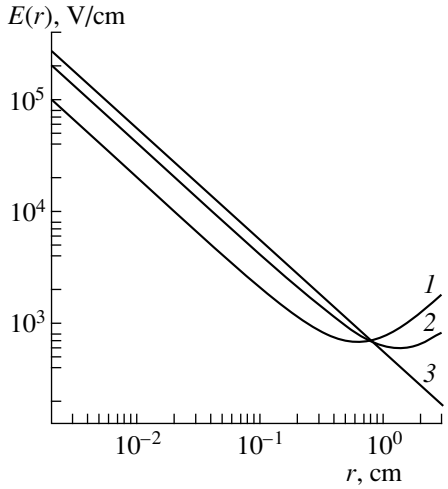

Fig. 1. Electric field as a function of r for an axial HPGe detector of the p type with $V = 4000$ V, $R_1 = 0.002$ cm, and $R_2 = 3.0$ cm for the impurity concentrations of $N = (1)\ 10^{10}$, $(2)\ 4 \times 10^9$, and $(3)\ 0$ (no volume charge) cm^{-3}.

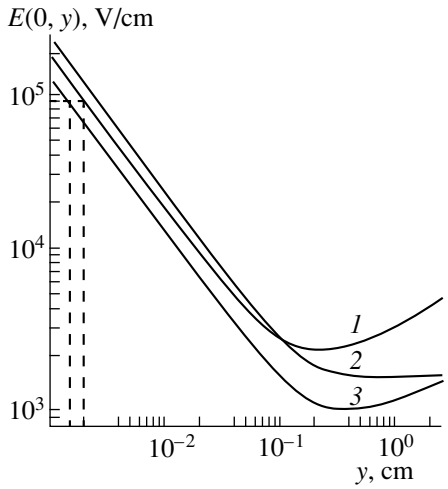

Fig. 2. Dependence $E(0, y)$ for a planar HPGe detector of the p type with $d = 20$ μm and various values of other parameters: $(1)\ N = 10^{10}$ cm^{-3}, $L = 1.5$ cm, and $s = 0.3$ cm; $(2)\ N = 0$ (no volume charge is present), $L = 2.0$ cm, and $s = 0.5$ cm; and $(3)\ N = 2 \times 10^9$ cm^{-3}, $L = 3.0$ cm, and $s = 0.5$ cm. For the options characterized by the parameter values in items (*1*) and (*3*), the length of the avalanche region is 10 and 5 μm, respectively.

ume. Under the assumption that $R_2 \gg R_1$, V_d for the coaxial detector is given by

$$V_d \approx -\frac{Nq}{4\epsilon}R_2^2. \tag{3}$$

Equation (2) can be recast into the final form

$$E(r) = -\frac{2V_d}{R_2^2}r - \frac{V - V_d}{r\ln(R_2/R_1)}. \tag{4}$$

The dependence of E on r is shown in Fig. 1 for a coaxial HPGe detector. The electric field near the anode reaches E_{cr}, which is required for the avalanche multiplication of electrons. The coaxial germanium detector with an internal amplification is more appropriate for low-background spectrometers, but the possibility of manufacturing the inner electrode of radius 20 μm is highly doubtful at present. Therefore, we consider a more realistic problem—a fabrication of a planar germanium detector with an internal amplification by using modern technology. A multistrip planar germanium detector is similar in design to an MWPC. The electric field in the MWPC has the form (one-dimensional case)

$$E(0, y) = \frac{\pi V}{s\left[\frac{\pi L}{s} - \ln\frac{\pi d}{s}\right]}\coth\frac{\pi y}{s}, \tag{5}$$

where V is the applied voltage, s is the wire spacing, d is the diameter of the wire, and L is the thickness of the planar detector. As in the case of a coaxial germanium detector, one should take into account the depletion voltage V_d for the multistrip germanium detector (MGD). For a planar germanium detector, $V_d = -\frac{Ne}{2\epsilon}L^2$. The electric field for the MGD has the form

$$E(0, y) = -\frac{2V_d}{L^2}y - \frac{\pi(V - V_d)}{s\left[\frac{\pi L}{s} - \ln\frac{\pi d}{s}\right]}\coth\frac{\pi y}{s}, \tag{6}$$

where d is the strip width. The dependence $E(0, y)$ for an MGD is shown in Fig. 2. In both cases considered, the electric field near the anode is sufficient for giving rise to an avalanche multiplication of electrons ($E > 10^5$ V/cm). The amplification factor can be estimated as $K = 2^{h/l}$; here, l is the free electron path for inelastic scattering, and h is the length of the avalanche region where $E > E_{cr}$. The free electron path in germanium at 77 K is 0.5 μm, and, for $L = 3$ cm, h is equal to 5 μm (Fig. 2); therefore, it is possible to achieve $K = 10^3$. If one does not need a high amplification factor, it is possible to decrease V or to increase the strip width s.

It is assumed to use a GDA for investigating rare processes; therefore, a spectrometer with a GDA must have a large mass of the detector. It can be manufactured from separate modules of weight about 0.7 kg each. One module includes a multistrip planar germanium detector constructed from HPGe (p type) with an impurity contamination less than 10^{10} cm^{-3} and a volume of $70 \times 70 \times 30$ mm^3 (Fig. 3). Twelve anode strips 20 μm wide and 65 mm long are manufactured by the photomask method [5]. The cathode area is 65×65 mm^2, and the fiducial volume is 130 cm^3. There are guard electrodes in the anode and cathode planes. The anode strips can be connected together; however, it is more convenient to pick up signals from separate strips to suppress the background Compton photons.

In order to manufacture a GDA, it is necessary to use germanium crystals with a uniform distribution of impurities to provide a uniform electric field near the anode. Second, it is important to provide a small depth and width of the junction layer under the strips, which allows the electric field near the strips to be determined by junction dimensions. The design of the GDA must provide stable cooling of the crystal since the critical electric field and the amplification factor depend on the free path of charge carriers, which in turn depends on temperature.

3. ENERGY RESOLUTION AND THRESHOLD OF GDA

The energy resolution of a semiconductor detector is given by

$$\Delta E = \sqrt{(\Delta E_{\text{int}})^2 + (\Delta E_{\text{el}})^2}, \quad (7)$$

where ΔE_{int} is a quantity that has the meaning of an intrinsic energy resolution of the detector and which is determined by statistical fluctuations in the number of charge carriers created in the detector sensitive volume, while ΔE_{el} is the energy resolution determined by associated electronics. In the case of a GDA, these two terms are

$$\Delta E_{\text{int}} = 2.34\sqrt{\varepsilon E(F + f)K^2}, \quad (8)$$

$$\Delta E_{\text{el}} = \frac{4.52\varepsilon}{e}\sqrt{\frac{0.6kT}{\tau S}C^2 + kT\tau\left[\frac{1}{R_\Sigma} + \frac{e}{2kT}(I_s + I_b f K^2)\right]}, \quad (9)$$

where ε is the energy required for creating one pair of charge carriers, E is the energy deposited in the detector, F is the Fano factor, f is the excess noise factor due to the fluctuation of the multiplication, K is the amplification factor, e is the electron charge, T is the absolute temperature of the resistors, C is the total capacitance at the input of the preamplifier, τ is the time constant of the RC circuits of the preamplifier, S is the steepness of the field-effect transistor, R_Σ is the resistance at the input of the preamplifier, I_s is the surface leakage current of the detector, and I_b is the bulk leakage current of the detector due to a thermal generation of charge carriers. According to the calculation for a GDA with $K > 10$, one must take into account, in the formula for ΔE_{el}, only the last term due to the bulk leakage current, and formula (7) for the GDA can be rewritten as

$$\Delta E \approx 2.36K\sqrt{\varepsilon E(F + f) + 10^4 I_b \tau f}, \quad (10)$$

where ε and E are in eV, I_b is in nA, and τ is in μs. The GDA energy threshold is determined by I_b, or, more precisely, by the last term in (10):

$$E_{\text{th}} \geq \sqrt{5.8 \times 10^4 I_b \tau f}. \quad (11)$$

Relative energy resolution $\Delta E/E$ versus energy

E, eV	50	200	400	600	800	1000	5000
$\Delta E/E$, %	57	25	17	13	11	10	4.3

One can estimate E_{th} for a microstrip planar HPGe detector with an internal amplification of volume 100 cm^3 as follows. At $N = 10^{10}$ cm^{-3}, $I_b = 0.01$ nA per strip, $\tau = 0.5$ μs, and $f = 0.5$, one has $E_{\text{th}} \geq 12$ eV. The dependence of the relative energy resolution $\Delta E/E$ on energy in the more interesting energy range 50–5000 eV for a GDA is shown in the table.

The internal amplification of the GDA somewhat degrades the performance, but this energy resolution of the GDA is adequate to the investigation of the above problems. It is interesting to note that a common planar HPGe detector of volume 100 cm^3 produced by Canberra (type GL3825R) has a relative energy resolution of about 8% at $E = 5900$ eV.

4. PROSPECTS FOR USING GDA

Presently, germanium detectors are in considerable use in low-background measurements for high purity of germanium crystals: their radioactive-impurity content does not exceed 10^{-13} g/g. If the internal amplification is realized in germanium detectors and if their threshold is lowered to a few eV, the possibility of using them will considerably increase.

In dark-matter experiments, the main effort is presently aimed at suppressing the background and at lowering the energy threshold. In searches for dark-matter

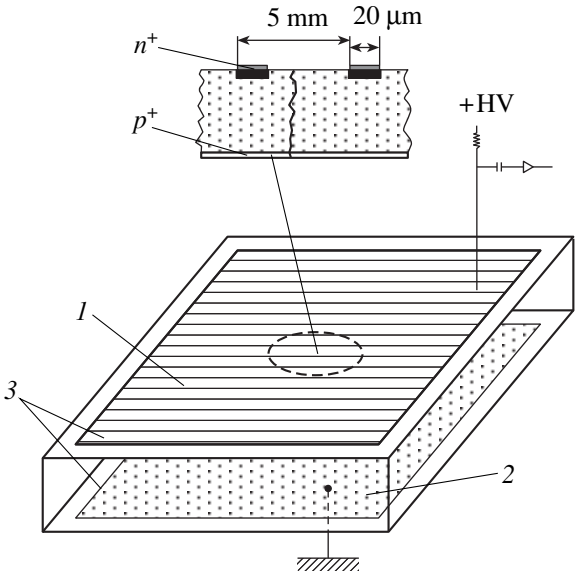

Fig. 3. Germanium detector with an internal amplification (schematic view): (*1*) anode strips, (*2*) cathode, and (*3*) guard electrodes. The scheme of n^+ and p^+ layers is shown in the upper part of the figure.

particles in the low-mass range, the CRESST collaboration is planning to use a cryogenic detector with four 250-g sapphire detectors having a threshold energy of 500 eV [6]. The use of several GDAs of mass 1 kg each with a threshold about 10 eV would be very effective in this investigations.

Nowadays, there are several projects devoted to measuring the neutrino magnetic moment (NMM). In this case, one needs a low-background and low-threshold detector again. In general, the threshold of the detectors aimed at searches for the neutrino magnetic moment is about a few hundred keV, but, in [7], the authors plan to use a low-background germanium spectrometer of mass 2 kg with a threshold of 4 keV to achieve the limit on the neutrino magnetic moment about $4 \times 10^{-11}\mu_B$ (μ_B is the Bohr magneton) within two years of reactor measurements. Now, there is a project that combines an artificial tritium antineutrino source of 40 MCi with a cryogenic silicon detector having a mass of 3 kg and a threshold of a few eV [8]. The goal of this project is to push the limit on the neutrino magnetic moment down to $3 \times 10^{-12}\mu_B$ within one year of measurements.

Detectors of the GDA type can open up the possibility of investigating coherent neutrino scattering by nuclei. This interaction is of great importance in interstellar processes; so far, it has not been observed in a laboratory because of very low kinetic-energy transfer to a nucleus. For the germanium nucleus and the reactor-antineutrino spectrum, the maximum kinetic recoil energy is about 2.5 keV, and only one third of the energy is imparted to the electron on ionization. If, in a reactor experiment, one uses a GDA with a threshold of 10 eV, it is possible to detect about 70 event/(kg d) at the antineutrino intensity of 2×10^{13} ν/cm^2 s due to weak interaction. The counting rate due to electromagnetic interaction (at $\mu_\nu = 3 \times 10^{-11}\mu_B$) will be about 0.15 event/(kg d). Thus, the measurement of coherent neutrino scattering with a GDA makes it possible (i) to refine our knowledge of the weak-interaction constants; (ii) to investigate neutrino oscillations in an alternative way; (iii) to set the more stringent limit on the NMM; and (iv) to measure more accurately the quenching factor for germanium at low energy transfer, which is of interest for dark-matter experiments.

The investigation of the solar-neutrino problem with a GDA can allow a simultaneous measurement of the whole neutrino spectrum, but one needs a large-mass detector in this case. It is believed that GDAs will find wide use in applied fields.

ACKNOWLEDGMENTS

We are grateful to V.S. Kaftanov for his participation in this work and to Yu. Kamishkov for his interest in this work and for enlightening discussions.

This work was supported by the ISTC grant no. 608.

REFERENCES

1. J. P. Pansart, Nucl. Instrum. Methods A **387**, 186 (1997).
2. R. Farrel, F. Olschner, K. Shah, and M. R. Squillante, Nucl. Instrum. Methods A **387**, 194 (1997).
3. G. Bertolini and A. Coche, *Semiconductor Detectors* (North-Holland, Amsterdam, 1968), p. 71; E. Sakrai, H. L. Malm, and I. L. Fovler, paper presented at the Gatlinburg Conference, 1967.
4. J. M. Marler and P. V. Hewka, IEEE Trans. Nucl. Sci. **NS-21**, 287 (1974).
5. D. Gutknecht, Nucl. Instrum. Methods A **288**, 13 (1990).
6. M. Buhler, L. Zerle, F. Probst, *et al.*, Nucl. Instrum. Methods A **370**, 237 (1996).
7. A. G. Beda, E. V. Demidova, A. S. Starostin, and M. B. Voloshin, Yad. Fiz. **61**, 72 (1998) [Phys. At. Nucl. **61**, 66 (1998)].
8. V. N. Trofimov, B. S. Neganov, and A. A. Yukhimchuk, Yad. Fiz. **61**, 1373 (1998) [Phys. At. Nucl. **61**, 1271 (1998)].

Physics of Atomic Nuclei, Vol. 63, No. 7, 2000, pp. 1301–1303. Fom Yadernaya Fizika, Vol. 63, No. 7, 2000, pp. 1374–1376.

EXPERIMENTAL RESULTS, METHODS, AND FACILITIES

Method for Background Reduction in an Experiment Devoted to WIMP Searches with a Liquid-Xenon (Liquid-Argon) Ionization Chamber*

B. M. Ovchinnikov and V. V. Parusov

Institute for Nuclear Research, Russian Academy of Sciences, pr. Shestidesyatiletiya Oktyabrya 7a, Moscow, 117312 Russia

Abstract—A method for detecting ultraviolet photons from Xe_2^* deexitation with an efficiency of nearly 100% is proposed. This method allows a reliable discrimination between Xe (Ar) recoil nuclei and background electrons. As a result, the β and γ background is almost completely suppressed. The neutron background can be reduced by water shielding and by selection of events involving only one recoil nucleus. The developed grid screen will remove the photon feedback. The small prototype TPC with a preliminary multiplication of ionization electrons in a proportional gap and a subsequent detection of the multiplied charges in the induction gap is constructed. The shape of an electron component of the proportional signal is obtained in this chamber for Penning mixtures. A chamber 636 mm long is now being prepared for WIMP searches. A background of about 10^{-5} event/(keV kg d) can be obtained in this experiment. © *2000 MAIK "Nauka/Interperiodica".*

The main problem in experiments aimed at directly detecting WIMPs is a reduction of the background, which is mainly caused by β and γ radiation from radioactive impurities in the detector and in environments. Liquid-xenon and liquid-argon detectors are the most promising for background suppression because, in liquid Ar and Xe, the shape of scintillation signals and the scintillation-to-ionization signal ratio are different for recoil nuclei and for background electrons. In order to suppress this background, it is necessary to detect these signals with a high efficiency. However, the detection of scintillation light with photomultipliers ensures only about a few percent efficiency.

We propose increasing the detection efficiency for ultraviolet photons from Xe and Ar scintillation by dissolving, in liquid Ar and Xe, photosensitive additions with an ionization potential less than the energy of such photons [1]. For example, the TMA has the ionization threshold equal to 6.6 eV in liquid Xe, the energies of ultraviolet photons being within the range 6.6–8.4 eV.

We consider liquid Xe with an addition of TMA at a concentration of 43 ppm. The mean free path with respect to photon absorption is 1 cm with TMA at this concentration [2]. The ranges of recoil nuclei from WIMP scattering in liquid Xe are equal to a few mg cm^{-2}; that is, their tracks are nearly pointlike.

Thus, the pointlike ionization track of a recoil nucleus is surrounded by a volumetric photoelectron cloud with a mean diameter of 2 cm. The primary ratio $\frac{N_{\text{exitons}}}{N_{\text{ion-pairs}}}$ is 0.2 for recoil nuclei and background electrons. Only a few percent of ionization electrons for a recoil nucleus in liquid Xe avoid recombination for E = 3 kV/cm; the rest of the electrons (more than 90%) recombine with the formation of Xe_2^*, which emits ultraviolet photons. As the result of these processes, a recoil nucleus with an energy of 20 keV at 3 kV/cm will produce about 14 free ionization electrons on its track and a cloud of about 242 free photoelectrons. For a recoil nucleus of energy 20 keV at 3 kV/cm, we therefore have the ratio

$$\left(\frac{N_{\text{phe}^-}}{N_{\text{ione}^-}}\right)_{\text{r.n.}} = \frac{242}{14} = 17.3.$$

For the sake of comparison, we take a background electron with an energy of 3.8 keV, which produces approximately the same total number of free electrons as a recoil nucleus of energy 20 keV at a field of 3 kV cm^{-1}. This electron gives about 173 free ionization electrons on the pointlike track and about 75 free photoelectrons distributed as a cloud with a mean diameter of 2 cm [3]. For the electron, we have the ratio

$$\left(\frac{N_{\text{phe}^-}}{N_{\text{ione}^-}}\right)_{\text{b.e.}} = \frac{75}{173} = 0.43.$$

Comparing the recoil nucleus and the background electron, we obtain

$$\left(\frac{N_{\text{phe}^-}}{N_{\text{ione}^-}}\right)_{\text{r.n.}} : \left(\frac{N_{\text{phe}^-}}{N_{\text{ione}^-}}\right)_{\text{b.e.}} = \frac{17.3}{0.43} = 40.$$

One can see that the probability for the imitation of a 20-keV recoil nucleus by a background electron is

* This article was submitted by the authors in English.

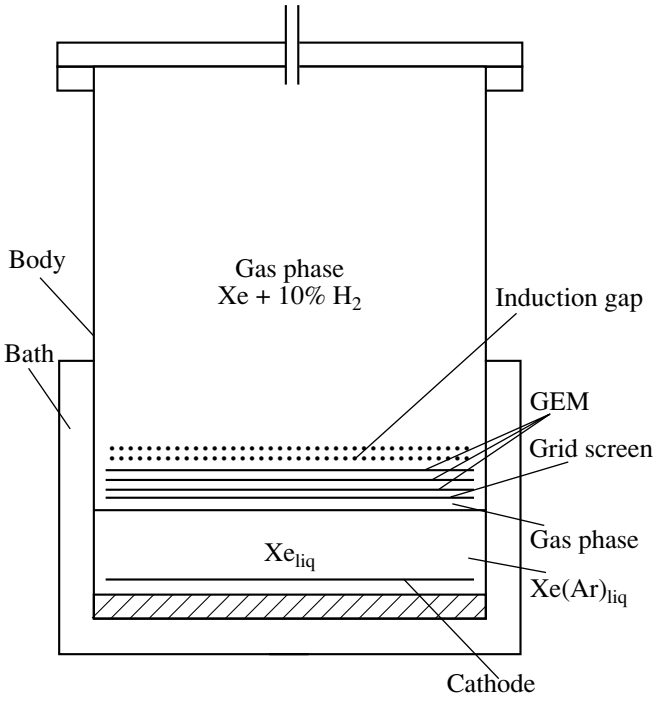

Fig. 1. Liquid Xe (Ar) two-phase ionization chamber.

very small. As a result, the β^- and γ background will be suppressed almost completely.

Fast neutrons produce the same recoil nucleus as a WIMP. In order to suppress this background, it is necessary to perform a deep-underground experiment with a water shielding of thickness about 2 m. While being moderated in Xe, a fast neutron strikes Xe nuclei a few hundred times. By selecting events featuring a single recoil nucleus, one will suppress the neutron background down to a level of about 10^{-5} event/(keV kg d). This will be a limit on the background in the experiment being discussed, because the β and γ background will be suppressed completely.

Chamber design. A Xe (Ar) two-phase chamber containing 30–70 l of liquid Xe (Ar) is under development for this experiment (Fig. 1). A layer of liquid Xe (Ar) above the cathode will have a thickness of 10–20 cm. The detecting electrodes will be placed in the gas phase above liquid Xe (Ar) and will contain a grid screen, three amplifying GEM grids, and an induction gap. Every GEM consists of a thin (~100 μm) polymer foil coated with metal on both sides and perforated to have a regular pattern of holes of about 100 μm in diameter with a pitch of about 200 μm. Three GEM grids will ensure a total amplification of about 10^5 for the detection of single electrons [4]. In the induction gap, we will detect the electron component of the proportional signal. The grid screen that we developed (Fig. 2) will remove the photon feedback. The transmission of the screen for ionization electrons is close to

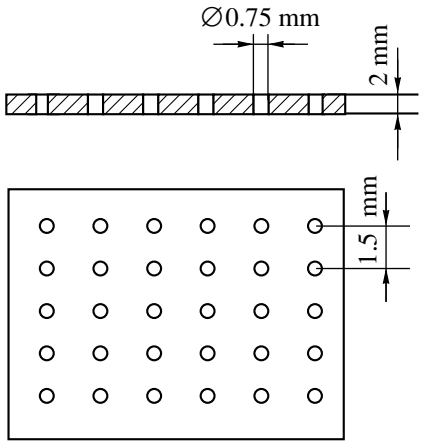

Fig. 2. Light screen.

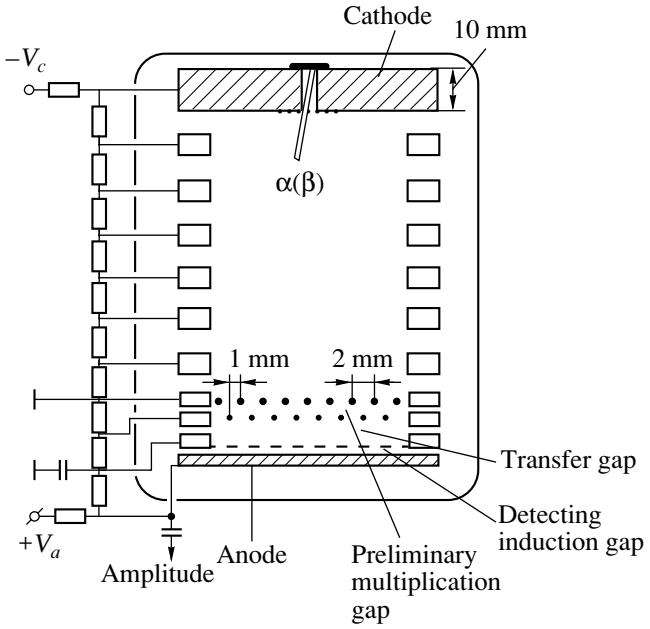

Fig. 3. Ionization chamber with a preliminary multiplication for electrons and an extraction of the electron component from the proportional signal.

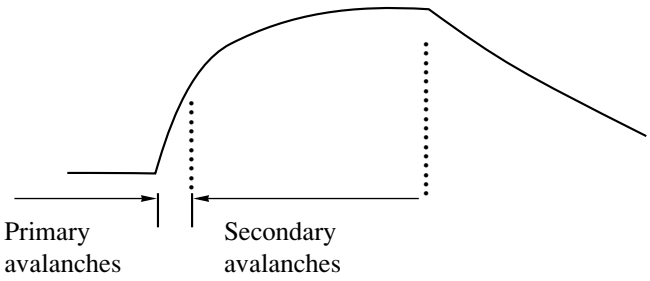

Fig. 4. Shape of the electron component of the proportional signal.

100%. The transmission of the screen for photons is equal to about 10^{-3}.

The spatial resolution of the detecting system must be about 1 mm along the *x*, *y*, and *z* axes in order to detect all photoelectrons and ionization bump separately.

In order to obtain a high resolution along the *z* axis, we have constructed a small prototype TPC with a preliminary multiplication for ionization electrons in a proportional gap and a subsequent detection of multiplied charges in the induction gap without multiplication (Fig. 3). The shape of the electron component of the proportional signal obtained in this chamber for Penning mixtures is shown in Fig. 4 [5]. This signal has a primary avalanche part and a secondary avalanche part. The tails of secondary avalanches have durations from about 10 to 100 μs for different mixtures. These tails will be removed by the differentiation of signals.

The background in the proposed experiment will be determined by neutrons and is expected to be about 10^{-5} event/(keV kg d).

REFERENCES

1. B. M. Ovchinnikov and V. V. Parusov, Preprint No. 0966/97, IYaI (Institute for Nuclear Research, Russian Academy of Sciences, Moscow, 1997).
2. S. Suzuki *et al.*, Nucl. Instrum. Methods A **245**, 78 (1986).
3. I. M. Obodovskiĭ and K. T. Ospanov, Prib. Tekh. Éksp. **1**, 55 (1995).
4. R. Bouclier *et al.*, Preprint No. CERN-PRE/96-177, CERN (Geneva, 1996).
5. B. M. Ovchinnikov and V. V. Parusov, Preprint No. 1008/99, IYaI (Institute for Nuclear Research, Russian Academy of Sciences, Moscow, 1999).